



Daya Bay Project
Technical Design Report (v2)
January 22, 2008



Daya Bay Collaboration

Beijing Normal University

Xinheng Guo, Naiyan Wang, Rong Wang

Brookhaven National Laboratory

Dana Beavis, Mary Bishai, Ralph L. Brown, Chellis Chasman, Milind Diwan, Jim Frank, Robert W. Hackenburg, Richard L. Hahn, Vladimir Issakov, David E. Jaffe, Steve Kettell, Kelvin Li, Laurence Littenberg, Nathaniel Tagg, Brett Viren, Zhe Wang, Lisa Whitehead, Yuping Williamson, Minfang Yeh, Kevin Zhang

California Institute of Technology

Dan Dwyer, Jianglai Liu, Christopher Mauger, Robert McKeown, Raymond H.M. Tsang

Charles University

Zdenek Dolezal, Rupert Leitner, Viktor Pec, Vit Vorobel

Chengdu University of Technology

Liangquan Ge, Haijing Jiang, Wanchang Lai, Yanchang Lin

China Guangdong Nuclear Power Holding Company

Jiliang Sun, Yixin Zhang

China Institute of Atomic Energy

Long Hou, Xichao Ruan, Zhaojun Wang, Biao Xin, Zuying Zhou

Chinese University of Hong Kong

Ming-Chung Chu, Joseph Hor, Kin Keung Kwan, Antony Luk, Jackie Wong

Dongguan University of Technology

Li Kang, Yi Li, Yue Song, Ning Wang, Donghe Xu, Lei Yang, Huaqiang Yuan

George Mason University

Phil Rubin

Illinois Institute of Technology

Brandon Seilhan, Alex Weiss, Christopher White, Qun Wu

Institute of High Energy Physics

Yuan An, Jinzhi Bai, Jun Cao, Jinfan Chang, Hesheng Chen, Mingjun Chen, Xiongxin Dai, Yayun Ding, Jinyu Fu, Mengyun Guan, Xiaolu Ji, Fei Li, Jin Li, Qiuju Li, Weidong Li, Xiaobo Li, Xiaonan Li, Jinchang Liu, Xuan Liu, Haoqi Lu, Weiguo Lu, Yusheng Lu, Xinhua Ma, Yuqian Ma, Xiangchen Meng, Huayi Sheng, Gongxin Sun, Xiao Tang, Xinchun Tian, Lijun Wang, Lingshu Wang, Lingyu Wang, Meng Wang, Ruiguang Wang, Wanliang Wang, Yifang Wang, Zheng Wang, Zhimin Wang, Liangjian Wen, Haisheng Xiang, Yuguang Xie, Zhizhong Xing, Jilei Xu, Xiongbo Yan, Changgen Yang, Mei Ye, Liang Zhan, Hongyu Zhang, Jiawen Zhang, Qingmin Zhang, Shuhua Zhang, Zhiyong Zhang, Yubin Zhao, Weili Zhong, Kejun Zhu, Honglin Zhuang

Iowa State University

Kerry Whisnant, Bing-Lin Young

Joint Institute for Nuclear Research

Yuri A. Gornushkin, Dmitri Naumov, Igor Nemchenok, Alexander Olshevski

Kurchatov Institute

Vladimir N. Vydrov

Lawrence Berkeley National Laboratory and University of California at Berkeley

Bill Edwards, Kelly Jordan, John Joseph, Jason Lee, Charles Leggett, Cheng-Ju Lin, Dawei Liu, Tak-Pui Lou, Kam-Biu Luk, Simon Patton, Herb M. Steiner, Craig Tull, Steve Virostek, Sergio Zimermann

Nanjing University

Shenjian Chen, Tingyang Chen, Guobin Gong, Ming Qi

Nankai University

Shengpeng Jiang, Xueqian Li, Ye Xu

National Chiao-Tung University

Feng-Shiu Lee, Guey-Lin Lin, Yung-Shun Yeh

National Taiwan University

Taihsiang Ho, Yee B. Hsiung

National United University

Simon Blyth, Yun Chang, Ming-Huey Alfred Huang, Chung-Hsiang Wang

Princeton University

Changguo Lu, Kirk T. McDonald

Rensselaer Polytechnic Institute

John Cummings, Johnny Goett, Jim Napolitano, Paul Stoler

Shandong University

Xingtao Huang, Jianbin Jiao, Cheng-guang Zhu

Shenzhen University

Yu Chen, Hanben Niu, Lihong Niu

Sun Yat-Sen (Zhongshan) University

Zhibing Li

Tsinghua University

Shaomin Chen, Hui Gong, Guanghua Gong, Li Liang, Beibei Shao, Qiong Su, Tao Xue

University of California at Los Angeles

Vahe Ghazikhanian, Huan Z. Huang, Stephen Trentalange, Oleg Tsai, Charles A. Whitten

University of Hong Kong,

K.S. Cheng, Talent T.N. Kwok, Maggie K.P. Lee, John K.C. Leung, Jimmy H.Y. Ngai, Jason C.S. Pun, Heymans H.C. Wong

University of Houston

Michael Ispiryan, Kwong Lau, Logan Lebanowski, Bill Mayes, Lawrence Pinsky, Guanghua Xu

University of Illinois at Urbana-Champaign

S. Ryland Ely, Wah-Kai Ngai, Jen-Chieh Peng

University of Science and Technology of China

Qi An, Yi Jiang, Hao Liang, Shubin Liu, Wengan Ma, Xiaolian Wang, Jian Wu, Ziping Zhang,
Yongzhao Zhou

University of Wisconsin and Physical Sciences Laboratory

A. Baha Balantekin, Jeff Cherwinka, Farshid Feyzi, Lee Greenler, Karsten M. Heeger, Bryce Little-
john, Michael McFarlane, Daniel Passmore, Wei Wang, Thomas S. Wise

Virginia Polytechnic Institute and State University

Jonathan M. Link, Leo E. Piilonen

Executive Summary

This document describes the design of the Daya Bay reactor neutrino experiment to be constructed at the Daya Bay nuclear power complex in Shenzhen, China. This is an international project with collaborating institutions from China, the United States, Russia and the Czech Republic. This experiment will precisely determine the last unknown neutrino mixing angle θ_{13} with a sensitivity of 0.01 or better in $\sin^2 2\theta_{13}$ at the 90% confidence level through a measurement of the relative rates and energy spectra of reactor antineutrinos at different baselines.

Experimental Site

The Daya Bay nuclear power complex is one of the most prolific sources of antineutrinos in the world. Currently the two pairs of reactor cores (Daya Bay and Ling Ao, separated by about 1.1 km) generate 11.6 GW_{th} of thermal power; this will increase to 17.4 GW_{th} by early 2011 when a third pair of reactor cores (Ling Ao II) is put into operation and Daya Bay will be among the five most powerful reactor complexes in the world.

The site is located adjacent to mountainous terrain, ideal for siting underground detectors that are well shielded from cosmogenic backgrounds. The basic experimental layout of Daya Bay consists of three underground experimental halls, one far and two near, linked by horizontal tunnels as shown in Fig. 0.1.



Fig. 0.1. Default configuration of the Daya Bay experiment, optimized for best sensitivity in $\sin^2 2\theta_{13}$. Four detector modules are deployed at the far site and two each at each of the near sites.

Experimental Setup

Figure 0.1 shows the detector deployment in the underground halls. Eight identical cylindrical detectors,

each consisting of three nested cylindrical zones contained within a stainless steel tank, will be deployed to detect antineutrinos via the inverse beta-decay reaction. To maximize the experimental sensitivity four detectors are deployed in the far hall near the first oscillation maximum. The rate and energy distribution of antineutrinos from the reactors are monitored with two detectors in each near hall at relatively short baselines from their respective reactor cores, reducing the systematic uncertainty in $\sin^2 2\theta_{13}$ due to uncertainties in the reactor power levels to about 0.1%. This configuration significantly improves the statistical precision over previous experiments (0.2% in three years of running) and enables cross-calibration to verify that the detectors are identical. Each detector will have 20 metric tons of 0.1% Gd-doped liquid scintillator in the inner-most, antineutrino target zone. A second zone, separated from the target and outer buffer zones by transparent acrylic vessels, will be filled with undoped liquid scintillator for capturing γ rays that escape from the target thereby improving the antineutrino detection efficiency. A total of 192 photomultiplier tubes are arranged along the circumference of the stainless steel tank in the outer-most zone, which contains mineral oil to attenuate γ rays from trace radioactivity in the photomultiplier tube glass and nearby materials including the outer tank. The detector dimensions are summarized in Table 0.1.

Dimensions	Inner Acrylic	Outer Acrylic	Stainless Steel
Diameter (mm)	3100	3970	4976
Height (mm)	3100	3970	4976
Wall thickness (mm)	10	15	12
Vessel Weight (ton)	0.6	1.4	20
Liquid Weight (ton)	~20	~20	~40

Table 0.1. Summary of antineutrino detector properties. The dimensions are for the inner diameters. The liquid weights are for the mass of liquid contained only within that zone.

With reflective surfaces at the top and bottom of the detector the energy resolution of the detector is about 12% at 1 MeV.

The mountainous terrain provides sufficient overburden to suppress cosmic muon induced backgrounds to less than 1% of the antineutrino signal. The detectors in each experimental hall are shielded by 2.5 m of water against radioactivity and spallation neutrons from the surrounding rock. The detector halls include a muon detector system, consisting of an instrumented water shield and tracker, for tagging the residual cosmic muons. The signal and background rate in the underground halls are summarized in Table 0.2.

Careful construction, filling, calibration and monitoring of the detectors will reduce detector-related systematic uncertainties to a level comparable to or below the statistical uncertainty. Table 0.3 summarizes the systematic uncertainties for the experiment. The horizontal tunnels connecting the detector halls will facilitate cross-calibration and offer the possibility of swapping the detectors to further reduce systematic uncertainties.

Schedule

Civil construction started in the fall of 2007. Deployment of the first pair of the detectors in the Daya Bay near hall will start in July 2009. Data taking using the baseline configuration of the two near halls and far hall will begin in November 2010. After three years of running the sensitivity of Daya Bay for $\sin^2 2\theta_{13}$ will be 0.008, relatively independent of the value of Δm_{31}^2 within its allowed range.

	Daya Bay Near	Ling Ao Near	Far Hall
Baseline (m)	363	481 from Ling Ao 526 from Ling Ao II	1985 from Daya Bay 1615 from Ling Ao
Overburden (m)	98	112	350
Radioactivity (Hz)	<50	<50	<50
Muon rate (Hz)	36	22	1.2
Antineutrino Signal (events/day)	930	760	90
Accidental Background/Signal (%)	<0.2	<0.2	<0.1
Fast neutron Background/Signal (%)	0.1	0.1	0.1
${}^8\text{He}+{}^9\text{Li}$ Background/Signal (%)	0.3	0.2	0.2

Table 0.2. Summary of signal and background rates for each detector module at the different experimental sites.

Source	Uncertainty
Reactor Power	0.087% (4 cores) 0.13% (6 cores)
Detector (per module)	0.38% (baseline) 0.18% (goal)
Signal Statistics	0.2%

Table 0.3. Summary of uncertainties. The baseline value is realized through proven experimental methods, whereas the goal value should be attainable with improved calibration and analysis techniques.

Contents

Executive Summary	I
1 Overview	1
1.1 Neutrino Oscillation Phenomenology	1
1.1.1 Neutrino Mixing	1
1.1.2 Current Knowledge of Mixing Parameters	1
1.1.3 Significance of the Mixing Angle θ_{13}	2
1.2 Determining θ_{13} with Nuclear Reactors	2
1.2.1 Energy Spectrum and Flux of Reactor Antineutrinos	3
1.2.2 Inverse Beta-Decay Reaction	4
1.2.3 Observed Antineutrino Rate and Spectrum at Short Distance	5
1.2.4 Reactor Antineutrino Disappearance Experiments	6
1.2.5 Precision Measurement of θ_{13}	8
1.3 The Daya Bay Reactor Antineutrino Experiment	10
1.3.1 Experimental layout	11
1.3.2 Detector Design	13
1.3.2.1 Antineutrino detector	15
1.3.2.2 Muon detector	18
1.3.2.3 WBS	18
2 Sensitivity & Systematic Uncertainties	21
2.1 Reactor Related Uncertainties	21
2.1.1 Power Fluctuations	22
2.1.2 Location Uncertainties	23
2.1.3 Spent Fuel Uncertainties	23
2.2 Detector Performance	23
2.2.1 Fabrication, Assembly, and Filling	24
2.2.2 Calibration/Monitoring Program	24
2.2.2.1 Commissioning	25
2.2.2.2 Automated Monitoring	25
2.2.2.3 Cosmogenic Events	26
2.2.2.4 PMT Calibration and Monitoring	27
2.2.2.5 Determination of Detector Optical Parameters	27
2.2.3 Detector Related Uncertainties	32
2.2.3.1 Number of Target Protons	33
2.2.3.2 Position Cuts	34
2.2.3.3 Positron Energy Cut	34
2.2.3.4 Neutron Detection Efficiency	34
2.2.3.5 Neutron Multiplicity	37
2.2.3.6 Trigger	37
2.2.3.7 Live Time	37
2.2.4 Detector Swapping	37
2.2.5 Detector Cross-calibration	38
2.3 Backgrounds	38
2.3.1 Cosmic Muons in the Underground Laboratories	39
2.3.2 Simulation of Neutron Backgrounds	41

2.3.3	Cosmogenic Isotopes	43
2.3.4	Radioactivity	45
2.3.5	Background Subtraction Uncertainty	47
2.4	Sensitivity	48
2.4.1	Global χ^2 Analysis	49
2.4.2	θ_{13} Sensitivity	51
3	Experimental Site and Laboratories	54
3.1	General Laboratory Facilities	54
3.1.1	Tunnels	55
3.2	Site Survey	57
3.2.1	Topographic Survey	57
3.2.2	Engineering Geological Mapping	58
3.2.3	Geophysical Exploration	62
3.2.4	Engineering Drilling	62
3.2.5	On-site Tests at Boreholes	62
3.2.6	Laboratory Tests	64
3.2.7	Survey Summary	66
3.3	Civil Design	68
3.3.1	Transportation Vehicle for the Antineutrino Detectors	68
3.3.2	Lifting System for the Antineutrino Detectors	69
3.3.3	Experimental Hall Layout	70
3.3.4	Central Water Purification Station	73
3.3.5	LS Hall	73
3.3.6	Design of Tunnel	73
3.3.7	Design of Surface Buildings	75
3.3.8	Electricity	79
3.3.9	Ventilation System	79
3.3.10	Water Supply and Drainage	79
3.3.11	Communication	79
3.3.12	Safety Systems	79
3.3.13	Blast Control	80
3.3.14	Environmental Effect Evaluations	80
3.4	Civil Construction Overview	80
4	Antineutrino Detector	84
4.1	Detector Geometry and Dimensions	84
4.1.1	Target Mass	85
4.1.2	Antineutrino Detector with Three Zones	86
4.1.3	Antineutrino Target	87
4.1.4	Gamma Catcher	88
4.1.5	Oil Buffer	89
4.1.6	Optical Reflective Panels	91
4.2	Antineutrino Detector Performance	93
4.3	Mechanical Design and Structure of the Antineutrino Detector	93
4.3.1	Detector Tank	93
4.3.2	Lifting of AD	98
4.3.3	Surface Coating of Detector Tank and Optical Barriers	98

4.3.4	Detector Target and Acrylic Vessels	98
4.3.5	Overflow Tanks, Calibration Ports, and Vessel Penetrations	106
4.3.6	Thermal Modeling of the Antineutrino Detector	110
4.3.7	Fill and Drain Mechanism	110
4.4	Liquid Scintillator and Detector Liquids	113
4.4.1	Selection of Solvents	115
4.4.2	Preparation of Gadolinium Complexes	115
4.4.3	Purification of Gd-LS	117
4.4.4	Characterization of Gd-LS	118
4.4.5	Large Scale Production of Gd-LS	122
4.4.6	Storage of Gd-LS, LS and Mineral Oil at Daya Bay	125
4.5	PMT System	127
4.6	PMT System	127
4.6.1	PMT Requirements	127
4.6.1.1	Efficiency for detecting antineutrinos	127
4.6.1.2	Energy resolution	128
4.6.1.3	Timing response	128
4.6.1.4	Radiopurity	128
4.6.1.5	Mechanical strength	128
4.6.1.6	Uniformity and long-term reliability	128
4.6.2	PMT Acquisition	130
4.6.3	PMT Burn-in	130
4.6.4	PMT Testing	131
4.6.5	PMT Base	133
4.6.6	PMT High Voltage System	133
4.6.7	PMT Signal and HV Coupling	137
4.6.8	PMT Support Structure	140
4.6.9	PMT Cable Penetrations and Cable Routing	143
4.6.9.1	PMT Cable Penetrations in AD Wall	145
4.6.9.2	PMT Cables and Cable Trays Outside AD in Muon Pool	149
4.6.9.3	PMT Cable Penetrations in Muon Pool Cover	149
4.6.10	PMT R&D Results	149
4.6.10.1	Radioactivity background	149
4.6.10.2	Single Photo-electron Spectrum	149
4.6.10.3	Effect of Local magnetic Field	149
4.6.10.4	Absolute Gain and Linearity	150
4.6.10.5	Dark Rate	151
4.6.10.6	Pre- and After-pulsing	151
4.6.10.7	Quantum Efficiency	152
4.7	Monitoring and Instrumentation for the Antineutrino Detectors	153
4.7.1	Survey of As-Built Detector Geometry	154
4.7.2	Visual Monitoring of Inside of Antineutrino Detector	155
4.7.3	Monitoring of Acrylic Vessel Positions	155
4.7.4	Motion Monitoring	156
4.7.5	Target Mass Monitoring During Filling and Operation	156
4.7.6	Gas Supply Monitoring (dry N ₂ and ambient)	157
4.7.7	Temperature Monitoring	158
4.7.8	Monitoring of LS Leaks	160

4.7.9	In-Situ Monitoring of the Mineral Oil Attenuation Length	161
4.8	Filling the Antineutrino Detectors and Measuring the Target Mass to High Precision	161
4.8.1	The Filling Process	162
4.8.2	Measuring the Target Mass to High Precision of <0.1%	165
4.8.3	Control and Operation of the AD Filling and Target Mass Measurement	169
4.8.4	Use of the Liquid Scintillator (LS) Hall for Detector Filling	170
4.8.5	Materials Compatibility of Liquid Scintillator with the Target Mass Measurement and AD Filling System	171
4.8.6	Emptying the Antineutrino Detectors	171
4.9	Risk Assessment	173
4.10	R&D Plan	174
4.10.1	PMT System	174
4.10.2	Acrylic Vessels	175
4.10.3	Instrumentation&Monitoring	175
4.10.4	Assembly&Integration	176
4.11	Manufacturing Plan	176
4.12	Quality Assurance During Fabrication and Assembly	180
4.13	ES&H	181
5	Calibration and Monitoring Systems	182
5.1	Radioactive Sources	182
5.2	LED Calibration System	183
5.3	In-situ Detector Monitoring	185
5.4	Detector monitoring with data	186
5.5	Automated Deployment System	187
5.6	Manual deployment system	192
5.7	Manufacturing Plan	192
5.8	Quality Assurance	193
5.9	ES&H	193
5.10	Risk Assessment	194
6	Muon System	195
6.1	Muon System Specifications	195
6.1.1	Muon Detection Efficiency	196
6.1.2	Muon System Redundancy	196
6.1.3	Spatial Resolution	197
6.1.4	Timing Resolution	197
6.1.5	Water Shield Thickness	197
6.1.6	Summary of Requirements	197
6.2	Water Shield	198
6.2.1	Water Shield Design	198
6.2.2	Water Shield PMT layout	200
6.2.3	Water Shield Front-End Electronics	202
6.2.4	Calibration of the Water Shield PMTs	202
6.2.5	Water Conditioning	203
6.2.6	Inner Water Shield	207
6.2.6.1	Inner Water Shield Simulation Studies	207
6.2.7	Outer Water Shield	208

6.2.7.1	Performance of the Outer Water Shield	208
6.3	Resistive Plate Chambers (RPC)	209
6.3.1	RPC Design	211
6.3.1.1	Overall considerations	211
6.3.1.2	Module Design	212
6.3.1.3	Module mechanical structure	215
6.3.1.4	Signal Readout	215
6.3.1.5	Gas Distribution	218
6.3.1.6	High Voltage Connector Arrangement	218
6.3.2	RPC Gas System	218
6.3.3	RPC High Voltage System	222
6.3.4	RPC Performance	222
6.3.5	RPC Support Structure	223
6.3.5.1	Physics Requirements	223
6.3.5.2	Mechanical Structure Requirements	223
6.3.5.3	Moving Mechanism Requirements	224
6.3.5.4	Design details	225
6.3.5.5	Strength Analysis of the Mechanical Structure	225
6.3.5.6	RPC Support Structure Finite Element Analysis	226
6.4	Manufacturing Plan.	226
6.4.1	Commercial Components	226
6.4.1.1	Commercial Components for the Water Shield	226
6.4.1.2	Commercial Components for RPCs	228
6.4.2	Components to be Fabricated In-house	229
6.4.2.1	Components to be Fabricated In-house for Water Shield and Outer Water Sections	229
6.4.2.1.1	PMT base fabrication	229
6.4.2.1.2	PMT supports	230
6.4.2.2	Components to be Fabricated In-house for RPCs	230
6.4.2.2.1	RPC module fabrication	230
6.4.2.2.2	RPC support manufacture	231
6.4.2.3	Quality Assurance During Fabrication and Assembly	231
6.4.3.1	Quality Assurance During Fabrication and Assembly of the RPCs	231
6.4.3.1.1	Quality Assurance of Raw Materials	231
6.4.3.1.2	Quality Control of the Production Process of the the RPCs	232
6.4.3.1.3	RPC Module Assembly and Testing	233
6.4.3.2	RPC Installation	233
6.4.3.3	Quality Assurance During Fabrication and Assembly of the RPC support structure	233
7	Electronics, Trigger, and Data Acquisition Systems	235
7.1	PMT Front-End Electronics	235
7.1.1	Requirements for the PMT Front-End Electronics	235
7.1.2	PMT Front-End Electronics (FEE) Boards	236
7.1.3	RPC Front-End Electronics	238
7.2	The Trigger System	240
7.2.1	Trigger System Requirements	240
7.2.2	The Antineutrino Detector Trigger System	242
7.2.3	The Muon Trigger System	244
7.3	The Timing System	245

7.3.1	GPS Driver Module	246
7.3.2	Central Clock Generator	246
7.3.3	Local Clock Fanout	247
7.4	The Data Acquisition System	247
7.4.1	Requirements	247
7.4.2	The DAQ System Architecture	249
7.4.2.1	VME front-ends readout	250
7.4.2.2	Event Builder	250
7.4.2.3	Data Storage and Logging	250
7.4.2.4	Online Software	251
7.5	Detector Control and Monitoring	251
7.6	Manufacturing Plan, Quality Assurance, ES&H (Environment, Safety and Health) and Risk Assessment	252
7.6.1	Manufacturing Plan	252
7.6.2	Quality Assurance	252
7.6.3	Environment, Safety, and Health	253
7.6.4	Risk Assessment	253
8	Offline	254
8.1	Offline Requirements	254
8.1.1	Networking, Computing and Software Distribution	255
8.1.2	Simulation	256
8.1.3	Data Processing and Analysis	256
8.1.4	Data Movement and Networking	257
8.1.5	Online Interface	258
8.2	Data Management, Networking and Computing	258
8.2.1	Data Movement	258
8.2.2	Networking	259
8.2.3	Data Archiving	261
8.2.4	Databases	261
8.2.5	Computing Resources, Operations, and Data Processing	261
8.2.5.1	BNL Cluster	262
8.2.5.2	IHEP Cluster and Tape Archive	262
8.2.5.3	LBNL Cluster and Tape Archive	262
8.3	Offline Core Software and Infrastructure	263
8.3.1	Processing and Analysis Software	263
8.3.2	Simulation Software	265
8.3.3	Infrastructure and Process	265
8.4	Risk Assessment	265
8.4.1	Schedule	266
8.4.2	Cybersecurity	266
9	Installation and Testing Plan	269
9.1	AD Deployment Plan	270
9.2	Receiving and Storage of Detector Components	271
9.2.1	Surface Assembly Building	271
9.3	AD Assembly, Testing and Transport	272
9.3.1	Assembly of the Antineutrino Detectors	273

9.3.2	Precision Survey of the Antineutrino Detectors	273
9.3.3	Antineutrino Detector Subsystem Testing	274
9.3.4	Antineutrino Detector Transport to LS Hall	275
9.3.5	Filling the Antineutrino Detector Modules	276
9.3.5.1	Antineutrino Detector Transport from the LS Hall to the Experimental Halls	278
9.4	Detector Installation in the Experimental Halls	278
9.4.1	Installation of the Muon Veto System	281
9.4.2	Installation of the Antineutrino Detectors	283
9.4.3	Precision Alignment and Survey	287
10	Integration	288
10.1	Mechanical Systems Integration	288
10.2	Electrical Systems Integration	289
10.3	Experimental Assembly	289
10.4	Safety Systems Integration	289
10.5	Subsystem Management	290
11	Value Engineering	291
11.1	Antineutrino Detector	291
11.1.1	Comparison of 3-zone vs. 2-zone Detectors	291
11.1.2	PMT Magnetic Shields	292
11.1.3	PMT Size	293
11.1.4	LS Process	294
11.1.4.1	Handling and storage of AD organic liquids underground	295
11.1.5	LS Storage	295
11.1.6	AV Supports	295
11.1.7	Cable Feedthroughs	296
11.1.8	Optimization of the AD Stainless Steel Vessel	296
11.2	Muon System	297
11.2.1	PMT Optimization	297
11.2.2	Water Hall	297
11.2.3	Pool Shape	297
11.2.4	RPC Strip Size	298
11.3	Electronics	298
11.4	Offline	298
11.5	Civil/Installation	299
11.5.1	SAB Design	299
11.5.2	Transporter	300
12	Operations of the Daya Bay Experiment	303
12.1	Configurations of Detector Modules	304
12.2	Early Occupancy of the Experimental Halls	305
12.3	Servicing and Maintenance of the Antineutrino Detector	305
12.4	Detector Swapping	306
12.4.1	Logistics of Detector Swapping	306
12.5	Maintenance and Operations Costs	307
12.5.1	Pre-operations Costs	307
12.5.2	Operations Costs	308

12.6 Decommissioning of Experiment	309
13 Environment, Safety and Health	310
13.1 Identification and Mitigation of Safety and Environmental Hazards	312
13.2 Environmental Stewardship	312
13.3 Underground Safety	313
14 Quality Assurance	314
14.1 Quality Assurance and Testing	314
14.1.1 Quality Management Plan	314
14.1.2 Design Codes and Standards	315
14.1.3 Drawing Exchange and Archiving	315
14.1.4 Design Reviews	315
14.1.5 Test Plans	315
15 R&D Plan	316
15.1 Risk Assessment and Tracking	316
15.2 Risk Mitigation	316
15.3 R&D Program	316
15.3.1 Antineutrino Detector Prototype	317
15.3.1.1 Prototype Detector Design	317
15.3.1.2 Prototype Detector Test Results	319
16 Organization and Management	322
16.1 Daya Bay Project Organization	322
16.1.1 U.S. and China Project Management Offices	323
16.1.2 Project Subsystem Organization	324
16.2 Technical Reviews	324
16.3 Change Control	324
17 Schedule, Scope and Cost	325
17.1 Project Schedule	325
17.2 Project Scope	325
17.2.1 U.S. Project Scope	325
17.2.2 U.S. Project Cost	327
A Acknowledgements	328
B Acronyms	329
C Requirements	332
D AD simulation parameters and studies	343
D.1 Simulation parameters	343
D.2 Simulation geometry	344
D.3 Evaluation metrics	345
D.4 Main structures	345
D.4.1 The thickness of the AV wall	345
D.4.2 Small variations of the outer AV size	347

D.4.3 Additional simulation of main structure variations	347
D.5 Contained structures	348
D.5.1 The effects of ribs in the outer AV	348
D.5.2 The effects of the inner AV kinematic mounts	349
D.5.3 General features of effects due to acrylic in the outer AV	349
D.5.4 Discussion	351
D.6 Penetration structures	351
D.7 Summary and future plans	352

List of Figures

0.1	Default configuration of the Daya Bay experiment, optimized for best sensitivity in $\sin^2 2\theta_{13}$. Four detector modules are deployed at the far site and two each at each of the near sites.	I
1.1	Exclusion contours determined by Chooz, Palo Verde along with the allowed region obtained by Kamiokande.	2
1.2	Fission rate of reactor isotopes as a function of time.	3
1.3	Antineutrino energy spectrum for four isotopes.	4
1.4	Total cross section for inverse beta-decay calculated in leading order and next-to-leading order. .	5
1.5	Recoil neutron energy spectrum from inverse beta-decay weighted by the antineutrino energy spectrum.	6
1.6	Angular distributions of positrons and recoil neutrons from inverse beta-decay in the laboratory frame.	6
1.7	Antineutrino energy spectrum (red dotted curve), total inverse beta-decay cross section (blue dotted-dash curve), and count rate (black solid curve) as a function of antineutrino energy.	7
1.8	Reactor antineutrino disappearance probability as a function of distance from the source. . . .	8
1.9	Reactor antineutrino disappearance probability due to the mixing angle θ_{13} as a function of the baseline L over the allowed 2σ range in Δm_{32}^2	9
1.10	Daya Bay and vicinity: The nuclear power complex (indicated by the red dot at the upper right of the map) is located 55 km from central Hong Kong.	10
1.11	The Daya Bay nuclear power complex. The Daya Bay nuclear power plant is in the foreground. The Ling Ao nuclear power plant is in the background. The experimental halls will be underneath the hills to the left.	11
1.12	Layout of the Daya Bay experiment.	12
1.13	Site optimization using the global χ^2 analysis. The optimal sites are labelled with red triangles. The stars show the reactors. The black contours show the sensitivity when one site's location is varied and the other two are fixed at optimal sites. The red lines with tick marks are the perpendicular bisectors of various combinations of reactors. The mountain contours are also shown on the plot (blue lines).	13
1.14	Layout of the baseline design of the Daya Bay detector at the far site. Four antineutrino detector modules are shielded by a 1.5 m-thick active water Cherenkov shield. Surrounding this shield and optically isolated from it is another 1-meter of water Cherenkov shield. (The optical barrier between the two water shields is not shown, nor are the PMTs.) The muon system is completed with RPCs at the top (which are shown in the retracted position).	16
1.15	Cross sectional slice of a 3-zone antineutrino detector module showing the inner acrylic vessel holding the Gd-LS at the center (20 ton), LS between the acrylic vessels (20 ton) and mineral oil (40 ton) in the outer region. The PMTs are mounted on the inner surface of the stainless steel tank in the mineral oil.	17
2.1	Illustration of the source deployment axes.	26
2.2	The Gd capture p.e. yield for the spallation neutrons (normalized to the yield at the detector center) as a function of the neutron vertex (R, z). The assumed attenuation length of the scintillator is 18 m.	27
2.3	A diagram for measuring the attenuation lengths in all three zones. The calibration PMTs are shown as blue blocks with yellow faces. The red balls indicate the LED diffuser ball positions for measurements of the buffer oil transparency. The magenta thick lines on the top and bottom represent the reflectors. The vertical dashed lines indicate regions of deployment for the LED ball for measurement of the transparencies of the central region and gamma catcher, as well as determination of the reflectivity of the top/bottom reflectors.	29

2.4	Determination of the gamma catcher attenuation length by deploying the LED at different z locations.	29
2.5	The hits timing of PMT #1 for direct and reflected light from a pulsing LED at the detector center.	30
2.6	The results of a scan of ^{60}Co source along the central z axis for a detector with bottom acrylic plate having a short 1 cm optical attenuation to simulate the effect of a precipitate.	31
2.7	Energy spectra associated with the positron's true energy (Red = kinetic energy + 1.022 MeV annihilation energy), the GEANT4 visible energy (Blue = dE/dx in the active detector region, i.e. the target or gamma catcher), and reconstructed energy (Black) close to the 1 MeV threshold. The reconstructed energy is calculated by scaling the total detected charge based on (simulated) calibration data from ^{68}Ge (1.022 MeV) and spallation neutrons (8 MeV). The full spectrum is shown in the upper insert, and a zoom in of the high energy tail region is shown in the lower insert. In both inserts, the red histogram corresponds to the true energy and the black corresponds to the reconstructed energy. Statistics comparable to a far site module in 1000 days.	35
2.8	Spallation neutron response for detector modules with scintillator optical attenuation lengths of $4.5 \leq d \leq 18$ m. The left panel shows the raw photoelectron spectra, whereas the right panel shows the spectra rescaled according to a non-linear rescaling procedure we have developed. The rescaled 6 MeV effective energy threshold produces a constant value of $\epsilon_E = 93\%$ to within 0.4% over this extreme range of attenuation length.	36
2.9	Three dimensional profile of Pai Ya Mountain, where the Daya Bay experimental halls will be located, generated from a 1:5000 topographic map of the Daya Bay area.	40
2.10	Comparison of the modified formula (solid lines) with data. Calculations with the standard Gaisser's formula are shown in dashed lines.	40
2.11	Muon flux as a function of the energy of the surviving muons. The three curves from upper to lower correspond to the Daya Bay near site, the Ling Ao near site and the far site, respectively.	40
2.12	The prompt energy spectrum of fast neutron background at the Daya Bay far detector. The inset is an expanded view of the spectrum from 1 to 10 MeV.	42
2.13	Fitting results as a function of the muon rate. The uncertainty bars show the precision of the fitting. The χ^2 fitting uses the same muon rate as the maximum likelihood fitting and is shown to the right of it.	44
2.14	The fitting precision as a function of the muon rate, comparing with the analytic estimation of Eq. 28. The y-axis shows the relative resolution of the background-to-signal ratio.	44
2.15	Spectrum of natural radioactivity measured with a Ge crystal in the Hong Kong Aberdeen Tunnel. Prominent peaks for ^{40}K (1.461 MeV) and ^{208}Tl (2.615 MeV) are clearly evident along with many other lines associated with the U/Th series.	46
2.16	Spectra of three major backgrounds for the Daya Bay experiment and their size relative to the oscillation signal, which is the difference of the expected neutrino signal without oscillation and the 'observed' signal with oscillation for $\sin^2 2\theta_{13} = 0.01$	48
2.17	Expected $\sin^2 2\theta_{13}$ sensitivity at 90% C.L. with 3 years of data, as shown in solid black line. The red line shows the current upper limit measured by Chooz.	51
2.18	Expected 3σ discovery limit for $\sin^2 2\theta_{13}$ at Daya Bay with 3 years of data.	51
2.19	Expected $\sin^2 2\theta_{13}$ sensitivity at 90% C.L. versus time. The curve is calculated with the assumption of two near sites and one far site with data acquisition beginning in Dec. 2010. The value of Δm_{31}^2 is taken to be 2.5×10^{-3} eV 2	52

3.1	Layout of the Daya Bay and Ling Ao cores, the future Ling Ao II cores and possible experiment halls. The entrance portal is shown at the bottom-left. Five experimental halls marked as #1 (Daya Bay near hall), #2 (Ling Ao near hall), #3 (far hall), #4 (water hall), #5 (LS hall) are shown. The green line represents the access tunnel, the blue lines represent the main tunnels and the pink line represents the construction tunnel. The total tunnel length is about 3000 m.	55
3.2	The original plan view of the experimental halls and tunnels from the site survey. Note the length here is slightly different from the presently optimized experiment halls, therefore the lengths of tunnels are also slightly different (see, Fig. 3.1). All distances are in meters. Line A{1-2-3-7-4-5-far site} has a total length of 2002 m; Line B{7-6} has a total length of 228 m; Line C{8-9} has a total length of 607 m; Line D{4-8-Ling Ao near} has a total length of 465 m. Line E is the dashed line on the top across far site. Line F is the construction tunnel for bidding. The four bore hole sites are marked as ZK1, ZK2, ZK3, ZK4 from north to south. They will be referred to later in the discussions of geological exploration in Section 3.2.3 and engineering drilling in Section 3.2.4.	56
3.3	Topographical map in the vicinity of the far site. The location of the far detector hall is marked by a red square in the middle of the map.	58
3.4	Geological map of the experimental site. The faults are shown as red line segments and marked by blue ellipses. Faults F2, F6, F7, and F8 are revealed by the Geological Mapping (see Section 3.2.2) and Faults F1, F3, F4, and F5 by Geological Exploration (see Section 3.2.3). Four weathering bags marked as black areas and as indicated explicitly are also revealed, two each, by the Mapping and Exploration.	60
3.5	Monthly average temperature and rainfall from data provided by the Da Ken weather station. The horizontal axis gives the months from January (1) to December (12) and the vertical axis is the average temperature in centigrade in the top figure and the rainfall in mm in the bottom figure.	61
3.6	Seismic refraction, electrical resistivity and high resolution density maps along the tunnel cross section from the Daya Bay experimental hall (left end) to the far hall (right end).	63
3.7	Rock samples from borehole ZK1.	64
3.8	Water level variation vs time in the four boreholes from Dec. 22, 2005 to early June, 2006. There is no measurement during holidays in January 2006 in ZK2. The cause of the sudden drop of the water level in April 2006 is unknown. The horizontal axis coordinate is in units of 7 days, the date reads as year/month/day. The vertical axis is the water level in meters into the borehole.	65
3.9	Engineering geological section in line A: the faults, weathering bags and tunnel are shown on the figure. The first curve down from the surface shows the boundary of the weathered granite and the second curve down shows the boundary of the slightly weathered granite. The tunnel passes through one region of slightly weathered granite.	67
3.10	Photo of a Doerfer 140-ton capacity transporter from underside showing multiple dual wheel modules under vehicle load bed.	69
3.11	A photo of a bridge style crane, the crane rail is fixed to the wall of the experimental hall.	70
3.12	Layout of the Daya Bay near hall. The gas mixing, electronics and water purification rooms are along one side of the hall.	71
3.13	Plane view of the Daya Bay hall cavern, with crane shown on the top. The detector is housed in the water pool in the bottom and supported by four vertical columns.	72
3.14	Top view of the central water station, the makeup system of the water is located between the storage pool and the tunnel.	73

3.15	Top view of the LS hall, including several storage tanks for the normal scintillator, loaded scintillator, and mineral oil. The AD detector is also shown.	74
3.16	An engineering schematic diagram of the tunnel layout. The dimensions are in meters.	75
3.17	A schematic diagram of the the main access portal and the layout of the auxiliary buildings. Building marked 1,2,3,4 from top to bottom, 1: Electricity distribution and control building (including the experimental control room); 2: Pump and ventilation building; 3: Water storage for fire control; 4: SAB. At the lower middle is the local hospital.	76
3.18	An artist's conception of the SAB situated adjacent to the access tunnel portal.	77
3.19	A corner of the SAB where ADs will be assembled. The stainless steel tank, acrylic vessel, and clean room are shown.	78
4.1	Sensitivity of $\sin^2 2\theta_{13}$ at the 90% C.L. as a function of the target mass at the far site. The solid line corresponds to the current best-fit central value of Δm_{31}^2 and the dashed line corresponds to the 90% C.L. lower limit on Δm_{31}^2	85
4.2	Cross-sectional model of the antineutrino detectors. The models show the complete antineutrino detectors including the automated calibration boxes and overflow tanks on top of the AD lid.	86
4.3	<i>Left:</i> Transparent cross-section of the antineutrino detector. This figure shows a complete design of one of the options of the antineutrino detector with the automated calibration boxes and overflow tanks on the lid. <i>Right:</i> Schematic top view of the three different zones of the antineutrino detector.	87
4.4	Cross-section of the tunnel and antineutrino detector on the transporter in the horizontal tunnel connecting the experimental halls. The outline of the tunnel cross-section including the air ducts and other infrastructure are shown in yellow.	87
4.5	The neutron capture energy spectrum as obtained from the Geant4 simulation (reconstructed by scaling the total charge). The peak at ~ 8 MeV corresponds to the n-capture on gadolinium. The tail to lower energies is from events with at least one escaping gamma.	88
4.6	The neutron detection efficiency as a function of the thickness of the γ -catcher. The neutron energy cut is set at 6 MeV. The thickness of the γ catcher of the Daya Bay experiment will be 42.5 cm.	89
4.7	Antineutrino detector response (in number of photoelectrons) as a function of the square of the radial location of a 1 MeV electron energy deposit. The mineral oil volume has been removed and the PMTs are positioned directly outside the γ -catcher volume. The vertical blue line is 15 cm from the PMT surface and indicates the need for at least 15 cm of buffer between the PMT surface and the region of active energy deposit in order to maintain uniform detector response.	90
4.8	Left: Measured reflectivity of ESR film. The red line is that for specular reflectivity and the blue line corresponds to total reflectivity including diffuse light. Right: Comparison of reflectivity of the reflector for different sandwich methods. See text for details.	91
4.9	The emission spectrum of Gd-LS with 5 g/L PPO and 10 mg/L bis-MSB. The Gd concentration is 0.2% and the complexant is TMHA.	92
4.10	Total reflectivity of Aluminum film MIRO-silver.	92
4.11	<i>Left:</i> The reconstructed energy resolution using the maximum likelihood method for electron events uniformly generated in the target region is $11.6\%/\sqrt{E(MeV)}$ using the total PMT digitized charge and $10.5\%/\sqrt{E(MeV)}$ using the undigitized total charge. <i>Right:</i> The vertex reconstruction resolution for 8 MeV electron events uniformly generated in the target region using the maximum likelihood fit to the energy and position. The x-axis is the distance of the reconstructed vertex to the true vertex and the y-axis is the number of events.	94
4.12	Stainless steel detector tank. <i>Left:</i> Barrel and bottom. <i>Right:</i> The inner side of the tank lid.	95

4.13	End flange of the stainless steel tank.	96
4.14	Model of the stainless steel tank in FEA.	96
4.15	An example of the FEA on SST, the stress (left) and the deformation (right) of the bottom of the fully-loaded tank when lifting at an acceleration of 0.1 g	97
4.16	Technical drawing of the lifting fixture for the Antineutrino Detector.	99
4.17	Engineering model of the 3-m and 4-m acrylic vessels with support ribs at the bottom and lids. The lid of the 4m vessel is removable while the lid for the 3m vessel is bonded to the vessel. A shaped top is used to avoid the trapping of bubbles and air during filling of the detectors. The conical shape is formed out of a sheet of flat cast acrylic. Latches on the support ribs of the 4m vessel are used to hold down the inner 3-m vessel.	100
4.18	Finite element analysis (FEA) of the 4-m acrylic vessel. The top plot shows the deflections and the lower figure gives the stresses during a worst case scenario of unequal filling. In this case a load equivalent to 30cm of liquid applies to the 15mm walls of the acrylic vessel.) . .	102
4.19	Results form a FEA of the 4-m acrylic vessel under different load conditions during the assembly, transport, lifting, and filling of the detector)	103
4.20	Prototype 3-m vessel under fabrication at the Gold Aqua Technical Company. in Taiwan. The diameter and height are approximately 3 m. The design of this prototype closely resembles the design of the fabrication vessels for the experiment.	103
4.21	Prototype 4-m acrylic vessel with rib bottom and shaped, conical lid under fabrication at Reynolds Polymer Technology in Grand Junction, Colorado, for the Daya Bay experiment. The dimensional specifications of this cylinder are essentially identical to the vessels we propose to build for the Daya Bay project. This picture shows the vessel without the bottom and with unfinished bond lines. After fabrication all bonds are polished to optical clarity. . .	104
4.22	Top: Example of large cylindrical acrylic objects that are being produced routinely by Reynolds Polymer Technology (RPT) in Grand Junction, Co. Bottom: Heat-room at Reynolds Polymer Technology for the bonding and curing of large-scale acrylic objects. In addition, several smaller ovens exist for the forming and curing of objects in size up to 3×3 m.	105
4.23	Fabrication hall and facilities for the production of large-scale acrylic objects at Reynolds Polymer Technology (RPT). Cranes and other infrastructure at RPT can be used for the lifting tests of the acrylic vessels and for the quality acceptance tests after production.	106
4.24	Top: Engineering model of the top of the antineutrino detectors. The overflow tanks for the mineral oil volume are shown in blue, the automated calibration boxes in orange, and the central overflow tank in green. Various ports and distribution boxes are used cabling of monitoring to the inside of the detector and the distribution of gas and electrical cables. Three penetrations connect the calibration boxes (orange) and overflow tanks (blue to the two different target vessel volumes. The ports can be sealed with gate valves when the calibration boxes are removed during transport or filling of the detectors. Bottom: Cross-sectional view of the top of the antineutrino detector.	107
4.25	Top: Detailed view of the central, concentric, nested overflow tanks for the Gd-LS and LS. Bottom: Cross-sectional drawing of the central calibration pipe and tank assembly.	108
4.26	Prototype of a plate to plate and a tube to plate bond for attaching penetration tubing to acrylic tank tops. If required all clamping hardware could be acrylic by use of threaded studs and acrylic nuts.	109
4.27	The temperature evolution of the fluids within the AD are shown along with the average AD temperature as predicted using a FLUENT thermal simulation. The simulation assumes that the AD was initially in thermal equilibrium at 291 K and that the external temperature is held constant at 284 K. The dashed line is the result using a coarse grid while the solid line is the result using a finer grid.	111

4.28 Schematic drawing of a filling system for the Gd-loaded liquid scintillator. A probe is inserted through the calibration port and the overflow tank into the inner target vessel. All connections are made leak tight under a back-pressure of nitrogen to avoid air and radon to enter the detector. Filling of the undoped liquid scintillator into the γ -catcher would occur using a duplicate system located over the appropriate calibration penetration. This figure shows the option of nested, concentric overflow tanks located in the center of the top lid of the antineutrino detector.	113
4.29 Comparison of the UV-visible spectra of LAB samples as received from the Fushun and Petresa companies	116
4.30 Variation of the light output of LS containing different concentrations of PPO.	118
4.31 The UV absorption values of Gd-LS prepared by solvent extraction, and measured at 430 nm over the period 2004-2007	119
4.32 Long-term Stability Test of Gd-LS with 0.2% Gd as a function of time (from phase II of the IHEP prototype: LAB with 5 g/L PPO and 10 mg/L bis-MSB).	120
4.33 Left: an example of the attenuation length measurement using the 1-m vertical tube system. The transmission values for different pathlengths are fitted with an exponential curve. Right: Closed and open circles are attenuation lengths obtained with samples of the 700-L LAB-based Gd-LS used in the prototype at IHEP. Squares are for PC-based unloaded LS; triangles are for mineral oil.	120
4.34 The variation of the light yield vs. time of the Gd-LS taken from the Daya Bay Phase II prototype, measured over a period \sim 120 days for two different γ -ray sources.	121
4.35 Flow chart for the chemical processes that will be used to prepare the solid Gd carboxylate. .	123
4.36 Flow chart for the dissolution processes that will be done to prepare the final Gd-LS in the LS Hall at Daya Bay.	124
4.37 Lining of acrylic on the side wall of the storage pool.	126
4.38 One option to glue the acrylic lid of the storage pool to the wall using silicone sealant. . . .	127
4.39 Block diagram of the PMT test system.	131
4.40 Block diagram of the PMT test DAQ system.	132
4.41 Schematics of the tapered voltage divider used for Hamamatsu R5912 PMT.	134
4.42 A view of the two layer PC board base for the Hamamatsu R5912 PMT.	135
4.43 Photograph of the PMT base assembled on the Hamamatsu R5912 PMT.	135
4.44 A block diagram view of the AD PMT system showing different components of the system. .	136
4.45 Oscilloscope trace of a large PMT pulse AC coupled via a 10 nF capacitor to the DC coupled $50\ \Omega$ terminated Oscilloscope.	137
4.46 Schematic diagram of the three channel BLR circuit.	138
4.47 Photograph of the three channel printed circuit board designed for testing the functionality and performance of the BLR circuit.	139
4.48 The response of the BLR to small signals.	139
4.49 The baseline restoration of the BLR circuit on long time scales.	140
4.50 Installation sequence of the PMT support structure. All the PMTs are premounted on the support structure.	141
4.51 Engineering model of the PMT mounts. The entire mount is fabricated out of strips of stainless steel. The circumference of this holder is adjusted with a screw.	141
4.52 Engineering model of the PMT support structure. The support structure is made of eight angular sections. Each section carries 24 PMTs in equal circular spacing. Together they form a complete ring. The sections can be vertically lowered into the antineutrino detector and secured. The PMTs are held by the mounts shown in the above figure on a ladder.	142

4.53	Cross-sectional view and detail of the PMT ladder structure inside the antineutrino detector. The PMTs are arranged radially looking inward towards the center of the detector. A dry box on the outside of the detector wall in form of a right-angle tube is used to make the connection between the cables inside the AD and outside.	142
4.54	Transparent antineutrino detector model with view of the PMT support ladders and the dry-boxes that are used to make the cable connections between the inside of the antineutrino detector and the outside. The dry boxes are arranged symmetrically around the detector to line up with the PMT ladders and to minimize the cable lengths between the PMT ladders and their respective dry box.	143
4.55	Engineering model of the dry boxes for the PMT cable feedthroughs on the antineutrino detector. They are made of commercial stainless steel elbows with vacuum flanges and a patch panel inside.	144
4.56	Engineering and assembly model of the dry boxes for the PMT cable feedthroughs. Upper left: Patch panel and flange with cables from outside AD. Upper right: Flange on AD tank wall with cable ends from inside the AD. Lower left: Complete assembly of dry box. Lower right: flange in AD tank wall with seal plugs.	144
4.57	Engineering model of a bonded seal plug for each AD PMT cable. O-rings provide the seal between the seal plug and the flange to the dry box. Both the PMT cables inside and outside the AD are prepared with the seal plugs. This design is the baseline method.	146
4.58	Engineering model of a mechanical seal plug for each AD PMT cable. In this case the seal plug is not bonded to the cable jacket. Instead an O-ring compression seal provides the seal to the cable jacket.	146
4.59	Drawing of the seal plugs on the PMT cables inside and outside the AD. The inside cables go through mineral oil while the outside cables go through ultrapure water.	147
4.60	Schematic of the full-wire seal plug for bonding to Teflon cables. For achieving a reliable, leaktight seal plug with Teflon jacketed cables it is necessary to create a full-wire seal. Studies have shown that the electrical characteristics of the cable and the frequency response remain the same with this bonding method.	148
4.61	Single photo-electron spectrum of an R5912 PMT running at a gain of 1×10^7 . The x-axis is the ADC channel.	150
4.62	Single photo-electron spectrum of an R5912 PMT running at a gain of 1×10^7 . The y-axis is in log scale.	150
4.63	Measured charge of ET 9354KB PMTs as a function of orientation in local magnetic field.	150
4.64	Measured charge of Hamamatsu R5912 PMTs as a function of orientation in local magnetic field.	150
4.65	Absolute gain of R5912.	151
4.66	Measured dark rate of an ET 9354KB as a function of time. The PMT is first exposed to light before high-voltage is applied to the tube in the dark. High voltage is power-cycled when the dark rate has reached an asymptotic value.	152
4.67	Dark rate of an ET 9354KB as a function of threshold. The threshold corresponding to a 0.25-p.e. (s.p.e.) cut is about 2 mV (10 mV).	152
4.68	Pre-pulse distribution of a Hamamatsu R5912 as a function of time (ns). The negative value means the signal arrives earlier than the main pulse.	153
4.69	Time distribution of the after-pulse of a Hamamatsu R5912.	153
4.70	Engineering model of the antineutrino detector lid with indications of the various instrumentation used for liquid level sensing and monitoring during filling and operation of the antineutrino detectors.	154

- 4.71 Top: Schematic of the N₂ cover gas supply and ballast system for the antineutrino detectors. Boil-off nitrogen is used as a source of clean, radiopure cover gas for the detector. Bottom: Conceptual layout of the supply lines for the N₂ cover gas system. 159
- 4.72 Schematic of the N₂ supply and return lines for the overflow tanks and calibration boxes on top of the AD. The supply and return lines run through common supply and return manifolds so that potential pressure differences between the calibration box and the overflow volumes or across the gate valve can be avoided. 160
- 4.73 Schematic of the different liquid zones of the antineutrino detector during filling. Zone A: only mineral oil is filled into the detector. Zone B: Mineral oil and LS are filled simultaneously into the detector. Zone C: MO, LS, and Gd-LS are filled simultaneously into the detector. Zone D: This is almost the complete reverse of the previous situation except that calibration pipes penetrate the different regions at the top of the detector. Mostly MO and LS are filled into the detector with some Gd-LS going into the calibration pipes. Zone E: In this zone the detector is filled mostly with MO until it is full with LS and Gd-LS going into the calibration pipes. Zone F: Once the detector is completely full all liquids MO, LS, and Gd-LS will rise into the overflow tanks. 163
- 4.74 *Top:* Mass flow rate of the three different detector liquids for a detector fill with a total duration of 24 hrs. The discontinuities indicate the points where the liquids reach acrylic vessel boundaries. *Bottom:* Cumulative liquids volumes during the detector fill. Again, we assume a total fill duration of 24 hrs. The contribution of liquids in the calibration pipes at the top of the AD is neglected in this graph. 164
- 4.75 A central element of the target mass measurement system is the precision scale for \sim 25 T of liquid scintillator. An ISO reference tank mounted on precision load cells will be used to measure the target mass to $<0.1\%$. The top panel shows the picture of a standard, commercial ISO tank. The bottom pictures show a commercial C6 load cell (left) and the arrangement of the load cells underneath the ISO tank. 166
- 4.76 ISO tank mounting details showing orientation of the free motions of the load cell mounts and the application of spherical swivel mounts to absorb load-induced tank frame distortions. 167
- 4.77 Top panel: Schematic of the filling system for the Gd-LS target liquid. The liquid is pumped through an intermediate ISO storage and weighing tank. Mass and volume flowmeters provide independent measurements of the target mass. Bottom Panel: Schematic of the filling system for the LS and MO filling systems. In this case the mass is determined based on mass and volume flowmeters alone. A total of three, parallel filling systems will be installed in the LS Hall. One for each kind of liquid. 168
- 4.78 Photograph of the facilities of the Physical Sciences Laboratory (PSL) at the University of Wisconsin. The assembly space at PSL allows us to completely assemble and test the ISO tank load scale and AD filling tank system before shipment to Daya Bay. 170
- 4.79 Top panel: Layout of the LS Hall for the filling of the antineutrino detectors. The ADs will be filled one at a time from the MO, LS, and Gd-LS storage tanks. An ISO tank instrumented with load cells is used for the precision mass measurement of the Gd-LS target mass. Bottom panel: To prevent contamination of the inner detector and the Gd-LS during filling the top of the AD will be enclosed in a class-10,000 clean room. Personnel will enter the clean room to insert the AD filling probe and to connect the AD to the filling system. 172
- 4.80 Color-coded model of the antineutrino detector showing the various contributions to the detector from the different countries: China (grey), US (blue), and Taiwan (yellow). 176

5.1	Same figure as Fig. 2.3. A diagram illustrating the deployment scheme for the LED diffuser balls. Three vertical dashed lines indicate the range of the automated deployment axes. The red balls represent the fixed diffuser balls in the oil buffer. The 2" calibration PMTs are shown as blue blocks with yellow faces. The magenta thick lines on the top and bottom represent the reflectors.	184
5.2	Conceptual diagram of the LED deployment system.	184
5.3	Scope capture of the LED light pulse detected by a phototube.	185
5.4	TDC spectrum of the LED light pulse. For details see text.	185
5.5	Diagram illustrating the variety of monitoring tools to be integrated into the design of the antineutrino detector modules.	186
5.6	Design drawing of the automated source deployment system. The central motor and gear box to rotate turntable is omitted for visual clarity. The bottom plate of the calibration box (with the eye bolt) is 35 inches in diameter.	187
5.7	The measured and simulated delayed energy spectra of a ^{252}Cf in the prototype detector.	189
5.8	Schematic diagrams showing designs of radioactive sources for the automated deployment system. On the left is the combination gamma source and on the right is the Pu(C) source.	190
5.9	A schematic diagram of the cabling scheme for the automated calibration system, and the concept of an interface box.	191
5.10	Screen shot of the LABVIEW control/monitoring program for the automated calibrate sys- tem (one turntable and three deployment unit).	192
5.11	Schematic diagram of the manual source deployment system.	193
5.12	Details of the rotating joint.	193
6.1	Elevation view of an experimental hall, showing the baseline design for the muon system. This includes a layer of RPCs above a water pool with at least 2.5 m of shielding for the antineutrino detectors, two layers of 8" photomultipliers in the water, with compartmentalization of the outer 1 m of water for position resolution and redundancy.	196
6.2	Section of pool with PMT support frames (shown without Tyvek panels).	199
6.3	Support pad/anchor bolted to the concrete. Half of one anchor is shown so that the method of fastening can be seen. Each anchor is bolted on, then leveled by a separate set of screws and finally grout is inserted between the anchor and the concrete.	199
6.4	Intersection of the side and bottom PMT support frames at one corner of the pool. Support leg of the AD table is also visible.	200
6.5	Scheme for covering antineutrino detectors with a reflective covering	200
6.6	Plan view of Far Hall configuration.	201
6.7	Design of a phototube base enclosure suitable for use in ultra-pure water.	202
6.8	PMT support scheme for water pool.	203
6.9	Schematic diagram of the water conditioning system designed for the three experimental halls and central storage pool.	206
6.10	Track length of muons in the inner water shield for the Far Hall. The edge at around 4 m is due to muons that penetrate the water and the ADs approximately vertically while the edge around 9 m is due to those that miss the ADs.	207
6.11	Total number of photoelectrons observed in baseline configuration in the inner shield of the Far Hall.	207
6.12	Number of inner shield phototubes hit in baseline configuration of the Far Hall.	208
6.13	Photoelectrons observed per inner shield PMT in baseline configuration of the Far Hall.	208

6.14 Muon efficiency of the inner and outer water shields as a function of the number of hit PMTs demanded. For the inner shield the threshold level needed to reduce the random rate to 50 Hz is 11 PMTs, for the outer it is 13 PMTs. Approximately 12,000 muons are simulated for each curve.	209
6.15 Distribution of reconstructed minus actual muon distance of closest approach to the center of the Far Hall pool.	209
6.16 Inner and outer sections of a near hall water pool.	209
6.17 Tyvek pool liner and inner-outer pool separator on PMT support frame.	210
6.18 Anchoring scheme for separator panels.	210
6.19 Track length of muons in the outer water shield for the Far Hall. The structure starting just below 3 m is due to muons that enter the side and exit the bottom section of the outer shield.	210
6.20 Total number of photoelectrons observed in the outer shield PMT in baseline configuration of the Far Hall.	210
6.21 Number of outer shield phototubes hit in baseline configuration of the Far Hall.	211
6.22 Photoelectrons observed per PMT in baseline configuration of the outer shield of the Far Hall.	211
6.23 Total track length of muons in the water shield for the Far Hall. Red histogram is events that were missed by both the inner and outer shields.	212
6.24 Efficiency of the BES-III RPC versus high voltage for different thresholds.	213
6.25 Noise rate of the BES-III RPC versus high voltage for different thresholds.	213
6.26 Distributions of a tested RPC a) Efficiencies. b) Singles rates.	213
6.27 Two 3-D models of the slanting mode. Left: the columns are aligned (the white space is a module removed to reveal the overlap). Right: there is an additional offset in the even (middle) row, with all the even modules offset slightly to the left.	213
6.28 The layer structure of the "IM_R IV" module design	214
6.29 Module dimensions and overlap width. See also Fig. 6.27.	214
6.30 Stacking scheme of the RPC layers within a module. The layers are shown, expanded vertically, with a projection of all four layers shown at the right.	215
6.31 Comparison of the trigger efficiency for the four stacking schemes.	216
6.32 RPC module mechanical and services structure. The gas and HV connections are at the top. The lifting rings (red) are connected to the steel vertical supports (gold/brown, two of the four are shown). Two of the four aluminum horizontal supports are shown in light gray.	216
6.33 RPC module support structure.	217
6.34 Module size and overlap width.	217
6.35 The assembly structure of the electronic box.	218
6.36 Arrangement of two-in two-out gas flow.	219
6.37 Two-in two-out high voltage arrangement.	219
6.38 Overall process diagram of the RPC gas system in one of the Near Halls. From [19].	220
6.39 Process diagram for the gas mixing subsystem. From [19].	220
6.40 Concept, circuit diagram and photographs of the electron bubbler system. From [13].	221
6.41 Flammability regions for isobutane gas mixtures. There is no region of flammability for a gas mixture in which the ratio of isobutane to the inert component of the RPC gas is 4% or less. From [20].	221
6.42 Layout of the RPC gas system in the Daya Bay Near Hall.	222
6.43 Efficiency as a function of gap voltage for the individual modules of the Daya Bay prototype RPCs (blue) and for the system when two out of three hit modules are required (red).	223
6.44 Diagram showing RPC main mechanical support.	224
6.45 RPC support structure for the far hall (18 m × 18 m).	224
6.46 Wheels and track.	225

6.47	Subunits assembled into a unit.	226
6.48	Units assembled together.	226
6.49	Model for calculations.	227
6.50	Maximum deflection 30.36 mm.	227
6.51	Maximum stress 70.2 MPa.	228
6.52	Prototype water-proof base for muon system PMTs.	229
7.1	Block diagram of front-end electronics module for PMT readout.	237
7.2	Configuration of the RPC electronics & readout system.	238
7.3	Block diagram for the FEC.	238
7.4	Diagram of the FEC threshold forming circuit.	239
7.5	Diagram of the FEC discriminator circuit.	239
7.6	A block diagram of the Daya Bay trigger system.	240
7.7	Simplified trigger board.	243
7.8	Calculated trigger rates caused by PMT dark current as a function of the multiplicity threshold. For this study, we assumed that the maximum number of PMTs was 200. The PMT dark current rate used was 50k with a 100 ns coincidence window.	244
7.9	Schematic layout of the global clock.	246
7.10	Block diagram of data acquisition system.	249
7.11	Internal interaction between the Online Software packages.	252
9.1	Diagram of the planned deployment of the AD modules into the experiment.	270
9.2	Schematic layout of the proposed surface assembly building showing locations for storage and assembly of detector subsystems.	271
9.3	Illustration of the envisioned detector assembly process in the SAB outside the underground tunnel at Daya Bay.	274
9.4	<i>Top:</i> Antineutrino detector on transporter during transport down the access tunnel. <i>Bottom:</i> Illustration of the Wheelift transporter being considered for the transport of the antineutrino detectors [1].	276
9.5	Schematic plan view of the LS hall during filling of one AD with load-cell reference tank and pumping systems.	277
9.6	Daya Bay near hall at Beneficial Occupancy shows tunnel entrance to hall, overhead crane coverage (green floor area), water pool and equipment rooms.	280
9.7	Installation of RPC and muon PMT detectors shown proceeding in parallel in the Daya Bay near hall.	281
9.8	One AD shown installed in water pool on support stand while a second AD is transported into the Daya Bay near hall for installation using the overhead crane.	284
9.9	ADs shown installed in the water pool at Daya Bay near hall. Personnel can gain access to an AD using an access bridge, stairs and work platform atop the AD, as shown.	286
11.1	The energy distribution observed by Chooz, horizontal axis is the prompt signal energy; the vertical axis is the delayed signal energy. In the region labelled D there are many background events with delayed signal falling into the 3–5 MeV energy range.	292
11.2	<i>Top:</i> Hemispherical magnetic shield. Image from [4]. <i>Bottom:</i> Variation of the PMT efficiency with and without mu-metal cage.	293
11.3	Early civil layout of the above ground facilities showing the SAB in the south region, the site utilities in the north region and the tunnel portal entrance.	300
11.4	Photo looking east at demolition of warehouse at the site of the SAB. Road to the left will be the tunnel portal entrance.	300

11.5 At left is a flatbed high capacity vehicle with a load bed close to 2-m above the ground. At right is a typical low-boy tractor trailer combination that can't be reversed out of tunnel and with a load bed height of 1-m.	301
11.6 Typical tunnel cross-section based on most common heavy capacity vehicles available.	301
11.7 Photo of typical automatic-guided-vehicle produced by Wheelift, a division of Doerfer Company.	302
12.1 Commissioning run of the first pair of detectors at the Daya Bay near site. With sufficient runtime of several months, systematic checks of the detectors and a relative comparison of the detector response is possible.	304
13.1 Daya Bay Project Safety organization chart.	310
15.1 Sketch of the antineutrino detector prototype (Left) Top view, (Right) Side view.	318
15.2 The antineutrino detector: before (left) and after (right) the muon detectors were mounted. .	318
15.3 Energy response of the prototype to ^{137}Cs (left) and ^{60}Co (right) sources at the center of the detector with a comparison to Monte Carlo simulation.	319
15.4 Linearity of energy response of the prototype to various sources at the center of the detector (left), and the energy resolution (right).	320
15.5 Energy response of the prototype to a ^{137}Cs source as a function of z position, and a Monte Carlo simulation.	320
15.6 Data and MC comparison of ^{252}Cf . Left: the prompt signal. Right: the delayed signal. . . .	321
15.7 Data and MC comparison of Pu-C source. Left: the prompt signal. Right: the delayed signal.	321
16.1 U.S. Daya Bay Project reporting and responsibility organization chart, with an emphasis on the relationship to DOE.	322
16.2 Daya Bay Project organization chart.	323
D.1 Antineutrino detector geometry in G4dyb, the GEANT4 simulation code of Daya Bay. . .	344
D.2 Energy smearing to simulate the detector response based on the estimated energy resolution. .	346
D.3 The rib structure to support and to constrain the inner AV inside LS.	348
D.4 The simplified geometrical model of acrylic kinematic mounts in GEANT4.	349
D.5 A cylinder-shaped acrylic dead volume at the bottom of the outer AV.	350
D.6 The dependence of neutron energy cut efficiency on the percentage of acrylic volume in the LS. The blue points "DV Study" correspond to Table D.8. The red points "Rib Study" correspond to Table D.4.	352
D.7 The dependence of the systematic uncertainty of neutron efficiency on the percentage of acrylic volume in LS	353

List of Tables

0.1	Summary of antineutrino detector properties. The dimensions are for the inner diameters. The liquid weights are for the mass of liquid contained only within that zone.	II
0.2	Summary of signal and background rates for each detector module at the different experimental sites.	III
0.3	Summary of uncertainties. The baseline value is realized through proven experimental methods, whereas the goal value should be attainable with improved calibration and analysis techniques.	III
1.1	Distances (in meters) from each detector site to the centroid of each pair of reactor cores.	13
1.2	Summary of scientific requirements.	14
1.3	Daya Bay Work Breakdown Structure (WBS) shown at L2.	18
2.1	Requirements on uncertainties necessary to achieve the sensitivity goal of $\sin^2 2\theta_{13} < 0.01$ at 90% C.L.	21
2.2	Reactor-related systematic uncertainties for different reactor configurations. The uncorrelated uncertainty of the power of a single core is assumed to be 2%.	23
2.3	Requirements for the full manual calibration procedure.	25
2.4	Requirements for automated calibration procedure.	25
2.5	Estimated production rates (per 20 ton detector module) for spallation neutron and ^{12}B events in the Daya Bay experiment.	26
2.6	The nominal precision requirements for detector parameters as determined in this study. See text for explanations.	28
2.7	A comparison of the input and fitted values of various sets of parameters in the likelihood fitter.	31
2.8	Comparison of detector-related systematic uncertainties (all in percent, per detector module) of the Chooz experiment (<i>absolute</i>) and projections for Daya Bay (<i>relative</i>). Baseline values for Daya Bay are conservative values achievable through essentially proven methods, whereas the goals should be attainable through additional calibration and analysis efforts described in the text. In addition, the potential improvement from detector swapping is indicated in the last column.	33
2.9	Vertical overburden of the detector sites and the corresponding muon flux and mean energy.	41
2.10	Neutron production rates in a 20-ton module at the Daya Bay sites. The rows labeled "tagged" refer to the case where the parent muon traversed and was detected by the muon detectors, and thus it could be tagged. Rows labeled "untagged" refer to the case where the muon was not identified by the muon detectors.	42
2.11	$^{8}\text{He} + ^{9}\text{Li}$ rates in a 20-ton module at the Daya Bay sites.	43
2.12	Cosmogenic radioactive isotopes without neutron emission but with beta decay energy greater than 6 MeV. Cross sections are taken from KamLAND [16] ($^{12}\text{B}/^{12}\text{N}$) and Hagner [11] (others).	45
2.13	Summary of signal and background rates in the antineutrino detectors at Daya Bay. A neutron detection efficiency of 78% has been applied to the antineutrino and single-neutron rates.	48
2.14	Sources of inefficiency leading to loss of statistical precision.	49
2.15	90% C.L. sensitivity limit for $\sin^2 2\theta_{13}$ at $\Delta m_{31}^2 = 2.5 \times 10^{-3} \text{ eV}^2$ for different assumptions of detector related systematic uncertainties as considered in Section 2.2.3. We assume 3 years running for each scenario.	51
3.1	Average values of meteorological data from the Da Ken station in 1985.	61
3.2	Table of the main civil construction work items.	80

3.3	Cost estimation of the civil construction.	81
3.4	Cost estimation of utilities and safety systems.	82
3.5	Milestones of the civil construction.	82
4.1	Physical requirements of the antineutrino detector.	84
4.2	Radiation from the PMT glass detected in the Gd-scintillator (in Hz) as a function of the oil-buffer thickness (in cm). An oil buffer of more than 45 cm thickness will provide 20 cm of shielding against radiation from the PMT glass.	89
4.3	Radioactivity and single rates of the stainless steel tank.	90
4.4	Dimensions of the mechanical structure and materials of the antineutrino detector modules.	91
4.5	Requirements on the steel tank of the antineutrino detector.	94
4.6	Maximum stress and deformation for two worst cases: that of tank bottom during lifting at an acceleration of 0.1 g, and that of the tank lid happen when submerged the AD in 2.5-m deep water.	97
4.7	Requirements on the acrylic vessels for the antineutrino detector.	99
4.8	Requirements on the overflow tanks of the antineutrino detector.	109
4.9	Input parameters for the FLUENT thermal simulation of the AD.	110
4.10	Technical requirements for the fill/drain mechanism of the antineutrino detector.	112
4.11	Requirements on the liquid scintillator of the antineutrino detector.	114
4.12	Properties of Selected Liquid Scintillators, abs_{430} is the absorption of 430 nm light measured in a 10-cm optical cell.	115
4.13	Light yield for several Gd-LS samples measured relative to an anthracene crystal.	121
4.14	Sizes of the storage pools. The oil pool is designed to contain only one half of the total mineral oil, which will have to be delivered in two batches.	125
4.15	Requirements on the PMTs.	129
4.16	Measured natural radioactivity of glass samples used in R5912, 9354KB, and XP1806 PMTs. 149	
4.17	Requirements on instrumentation/monitoring of the antineutrino detector.	154
5.1	Radioactive sources to be used for calibrations. All of these sources can be used in the manual calibration system with few constraints on the source activity. For the automated calibration system, we choose to use ^{68}Ge and low rate ^{252}Cf neutron sources.	182
5.2	Summary of a typical automated calibration cycle. The left table lists the sources and positions for the two calibration axes in the target region, and the right table is for the axis in the gamma catcher. Note the difference in the z accessibility between the two table, reflecting the larger height occupied by the gamma catcher. The origin of z is defined at the “equator” of the detector. The time to deploy the source to a given position is taken into account in the “Duration” column.	191
6.1	Requirements for Muon system.	197
6.2	Number of PMTs for the water shield.	202
6.3	Water conditioning systems used in previous experiments.	203
6.4	Trigger efficiency as a function of layers and coincidence level	212
6.5	Components of muon system	228
7.1	Requirements for the electronics used to read out the PMTs.	236
7.2	Requirements for the trigger system.	241
7.3	Summary of data rate estimations. kB/s = 1000 bytes per second.	245
8.1	Requirements for Offline.	255
9.1	Positioning accuracy of the principal elements of the Daya Bay experiment.	287

11.1 Uncertainty of the neutron energy threshold efficiency caused by uncertainty in the energy scale for 2-zone and 3-zone detector modules. The energy scale uncertainty is taken to be 1% and 1.2% at 6 MeV and 4 MeV, respectively.	291
16.1 The Daya Bay Subsystem Managers. * Chris Laughton of FNAL has been providing valuable consultation services to the Daya Bay Collaboration on civil construction issues.	324
17.1 Selected Daya Bay milestones.	326
C.1 Summary of scientific requirements.	332
C.2 Requirements on uncertainties necessary to achieve the sensitivity goal of $\sin^2 2\theta_{13} < 0.01$ at 90% C.L.	333
C.3 Physical requirements of the antineutrino detector.	334
C.4 Requirements on the steel tank of the antineutrino detector.	334
C.5 Requirements on the PMTs.	335
C.6 Requirements on the acrylic vessels for the antineutrino detector.	336
C.7 Requirements on the liquid scintillator of the antineutrino detector.	336
C.8 Technical requirements for the fill/drain mechanism of the antineutrino detector.	337
C.9 Requirements on the overflow tanks of the antineutrino detector.	338
C.10 Requirements on instrumentation/monitoring of the antineutrino detector.	338
C.11 Requirements for Muon system.	339
C.12 Positioning accuracy of the principal elements of the Daya Bay experiment.	339
C.13 Requirements for the full manual calibration procedure.	340
C.14 Requirements for automated calibration procedure.	340
C.15 Requirements for the electronics used to read out the PMTs.	341
C.16 Requirements for the trigger system.	341
C.17 Requirements for Offline.	342
C.18 Requirements for Installation.	342
C.19 Requirements for Integration.	342
D.1 Effects of the inner AV wall thickness on the positron energy cut efficiency.	347
D.2 Effects of the inner AV wall thickness on the neutron energy cut efficiency.	347
D.3 Effects of the outer AV dimension changes.	347
D.4 Effects of the rib thickness to energy cut efficiencies and their uncertainties	349
D.5 Effects on the energy cut efficiencies of the inner AV kinematic mounts	350
D.6 Z-dependence of the effects on the energy cut efficiencies due to acrylic in the outer AV	351
D.7 Radial dependence of the neutron energy cut efficiencies of acrylic cylinders in LS	351
D.8 Volume dependence of the neutron energy cut efficiencies of the acrylic presence (represented by a cylinder) in LS	352
D.9 Dimensions of the penetration tubes.	353

1 Overview

The goal of the Daya Bay reactor antineutrino experiment is to determine the unknown neutrino mixing angle θ_{13} with a sensitivity of 0.01 or better in $\sin^2 2\theta_{13}$, an order of magnitude better than the current limit. This section provides an overview of neutrino oscillation phenomenology and the scientific requirements of the experiment.

1.1 Neutrino Oscillation Phenomenology

Compelling evidence for transformation of one neutrino flavor to another (neutrino oscillations) has been observed in solar [1–4], atmospheric [5], reactor [6] and accelerator [7,8] experiments, using a wide variety of detector technologies. The only consistent explanation for these results is that neutrinos have mass and that the mass eigenstates are not the same as the flavor eigenstates (neutrino mixing).

1.1.1 Neutrino Mixing

For three neutrino flavors, the mixing matrix, usually called the Maki-Nakagawa-Sakata-Pontecorvo [9] mixing matrix, is defined to transform the mass eigenstates (ν_1, ν_2, ν_3) to the flavor eigenstates (ν_e, ν_μ, ν_τ) and can be parameterized as

$$\begin{aligned} U_{\text{MNSP}} &= \begin{pmatrix} 1 & 0 & 0 \\ 0 & C_{23} & S_{23} \\ 0 & -S_{23} & C_{23} \end{pmatrix} \begin{pmatrix} C_{13} & 0 & \hat{S}_{13}^* \\ 0 & 1 & 0 \\ -\hat{S}_{13} & 0 & C_{13} \end{pmatrix} \begin{pmatrix} C_{12} & S_{12} & 0 \\ -S_{12} & C_{12} & 0 \\ 0 & 0 & 1 \end{pmatrix} \begin{pmatrix} e^{i\phi_1} & & \\ & e^{i\phi_2} & \\ & & 1 \end{pmatrix} \\ &= \begin{pmatrix} C_{12}C_{13} & C_{13}S_{12} & \hat{S}_{13}^* \\ -S_{12}C_{23} - C_{12}\hat{S}_{13}S_{23} & C_{12}C_{23} - S_{12}\hat{S}_{13}S_{23} & C_{13}S_{23} \\ S_{12}S_{23} - C_{12}\hat{S}_{13}C_{23} & -C_{12}S_{23} - S_{12}\hat{S}_{13}C_{23} & C_{13}C_{23} \end{pmatrix} \begin{pmatrix} e^{i\phi_1} & & \\ & e^{i\phi_2} & \\ & & 1 \end{pmatrix} \quad (1) \end{aligned}$$

where $C_{jk} = \cos \theta_{jk}$, $S_{jk} = \sin \theta_{jk}$, $\hat{S}_{13} = e^{i\delta_{CP}} \sin \theta_{13}$. The neutrino oscillation phenomenology is independent of the Majorana phases ϕ_1 and ϕ_2 .

Neutrino oscillations of three flavors are completely described by six parameters: three mixing angles $\theta_{12}, \theta_{13}, \theta_{23}$, two independent mass-squared differences, $\Delta m_{21}^2 \equiv m_2^2 - m_1^2$, $\Delta m_{32}^2 \equiv m_3^2 - m_2^2$, and one CP -violating phase δ_{CP} (note that $\Delta m_{31}^2 \equiv m_3^2 - m_1^2 = \Delta m_{32}^2 + \Delta m_{21}^2$).

1.1.2 Current Knowledge of Mixing Parameters

Results from solar, atmospheric, reactor, and accelerator neutrino experiments have been used to determine the mixing parameters separately and in global fits. The sixth parameter, the CP -violating phase δ_{CP} , is inaccessible to the present and near future oscillation experiments. We quote here the result of a recent global fit with 2σ (95% C.L.) ranges [10]:

$$\Delta m_{21}^2 = 7.92(1.00 \pm 0.09) \times 10^{-5} \text{ eV}^2 \quad \sin^2 \theta_{12} = 0.314(1.00^{+0.18}_{-0.15}) \quad (2)$$

$$|\Delta m_{32}^2| = 2.4(1.00^{+0.21}_{-0.26}) \times 10^{-3} \text{ eV}^2 \quad \sin^2 \theta_{23} = 0.44(1.00^{+0.41}_{-0.22}) \quad (3)$$

$$\sin^2 \theta_{13} = (0.9^{+2.3}_{-0.9}) \times 10^{-2} \quad (4)$$

Due to the absence of a signal, the global fits on θ_{13} result in upper bounds which vary significantly from one fit to another.

Another very recent global fit [11] with different inputs finds allowed ranges for the oscillation parameters that overlap significantly with the above results even at 1σ (68% C.L.). The latest MINOS neutrino oscillation results [8] significantly overlap those in the global fit [10]. All these signify the convergence to a set of accepted values of neutrino oscillation parameters Δm_{21}^2 , $|\Delta m_{32}^2|$, $\sin^2 \theta_{12}$, and $\sin^2 \theta_{23}$.

The central value of θ_{13} extracted from Eq. 4 is about 5° . This corresponds to a value of 0.036 for $\sin^2 2\theta_{13}$, which should be compared to the best upper limit of 0.17 at 90% C.L. for $\Delta m_{31}^2 = 2.5 \times 10^{-3}$

eV² obtained by Chooz (see Fig. 1.1). We can conclude that, unlike θ_{12} and θ_{23} , the mixing angle θ_{13} is relatively small. The three parameters that are not determined by present data are θ_{13} , the sign of Δm_{32}^2

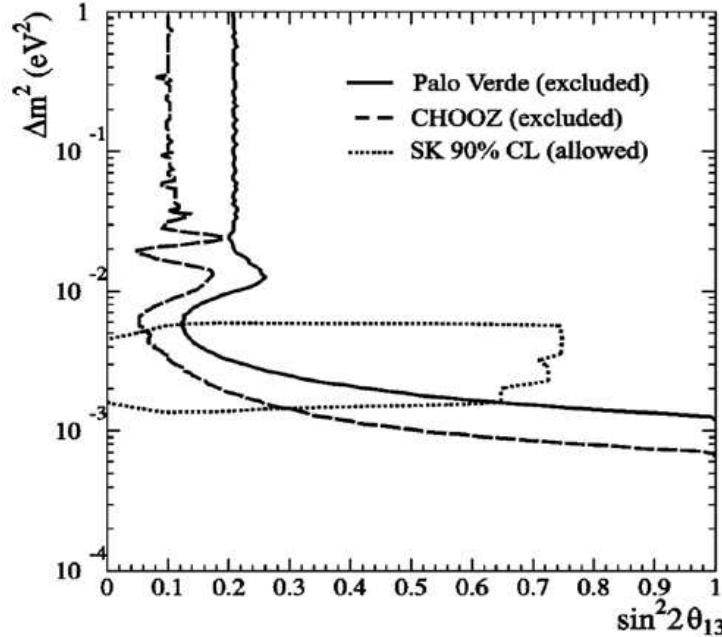


Fig. 1.1. Exclusion contours determined by Chooz, Palo Verde along with the allowed region obtained by Kamiokande. [12]

(which fixes the hierarchy of neutrino masses), and the Dirac CP -violating phase δ_{CP} .

1.1.3 Significance of the Mixing Angle θ_{13}

As one of the six neutrino mass parameters measurable in neutrino oscillations, θ_{13} is important in its own right and for further studies of neutrino oscillations. We need to know the value of θ_{13} to sufficient precision to design experiments to measure δ_{CP} . The matter effect, which can be used to determine the mass hierarchy, also depends on the size of θ_{13} . If $\theta_{13} > 0.01$, then the design of future experiments searching for CP violation is relatively straightforward [13]. However, for smaller θ_{13} new experimental techniques and accelerator technologies are likely required to carry out the measurements. In addition, θ_{13} is important in theoretical model building of the neutrino mass matrix, which can serve as a guide to the theoretical understanding of physics beyond the standard model. Based on these many considerations it is highly desirable to significantly improve our knowledge of θ_{13} in the near future. The February 28, 2006 report of the Neutrino Scientific Assessment Group (NuSAG) [14], which advises the DOE Offices of Nuclear Physics and High Energy Physics and the National Science Foundation, and the APS multi-divisional study's report on neutrino physics, *the Neutrino Matrix* [15], both recommend with high priority a reactor antineutrino experiment to measure $\sin^2 2\theta_{13}$ at the level of 0.01.

1.2 Determining θ_{13} with Nuclear Reactors

Reactor-based antineutrino experiments have the potential of uniquely determining θ_{13} at low cost and in a timely fashion. In this section we summarize the important features of nuclear reactors which are crucial to reactor-based antineutrino experiments.

1.2.1 Energy Spectrum and Flux of Reactor Antineutrinos

Many reactor antineutrino experiments to date have been carried out at pressurized water reactors (PWRs). Such a nuclear power plant derives its power from the fission of uranium and plutonium isotopes (mostly ^{235}U and ^{239}Pu) which are embedded in the fuel rods in the reactor core. The fission produces daughters, many of which beta decay because they are neutron-rich. Each fission on average releases approximately 200 MeV of energy and six antineutrinos. A typical reactor with 3 GW of thermal power (3 GW_{th}) emits 6×10^{20} antineutrinos per second with antineutrino energies up to 8 MeV. The majority of the antineutrinos have very low energies; about 75% are below 1.8 MeV, the threshold of the inverse beta-decay reaction (IBD) that will be discussed in Section 1.2.2.

The antineutrino flux and energy spectrum of a PWR depend on several factors: the total thermal power of the reactor, the fraction of each fissile isotopes in the fuel, the fission rate of each fissile isotope, and the energy spectrum of antineutrinos of the individual fissile isotopes.

The antineutrino yield is directly proportional to the thermal power that is determined by measuring the temperature, pressure and the flow rate of the cooling water. The reactor thermal power is measured continuously by the power plant with a typical precision of about 1%.

Fissile materials in a reactor are continuously consumed while new fissile isotopes are produced from other fissionable isotopes in the fuel (mainly ^{238}U) by fast neutrons. Since the antineutrino energy spectra are slightly different for the four main isotopes, ^{235}U , ^{238}U , ^{239}Pu , and ^{241}Pu , the knowledge on the fission composition and its evolution over time are therefore critical to the determination of the antineutrino flux and energy spectrum. From the average thermal power and the effective energy released per fission [16], the average number of fissions per second of each isotope can be calculated as a function of time. Figure 1.2 shows the results of a computer simulation of the Palo Verde reactor cores [17].

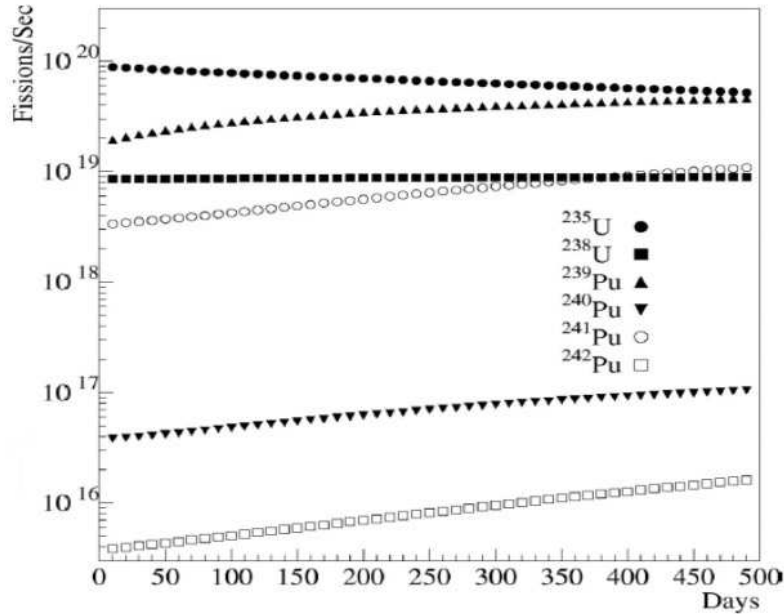


Fig. 1.2. Fission rate of reactor isotopes as a function of time from a Monte Carlo simulation [17].

It is common for a nuclear power plant to replace some of the fuel rods in the core periodically as the fuel is used up. Typically, a core will have 1/3 of its fuel changed every 12 to 18 months. At the beginning of each refueling cycle, 69% of the fissions are from ^{235}U , 21% from ^{239}Pu , 7% from ^{238}U , and 3% from

^{241}Pu . During operation the fissile isotopes ^{239}Pu and ^{241}Pu are produced continuously from ^{238}U . Toward the end of the fuel cycle, the fission rates from ^{235}U and ^{239}Pu are about equal. The average (“standard”) fuel composition responsible for the fission processes is 58% of ^{235}U , 30% of ^{239}Pu , 7% of ^{238}U , and 5% of ^{241}Pu [18].

In general, the composite antineutrino energy spectrum is a function of the time-dependent contributions of the various fissile isotopes to the fission process. The Bugey 3 experiment compared three different models of the antineutrino spectrum with its measurement [19]. Good agreement was observed with the model that made use of the $\bar{\nu}_e$ spectra derived from the β spectra [20] measured at the Institute Laue-Langevin (ILL). However, there is no data for ^{238}U ; only the theoretical prediction is used. The possible discrepancy between the predicted and the real spectra should not lead to significant errors since the contribution from ^{238}U is never higher than 8%. The overall normalization uncertainty of the ILL measured spectra is 1.9%. A global shape uncertainty is also introduced by the conversion procedure.

A widely used three-parameter parameterization of the antineutrino spectrum for the four main isotopes, as shown in Fig. 1.3, can be found in [21]. Per fission, ^{238}U produces the highest number of antineutrinos whereas ^{239}Pu generates the least. In addition, the spectra associated with ^{235}U and ^{241}Pu are almost identical.

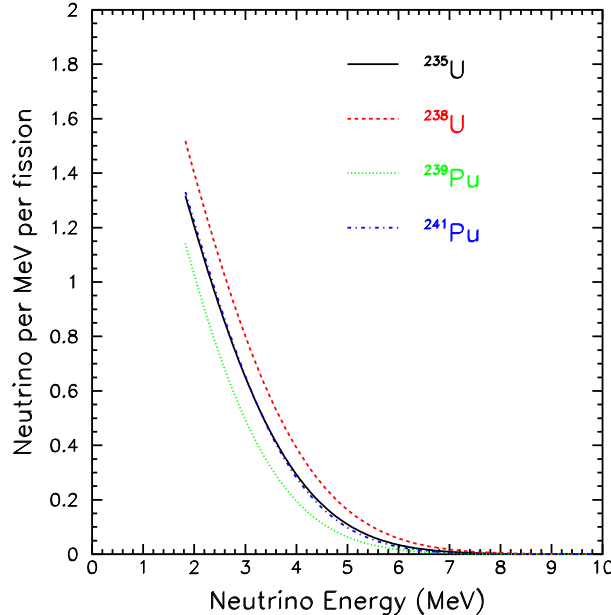


Fig. 1.3. Antineutrino energy spectrum for four isotopes following the parameterization of Vogel and Engel [21].

1.2.2 Inverse Beta-Decay Reaction

The reaction employed to detect the $\bar{\nu}_e$ from a reactor is the inverse beta-decay $\bar{\nu}_e + p \rightarrow e^+ + n$. The total cross section of this reaction, neglecting terms of order E_ν/M , where E_ν is the energy of the antineutrino and M is the nucleon mass, is

$$\sigma_{tot}^{(0)} = \sigma_0(f^2 + 3g^2)(E_e^{(0)} p_e^{(0)}/1\text{MeV}^2) \quad (5)$$

where $E_e^{(0)} = E_\nu - (M_n - M_p)$ is the positron energy when neutron recoil energy is neglected, and $p_e^{(0)}$ is the positron momentum. The weak coupling constants are $f = 1$ and $g = 1.26$, and σ_0 is related to the Fermi

coupling constant G_F , the Cabibbo angle θ_C , and an energy-independent inner radiative correction. The inverse beta-decay process has a threshold energy in the laboratory frame $E_\nu = [(m_n + m_e)^2 - m_p^2]/2m_p = 1.806$ MeV. The leading-order expression for the total cross section is

$$\sigma_{tot}^{(0)} = 0.0952 \times 10^{-42} \text{cm}^2 (E_e^{(0)} p_e^{(0)} / 1 \text{MeV}^2) \quad (6)$$

Vogel and Beacom [22] have recently extended the calculation of the total cross section and angular distribution to order $1/M$ for the inverse beta-decay reaction. Figure 1.4 shows the comparison of the total cross sections obtained in the leading order and the next-to-leading order calculations. Noticeable differences are

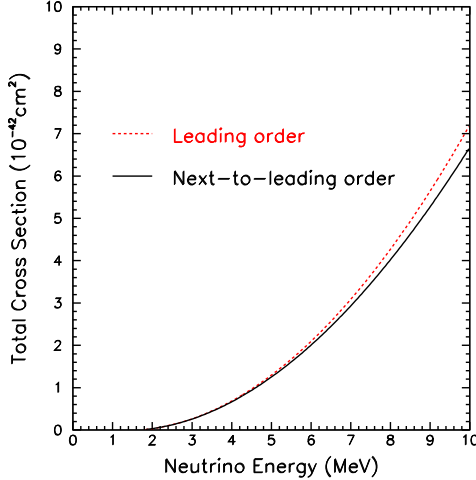


Fig. 1.4. Total cross section for inverse beta-decay calculated in leading order and next-to-leading order.

present for high antineutrino energies. We adopt the order $1/M$ formulae for describing the inverse beta-decay reaction. The calculated cross section can be related to the neutron lifetime, whose uncertainty is only 0.2%.

The expected recoil neutron energy spectrum, weighted by the antineutrino energy spectrum and the $\bar{\nu}_e + p \rightarrow e^+ + n$ cross section, is shown in Fig. 1.5. Due to the low antineutrino energy relative to the mass of the nucleon, the recoil neutron has low kinetic energy. While the positron angular distribution is slightly backward peaked in the laboratory frame, the angular distribution of the neutrons is strongly forward peaked, as shown in Fig. 1.6.

1.2.3 Observed Antineutrino Rate and Spectrum at Short Distance

The observed antineutrino spectrum is a product of the reactor antineutrino spectrum and the inverse beta-decay cross section. Figure 1.7 shows the differential antineutrino energy spectrum, the total cross section of the inverse beta-decay reaction, and the expected count rate as a function of the antineutrino energy. The differential energy distribution is the sum of the antineutrino spectra of all the radio-isotopes in the fuel. It is thus sensitive to the variation of thermal power and composition of the nuclear fuel.

By integrating over the energy of the antineutrino, the number of events can be determined. With one-ton* of LS, a typical rate is about 100 antineutrinos per day per GW_{th} at 100 m from the reactor.

*Throughout this document we will use the term ton to refer to a metric ton of 1000 kg.

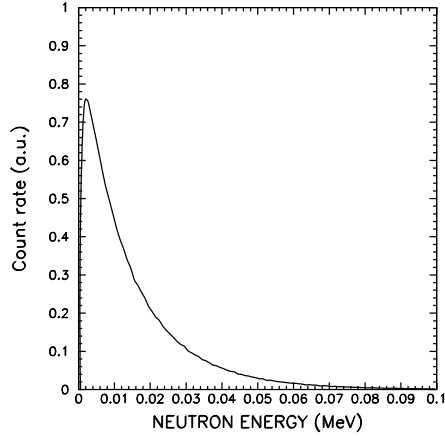


Fig. 1.5. Recoil neutron energy spectrum from inverse beta-decay weighted by the antineutrino energy spectrum.

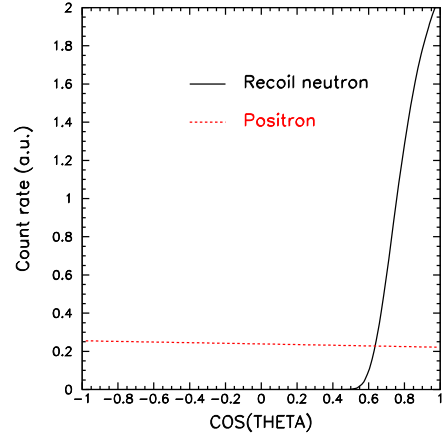


Fig. 1.6. Angular distributions of positrons and recoil neutrons from inverse beta-decay in the laboratory frame.

A small amount of Gd can be dissolved in the LS. After a moderation time of about ten μs , the neutron is captured by a Gd nucleus,[†] emitting several γ -ray photons with a total energy of about 8 MeV. This signal is called the delayed energy, E_d . The temporal correlation between the prompt energy (the positron signal) and the delayed energy constitutes a powerful tool for identifying the $\bar{\nu}_e$ and for suppressing backgrounds.

1.2.4 Reactor Antineutrino Disappearance Experiments

In a reactor-based antineutrino experiment the measured quantity is the survival probability for $\bar{\nu}_e \rightarrow \bar{\nu}_e$ at a baseline of the order of hundreds of meters to about a couple hundred kilometers with the $\bar{\nu}_e$ energy from about 1.8 MeV to 8 MeV. The matter effect is totally negligible and so the vacuum formula for the survival probability is valid. In the notation of Eq. 1, this probability has a simple expression

$$P_{\text{sur}} = 1 - C_{13}^4 \sin^2 2\theta_{12} \sin^2 \Delta_{21} - C_{12}^2 \sin^2 2\theta_{13} \sin^2 \Delta_{31} - S_{12}^2 \sin^2 2\theta_{13} \sin^2 \Delta_{32} \quad (7)$$

where

$$\begin{aligned} \Delta_{jk} &\equiv 1.267 \Delta m_{jk}^2 (\text{eV}^2) \times 10^3 \frac{L(\text{km})}{E(\text{MeV})} \\ \Delta m_{jk}^2 &\equiv m_j^2 - m_k^2 \end{aligned} \quad (8)$$

L is the baseline in km, E the antineutrino energy in MeV, and m_j the j -th antineutrino mass in eV. The $\nu_e \rightarrow \nu_e$ survival probability is given by Eq. 7 which is independent of the CP phase angle δ_{CP} and the mixing angle θ_{23} .

To obtain the value of θ_{13} , the depletion of $\bar{\nu}_e$ has to be extracted from the experimental $\bar{\nu}_e$ disappearance probability,

$$\begin{aligned} P_{\text{dis}} &\equiv 1 - P_{\text{sur}} \\ &= C_{13}^4 \sin^2 2\theta_{12} \sin^2 \Delta_{21} + C_{12}^2 \sin^2 2\theta_{13} \sin^2 \Delta_{31} + S_{12}^2 \sin^2 2\theta_{13} \sin^2 \Delta_{32} \end{aligned} \quad (9)$$

[†]The cross section of neutron capture on H is 0.3 b and 50,000 b on Gd.

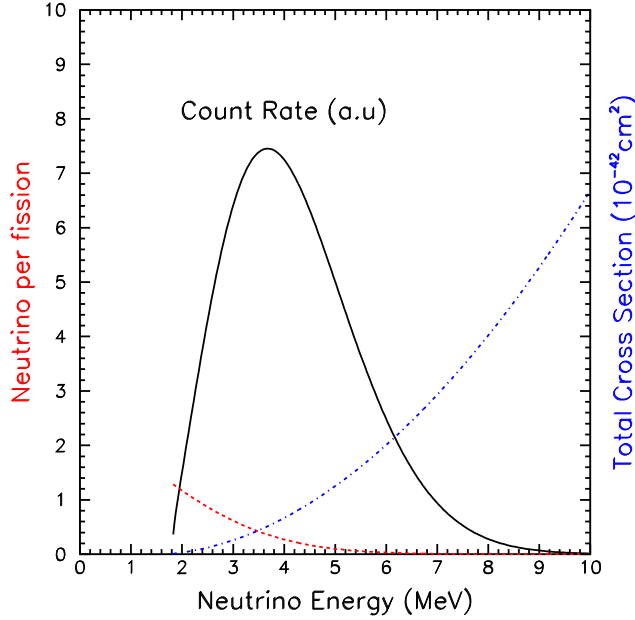


Fig. 1.7. Antineutrino energy spectrum (red dotted curve), total inverse beta-decay cross section (blue dotted-dash curve), and count rate (black solid curve) as a function of antineutrino energy.

Since θ_{13} is known to be less than 10° , we define the term that is insensitive to θ_{13} as

$$P_{12} = C_{13}^4 \sin^2 2\theta_{12} \sin^2 \Delta_{21} \approx \sin^2 2\theta_{12} \sin^2 \Delta_{21} \quad (10)$$

Then the part of the disappearance probability directly related to θ_{13} is given by

$$\begin{aligned} P_{13} &\equiv P_{\text{dis}} - P_{12} \\ &= C_{12}^2 \sin^2 2\theta_{13} \sin^2 \Delta_{31} + S_{12}^2 \sin^2 2\theta_{13} \sin^2 \Delta_{32} \end{aligned} \quad (11)$$

The above discussion shows that in order to obtain θ_{13} we have to subtract the θ_{13} -insensitive contribution P_{12} from the experimental measurement of P_{dis} . To see their individual effect, we plot P_{13} in Fig. 1.8 together with P_{dis} and P_{12} as a function of the baseline from 100 m to 250 km. The antineutrino energy is integrated from 1.8 MeV to 8 MeV. We also take $\sin^2 2\theta_{13} = 0.10$, which will be used for illustration in most of the discussions in this section. The other parameters are taken to be

$$\theta_{12} = 34^\circ, \quad \Delta m_{21}^2 = 7.9 \times 10^{-5} \text{ eV}^2, \quad \Delta m_{31}^2 = 2.5 \times 10^{-3} \text{ eV}^2 \quad (12)$$

The behavior of the curves in Fig. 1.8 are quite clear from their definitions, Eqs. (9), (10), and (11). Below a couple kilometers P_{12} is very small, and P_{13} and P_{dis} track each other well. This suggests that the measurement can be best performed at the first oscillation maximum of $P_{13}(\text{max}) \simeq \sin^2 2\theta_{13}$. Beyond the first minimum P_{13} and P_{dis} deviate from each other more and more as L increases when P_{12} becomes dominant in P_{dis} .

When we determine $P_{13}(\text{max})$ from the difference $P_{\text{dis}} - P_{12}$, the uncertainties on θ_{12} and Δm_{21}^2 will propagate to P_{13} . It is easy to check that, given the best fit values in Eq. 2, when $\sin^2 2\theta_{13}$ varies from 0.01 to

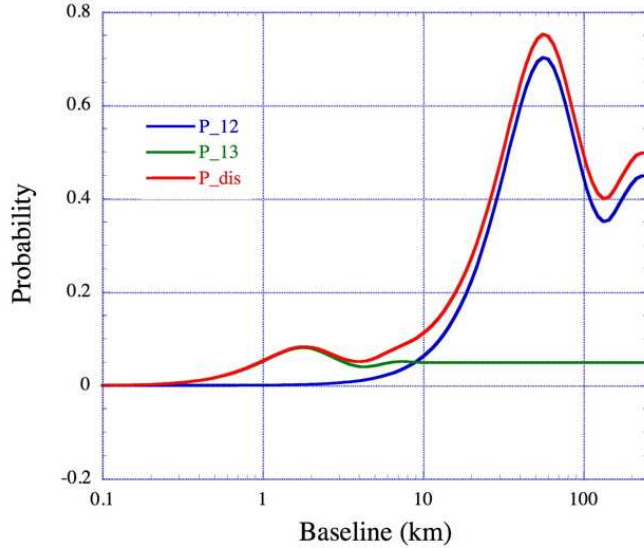


Fig. 1.8. Reactor antineutrino disappearance probability as a function of distance from the source. The values of the mixing parameters are given in Eq. 12. P_{12} is the slowly rising blue curve. P_{13} is the green curve that has a maximum near 2 km. The total disappearance probability P_{dis} is the red curve.

0.10 the relative size of P_{12} compared to P_{13} is about 25% to 2.6% at the first oscillation maximum. Yet the contribution of the uncertainty of P_{12} to the uncertainty in determining $\sin^2 2\theta_{13}$ is always less than 0.005.

In Fig. 1.9, P_{dis} integrated over E from 1.8 to 8 MeV is shown as a function of the baseline L for three values of Δm_{32}^2 that cover the allowed range of Δm_{32}^2 at 95% C.L. as given in Eq. 3. The curves show the location of the oscillation maximum is sensitive to Δm_{32}^2 . For $\Delta m_{32}^2 = (1.8, 2.4, 2.9) \times 10^{-3} \text{ eV}^2$, the oscillation maximum occurs at a baseline of 2.5 km, 1.9 km, and 1.5 km, respectively.[‡] From this simple study, placing the detector between 1.5 km and 2.5 km from the reactor looks to be a good choice.

We conclude from this phenomenological investigation that the choice of L be made so that it can cover as large a range of Δm_{31}^2 as possible. A baseline near 2 km is particularly attractive since it is least sensitive to the value of Δm_{31}^2 .

1.2.5 Precision Measurement of θ_{13}

The value of $\sin^2 2\theta_{13}$ can be determined by comparing the observed antineutrino rate and energy spectrum with predictions assuming no oscillations. The number of detected antineutrinos N_{det} is given by

$$N_{\text{det}} = \frac{N_p}{4\pi L^2} \int \epsilon \sigma P_{\text{sur}} S dE \quad (13)$$

where N_p is the number of free protons in the target, L is the distance of the detector from the reactor, ϵ is the efficiency of detecting an antineutrino, σ is the total cross section of the inverse beta-decay process, P_{sur}

[‡]The latest MINOS results [8] yielded a mean value of Δm_{32}^2 almost identical to that shown in Eq. 3 but with smaller uncertainties such that the 2σ limits are $2.0 \times 10^{-3} \text{ eV}^2$ and $2.8 \times 10^{-3} \text{ eV}^2$. Hence, the curve responding to the lower range of Δm_{32}^2 in Fig. 1.9 will shift closer towards the solid curve if the MINOS error is used in the calculation.

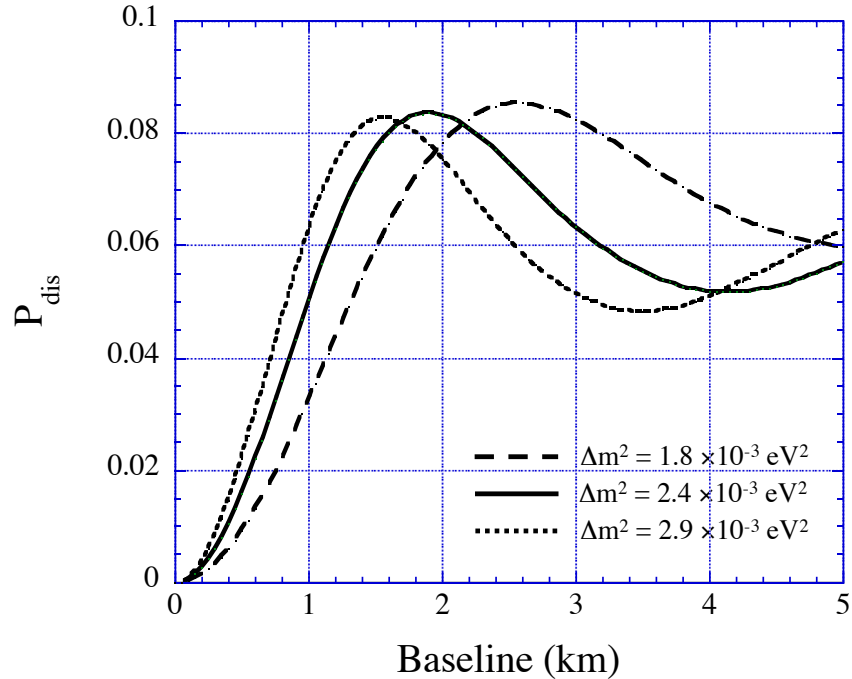


Fig. 1.9. Reactor antineutrino disappearance probability due to the mixing angle θ_{13} as a function of the baseline L over the allowed 2σ range in Δm_{32}^2 .

is the survival probability given in Eq. 7, and S is the differential energy distribution of the antineutrino at the reactor shown in Fig. 1.7.

With only one detector at a fixed baseline from a reactor, according to Eq. 13, we must determine the absolute antineutrino flux from the reactor, the absolute cross section of the inverse beta-decay reaction, and the efficiencies of the detector and event-selection requirements in order to measure $\sin^2 2\theta_{13}$. The prospect for determining $\sin^2 2\theta_{13}$ precisely with a single detector is not promising. It is a challenge to reduce the systematic uncertainties of such an absolute measurement to sub-percent level, especially for reactor-related uncertainties.

Mikaelyan and Sinev pointed out that the systematic uncertainties can be greatly suppressed or totally eliminated when two detectors positioned at two different baselines are utilized [23]. The near detector close to the reactor core is used to establish the flux and energy spectrum of the antineutrinos. This relaxes the requirement of knowing the details of the fission process and operational conditions of the reactor. In this approach, the value of $\sin^2 2\theta_{13}$ can be measured by comparing the antineutrino flux and energy distribution observed with the far detector to those of the near detector after scaling with distance squared. According to Eq. 13, the ratio of the number of antineutrino events with energy between E and $E + dE$ detected at distance L_f (far detector) to that at a baseline L_n (near detector) is given by

$$\frac{N_f}{N_n} = \left(\frac{N_{p,f}}{N_{p,n}} \right) \left(\frac{L_n}{L_f} \right)^2 \left(\frac{\epsilon_f}{\epsilon_n} \right) \left[\frac{P_{\text{sur}}(E, L_f)}{P_{\text{sur}}(E, L_n)} \right] \quad (14)$$

By placing the near detector close to the core such that there is no significant oscillating effect and the contribution of θ_{12} is negligible, $\sin^2 2\theta_{13}$ is approximately given by

$$\sin^2 2\theta_{13} \approx \frac{1}{A(E, L_f)} \left[1 - \epsilon_r \left(\frac{N_f}{N_n} \right) \left(\frac{L_f}{L_n} \right)^2 \right] \quad (15)$$

where $A(E, L_f) = \sin^2 \Delta_{31}$ with Δ_{31} defined in Eq. 8 is the analyzing power and ϵ_r is the relative efficiency of the near and far detectors. The relative detector efficiency can be determined more precisely than the absolute efficiency. Since this is a *relative* measurement, the detector-related systematic uncertainty in this approach is greatly reduced. Indeed, from this simplified picture, it is clear that the two-detector scheme is an excellent approach for precisely determining the value of $\sin^2 2\theta_{13}$. In practice, we need to extend this idea to handle more complicated arrangements involving multiple reactors and multiple detectors as in the case of the Daya Bay experiment.

1.3 The Daya Bay Reactor Antineutrino Experiment

The objective of the Daya Bay experiment is to determine $\sin^2 2\theta_{13}$ with sensitivity of 0.01 or better. In order to meet this goal, it is important to reduce the statistical and systematic uncertainties as well as to suppress backgrounds. A sensitivity of 0.01 (90% C.L.) implies the standard deviation of the measurement is about 0.0061 for a one-parameter fit (namely, $\sin^2 2\theta_{13}$).

This experiment will be located at the Daya Bay nuclear power complex in southern China. Its location is shown in Fig. 1.10. The experimental site is about 55 km north-east from Victoria Harbor in Hong Kong.

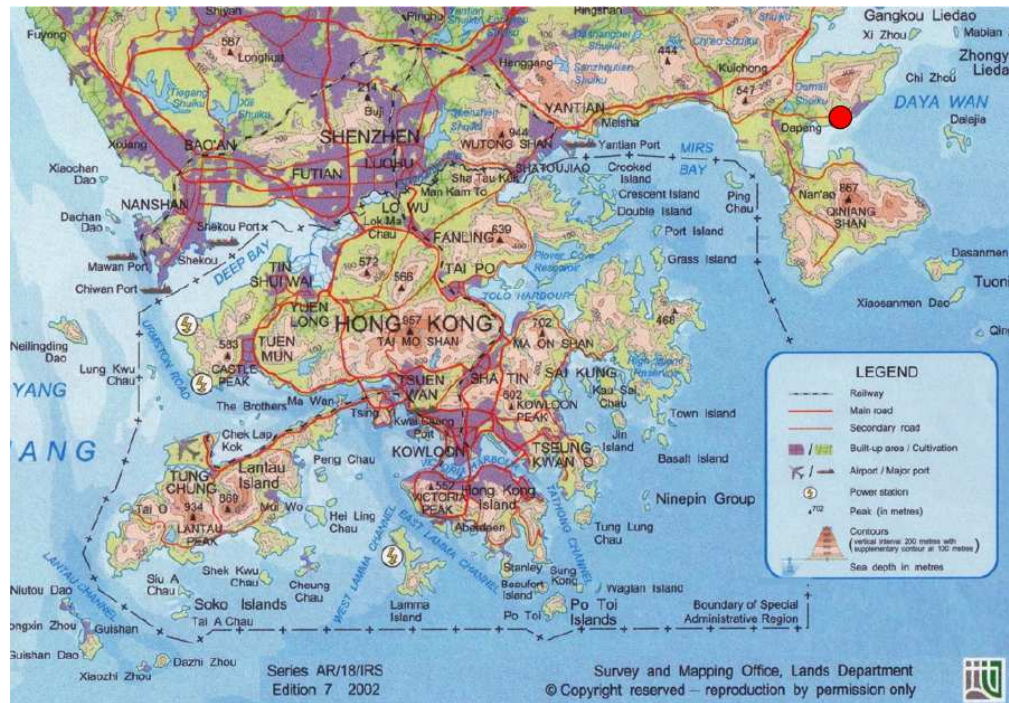


Fig. 1.10. Daya Bay and vicinity: The nuclear power complex (indicated by the red dot at the upper right of the map) is located 55 km from central Hong Kong.

Figure 1.11 is a photograph of the complex. The complex consists of three nuclear power plants (NPPs): the Daya Bay NPP, the Ling Ao NPP, and the Ling Ao II NPP. The Ling Ao II NPP is under construction and will be operational by 2010–2011. Each plant has two identical reactor cores. Each core generates 2.9 GW_{th} during normal operation. The distance between the two cores in each NPP is about 88 m. The Ling Ao cores are about 1.1 km east of the Daya Bay cores, and about 400 m west of the Ling Ao II cores. There are mountain ranges to the north which provide sufficient overburden to suppress cosmogenic backgrounds in the underground experimental halls. Within 2 km of the site the elevation of the mountain varies generally from 185 m to 400 m.



Fig. 1.11. The Daya Bay nuclear power complex. The Daya Bay nuclear power plant is in the foreground. The Ling Ao nuclear power plant is in the background. The experimental halls will be underneath the hills to the left.

The six cores can be roughly grouped into two clusters, the Daya Bay cluster of two cores and the Ling Ao cluster of four cores. We plan to deploy two identical sets of detectors near their respective cluster of cores, one primarily for the Daya Bay cores and the other for the Ling Ao—Ling Ao II cores, to monitor the antineutrino fluxes as precisely as possible. Another set of identical detectors, the far detectors, will be located north of the two near detector sets. Since the overburden of the experimental site increases with distance from the cores, the cosmogenic background decreases as the signal decreases, hence keeping the background-to-signal ratio roughly constant. This is beneficial to controlling systematic uncertainties.

1.3.1 Experimental layout

Taking the current value of $\Delta m_{31}^2 = 2.5 \times 10^{-3}$ eV² (see equation 12), the first maximum of the oscillation associated with θ_{13} occurs at ~ 1800 m. (This also minimizes the dependence on Δm_{31}^2 as discussed in Section 1.2.4). Considerations based on statistics alone will result in a somewhat shorter baseline, especially when the statistical uncertainty is larger than or comparable to the systematic uncertainty. For the Daya Bay experiment, the overburden influences the optimization since it varies along the baseline. In addition, a shorter tunnel will decrease the civil construction cost.

Three major factors are involved in optimizing the locations of the near sites. The first one is overburden. The locations of all the underground detector halls are optimized to provide sufficient overburden to reduce the cosmogenic backgrounds to a level that can be measured with certainty. Since Chooz [12] had an overburden of ~ 300 m.w.e. and achieved a background-to-signal ratio of approximately 0.09, this experiment should have more overburden. The slope of the hills near the site is around 30 degrees. Hence, the overburden falls rapidly as the detector site is moved closer to the cores. The second concern is oscillation loss. The oscillation probability is appreciable even at the near sites. For example, for the near detectors placed approximately 500 m from the center of gravity of the cores, the integrated oscillation probability is $0.19 \times \sin^2 2\theta_{13}$ (computed with $\Delta m_{31}^2 = 2.5 \times 10^{-3}$ eV²). The oscillation contribution of the other pair of cores, which is around 1100 m away, has been included. The third concern is the near-far cancellation of reactor uncertainties.

After careful study of many different experimental designs, the best configuration of the experiment is shown in Fig. 1.12 together with the tunnel layout. Based on this configuration, a global χ^2 fit (see Eq. 29) for the best sensitivity and baseline optimization was performed, taking into account backgrounds, mountain profile, detector systematics and residual reactor related uncertainties. The result is shown in Fig. 1.13.

Ideally each near detector site should be positioned equidistant from the cores that it monitors so that the uncorrelated reactor uncertainties are cancelled. However, taking overburden and statistics into account

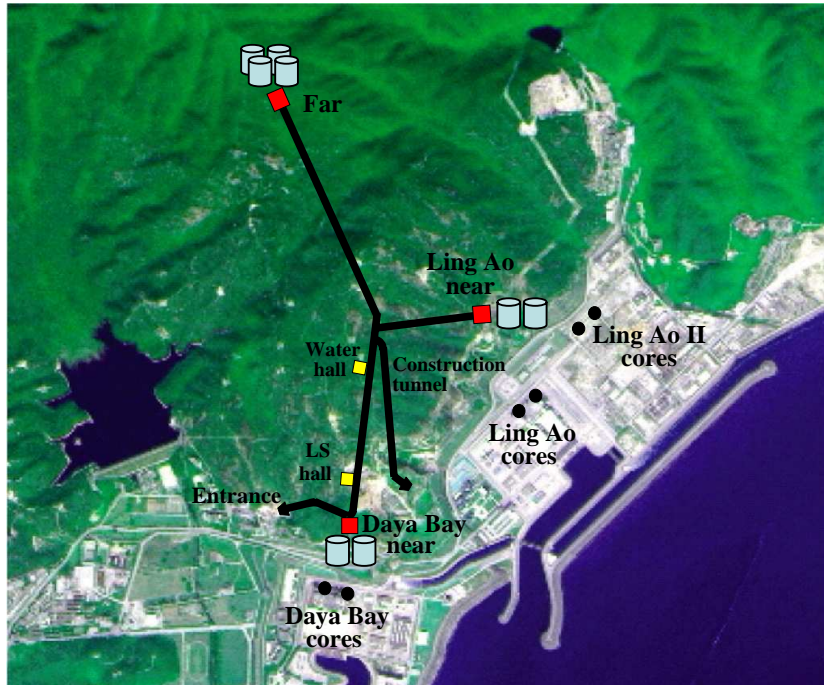


Fig. 1.12. Layout of the Daya Bay experiment.

while optimizing the experimental sensitivity, the Daya Bay near detector site is best located 363 m from the center of the Daya Bay cores. The overburden at this location is 98 m (255 m.w.e.).[§] The Ling Ao near detector hall is optimized to be 481 m from the center of the Ling Ao cores, and 526 m from the center of the Ling Ao II cores[¶] where the overburden is 112 m (291 m.w.e).

The far detector site is about 1.5 km north of the two near sites. Ideally the far site should be equidistant between the Daya Bay and Ling Ao—Ling Ao II cores; however, the overburden at that location would be only 200 m (520 m.w.e). At the optimized locations, the distances from the far detector to the midpoint of the Daya Bay cores and to the mid point of the Ling Ao—Ling Ao II cores are 1985 m and 1615 m, respectively. The overburden is about 350 m (910 m.w.e). A summary of the distances to each detector is provided in Table 1.1. The reactor-related systematic uncertainties cannot be cancelled completely, but can be reduced to a negligible level. From the global fit, a residual reactor uncertainty of <0.1% is obtained.

There are three branches for the main tunnel extending from a junction near the middle of the site to the near and far underground detector halls. There are also access and construction tunnels. The length of the access tunnel, from the portal to the Daya Bay near site, is 292 m. It has a grade of 9.6% [28], which allows the underground facilities to be located deeper with more overburden. The layout of the underground facility is shown in Figure 1.12.

From the global baseline optimization, by comparing the antineutrino fluxes and energy spectra between the near and far detectors, we also conclude we need to collect at least 170,000 events with the far detector

[§]The Daya Bay near detector site is about 40 m east of the perpendicular bisector of the Daya Bay two cores to gain more overburden.

[¶]The Ling Ao near detector site is about 50 m west of the perpendicular bisector of the Ling Ao-Ling Ao II clusters to avoid installing it in a valley which is likely to be geologically weak, and to gain more overburden.

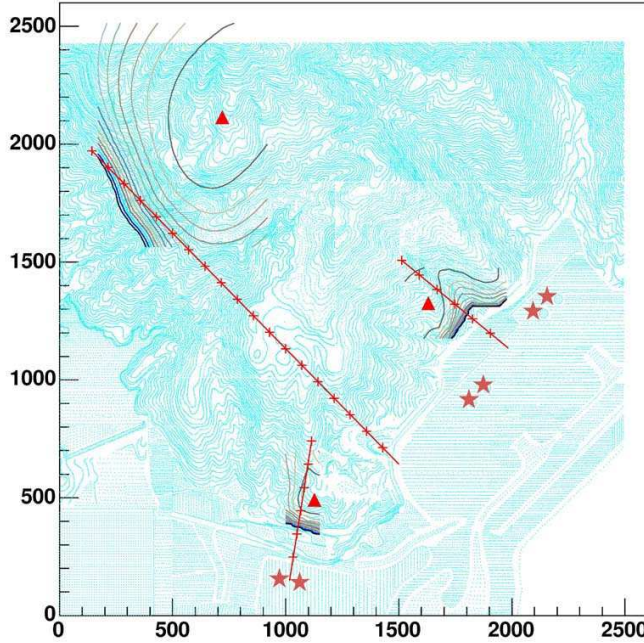


Fig. 1.13. Site optimization using the global χ^2 analysis. The optimal sites are labelled with red triangles. The stars show the reactors. The black contours show the sensitivity when one site's location is varied and the other two are fixed at optimal sites. The red lines with tick marks are the perpendicular bisectors of various combinations of reactors. The mountain contours are also shown on the plot (blue lines).

	DYB	LA	Far
DYB cores	363	1347	1985
LA cores	857	481	1618
LA II cores	1307	526	1613

Table 1.1. Distances (in meters) from each detector site to the centroid of each pair of reactor cores.

in order to establish the presence of neutrino oscillation due to θ_{13} to reach the sensitivity goal. Since the standard error will be 0.0061, Daya Bay would determine the central value of $\sin^2 2\theta_{13}$ derived from Eq. 4 with approximately a six-sigma significance. Table 1.2 is a summary of the scientific requirements for determining $\sin^2 2\theta_{13}$ with a sensitivity of 0.01 at the 90% confidence level.

1.3.2 Detector Design

Besides collecting at least 170,000 antineutrino events at the far site, systematic uncertainties in the ratios of the near-to-far detector acceptance, antineutrino flux and background have to be controlled to a level almost an order of magnitude better than the previous experiments. Based on the recent single-detector reactor experiments such as Chooz, Palo Verde and KamLAND, there are three main sources of systematic uncertainty: reactor-related uncertainty of (2–3)% , background-related uncertainty of (1–3)% , and detector-related uncertainty of (1–3)% . Each source of uncertainty can be further classified into correlated and uncorrelated uncertainties. The experiment must be designed carefully with particular attention to the detector

Item	Requirement	Justification
Sensitivity in $\sin^2 2\theta_{13}$ (90% C.L.)	≤ 0.01	Goal of the experiment as recommended by NuSAG
Standard error of $\sin^2 2\theta_{13}$	0.006	The value corresponding to 90% C.L. is 1.67 times the standard error for one-parameter
Baseline of the far detector	$1.5 \text{ km} \leq L \leq 2 \text{ km}$	Location of the first oscillation maximum due to Δm_{31}^2
Number of events at the far site	$\geq 170,000$	The minimum number of events to reach the designed sensitivity
Background/signal	$\ll 0.09$	This ratio should be much better than that obtained by Chooz since reactor off data is not expected

Table 1.2. Summary of scientific requirements.

mass, efficiency and background control. The primary factors leading to the improved performance are listed below:

- **identical near and far detectors** As discussed in Section 1.2.5, identical antineutrino detectors will be deployed at the near and far sites to minimize the reactor- and detector-related systematic uncertainties. The event samples collected with the near detectors will be used to predict the characteristics of the events observed at the far detectors. Even with several cores at Daya Bay, reactor-related uncertainties can be controlled to a negligible level by carefully optimizing the near and far site locations.
- **multiple modules** multiple identical modules will be installed at the near and far sites to reduce detector-related uncorrelated uncertainties. The use of multiple modules in each site enables internal consistency checks (to the limit of statistics). In addition, multiple modules implies smaller detectors which are easier to move. Furthermore, small detectors intercept fewer cosmic-ray muons, resulting in less dead time, less cosmogenic background and hence smaller systematic uncertainty. Taking calibration and monitoring of the detectors, redundancy and cost into account, we have selected a design with two modules at each near site and four modules at the far site.
- **three-zone detector module** Each module is partitioned into three concentric zones. The innermost zone, filled with Gd-loaded liquid scintillator (Gd-LS), is the antineutrino target which is surrounded by a zone filled with unloaded LS called the γ -catcher. This middle zone is used to capture γ rays, from IBD events, that escape from the target. This arrangement can substantially reduce the systematic uncertainties related to the target volume and mass, positron energy threshold, and position cut. The outermost zone, filled with transparent mineral oil that does not scintillate, shields against external γ rays entering the active LS volume.
- **shielding** In addition to overburden, the antineutrino detector modules will be enclosed with sufficient amount of passive shielding to attenuate natural radiation and energetic spallation neutrons from the surrounding rocks and materials used in the experiment.
- **multiple muon detectors** By tagging the incident muons, the associated cosmogenic background can be suppressed to a negligible level. This requires the muon detectors surrounding the antineutrino detectors to have a high efficiency that is known to high precision. Monte Carlo study shows that the

efficiency of the muon detector should be $\geq 99.5\%$ (with $\sigma_\epsilon \leq 0.25\%$). The muon system is designed to have at least two detector systems in each direction. One system utilizes the water shield as a Cherenkov detector, and another employs muon tracking detectors with a position resolution about 50–100 cm. Each muon detector can easily be constructed with an efficiency of (90–95)% such that the overall efficiency of the muon system will be better than 99.5%. In addition, the two muon detectors can be used to measure the efficiency of each other to a uncertainty of better than 0.25%.

- **movable detectors** The detector modules are movable, such that swapping of modules between the near and far sites can be employed to provide an even higher level of cancellation of the detector-related uncertainties (to the extent that they remain unchanged before and after swapping). The residual uncertainties, being secondary, are caused by the energy scale uncertainties not completely taken out by calibration, as well as other site-dependent uncertainties. The goal is to reduce the systematic uncertainties as much as possible by careful design and construction of detector modules such that swapping of detectors is not necessary. Further discussion of detector swapping will be given in Chapters 2 and 12.

With these improvements, the total detector-related systematic uncertainty is expected to be $\sim 0.2\%$ in the near-to-far ratio per detector site. As discussed above, the antineutrino detector employed at the near (far) site has two (four) modules while the muon detector consists of a cosmic-ray tracking device and active water shield. The antineutrino detector modules are submerged in the water pool, shielding them from ambient radiation and spallation neutrons. The water shield and muon tracking detector are discussed in Section 6. The baseline design of the far site is shown in Fig. 1.14.

The water shield is instrumented with photomultiplier tubes (PMTs) to serve as a Cherenkov detector. The outer region of the water pool is separated from the inner region by an optical barrier to provide two independent systems for detecting muons. Above the pool the muon tracking detector is made of light-weight resistive-plate chambers (RPCs). RPCs offer good performance and excellent position resolution at low cost.

1.3.2.1 Antineutrino detector

As discussed in Sections 1.2.2 and 1.2.3 antineutrinos are detected via the inverse beta-decay reaction in Gd-LS. The prompt positron signal and delayed neutron-capture signal (8 MeV and capture time of 28 μ s) are combined to define a neutrino event with timing and energy requirements on both signals. Both Chooz [29] and Palo Verde [30] used 0.1% Gd-loaded LS that yielded a capture time of 28 μ s, about a factor of seven shorter than in the undoped LS. The large energy release and relatively short capture time provide good suppression of accidental backgrounds.

The specifications for the design of the Daya Bay antineutrino detector modules are given as follows:

- Employ three-zone detector modules partitioned with two acrylic tanks as shown in Fig. 1.15. The target volume is defined by the physical dimensions of the central region of Gd-LS. This target volume is surrounded by an intermediate region filled with normal LS to catch γ rays escaping from the central region. The LS regions are embedded in a volume of mineral oil to separate the PMTs from the LS and suppress natural radioactivity from the PMT glass and other external sources.

Four of these modules, each with 20 ton target mass, will be deployed at the far site to obtain sufficient statistics and two modules will be deployed at each near site, enabling cross calibrations. Deploying an equal number of near and far detectors allows for flexibility in analyzing the data to minimize the systematic uncertainties, such as analyzing with matched near-far pairs.

In this design, the homogeneous target volume is well determined without a position cut since antineutrinos interacting in the unloaded LS will not in general satisfy the high neutron-capture energy

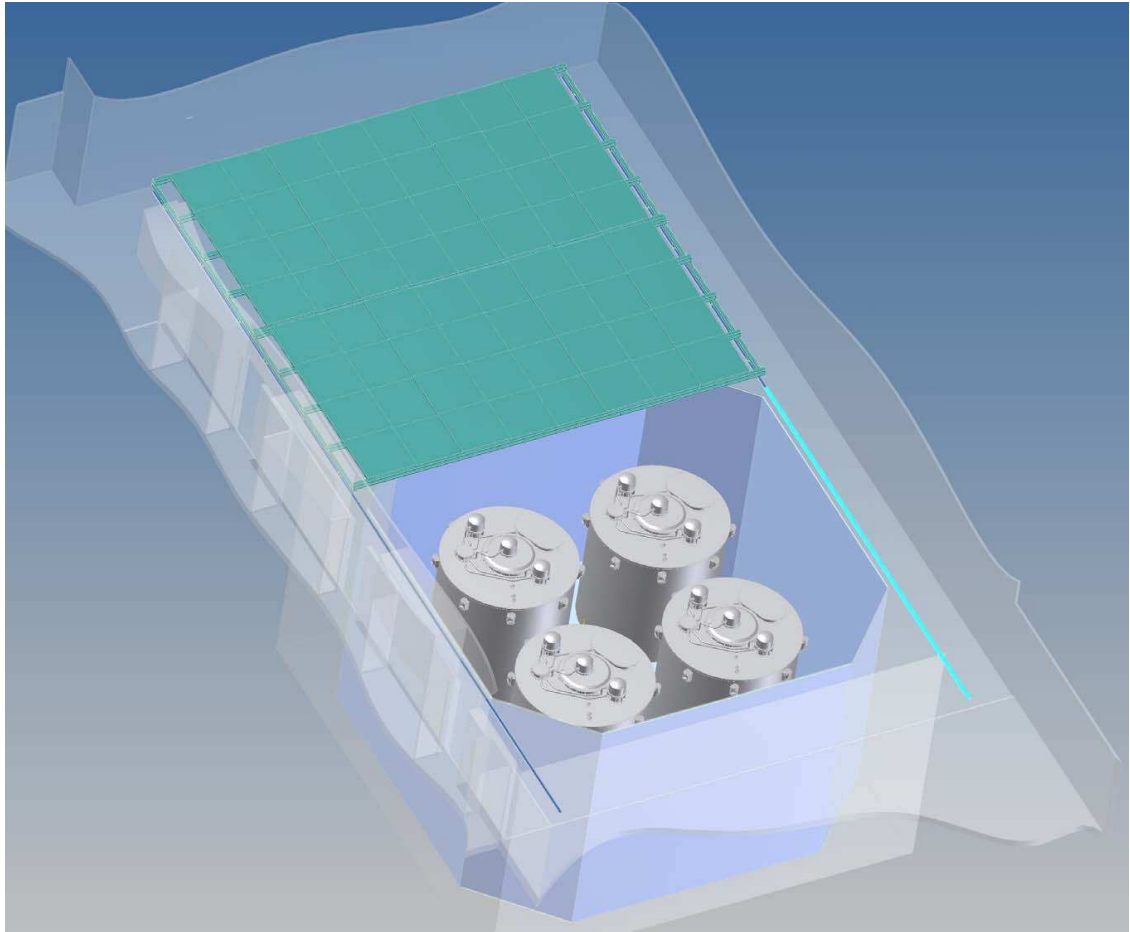


Fig. 1.14. Layout of the baseline design of the Daya Bay detector at the far site. Four antineutrino detector modules are shielded by a 1.5 m-thick active water Cherenkov shield. Surrounding this shield and optically isolated from it is another 1-meter of water Cherenkov shield. (The optical barrier between the two water shields is not shown, nor are the PMTs.) The muon system is completed with RPCs at the top (which are shown in the retracted position).

requirement with Gd. Each vessel will be carefully measured to determine its volume and each vessel will be filled with the same set of mass-flow and volumetric flow meters to minimize any variation in the relative detector volume and mass. The effect of neutron spill-in and spill-out across the boundary between the two LS regions will be cancelled when pairs of identical detector modules are used at the near and far sites. With the shielding of mineral oil, the singles rate will be reduced substantially. The trigger threshold can thus be lowered to below 1.0 MeV, providing \sim 100% detection efficiency for the prompt positron signal.

- The Gd-LS, which is the antineutrino target, should have the same composition and fraction of hydrogen for each pair of detectors (one at a near site and the other at the far site). The detectors will be filled from a common storage vessel to assure that the composition of the LS is the same. Other detector components such as unloaded LS and PMTs will be characterized and distributed evenly to a pair of detector modules during assembly to equalize the properties of the modules.

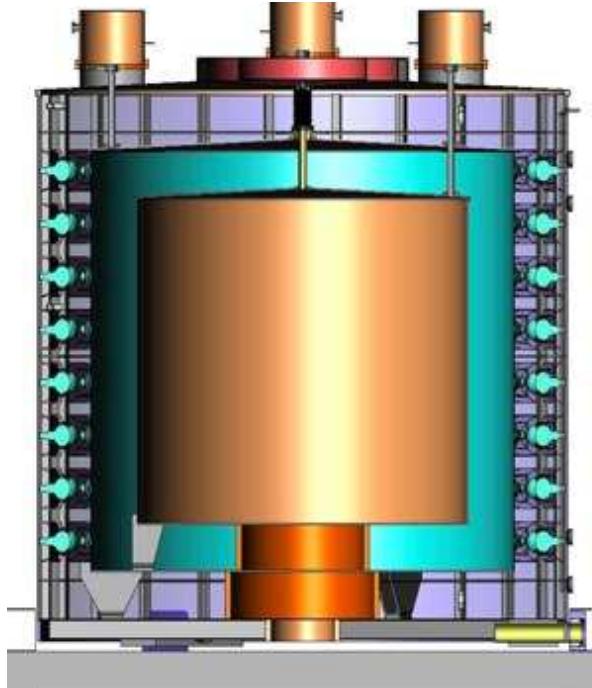


Fig. 1.15. Cross sectional slice of a 3-zone antineutrino detector module showing the inner acrylic vessel holding the Gd-LS at the center (20 ton), LS between the acrylic vessels (20 ton) and mineral oil (40 ton) in the outer region. The PMTs are mounted on the inner surface of the stainless steel tank in the mineral oil.

- The energy resolution should be better than 15% at 1 MeV. Good energy resolution is desirable for reducing the energy-related systematic uncertainty on the neutron energy cut. Good energy resolution is also important for studying spectral distortion as a signature of neutrino oscillation. The primary driver for the energy resolution is to achieve sufficient energy calibration precision for neutron captures throughout the detector volume in a reasonable time.
- The time resolution should be better than 1 ns for determining the event time and for studying backgrounds.

Detector modules of different shapes, including cubical, cylindrical, and spherical, have been considered. From the point of view of ease of construction cubical and cylindrical shapes are particularly attractive. Monte Carlo simulation shows that cylindrical modules can provide better energy and position resolutions for the same number of PMTs. Figure 1.15 shows the structure of a cylindrical module. The PMTs are arranged along the circumference of the outer cylinder. The surfaces at the top and the bottom of the outermost acrylic cylinder are covered with a reflective material. Such an arrangement is feasible since 1) the event vertex is determined only with the center of gravity of the charge, not relying on the time-of-flight information,^{||} 2) the fiducial volume is well defined with a three-zone structure, thus no accurate vertex information is required. Details of the antineutrino detector will be discussed in Chapter 4.

^{||}Although time information may not be used in reconstructing the event vertex, it will be used in background studies. A time resolution of 0.5 ns can be easily realized in the readout electronics.

1.3.2.2 Muon detector

Since most backgrounds originate from cosmic-ray muon interactions with nearby materials, it is desirable to have a very efficient muon detector with some tracking capability. This enables the study and rejection of cosmogenic backgrounds. The two selected detector technologies are water Cherenkov counters and RPCs. The combined water Cherenkov detector and RPC can achieve muon detection efficiencies close to 100%. Furthermore, these two independent detectors can cross check each other. Their inefficiencies and the associated uncertainties can be well determined by cross calibration during data taking. We expect the inefficiency will be smaller than 0.5% and the uncertainty of the inefficiency will be better than 0.25%.

Besides being a shield against ambient radiation, the water shield can also be utilized as a water Cherenkov counter by installing PMTs in the water. The water Cherenkov detector is based on proven technology, and known to be very reliable. With sufficient PMT coverage and reflective surfaces, the efficiency of detecting muons should exceed 95%. The current baseline design of the water shield is a water pool, similar to a swimming pool with a dimensions of 16 m (length) \times 16 m (width) \times 10 m (height) for the far hall containing four detector modules, as shown in Fig. 1.14. The PMTs of the water Cherenkov counters are mounted facing the inside of the water volume. This is a simple and proven technology with very limited safety concerns. The water will effectively shield the antineutrino detectors from radioactivity in the surrounding rocks and from radon, with the attractive features of being simple, cost-effective and rapidly deployable.

RPCs are very economical for instrumenting large areas and are simple to fabricate. The Bakelite-based RPC developed by IHEP for the BES-III detector has a typical efficiency of 95% and noise rate of 0.1 Hz/cm² per layer [31]. A possible configuration is to build four layers of RPC, and require three out of four layers to have a hit within a time window of 20 ns to define a muon event. Such a scheme has high efficiency and low noise rate. Although RPCs provide an ideal large-area muon detector due to their light weight, good performance, excellent position resolution and low cost, it is impractical to put them in water. Therefore they will only be deployed on top of the water pool.

1.3.2.3 WBS

The plan for construction of the Daya Bay detector is described by the Daya Bay work breakdown structure (WBS), which has ten major categories as shown in Table 1.3. More details can be found in the Resource Loaded Schedule (RLS).

WBS element	Task Name
1.1	Antineutrino Detector
1.2	Muon System
1.3	Calibration and Monitoring Systems
1.4	Electronics, Trigger, DAQ and Online
1.5	Offline
1.6	Conventional Construction and Equipment
1.7	Installation and Test
1.8	Integration
1.9	PMT
1.10	Project Management

Table 1.3. Daya Bay Work Breakdown Structure (WBS) shown at L2.

REFERENCES

1. B. T. Cleveland *et al.*, *Astrophys. J.* **496** (1998) 505.
2. Y. Fukuda *et al.* (SuperK Collaboration), *Phys. Rev. Lett.*, **81** (1998) 1158 [arXiv:hep-ex/9805021]; **82** (1999) 2430 [arXiv:hep-ex/9812011]; S. Fukuda *et al.*, *Phys. Rev. Lett.* **86** (2001) 5651 [arXiv:hep-ex/010302]; M. B. Smy *et al.*, *Phys. Rev.* **D69** (2004) 011104 [arXiv:hep-ex/0309011].
3. J. N. Abdurashitov *et al.* (SAGE Collaboration), *J. Exp. Theor. Phys.* **95** (2002) 181 [arXiv:astro-ph/0204245]; W. Hampel *et al.* (GALLEX Collaboration), *Phys. Lett.* **B447** (1999) 127; M. Altman *et al.* (GNO Collaboration), *Phys. Lett.* **B490** (2000) 16 [arXiv:hep-ex/0006034].
4. Q.R. Ahmad et at. (SNO Collaboration), *Phys. Rev. Lett.* **87** 071301 [arXiv:nucl-ex/0106015]; **89** (2002) 011301 [arXiv:nucl-ex/0204008]; **89** (2002) 011302 [arXiv:nucl-ex/0204009]; **92** (2004) 181301 [arXiv:nucl-ex/0309004]; *Phys. Rev.* **C72** (2005) 055502 [arXiv:nucl-ex/0502021].
5. Y. Fukuda *et al.* (SuperK Collaboration), *Phys. Lett.* **B433** (1998) 9 [arXiv:hep-ex/9803006]; **B436** (1998) 33 [arXiv:hep-ex/9805006]; *Phys. Rev. Lett.*, **81** (1998) 1562 [arXiv:hep-ex/9807003]; S. Fukuda *et al.*, *Phys. Rev. Lett.* **85** (2000) 3999 [arXiv:hep-ex/0009001]; Y. Ashie *et al.*, *Phys. Rev. Lett.* **93** (2004) 101801 [arXiv:hep-ex/0404034].
6. K. Eguchi *et al.* (KamLAND Collaboration), *Phys. Rev. Lett.*, **90** (2003) 021802 [arXiv:hep-ex/0212021]; **94** (2005) 081801 [arXiv:hep-ex/0406035].
7. E. Aliu *et al.* (K2K Collaboration), *Phys. Rev. Lett.* **94** (2005) 081802 [arXiv:hep-ex/0411038].
8. The MINOS Collaboration, arXiv:0708.1495 [hep-ex].
9. Z. Maki, M. Nakagawa, and S. Sakata, *Prog. Theor. Phys.* **28** (1962) 870; B. Pontecorvo, *Sov. Phys. JETP* **26** (1968) 984; V.N. Gribov and B. Pontecorvo, *Phys. Lett.* **28B** (1969) 493.
10. G.L. Fogli, E. Lisi, A. Marrone, and A. Palazzo, and A.M. Rotunno, 40th Rencontres de Moriond on Electroweak Interactions and Unified Theories, La Thuile, Aosta Valley, Italy, 5-12 March 2005 [arXiv:hep-ph/0506307].
11. T. Schwetz, Talk given at 2nd Scandinavian Neutrino Workshop (SNOW 2006, Stockholm Sweden, 2-6 May 2006 [arXiv:hep-ph/0606060].
12. M. Apollonio *et al.* (Chooz Collaboration), *Eur. Phys. J.* **C27**, 331 (2003) [arXiv:hep-ex/0301017].
13. K. Anderson, *et al.*, *White paper report on using nuclear reactors to search for a value of θ_{13}* , arXiv:hep-ex/0402041.
14. ‘Recommendations to the Department of Energy and the National Science Foundation on a U.S. Program of Reactor- and Accelerator-based Neutrino Oscillations Experiments’, <http://www.science.doe.gov/hep/NuSAG2ndRptFeb2006.pdf>
15. The Neutrino Matrix, <http://www.aps.org/neutrino/>
16. M.F. James, *J. Nucl. Energy* **23** 517 (1969).
17. L. Miller, Ph.D Thesis, Stanford University, 2000, unpublished.
18. V.I. Kopeikin, *Phys. Atom. Nucl.* **66** (2003) 472 [arXiv:hep-ph/0110030].
19. B. Achkar *et al.*, *Phys. Lett.* **B374** 243 (1996).
20. K. Schreckenbach *et al.*, *Phys. Lett.* **B160**, 325 (1985); A. A. Hahn *et al.*, *Phys. Lett.* **B218**, 365 (1989).
21. P. Vogel and J. Engel, *Phys. Rev.* **D39**, 3378 (1989).
22. P. Vogel and J. F. Beacom, *Phys. Rev.* **D60**, 053003 (1999) [arXiv:hep-ph/9903554].
23. L.A. Mikaelyan and V.V. Sinev, *Phys. Atomic Nucl.* **63** 1002 (2000) [arXiv:hep-ex/9908047].
24. M. Kuze *et al.*, *The KASKA project - a Japanese medium-baseline reactor-neutrino oscillation experiment to measure the mixing angle θ_{13}* , arXiv:hep-ex/9908047.
25. K.K.Joo, *Progress Report on RENO*, talk presented at NOW 2006, Otranto, Italy, September 9-16, 2006.
26. F. Ardellier *et al.* (Double Chooz Collaboration), *Double Chooz: A Search for the Neutrino Mixing Angle θ_{13}* , arXiv:hep-ex/0606025.
27. L.A. Mikaelyan and V. V. Sinev, *Phys. Atom. Nucl.* **63**, 1002 (2000); L. Mikaelyan, *Nucl. Phys. Proc. Suppl.* **91**, 120 (2001); L.A. Mikaelyan, *Phys. Atom. Nucl.* **65**, 1173 (2002).

28. *Report of Preliminary Feasibility Study of Site Selection for the Daya Bay Neutrino Experiment*, prepared by Beijing Institute of Nuclear Energy, September, 2004.
29. M. Apollonio *et al.* (Chooz Collaboration), Phys. Lett. **B420**, 397 (1998); Phys. Lett. **B466**, 415 (1999); Eur. Phys. J. **C27**, 331 (2003).
30. F. Boehm *et al.* (Palo Verde Collaboration), Phys. Rev. Lett. **84**, 3764 (2000) [arXiv:hep-ex/9912050]; Phys. Rev. **D62**, 072002 (2000) [arXiv:hep-ex/0003022]; Phys. Rev. **D64**, 112001 (2001) [arXiv:hep-ex/0107009]; A. Piepke *et al.*, Nucl. Instr. and Meth. **A432**, 392 (1999).
31. J.W. Zhang *et al.*, High Energy Phys. and Nucl. Phys., **27**, 615 (2003); JiaWen Zhang *et al.*, Nucl. Inst. Meth. **A540**, 102 (2005).

2 Sensitivity & Systematic Uncertainties

The control of systematic uncertainties is critical to achieving the $\sin^2 2\theta_{13}$ sensitivity goal of this experiment. The most relevant previous experience is the Chooz experiment [1] which obtained $\sin^2 2\theta_{13} < 0.17$ for $\Delta m_{31}^2 = 2.5 \times 10^{-3} \text{ eV}^2$ at 90% C.L., the best limit to date, with a systematic uncertainty of 2.7% and statistical uncertainty of 2.8% in the ratio of observed to expected events at the ‘far’ detector. In order to achieve a $\sin^2 2\theta_{13}$ sensitivity below 0.01, both the statistical and systematic uncertainties need to be an order of magnitude smaller than Chooz. The requirements on the statistical uncertainties, systematic uncertainties, and background measurements for the Daya Bay experiment to reach the design sensitivity are listed in Table 2.1.

Requirement	Near Site	Far Site	Justification
Statistical uncertainty	0.07% per site	$\leq 0.24\%$	Far site should be less than the systematic uncertainty and allow a total uncertainty of less than 0.006. Near sites will have very good statistics.
Detector systematic uncertainty	$\leq 0.38\%/\text{module}$		Must allow a total uncertainty of less than 0.006, should not be much larger than the statistical or background uncertainties
Reactor power systematic	$\leq 0.2\%$		Should be small compared to other uncertainties, is satisfied with two near sites and any reasonable assumption on the uncorrelated power uncertainty on a single core
Background uncertainty	0.3% per site	0.2%	Dominated by ${}^9\text{Li}$; sets a limit on the size of a detector, and is improved by putting detectors deeper. (Motivates siting the halls 20 m below sea level.)

Table 2.1. Requirements on uncertainties necessary to achieve the sensitivity goal of $\sin^2 2\theta_{13} < 0.01$ at 90% C.L.

In this chapter we discuss our strategy for achieving the levels of uncertainty in Table 2.1. Achieving these goals will require special care and substantial effort, and can only be realized by incorporating rigid constraints in the design of the experiment.

There are three main sources of systematic uncertainties: reactor, background, and detector. Each source of uncertainty can be further classified into correlated and uncorrelated uncertainties.

2.1 Reactor Related Uncertainties

For a reactor with only one core, all uncertainties from the reactor, correlated or uncorrelated, can be canceled precisely by using one far detector and one near detector (assuming the distances are precisely known) and forming the ratio of measured antineutrino fluxes [2]. In reality, the Daya Bay nuclear power complex has four cores in two groups, the Daya Bay NPP and the Ling Ao NPP. Another two cores will be installed adjacent to Ling Ao, called Ling Ao II, which will start to generate electricity in 2010–2011. Figure 1.12 shows the locations of the Daya Bay cores, Ling Ao cores, and the future Ling Ao II cores. Superimposed on the figure are the tunnels and detector sites. The distance between the two cores at each NPP is about 88 m. The midpoint of the Daya Bay cores is 1100 m from the midpoint of the Ling Ao

cores, and will be 1600 m from the Ling Ao II cores. For this type of arrangement, with more reactor cores than near detectors, one must rely upon the measured reactor power levels in addition to forming ratios of measured antineutrino fluxes in the detectors. Thus there is a residual uncertainty in the extracted oscillation probability associated with the uncertainties in the knowledge of the reactor power levels. In addition to the reactor power uncertainties, there are uncertainties in the effective locations of the cores relative to the detectors. The effects of different fuel composition in the reactor cores are higher order and their contribution to the uncertainty is negligible.

2.1.1 Power Fluctuations

Typically, the measured power level for each reactor core will have a correlated (common to all the reactors) uncertainty of the order of 2% and an uncorrelated uncertainty of similar size. Optimistically, we may be able to achieve uncorrelated uncertainties of 1%, but we conservatively assume that each reactor has 2% uncorrelated uncertainty in the following. (We note that both Chooz and Palo Verde achieved total reactor power uncertainties of 0.6–0.7%. The appropriate value for the Daya Bay reactors will need to be studied in detail with the power plant and could hopefully be reduced below 2% per core.) If the distances are precisely known, the correlated uncertainties will cancel in the near/far ratio.

For the geometry of the Daya Bay experiment, we have (effectively) two near detectors. One near site primarily samples the rate from the two Daya Bay cores and the other primarily samples the rate from the (two or four) Ling Ao cores. The detectors at the far site do not sample the reactor cores equally, so one needs to consider the weighting of the data from the near sites relative to the far site. In order to provide optimal relative weights of the near sites one can utilize the following combination of ratios in the event rates of the far and near detectors:

$$\rho = \left[\alpha \sum_r \frac{\phi_r}{(L_r^{DB})^2} + \sum_r \frac{\phi_r}{(L_r^{LA})^2} \right] \Bigg/ \sum_r \frac{\phi_r}{(L_r^f)^2} \quad (16)$$

where ϕ_r is the antineutrino flux at unit distance from core r , L_r^f is the distance from reactor r to the far site, L_r^{DB} (L_r^{LA}) is the distance from reactor r to the near Daya Bay (Ling Ao) site, and α is a constant chosen to provide the proper weighting of the near site data and minimize the sensitivity of ρ to the uncertainties in the relative reactor power levels. (Note that $\sum_r \phi_r / L_r^2$ is the event rate to be measured at each site in the absence of neutrino oscillations. In Eq. 16 we have neglected neutrino oscillations. In the absence of oscillations and given a value of α , the quantity ρ is completely determined by the geometry. Thus a measurement of ρ that differs from this value could then be used to determine the oscillation probability that depends upon $\sin^2 2\theta_{13}$ with minimal systematic uncertainty due to the uncorrelated reactor power uncertainties.)

To illustrate the utility of the ratio ρ in Eq. 16, we can consider a slightly simplified geometry where there are only two cores and two near detectors. Each near detector is located at the same close distance from one reactor core. Assuming the cross-talk in a near detector from the other core can be neglected then the value of $\alpha = (L_{LA}^f / L_{DB}^f)^2$ will correct the ratio ρ for the fact that the two reactors are not sampled equally by the far detector. (Here L_{DB}^f and L_{LA}^f are the distances of the far detector from the two reactor cores.) Then the ratio ρ would be independent of the reactor power uncertainties.

For the more complex situation as in Fig. 1.12, the optimal choice of the weighting factor α is somewhat different, and can be computed from knowledge of the relative distances and powers of the reactor cores. One can also determine α by Monte Carlo simulations that minimize the systematic uncertainty in ρ due to uncorrelated reactor power uncertainties. The weighting of near sites using α does introduce a slight degradation (in our case <11% fractional increase) in the statistical uncertainty. The correlated uncertainties of the reactors are common to both the numerator and denominator of the ratio ρ , and therefore will cancel.

Using the detector configuration shown in Fig. 1.12, with two near sites at ~ 500 m baselines to sample the reactor power and a far site at an average baseline of ~ 1800 m, an uncorrelated uncertainty of 2% for

each core and optimal choice of α leads to the estimated reactor power contribution to σ_ρ (i.e., the fractional uncertainty in the ratio ρ) shown in Table 2.2 for the case of four (six) reactor cores. In Section 2.4.1 below,

Number of cores	α	$\sigma_\rho(\text{power})$	$\sigma_\rho(\text{location})$	$\sigma_\rho(\text{total})$
4	0.338	0.035%	0.08%	0.087%
6	0.392	0.097%	0.08%	0.126%

Table 2.2. Reactor-related systematic uncertainties for different reactor configurations.
The uncorrelated uncertainty of the power of a single core is assumed to be 2%.

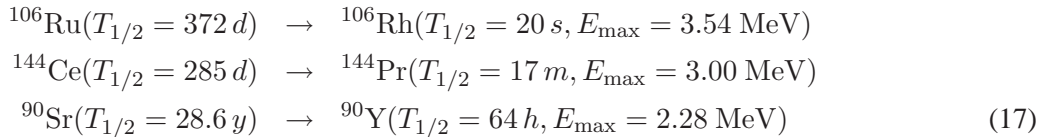
we study the sensitivity of the Daya Bay experiment to neutrino oscillations and $\sin^2 2\theta_{13}$ using a more general χ^2 analysis that includes all the significant sources of systematic uncertainty. The optimal weighting of near sites in that analysis is implemented by allowing all the reactor core powers to vary in the χ^2 minimization associated with the measured rates in the different detectors.

2.1.2 Location Uncertainties

The center of gravity of the antineutrino source in each core will be determined to a precision of about 30 cm. We assume that the location uncertainties are uncorrelated, and so their combined effect will be reduced by $\sim \sqrt{N_r}$ where N_r is the number of reactor cores. The resulting fractional uncertainty in the near/far event ratio is estimated to be 0.08% for the near baseline of ~ 500 m.

2.1.3 Spent Fuel Uncertainties

In addition to fission, beta decay of some fission products can also produce antineutrinos with energy higher than the inverse beta decay threshold 1.8 MeV. Some of these have long lifetimes, such as [3]



These isotopes will accumulate in the core during operations. Normally a fuel rod will produce power in the core for 2–3 years. The inverse beta decay rate arising from these fission products will increase to 0.4–0.6% of the total event rate. In the 1.8–3.5 MeV range, the yield will increase to about 4%. Neutron capture by fission products will also increase the total rate by 0.2% [3].

The Daya Bay and Ling Ao NPPs store their spent fuel in water pools adjoining the cores. A manipulator moves the burnt-out fuel rods from the core to the water pool during refueling. The long lived isotopes mentioned in the previous paragraph will continue to contribute to the antineutrino flux. The spent fuel data, as well as the realtime running data, will be provided to the Daya Bay Collaboration by the power plant.

Taking the average of all fuel rods at different life cycles, and the decay in the spent fuel, these isotopes are estimated to contribute <0.5% to the event rate (prior to receiving the detailed reactor data). All of these events are in the low energy region. Since the spent fuel is stored adjoining to the core, the uncertainty in the flux will be canceled by the near-far relative measurement, in the same way as the cancellation of the reactor uncertainties. The uncertainty associated with the spent fuel is much smaller than the assumed 2% uncorrelated uncertainty of reactor fission, and thus we expect it will have negligible impact on the θ_{13} sensitivity.

2.2 Detector Performance

The measurement of $\sin^2 2\theta_{13}$ to a precision of 0.01 in the Daya Bay experiment will require special care in detector building, characterization of the detector properties, and frequent monitoring of the detector

performance and condition. We begin this section by discussing our strategies and methods for addressing the fabrication and deployment issues that will result in well-understood detector modules. The properties of the detector affecting the performance goals must be then calibrated and monitored, and we will implement a comprehensive program for calibrating and monitoring the detector modules. Finally we then estimate the resulting expected detector-related systematic uncertainties.

2.2.1 Fabrication, Assembly, and Filling

The most stringent requirement for the detector construction is the control of detector geometry, the target mass, and the chemical composition of the scintillator liquid. Before transporting the detector modules underground, the geometry of the detector modules will be surveyed carefully with laser devices, which can achieve $<25\text{ }\mu\text{m}$ precision in measuring detector dimensions. (Note that $<0.1\text{ mm}$ precision is required to achieve a 0.01% precision in target volume measurement.) In-situ monitoring equipment inside the detector modules will then be used to track any changes during the transport or filling of the modules.

The filling of the detectors will be performed underground. Liquids from a common storage tank will be used to fill a pair of detectors in close time sequence to ensure the same chemical composition. During the filling, the flow rate will be monitored constantly with high precision mass flowmeters to ensure the same target mass between the pair. In each detector module, we will have load sensors, liquid level sensors in each zone, as well as CCD cameras to monitor the detector conditions continuously.

2.2.2 Calibration/Monitoring Program

As discussed in Section 9.3.4, the filled detector modules will then be transported to the designated experimental halls where they will be located for operations. At this point, critical differences between detector modules will be studied and understood at the level of normalization uncertainty of $\sim 0.1\%$. Subsequent changes in a particular detector module (over time or after relocation at another site) will be monitored to insure that the normalization uncertainty remains below $\sim 0.1\%$. Achieving these goals will be accomplished through a comprehensive program of detector calibration and monitoring.

We have designed a program with three different classes of procedures:

1. “complete” characterization of a detector module,
2. “partial” characterization, and
3. routine monitoring.

We envision that the complete characterization (procedure #1) will generally be performed once during initial commissioning of a detector module before taking physics data. Procedure #2 would be employed after relocation of a detector module or after some other change that requires a careful investigation of the detector properties and will involve a subset of the activities in procedure #1. If substantial changes are detected during procedure #2, then we would likely opt for reverting to procedure #1. Finally, procedure #3 will involve both continuous monitoring of some detector parameters as well as frequent (i.e., daily or weekly) automated procedures to acquire data from LED light sources and radioactive sources deployed into the detector volume.

The requirements and proposed solutions for procedure #1 are listed in Table 2.3. These will be manually operated procedures using equipment and systems to be described below, and will likely entail several weeks activity.

Procedure #2 will be a subset (to be determined) of the activities in procedure #1. These will also be manually operated procedures using equipment and systems to be described below, and will likely entail several days activity.

The requirements and proposed solutions for procedure #3 are listed in Table 2.4.

Requirement	Description	Proposed Solution(s)
Optical Integrity	Spatial uniformity of response, light attenuation	LED , γ sources
PMT gains	Match gains of all PMTs	LED - single p.e. matching
PMT timing	~ 1 ns timing calibration for each PMT	Pulsed LED
Energy scale	Set scale of energy deposition	Gamma sources
H/Gd ratio	Measure relative Gd fraction	Neutron sources

Table 2.3. Requirements for the full manual calibration procedure.

Requirement	Description	Proposed Solution(s)
Mechanical/thermal	Verify these properties are stable	Load sensors, thermometers, etc.
Optical stability	Track variations in light yield	γ sources, spallation products
Uniformity, light attenuation	Monitor spatial distribution of light	γ sources, spallation products
Detection efficiency	Monitor ϵ for neutrons and positrons	γ sources, neutron sources
PMT gains	Monitor 1 p.e. peaks	LED source

Table 2.4. Requirements for automated calibration procedure.

Procedure #3 will entail continuous in-situ monitoring (Section 5.3), monitoring of continuously produced spallation-induced activity (Section 2.2.2.3), and regularly scheduled automated deployment of sources (Section 2.2.2.2).

2.2.2.1 Commissioning

In the commissioning phase, a manual calibration system will be employed to characterize the entire (inner) detector response. During this procedure, the water pool must be drained to below the top of the AD lid to install the manual system and then refilled to 1 meter above the AD lid in order to reduce the singles rate and maintain thermal stability of the detector. In each detector, we plan to deploy a few radioactive sources, and make point-to-point sampling of the inner detector volume every 40 cm, leading to about 200 measurements per source per detector. We also envision using common sources in different detectors to measure absolute rates and detection efficiency.

2.2.2.2 Automated Monitoring

Automated deployment systems will be used to monitor all detector modules on a routine (e.g., weekly) basis. Each detector module will be instrumented with a few identical automated deployment systems, each will allow the full z access inside the detector. There will be three such ports, one along the central z axis, one in the gamma catcher, and the other one along an off-center z axis. The configuration three axes are illustrated in Fig. 2.1.

Each deployment system will be capable of deploying three different sources into the detector. Currently, we plan to include ^{68}Ge (e^+), neutron (^{252}Cf), and a LED diffuser ball.

The automated deployment of sources will be scheduled simultaneously for all eight detector modules, and is expected to require about 2–3 hours. Data acquisition for antineutrino measurements will be suspended during this period, and these data runs will be designated as calibration runs. The automated calibration source system control computer will need to communicate and coordinate with the data acquisition system during these calibration runs so all the data are properly recorded and labeled.

Simulation studies have indicated that with the source data along these three axes, plus a few additional

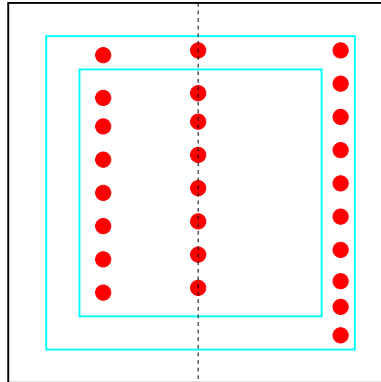


Fig. 2.1. Illustration of the source deployment axes.

diagnostic measurements, one can monitor the detector conditions and achieve quantitative measurement of detector parameters to give a 0.20–0.38% detector-related systematic uncertainty. See more details in Section 2.2.2.5.

2.2.2.3 Cosmogenic Events

Cosmic muons passing through the detector modules will produce useful short-lived radioactive isotopes and spallation neutrons. These events will follow the muon signal (detected in the muon system as well as the detector) and will be uniformly distributed throughout the detector volume. Therefore, these provide very useful information on the full detector volume which is complementary to the information obtained by deploying point sources. Such events are used by KamLAND to study the energy and position reconstruction as well as to determine the fiducial volume. As with KamLAND, the Daya Bay experiment will use primarily spallation neutron capture and ^{12}B decay ($\tau = 29.1$ ms and $Q = 13.4$ MeV).

The rates of these events for Daya Bay are given in Table 2.5. These rates are sufficient to determine the energy stability relevant to the neutron capture efficiency to $\sigma_E/E \sim 0.5\%$ for 100 pixels (200 kg each) in each detector on time scales of 1(10) days for the near(far) detector modules, respectively.

Event type	Near Site Rate	Far Site Rate
Neutrons	13500/day	1100/day
^{12}B	300/day	28/day

Table 2.5. Estimated production rates (per 20 ton detector module) for spallation neutron and ^{12}B events in the Daya Bay experiment.

As an example, the simulated detector response (total charge) for the 8 MeV n-Gd capture signals throughout the detector target volume is shown in Fig. 2.2. Regular monitoring of the full-volume response for these events, compared with the regular automated source deployments, will provide precise information on the stability (particularly of optical properties of the detector, but also general spatial uniformity of response) of the detector modules. With the addition of Monte Carlo simulations, this comparison can be used to accurately assess the relative efficiency of different detector modules as well as the stability of the efficiency of each module.

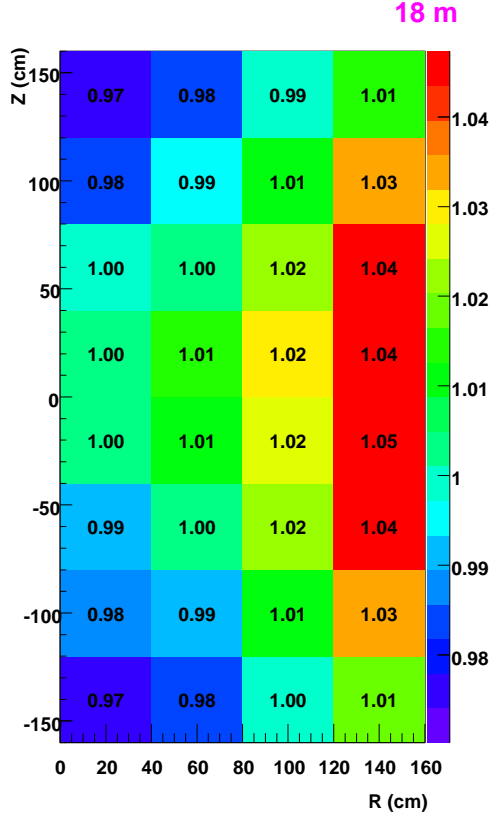


Fig. 2.2. The Gd capture p.e. yield for the spallation neutrons (normalized to the yield at the detector center) as a function of the neutron vertex (R, z). The assumed attenuation length of the scintillator is 18 m.

2.2.2.4 PMT Calibration and Monitoring

The timing, gain, and quantum efficiencies of the PMTs are crucial input to the energy measurement and position reconstruction. An LED system (470 nm) with a control trigger can be used to calibrate the PMT timing. Due to the cylindrical symmetry of the detector, we can deploy the LED diffuser ball along the central z axis and calibrate the PMT timing ring by ring so that we obtain 1 ns precision in the relative timing of all PMTs in a module. At the same time, the absolute gain of the PMTs can be calibrated by the ADC peaks of the single photoelectrons, after which individual discriminator thresholds can be set. Assuming azimuthal symmetry, the relative quantum efficiencies for different tubes in the same ring can be calibrated based on the measured rate during the same z scan scheme with a radioactive source (e.g. ^{68}Ge). A tight timing cut may be necessary to remove the background counts as well as photons reflected from the wall. In principle, only a global factor in QE will be left undetermined after this step for all the tubes in a detector module. Each PMT can be tracked on a weekly (or even daily, if necessary) basis using automated deployment of the LED ball.

2.2.2.5 Determination of Detector Optical Parameters

The generation, transmission, and reflection of optical photons in each detector must be well-understood. The associated detector optical parameters will be employed in the event reconstruction, so that reconstructed positron and neutron energies for all the detectors are “identical” to the required precision (generally

<0.5%).

In general, the relevant optical properties of an AD can be characterized by the following set of parameters: the light yields in the target region (Y_{tgt}) and the gamma catcher (Y_{gcat}), the attenuation lengths of the target (L_{tgt}), gamma catcher (L_{gcat}), and mineral oil (L_{mo}), the reflectivity of the top and bottom reflectors (R_{top} and R_{bottom}). (The reflectivity of the side walls will be small so this should not be a significant factor in the optical properties.) Simulation studies have indicated that using the ^{68}Ge source, one can calibrate the positron efficiency readily to $\sim 0.05\%$ precision. The 6 MeV visible energy cut for the neutrons, on the other hand, is in the middle of a rather long tail in the delayed energy spectrum, which is more difficult to calibrate. In the following Table 2.6, we summarize the required precision on individual parameters, determined from simulation, to achieve a $<0.2\%$ precision on the neutron efficiency. These specs should be interpreted

Parameter	Tolerance
Y_{tgt}	$\pm 1.0\%$
Y_{gcat}	$\pm 1.6\%$
L_{tgt}	$\pm 5.4\%$
L_{gcat}	$\pm 11.2\%$
L_{mo}	$\pm 15.0\%$
R_{top}	$\pm 7.3\%$
R_{bottom}	$\pm 7.3\%$

Table 2.6. The nominal precision requirements for detector parameters as determined in this study. See text for explanations.

as the precision to which one needs to calibrate a given parameter, rather than an absolute tolerance from a nominal value. That is, we need only know the measured values among all the detectors with this precision in order to meet the requirement on the detector systematic uncertainty and its effect on the measurement of $\sin^2 2\theta_{13}$. In what follows, we shall outline a comprehensive program, which can determine all of the parameters listed in Table 2.6.

Attenuation Lengths

Fixed LEDs can be deployed at three different positions in the oil buffer, as shown in Fig. 2.3. Two opposing phototubes (PMTs #5 and #6) are located at the top and bottom of the oil buffer as shown. The ratio of the rates measured for the three LED locations, corrected for the differing acceptance and reflections from the wall (see below), leads directly to the attenuation length of the mineral oil. With two such phototubes, the attenuation of the oil is determined with redundancy. Since the understanding of the acceptance is crucial for this application, it is desirable to use smaller phototubes.

A similar scheme can be used to determine the attenuation length of the gamma catcher. To have a longer lever arm, the LED ball should be placed at different vertical locations in the gamma catcher, as illustrated in Fig. 2.3. Light that is vertically transmitted through the gamma catcher region will be detected by phototubes located at the top and bottom of the tank (PMTs #3 and #4). By taking the ratio of rates for the diffuser ball at different z , the (constant) attenuation from the oil buffer will cancel. This leads to a clean determination of the attenuation in the gamma catcher. Preliminary simulation of this procedure is illustrated Fig. 2.4, where 2" phototubes are implemented in the Monte Carlo. With careful study of the phototube acceptance, we anticipate a very precise determination of the attenuation length.

Similarly, if one deploys the light source along the center or edge of the central target region, the attenuation length of the target region can be determined using PMTs deployed at the top and bottom of the detector (PMTs #1 and #2 in Fig. 2.3).

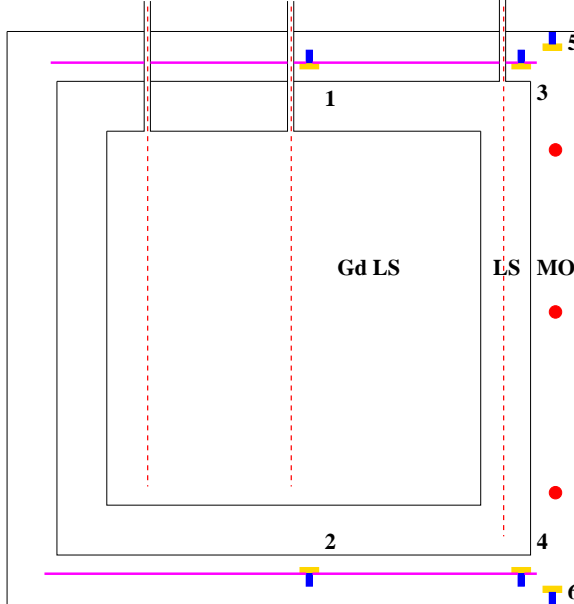


Fig. 2.3. A diagram for measuring the attenuation lengths in all three zones. The calibration PMTs are shown as blue blocks with yellow faces. The red balls indicate the LED diffuser ball positions for measurements of the buffer oil transparency. The magenta thick lines on the top and bottom represent the reflectors. The vertical dashed lines indicate regions of deployment for the LED ball for measurement of the transparencies of the central region and gamma catcher, as well as determination of the reflectivity of the top/bottom reflectors.

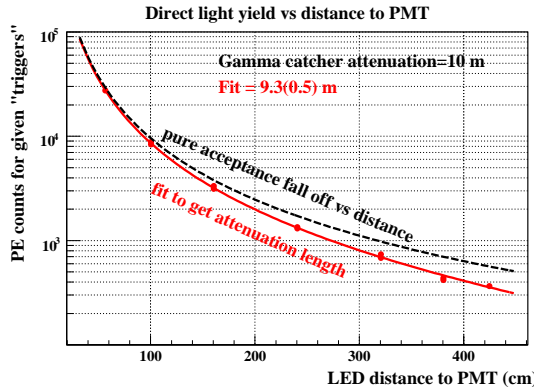


Fig. 2.4. Determination of the gamma catcher attenuation length by deploying the LED at different z locations.

Top/Bottom Reflectivity

The top/bottom reflectivity can also be determined using the scheme in Fig. 2.3. Separation of the direct and reflected light is facilitated by using the time of arrival of the light. In Fig. 2.5, the hit timing of PMT #1 (Fig. 2.3) is illustrated with an LED deployed at the center of the detector. The separation of direct and reflected light can be achieved easily with a multi-hit TDC with \sim ns precision. By comparing the measured

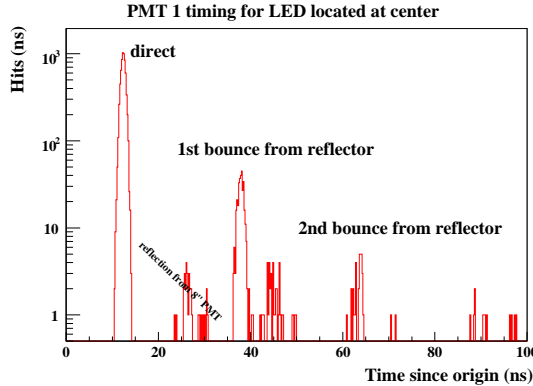


Fig. 2.5. The hits timing of PMT #1 for direct and reflected light from a pulsing LED at the detector center.

reflected/direct light ratio with the Monte Carlo (with precisely measured attenuation lengths as inputs), the top/bottom reflectivity can then be determined accurately.

Global Fit Determination of Detector Optical Properties

Since we will not have absolute quantum efficiency values for all PMTs, it is not possible to determine the absolute light yield of the liquid scintillator. The total photoelectron (p.e.) yields of radioactive sources (like ^{60}Co) can be measured at the central region and this can be used to establish the energy calibration for each detector.

By studying the p.e. yields in different regions of the detector we can determine the ratio $Y_{\text{tgt}}/Y_{\text{gcat}}$. To first order, assuming that a calibration source deposits energy only locally, the ratio of light yields for the two regions can be determined after correction for the attenuation lengths. The attenuation length, on the other hand, causes the response of a given phototube to vary with vertex position. Therefore, by deploying a source at different locations in the detector module, and by analyzing the total light yield as well as the distribution of p.e. yields in the PMTs, one can make a simultaneous fit to determine L_{tgt} and the ratio $Y_{\text{tgt}}/Y_{\text{gcat}}$. In principle, all the detector optical properties can be determined using a global fit to a sufficiently complete set of data.

The feasibility of this approach was studied with simulation. We simulated the detector with various sets of $Y_{\text{tgt}}/Y_{\text{gcat}}$ and L_{tgt} . In each case the detector was calibrated by a 1 MeV electron source* in different locations according to Fig. 2.1 along three z axes. The simulated data (p.e. for each PMT) were fitted by a likelihood function, which was constructed based on the Poisson probability of hits in individual phototubes. The expected rate in each tube is a function of the geometry (known), light yields, and the attenuation. To avoid complications due to the light reflection, timing cuts were applied to the tube hits. In Table 2.7, a comparison between the input and fitted values of $Y_{\text{tgt}}/Y_{\text{gcat}}$ and L_{tgt} for three example fits is made. One sees that this fitting method is able to disentangle the change of light yield from a change of attenuation. We expect that the precision of the procedure can be improved to the desired level with additional simulation studies.

Precipitate at the Bottom of the Acrylic Vessel

Over time, some particulates or other material from the liquid scintillator may precipitate onto the bottom of the acrylic tank, making the bottom acrylic more opaque than the top. A top/bottom asymmetry in detector response will develop as a result. For illustration, in Fig. 2.6, the total p.e. yield of the detector as a function of the z position of a ^{60}Co source is plotted, for a rather opaque acrylic bottom with only 1 cm of

*For simplicity we used an electron source instead of a gamma source so that the ionization energy is deposited locally.

Quantity	Input	Fit result
$Y_{\text{tgt}}/Y_{\text{gcat}}$	0.667	0.674
L_{tgt} (m)	9.0	9.32
$Y_{\text{tgt}}/Y_{\text{gcat}}$	0.75	0.743
L_{tgt} (m)	9.0	9.95
$Y_{\text{tgt}}/Y_{\text{gcat}}$	1.0	0.978
L_{tgt} (m)	4.5	4.6

Table 2.7. A comparison of the input and fitted values of various sets of parameters in the likelihood fitter.

attenuation length. Clearly the light originating from the bottom half of the detector is absorbed more than

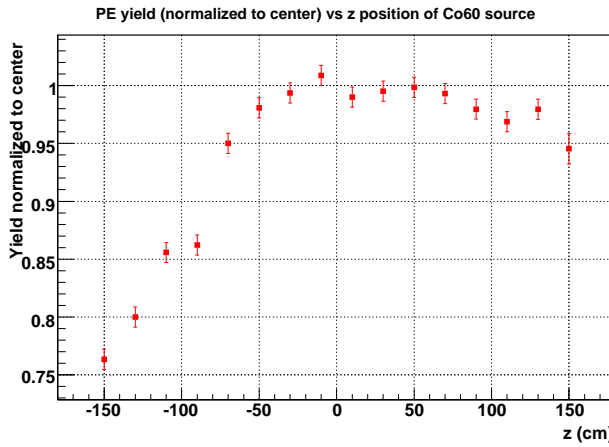


Fig. 2.6. The results of a scan of ^{60}Co source along the central z axis for a detector with bottom acrylic plate having a short 1 cm optical attenuation to simulate the effect of a precipitate.

the top half. The precipitate also suppresses the yield in the bottom PMT ring, which is another symptom of this problem. One effective correction procedure is a brute force “fix” such that the p.e. measured by the bottom ring is scaled according to the top ring. (This should yield similar results to a more correct procedure using a maximum likelihood method to determine the energy.) Simulations indicate that even under the extreme situation considered (with a 1 cm attenuation length) in Fig. 2.6 the positron efficiency is stable to 0.2%.

We are also exploring the possibility of using 2.2 MeV n-p capture signal in the bottom gamma catcher to detect and make corrections to this region of the gamma catcher which is not directly accessible to source deployments.

Additional Constraints from Spallation Neutrons

In addition to the calibration devices discussed above, spallation neutron events serve as a unique and powerful calibration tool. The 2.2 MeV n-p and 8 MeV n-Gd capture signals are distributed uniformly throughout the detector. With a reconstruction of the vertex, one can produce a full volume map of the detector response, as shown earlier in Fig. 2.2. Effectively, the topology of this map captures the combined effect of all detector parameters. Simulation has shown that even without detailed knowledge of individual parameters, we can use the spallation neutron capture peak to set the overall energy scale and achieve near/far

“identical”neutron efficiency.

The detection of spallation neutrons is straightforward. One requires a prompt (large) muon signal in the antineutrino and muon detectors, and a delayed neutron capture signal.[†] Such a delayed energy spectrum consists of two clean 2.2 and 8 MeV peaks, with very small background from cosmogenic beta emitters (e.g. ¹²B) and accidentals. Clearly, such a measurement requires that the electronics become “live” shortly after the muon passage — this has become one of the key design requirements for the electronics system (see Sec. 7).

In terms of constraining the detector parameters, the anticipated utility of the spallation neutrons events is summarized below

- The spallation neutron capture events that reconstruct close to each of the three calibration axes should give the same energy response as the neutron source data from the corresponding axis. This provides essential validation of the calibration program by directly cross-checking the source data with the spallation data.
- The n-p capture signals in the gamma catcher can provide further information about the detector properties there. This is particularly useful at the bottom of the gamma catcher, where direct calibration device has no access.
- The reconstructed n-p capture peak should be at 2.2 MeV, and that of n-Gd capture should be at 8 MeV, *regardless of the vertex position*. If position non-uniformity is found, it either indicates that some parameters in the model are off, or that our detector modeling is imperfect. Ideally one should diagnose and fix the problem, in effect, turning Fig. 2.2 into a flat energy map.
- It is conceivable that after exhausting all techniques, some residual non-uniformity in the neutron energy map remains. Then one could consider taking the residual map to make the final position dependent energy correction.

The effectiveness of the 2nd bullet requires further Monte Carlo studies.

2.2.3 Detector Related Uncertainties

For the detector-related systematic uncertainties, we utilize two values for the Daya Bay experiment: baseline and goal. The baseline value is what we conservatively expect to achieve through essentially proven methods with perhaps straightforward improvement in technique. The goal value is that which we consider achievable through improved calibration and analysis techniques as described below.

As emphasized in Section 1.2.5, we are essentially measuring a ratio of rates in near and far detector pairs. Therefore, we do not need to determine the *absolute* efficiency for each detector, but only the ratio for the two detectors in a pair. This ratio can be determined by measuring components of the efficiency for each detector using identical methods for the two detectors. If the measurement method has some common systematic uncertainty for the two detectors, this is not relevant for the ratio. We only need consider the uncorrelated uncertainties that will actually contribute to the uncertainty in the efficiency ratio. We will use the term “*relative uncertainty*” to refer to the contributions of such uncorrelated effects to the detector related uncertainties, as opposed to the term “*absolute uncertainty*” which refers to the uncertainty that contributes to the *absolute* efficiency. That is, the *relative* uncertainties are the only ones relevant to measurement of ratios of rates in the near and far detector pairs.

The estimated values of detector-related systematic uncertainties are summarized in Table 2.8 and discussed in the rest of this section.

[†]One might need to cut the first few microseconds after muon passage to ensure electronics baseline recovery and to minimize the effects of PMT afterpulsing.

Source of uncertainty	Chooz (absolute)	Daya Bay (<i>relative</i>)		
		Baseline	Goal	Goal w/Swapping
# protons	0.8	0.3	0.1	0.006
Detector Efficiency	Energy cuts	0.8	0.2	0.1
	Position cuts	0.32	0.0	0.0
	Time cuts	0.4	0.1	0.03
	H/Gd ratio	1.0	0.1	0.0
	n multiplicity	0.5	0.05	0.05
	Trigger	0	0.01	0.01
	Live time	0	<0.01	<0.01
Total detector-related uncertainty	1.7%	0.38%	0.18%	0.12%

Table 2.8. Comparison of detector-related systematic uncertainties (all in percent, per detector module) of the Chooz experiment (*absolute*) and projections for Daya Bay (*relative*). Baseline values for Daya Bay are conservative values achievable through essentially proven methods, whereas the goals should be attainable through additional calibration and analysis efforts described in the text. In addition, the potential improvement from detector swapping is indicated in the last column.

2.2.3.1 Number of Target Protons

The antineutrino targets are the free protons in the detector, so the event rate in the detector is proportional to the total number of free protons. As discussed in Chapter 4, the antineutrino detectors will be filled in pairs, each pair from a common batch of liquid scintillator carefully controlled so that there will be no difference in chemical composition between the two detectors. Then one of the two detectors will be deployed at a near site, and the other at the far site. Then the near and far members of a pair will have liquid scintillator with the same chemical composition and exactly the same number of protons per unit mass of liquid scintillator. The ratio of masses in the central volumes then provides the ratio of proton targets for the two detectors.

The mass of the antineutrino target is accurately determined in several ways. The primary measurement of the target mass will rely on load cell measurements of the Gd-LS fill tank before and after filling the AD.

The detector modules will be built to specified tolerance so that the volume is known to $\sim 0.6\%$ (typically <5 mm dimension out of a radius of 1.6 meters). We will make a survey of the detector geometry and dimensions after construction to characterize the detector volumes to higher precision than 0.3%. Using optical measuring techniques and reflective survey targets built into the detector modules and attached to the surfaces of the acrylic vessels sub-mm precision is easily achievable with conventional surveying techniques.

Once the detectors are underground, we plan to fill each detector from a common tank using a variety of instrumentation to directly measure the mass and volume flow into the detector. A combination of load cells, Coriolis mass flow meters and volume flow meters and thermometers in the filling station and the fill tank will allow us to determine the mass of the liquid scintillator reliably and with independent methods.

The detailed filling plan for the anti-neutrino detectors will be discussed in Sec. 4.6. With commercial load cells and flow meters, we conservatively quote a baseline uncertainty of 0.3% for the detector mass. The goal value of 0.1% is based on the expected load cell performance.

The absolute H/C ratio was determined by Chooz using scintillator combustion and analysis to 0.8% precision based on combining data from several analysis laboratories. By filling the near/far pairs from a common batch of scintillator, we expect to essentially eliminate this systematic uncertainty. Nevertheless,

we will analyze samples from each detector to check that no difference is observed. These samples will be analyzed with a common apparatus, so common sources of systematic uncertainty will not contribute to the relative determination of the H/C ratio in different samples. The *relative* H/C ratio for different samples thus can be determined with an improved precision, perhaps 0.1% or better. (R&D results indicate the H/C ratio can indeed achieve a precision of 0.1% or better using a combination of NMR methods, chemical analysis, and neutron capture.)

We note that the γ -catcher will also be filled using scintillator from a common tank for both members of the detector pair. Thus there should also be no possibility of a systematic difference in the H/C ratio for the gamma catcher liquid. For the γ -catcher we need to control the H/C ratio to about 1% to constrain the amount of “spill-in” events. These “spill-in” events are where a neutron generated in the γ -catcher is captured in the Gd-loaded scintillator after thermal diffusion. We will also analyze samples of the γ -catcher to verify the H/C ratio is the same for detector pairs.

2.2.3.2 Position Cuts

Due to the design of the detector modules, the event rate is measured without resort to reconstruction of the event location. Therefore the uncertainty in the event rate is related to the physical parameters of the antineutrino volume. We do not anticipate employing cuts on reconstructed position to select events, and there should be no uncertainty related to this issue.

2.2.3.3 Positron Energy Cut

Due to the high background rates at low energy, Chooz employed a positron energy threshold of 1.3 MeV. This cut resulted in an estimated uncertainty of 0.8%. The improved shielding design of the Daya Bay detectors makes it possible to lower this threshold to below 1 MeV while keeping uncorrelated backgrounds as low as 0.1%. The threshold of visible energy of neutrino events is 1.022 MeV. Due to the finite energy resolution of \sim 12% at 1 MeV, the reconstructed energy will have a tail below 1 MeV.

The systematic uncertainty associated with this cut efficiency is studied by Monte Carlo simulation. The baseline antineutrino detector configuration (20 T target with 192 8" PMTs) was assumed in this simulation, yielding an energy resolution of \sim 12% at 1 MeV. The threshold region of the simulated energy spectrum is shown in Fig. 2.7. The full spectrum and the high energy tail of the spectrum are shown in the figure as the upper and lower inserts, respectively.

In Daya Bay, the positron energy threshold at 1 MeV will be established with the ^{68}Ge source (see Sec. 5). The uncertainty of this cut is estimated conservatively to be 2% based on KamLAND experience). For a varying positron cut at 1.0, 1.02, and 1.04 MeV, the simulation above predicts a positron inefficiency of 0.15%, 0.19%, and 0.24%, which leads to a 0.05% uncertainty in the detected antineutrino rate.

The upper energy requirement for the positron signal will be $E < 8$ MeV. An 1% uncertainty of the 8 MeV energy scale (established by n-Gd capture signals) contributes to a negligible uncertainty to the positron detection efficiency.

2.2.3.4 Neutron Detection Efficiency

The delayed neutron from the inverse beta decay reaction is produced with \sim 10 keV of kinetic energy. The neutron loses energy in the first few interactions with H and C in the scintillator, and reaches thermal energy in a few microseconds. The neutrons can capture on either H or Gd during or after the thermalization process. We will detect the neutrons that capture on Gd, yielding at least 6 MeV of visible energy from the resulting capture γ rays, during the time period $0.3 < T < 200 \mu\text{s}$.

In order to measure the rates for two detectors (near and far) with a precision to reach $\sin^2 2\theta_{13} = 0.01$ the baseline requirement for the uncertainty on *relative* neutron detection efficiencies is 0.25%. The ϵ_n for neutrons at the center of a detector module can be determined directly by using a tagged neutron source

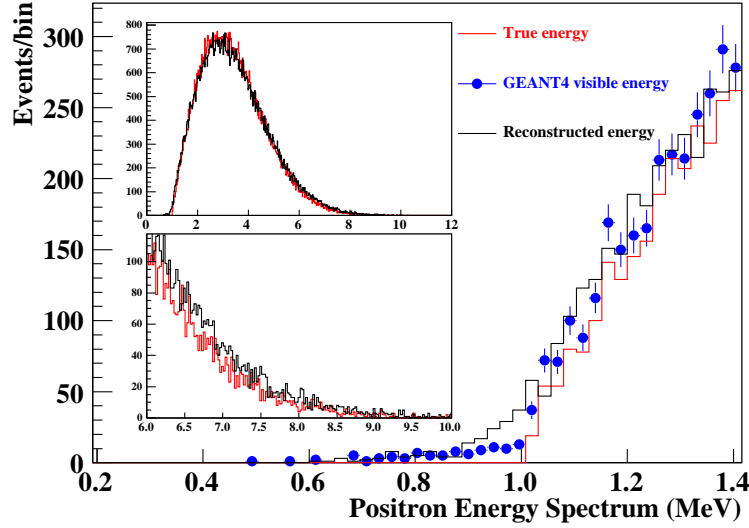


Fig. 2.7. Energy spectra associated with the positron's true energy (Red = kinetic energy + 1.022 MeV annihilation energy), the GEANT4 visible energy (Blue = dE/dx in the active detector region, i.e. the target or gamma catcher), and reconstructed energy (Black) close to the 1 MeV threshold. The reconstructed energy is calculated by scaling the total detected charge based on (simulated) calibration data from ^{68}Ge (1.022 MeV) and spallation neutrons (8 MeV). The full spectrum is shown in the upper insert, and a zoom in of the high energy tail region is shown in the lower insert. In both inserts, the red histogram corresponds to the true energy and the black corresponds to the reconstructed energy. Statistics comparable to a far site module in 1000 days.

(either ^{252}Cf , Am-Be or Pu(C) can be used) and counting the number of neutrons using the time and energy cuts after a neutron producing event. (Corrections associated with uniformly distributed neutrons are studied with spallation neutrons, as discussed in Section 2.2.2.3.) This will require measurement of order a million neutron captures, and would likely require several hours of measurement. This will be established during the initial comprehensive calibration of each detector.

The efficiency for detecting the neutron can be written

$$\epsilon_n = P_{Gd}\epsilon_E\epsilon_T \quad (18)$$

in which P_{Gd} is the probability to capture on Gd (as opposed to H), ϵ_E is the efficiency of the $E>6$ MeV energy cut for Gd capture, and ϵ_T is the efficiency of the delayed time period cut. The individual components P_{Gd} , ϵ_E , and ϵ_T can be monitored separately as an additional check on the measurement of ϵ_n .

H/Gd ratio

Neutrons are thermalized during their first $10\ \mu\text{s}$ of existence in the detector central volume. Thus for times longer than $10\ \mu\text{s}$ the delayed neutron capture events will exhibit an exponential time constant, τ , related to the average concentration of Gd in the detector module. The rate of capture, $\Gamma \equiv 1/\tau$, is given by:

$$\Gamma = \Gamma_{Gd} + \Gamma_H = [n_{Gd}\sigma_{Gd} + n_H\sigma_H]v \quad (19)$$

where $n_{H(Gd)}$ is the number density of hydrogen (Gd) in the liquid scintillator and $\sigma_{H(Gd)}$ is the neutron capture cross section on hydrogen (Gd) and v is the thermal velocity. For liquid scintillator one generally

obtains $1/\Gamma_H \sim 200 \mu\text{sec}$, whereas for 0.1% Gd fraction in Gd-LS we expect $\tau \sim 30 \mu\text{sec}$. The fraction of neutrons that capture on Gd rather than H is then

$$P_{Gd} = \frac{1}{1 + \Gamma_H/\Gamma_{Gd}} \quad (20)$$

and we would like to know this *relative* fraction between different detector modules to $\sim 0.1\%$. Thus we must measure the time constants τ for different detector modules to a *relative* precision of $0.2 \mu\text{s}$, or about 0.5%. Such a measurement requires measuring about 30,000 neutron captures, which can be done in an hour with a 10 Hz neutron source (in the manual calibration system). The Chooz experiment measured the (*absolute*) $\sim 30 \mu\text{s}$ capture time to $\pm 0.5 \mu\text{s}$ precision.

Measurement of τ to 0.5% precision will provide a relative value of P_{Gd} to 0.1% uncertainty, which is the baseline and goal value in Table 2.8.

Energy cut efficiency

Another issue is the neutron detection efficiency associated with the signal from capture of neutrons on Gd in the antineutrino detector volume. An energy threshold of about 6 MeV will be employed to select these delayed events, and the efficiency ($\sim 93\%$) of this criterion may vary between detector modules depending upon the detailed response of the module. However, this can be calibrated through the use of radioactive sources (see Section 5) and spallation neutron captures. The KamLAND detector gain is routinely (every two weeks) monitored with sources, and a relative long-term gain drift of $\sim 1\%$ is readily monitored with a precision of 0.05%. Monte Carlo simulations of the Daya Bay detector response for the Gd capture γ s indicate that 1% energy scale uncertainty will lead to 0.2% uncertainty in ϵ_E , and we use this value as the baseline systematic uncertainty.

We have also performed detailed Monte Carlo simulations of the detector response to neutron sources and spallation neutrons. The results of these studies indicate that we can indeed establish the relative value of ϵ_E to 0.1%, even for reasonable variations of detector properties (such as scintillator attenuation length). As an example, Fig. 2.8 shows how the source data can be used with uniform spallation neutrons to bootstrap a non-linear energy scale that corrects the spectrum, independent of attenuation length over the extreme range of 4.5–18 m. Therefore, we estimate a value of 0.1% for the goal systematic uncertainty in ϵ_E .

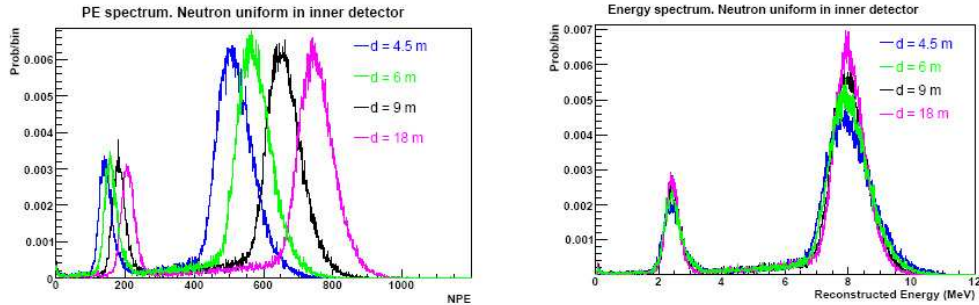


Fig. 2.8. Spallation neutron response for detector modules with scintillator optical attenuation lengths of $4.5 \leq d \leq 18 \text{ m}$. The left panel shows the raw photoelectron spectra, whereas the right panel shows the spectra rescaled according to a non-linear rescaling procedure we have developed. The rescaled 6 MeV effective energy threshold produces a constant value of $\epsilon_E = 93\%$ to within 0.4% over this extreme range of attenuation length.

Finally, we note that deployment of $^{238}\text{Pu}-^{13}\text{C}$ neutron sources during commissioning of the detector will enable establishing a very precise energy threshold using the 6.13 MeV gamma ray line in ^{16}O .

Time cuts

The time correlation of the prompt (positron) event and the delayed (neutron) event is a critical aspect of the event signature. Matching the time delays of the start and end times of this time window between detector modules is crucial to reducing systematic uncertainties associated with this aspect of the antineutrino signal. If the starting time ($\sim 0.3 \mu\text{s}$) and ending time ($\sim 200 \mu\text{s}$) of the delayed event window is determined to $\sim 10 \text{ ns}$ precision, the resulting uncertainty associated with missed events is $\sim 0.03\%$. We will insure that this timing is equivalent for different detector modules by slaving all detector electronics to one master clock. We estimate that with due care, the relative neutron efficiency for different modules due to timing is known to $\sim 0.03\%$, and we use this value as the estimated goal systematic uncertainty. We use a more conservative 0.1% value for the baseline value.

2.2.3.5 Neutron Multiplicity

Chooz required a cut on the neutron multiplicity to eliminate events where it appeared that there were two neutron captures following the positron signal, resulting in a 2.6% inefficiency and associated 0.5% systematic uncertainty. These multiple neutron events are due to muon-induced spallation neutrons, and will be reduced to a much lower level by the increased overburden available at the Daya Bay site. For the near site at 500 m baseline, the muon rate relative to the signal rate will be more than a factor nine lower than for the Chooz site. Therefore, events with multiple neutron signals will be reduced by this factor relative to Chooz, and should present a much smaller problem for the Daya Bay site. We therefore estimate a 0.05% value for this systematic uncertainty and use this for both the baseline and goal values.

2.2.3.6 Trigger

The trigger efficiency can be measured to high precision (0.01%) using studies with pulsed light sources in the detector. (We note that KamLAND has used this method to determine 99.8% absolute trigger efficiency [4].) In addition, we will employ redundant triggers so that they can be used to cross-check each other to high precision. We estimate a systematic uncertainty of 0.01% can be achieved, and use this for both the baseline and goal values.

2.2.3.7 Live Time

The detector live time can be measured accurately by counting a 80 MHz clock using the detector electronics, and normalizing to the number of clock ticks in a second (as defined by a GPS receiver signal). The uncertainty associated with this procedure should be extremely small, and certainly negligible relative to the other systematic uncertainties. For example, SNO measured the relative live times for their day/night analysis with a fractional uncertainty of 5×10^{-7} .

2.2.4 Detector Swapping

The connection of the two near detector halls and the far hall by horizontal tunnels provides the Daya Bay experiment with the unique option of swapping detectors between locations. This could enable the further reduction of detector-related systematic uncertainties in the measurement of the ratio of neutrino fluxes at the near and far locations. Although the estimated baseline and goal systematic uncertainties in Table 2.8 are sufficient to achieve a sensitivity of 0.01 in $\sin^2 2\theta_{13}$, implementation of detector swapping could provide an important method to further reduce systematic uncertainties and increase confidence in the experimental results.

The swapping concept is easy to demonstrate for a simple scenario with a single neutrino source and only two detectors deployed at two locations, near and far. The desired measurement is the ratio of event rates at the near and far locations: N/F . With detector #1 (efficiency ϵ_1) at the near location and detector #2

(efficiency ϵ_2) at the far location we would measure

$$\frac{N_1}{F_2} = \left(\frac{\epsilon_1}{\epsilon_2} \right) \frac{N}{F} \quad (21)$$

By swapping the two detectors and making another measurement, we can measure

$$\frac{N_2}{F_1} = \left(\frac{\epsilon_2}{\epsilon_1} \right) \frac{N}{F} \quad (22)$$

where we have assumed that the detector properties (e.g., efficiencies) do not change when the detector is relocated. We can now combine these two measurements to obtain a value of N/F that is, to first order, independent of the detector efficiencies:

$$\frac{1}{2} \left(\frac{N_1}{F_2} + \frac{N_2}{F_1} \right) = \frac{N}{F} \left(1 + \frac{\delta^2}{2} \right) \quad (23)$$

where we have defined

$$\delta \equiv \frac{\epsilon_2}{\epsilon_1} - 1 \quad (24)$$

Note that even if the detector efficiencies are different by as much as 1%, we can determine N/F to a fractional precision better than 10^{-4} .

We plan on running the experiment for a period of time (probably 3 years) before considering implementation of the swapping option.

2.2.5 Detector Cross-calibration

Another important feature of the design of the Daya Bay experiment is the presence of two detector modules at each near site. Each near detector module will measure the neutrino rate with 0.23% statistical precision every 8 months. If the systematic uncertainties are smaller than this, the two detectors at the near site should measure the same rate, giving a detector asymmetry of $0 \pm 0.34\%$ (statistical uncertainty only). These asymmetries are an important check to ensure that the detector-related systematic uncertainties are under control. In addition, this analysis can provide information on the degree to which the detector-related systematic uncertainties are correlated or uncorrelated so that we know how to handle them in the full analysis including the far site.

Finally, the near detector data can provide important information on the reactor power measurements. We will measure the ratio

$$R_{\text{near}} = \frac{S_{DB}}{S_{LA}} \quad (25)$$

where S_{DB} (S_{LA}) is the detector signal (background subtracted, normalized to the reactor power) for the Daya Bay (Ling Ao) near site. If the reactor powers are correct (and the detector systematic uncertainties are under control) then we expect $R_{\text{near}} = 1.0 \pm 0.24\% \pm 0.51\%$, where the first uncertainty is statistical (during each 8 month running periods) and the second uncertainty is the detector (baseline) systematic uncertainty. Note that these uncertainties are small relative to the expected 2% uncorrelated reactor power uncertainty, so measurement of R_{near} will provide an important check (and even perhaps additional information) on the reactor powers. Furthermore, studies of the measured neutrino spectra in the different near detectors during different parts of the reactor fuel cycle can help provide constraints on the fuel cycle effects on the spectrum.

2.3 Backgrounds

In the Daya Bay experiment, the signal events (inverse beta decay reactions) have a distinct signature: a prompt positron followed by a neutron-capture. Background events are logically divisible into two

categories, correlated and uncorrelated. A correlated background is one in which two reactions triggered by a single source, such as a cosmic muon, mimic the time-ordered pattern of a signal. An uncorrelated background is one in which the two-component pattern is accidentally formed by two distinct sources.

There are three important sources of backgrounds in the Daya Bay experiment: fast neutrons, ${}^8\text{He}/{}^9\text{Li}$, and natural radioactivity. A fast neutron produced by cosmic muons in the surrounding rock or the detector can produce a signal mimicking the inverse beta decay reaction in the detector: the recoil proton generates the prompt signal and the capture of the thermalized neutron provides the delayed signal. The ${}^8\text{He}/{}^9\text{Li}$ isotopes produced by cosmic muons have substantial beta-neutron decay branching fractions, 16% for ${}^8\text{He}$ and 49.5% for ${}^9\text{Li}$. The beta energy of the beta-neutron cascade overlaps the positron signal of neutrino events, simulating the prompt signal, and the neutron emission forms the delayed signal. Fast neutrons and ${}^8\text{He}/{}^9\text{Li}$ isotopes create correlated backgrounds since both the prompt and delayed signals are from the same single parent muon. Some neutrons produced by cosmic muons are captured in the detector without proton recoil energy. A single neutron capture signal has some probability to fall accidentally within the time window of a preceding signal due to natural radioactivity in the detector, producing an accidental background. In this case, the prompt and delayed signals are from different sources, forming an uncorrelated background. Such uncorrelated backgrounds can be accurately measured as described in Section 2.3.4 below.

All three major backgrounds are related to cosmic muons. Locating the detectors at sites with adequate overburden is the only way to reduce the muon flux and the associated background to a tolerable level. The overburden requirements for the near and far sites are quite different because the signal rates differ by more than a factor of 10. Supplemented with a good muon identifier outside the detector, we can tag the muons going through or near the detector modules and reject backgrounds efficiently.

In this section, we describe our background studies and our strategies for background management. We conclude that the background-to-signal ratio will be around 0.3% at the near sites and around 0.2% at the far site, and that the major sources of background can be quantitatively studied *in-situ*.

2.3.1 Cosmic Muons in the Underground Laboratories

The most effective and reliable approach to minimize the backgrounds in the Daya Bay experiment is to have sufficient amount of overburden over the detectors. The Daya Bay site is particularly attractive because it is located next to a 700-m high mountain. The overburden is a major factor in determining the optimal detector sites. The location of detector sites has been optimized by using a global χ^2 analysis described in Section 2.4.1.

Detailed simulation of the cosmogenic background requires accurate information of the mountain profile and rock composition. Figure 2.9 shows the mountain profile converted from a digitized 1:5000 topographic map. The horizontal tunnel and detector sites are designed to be about -20 m PRD.[‡] Several rock samples at different locations of the Daya Bay site were analyzed by two independent groups. The measured rock density ranges from 2.58 to 2.68 g/cm 3 . We assume an uniform rock density of 2.60 g/cm 3 in the present background simulation. A detailed description of the topography and geology of the Daya Bay area is given in Chapter 3.

The standard Gaisser formula [5] is known to poorly describe the muon flux at large zenith angle and at low energies. This is relevant for the Daya Bay experiment since the overburden at the near sites is only ~ 100 m. We modified the Gaisser formula as

$$\frac{dI}{dE_\mu d \cos \theta} = 0.14 \left(\frac{E_\mu}{\text{GeV}} \left(1 + \frac{3.64 \text{ GeV}}{E_\mu (\cos \theta^*)^{1.29}} \right) \right)^{-2.7} \left[\frac{1}{1 + \frac{1.1 E_\mu \cos \theta^*}{115 \text{ GeV}}} + \frac{0.054}{1 + \frac{1.1 E_\mu \cos \theta^*}{850 \text{ GeV}}} \right] \quad (26)$$

[‡]PRD is the height measured relative to the mouth of the Zhu Jiang River (Pearl River), the major river in South China.

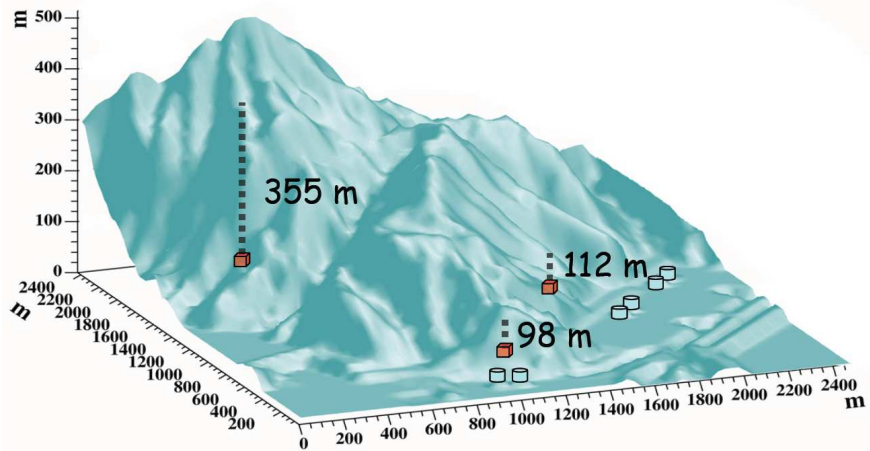


Fig. 2.9. Three dimensional profile of Pai Ya Mountain, where the Daya Bay experimental halls will be located, generated from a 1:5000 topographic map of the Daya Bay area.

which is the same as the standard formula, except that the polar angle θ is substituted with θ^* ,

$$\cos \theta^* = \sqrt{\frac{(\cos \theta)^2 + P_1^2 + P_2(\cos \theta)P_3 + P_4(\cos \theta)P_5}{1 + P_1^2 + P_2 + P_4}} \quad (27)$$

as defined in [6]. The parameters are determined to be $P_1 = 0.102573$, $P_2 = -0.068287$, $P_3 = 0.958633$, $P_4 = 0.0407253$, and $P_5 = 0.817285$, by using CORSIKA to simulate the muon production in the atmosphere. The comparison of the modified formula with data is shown in Fig. 2.10, where the calculations with the standard Gaisser formula are also shown. At muon energies of several tens of GeV, the

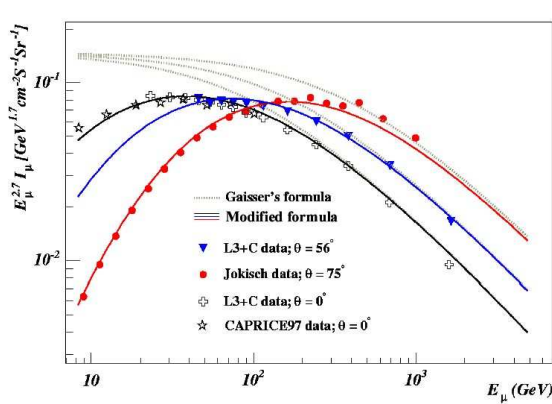


Fig. 2.10. Comparison of the modified formula (solid lines) with data. Calculations with the standard Gaisser's formula are shown in dashed lines. The data are taken from Ref. [7,8].

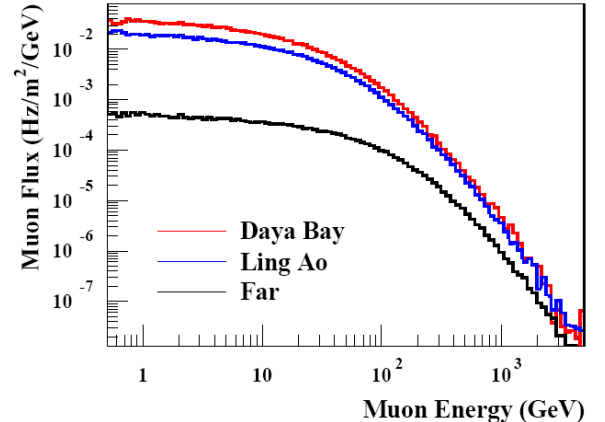


Fig. 2.11. Muon flux as a function of the energy of the surviving muons. The three curves from upper to lower correspond to the Daya Bay near site, the Ling Ao near site and the far site, respectively.

standard Gaisser formula has large discrepancies with data while the modified formula agrees with data in

the whole energy range.

Using the mountain profile data, the cosmic muons are transported from the atmosphere to the underground detector sites using the MUSIC package [9]. Simulation results are shown in Table 2.9 for the optimal detector sites. The muon energy spectra at the detector sites are shown in Fig. 2.11. The three curves

	DYB site	LA site	Far site
Vertical overburden (m)	98	112	355
Muon Flux (Hz/m ²)	1.16	0.73	0.041
Muon Mean Energy (GeV)	55	60	138

Table 2.9. Vertical overburden of the detector sites and the corresponding muon flux and mean energy.

from upper to lower correspond to the Daya Bay near site, the Ling Ao near site and the far site, respectively.

2.3.2 Simulation of Neutron Backgrounds

The neutron production rates will depend upon the cosmic muon flux and average energy at the detector. However, the neutron backgrounds in the detector also depend on the local detector shielding. The neutrino detectors will be shielded by at least 2.5 meters of water. This water buffer will be used as a Cherenkov detector to detect muons. Thus neutrons produced by muons in the detector module or the water buffer will be identified by the muon signal in the water Cherenkov detector. In addition, neutrons created by muons in the surrounding rock will be effectively attenuated by the 2.5 m water buffer. Together with another muon tracker above the water buffer, the combined muon tag efficiency is designed to be 99.5%, with an uncertainty smaller than 0.25%.

From the detailed muon flux and mean energy at each detector site, the neutron yield, energy spectrum, and angular distribution can be estimated with an empirical formula [10] which has been tested against experimental data. A Monte Carlo simulation has been carried out to propagate primary neutrons produced by muons in the surrounding rocks, the water buffer, and the oil buffer layer of the neutrino detector, to the detector. Neutrons produced in the liquid scintillator neutrino detector will be tagged by the muon system with 100% efficiency. Neutrons produced in the water buffer will be tagged with an efficiency of more than 99.5%, since their parent muons must pass through the muon system as well (this point will be further elaborated below). About 70% of the neutrons that enter the detector modules from the surrounding rock are also tagged by the muon system. Thus the remaining neutron background after muon rejection is due to the 30% of rock neutrons plus the neutrons produced in the water without detection of the parent muon (due to inefficiency of the muon tagging system), and we call these “untagged” neutron events.

Some energetic neutrons will produce tertiary particles, including neutrons. For those events that have energy deposited in the liquid scintillator, many have a complex time structure due to multiple neutron scattering and captures. These events are split into sub-events in 50 ns time bins. We are interested in two kinds of events. The first kind has two sub-events. The first sub-event has deposited energy in the range of 1–8 MeV, followed by a sub-event with deposited energy in the range of 6–12 MeV in a time window of 1–200 μ s. These events, called fast neutron events, can mimic the antineutrino signal as correlated backgrounds. The energy spectrum of the prompt signal of the fast neutron events, e.g. at the far site, is shown in Fig. 2.12 up to 50 MeV. The other kind of events has only one sub-event with deposited energy in range of 6 to 12 MeV. These events, when combined with the natural radioactivity events, can provide the delayed signal to form the uncorrelated backgrounds. We call them single neutron events. Most of the single neutron events are real thermalized neutrons while others are recoil protons that fall into the 6–12 MeV energy range accidentally. A few thermalized neutrons will survive beyond the 200 μ s cut, even though

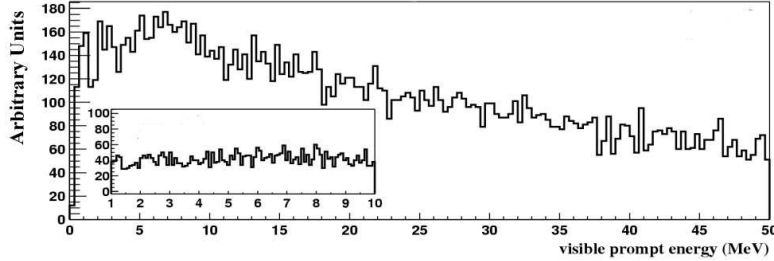


Fig. 2.12. The prompt energy spectrum of fast neutron background at the Daya Bay far detector. The inset is an expanded view of the spectrum from 1 to 10 MeV.

the parent muon is tagged. These neutrons contribute to the untagged single neutron rate, along with those where the veto misses the muon due to inefficiency. The neutron simulation results are listed in Table 2.10.

		DYB site	LA site	far site
fast neutron (/day/module)	tagged	19.6	13.1	2.0
	untagged	0.5	0.35	0.03
single neutron (/day/module)	tagged	476	320	45
	untagged	8.5	5.7	0.63

Table 2.10. Neutron production rates in a 20-ton module at the Daya Bay sites. The rows labeled “tagged” refer to the case where the parent muon traversed and was detected by the muon detectors, and thus it could be tagged. Rows labeled “untagged” refer to the case where the muon was not identified by the muon detectors.

As mentioned in the above, the “untagged” neutron background in Table 2.10 is due to 2 sources: (a) neutrons that are produced in the water but are untagged due to the detector inefficiency, and (b) neutrons produced in the rock. We note that events of type (b) are the dominant background.

As mentioned above, simulation studies indicate that the actual efficiency for tagging muons associated with neutrons in the ADs is *more* than 99.5% (the average value for all incident muons). This is because muons that produce neutrons in the ADs are much more likely to fire the water shield than the average muon that traverses the water shield. (The 0.5% average muon inefficiency is largely due to muons near the rock walls and corners; these muons are less likely to produce neutrons in the ADs. Thus the inefficiency for muons that produce neutrons in the ADs is much less than 0.5%.) In addition, the rate and energy spectrum of background (a) can be estimated through Monte Carlo studies constrained by the tagged data sample. Thus, background (a) is quite small and relatively well-controlled.

From the systematics point of view, it is then desirable to obtain additional handles on background (b). Simulation studies have been made on a muon system with a “roof” detector above the water Cherenkov detector (e.g. RPC), extending some distance into the surrounding rock. With 1 m rock “overhang”, the “roof” detector can tag $\sim 1/3$ of background (b), which would have otherwise been totally missed by the water Cherenkov detector. These additional tagged events will allow us to validate/tune the Monte Carlo in order to calculate the residual untagged rock neutron background.

2.3.3 Cosmogenic Isotopes

Cosmic muons, even if they are tagged by the muon identifier, can produce radioactive isotopes in the detector scintillator which decay by emitting both a beta and a neutron (β -neutron emission isotopes). Some of these so-called cosmogenic radioactive isotopes live long enough such that their decay cannot be reliably associated with the last tagged muon. Among them, ${}^8\text{He}$ and ${}^9\text{Li}$ with half-lives of 0.12 s and 0.18 s, respectively, constitute the most serious correlated background sources. The production cross section of these two isotopes has been measured with muons at an energy of 190 GeV at CERN [11]. Their combined cross section is $\sigma({}^8\text{He} + {}^9\text{Li}) = (2.12 \pm 0.35) \mu\text{barn}$. Since their lifetimes are so close, it is hard to extract individual cross sections. About 16% of ${}^8\text{He}$ and 49.5% of ${}^9\text{Li}$ will decay by β -neutron emission. Using the muon flux and mean energy at each detector site (from Section 2.3.1) and an energy dependent cross section, $\sigma_{\text{tot}}(E_\mu) \propto E_\mu^\alpha$, with $\alpha = 0.73$, the estimated ${}^8\text{He}+{}^9\text{Li}$ backgrounds are listed in Table 2.11.

	DYB site	LA site	Far site
$({}^8\text{He}+{}^9\text{Li})/\text{day/module}$	3.7	2.5	0.26

Table 2.11. ${}^8\text{He}+{}^9\text{Li}$ rates in a 20-ton module at the Daya Bay sites.

The recent Double Chooz paper [14] includes new reactor-off data from Chooz [1] that allow a better separation of ${}^9\text{Li}$ from fast neutron background. This basically comes from including previously unreleased high energy data in the fit. The extracted ${}^9\text{Li}$ background level was 0.7 ± 0.2 events/day. The mean muon energy in Chooz was ~ 60 GeV, almost the same as the Daya Bay near site (55 GeV) and the Ling Ao near site (60 GeV). The fitting is based on the assumption that the fast neutron background is flat in energy spectrum. Scaling from the Chooz result, the Daya Bay experiment will have 8.0, 5.4, and 0.57 ${}^9\text{Li}$ events per module per day at the Daya Bay near site, the Ling Ao near site, and the far site, respectively. These estimates are twice as large as the estimates from the CERN cross section.

The KamLAND experiment [15] measures this ${}^8\text{He}/{}^9\text{Li}$ background very well by fitting the time interval since last muon. The muon rate is 0.3 Hz in the active volume of KamLAND detector. The mean time interval of successive muons is ~ 3 seconds, much longer than the lifetimes of ${}^8\text{He}/{}^9\text{Li}$. For the Daya Bay experiment, the target volume of a 20 ton detector module has a cross section around 10 m^2 , thus the muon rate is around 10 Hz at the near sites, resulting in a mean time interval of successive muons shorter than the lifetimes of ${}^8\text{He}/{}^9\text{Li}$. With a modified fitting algorithm, we find that it is still feasible to measure the isotope background *in-situ*.

From the decay time and β -energy spectra fit, the contribution of ${}^8\text{He}$ relative to that of ${}^9\text{Li}$ was determined by KamLAND to be less than 15% at 90% confidence level [16]. Furthermore, the ${}^8\text{He}$ contribution can be identified by tagging the double cascade ${}^8\text{He} \rightarrow {}^8\text{Li} \rightarrow {}^8\text{Be}$. So we assume that all isotope backgrounds are ${}^9\text{Li}$. They can be determined with a maximum likelihood fitting even at 10 Hz muon rate, by taking all contributions from the preceding muons into account. The resolution of the background-to-signal ratio can be determined to be [17]

$$\sigma_b = \frac{1}{\sqrt{N}} \cdot \sqrt{(1 + \tau R_\mu)^2 - 1} \quad (28)$$

where N is the total number of neutrino candidates, τ is the lifetime of ${}^9\text{Li}$, and R_μ is the muon rate in the target volume of detector. The resolution is insensitive to the ${}^9\text{Li}$ level since the statistical fluctuation of neutrino events dominates the uncertainty. The ${}^9\text{Li}$ background can be measured to a $\sim 0.3\%$ fraction of the antineutrino signal with two 20-ton modules at the near sites of the Daya Bay experiment and $\sim 0.1\%$ at the far site with four 20-ton modules, with the data sample of three years of running. The fitting uses time information only. Inclusion of energy and vertex information could further improve the precision.

A Monte Carlo has been carried out to check the fitting algorithm. The background-to-signal ratio is fixed at 1%. The total number of neutrino candidates is 2.5×10^5 , corresponding to the far site statistical uncertainty, 0.2%. Figure 2.13 shows the fitting results as a function of muon rate. The data sample genera-

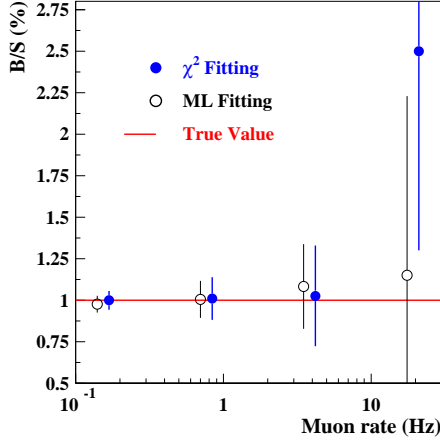


Fig. 2.13. Fitting results as a function of the muon rate. The uncertainty bars show the precision of the fitting. The χ^2 fitting uses the same muon rate as the maximum likelihood fitting and is shown to the right of it.

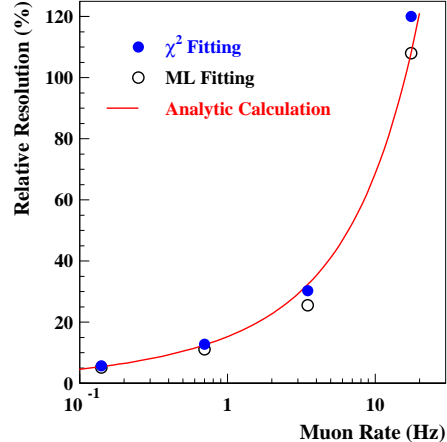


Fig. 2.14. The fitting precision as a function of the muon rate, comparing with the analytic estimation of Eq. 28. The y-axis shows the relative resolution of the background-to-signal ratio.

tion and fitting were performed 400 times for each point to get the fitting precision. In Fig. 2.14 the fitting precision is compared to the analytic formula Eq. 28 with the same Monte Carlo samples. The Monte Carlo results for minimizing χ^2 , the maximum likelihood fit, and the simple analytical estimation are in excellent agreement.

KamLAND also found that most ${}^8\text{He}/{}^9\text{Li}$ background are produced by showering muons [15,16]. A 2-second veto of the whole detector is applied at KamLAND to reject these backgrounds. Roughly 3% of cosmic muons shower in the detector. It is not feasible for Daya Bay to apply a 2-second veto since the dead time of the near detector would be more than 50%. However, if the Daya Bay detector is vetoed for 0.5 s after a showering muon, about 85% of the ${}^8\text{He}/{}^9\text{Li}$ backgrounds caused by shower muons can be rejected. Approximately 30% of the ${}^8\text{He}/{}^9\text{Li}$ background will remain: $\sim 15\%$ from non-showering muons and $\sim 15\%$ from showering muons. Although additional uncertainties may be introduced due to the uncertainties in the relative contributions from showering and non-showering muons and the uncertainties arising from the additional cuts (e.g., increased dead time), this rejection method can cross check the fitting method and firmly determine the background-to-signal ratio to 0.3% at the near sites and to 0.1% at the far site.

Some other long-lived cosmogenic isotopes, such as ${}^{12}\text{B}/{}^{12}\text{N}$, beta decay without an accompanying neutron. They can not form backgrounds themselves but can fake the delayed ‘neutron’ signal of an accidental background if they have beta decay energy in the 6–10 MeV range. The expected rates from these decays in the antineutrino detector are listed in Table 2.12. The ${}^{12}\text{B}/{}^{12}\text{N}$ cross section is taken from KamLAND [16] and the others are taken from measurement at CERN [11]. They are extrapolated to Daya Bay mean muon energies using the power law $\sigma_{\text{tot}}(E_\mu) \propto E_\mu^{0.73}$. The total rates of all these isotopes of visible energy in detector in the 6–10 MeV range, where they can be misidentified as a neutron capture signal on Gadolinium, are 210, 141, and 14.6 events per module per day at the Daya Bay near site, the Ling Ao near

site, and the far site, respectively. The dominant contribution is from $^{12}\text{B}/^{12}\text{N}$. KamLAND found that ^{12}N yield is smaller than 1% of ^{12}B . Since the half-life of ^{12}B is short comparing to the mean muon interval, the rate can be well determined *in situ* by fitting the time since last muon. Using Eq. 28, the yield can be determined to a precision of 0.34, 0.25, and 0.015 events per module per day at the Daya Bay near site, the Ling Ao near site, and the far site, respectively, using three years' data sample. Therefore, we expect those isotopes will introduce very little uncertainties in the background subtraction. On the other side, these isotopes, uniformly produced inside the detector, can be used to monitor detector response.

isotopes	E_{\max} (MeV)	$T_{1/2}$ (s)	DYB site (/day/module)	LA site (/day/module)	far site (/day/module)
$^{12}\text{B}/^{12}\text{N}$	13.4 (β^-)	0.02/0.01	396	267	27.5
^9C	16.0 (β^+)	0.13	16.6	11.2	1.15
^8B	13.7 (β^+)	0.77	24.5	16.5	1.71
^8Li	16.0 (β^-)	0.84	13.9	9.3	0.96
^{11}Be	11.5 (β^-)	13.8	<8.0	<5.4	<0.56
Total in 6-10 MeV			210	141	14.6

Table 2.12. Cosmogenic radioactive isotopes without neutron emission but with beta decay energy greater than 6 MeV. Cross sections are taken from KamLAND [16] ($^{12}\text{B}/^{12}\text{N}$) and Hagner [11] (others).

2.3.4 Radioactivity

Natural radioactivity and the single neutron events induced by cosmic muons may occur within a given time window accidentally to form an uncorrelated background. The coincidence rate is given by $R_\gamma R_n \tau$, where R_γ is the rate of natural radioactivity events, R_n is the rate of spallation neutron, and τ is the length of the time window. With the single neutron event rate given in the previous section, the radioactivity should be controlled to 50 Hz to limit the accidental backgrounds <0.1%. The accidental backgrounds can be well determined *in-situ* by measurement of the individual single rates from radioactivity and the single neutrons. The energy spectrum can be also well determined.

Past experiments suppressed uncorrelated backgrounds with a combination of carefully selected construction materials, self-shielding, and absorbers with large neutron capture cross section. However, additional care is necessary to lower the detector energy threshold much below 1 MeV. A higher threshold will introduce a systematic uncertainty in the efficiency of detecting the positron. In the following, the singles rate is from radioactivity depositing >1 MeV of visible energy in detector.

Radioactive background can come from a variety of sources. For simplicity, U, Th, K, Co, Rn, Kr in the following text always mean their radioactive isotopes ^{238}U , ^{232}Th , ^{40}K , ^{60}Co , ^{222}Rn , ^{85}Kr . The radioactive sources include

- U/Th/K in the rocks around the detector hall.
- U/Th/K in the water buffer.
- Co in the detector vessel and other supporting structures.
- U/Th/K in weld rods.
- U/Th/K in the PMT glass.
- U/Th/K in the scintillator.

- U/Th/K in materials used in the detector.
- Dust and other impurities
- Rn and Kr in air.
- Cosmogenic isotopes.

The radioactivity of rock samples from the Daya Bay site has been measured by several independent groups, including the Institute for Geology and Geophysics (IGG). The concentrations are: ~ 10 ppm for U, ~ 30 ppm for Th, and ~ 5 ppm for K. The effect of the rock radioactivity on the antineutrino detectors has been studied with Monte Carlo. With the shielding of 2.5-meter water buffer and 45 cm oil buffer, there are 0.65 Hz, 2.6 Hz, and 0.26 Hz singles rates with visible energy greater than 1 MeV in each antineutrino detector module for U/Th/K, respectively. The total rate is ~ 3.5 Hz.

The geological environment and rock composition are very similar in Hong Kong and Daya Bay. The spectrum of natural radioactivity that we have measured of the rock in the Aberdeen Tunnel in Hong Kong is shown in Fig. 2.15.

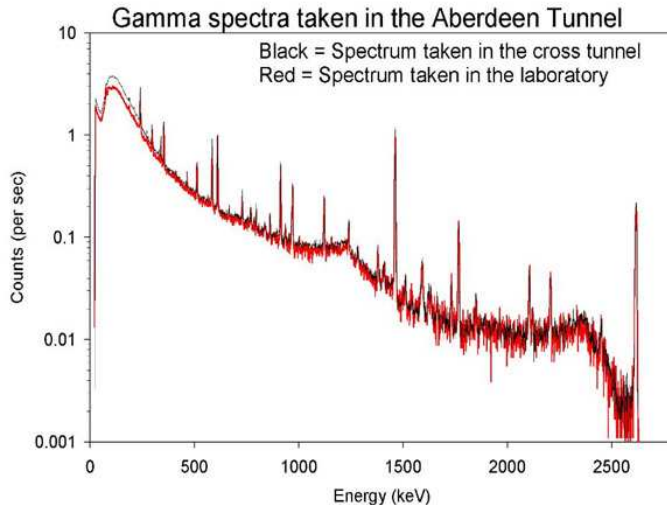


Fig. 2.15. Spectrum of natural radioactivity measured with a Ge crystal in the Hong Kong Aberdeen Tunnel. Prominent peaks for ^{40}K (1.461 MeV) and ^{208}Tl (2.615 MeV) are clearly evident along with many other lines associated with the U/Th series.

The water buffer will be circulated and purified to achieve a long attenuation length for Cherenkov light as well as low radioactivity. Normally tap water has less than 1 ppb U, Th, and K. If filling with tap water, the water buffer will contribute 1.8 Hz, 0.4 Hz, and 6.3 Hz single rates from U/Th/K, respectively. Purified water in the water pool will have much lower radioactivity and can be ignored. The specification for radon in the water is $< 5 \text{ Bq/m}^3$ (see Section 6.2.5), which will contribute a singles rate of < 0.9 Hz.

The Co in stainless steel varies from batch to batch and should be measured before use as detector material, such as the outer vessel. U/Th/K concentration in normal weld rods are very high. There are non-radioactivity weld rods commercially available. Weld rods TIG308 used in KamLAND were measured to have < 1 ppb Th, 0.2 ± 0.08 ppb U, 0.1 ± 0.03 ppb K, and $2.5 \pm 0.04 \text{ mBq/kg}$ Co, five orders of magnitude lower than normal weld rods. The welded stainless steel in KamLAND has an average radioactivity of 3 ppb Th, 2 ppb U, 0.2 ppb K, and 15 mBq/kg Co. Assuming the same radioactivity for the vessel of the Daya

Bay neutrino detector module, the corresponding rates from a 20-ton welded stainless steel vessel are 7 Hz, 4.6 Hz, 1.5 Hz, 4.5 Hz for U/Th/K/Co, respectively for a total of 17.6 Hz.

A potential PMT candidate is the Hamamatsu R5912[§] with low radioactivity glass. The concentrations of U and Th are both less than 150 ppb in the glass, and that of ⁴⁰K is 15 ppb. The Monte Carlo study shows that the single rate is 5.5 Hz, 3.8 Hz, 2.7 Hz for U/Th/K, respectively, with a 20 cm oil buffer from the PMT surface to the liquid scintillator. The total rate from the PMT glass is 12 Hz.

Following the design experience of Borexino and Chooz, backgrounds from impurities in the liquid scintillator can be reduced to the required levels. A major source is the U/Th contamination in the Gadolinium, which can be purified before doped into liquid scintillator. The U/Th/K concentration of $10^{-12} g/g$ in liquid scintillator will contribute only 0.8 Hz of uncorrelated background in a 20-ton detector module.

The radioactivity inside the liquid scintillator can also make *correlated* background. The alpha particles from the U/Th impurity can make $(\alpha, n)^{16}\text{O}$ reaction with ¹³C in the liquid scintillator, which leads to a correlated background if (a) the neutron is fast enough, or (b) there is an accompanying photon from the excited state of ¹⁶O. Assuming a $10^{-12} g/g$ U/Th concentration, this contributes to a correlated background rate of $\sim 4/\text{year/module}$. Compared to Table 2.10, this is about 40% of the muon-induced fast neutron rate at the far site. The cross section of $^{13}\text{C}(\alpha, n)^{16}\text{O}$ is known to $\sim 20\%$ for an alpha energy $< 10 \text{ MeV}$ (highest energy α from U/Th is about 9 MeV). Thus for a given U/Th concentration, this background can be evaluated relatively precisely. Therefore, we shall omit it in the systematic uncertainty calculation in Section 2.3.5.

The alpha particles from U/Th chains in the rock or PMT glasses can also make (α, n) reaction with ¹⁸O, ²⁹Si, and ³⁰Si (0.20%, 4.68%, and 3.09% naturally abundant, respectively) in these materials. Similar to ¹³C above, gamma rays can be released from these reactions due to excited final states. The upper limit of the gamma rate is estimated to be $\sim 1/\text{day/module}$, based on the total (α, n) reaction cross section on the three nuclei [13]. A small fraction of these gammas can have rather high energy, and generate “neutron-like” signals ($> 6 \text{ MeV}$) in the scintillator. Nevertheless, compared to the “neutron-like” rate due to cosmogenic beta emitters in Table 2.12, this contribution is negligible. The average emitting neutron energies from these reactions are about 2.5 MeV. Even for those neutrons from the PMT glass, they will be attenuated by $\sim 10^{-5}$ due to the shielding of the mineral oil and gamma catcher before entering the target. Therefore, the *correlated* (γ and neutron) background here is also negligible compared to, for example, the fast neutron background in Table 2.10.

Radon is one of the radioactive daughters of ²³⁸U, which can increase the background rate of the experiment. The Radon concentration in the experimental halls can be kept to an acceptable level by ventilation with fresh air from outside. Since the neutrino detector modules are immersed in a 2.5-meter thick water buffer, it is expected that the radon contribution, as well as the krypton, can be safely ignored for the water pool design.

The β decay of long lived radioactive isotopes produced by cosmic muons in the scintillator will contribute a couple of Hz at the near detector, and less than 0.1 Hz at the far detector. The rate of muon decay or muon capture are 2–6% of the muon rate. So they can be ignored when viewed as a source of singles.

2.3.5 Background Subtraction Uncertainty

There are additional sources of backgrounds, such as other cosmogenic nuclei, stopped-muon decay, and muon capture. While they are important for a shallow site, our study shows that they can be safely ignored at Daya Bay.

The major backgrounds are summarized in Table 2.13. The rates assume a muon tagging efficiency of 99.5% and a neutron efficiency of 78% (product of 0.85 Gd fraction and 0.93 energy cut). In our sensitivity study, the uncertainties were taken to be 100% for the accidental and fast neutron backgrounds. The ⁸He/⁹Li background can be measured to an uncertainty of 0.3% and 0.1% relative to the antineutrino signal at the

[§]The R5912 is a newer version of the R1408 used by SNO [12].

	DYB site	LA site	far site
Antineutrino rate (/day/module)	930	760	90
Natural radiation (Hz)	<50	<50	<50
Single neutron (/day/module)	18	12	1.5
β -emission isotopes (/day/module)	210	141	14.6
Accidental/Signal	<0.2%	<0.2%	<0.1%
Fast neutron/Signal	0.1%	0.1%	0.1%
${}^8\text{He} {}^9\text{Li}$ /Signal	0.3%	0.2%	0.2%

Table 2.13. Summary of signal and background rates in the antineutrino detectors at Daya Bay. A neutron detection efficiency of 78% has been applied to the antineutrino and single-neutron rates.

near and far sites, respectively.

The rates and energy spectra of all three major backgrounds can be measured *in-situ*. Thus the backgrounds at the Daya Bay experiment are well controlled. The simulated energy spectra of backgrounds are shown in Fig. 2.16. The background-to-signal ratios are taken at the far site.

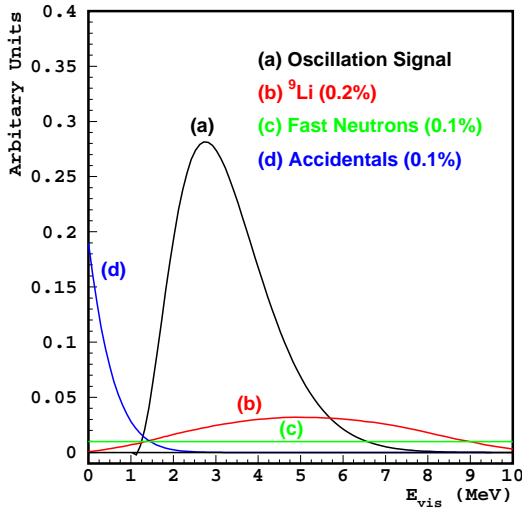


Fig. 2.16. Spectra of three major backgrounds for the Daya Bay experiment and their size relative to the oscillation signal, which is the difference of the expected neutrino signal without oscillation and the ‘observed’ signal with oscillation for $\sin^2 2\theta_{13} = 0.01$.

2.4 Sensitivity

If θ_{13} is non-zero, a rate deficit will be present at the far detector (primarily) due to oscillation. At the same time, the energy spectra of neutrino events at the near and far detectors will be different because neutrinos of different energies oscillate at different frequencies. Both rate deficit and spectral distortion of neutrino signal will be exploited in the final analysis to obtain maximum sensitivity. When the neutrino event statistics are low ($<400 \text{ ton}\cdot\text{GW}_{\text{th}}\cdot\text{y}$), the sensitivity is dominated by the rate deficit. For luminosity higher than $8000 \text{ ton}\cdot\text{GW}_{\text{th}}\cdot\text{y}$, the sensitivity is dominated by the spectral distortion [18]. The Daya Bay

experiment will have $\sim 4000 \text{ ton}\cdot\text{GW}_{\text{th}}\cdot\text{y}$ exposure in three years, so both rate deficit and shape distortion effects will be important to the analysis.

The antineutrino rates in the detector modules determine the statistical uncertainty contribution to the experimental sensitivity. The efficiency factors that have been assumed to compute the expected rates (no oscillation) are given in Table 2.14.

Source	Efficiency	
	Near	Far
Neutron detection	0.78	0.78
Positron detection	0.98	0.98
Muon Veto deadtime	0.95	0.95
Calibration runs	0.99	0.99
Reactor/experiment downtime	0.82	0.82

Table 2.14. Sources of inefficiency leading to loss of statistical precision.

2.4.1 Global χ^2 Analysis

Many systematic uncertainties will contribute to the final sensitivity of the Daya Bay experiment, and many of them are correlated. The correlation of the uncertainties must be taken into account correctly. A rigorous analysis of systematic uncertainties can be done by constructing a χ^2 function with pull terms, where the uncertainty correlations can be introduced naturally [18–21]:

$$\begin{aligned} \chi^2 = & \min_{\gamma} \sum_{A=1}^8 \sum_{i=1}^{N_{bins}} \frac{\left[M_i^A - T_i^A \left(1 + \alpha_c + \sum_r \omega_r^A \alpha_r + \beta_i + \varepsilon_D + \varepsilon_d^A \right) - \eta_f^A F_i^A - \eta_n^A N_i^A - \eta_s^A S_i^A \right]^2}{T_i^A + (\sigma_{b2b} T_i^A)^2} \\ & + \frac{\alpha_c^2}{\sigma_c^2} + \sum_r \frac{\alpha_r^2}{\sigma_r^2} + \sum_{i=1}^{N_{bins}} \frac{\beta_i^2}{\sigma_{shp}^2} + \frac{\varepsilon_D^2}{\sigma_D^2} + \sum_{A=1}^8 \left[\left(\frac{\varepsilon_d^A}{\sigma_d} \right)^2 + \left(\frac{\eta_f^A}{\sigma_f^A} \right)^2 + \left(\frac{\eta_n^A}{\sigma_n^A} \right)^2 + \left(\frac{\eta_s^A}{\sigma_s^A} \right)^2 \right] \end{aligned} \quad (29)$$

where A sums over detector modules, i sums over energy bins, and γ denotes the set of minimization parameters, $\gamma = \{\alpha_c, \alpha_r, \beta_i, \varepsilon_D, \varepsilon_d^A, \eta_f^A, \eta_n^A, \eta_s^A\}$. The γ 's are used to introduce different sources of systematic uncertainties. The standard deviations of the corresponding parameters are $\{\sigma_c, \sigma_r, \sigma_{shp}, \sigma_D, \sigma_d, \sigma_f^A, \sigma_n^A, \sigma_s^A\}$. They will be described in the following text. T_i^A is the expected events in the i -th energy bin in detector A , and M_i^A is the corresponding measured events. F_i^A, N_i^A, S_i^A are number of fast neutron, accidental, and ${}^8\text{He}/{}^9\text{Li}$ backgrounds, respectively. For each energy bin, there is a variance T_i^A and a bin-to-bin systematic uncertainty σ_{b2b} . For each point in the oscillation space, the χ^2 function is minimized with respect to the parameters γ .

Assuming each uncertainty can be approximated by a Gaussian, this form of χ^2 can be proven to be strictly equivalent to the more familiar covariance matrix form $\chi^2 = (M - T)^T V^{-1} (M - T)$, where V is the covariance matrix of $(M - T)$ with systematic uncertainties included properly [19].

To explore the sensitivity to θ_{13} , we use the single parameter raster scan method. We make an assumption of no oscillations so that T_i^A are the event numbers without oscillation. For each given Δm_{31}^2 , the “measured” event numbers M_i^A are calculated with different $\sin^2 2\theta_{13}$. The $\sin^2 2\theta_{13}$ value corresponding to a $\Delta\chi^2$ 2.71 greater than the minimum is the limit of the experiment to exclude the “no oscillation” assumption at 90% confidence level.

The systematic uncertainties are described in detail:

- The reactor-related correlated uncertainty is $\sigma_c \approx 2\%$. This fully correlated uncertainty will be cancelled by the near-far relative measurement and has little impact on the sensitivity.
- The reactor-related uncorrelated uncertainty for core r is $\sigma_r \approx 2\%$. These enter the normalization of the predicted event rate for each detector A according to the weight fractions ω_r^A . After minimization, the σ_r contribute a total of $\sim 0.1\%$ to the relative normalization of neutrino rate. This is essentially equivalent to the analysis described in Section 2.1, and takes into account the correlations of this uncertainty with the others (like the detector efficiencies ε_d^A).
- The spectrum shape uncertainty is $\sigma_{\text{shp}} \approx 2\%$: The shape uncertainty is the uncertainty in the neutrino energy spectra calculated from the reactor information. This uncertainty is uncorrelated between different energy bins but correlated between different detectors. Since we have enough statistics at near detector to measure the neutrino energy spectrum to much better than 2%, it has little effect on the Daya Bay sensitivity.
- The detector-related correlated uncertainty is $\sigma_D \approx 2\%$. Some detection uncertainties are common to all detectors, such as H/Gd ratio, H/C ratio, neutron capture time on Gd, and spill in/out effects, assuming we use the same batch of liquid scintillator and identical detectors. Based on the Chooz experience, σ_D is (1–2)%. Like other fully correlated uncertainties, it has little impact on sensitivity.
- The detector-related uncorrelated uncertainty is $\sigma_d = 0.38\%$. We take the baseline systematic uncertainty as described in Section 2.2.3. The goal systematic uncertainty with swapping is estimated to be 0.12%.
- The background rate uncertainties σ_f^A , σ_n^A , and σ_s^A , corresponding to the rate uncertainty of fast neutron, accidental backgrounds, and ${}^8\text{He}/{}^9\text{Li}$ isotopes. They are listed in Section 2.3.5.
- Bin-to-bin uncertainty σ_{b2b} : The bin-to-bin uncertainty is the systematic uncertainty that is uncorrelated between energy bins and uncorrelated between different detector modules. The bin-to-bin uncertainties normally arise from the different energy scale at different energies and uncertainties of background energy spectra during background subtraction. The only previous reactor neutrino experiment that performed spectral analysis with large statistics is Bugey, which used a bin-to-bin uncertainty of order of 0.5% [22,23]. With better designed detectors and much less background, we should have much smaller bin-to-bin uncertainties than Bugey. The bin-to-bin uncertainty can be studied by comparing the spectra of two detector modules at the same site. We will use 0.3%, the same level as the background-to-signal ratio, in the sensitivity analysis. The sensitivity is not sensitive to σ_{b2b} at this level. For example, varying σ_{b2b} from 0 to 0.5% will change the $\sin^2 2\theta_{13}$ sensitivity from 0.0082 to 0.0087 at the best fit Δm_{31}^2 .

There are other uncertainties not included in the χ^2 function. 1) Due to the energy resolution, the spectra are distorted. However, the energy bins used for sensitivity analysis (~ 30 bins) are $2\sim 6$ times larger than the energy resolution, and the distortion happens at all detectors in the same way. It has little impact on the final sensitivity. 2) Detector energy scale uncertainty has significant impact on detection uncertainties (neutron efficiency and positron efficiency) which has been taken into account in σ_d . An energy scale uncertainty will shift the whole spectrum, thus directly impacting the analysis, especially on the best fit values. However, this shift has very little impact on our sensitivity computations. 3) Current knowledge on θ_{12} and Δm_{21} has around 10% uncertainties. Although the primary oscillation effect at the Daya Bay baseline is related to θ_{13} only, the subtraction of θ_{12} oscillation effects introduce very small uncertainties (see Section 1.2.4). We have studied the above three sources of uncertainty and found that none of them have a significant impact on the sensitivity of the Daya Bay experiment. For simplicity, they are ignored in our χ^2 analysis of sensitivity.

2.4.2 θ_{13} Sensitivity

Figure 2.17 shows the sensitivity contour in the $\sin^2 2\theta_{13}$ versus Δm_{31}^2 plane for three years (we assume 1 year $\equiv 300$ live days) of data, using the global χ^2 analysis and the baseline values for detector-related systematic uncertainties. The green shaded area shows the 90% confidence region of Δm_{31}^2 determined by

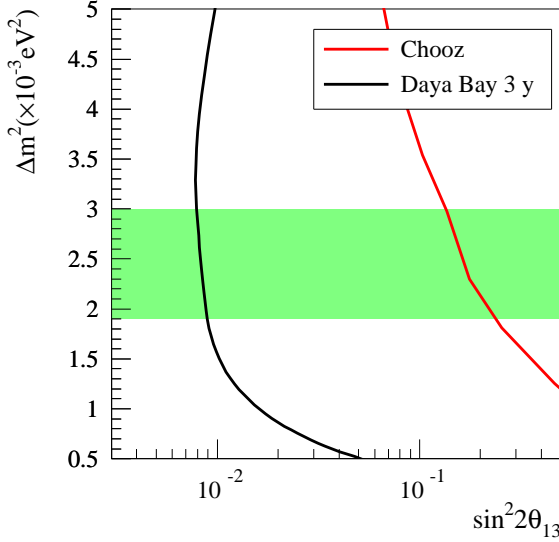


Fig. 2.17. Expected $\sin^2 2\theta_{13}$ sensitivity at 90% C.L. with 3 years of data, as shown in solid black line. The red line shows the current upper limit measured by Chooz.

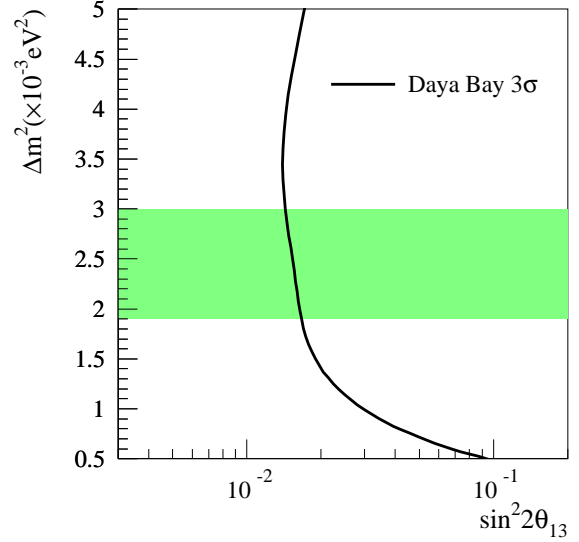


Fig. 2.18. Expected 3σ discovery limit for $\sin^2 2\theta_{13}$ at Daya Bay with 3 years of data.

atmospheric neutrino experiments. Assuming four 20-ton modules at the far site and two 20-ton modules at each near site, the statistical uncertainty is around 0.2%. The sensitivity of the Daya Bay experiment with this design can achieve the challenging goal of 0.01 with 90% confidence level over the entire allowed (90% C.L.) range of Δm_{31}^2 . At the best fit $\Delta m_{31}^2 = 2.5 \times 10^{-3} \text{ eV}^2$, the sensitivity is around 0.008 with 3 years of data. The corresponding values for other assumptions of systematic uncertainties are shown in Table 2.15.

Systematic Uncertainty Assumptions:	Baseline	Goal	Goal with swapping
90% C.L. Limit:	0.008	0.007	0.006

Table 2.15. 90% C.L. sensitivity limit for $\sin^2 2\theta_{13}$ at $\Delta m_{31}^2 = 2.5 \times 10^{-3} \text{ eV}^2$ for different assumptions of detector related systematic uncertainties as considered in Section 2.2.3. We assume 3 years running for each scenario.

Figure 2.18 shows the 3σ discovery limit for $\sin^2 2\theta_{13}$ at Daya Bay with 3 years of data. At $\Delta m_{31}^2 = 2.5 \times 10^{-3} \text{ eV}^2$, the corresponding $\sin^2 2\theta_{13}$ discovery limit is 0.015. Figure 2.19 shows the sensitivity versus time of data taking. After one year of data taking, $\sin^2 2\theta_{13}$ sensitivity will reach 0.014 (1.4%) at 90% confidence level.

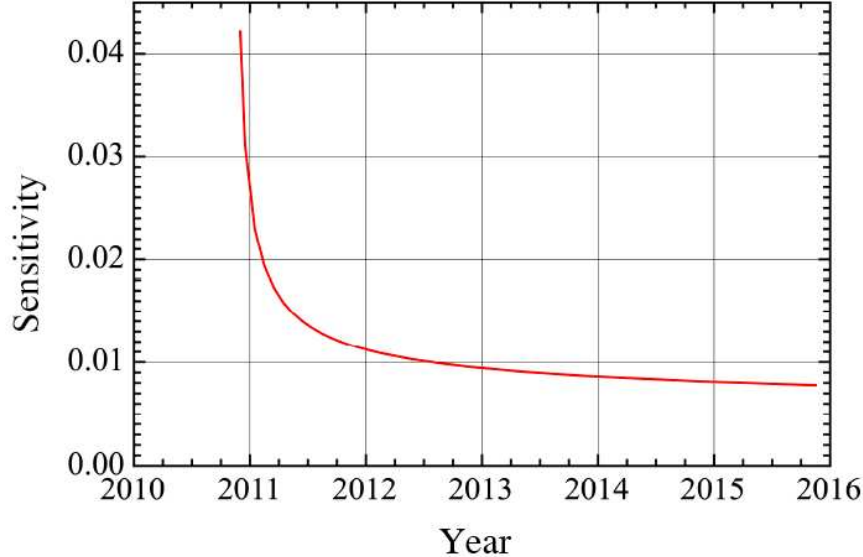


Fig. 2.19. Expected $\sin^2 2\theta_{13}$ sensitivity at 90% C.L. versus time. The curve is calculated with the assumption of two near sites and one far site with data acquisition beginning in Dec. 2010. The value of Δm_{31}^2 is taken to be 2.5×10^{-3} eV².

REFERENCES

1. M. Apollonio *et al.*, Phys. Lett. **B420**, 397 (1998); Phys. Lett. **B466**, 415 (1999); Euro. Phys. J. C **27**, 331 (2003).
2. L. A. Mikaelyan and V. V. Sinev, Phys. Atom. Nucl. **63**, 1002 (2000); L. Mikaelyan, Nucl. Phys. Proc. Suppl. **91**, 120 (2001); L. A. Mikaelyan, Phys. Atom. Nucl. **65**, 1173 (2002).
3. V. Kopeikin, L. Mikaelyan, V. Sinev, Phys. Atom. Nucl. **64**, 849 (2001); V. Kopeikin, L. Mikaelyan, V. Sinev, hep-ph/0412044.
4. K. Eguchi *et al.*, Phys. Rev. Lett. **90**, 021802 (2003).
5. T. Gaisser, *Cosmic Rays and Particle Physics*, Cambridge University Press, 1991.
6. D. Chirkin, hep-ph/0407078.
7. J. Kremer *et al.*, Phys. Rev. Lett. **83**, 4241 (1999)
8. H. Jokisch *et al.*, Phys. Rev. **D19**, 1368 (1979).
9. P. Antonioli *et al.*, Astro. Phys. **7**, 357 (1997).
10. Y. F. Wang *et al.*, Phys. Rev. **D64**, 013012 (2001).
11. T. Hagner *et al.*, Astro. Phys. **14**, 33 (2000).
12. J. Boger *et al.*, Nucl. Instr. and Meth. **A449**, 172 (2000).
13. JENDL (α, n) Reaction Data File 2005, <http://wwwndc.tokai-sc.jaea.go.jp/ftpnd/jendl/jendl-an-2005.html>
14. F. Ardellier, *et al.*, hep-ex/0606025.
15. KamLAND collaboration, private communication.
16. T. Araki *et al.*, (KamLAND Collaboration) Phys. Rev. Lett. **94**, 081801 (2005).
17. Liangjian Wen *et al.*, Nucl. Instr. and Meth. **A564**, 471 (2006).
18. P. Huber, M Lindner, T. Schwetz, and W. Winter, Nucl. Phys. **B665**, 487 (2003); Nucl. Phys. **B645**, 3 (2002).
19. D. Stump *et al.*, Phys. Rev. **D65**, 014012 (2001).
20. Y. Fukuda *et al.*, Phys. Rev. Lett. **81**, 1562 (1998); Y. Ashie *et al.*, hep-ex/0501064.
21. H. Minakata, H. Sugiyama, O. Yasuda, K. Inoue, and F. Suekane, Phys. Rev. **D68**, 033017 (2003); H. Minakata and H. Sugiyama, Phys. Lett. **B580**, 216 (2004).

22. Y. Declais *et al.*, Phys. Lett. **B338**, 383 (1994). B. Ackar *et al.*, Nucl. Phys. **B434**, 503 (1995); B. Ackar *et al.*, Phys. Lett. **B374**, 243 (1996).
23. H. Sugiyama and O. Yasuda, hep-ph/0508090.

3 Experimental Site and Laboratories

The Daya Bay site is an ideal place to search for oscillations of antineutrinos from reactors. The nearby mountain range provides excellent overburden to suppress cosmogenic background at the underground experimental halls. Since the Daya Bay nuclear power complex consists of multiple reactor cores, there will be two near detector sites to monitor the yield of antineutrinos from these cores and one far detector site to look for disappearance of antineutrinos. It is possible to instrument another detector site about half way between the near and far detectors to provide independent consistency checks.

The proposed experimental site is located at the east side of the Dapeng peninsula, on the west coast of Daya Bay, where the coastline goes from southwest to northeast (see Fig. 1.10). It is in the Dapeng township of the Longgang Administrative District, Shenzhen Municipality, Guangdong Province. Two mega cities, Hong Kong and Shenzhen are nearby. Shenzhen City* is 45 km to the west and Hong Kong is 55 km to the southwest (all measured in a straight line). The geographic location is east longitude $114^{\circ}33'00''$ and north latitude $22^{\circ}36'00''$. Daya Bay is semi-tropical and the climate is dominated by the south Asia tropical monsoon. It is warm and rainy with frequent rainstorms during the typhoon season in one half of the year, while relatively dry in the other half. Frost is rare.

The Daya Bay Nuclear Power Plant (NPP) is situated to the southwest and the Ling Ao NPP to the northeast along the coastline. Each NPP has two cores that are separated by 88 m. The distance between the centers of the two NPPs is about 1100 m. The thermal power of each core is $2.9 \text{ GW}_{\text{th}}$. Hence the total thermal power available is $11.6 \text{ GW}_{\text{th}}$. A third NPP, Ling Ao II, is under construction and two cores are scheduled to come online by 2010–2011. This new NPP is built roughly along the line extended from Daya Bay to Ling Ao, about 400 m northeast of Ling Ao. The core type is the same as that of the Ling Ao NPP. When the Daya Bay, Ling Ao and Ling Ao II NPP are all in operation, the complex will provide a total thermal power of $17.4 \text{ GW}_{\text{th}}$.

The site is surrounded to the north by a group of hills which slope upward from southwest to northeast. The slopes of the hills vary from 10° to 45° . The ridges roll up and down with smooth round hill tops. Within 2 km of the site the elevation of the hills are generally vary from 185 m to 400 m. The summit, called Pai Ya Shan, is 707 m PRD[†]. Due to the construction of the Daya Bay and Ling Ao NPPs, the foothills along the coast from the southwest to the northeast have been levelled to a height of 6.6 m to 20 m PRD. The Daya Bay experimental halls are to be located inside the mountain north of the Daya Bay and Ling Ao NPPs.

There is no railway within a radius of 15 km of the site. The highway from Daya Bay NPP to Dapeng Township (Wang Mu) is of second-class grade and 12 m wide. Dapeng Town is connected to Shenzhen, Hong Kong, and the provincial capital Guangzhou by highways which are either of first-class grade or expressways.

There are two maritime shipping lanes near the site in Daya Bay, one on the east side and the other on the west side. Oil tankers to and from Nanhai Petrochemical use the east side. Huizhou Harbor, which is located in Daya Bay is 13 km to the north. Two general-purpose 10,000-ton docks were constructed in 1989. Their functions include transporting passengers, dry goods, construction materials, and petroleum products. The ships using these two docks take the west line. The minimum distance from the west line to the power plant site is about 6 km. Two restricted docks of 3000-ton and 5000-ton capacity, respectively, have been constructed on the power plant site during the construction of the Daya Bay NPP [1].

3.1 General Laboratory Facilities

The laboratory facilities include access tunnels connected to the entrance portal, a construction tunnel for waste rock transfer, a main tunnel connecting all the three underground detector halls, a liquid scintillator

*Shenzhen is the first Special Economic Zone in China. Many international corporations have their Asian headquarters there. It is both a key commercial and tourist site in South China.

[†]PRD is the height measured relative to the mouth of the Zhu Jiang River (Pearl River), the major river in South China.

filling and mixing hall (LS hall), a central water purification station (Water hall), counting rooms, water and electricity supply, air ventilation, and communication. There is an SAB and a control room near the entrance portal on surface. The location of the experiment halls and the layout of the tunnels are shown in Fig. 3.1. All experimental halls are located at similar elevations, approximately -20 m PRD.



Fig. 3.1. Layout of the Daya Bay and Ling Ao cores, the future Ling Ao II cores and possible experiment halls. The entrance portal is shown at the bottom-left. Five experimental halls marked as #1 (Daya Bay near hall), #2 (Ling Ao near hall), #3 (far hall), #4 (water hall), #5 (LS hall) are shown. The green line represents the access tunnel, the blue lines represent the main tunnels and the pink line represents the construction tunnel. The total tunnel length is about 3000 m.

3.1.1 Tunnels

A sketch of the layout of the tunnels, which consist of the entrance portal and access tunnel, the main tunnels, experimental halls, and the construction portal and tunnel, is shown in Fig. 3.2. There are three major branches of the main tunnels, which are represented by line{3-7-4-5}, line{4-8-Ling Ao near} and line{5-Far}. They are horizontal tunnels extending from junctions 4 and 5 to the near and far underground detector halls. The lines marked as A, B, C, D and E are for the geophysical survey. Line E, which is a dashed line on the top of figure across the far site, is the line of the geophysical survey made to investigate if the far site needs to be pushed further from the reactor cores for future optimizations. Line{1-2-3} is the access tunnel with a length of 292 m. The lines B and C are survey lines for alternate construction tunnel designs. The current design for the construction tunnel is marked as line F which is very close to the survey line C.

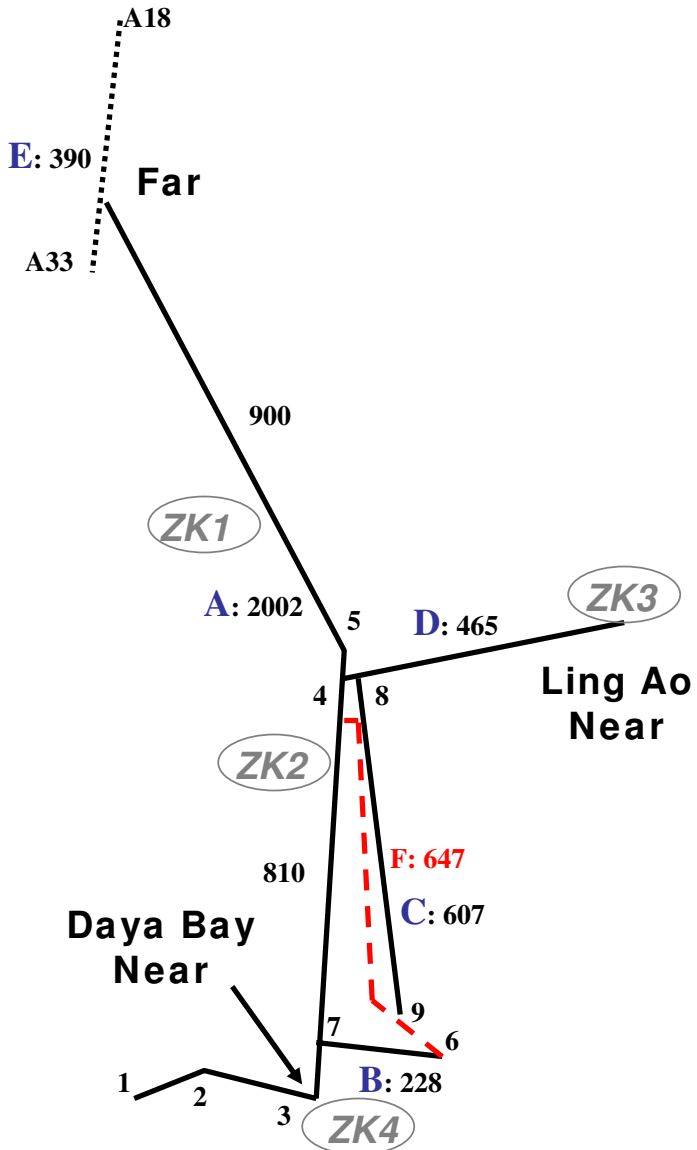


Fig. 3.2. The original plan view of the experimental halls and tunnels from the site survey. Note the length here is slightly different from the presently optimized experiment halls, therefore the lengths of tunnels are also slightly different (see, Fig. 3.1). All distances are in meters. Line A{1-2-3-7-4-5-far site} has a total length of 2002 m; Line B{7-6} has a total length of 228 m; Line C{8-9} has a total length of 607 m; Line D{4-8-Ling Ao near} has a total length of 465 m. Line E is the dashed line on the top across far site. Line F is the construction tunnel for bidding. The four bore hole sites are marked as ZK1, ZK2, ZK3, ZK4 from north to south. They will be referred to later in the discussions of geological exploration in Section 3.2.3 and engineering drilling in Section 3.2.4.

As shown in the enlarged insert of Fig. 3.1 the entrance portal to the underground site is located behind the on-site hospital and lies to the west of the Daya Bay near site. The access tunnel from the portal to the Daya Bay near hall is sloped downward with a 9.6% grade. The downward sloping access tunnel allows the

underground facilities to be located deeper with more overburden.

The access and main tunnels will be able to accommodate vehicles transporting equipment of different size and weight. The grade of the main tunnel will be 0.3% upward from the Daya Bay near hall to both the Ling Ao hall and the far hall. The slightly sloped tunnel has two important functions: to ensure a nearly level surface for the movement of the heavy detectors filled with liquid scintillator and to channel any water seeping into the tunnel to a collection pit located at the lowest point, near the Daya Bay near site. The collected water will be pumped to the surface.

The entrance portal of the construction tunnel (red dashed Line F in Fig. 3.2) is near the lower level of the Daya Bay Quarry. The length of this tunnel is 647 m from the entrance to the junction point with the main tunnel near ZK2. The slope of this construction tunnel is 10%. During the tunnel construction, most of the waste rock and dirt will be transferred through this tunnel to the outside in order to minimize the interference with the operation of the hospital and speed up the tunnel construction. However, completion of the Daya Bay near hall will be advanced by transportation of some dirt through the main portal to dump site. The access tunnel and the Daya Bay near hall will be finished earlier than the far and Ling Ao halls since much less tunnelling is required. After the work on this section of tunnel is finished (construction and outfitting) and a barrier is installed between the tunnel construction and the experimental area, the Daya Bay near, Water and LS halls will be available for detector installation. Because the construction tunnel is far from the access tunnel and the Daya Bay near hall, the excavation activities for the rest of the main tunnel and the detector assembly in the Daya Bay near site can proceed in parallel with minimal interference. We expect beneficial occupancy of the Daya Bay near site about 14 months after the start of civil construction.

Excavations will begin from both the main portal and the construction portal. When the excavation of the construction tunnel reaches the main tunnel, excavation will proceed in parallel to both the Daya Bay near hall and the other two halls, subject to the condition that beneficial occupancy of the Daya Bay near hall should occur as early as possible. At the junction marked as 4 in Fig. 3.2, the main tunnels to the far hall and the Ling Ao hall will also proceed in parallel.

The total length of the tunnel is about 3000 m. The amount of waste to be removed will be about 200,000 m³. About half of the waste will be dumped in the Daya Bay Quarry to provide additional overburden for the Daya Bay near site which is close to the Quarry. This requires additional protection and retaining walls. The rest of the waste will be disposed of along with waste from the construction of the Ling Ao II NPP. Our tunnel waste is about one tenth that of the Ling Ao II NPP.

3.2 Site Survey

The geological integrity of the Daya Bay site was studied in order to determine its suitability for the construction of the underground experimental halls and the tunnels connecting them. The survey consisted of a set of detailed geological surveys and studies: (1) topographic survey, (2) engineering geological mapping, (3) geophysical exploration, (4) engineering drilling, (5) On-site tests at boreholes and (6) laboratory tests. The site survey has been conducted by the Institute of Geology and Geophysics (IGG) of the Chinese Academy of Sciences (CAS). The work started in May 2005 and was completed in June 2006.

3.2.1 Topographic Survey

The topographic survey is essential for determining the position of the tunnels and experimental halls. From the topographic survey the location of the reactor cores relative to the experimental halls is determined, as are the overburdens above each of the experimental halls. The overburdens are input in the optimization of the experimental sensitivity. They are also relevant for the portal design and construction. Appropriate maps are constructed out of this measurement. The area surveyed lies to the north of the Daya Bay complex. The area of the survey extends 2.5 km in the north-south direction and varies from 450 m to 1.3 km in the east-west direction as determined by the locations of the experimental halls and tunnels. The total area measured is 1.839 km². The results of the survey are plotted in a scale of 1:2000.

The instrument used for the topographic measurement is a LEICA TCA2003 Total Station, with a precision of $\pm 0.5''$ in angle and ± 1 mm in distance. Based on four very high standard control points that exist in the area, twenty-six high grade control points and forty-five map baseline points are selected. In total, 7000 points are used to obtain the topographic map. As an example, Fig. 3.3 shows part of the topographic map around the far site. The altitude difference between adjacent contour lines is one meter. The area around

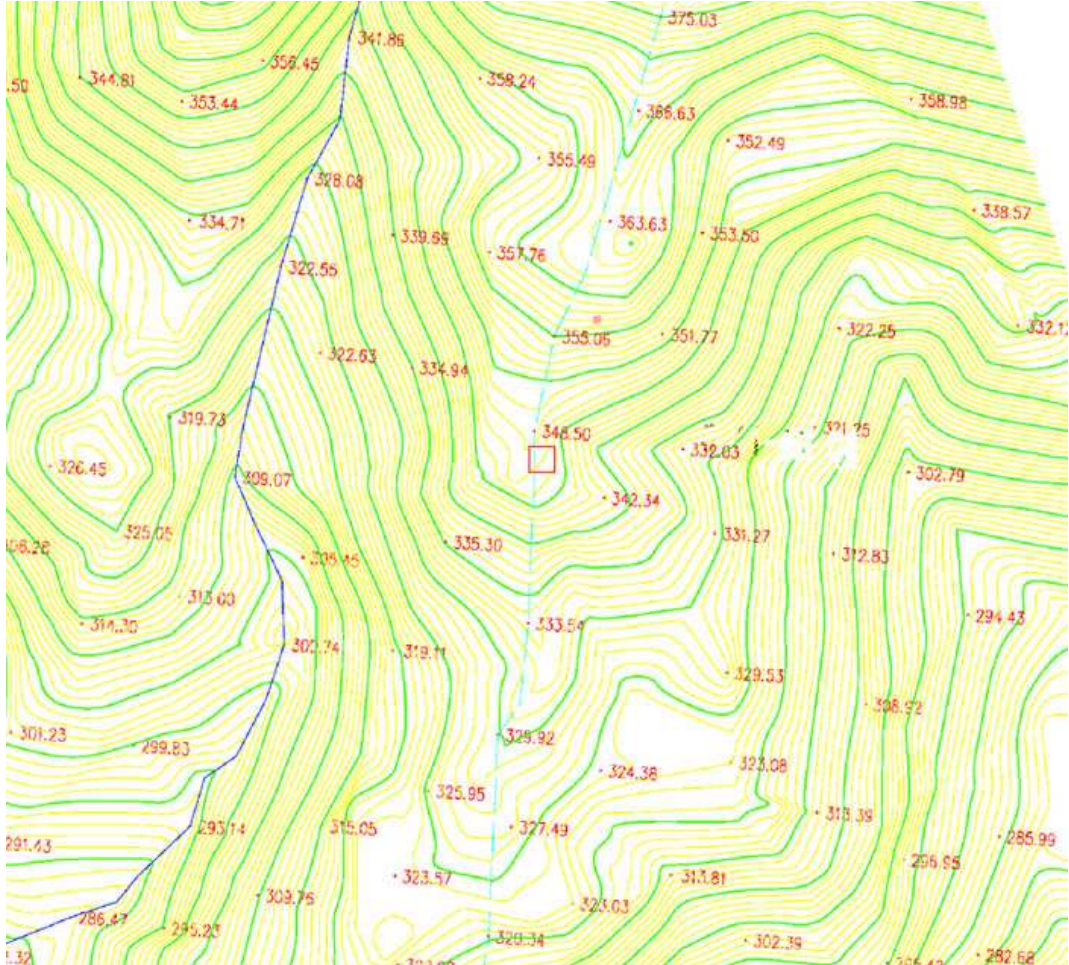


Fig. 3.3. Topographical map in the vicinity of the far site. The location of the far detector hall is marked by a red square in the middle of the map.

the entrance portal behind the local hospital, and two possible construction portals are measured at a higher resolution of 1:500. The cross sections along the tunnel line for the access and construction portals are measured at an even higher resolution of 1:200. The positions of the experimental halls, the entrance portal, and the construction portal are marked on the topographic map.

3.2.2 Engineering Geological Mapping

Geological mapping has been conducted in an area extending about 2.5 km in the north-south direction and about 3 km in the east-west direction. From an on-the-spot survey to fill in the geological map of the area, a list of the geological faults, underground water distribution and contact interface between different types of rocks and weathering zones can be deduced. The statistical information on the orientation of joints is used to deduce the general property of the underground rocks, and the determination of the optimal tunnel

axes. The survey includes all the areas through which the tunnels will pass and in which the experimental halls are to occupy. Reconnaissance has been performed along 28 geological routes, of 18.5 km total length. Statistics of 2000 joints and rock mine skeletons are collected at 78 spots. Rock mine appraisals are made with 36 sliced samples.

Surface exploration and trenching exposure show that the landform and terrains are in good condition. There are no karsts, landslides, collapses, mud slides, empty pockets, ground sinking asymmetry, or hot springs that would affect the stability of the site. There are only a few pieces of weathered granite scattered around the region.

The mountain slopes in the experimental area, which vary from 10° to 30°, are stable and the surface consists mostly of lightly effloresced granite. The rock body is comparatively integrated. Although there is copious rainfall which can cause erosion in this coastal area, there is no evidence of large-scale landslide or collapse in the area under survey. However, there are small-scale isolated collapses due to efflorescence of the granite, rolling and displacement of effloresced spheroid rocks.

The engineering geological survey found mainly four types of rocks in this area: (1) hard nubby and eroded but hard nubby mid-fine grained biotite granite, (2) gray white thick bedding conglomerate and gravel-bearing sandstone, (3) siltstone, (4) sandy conglomerate sandstone. Most of the areas are of hard nubby granite, extended close to the far detector site in the north and reaching to the south, east, and west boundaries of the investigated area. There exists a sub-area, measured about 150 m (north-south) by 100 m (east-west), which contains eroded but still hard nubby granite north of a conspicuous valley existing in this region.[‡] Mildly weathered and weathered granite lies on top of the granite layer. Devonian sandstones are located in the north close to the far detector site. There are also scattered sandstones distributed on the top of the granite. The granite is generally very stable, with only three small landslides found around the middle of the above mentioned valley. The total area of the slide is about 20 m² and the thickness is about 1 m. Four faults and two weathering bags have been identified. The weathering bags are shallow with no or at most a slight effect for the rocks at the tunnel depth. The faults are all of widths of tens centimeter and can be crossed quickly during tunnelling. A detailed geological map is shown in Fig. 3.4 and explained in the caption.

The accumulation and distribution of underground water depends generally on the local climate, hydrology, landform, lithology of stratum, and detailed geological structure. In the investigated area of the Daya Bay site, the amount of underground water flux depends, in a complicated way, on the atmospheric precipitation and the underground water seeping that occurs. The sandstone area is rich in underground water seeping in, mainly through joints caused by weathering of crannies that formed in the structure. No circulation is found between the underground water and outside boundary water in this area. Underground water mainly comes from the atmospheric precipitation, and emerges in the low land and is fed into the ocean.

Table 3.1 gives the values of various aspects of the meteorology of the Daya Bay area. A direct comparison shows that the weather elements in Daya Bay are similar to those in the Hong Kong—Shenzhen area. Plots of the average monthly rainfall and temperature at the Da Ken station for 1985 are shown in Fig. 3.5.

According to the historical record back to December 31, 1994, there have been 63 earthquakes above magnitude 4.7 on the Richter scale (RS), including aftershocks, within a radius of 320 km of the site.[§] Among the stronger ones, there was one 7.3 RS, one 7.0 RS, and ten 6.0–6.75 RS. There were 51 medium quakes between 4.7 and 5.9 RS. The strongest, 7.3 RS, took place in Nan Ao, 270 km northeast of Daya Bay, in 1918. The most recent one happened in 1969 in Yang Jiang at 6.4 RS. In addition, there have been earthquakes in the southeast region of China and one 7.3 RS quake occurred in the Taiwan Strait on Sept.

[‡]The valley extends in the north-east direction from the north-east edge of the reservoir. The valley can be seen in Fig. 3.1, as a dark strip crossing midway along the tunnel to the far hall.

[§]The seismic activity quoted here is taken from a Ling Ao NPP report [2].

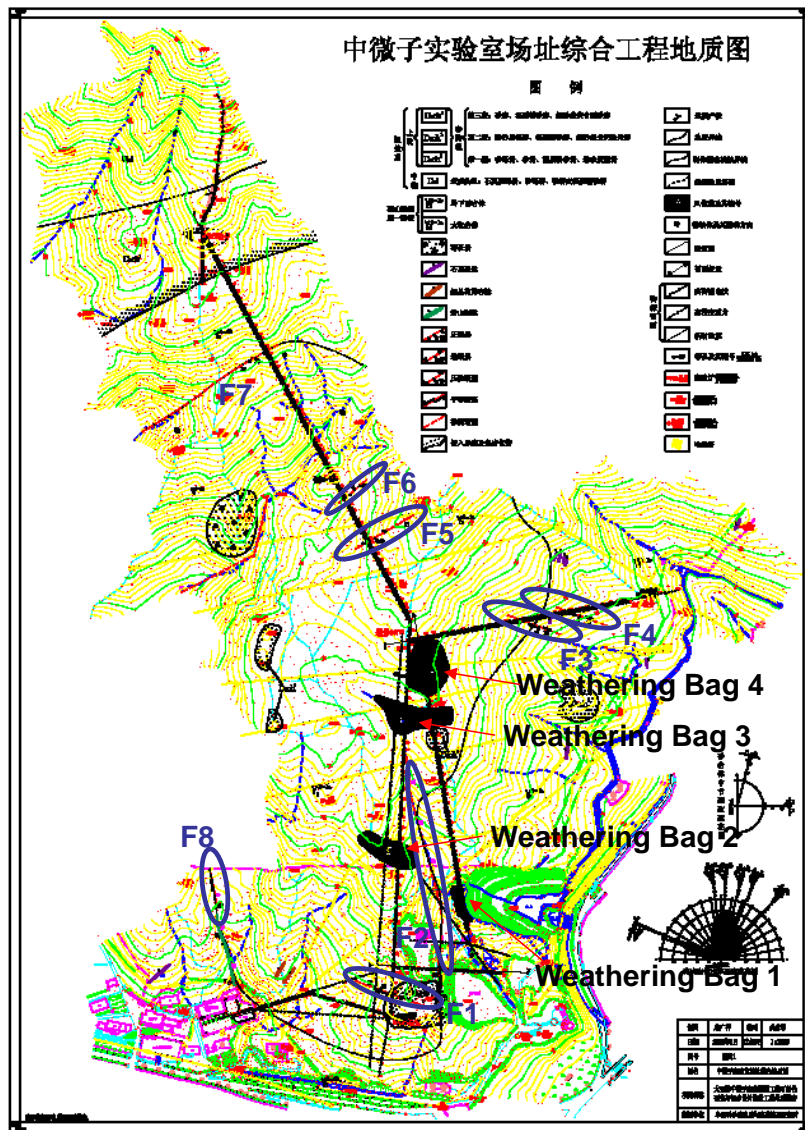


Fig. 3.4. Geological map of the experimental site. The faults are shown as red line segments and marked by blue ellipses. Faults F2, F6, F7, and F8 are revealed by the Geological Mapping (see Section 3.2.2) and Faults F1, F3, F4, and F5 by Geological Exploration (see Section 3.2.3). Four weathering bags marked as black areas and as indicated explicitly are also revealed, two each, by the Mapping and Exploration.

16, 1994. The epicenters of the quakes were at a depth of roughly 5 to 25 km. These statistics show that the seismic activities in this region originate from shallow sources which lie in the earth crust. The strength of the quakes generally decreases from the ocean shelf to inland.

Within a radius of 25 km of the experimental site, there is no record of earth quakes of $M_s \geq 3.0$ ($M_L \geq 3.5$),[¶] and there is no record of even weak quakes within 5 km of the site. The distribution of the weak quakes

[¶] M_s is the magnitude of the seismic surface wave and M_L the seismic local magnitude. M_s provides the information of the normal characteristics of an earthquake. There is a complicated location-dependent relationship between M_s and M_L . In Daya Bay $M_s \geq 3.0$ is equivalent to $M_L \geq 3.5$.

Meteorological Data	Units	Magnitude
Average air speed	m/s	3.29
Yearly dominant wind direction		E
Average temperature	°C	22.3
Highest temperature	°C	36.9
Lowest temperature	°C	3.7
Average relative humidity	%	79
Average pressure	hPa	1012.0
Average rainfall	mm	1990.8

Table 3.1. Average values of meteorological data from the Da Ken station in 1985.

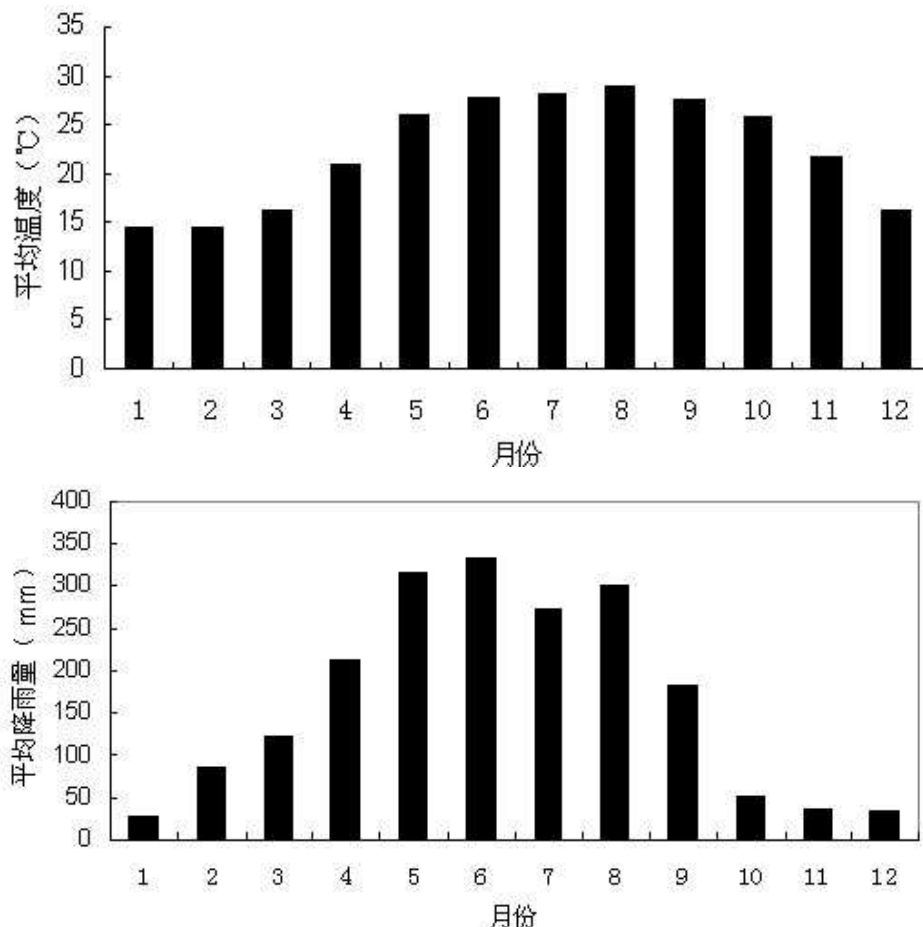


Fig. 3.5. Monthly average temperature and rainfall from data provided by the Da Ken weather station. The horizontal axis gives the months from January (1) to December (12) and the vertical axis is the average temperature in centigrade in the top figure and the rainfall in mm in the bottom figure.

is isolated in time and separated in space from one another, and without any obvious pattern of regularity.

According to the Ling Ao NPP site selection report [3], activity in the seismic belt of the southeast sea has shown a decreasing trend. In the next one hundred years, this region will be in a residual energy-releasing period to be followed by a calm period. It is expected that no earthquake greater than 7 RS will likely occur within a radius of 300 km around the site; the strongest seismic activity will be no more than 6 RS. In conclusion, the experimental site is in a good region above the lithosphere, as was ascertained when the NPP site was selected.

3.2.3 Geophysical Exploration

Three methods are commonly used in geophysical prospecting: the high density electrical resistivity method, high resolution gravity method, and seismic refraction image method using mechanical hammer. The first two methods together with the third as supplement have been used for the Daya Bay geophysical study^{||}. The combination of these three methods reveal the underground structure, including: faults, type of granite, rock mine contact interface, weathering zone interface, and underground water distribution.

Geophysical exploration revealed another four faults and two weathering bags along the tunnels. Figure 3.6 shows the geophysical survey, including the experimental halls and tunnel sections from the Daya Bay near hall to the far hall. The experimental halls (0 marks the near hall and 1800 the far hall), the tunnel sections (the white horizontal line at the lower part of the top and bottom figures with the three small white squares to indicate the experimental halls), faults and weathering bags are marked by blue and green. The electrical resistivity measurements are shown in the middle part of the figures, represented by the almost overlapping solid and dashed lines. The high resolution density measurements is given in the bottom figure, and two sections of seismic refraction measurement is in the top figure. Because of the complexity and variation of the underground structures, the electrical resistivity was measured in the boreholes ZK1 and ZK2 (see, Fig. 3.2). The resistivity and density of the rock samples from the boreholes were used for calibration of the resistivity map. Depending on the characteristics of the granite and its geological structure, the electrical resistivity of this area can vary from tens of $\Omega\text{-m}$ to more than $10k\Omega\text{-m}$. The non-weathered granite has the highest electrical resistivity, whereas the sandstone has medium resistivity due to trapped moisture. The weathered zone, consisting of weathered bursa and faults, has relatively low resistivity.

3.2.4 Engineering Drilling

Based on the information available for the faults, zones with relative high density of joints, weathering bags, and low resistivity areas revealed from previous geological survey, the position of four borehole were determined. The purpose of the boreholes was essentially to confirm or exclude the inferences from the previous survey approaches above ground. These four boreholes are labelled as ZK1, ZK2, ZK3, ZK4 from north to south in Fig. 3.2. The depths of the four boreholes are 213.1 m, 210.6 m, 130.3 m, and 133.0 m respectively (all to at least the tunnel depth). Figure 3.7 shows sections of rock samples obtained from borehole ZK1. Similar samples are obtained in the other three boreholes. The samples are used for various laboratory tests as described below.

3.2.5 On-site Tests at Boreholes

A number of on-site tests have been performed based on rock samples obtained from the boreholes or in situ in the boreholes:

1. High density electrical resistivity measurement in boreholes ZK1 and ZK2.

^{||}In order not to affect the construction work of Ling Ao II, a heavy blaster cannot be used as a source of the seismic refraction measurement, as required for deep underground measurement. Therefore seismic refraction cannot be used as a major tool for the Daya Bay prospecting.

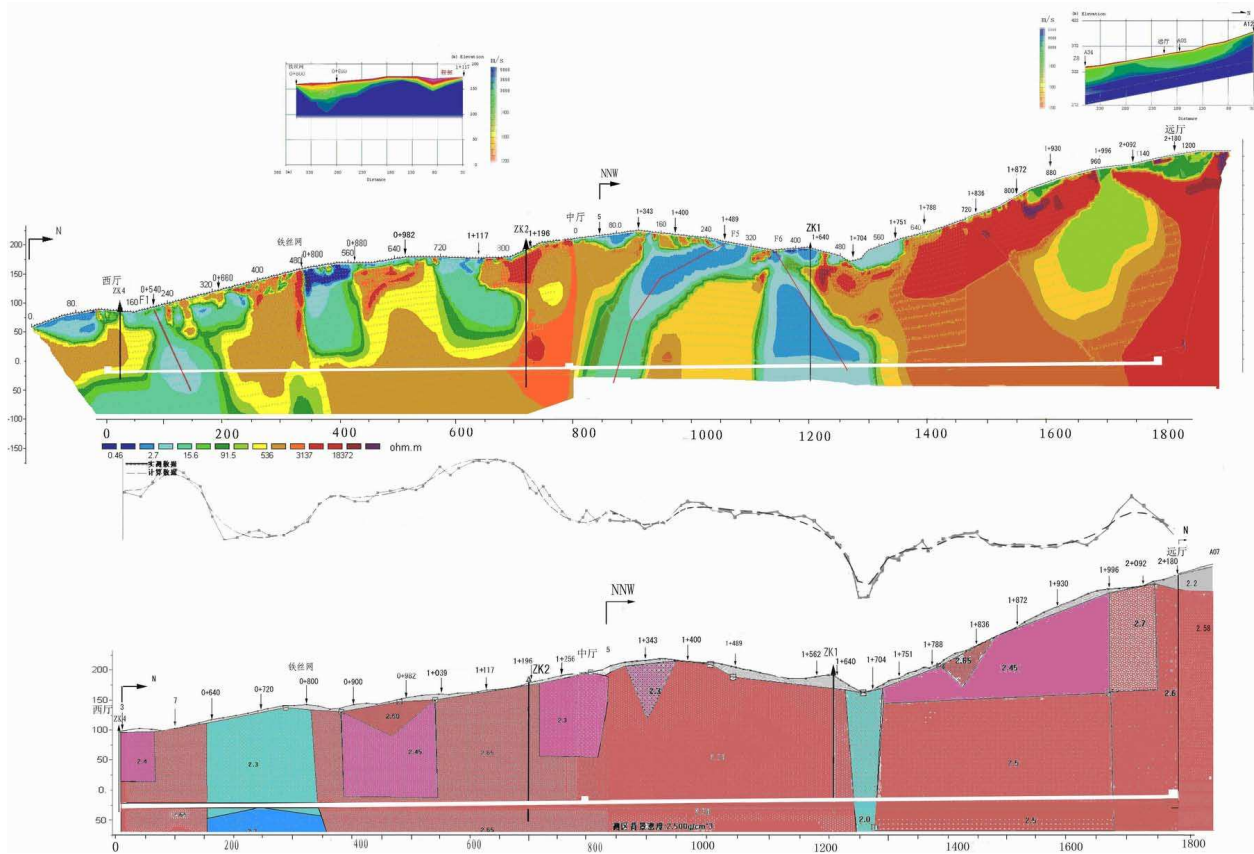


Fig. 3.6. Seismic refraction, electrical resistivity and high resolution density maps along the tunnel cross section from the Daya Bay experimental hall (left end) to the far hall (right end).

2. Permeability tests at different time and depth are made in the boreholes during borehole drilling and at completion. The test shows that all measured values of the permeability parameter K are less than 0.0009 m/d . The K values in ZK2, ZK3 are smaller than that in ZK1 and ZK4. Figure 3.8 shows the water level variation vs time from pouring tests in the four boreholes during the five months period, from December 22, 2005 to June 1, 2006. The horizontal axis is the date and the vertical axis is the water level measured in meters from 0 to 100 m.
3. Acoustic logging, which is tested at different segments of the boreholes separated by 0.5 m. There are 66, 26, 34, 23 segments tested in ZK1, ZK2, ZK3, ZK4 respectively. The combined results give the velocity of longitudinal wavelength $V_p = 5500 \text{ m/s}$ in the fresh granite.
4. Geo-stress tests.
5. Digital video for visual inspection.
6. The radon emanation rate inside the borehole ZK4 was measured up to a depth of 27 m with an electronic radon dosimeter inserted into the borehole. An average rate of $0.58 \times 10^{-3} \text{ Bq m}^{-2} \text{ s}^{-1}$ was determined at depths of 14–27 m after correction for back diffusion. These values generally agree with the rates $(0.13\text{--}2.56) \times 10^{-3} \text{ Bq m}^{-2} \text{ s}^{-1}$ measured directly from the rock samples extracted from the borehole.



Fig. 3.7. Rock samples from borehole ZK1.

7. Measurements of the rock chemical composition. Among the chemical elements of the rock measured, the amount of radioactive U was measured to be 10.7, 16.6, 14.5 and 14.2 ppm from the samples in each of the four boreholes, respectively. The Th concentrations were measured to be 25.2, 49.6, 29.4 and 41.9 ppm in each of the borehole respectively.
8. Water chemical analysis. Water samples from the four boreholes and a surface stream have a pH slightly smaller than 7.5, considered to be neutral. The water hardness is smaller than 42 mg/l which is considered to be very soft. The underground water is thus very weakly corrosive to the structure of steel, but is not corrosive to reinforced concrete.

3.2.6 Laboratory Tests

Laboratory tests performed includes: rock chemical properties, mineral elements, physical and mechanical property tests. The following data are some of the physical properties of slightly weathered or fresh rocks which are the most comment rock types found in the tunnel construction:

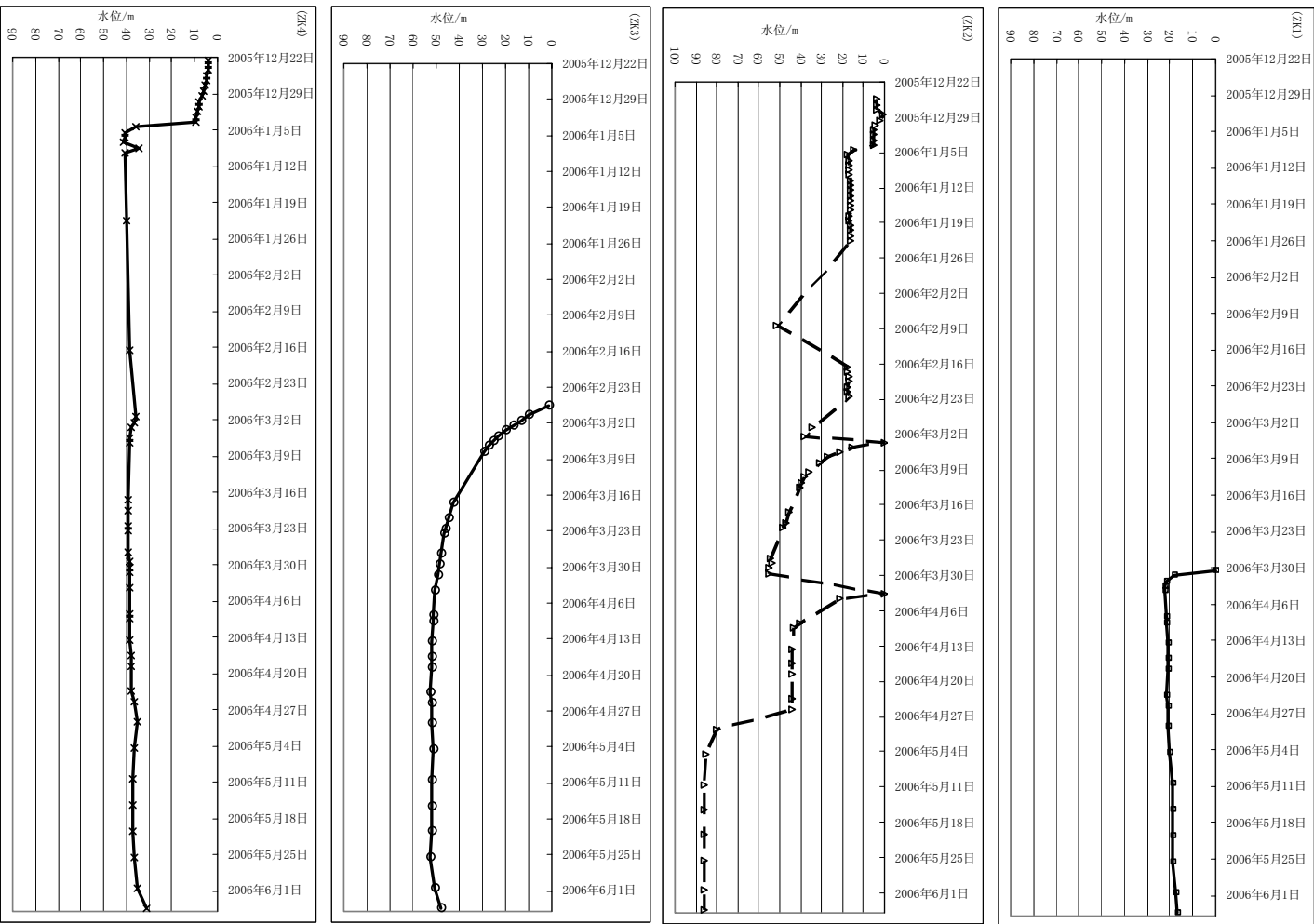


Fig. 3.8. Water level variation vs time in the four boreholes from Dec. 22, 2005 to early June, 2006. There is no measurement during holidays in January 2006 in ZK2. The cause of the sudden drop of the water level in April 2006 is unknown. The horizontal axis coordinate is in units of 7 days, the date reads as year/month/day. The vertical axis is the water level in meters into the borehole.

- Density of milled rock: $2.609 \sim 2.620 \text{ g/cm}^3$
- Density of bulk rock: $2.59 \sim 2.60 \text{ g/cm}^3$
- Percentage of interstice: $0.765\% \sim 1.495\%$
- Speed of longitudinal wave (V_p): $4800 \sim 5500 \text{ m/s}$
- Pressure resistance strength of a saturated single stalk: $85.92 \sim 131.48 \text{ MPa}$
- Pressure resistance strength of a dry single stalk: $87.88 \sim 125.79 \text{ MPa}$
- Softening coefficient: $0.924 \sim 1.000$
- Elastic modulus: $32.78 \sim 48.97 \text{ GPa}$
- Poisson ratio: $0.163 \sim 0.233$

3.2.7 Survey Summary

Based on the combined analyses of the survey and tests described above, IGG concludes that the geological structure of the proposed experimental site is rather simple, consisting mainly of massive, slightly weathered or fresh blocky granite. There are only a few small faults with widths varying from 0.5 m to 2 m, and the affected zone width varies from 10 m to 80 m. There are a total of four weathering bags along the tunnel from the Daya Bay near site to the far site (see, Fig. 3.4) and on the construction tunnel from the Daya Bay quarry. The weathering depth and width are 50–100 m. Just below the surface, the granite is mild to mid weathered. These weathered zones are well above the tunnel, more than three times tunnel diameter away, so the tunnel is not expected to be affected by these weathering bags. Nevertheless, there are joints around this region and some sections of the tunnel will need extra support.

The far hall, at a depth of 350 m is thought to consist of lightly effloresced or fresh granites; the far hall is most likely surrounded by hard granite. The distance to the interface with Devonian sandstone is about 100 m (to the North) as indicated by the present analysis.

The rock along the tunnel is lightly effloresced or fresh granite, and the mechanical tests found that it is actually hard rock. No circulation is found between the underground water and the outside boundary water in this area, and the underground water mainly comes from the atmospheric precipitation. Water borehole permeability tests show that underground water circulation is poor and no uniform underground water level at the tunnel depth. At the tunnel depth the stress is 10 MPa, which lies in the normal stress regime. The quality of most of the rock mass varies from grade II to grade III (RQD around 70% which indicates good and excellent rock quality). From the ZK1 and ZK2 stress measurements and structure analysis, the orientation of the main compressive stress is in the NWW (northwest to west) direction. For the east-west oriented excavation tunnel, this is a favorable condition for tunnel stability. For the 810 m segment of the main tunnel from the Daya Bay near hall (#1) to the junction the tunnel orientation will run nearly perpendicular to the orientation of the maximum principal stress and thus limits the area in the excavation perimeter to subject to high level of stresses. These limited high stress levels are not expected to cause significant stability problems due to the good strength of the granite rock mass. There are some tunnel sections, including the access tunnel, where the rock mass quality is of grade IV, and some belongs to grade V. Figure 3.9 shows the details of the engineering geological section along Line A of Fig. 3.2. Detailed results from the site survey by IGG can be found in references [4,7–12].

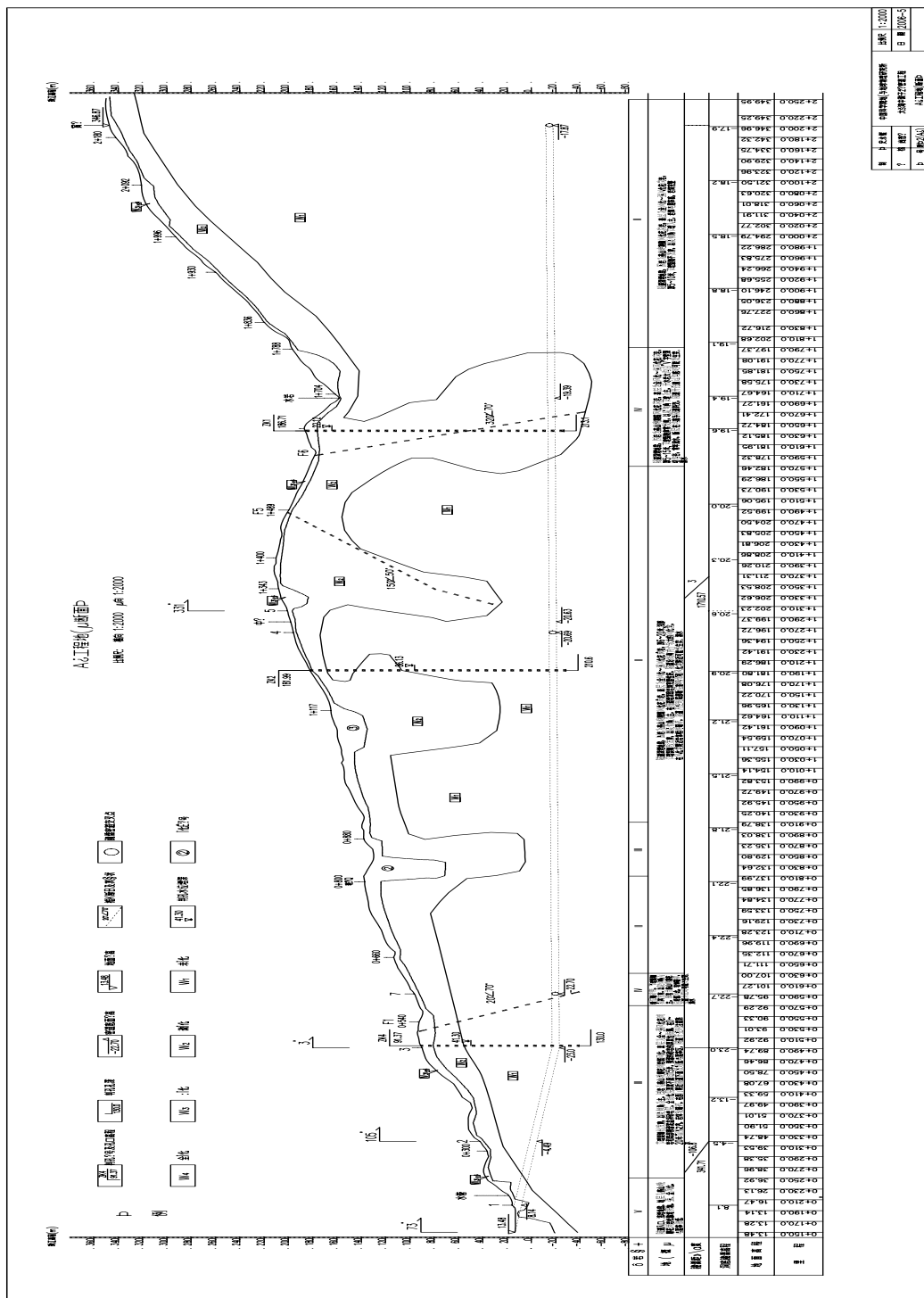


Fig. 3.9. Engineering geological section in line A: the faults, weathering bags and tunnel are shown on the figure. The first curve down from the surface shows the boundary of the weathered granite and the second curve down shows the boundary of the slightly weathered granite. The tunnel passes through one region of slightly weathered granite.

3.3 Civil Design

In June 2006 a bid package for the conceptual design of the civil construction of the Daya Bay project was released. The purpose of this effort was to further refine our understanding of the cost of various options and to make sure that no important points were left out of the final design specifications. The major items of the conceptual design included: (1) the underground experimental halls, the connecting, access, and construction tunnels; (2) the infrastructure buildings above ground; (3) the electric power, communication, monitor, ventilation system, water supply and drainage, safety, blast control, and environmental protection. Two design firms were selected: the Fourth Survey and Design Institute of China Railways (TSY) and the Yellow River Engineering Consulting Co. Ltd. (YREC). TSY has expertise in the design of railway tunnels, and YREC has a great deal of experience in underground hydroelectric engineering projects. These designs in the form of design reports were completed in early August 2006. The two reports were helpful in writing the specifications for the bid of the detailed tunnel design.

YREC was selected to draft a preliminary design for civil construction and their report was released in February 2007. Uncertainties in the previous designs were constrained and one design was selected. More optimization was made based on the conceptual designs and details of the civil design that were provided.

3.3.1 Transportation Vehicle for the Antineutrino Detectors

Suitable transportation facilities are a crucial component for the success of our experiment. The biggest item to transport through the tunnels is the antineutrino detector (AD). Each module is a 115 T cylinder with a 5.1 m diameter and 5 m height (with ports extending 30 cm above). It is clear that the transportation requirements for the antineutrino detectors determines the cross section of the tunnel and the tunnel construction plan.

The space in the tunnel is limited, so the AD transporter should be easy to operate, maneuverable, yet smooth and stable when operating in a straight line. The tunnel connecting the SAB and the underground halls will have parallel side walls 6.2 m in width with a domed ceiling less than 8 m in height at the apex. This tunnel configuration puts significant constraints on the transporter to be adopted. Commonly used heavy truck tractors with lowboy trailers (that must always be in a towing configuration) have limited maneuverability in tight quarters. They also require that the load be lifted on and off with overhead crane. For these reasons we have investigated a custom transport vehicle of the design supplied by such commercial manufacturers as Goldhofer and Doerfer Companies, Wheelift Systems Group**, as shown in Fig. 3.10. These transport vehicles have low flatbed load platforms supported by multiple independently computer controlled dual wheel sets with hydraulic lift capability. With an AD designed to perch atop vertical support legs at the base, a 3 m wide vehicle can maneuver under the AD and between support legs to gently lift the load for transport. The transporter flatbed top surface will be no greater in height than 0.5 m off the tunnel floor and will automatically maintain a load level orientation during transport of a filled AD. Such a vehicle is dynamically capable of either moving forward, reverse or in any transverse direction, with complete rotation about the load center (the turn radius is limited only by the length of the vehicle and load). The vehicle can be manually controlled by an operator or capable of pre-programmable unmanned operation. The vehicle can be powered by a diesel engine during long tunnel transports or connected to AC power when maneuvering at destination sites.

The Doerfer Companies has shown interest in this application and supplied the following operational parameters on an applicable transport vehicle for tunnel civil construction requirements.

- Rated capacity of a dual (12 inch diameter × 6 inch wide) wheel module is 12,700 kg; with 10 dual wheel modules the total capacity is 127,000 kg.
- Spacing between dual wheel modules is 1.04 m longitudinal × 2.1 m lateral.

**<http://www.wheelift.com/>



Fig. 3.10. Photo of a Doerfer 140-ton capacity transporter from underside showing multiple dual wheel modules under vehicle load bed.

- Floor contact area of each wheel under load is 92.5 cm^2 .
- Outer dimension of vehicle is $3.0 \text{ m} \times 7.1 \text{ m}$, and load platform is $3.0 \text{ m} \times 5.6 \text{ m}$.
- Load platform vertical lift range of motion is 0.46 m to 0.57 m .
- Maximum vehicle speed without load is 2.7 kph , and with load 1.5 kph .
- Smallest turn radius is on center rotation with programmable fixed turn radii.
- Minimum tunnel floor crown or valley is 25 m .
- Maximum floor height imperfection without load 19.0 mm and with load 3.0 mm , with a minimum flatness within 20.0 mm over a 30.0 cm span.
- Climb slope 3-5% preferred; 10% with optional driving train.
- Floor surface can be concrete, asphalt, tiles, or compressed rock with relatively uniform surface texture.
- Maximum slope correction by tilt of transporter surface is 3%.
- Will be outfitted with a diesel engine to satisfy the power plant requirements of not allowing LPG on site.

3.3.2 Lifting System for the Antineutrino Detectors

Lifting systems, mainly for handling the antineutrino detectors, have been investigated. The lifting system should be low in order to minimize the height of the experimental hall to gain overburden. Bridge style cranes are designed for our requirement. The required height of the experimental halls to lift and install the antineutrino detector is 15 m. Figure 3.11 show a picture of a bridge style crane. Sensitivity in handling the AD is extremely important and requires crane controls with variable frequency motor drives for smooth acceleration and speed control of bridge, trolley, and hoist motion. A digital load cell integrated into hoist motion will enhance operator feedback in handling and transfer of loads.



Fig. 3.11. A photo of a bridge style crane, the crane rail is fixed to the wall of the experimental hall.

3.3.3 Experimental Hall Layout

The important components of the experimental hall are the detectors, a water pool, auxiliary rooms, etc. A layout of the experimental hall is shown in Fig. 3.12. The auxiliary rooms are located adjacent to the pool on one side of the hall to minimize electronic cable length runs between detectors and counting room. The auxiliary rooms are designed for the gas system, data taking, water purification and refuge. A secondary personnel egress tunnel links these auxiliary rooms to the main access tunnel.

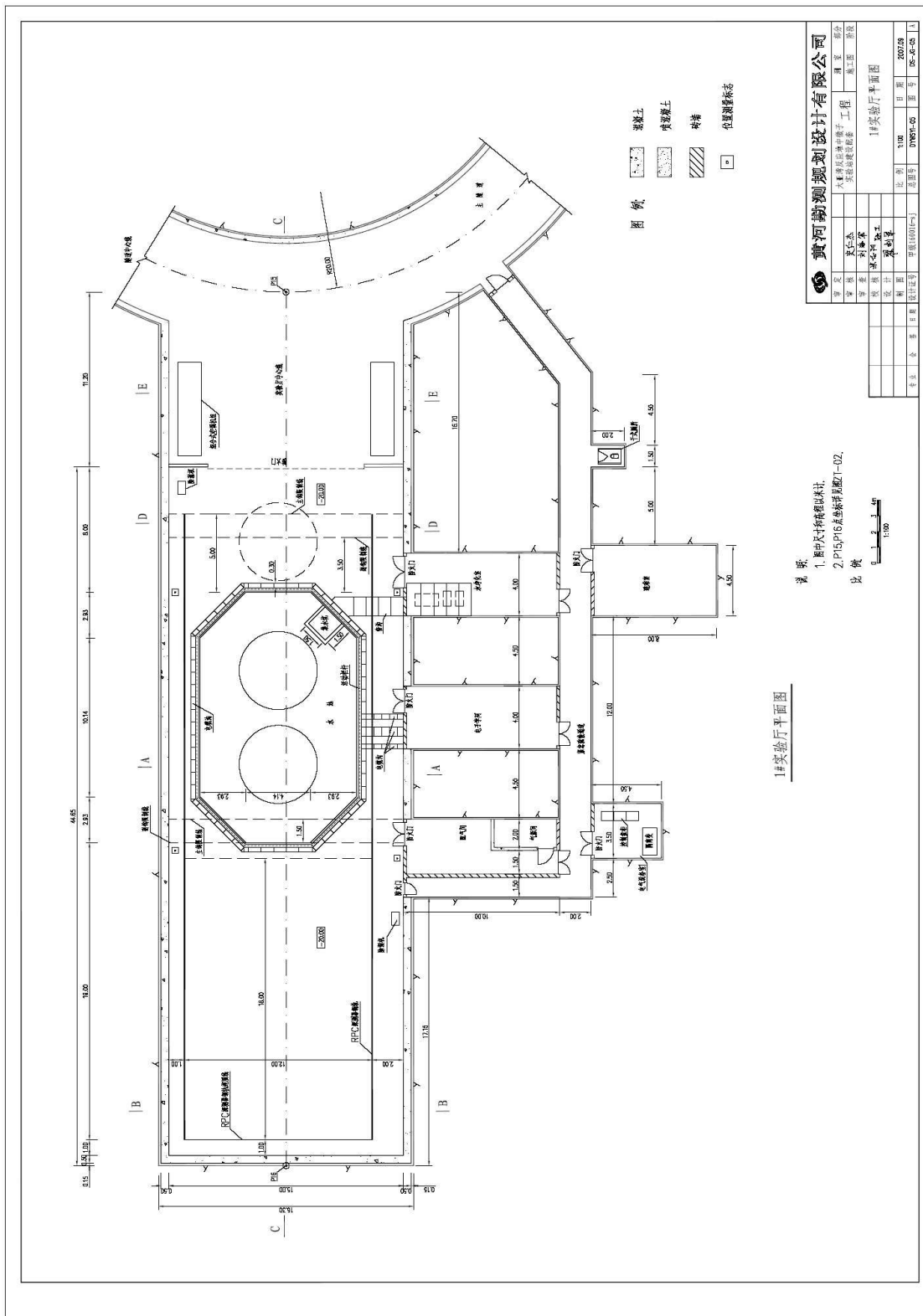


Fig. 3.12. Layout of the Daya Bay near hall. The gas mixing, electronics and water purification rooms are along one side of the hall.

A plane view along the longer axis of the experiment hall is shown in Fig. 3.13, with the crane at the top, the concrete pool, the lining in the pool, the drainage and cable ditches.

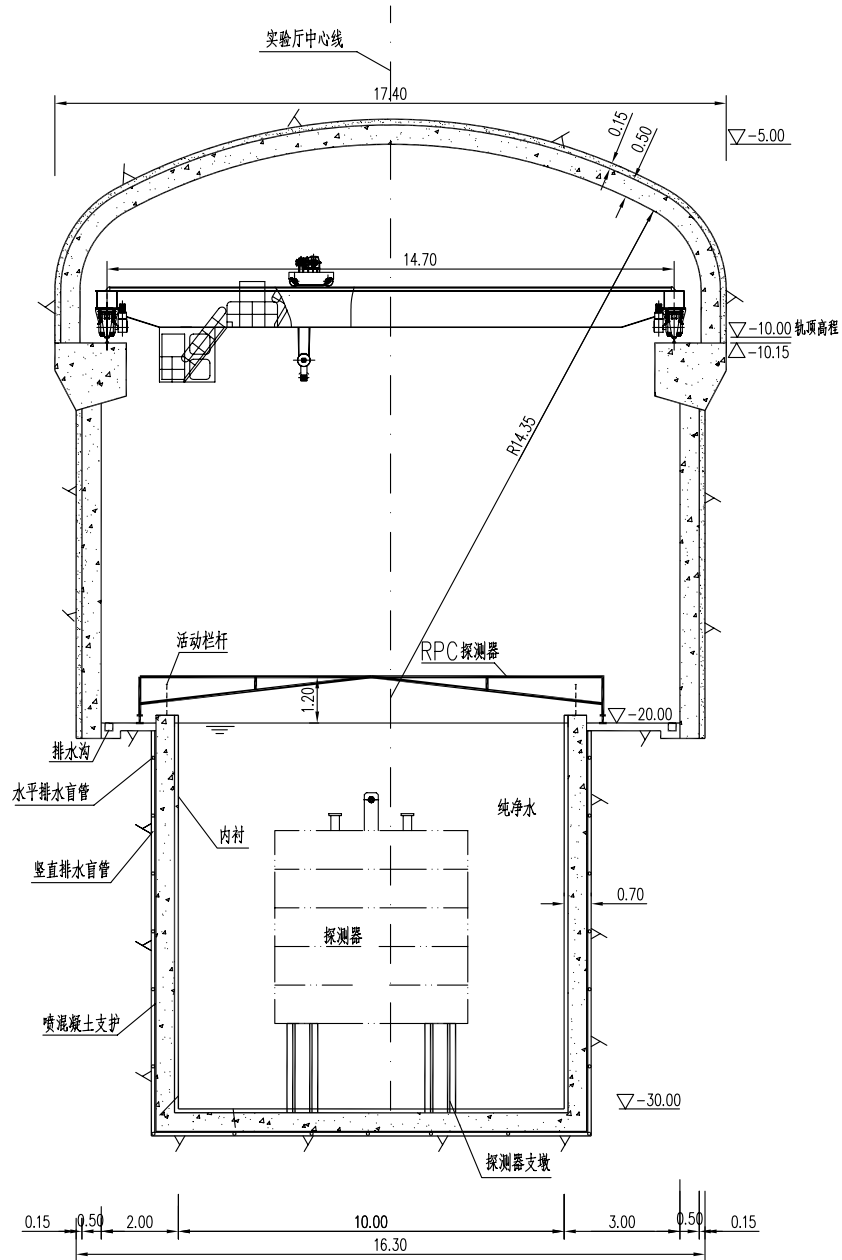


Fig. 3.13. Plane view of the Daya Bay hall cavern, with crane shown on the top. The detector is housed in the water pool in the bottom and supported by four vertical columns.

The experiment halls which are rectangular shaped and are oriented in such a way that their longer axes are as close to perpendicular as possible relative to the faults and joints as identified by the geological survey. The caverns will be more stable in such an orientation.

3.3.4 Central Water Purification Station

The central water purification station, which consists of a water pool, and the water purification system, is located near the intersection point of the main tunnels connecting the three experimental halls, called hall 4 in Fig. 3.1. The main water purification system will process city water to high purity to satisfy the requirements of the muon Cherenkov detectors. The water is transported via more or less equal length water pipe to the three detector halls (any degradation of the water in the pipes will be the same for the three pools). The storage pool, which has the same volume of the far pool, will be empty except when one of the detector pools needs to be emptied. That water will be pumped to the storage pool. Then when the detector pool needs refilling, the water in the storage pool is sent back through the makeup water system to the detector hall. Another option which uses this pool for water supply system is under consideration.

A layout of the central water station is shown in Fig. 3.14. The water makeup system is located between the storage pool and the tunnel.

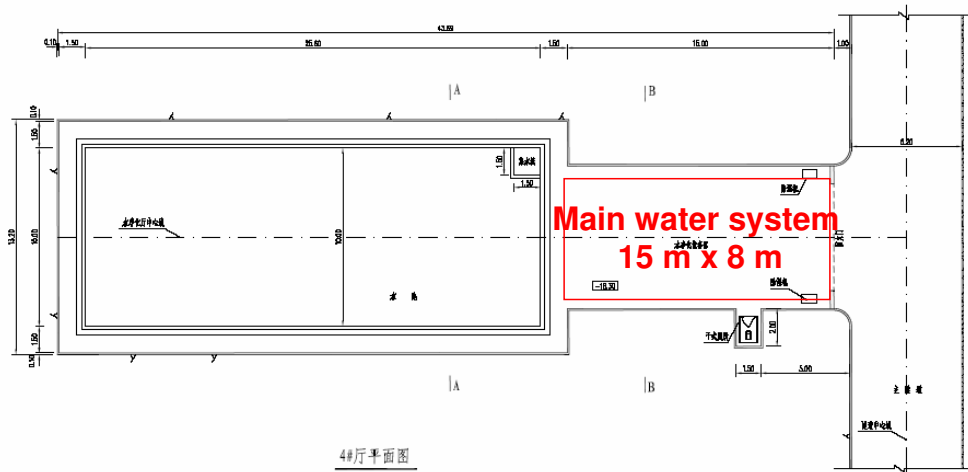


Fig. 3.14. Top view of the central water station, the makeup system of the water is located between the storage pool and the tunnel.

3.3.5 LS Hall

The LS hall (hall #5 in Fig. 3.1) will be $12 \text{ m} \times 30 \text{ m}$ and located near the Daya Bay hall (hall #1 in Fig. 3.1) to minimize the transport distance of liquid materials from the surface. The Gd loaded scintillator, normal scintillator and mineral oil will be mixed and stored in this room, and the AD filling will take place here. As with the experimental halls, relatively good rock conditions are required to minimize structural support costs of this hall. The top view of the LS hall is shown in Fig. 3.15.

3.3.6 Design of Tunnel

To minimize the excavation cost yet accommodate the antineutrino detectors, the cross section of the main tunnel is defined as:

- The total width of the tunnel: 6.2 m.
- The purified water supply pipe, fire suppression pipes and cable trays are mounted along one side of the tunnel wall extending out of the wall less than 20 cm.
- Safety clearance to each side of tunnel wall: 0.5 m.

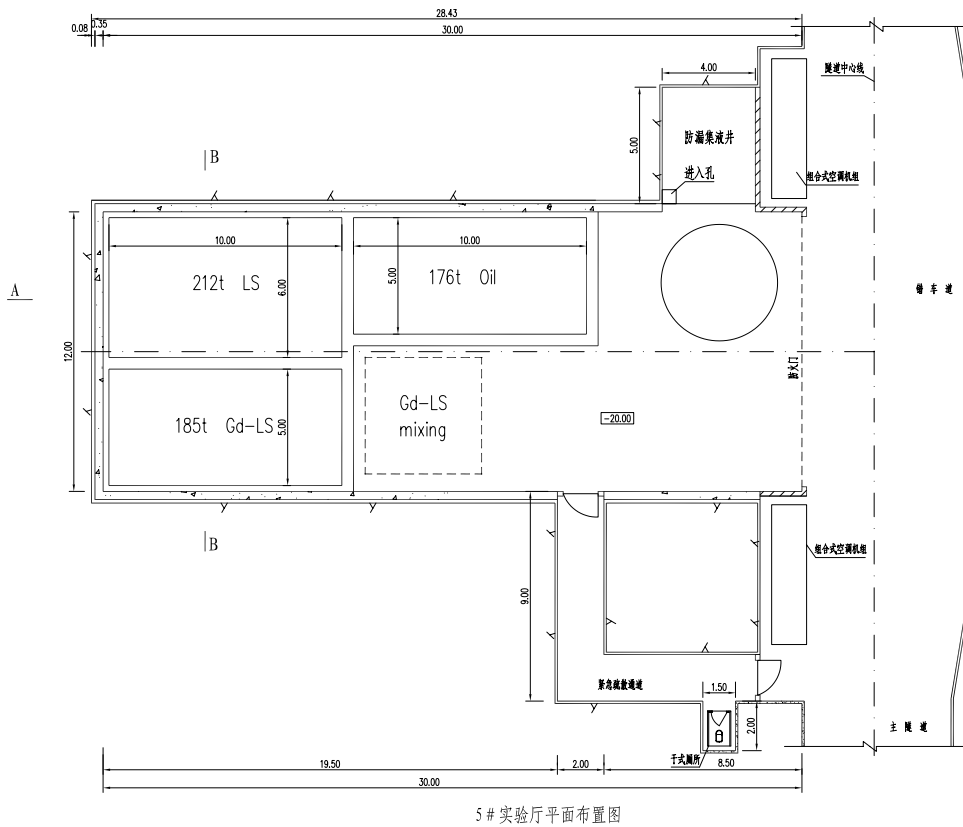


Fig. 3.15. Top view of the LS hall, including several storage tanks for the normal scintillator, loaded scintillator, and mineral oil. The AD detector is also shown.

- Approximately every 200 m along the tunnel there will be a by-pass to allow two vehicles to pass with full load transporter stop.
- Width of drainage channel: 0.5 m on each side of the tunnel
- Total height of the tunnel: 0.58 m (height of transporting vehicle) + 5.0 m (height of antineutrino detector) + 0.5 m (safety distance to the duct) + height of duct.

Figure 3.16 shows the cross section and the details of some of the layout of the main tunnel. As shown cable trays and water supply pipes will be installed along one of the side walls of the tunnel. At the locations where the tunnel branches, the height of the tunnel will be increased to allow for cable and ventilation duct crossover.

The lining of the tunnel depends on the rock quality. At the Daya Bay site the rock quality varies from grades I to V: grade I being excellent and grade V poor. According to the site survey, more than 90% of the rock is grade I, II or III (stable rocks). Some very short sections of the tunnel have grade IV rock with some grade V rock only in the first tens of meters at the main portal. The lining for different quality of rocks are designed according to the requirements for these rock types.

Most of the excavated rock will be transported by heavy truck through the construction tunnel as shown as orange lines in Fig. 3.1. The width of the construction tunnel is 4.6 m and height 6.0 m. There will be a passing section every 200 m along the tunnel for two trucks to cross in opposite directions. The total length of such a tunnel is 647 m.

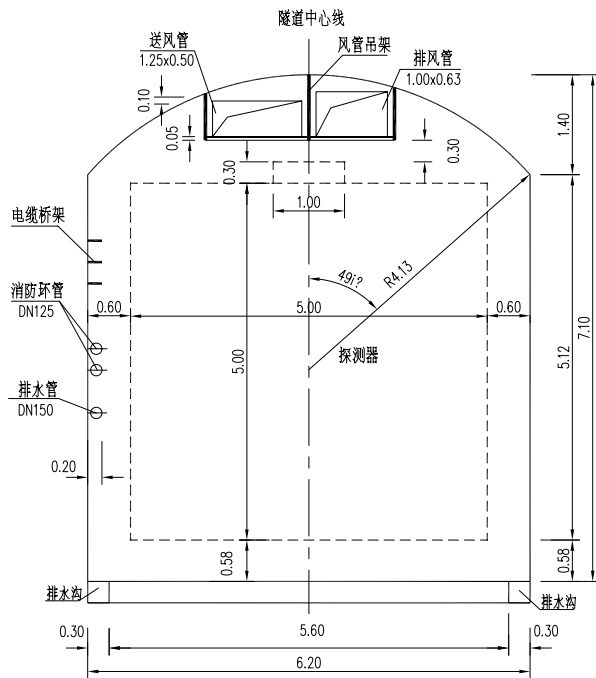


Fig. 3.16. An engineering schematic diagram of the tunnel layout. The dimensions are in meters.

3.3.7 Design of Surface Buildings

The layout of the main portal area behind the local hospital is shown in Fig. 3.17. An artist's conception of the portal area with the SAB is shown in Fig. 3.18. These surface buildings include a two-floor electricity and control building including the experimental control room, a two-floor pump and ventilation building, a water pool for fire control and a SAB of $\sim 2000 m^2$. A corner of the SAB for AD assembly is shown in Fig. 3.19.

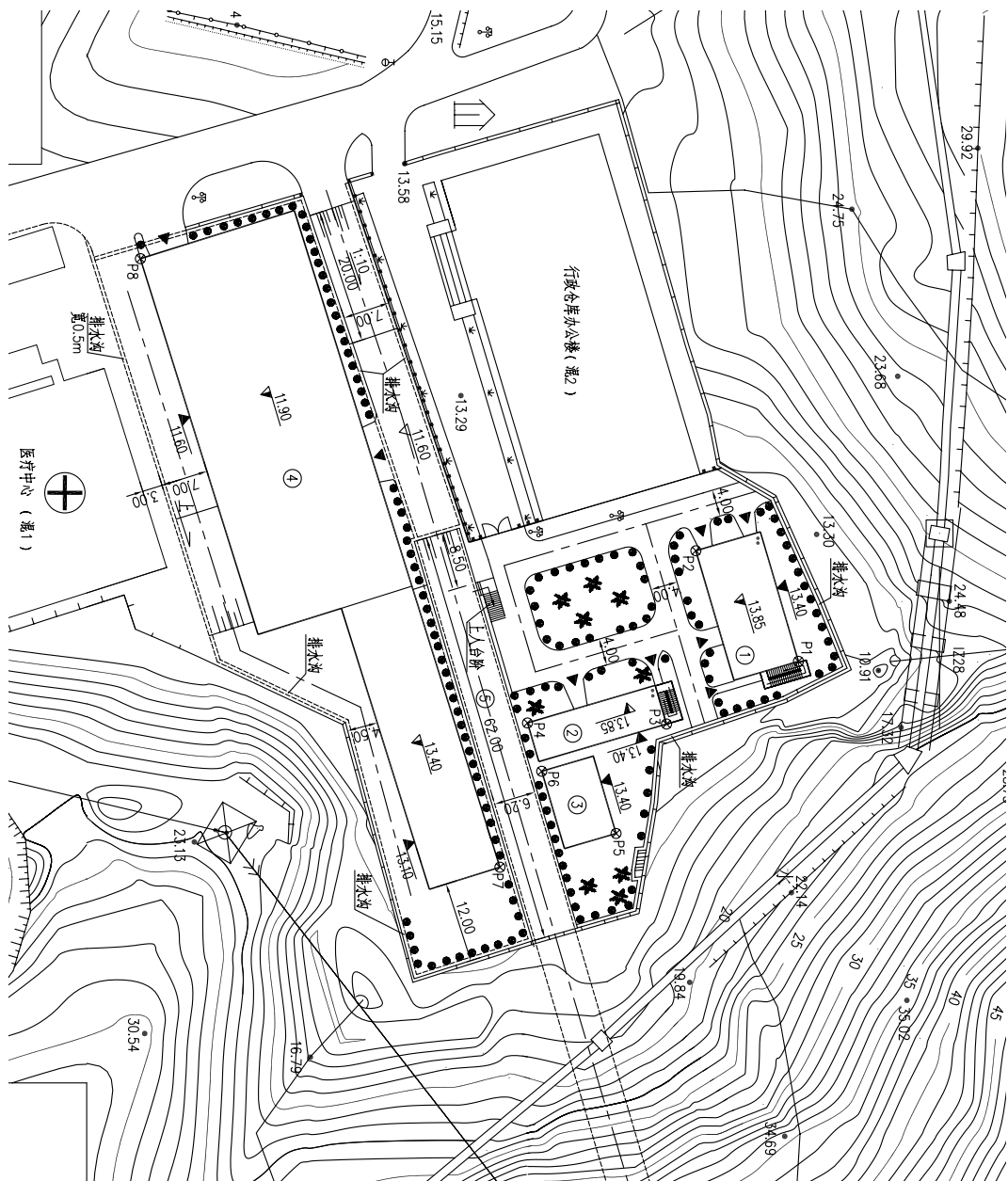


Fig. 3.17. A schematic diagram of the the main access portal and the layout of the auxiliary buildings. Building marked 1,2,3,4 from top to bottom, 1: Electricity distribution and control building (including the experimental control room); 2: Pump and ventilation building; 3: Water storage for fire control; 4: SAB. At the lower middle is the local hospital.



Fig. 3.18. An artist's conception of the SAB situated adjacent to the access tunnel portal.

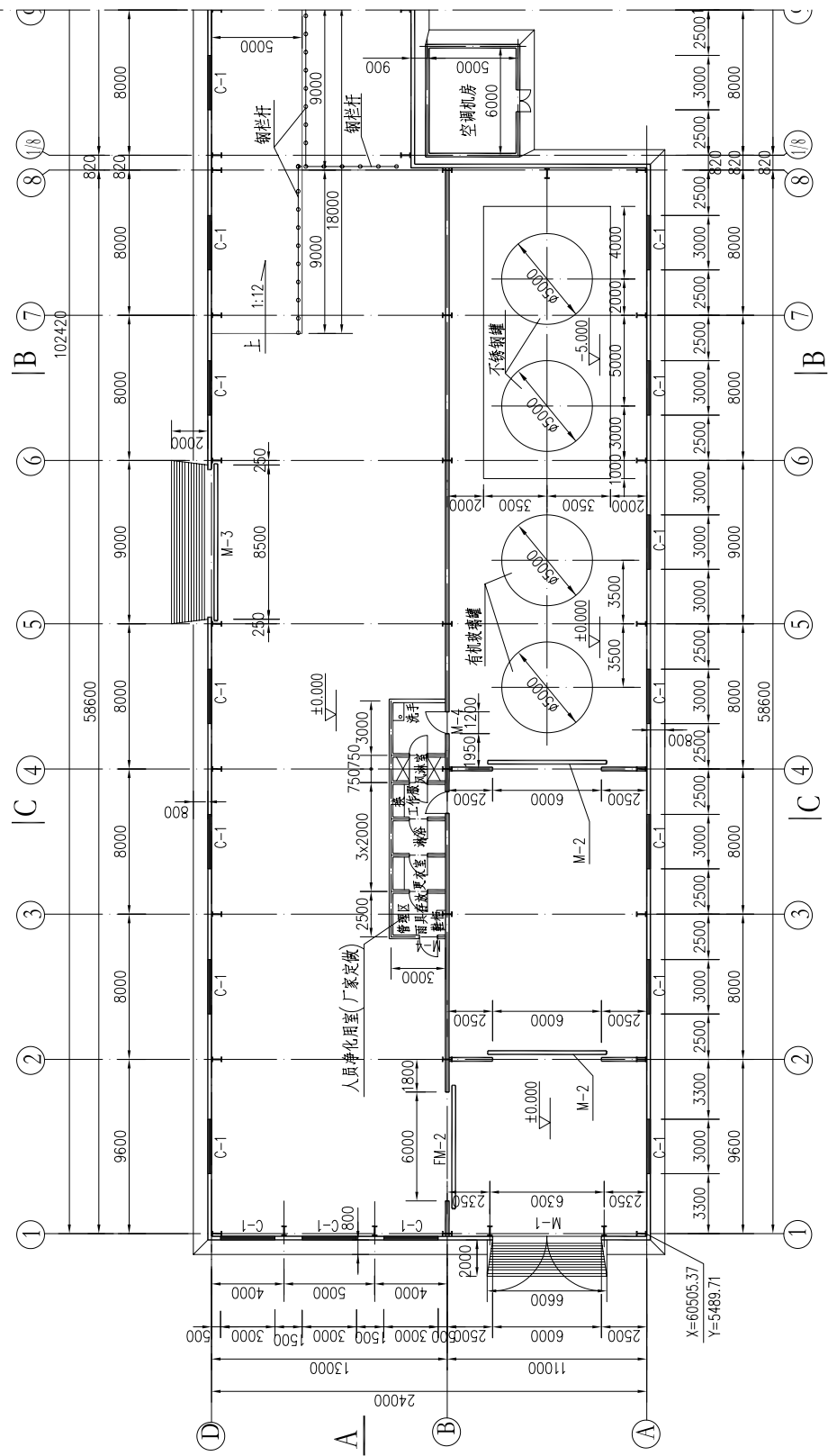


Fig. 3.19. A corner of the SAB where ADs will be assembled. The stainless steel tank, acrylic vessel, and clean room are shown.

3.3.8 Electricity

A 6.3 kV power line will be pulled from a local transformer, which is near the main portal, via two independent loops to provide an uninterrupted supply of power except for normal power maintenance and inspection for which we will be informed in advance.

There will be 6.3/0.4 kV, 630 kVA transformers at the power control room located at the main portal. Because the different distances from the electric control room to the different experimental halls, there will be local transformers in the far hall (#3) and the LA near hall (#2). There will be an isolation transformer for the power supply of the electronic equipment in each experimental hall.

Each experimental hall has two independent grounds, the resistance of each ground is smaller than 0.5Ω .

The lighting in the tunnel and experiment halls will meet Chinese regulations. The total power consumption includes those of the crane, heating, cooling, ventilation, water purification system, water supply, drainage, and experiment halls.

3.3.9 Ventilation System

The ventilation system is composed of inlet and outflow ducts. The ventilation rate is designed to replace the entire air volume of each experimental hall at least six times a day. The ventilation capacity is designed to allow a maximum of 30 workers simultaneously in each experimental hall. The ventilation system is designed to be quiet in operation while providing ambient air dehumidification, heating/cooling and filtration. Additional dehumidification units will be devoted to each experimental hall with large water pools. To reduce power consumption, the average temperature will be controlled close to the original (natural) temperature of the cavern to within $\pm 2^\circ\text{C}$.

3.3.10 Water Supply and Drainage

The experiment will use city water. The initial water usage will be large for filling the muon water pools ($5,000 \text{ m}^3$ or $1.32 \times 10^6 \text{ US-gal}$), but the filling of the three pools is not simultaneous. Daily operational water needs are minimal for purified experimental make-up water, personnel consumption and fire suppression. There will be a 300 m^3 water storage tank located at the main portal as a supply buffer.

The main source of waste water will be the drainage of seeped water from rock. This and other waste water from the muon system will be monitored when it is pumped out to the surface. The sump pit as shown in Fig. 3.12 will be about 9 m long, 6 m wide and 4.5 m deep, which can contain about 3 days of seepage water according to the seepage water flux estimation based on the survey report [4].

3.3.11 Communication

ShenZhen local telephone and a wire interphone system will be installed in the tunnel and the experiment halls. Internet connection will be available in the experimental areas and experimental control room.

3.3.12 Safety Systems

Environmental, Safety, Security and Health (ESSH) issues related to the project will fall within those policies established by the host country, China, and must meet minimum standards for all collaborative members working at the experimental complex. These polices will include life safety concerns for radiological controls, chemical inventory controls, emergency egress and access controls, fire protection and suppression systems, laser operation, cryogens, oxygen deficiency hazards, fall protection, personnel protective equipment, electrical and mechanical hazards, and liquid spill confinement and cleanup controls.

Equipment protection systems will also be incorporated into the experimental operational safety envelope. A system will be developed using a programmable logic controller (PLC) as the heart of a safety interlocks system to alarm subsystem fault conditions and automatically bring experimental hardware to a preprogrammed safe state. These fault interlock conditions will automatically valve off liquid and gas

sources and turn off electrical power to designated hardware based on cooling water leak detection and flammable gas detection. It will also alarm and interlock AC power based on smoke detection near electronics, and alarm and ventilate based on ODH and flammable gas conditions.

3.3.13 Blast Control

The maximum allowable force caused by blasts in the tunnel construction at the Daya Bay Complex is 0.01 g. Test blasts will be performed at the beginning of construction and the vibration caused by all blasts will be monitored during the construction period.

3.3.14 Environmental Effect Evaluations

The environmental impact evaluations include: (1) construction dust and noise; (2) rock disposal and treatment measurements; (3) temporary disruption and restoration after the construction work is completed.

All the details are included in the civil design report submitted by YREC [15].

3.4 Civil Construction Overview

Based on the conceptual designs and further work of the collaboration, the final civil construction design specs were developed. The Yellow River Engineering Consulting Co. Ltd. won the bid for the final civil construction design on January 22, 2007. The completed design took two months and was finished in March 2007. After the preparation of the bid documents (April–June), the bidding for civil construction was initiated in July and the contract was signed on September 15, 2007. The China Railway 15th Group Co. Ltd. began site preparation work on Sept. 20, 2007 and was scheduled to begin tunnel construction on Oct. 20, 2007. The tunnel construction start has been delayed by additional blast testing approvals. The civil construction will take about 22 months and finish in June 2009. The blue prints for the civil construction will be available ahead of the civil construction so that the design can accommodate some civil changes as the civil construction continue.

The civil construction contractor is responsible for the safety and risks during civil construction and is responsible for the prevention of accidents. The construction risks include: (1) safety of workers (2) the safety work in-situ (3) the mechanical instruments, materials, tools used on site (4) use of cranes (5) electricity (6) use of scaffold (7) chemicals (8) blast (9) ventilation and air condition monitoring (10) dangerous rock treatment (11) lighting (12) transportation (13) drainage (14) accident report and rescue. Technical activities of civil construction will follow the corespondent regulations in China.

The main civil construction work items are listed in Table 3.2.

Construction item	Number
Excavation debris from surface	6,876 (m^3)
Excavation debris from tunnel	174,961 (m^3)
Concrete	8,140 (m^3)
Eject concrete	4,782 (m^3)
Maximum ventilation	50 ($m^3/min.$)
Maximum water consumption	60 (m^3/h)
Maximum power of electricity	750 kW
Maximum number of manpower	640
Total number of manpower of civil	13.9k man · day

Table 3.2. Table of the main civil construction work items.

The costs for the civil construction are listed in Table 3.3. Taxes and fees are included in each item. The

design costs are covered in previous contracts.

Civil construction item	Unit (10K RMB)
Excavation debris above ground	48.8
Excavation of tunnel and EH	2392.2
support work	870.4
Concrete and Eject concrete	947.4
Permanent drainage	204.0
Installation of monitor sensors	44.6
Installation of rail, grounding etc.	112.9
Rock disposal treatment	23.4
Management	174.8
Total cost	4818.5

Table 3.3. Cost estimation of the civil construction.

During the tunnel excavation, the coding of geological conditions will be recorded, including: 1) the rock name, quality, age, type, rock boundary, deformation, and the mitigations 2) the shape of faults, zone of break up, weak interlayers, and the width, length, shape of other underground structures 3) the flux, format, location, water quality of underground drainage water 4) the rock fault shifting, widen, shift rate increase, water and sand avalanche, temperature changes, convention of cool air in the tunnel etc. Photos and records will be taken for important geological phenomena. Based on these codings, a geological forecast will be made during the civil construction. This forecast will be supplemented with other methods like Tunnel Seismic Prediction (TPS) and pre geological drilling. During the civil construction period, the deformation of the special locations in tunnel and halls will be monitored. The deformation of the sloping field near the main portal will also be monitored. The contract for this geological prediction and monitoring during civil construction period was awarded to YREC. The long term geological deformation during experimental operations will also be monitored by the sensors installed during the construction period and the data will be analyzed.

The Institute of Rock and Soil Mechanics (IRSM) of the CAS was selected for blast monitoring and control during the 22 months construction period. There are total 13 specified measurement sites. The most critical allowable force caused by blasts for the tunnel construction are at the Daya Bay and Ling Ao reactors, which is limited to 0.01 g. Each blast will be signed by IRSM to insure security and reliability. They will provide the measurements to adjust the blast plan and controls.

The bid for equipment and installation (outfitting) was awarded to China Railway 15th Group Co. Ltd. IHEP will participate in the equipment purchase contract.

The estimated utility and safety system costs are listed in Table 3.4.

YREC was selected as the construction management contractor. IHEP will have an on-site representative to oversee the civil construction. IHEP is also responsible for the interface with the power plant. Power and water needed during the construction will be provided by the power plant and this cost is included in the civil construction package.

YREC was selected as the oversight agency for the construction.

The milestones for the civil construction are summarized in Table 17.1 [15].

REFERENCES

1. *Report of Preliminary Feasibility Study of Site Selection for the Daya Bay Neutrino Experiment*, prepared by Beijing Institute of Nuclear Energy, September, 2004.

Utility and safety system item	Unit (10K RMB)
Electric system	822
Ventilation system	480
Fire suppression system	50
Water supply and drainage system	90
Communication and networks	75
Monitoring and control system	113
Clean room	100
Crane in surface assemble building	120
Crane in experiment halls	540
Transportation vehicle	500
Total cost	2890

Table 3.4. Cost estimation of utilities and safety systems.

Civil construction milestones	Schedule
Site preparation	Sept. 20, 2007
Tunnel excavation start	Oct. 15, 2007
Entering tunnel ready to use	June 15, 2008
Hall #1,#4 and #5 ready for installation	July 15, 2008
Hall #1,#4 and #5 beneficial occupancy	Sept. 15, 2008
Hall #2 ready for installation	Dec. 20, 2008
Hall #3 ready for installation	April 1, 2009
Hall #2 and #3 beneficial occupancy	July 15, 2009

Table 3.5. Milestones of the civil construction.

2. *Catalog of Chinese Earthquakes*, Quoted in the *Preliminary Safety Report on Ling Ao Nuclear Power Plant*.
3. *Report of Ling Ao Nuclear Power Plant*.
4. *Report on Geo-technical Survey(Feasibility Study and Conceptual Design)*, Institute of Geology and Geophysics, CAS, May, 2006.
5. *Final Report on Topographic Survey of the Neutrino Experimental Site*, Institute of Geology and Geophysics, CAS, June, 2006;
6. *Map obtained from Topographic Survey of the Neutrino Experimental Site*, Institute of Geology and Geophysics, CAS, December, 2005;
7. *Report on Engineering Geology of the Neutrino Experimental Site*, Institute of Geology and Geophysics, CAS, May 6, 2006;
8. *Report on Geophysical Survey of the Neutrino Experimental Site*, Institute of Geology and Geophysics, CAS, May 6, 2006;
9. *Report on Bore Drilling and In-situ Sonic Investigation of the Neutrino Experimental Site*, Institute of Geology and Geophysics, CAS, May, 2006;
10. *Report on Stress-loading in Bore Holes at the neutrino Experimental Site*, Institute of Geology and Geophysics, CAS, April 18, 2006;
11. *Report on Ultra-sonic Imaging in Bore holes at the Neutrino Experimental Site*, Institute of Geology and Geophysics, CAS, May, 2006;

12. *Report on Laboratory Study of the Neutrino Experimental Site*, Institute of Geology and Geophysics, CAS, May 6, 2006.
13. *Feasibility study About Daya Bay Neutrino Experiment Engineering Work*, The Fourth Survey and Design Inst. of China Railway, July 2006
14. *Feasibility Study About Daya Bay Neutrino Experiment Engineering Work*, Yellow River Engineering Consulting Co. Ltd., August 2006
15. *Civil Construction Layout Report of Daya Bay Neutrino Experiment Engineering Work*, Yellow River Engineering Consulting Co. Ltd., April 2007

4 Antineutrino Detector

The measurement of $\sin^2 2\theta_{13}$ to <0.01 is an experimental challenge. A value of 0.01 for $\sin^2 2\theta_{13}$ yields a tiny oscillation effect. This corresponds to a small difference in the number of antineutrino events observed at the far site from the expectation based on the number of events detected at the near site after correcting for the distance under the assumption of no oscillation. To observe such a small change, the detector must be carefully designed following the guidelines discussed in Chapter 1, and possible systematic uncertainties discussed in Chapter 2. To make this measurement the antineutrino detector must meet the physics performance requirements summarized in Table 4.1.

Item	Requirement	Justification
Target mass at far site	≥ 80 T	Achieve sensitivity goal in three years over allowed Δm_{31}^2 range
Precision on target mass	$\leq 0.3\%$	Meet detector systematic uncertainty baseline per module
Energy resolution	$\leq 15\%/\sqrt{E}$	Assure accurate calibration to achieve required uncertainty in energy-threshold cuts (dominated by energy threshold cut)
Detector efficiency error	$< 0.2\%$	Should be small compared to target mass uncertainty
Positron energy threshold	≤ 1 MeV	Fully efficient for positrons of all energies
Radioactivity singles rate	≤ 50 Hz	Limit accidental background to less than other backgrounds and keep data rate manageable

Table 4.1. Physical requirements of the antineutrino detector.

The technical requirements of the individual subsystems for the antineutrino detector are summarized in similar format at the beginning of each of the following sections.

In addition, the following considerations enter the design of the antineutrino detector:

1. The detector modules should be homogeneous to minimize edge effects.
2. It is important to precisely know the target mass and composition. The number of protons in the target liquid scintillator should be well known, implying that the scintillator mass and the proton to carbon ratio should be precisely determined. The target scintillator should come from the same batch for each pair of near-far detector modules or for all detectors, and the mixing procedure should be well controlled to ensure that the composition of each antineutrino target is the same.
3. The detector module should not be too large; otherwise, it would be difficult to move from one detector site to another for cross check to reduce systematic effects. In addition, beyond a certain size, the rate of cosmic-ray muons passing through the detector module is too high to be able to measure the ${}^9\text{Li}$ background.

4.1 Detector Geometry and Dimensions

Several previous neutrino experiments have designed spherical or ellipsoidal detectors to insure uniform energy response in the entire volume. This type of detector vessel is expensive and requires many PMTs for 4π coverage. Two types of alternative detector geometries have been investigated: cubic and cylindrical. Both are attractive from the viewpoint of construction. Monte Carlo simulation shows that a cylindrical

shape, as shown in Fig. 4.3, can deliver better energy and position resolution while maintaining good uniformity of light response over the volume, similar to that of a sphere or ellipsoid. This design is verified by prototype tests as discussed in Section 15.3.1. An optical reflector can be put at the top and bottom of the cylinder, so that PMTs are only positioned on the circumference of the cylinder, to reduce the number of PMTs by almost half.

This design, which allows a tremendous reduction of the detector cost including savings on the PMT readout, steel and acrylic vessel construction, is practical due to the following considerations:

1. The event vertex is determined by the charge pattern in the AD phototubes without reliance on time-of-flight, so that the light reflected from the top and bottom of the cylinder will not worsen the performance of the detector module. The hit times are measured to a resolution of 0.5 ns for background studies.
2. The fiducial volume is well defined with a three-zone-structure as discussed below wherein no accurate vertex information is needed.

4.1.1 Target Mass

The total target mass at the far site is determined by the sensitivity goal as is shown in Fig. 4.1 as a function of the far site detector mass. To measure $\sin^2 2\theta_{13}$ to better than 0.01, a total target mass of

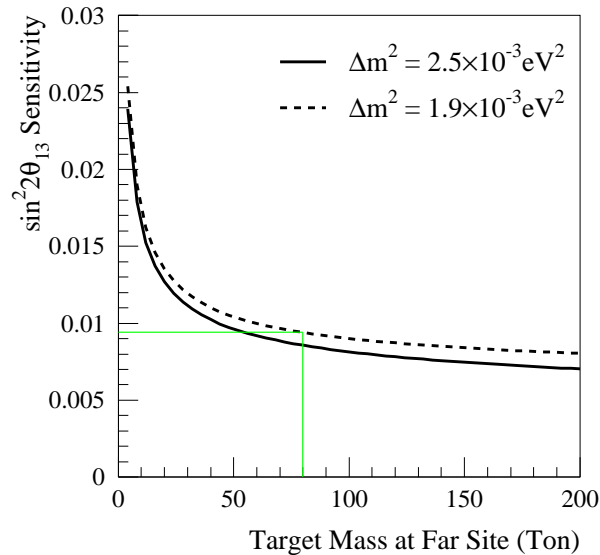


Fig. 4.1. Sensitivity of $\sin^2 2\theta_{13}$ at the 90% C.L. as a function of the target mass at the far site. The solid line corresponds to the current best-fit central value of Δm_{31}^2 and the dashed line corresponds to the 90% C.L. lower limit on Δm_{31}^2 .

80–100 T is needed, which corresponds to a statistical uncertainty of $\sim 0.2\%$ after three years data taking. A larger target mass is not attractive since the sensitivity improves rather slowly when the target mass goes beyond 100 T. By adopting a multiple-module-scheme as discussed in Chapter 1, two modules are chosen for each near site to allow a cross check of the systematic uncertainties (within the limit of statistical uncertainties at the near site). For the far detector site, at least four modules are needed for sufficient statistics to reach the designed sensitivity while maintaining the number of modules at a manageable level. A detector

scheme of eight identical modules, each with a target mass of 20 T, is chosen. About 930 events per day per module will be detected at the Daya Bay near site (300–500 m) with about 90 events per day per module at the far site (>1800 m).

4.1.2 Antineutrino Detector with Three Zones

A Chooz-type detector [2] with suitable upgrades satisfies the requirements. The energy threshold of a Chooz-type scintillator detector can be reduced by a three-zone structure as shown in Figure 4.3.

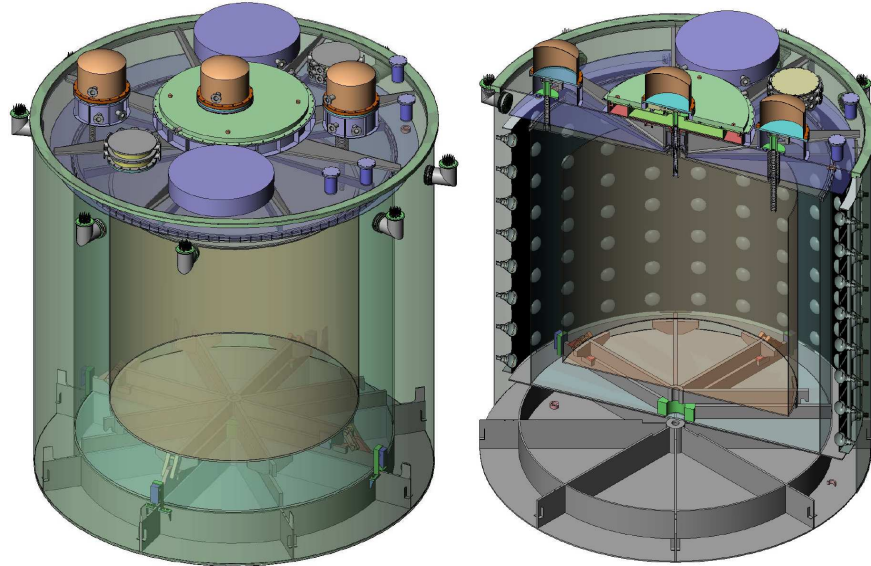


Fig. 4.2. Cross-sectional model of the antineutrino detectors. The models show the complete antineutrino detectors including the automated calibration boxes and overflow tanks on top of the AD lid.

The inner-most zone (region I) is the Gd-loaded liquid scintillator antineutrino target. The second zone (region II) is filled with normal liquid scintillator and serves as a γ -catcher to contain the energy of γ rays from neutron capture or positron annihilation. This zone does not serve as an antineutrino target as neutron-capture on hydrogen does not release sufficient energy to satisfy the 6 MeV offline neutron detection threshold. The outer-most zone (region III) contains mineral oil that shields external radiation from entering the fiducial volume. This buffer substantially reduces the singles rates and allows the threshold to be lowered below 1.0 MeV and improves the uniformity of light collection at the PMTs. The three regions are partitioned with transparent acrylic tanks so that the target mass contained in region I can be well determined without the need for event vertex reconstruction and a position cut.

The cost of the tunnel construction is proportional to the cross section of the tunnel. With optimization described in the following subsections, the minimum outer dimension of the detector that satisfy our physics requirement is found to be a cylinder with diameter of 5 m and height of 5 m. Figure 4.4 shows the fit of such a detector on a transporter in tunnel. The neutrino target is a cylinder of 3.1 m height and 1.55 m radius. The γ -catcher is 0.425 m thick and the oil buffer is 0.488 m thick. The diameter of the stainless steel vessel is 5.0 m, with a height of 5.0 m and a total mass of 100 T.

Appendix D contains a description of the detector geometry and parameters of the simulated antineutrino detectors used to optimize the detector design and verify detector performance.

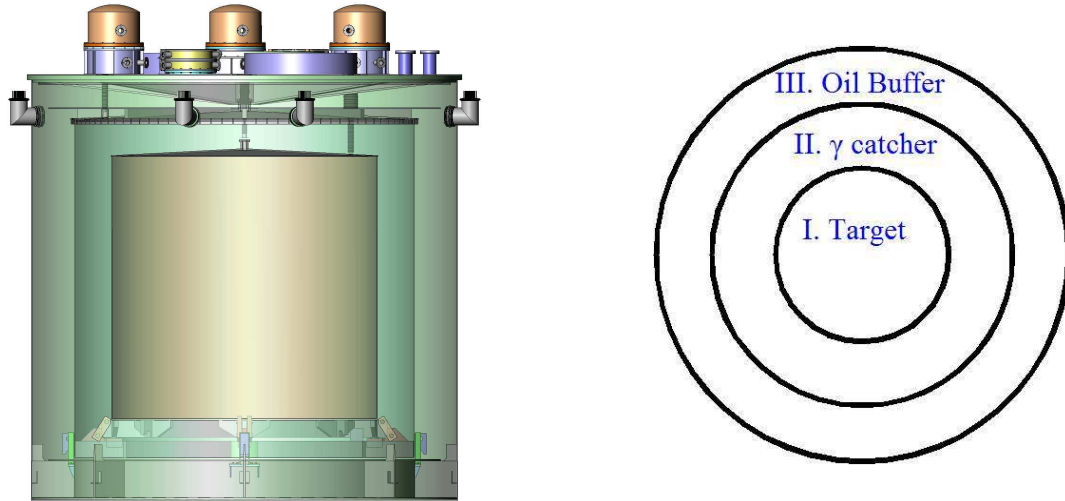


Fig. 4.3. *Left:* Transparent cross-section of the antineutrino detector. This figure shows a complete design of one of the options of the antineutrino detector with the automated calibration boxes and overflow tanks on the lid. *Right:* Schematic top view of the three different zones of the antineutrino detector.

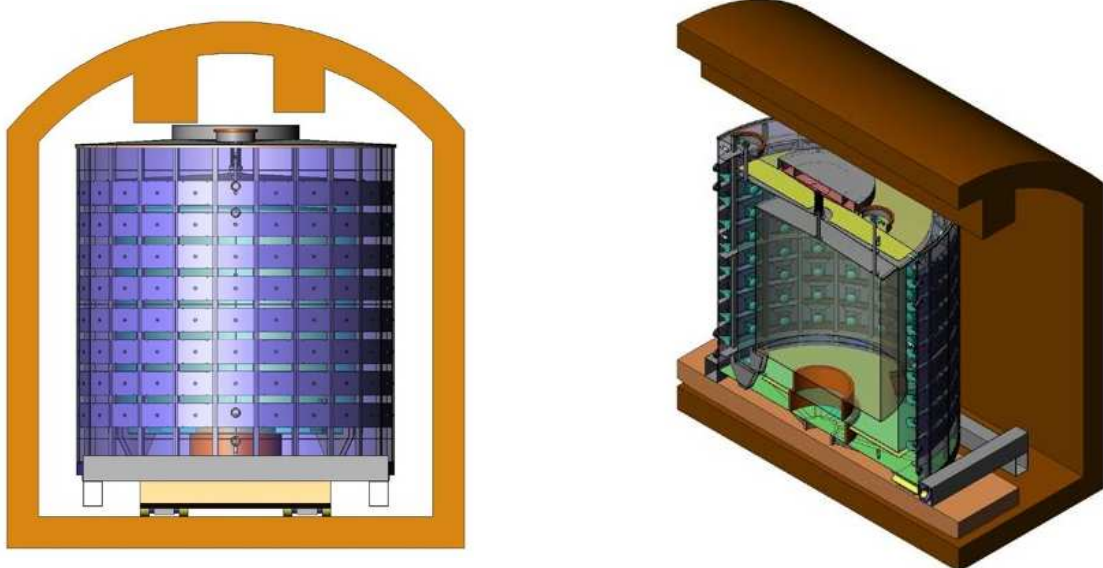


Fig. 4.4. Cross-section of the tunnel and antineutrino detector on the transporter in the horizontal tunnel connecting the experimental halls. The outline of the tunnel cross-section including the air ducts and other infrastructure are shown in yellow.

4.1.3 Antineutrino Target

The target vessel is designed to be a cylinder of an inner diameter of 3.1 m and inner height of 3.1 m. The density of the Gd-LS, consisting of 99% linear alkylbenzene, is 0.855–0.870 g/ml. The target mass is

20.0–20.3 T.

4.1.4 Gamma Catcher

The γ rays produced in the target region by positron annihilation or neutron capture will undergo many collisions to transfer most of their energy to the liquid scintillator before converting to visible scintillation light. However, the γ rays can also escape from this target region and deposit energy outside of this region. To capture the escaping γ rays a layer of undoped liquid scintillator surrounding the target zone is added, significantly reducing this energy loss mechanism. The energy spectrum of the delayed neutron capture signal is shown in Fig. 4.5. The tail to low energies is from events with at least one escaping γ . The Gd

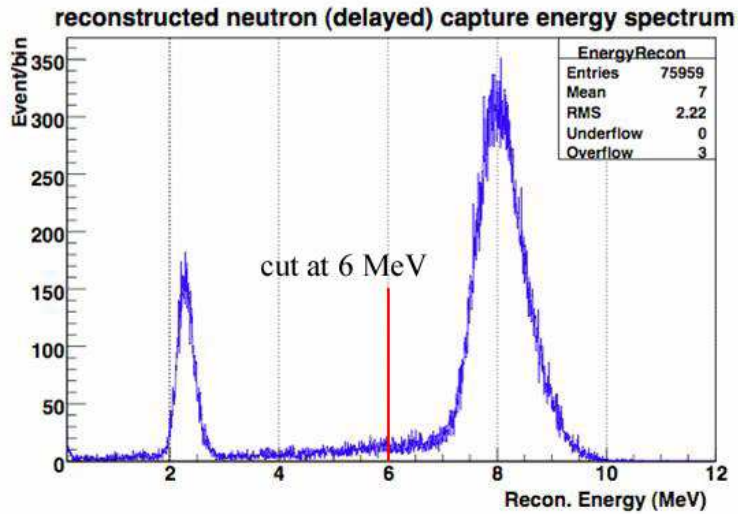


Fig. 4.5. The neutron capture energy spectrum as obtained from the Geant4 simulation (reconstructed by scaling the total charge). The peak at ~ 8 MeV corresponds to the n-capture on gadolinium. The tail to lower energies is from events with at least one escaping gamma.

capture peak at 8 MeV is dominated by the two most abundant isotopes of gadolinium, ^{155}Gd and ^{157}Gd , with total γ energies of 8.54 and 7.94 MeV, respectively.

A threshold of 6 MeV cleanly separates the 8 MeV neutron capture signal from the background due to natural radioactivity. However, this threshold will cause a loss of some neutron capture events and a corresponding loss of detection efficiency. A simulation of the detector giving the correlation between the thickness of the γ -catcher region and the neutron detection efficiency is shown in Fig. 4.6. The figure shows that with a γ -catcher thickness of 42.5 cm the neutron detection efficiency is 91%. Chooz had a smaller detector and a γ -catcher thickness of 70 cm, and neutron source tests showed a $(94.6 \pm 0.4)\%$ detection efficiency [2]. The uncertainty includes a vertex selection uncertainty that Daya Bay will not have. Chooz, Palo Verde and KamLAND all claimed an uncertainty on the energy scale at 6 MeV of better than 1%. Our detector simulation shows that a 1% uncertainty in energy calibration will cause a 0.2% uncertainty in the relative neutron detection efficiencies of different detector modules for a 6 MeV threshold. After subtracting the vertex selection uncertainty, the resulting efficiency values are consistent with simulation. After a comprehensive study of detector size, detection efficiency, and experimental uncertainties, we choose 42.5 cm as the thickness of the γ -catcher.

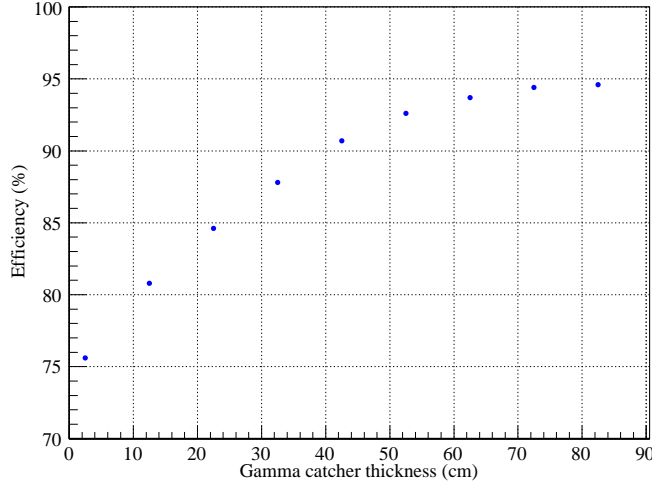


Fig. 4.6. The neutron detection efficiency as a function of the thickness of the γ -catcher. The neutron energy cut is set at 6 MeV. The thickness of the γ catcher of the Daya Bay experiment will be 42.5 cm.

4.1.5 Oil Buffer

The outermost zone of the detector module is composed of mineral oil. The PMTs will be mounted in the mineral oil next to the stainless steel vessel wall, facing radially inward. This mineral oil layer is optically transparent and emits very little scintillation light. There are two primary purposes for this layer: 1) to attenuate radiation from the PMT glass, steel tank and other sources outside of the module; and 2) to ensure that PMTs are sufficiently far from the liquid scintillator so that the light yield is quite uniform. Simulations indicate that the location of light emission should be at least 15 cm away from the PMT surface, as indicated in Fig. 4.7.

The oil buffer is also used to attenuate radiation from the PMT glass into the fiducial volume. Simulation shows that with 20 cm of oil buffer between the PMT glass and the liquid scintillator, the radiation from the PMT glass detected in the liquid scintillator is 7.7 Hz, as summarized in Table 4.2.

Isotope	Concentration	Distance of PMT Front Face to Gamma Catcher			
		20 cm (Hz)	25 cm (Hz)	30 cm (Hz)	40 cm (Hz)
^{238}U	100 ppb	5.5	4.0	2.8	1.5
^{232}Th	150 ppb	3.8	2.6	2.3	1.1
^{40}K	15 ppb	2.7	1.9	1.3	0.8
Total		12.	8.5	6.4	3.4

Table 4.2. Radiation from the PMT glass detected in the Gd-scintillator (in Hz) as a function of the oil-buffer thickness (in cm). An oil buffer of more than 45 cm thickness will provide 20 cm of shielding against radiation from the PMT glass.

The welded stainless steel in KamLAND has an average radioactivity of 3 ppb Th, 2 ppb U, 0.2 ppb K, and 15 mBq/kg Co. Assuming the same radioactivity levels for the vessel of the Daya Bay antineutrino

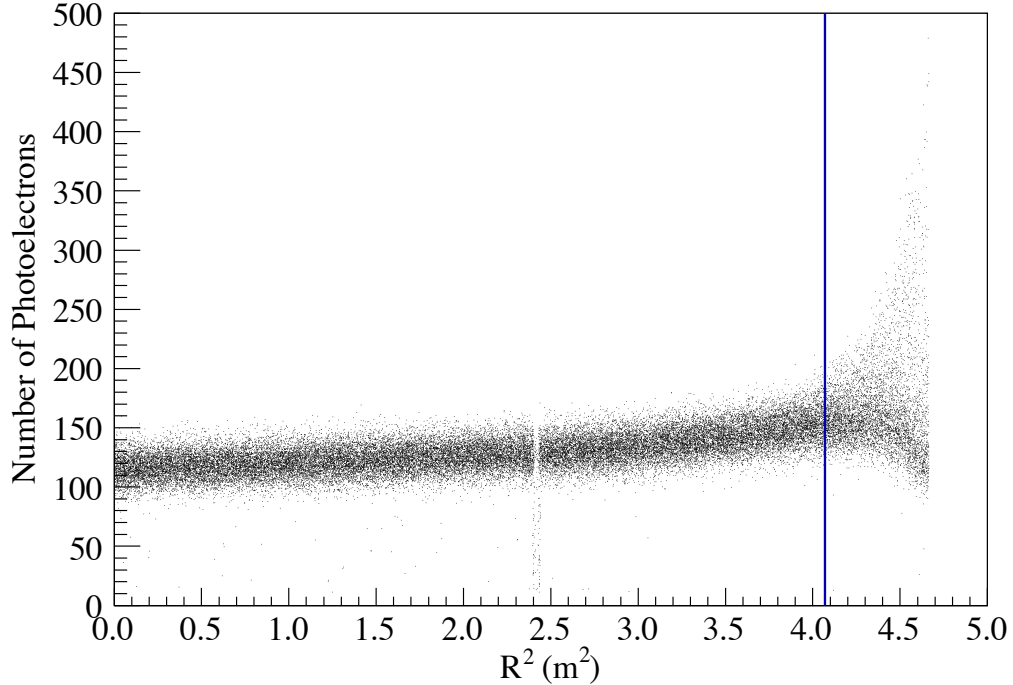


Fig. 4.7. Antineutrino detector response (in number of photoelectrons) as a function of the square of the radial location of a 1 MeV electron energy deposit. The mineral oil volume has been removed and the PMTs are positioned directly outside the γ -catcher volume. The vertical blue line is 15 cm from the PMT surface and indicates the need for at least 15 cm of buffer between the PMT surface and the region of active energy deposit in order to maintain uniform detector response.

detector module, the corresponding rate from the stainless steel tank can be found in Table 4.3. The total rate is ~ 20 Hz.

	Weight	^{232}Th	^{238}U	^{40}K	^{60}Co	Total
Radioactivity of SS	—	3 ppb	2 ppb	0.2 ppb	15 mBq/kg	—
Tank Wall Rate (Hz)	14 T	2.2	2.8	0.77	2.7	8.5
Rib Rate (Hz)	5 T	2.9	4.0	1.1	2.8	11
Radioactivity of Welds	-	5 ppb	2 ppb	1 ppb	10 mBq/kg	—
Welds Rate (Hz)	50 kg	0.015	0.014	0.020	0.010	0.060

Table 4.3. Radioactivity and single rates of the stainless steel tank.

The natural radioactivity of rock, buffer water, mineral oil, dust, radon and krypton in air play a minor role, as described in Section 2.3.4. The total γ rate is < 50 Hz. The oil buffer will be sufficient to suppress the γ rate and the subsequent uncorrelated backgrounds to an acceptable level.

The dimensions of the antineutrino detector modules are shown in Table 4.4.

Region	IR(m)	OR(m)	inner height(m)	outer height(m)	thickness(mm)	material
target	0.000	1.550	0.000	3.100	10.0	Gd-LS
γ -catcher	1.560	1.985	3.120	3.970	15.0	LS
buffer	2.000	2.488	4.000	4.976	12.0	Mineral oil

Table 4.4. Dimensions of the mechanical structure and materials of the antineutrino detector modules.

4.1.6 Optical Reflective Panels

Optical reflective panels will be put at the top and bottom of the cylinder. PMT numbers can be reduced to nearly one half comparing to the 4π PMT installation, while keeping the same photocathode coverage. The reflective panels can be put close to the top and bottom of the γ -catcher vessel to enlarge the photocathode coverage. As shown in Fig. 4.7, the photoelectron yield increases as the light source approaches the wall of the detector. However, the detector response will be uniform in the direction of the axis of the cylinder if a reflector with $\sim 100\%$ specular reflectivity is used. While specular and diffuse reflection have no difference in the total photoelectron yield, specular reflection is preferred because it will simplify vertex fitting algorithms (Sec. 4.2).

Using a reflector can also greatly simplify the mechanical design and assembly of the detector. To maximize the target volume within the constrained outer dimension of the steel vessel, reinforcing ribs for the vessel are inside the stainless steel vessel. This complicates the installation of the PMTs; however, since the detector volume is not sensitive beyond the reflector, support structures in this region do not adversely affect the target volume or detector response.

The baseline option of the reflective film is the Enhanced Specular Reflector (ESR) [3], a thin, mirror-like, non-metallic film that offers greater than 98% specular reflectivity across the entire visible spectrum. The measured reflectivity is shown in Fig. 4.8. For wavelength >400 nm, the total reflectivity (specular +

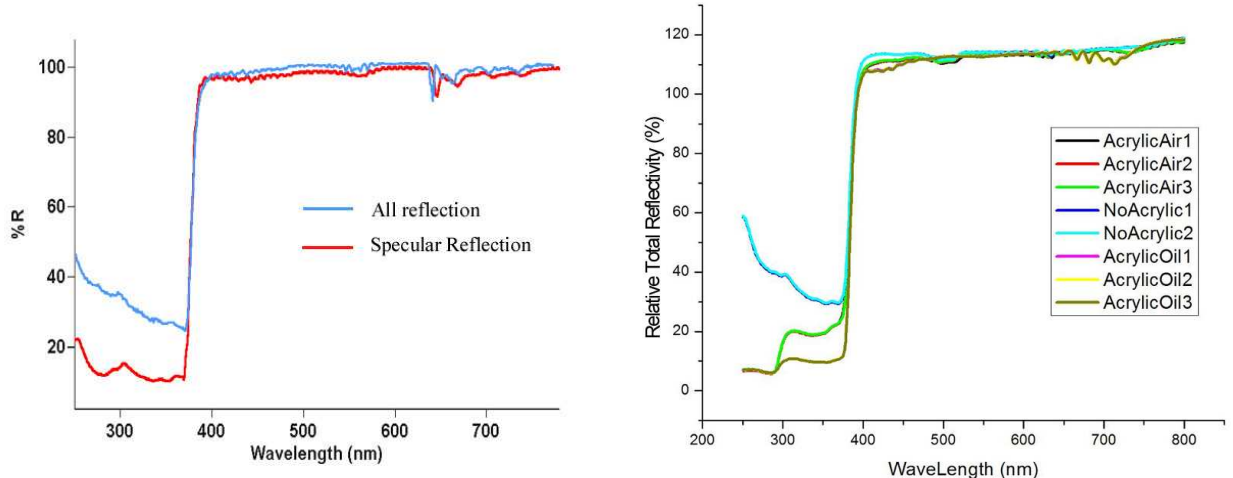


Fig. 4.8. Left: Measured reflectivity of ESR film. The red line is that for specular reflectivity and the blue line corresponds to total reflectivity including diffuse light. Right: Comparison of reflectivity of the reflector for different sandwich methods. See text for details.

diffuse) is greater than 99%. The rising edge is at 380–390 nm. Comparing to the light emission spectrum of

Gd-LS (see Fig. 4.9), the ESR has perfect reflectivity over almost the whole range of the scintillation light.

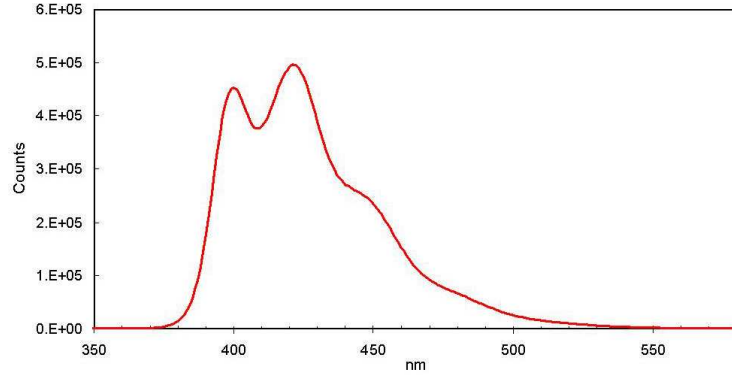


Fig. 4.9. The emission spectrum of Gd-LS with 5 g/L PPO and 10 mg/L bis-MSB. The Gd concentration is 0.2% and the complexant is TMHA.

Another attractive candidate is aluminum film. The total reflectivity of an aluminum film, MIRO-silver [4], is shown in Fig. 4.10, at three incident angles 10° , 40° and 60° . The reflectivity is slightly worse

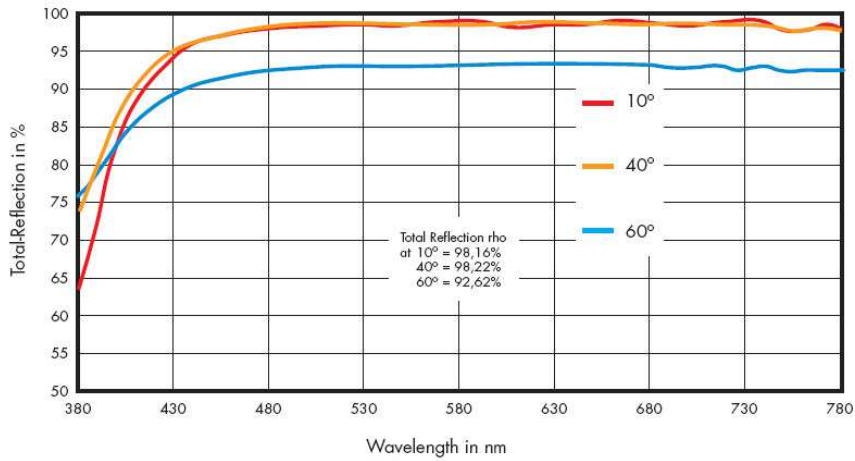


Fig. 4.10. Total reflectivity of Aluminum film MIRO-silver.

than ESR in the Gd-LS emission range but it is attractive in cost. Tyvek film for diffuse reflection has also been considered. Tyvek film will become semi-transparent when soaked in mineral oil. It has to be sealed to be used in the detector, thus has risk in case there is leakage of oil into the sealed structure.

The reflective film will be sandwiched between two acrylic panels. The sandwich structure can 1) protect the reflective film from scratch during assembly and installation; 2) avoid the possible contamination to mineral oil from the glue to stick the film in long term; 3) avoid the possible degradation of reflectivity when the film is immersed in mineral oil for years.

The maximum size of the commercial available ESR sheet is 17-in by 17-in. The ESR sheets will be bonded on one acrylic panel, while the other side facing to the target will not be bonded to avoid degradation of reflectivity. Epoxy has been used to bond the ESR or aluminum film on the acrylic panel in IHEP prototype detector. The reflector in the prototype is not sandwiched. The epoxy glue has direct contact with mineral

oil. No observable contamination to oil has been found in ~ 2 years test. The prototype reflector has been bent by a couple of cm and has experienced room temperature change from 10° to 30° . The bonding remains firm.

In the sandwich structure, there could be air gap between the reflective film and acrylic panel on the unbonded side. To have uniform reflectivity, a possible sealing method is to introduce a layer of mineral oil between the reflective film and the acrylic before sealing. Comparison of reflectivity for different sandwich methods is shown in the right side of Fig. 4.8. *NoAcrylic* means the reflectivity of the ESR, without an acrylic panel covering it. *AcrylicAir* means directly putting the acrylic panel on the reflective film, impacting and sealing it. There could be an air gap between the film and the panel. *AcrylicOil* means introducing a mineral oil layer between the film and the panel, impacting and sealing it. Each sandwich method has been prototyped several times and the reflectivity has been measured. There is no obvious difference between different methods. We will use the simplest way, without introducing an oil layer. In case there is oil leakage due to the break of sandwich sealing, the reflectivity won't change.

4.2 Antineutrino Detector Performance

With reflectors at the top and bottom, the effective photocathode coverage is 12% with 192 PMTs and the light yield is ~ 105 p.e./MeV (see Appendix D). We evaluate the expected energy resolution using both a simple total-charge method and a maximum likelihood fit. The total-charge method is robust and yields an unbiased estimate of the energy. The maximum likelihood method takes into account both direct and reflected light, the PMT efficiency and solid angle, and the attenuation of light in the Gd-LS, LS and mineral oil, and can yield a more precise estimate of the energy and vertex position than the total-charge method. However, the likelihood method relies on a number of parameters that must be determined either from *in situ* or external measurements, and incorrectly determined parameters can cause the method to yield biased results. The effect of digitization on the detector response is taken into account using a parameterization [1] of the measured PMT response in the prototype (Sec. 15.3.1). We expect an energy resolution of $\sim 5.9\%$ for 8 MeV electrons when the total-charge method is used, or $\sim 4.1\%$ with a maximum likelihood fit approach. The energy resolution of the 8-MeV γ 's from n-capture on Gd is 6.9% (total charge) and 5.7% (likelihood). The vertex can also be reconstructed with a resolution similar to a design with 12% PMT coverage on all surfaces. The vertex reconstruction resolution is ~ 12.5 cm for an 8 MeV electron event using the maximum likelihood fit, as shown in Fig. 4.11. Such a vertex resolution is acceptable since the neutron capture vertex has ~ 20 cm intrinsic smearing, as found by Chooz [2] and by our Monte Carlo simulation as well. The intrinsic smearing of the neutron capture vertex is caused by the difference in the position of the neutron capture vertex and the true center-of-gravity of the energy deposition of the γ 's emitted from the capture. The vertex position resolution will enable a study of the incoming neutrino direction to provide a check on the event reconstruction method and the simulation of neutron thermalization in the liquid scintillator.

4.3 Mechanical Design and Structure of the Antineutrino Detector

The detector's mechanical structure consists of the outer stainless steel detector tank, the structures for lifting the antineutrino detector, the surface coating of the stainless steel, the acrylic vessels, the overflow tanks and calibration ports, and the fill and drain mechanisms.

4.3.1 Detector Tank

The stainless steel vessel is the outer tank of the antineutrino detector module, and surrounds the buffer oil region. It will be built with low radioactivity 304L stainless steel and will satisfy the requirements listed in Table 4.5.

The stainless steel tank (SST) is a cylinder of 5000 mm height and 5000 mm diameter (external dimensions) with a 12 mm wall thickness. The flange extends to 5100 mm in diameter. There are support structures of height 300 mm on the lid for the overflow tanks and the calibration devices. The SST weighs about 24 T

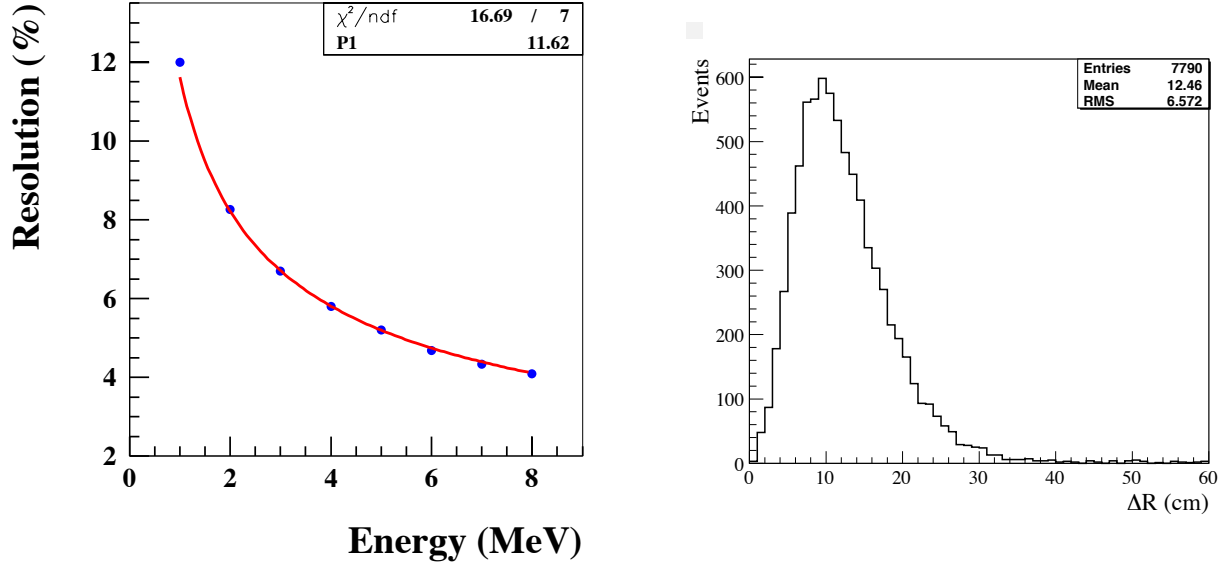


Fig. 4.11. *Left:* The reconstructed energy resolution using the maximum likelihood method for electron events uniformly generated in the target region is $11.6\%/\sqrt{E(\text{MeV})}$ using the total PMT digitized charge and $10.5\%/\sqrt{E(\text{MeV})}$ using the undigitized total charge. *Right:* The vertex reconstruction resolution for 8 MeV electron events uniformly generated in the target region using the maximum likelihood fit to the energy and position. The x-axis is the distance of the reconstructed vertex to the true vertex and the y-axis is the number of events.

Item	Requirement	Justification
Height	$\leq 5 \text{ m}$	Clear ducts at the ceiling of the tunnels
Diameter	$\leq 5.1 \text{ m}$	Clear cable trays and the walls of tunnels
Height of external ports	$\leq 0.3 \text{ m}$	Clear ducts at the ceiling of the tunnels
Wall thickness	$\leq 2 \text{ cm}$	Minimal material to reduce radioactivity while maintaining strength
Leak tightness	$> 5 \text{ years}$	Data taking requires at least 3 years
Tilt	9.6% when empty	Transport empty AD down sloped access tunnel
Ports	≥ 3	Insert calibration devices, fill and drain liquid
Vessel wall deflection	$< 2 \text{ mm}$	Lift full tank without perturbing acrylic vessels

Table 4.5. Requirements on the steel tank of the antineutrino detector.

(including the support structures) and has a volume of $\sim 95 \text{ m}^3$ (without the chimney). The structure of the SST is shown in Fig. 4.12.

There are eight radial internal reinforcing ribs and two circular ribs at the bottom as well as the tank lid to assure sufficient mechanical strength to be lifted fully-loaded, transported, and submerged under 2.5 m of water. To maximize the fiducial volume within the limitation of external dimensions, the reinforcing ribs

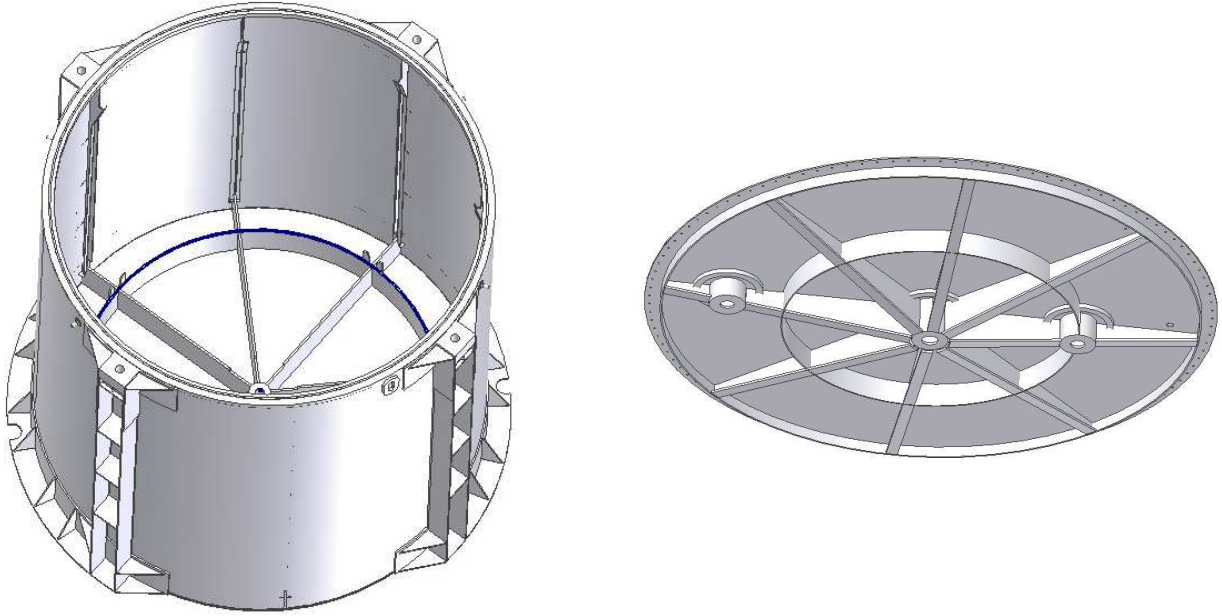


Fig. 4.12. Stainless steel detector tank. Left: Barrel and bottom. Right: The inner side of the tank lid.

are designed inside the tank, as shown in Fig. 4.12. The bottom ribs have height of 430 mm and thickness of 25 mm. The lid ribs have a maximum height of 340 mm and thickness of 20 mm. To leave enough space for assembly of the calibration tube penetrations, the strength of the lid ribs is enhanced by a ‘T-rib’, by welding a horizontal strip, instead of extending the height. On the wall there are 8 vertical ribs to enhance the cylinder. The vertical ribs are also used as the guide of the PMT ladders.

The detector is allowed to be more than 5.1 m in one direction, which is along the tunnel direction during transportation in the tunnel. The clamping plate at the tank bottom, which is used to fix the antineutrino detector on the stand in the water pool and on the transporter, and the lifting lugs and the external vertical ribs to distribute the stress during lifting, are designed to be located in this direction.

The lid is sealed to the SST barrel via an end flange. Again, to maximize the fiducial volume, the flange is designed to be internal, as shown in Fig. 4.13. The flange is a L-shape with 80 mm thick and 136 mm wide, which provides enough stiffness to avoid leakage during deformation. A Viton O-ring will be used to seal the detector tank.

The mechanical strength of the tank has been carefully analyzed using Finite Element Analysis (FEA). The model is depicted in Fig. 4.14. Stress and distortion has been calculated for all possible detector load cases, such as lifting empty without the lid, lifting fully-loaded with 0.1 g acceleration, transporting with 0.2 g horizontal acceleration, submerged in 2.5-m deep water, etc. The allowed stress is taken as 205 MPa.

An example of the FEA model is shown in Fig. 4.15. The stress and the deformation distribution of the tank bottom is shown for the load case of lifting the fully-loaded tank (~ 110 T) at an acceleration of 0.1 g. The maximum stress of 87.4 MPa occurs on the ribs at the center of the bottom. The safety factor is 2.35. The maximum deformation is 3.86 mm and occurs on the bottom plate between two radial ribs. The maximum deformation of the ribs is 2.85 mm and occurs at the center of the bottom.

For all possible load cases, the maximum stress and deformation of the tank bottom occurs when lifting at an acceleration of 0.1 g, and that of the tank lid occurs when submerged the antineutrino detector in 2.5-m deep water. The stress and deformation of the cylinder is relative small. The maximum stress and deformation are summarized in Table 4.6. Stability (buckling) of the cylinder is also analyzed. e.g. the

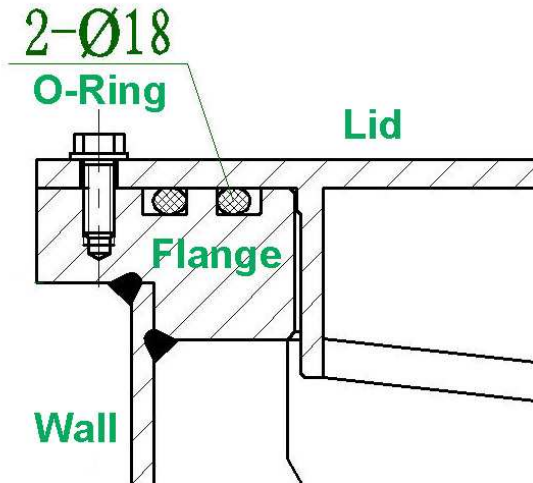


Fig. 4.13. End flange of the stainless steel tank.

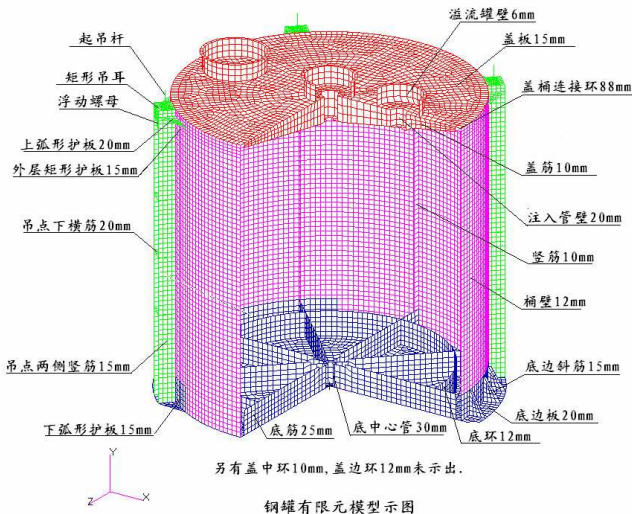


Fig. 4.14. Model of the stainless steel tank in FEA.

stability coefficient is 17.2 when lifting fully loaded ADs while the allowed critical factor is 5, resulting in a safety factor of 3.4.

The manufacturer has been selected from 5 bidding companies. The cylinder will be made of 3 parts. Each part will be welded and machined before being welded together. The bottom part (with bottom ribs) and the top part (with end flange) will have precision of ± 2 mm, while the mid part may have a larger error up to 5 mm. With machining, the flatness of the bottom rib surface will be <2 mm.

Quality Assurance and Quality Control (QA/QC) procedures is established before bidding, including

1. The material selection. Stainless steel and welds has natural radioactivities, which is not in the normal specification of the national standard or factory standard. They must be measured batch by batch and only the qualified material can be used for the manufacturing. The impact of radioactivities is shown

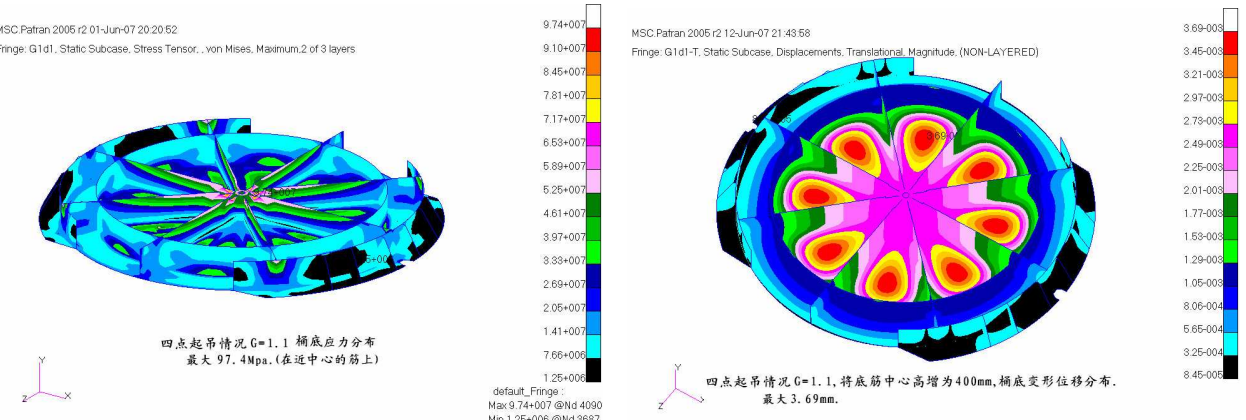


Fig. 4.15. An example of the FEA on SST, the stress (left) and the deformation (right) of the bottom of the fully-loaded tank when lifting at an acceleration of 0.1 g

Item	Bottom when lifting	Lid in water
Height of ribs (mm)	400	340 (+T-rib)
Thickness of ribs (mm)	25	20
Max. stress of ribs (MPa)	87.4	87.1
Safety factor	2.35	2.35
Deformation of ribs (mm)	2.85	1.92
Deformation of plate (mm)	3.86	2.6

Table 4.6. Maximum stress and deformation for two worst cases: that of tank bottom during lifting at an acceleration of 0.1 g, and that of the tank lid happen when submerged the AD in 2.5-m deep water.

in Table 4.3. IHEP will negotiate with the manufacturer and will be deeply involved in the material selection.

2. The welding strength will be measured for the selected stainless steel, the welding rods, and the welding method, before the manufacturing.
3. The ingredient of the stainless steel will be analyzed for each sheet after the point welding to make sure the right sheet is used.
4. The dimension of the SST will be measured after the point welding to ensure the required precision.
5. Vibration aging will be used to release 70% to 100% stress after welding and before machining.
6. The detector tank, especially the first one, will be lifted with water filled in the factory to test the mechanical strength.
7. The sealing of the detector tank will be tested with Helium leak detector.
8. Packing will be required during ocean shipping to protect from the corrosion of the sea water.

4.3.2 Lifting of AD

Transportation and installation of the AD require the fully-loaded AD, weighs around 110 T, can be lifted by crane. To reduce the stress and deformation during lifting, a lifting beam is designed. There are four lifting lugs on the cylinder of the SST, as shown in Fig. 4.12. The lifting lugs are welded to the cylinder via a patch. The stress is distributed through vertical external ribs. The maximum stress of the lifting lug and vertical ribs is 41.4 MPa, far below the allowed value. There could small differences between 8 detector tanks. Floating nut is designed so that all ADs can be lifted with the same lifting beam. The position floating is ± 5 mm.

The lifting beam will be designed with one main bridge and two girders, which connect to the four lifting lugs, shown in Fig. 4.16. The gear motors on each screw can be tuned individually to level the four lifting point. A rigid connection is adopted so that the lifting beam can serve as a reinforcing structure of the SST to have the minimal deformation during lifting. The total height of the lifting beam is required to be < 1.7 m to be fit in the experimental hall. The lifting beam weighs around 7 T and the designed capacity is 110 T. The safety factor is required to be > 4 . The design and fabrication of the lifting beam will be done before Feb. 2008 by Juli company, the largest professional lifting structure company in China, after the crane in the experimental hall has been contracted.

4.3.3 Surface Coating of Detector Tank and Optical Barriers

We plan to coat the inside of the antineutrino detectors with a black “paint” such that the PMTs only detect light directly from the antineutrino interaction in the liquid scintillator. This improves the position resolution of the positron interaction and of the neutron capture, at some expense in energy resolution.

Alternatively, we are considering the use of a black barrier offset from the steel vessel. It would occlude all of the PMT support structure and the PMT except for the photocathode. In this case, light produced behind the PMTs will be less troublesome just as light above and below the reflectors is less troublesome.

The outside of the AD steel tank is unfinished stainless steel. The reflectivity of (stainless) steel is about 60%, if its surface is not prepared for good optical performance. The outside of the AD will be covered in Tyvek to increase the light collection in the muon system as described in Chapter 6.

4.3.4 Detector Target and Acrylic Vessels

The acrylic vessels for Daya Bay consist of the following basic components:

- a pair of nested acrylic vessels
- a support structure (ribs, rings, or feet) for the acrylic vessels that support the assembly when empty
- three calibration pipes at the top to calibrate the detector along z at different radii
- a fill-drain mechanism to allow for the filling and emptying of all detector volumes
- closed overflow tanks that capture all liquids during expansion due to temperature variations of the antineutrino detector

and should meet the requirements outlined in Table 4.7.

The target vessel is a cylinder of 3120 mm height and 3120 mm diameter (external dimensions) with 10 mm wall thickness (acrylic). It weighs ~ 580 kg, and contains a volume of ~ 25 m³ (without chimneys). The γ -catcher vessel surrounding the target is a cylinder of 4000 mm height and 4000 mm diameter (external dimensions) with a 15 mm wall thickness (acrylic). It weighs 1420 kg, and contains a volume of 28 m³ (53 m³–25 m³) (without the chimneys). At the top of the inner target vessel, there are two chimneys for the insertion of radioactive calibration sources at the center as well as off-axis. There will be one chimney for the γ -catcher as well. The inner diameter of the calibration pipes will be ~ 50 mm.

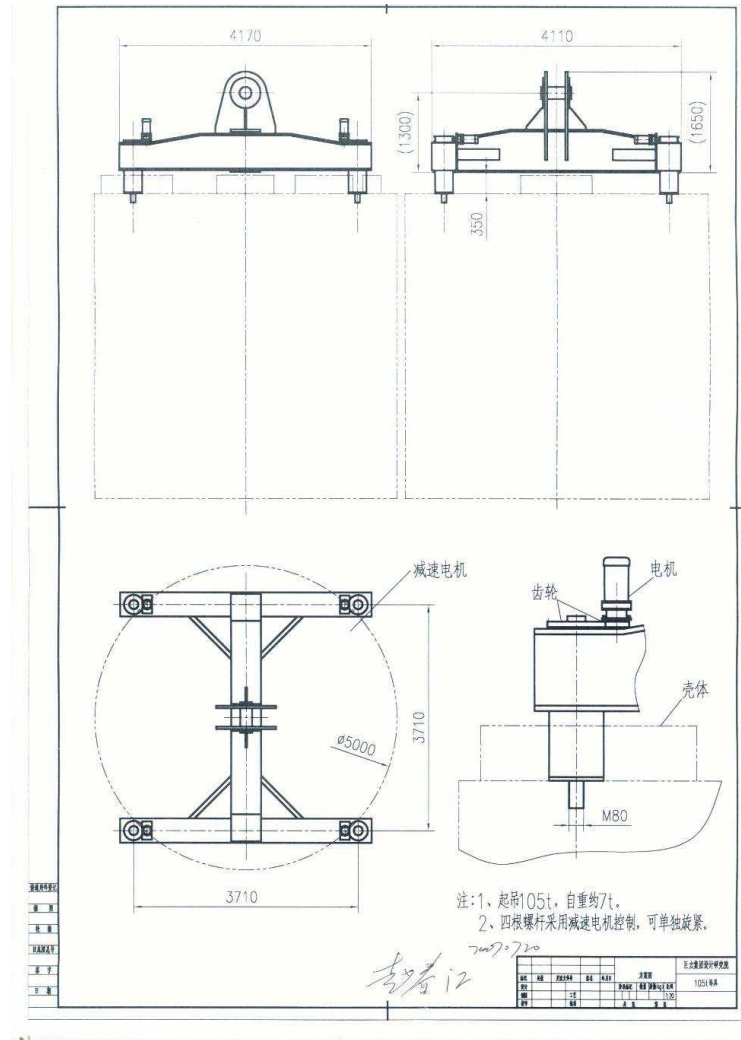


Fig. 4.16. Technical drawing of the lifting fixture for the Antineutrino Detector.

Item	Requirement	Justification
LS vessel volume	$\leq 1\%$	Matched pair filling
Gd-LS vessel volume	Matched to 0.3%	Matched pair filling
Dimension stability	$< 1 \text{ mm}$	Suppress time-dependent systematic problems
Optical properties	Transmittance $> 90\%$ at 400 nm	Maximize detection efficiency
Leakage	No leak at any interface for > 5 years	Simulations ongoing
Surface crazing	Minimal crazing after assembly and transport	Maintain good/stable optical properties

Table 4.7. Requirements on the acrylic vessels for the antineutrino detector.

The target and γ -catcher vessels will be built of acrylic which is transparent to photons with wavelength above ~ 300 nm (50% at 300 nm [5]). Both vessels are designed to contain aromatic liquids with a long term

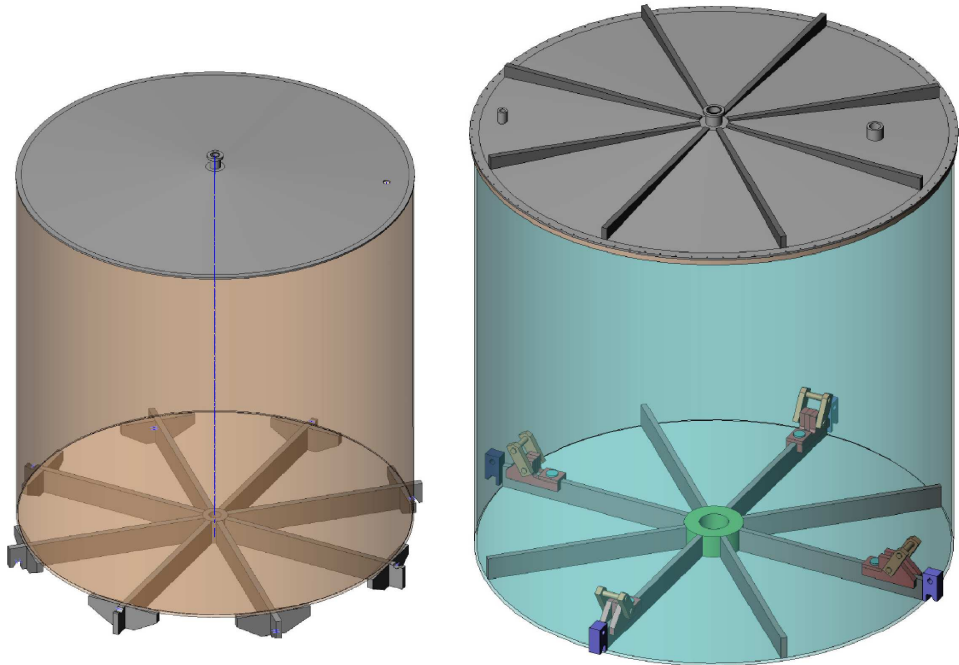


Fig. 4.17. Engineering model of the 3-m and 4-m acrylic vessels with support ribs at the bottom and lids. The lid of the 4m vessel is removable while the lid for the 3m vessel is bonded to the vessel. A shaped top is used to avoid the trapping of bubbles and air during filling of the detectors. The conical shape is formed out of a sheet of flat cast acrylic. Latches on the support ribs of the 4m vessel are used to hold down the inner 3-m vessel.

leak-tightness (free from leakage for ten years) and stability. The critical constraint is the chemical compatibility between the vessel and the scintillating liquids, for at least five years. There must be no degradation of the liquid properties (scintillation efficiency, absorption length) nor any significant degradation of the acrylic material (yellowing or crazing of more than a few percent of the acrylic surface area). The γ -catcher vessel will also be chemically compatible with the mineral oil in the buffer region.

Acrylic is normally PMMA plus additional ingredients to prevent aging and UV light absorption. Different manufacturing companies have different formulas and trade secrets for the additional ingredients, resulting in different appearance, chemical compatibility, and aging effects. For the material choice, we have surveyed many kinds of organic plastic and identified a number of suppliers and manufacturers. See below.

In the polymerization gluing method, they add the same raw materials as the acrylic (PMMA + ingredients) into the gap between the plates. Thus the joints consist of exactly the same acrylic material as the joined plates, and there is no difference in their mechanical, chemical and optical properties. During polymerization, UV light is used instead of heating, in order to prevent the bent sheets from rebounding. The speed of polymerization is controlled to minimize the remaining stress. Once the tank is fabricated in shape, it will be put in a thermally insulated enclosure for up to a month to be heated for releasing the stresses. The temperature will be controlled within $\pm 1^\circ \text{C}$. Different acrylic types, shapes, thicknesses, etc., need different temperature curves for bending and curing.

The Daya Bay detectors will consist of a pair of concentric, nested acrylic vessels inside a stainless steel tank. The nested design of the target vessels is a unique technical challenge, both in engineering and

fabrication. To allow the nesting of the 4-m acrylic vessel the outer 4-m acrylic vessel will have a removable lid with O-ring seal. The inner 3-m vessel will be completely sealed.

Modular Design of the Acrylic Vessels

In the modular design the acrylic vessel assembly consists of a pair of nested vessels with removable tops and calibration ports. This allows the on-site assembly of the nested arrangement inside the steel tank. The bottom of the vessels will be bonded to minimize the number of O-ring seals and flanges and to maximize the optical transparency of the vessels. In the modular assembly the calibration pipes are attached to the vessels by means of acrylic flanges and O-rings seals. See for example Fig. 4.17 for a prototype of an acrylic flange.

Penetrations through the γ -catcher vessel can be designed with double O-ring seals or flexible Teflon tubing that allows small lateral movements of the acrylic vessels with respect to each others.

Acrylic doesn't have a well defined yield point. It can creep slowly over time. The higher the stress the faster the creep. Below 5 or 10 MPa this creep can be taken to be zero. The safety factor given in the table is based on a maximum working load of 5 MPa which is quite conservative. For loads that are ramped up over minutes the failure stresses are a factor of 10 or more higher than this. The FEA shown is intended to give a big picture of stresses for guidance as the design is refined (based on prototyping experience). The current FEA is done with 15 mm acrylic top, bottom and wall. That is the thickness intended for the top and bottom of the 3m vessel. Although the wall of the 3m is only 10mm thick the walls of these vessels are not stressed very much. It is to be expected that the results for the the 3m vessel will be better than what was found for the 4m vessel.

We also note that the results for the level and tilted case are the same (cases 2 and 3). Tilting at 10% introduces very little additional stress or deflection.

Manufacturers and Fabrication

There are several manufacturers worldwide that have experience in the production of large-scale acrylic vessels of the size under consideration in Daya Bay. Only a few of them have the experience in working with scientific collaborations and manufacturing products for scientific work. The Daya Bay collaboration has investigated a number of vendors worldwide as suppliers for the acrylic raw material and manufacturers for the acrylic vessel. Two possible manufacturers of acrylic vessel have been identified. One in Taiwan and one in the US. Because the acrylic vessels are such a critical element of the detector the Daya Bay Collaboration has decided to pursue a prototyping program at both vendors.

Gold Aqua System Technical Co. [20] in Kaoshiung, Taiwan, is a subsidiary of Nakano Ltd. [21] They have experience in the design and construction of acrylic-based structures for aquariums, museums, and residential homes. They are interested in the development of acrylic vessels for the Daya Bay experiment. The approach of Gold Acqua is to use bent plate sheets to be glued together by the polymerization method. The vessel for the Hong Kong neutron detector (which is being built by a subset of the Daya Bay collaboration) has been ordered from Gold Aqua in Taiwan. An example of their work is shown in Fig. 4.20.

We have also been discussing the design of the Daya Bay vessels with Reynolds Polymer Technology [22] in Co, USA (RPT). Reynolds Polymer Technology is a large-scale manufacture of acrylic, acrylic casting, and acrylic objects. With their international reputation and impressive portfolio including experience in research projects such as the Sudbury Neutrino Observatory they are ideally suited to help develop the design of the Daya Bay vessels, provide consulting, and technical feedback. Examples of their work and production facilities are shown in Figs. 4.21, ??, 4.22, and 4.23.

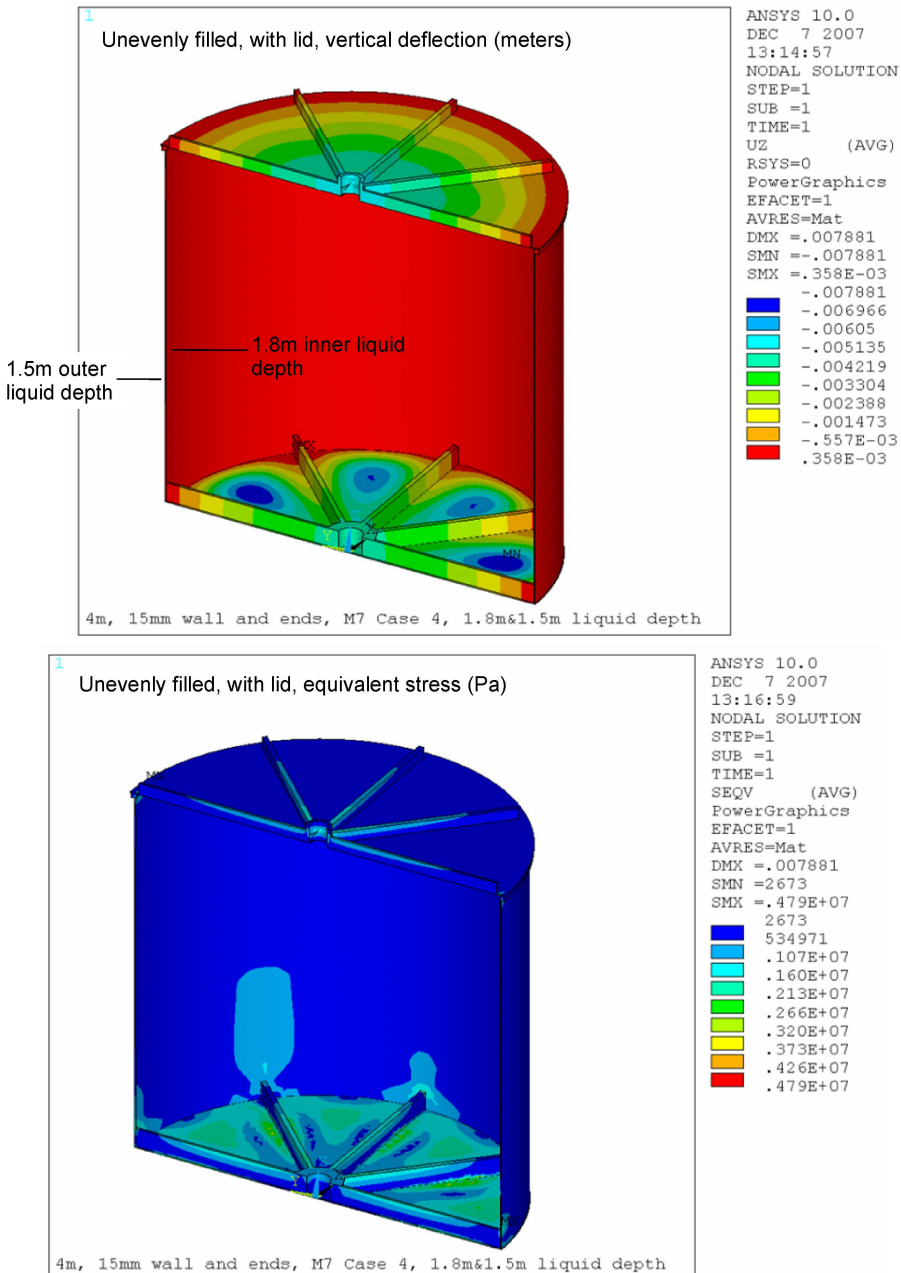


Fig. 4.18. Finite element analysis (FEA) of the 4-m acrylic vessel. The top plot shows the deflections and the lower figure gives the stresses during a worst case scenario of unequal filling. In this case a load equivalent to 30cm of liquid applies to the 15mm walls of the acrylic vessel.)

Case	Maximum vertical deflection (mm)	Maximum equivalent stress (MPa)	Safety factor against conservative working load of 5MPa (non-dim.)
Case 1 Empty, lid off	1.1 at center of bottom	1.3 at connection between rib and central hub	3.8
Case 2 Empty, lid on	5.5 center of lid under its own weight	1.9 at connection between lid ribs and hub	2.6
Case 3 Empty, lid on, sitting on 10% slope	5.5 center of lid under its own weight	1.9 at connection between lid ribs and hub	2.6
Case 4 Filled 1.8m deep inside, 1.5m deep outside, lid on, no slope	7.9 in floor panels between ribs	4.8 at connection between rib and vessel wall	1.0

Fig. 4.19. Results from a FEA of the 4-m acrylic vessel under different load conditions during the assembly, transport, lifting, and filling of the detector)



Fig. 4.20. Prototype 3-m vessel under fabrication at the Gold Aqua Technical Company. in Taiwan. The diameter and height are approximately 3 m. The design of this prototype closely resembles the design of the fabrication vessels for the experiment.

The US group of the Daya Bay collaboration has issued an R&D contract for the production of the 4-m full-size prototype at Reynolds Polymer Technology. Completion of this prototype is expected by the end of



Fig. 4.21. Prototype 4-m acrylic vessel with rib bottom and shaped, conical lid under fabrication at Reynolds Polymer Technology in Grand Junction, Colorado, for the Daya Bay experiment. The dimensional specifications of this cylinder are essentially identical to the vessels we propose to build for the Daya Bay project. This picture shows the vessel without the bottom and with unfinished bond lines. After fabrication all bonds are polished to optical clarity.

2007.

The default plan is for the US to build the 4-m vessels and support structure at Reynolds Polymer Technology and for Taiwan to build the 3-m vessels at Nakano. Both vessels would then be shipped to Daya Bay and assembled on-site.

An important consideration in the choice of vendor is the transportation of the vessels to Daya Bay and the assembly of the nested vessels. Simulations have shown that the transportation phase is hazardous for a double acrylic vessel which has been completely assembled. In general, upright transportation of the acrylic vessels is preferred as this is the strongest position for the vessels with the least risk of cracking, sagging, or damage during transport. Horizontal transport will require the design of a special transport container. Transportation equipment will be chosen to isolate shock and vibration loads. Investigation of the logistics have shown that it makes little cost difference if the vessels are transported from the US or Asia to Daya Bay. The shipping container and the shipping arrangements are part of the ongoing R&D program.



Fig. 4.22. Top: Example of large cylindrical acrylic objects that are being produced routinely by Reynolds Polymer Technology (RPT) in Grand Junction, Co. Bottom: Heat-room at Reynolds Polymer Technology for the bonding and curing of large-scale acrylic objects. In addition, several smaller ovens exist for the forming and curing of objects in size up to $3 \times 3\text{m}$.



Fig. 4.23. Fabrication hall and facilities for the production of large-scale acrylic objects at Reynolds Polymer Technology (RPT). Cranes and other infrastructure at RPT can be used for the lifting tests of the acrylic vessels and for the quality acceptance tests after production.

4.3.5 Overflow Tanks, Calibration Ports, and Vessel Penetrations

The detectors consist of three nested vessels: An inner target vessel filled with Gd-loaded liquid scintillator, the γ -catcher filled with liquid scintillator, and the outer steel tank containing the target vessels and a mineral oil buffer. The design of the acrylic vessels allows for the insertion of the calibration sources into the inner target volumes as well as the thermal expansion of the liquids during transport or data taking. The three volumes of the detectors are designed vacuum-tight to prevent mixing of the three fluids or their vapors.

Overflow tanks are positioned directly below the calibration hardware and they are connected to the calibration pipes and target vessels. A small gate valve separates the overflow tank from the calibration hardware during data collection. The overflow tanks provide a capacity of 100-150 L to accommodate the liquid expansion in temperature changes of up to 6–8° C.

In addition to the central chimney port, the buffer vessel lid will have two more ports, each of 50 mm diameter, to facilitate the deployment of radioactive calibration sources and light sources. These ports will have gate valves to isolate the calibration devices when they are not in use and facilitate their removal. Around the side wall of the stainless steel vessel there will be several ports for high voltage, signal, and instrumentation cables.

At first glance one is tempted to solve the penetration problem by long nested acrylic tubes bonded to the tops of the acrylic tanks. However, one pays for the simplicity of the penetrations in the following ways. The acrylic lids will require tubes of 1 m and 0.5 m length. This is a fragile protrusion, especially during

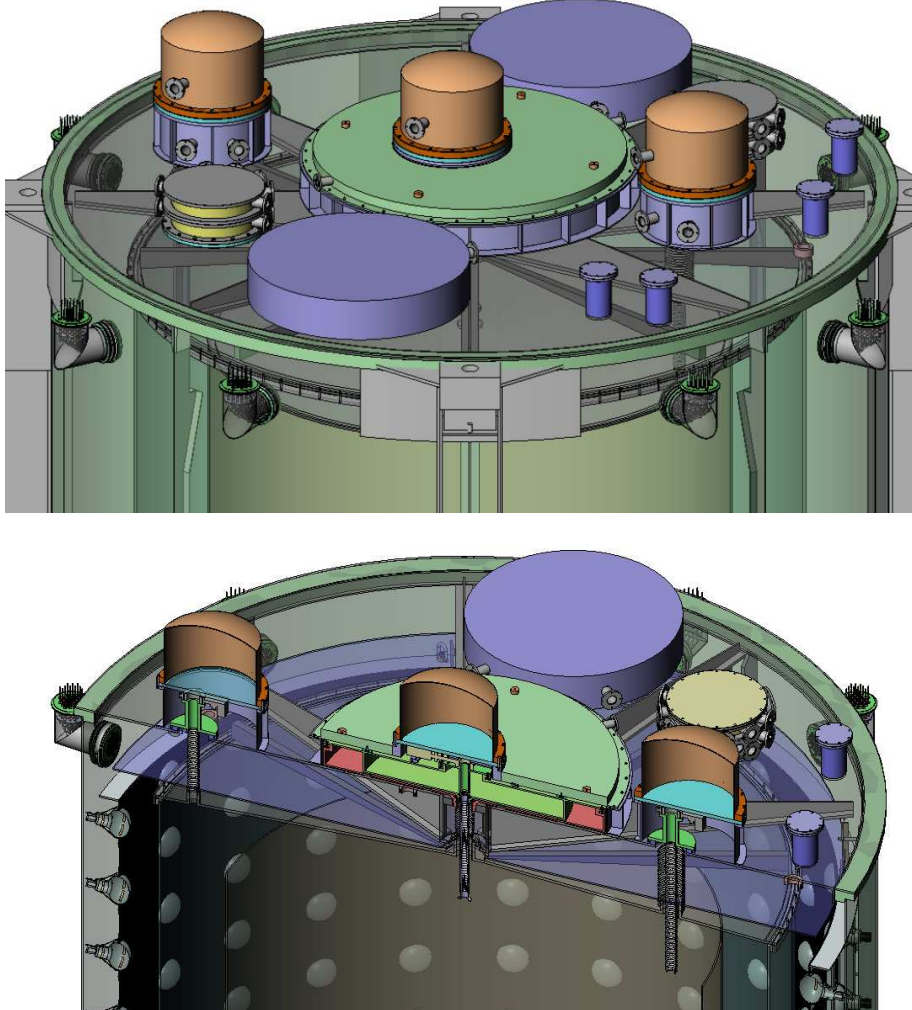


Fig. 4.24. Top: Engineering model of the top of the antineutrino detectors. The overflow tanks for the mineral oil volume are shown in blue, the automated calibration boxes in orange, and the central overflow tank in green. Various ports and distribution boxes are used cabling of monitoring to the inside of the detector and the distribution of gas and electrical cables. Three penetrations connect the calibration boxes (orange) and overflow tanks (blue) to the two different target vessel volumes. The ports can be sealed with gate valves when the calibration boxes are removed during transport or filling of the detectors. Bottom: Cross-sectional view of the top of the antineutrino detector.

transport and shipping. The outer lid must be lowered precisely during the assembly or damage will occur. With bonded calibration tubes any lateral motion of the vessels with respect to each other or with respect to the outer steel tank can damage the calibration pipes and penetrations.

The present design addresses these problems by using flexible Teflon joints along the acrylic tubes. These absorb translation and rotation motion in all possible directions [6]. Instead of long bonded acrylic tubes with bonded plates or stub tubes flanges with O-ring seals are used. The associated acrylic hardware can be manufactured in a machine shop separate from the acrylic tank company and attached in the surface

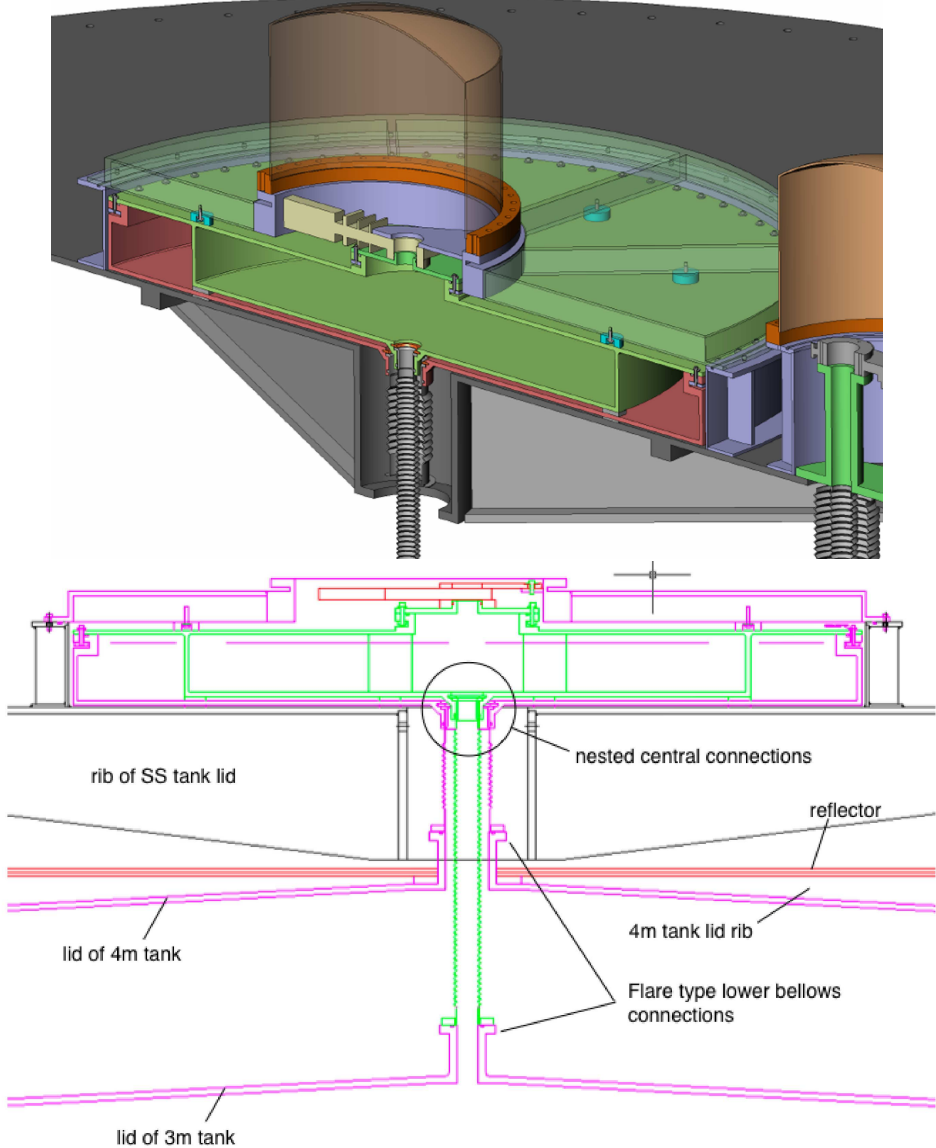


Fig. 4.25. Top: Detailed view of the central, concentric, nested overflow tanks for the Gd-LS and LS. Bottom: Cross-sectional drawing of the central calibration pipe and tank assembly.

assembly building. Support spools are required to mount the calibration boxes on the lid of the detector

A critical element in the current design are acrylic O-ring flanges. A prototype flange for connecting the calibration tube to a vessel flange has been constructed and is shown in Figure 4.26. Further R&D is necessary to test the reliability and leak tightness of such a flange.

After the detectors have been filled in the LS Hall, they will be transported to the experimental halls. During data taking they will operate under water in the pools of the experimental halls. During the course of their lifetime the detectors may experience temperature fluctuations of several $^{\circ}$ C. We expect that the range of temperatures the detectors are exposed to will be between 12–20 $^{\circ}$ C. The LS Hall and the tunnels will be air conditioned to 18–20 $^{\circ}$ C. The rock temperature at underground locations such as KamLAND is usually

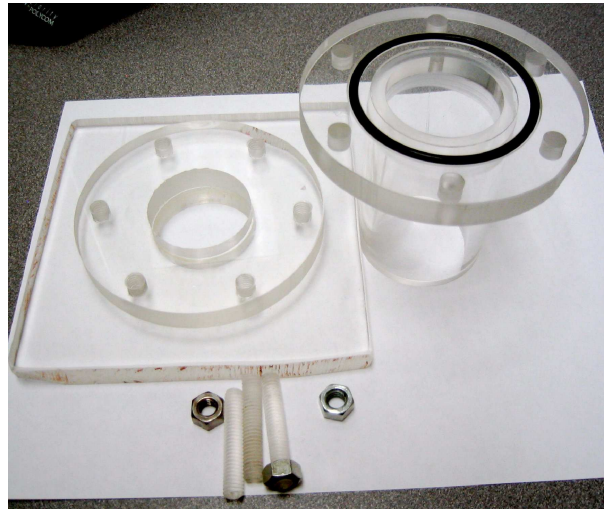


Fig. 4.26. Prototype of a plate to plate and a tube to plate bond for attaching penetration tubing to acrylic tank tops. If required all clamping hardware could be acrylic by use of threaded studs and acrylic nuts.

10–12° C. To allow for the expansion of the detector liquids, overflow tanks are part of the detector design. Based on the typical expansion of liquid scintillator and mineral oil of $\sim 7 \times 10^{-4}/^\circ\text{C}$ we expect the volume of the liquids to change by 15–20 L/ $^\circ\text{C}$. The overflow tanks are designed to accommodate 100–150 L of fluids for each one of the volumes. The volume in the overflow tank needs to be constantly monitored to a precision of about 1–2 L so that we can correct for the loss of events that the overflow fluid would have contributed. The entire overflow system is constrained to be inside a 300 mm high zone above the stainless tank top surface. The requirements for the overflow tanks are listed in Table 4.8.

Item	Requirement	Justification
Height	<300 mm	Tall enough to buffer anticipated fluid expansion/contraction from 5° C change in temperature
Geometry	Simple	Allow measurement of volume
Non-capturing overflow	Passive emptying back into main volume	Avoid loss of target mass and associated systematic uncertainty
Materials compatibility	scintillator compatibility for >5 years	Maintain structural integrity and avoid contamination of LS

Table 4.8. Requirements on the overflow tanks of the antineutrino detector.

The design of the concentric, nested overflow tanks for the Gd-LS and LS is shown in Figure 4.25.

In this design all overflow volumes for the LS and Gd-LS can be combined in one nested tank underneath the center calibration box. This option reduces the number of individual overflow tanks on top of the antineutrino detector but requires a set of concentric pipes at the center of the detector. This design permits domed top faces to the acrylic vessels which will provide additional structural strength and allow the escape of gas bubbles into the overflow volumes.

4.3.6 Thermal Modeling of the Antineutrino Detector

The thermal properties of the AD have been studied using a commercial FEA program, FLUENT [23]. The AD was assumed to initially be at thermal equilibrium (291 K) before immersion in a fluid at a temperature of 284 K. The temperature of the exterior fluid was held constant for the duration of the simulation. The AD was simulated as nested cylinders as specified in table 4.9. Meshing was done using two different grid sizes in order to test the stability of the simulation. The temperature of the fluid at a given point inside each cylinder was tracked as a function of time (as is the average AD temperature) and is shown in Fig. 4.27. The simulations indicate that the AD possesses significant thermal inertia and would require several months to approach thermal equilibrium.

Tank	material	thickness	radius	height	filling fluid
Outer	Stainless Steel	12 mm	2.5 m	5.0 m	mineral oil
Middle	Acrylic	15 mm	2.0 m	4.0 m	LAB
Inner	acrylic	10 mm	1.5 m	3.0 m	LAB

Table 4.9. Input parameters for the FLUENT thermal simulation of the AD.

4.3.7 Fill and Drain Mechanism

Filling the Daya Bay detector modules is a critical step of the assembly process. It involves the simultaneous filling of the Gd-loaded liquids scintillator, the undoped liquid scintillator, and the mineral oil into the detector volumes. The main purpose of this system is to provide a mechanism for filling the detector with the liquid scintillator and oil after assembly and for draining the detector for repair and decommissioning at the end of the experiment. The internal structure of the detector pose stringent mechanical constraints on the filling and draining process. All three regions in the antineutrino detector have to be filled simultaneously to minimize stresses on the acrylic target vessels. During the filling the mass of the Gd-loaded liquid scintillator has to be measured precisely to be able to determine the detector's target mass to < 0.1%. The filling process and measurement of the target mass are described below. The baseline design of the fill and drain mechanism is described below with a preliminary discussion of the characteristics and technical challenges. Design studies, prototyping, and R&D are underway to evaluate the conceptual design and develop a detailed technical solution. The basic requirements for the fill- and drain mechanism of the detector are summarized in Table 4.10.

Before and during filling the interior of the antineutrino detector is kept in a dry nitrogen atmosphere. The detector will first be purged after the assembly and cleaning in the surface assembly building, and then again before filling in the LS Hall. The purge gas will be dry, boil-off nitrogen supplied from a movable liquid nitrogen tank or nitrogen buggy. We may consider flowing the boil-off nitrogen through an activated charcoal trap for further reduction of radon but this may not be necessary. After filling it is necessary to maintain the flow of purge gas at all times to avoid degradation of the Gd-loaded liquid scintillator from oxygen and contaminants in the air. Liquid nitrogen will be delivered to the LS Hall and the experimental halls on a regular basis during the commissioning and operation of the experiment.

It is preferable that the liquid flow into the tank volumes be laminar with little or no splashing. This minimizes the creation of bubbles in the scintillator that can stick to the surface of the acrylic vessels during filling. It is possible to meet these requirements with a system using concentric filling tubes from the bottom of the nested tanks. But this requires additional and complicated penetrations. Fixed filling lines from the side are also possible but that system requires that tubes be left in place during data taking. The default solution is a removable fill/drain probe that can meet the above requirements. It is described below.

To minimize the number of penetrations into the detector we intend to use the calibration ports as fill ports. In this case the liquids are introduced from the top of the detector, as shown in Fig. 4.24.

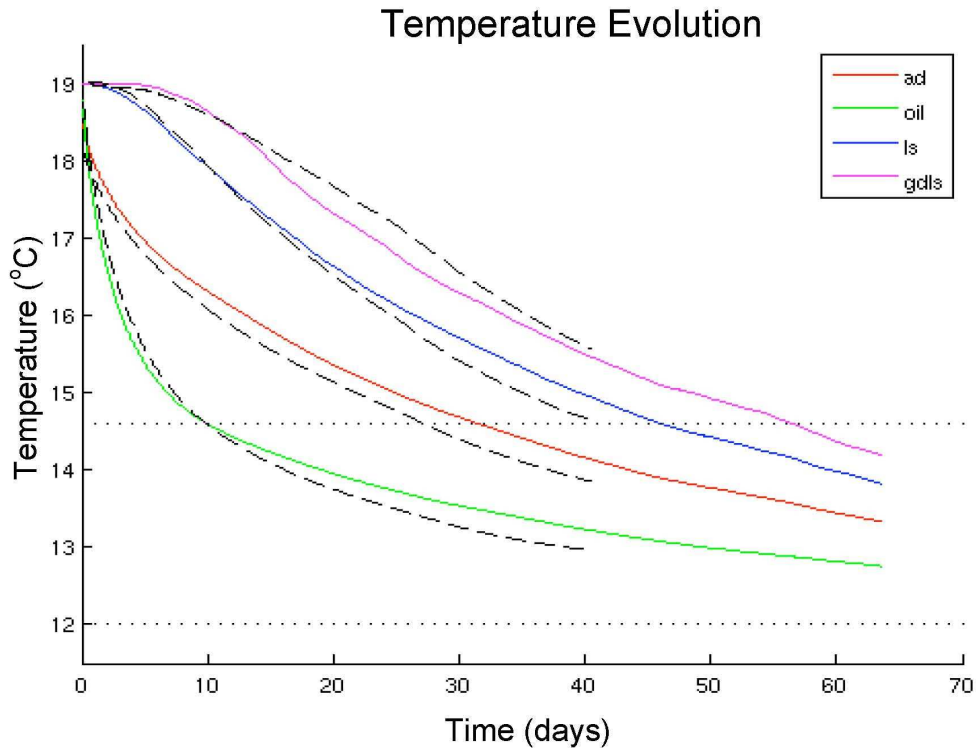


Fig. 4.27. The temperature evolution of the fluids within the AD are shown along with the average AD temperature as predicted using a FLUENT thermal simulation. The simulation assumes that the AD was initially in thermal equilibrium at 291 K and that the external temperature is held constant at 284 K. The dashed line is the result using a coarse grid while the solid line is the result using a finer grid.

To avoid splashing of the liquids under gravity into the empty vessels it we plan to insert small fill tubes down the calibration ports to the bottom of the target volume and the γ -catcher. These tubes can be used to fill the detectors from the bottom and to pump out the volumes when the detectors are emptied. When the detector are pumped with tubes from the top a small residual amount of scintillator is likely to remain in the vessels. This is unavoidable for all mechanisms that require pumping out the liquids to the top. The features of this mechanism are listed below:

- Small fill- and drain lines will run through the calibration ports to the bottom of the detector volumes.
- This design requires no additional penetrations to the acrylic vessels thus simplifying the construction and minimizing optical obstruction and interference in the detector.
- The interference of the insertion of calibration devices with the fill- and drain lines has to be studied.

Item	Requirement	Justification
Access to all three zones	Fill all volumes simultaneously	Minimize differential stress on the acrylic vessels
Fill Rate	1–2 days	Avoid extended filling time and bubbles from turbulent flow
Bubbles in scintillator	Minimize bubbles during filling	Avoid optical degradation at acrylic boundaries
Drain Rate	1–2 days	Rapid recovery from errors or emergency
Drained liquids	Discard drained liquids	Simplify technical challenges of fill/drain mechanism; Detector can be opened to air during emptying; drained liquids are likely contaminated
Residual liquids	<tens of liters after drain	Avoid standing LS in vessel during repair
Fluid pumping hardware	Non-contaminating vacuum tight; Reversible flow; Interlock to level sensors and emergency stop	Accurate fluid delivery, Radon protection, Preserve fluid properties, Suction flow during draining; drain without dismantling hardware or overstressing acrylic
Fluid measurements	Gd-LS to <0.3% LS & MO to <0.5% $\delta_p < 0.1\%$, $\delta_T < 0.5^\circ \text{C}$	satisfy detector systematic error Protect acrylic vessels Determine overflow tank fill levels.
Cover gas	Continuous N ₂ boil-off supply before, during and after filling	Minimize radon contamination

Table 4.10. Technical requirements for the fill/drain mechanism of the antineutrino detector.

The detectors will be filled in a dedicated filling station in the LS Hall. On the floor of the LS Hall the top flange connections on top of the detector will be at a height of about 5.7 m with an 8 m high ceiling height. Thus it is necessary to either insert flexible tubing or rigid tubing by sections. The latter is chosen for the fill-drain mechanism. During the filling or pumpout of the detector a temporary spool is clamped and sealed to the top plate of the overflow tank. This is the same plate that will later hold and locate the calibration domes. The temporary spool has a center passage allowing a sliding fit of the filling probe segments. Segments are inserted into the spool sequentially and attached to each other just above the spool. Elastomer seals at the joints contain the fluid flow to the inside of the probe sections. The probe diameter is in the range of 25 mm. During insertion, temporary safety clamps prevent accidental loss of probe sections. Welded to the last section is a commercial vacuum grade clamp flange (type KF-40). The KF flange provides a positive final stop for the probe assembly and permits leak tight attachment of the supply line to the probe.

Gas flow into the tanks is constrained to leave the system predominately through the normal overflow tank vent port because the sliding fit between the probe and the temporary spool has a low gas conductance. In addition there is a Teflon wiper on the inner spool surface to reduce fluid residue on the probes as they are withdrawn. Lowering and raising will either be by hand or by mechanical hand winch.

Once the fill-drain probe has been inserted the detector is filled until the liquid level raises into the overflow tanks. Level sensors in the overflow tanks will provide continuous monitoring of the liquid levels (and hence target mass) in the detectors.

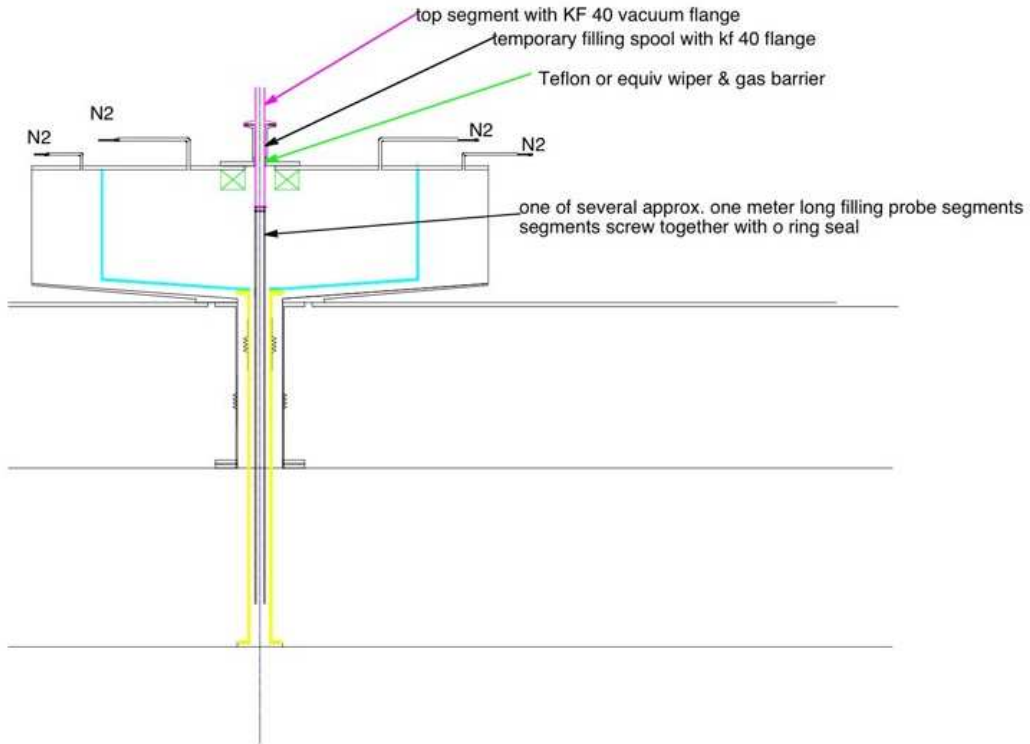


Fig. 4.28. Schematic drawing of a filling system for the Gd-loaded liquid scintillator. A probe is inserted through the calibration port and the overflow tank into the inner target vessel. All connections are made leak tight under a back-pressure of nitrogen to avoid air and radon to enter the detector. Filling of the undoped liquid scintillator into the γ -catcher would occur using a duplicate system located over the appropriate calibration penetration. This figure shows the option of nested, concentric overflow tanks located in the center of the top lid of the antineutrino detector.

4.4 Liquid Scintillator and Detector Liquids

The gadolinium-loaded organic liquid scintillator (Gd-LS) fills the central vessel of the antineutrino detector. The H atoms in the LS serve as the target for the inverse beta-decay (IBD) reaction, and the Gd atoms produce the delayed coincidence tag between the prompt positron and the delayed neutron from the IBD that is so important for background reduction. The LS contains $\sim 10\%$ hydrogen. Natural abundance Gd has a very large neutron-capture cross section, $\sigma = 49,000$ barns so that isotopic enrichment of the Gd is not required. Furthermore, neutron-capture on Gd leads to emission of γ rays with a total energy of ~ 8 MeV, that is much higher than the ≤ 3.5 MeV energies of the γ rays from natural radioactivity. Both Chooz and Palo Verde [7] used 0.1% Gd-doping (1 g Gd per kg LS) that yielded a capture time of $\tau \sim 28 \mu\text{s}$, about a factor of six shorter than that on protons in undoped liquid scintillator, ($\tau \sim 180 \mu\text{s}$).

To detect reactor antineutrinos with high precision, the Gd-LS must have the following key properties: a) high optical transparency (long optical attenuation length, on the order of several meters,) (b) high photon production (high light yield) by the scintillator, (c) ultra-low impurity content, mainly of the natural radioactive contaminants, such as U, Th, Ra, K, and Rn, and (d) long-term chemical stability, over a period of several years. It is necessary to avoid any chemical decomposition, hydrolysis, formation of colloids, or polymerization, which can lead over time in the LS to development of color, cloudy suspensions, or for-

mation of gels, emulsions or precipitates, all of which can degrade the optical properties of the LS. The requirements for the LS are described in Table 4.11.

Item	Requirement	Justification
Chemical stability of Gd-LS	>5 years	Unchanged during data taking
Attenuation length of oil, LS and Gd-LS	≥ 10 m	Ensure good light collection and maintain energy resolution
Light yield of liquid scintillators	>100 detected p.e./MeV	Meet energy-resolution requirement
Radioactive contamination	$<10^{-12}$ g/g	Reduce accidental background
Distribution of Gd in LS	Gd uniformly dissolved in LS	Maintain detection efficiency
Batch-to-batch identical properties of organic liquids	Every batch of each liquid (LS, Gd-LS, oil) to be the same as the other batches	Pair-wise filling to control target mass and ensure identical detector properties

Table 4.11. Requirements on the liquid scintillator of the antineutrino detector.

Because of the importance of the Gd-LS in the Daya Bay experiment, the groups at BNL in the U.S., IHEP in the Peoples Republic of China, and JINR in Russia, have for the past ~ 3 years been studying multiple approaches to synthesizing the Gd-LS. We have done R&D on topics such as: (1) selection of the proper organic LS, (2) development of chemical procedures to synthesize organo-Gd complexes that are soluble in the LS and chemically stable, (3) purification of the components of the Gd-LS, and (4) development of analytical chemical and physical methods to measure these key properties of the Gd-LS over time. These groups are briefly described in the following:

- A. The Solar-Neutrino/Nuclear-Chemistry Group in the BNL Chemistry Department has been involved since 2000 in R&D of chemical techniques for synthesizing and characterizing organic liquid scintillators loaded with metallic elements (M-LS). Mainly using solvent extraction techniques, they initially developed a proposed new low-energy solar-neutrino detector, LENS/Sol [8], in which relatively high concentrations of $\sim 5\text{--}10\%$ by weight of carboxylate complexes of ytterbium (Yb^{3+}) and indium (In^{3+}) were dissolved in the LS to serve as targets for solar neutrino capture. Beginning in 2004, BNL extended these chemical methods to the new reactor antineutrino experiments, doing R&D to synthesize Gd-LS (with Gd^{3+}) at the much lower concentrations required for neutron detection, $\sim 0.1\%$. See reference [9].
- B. Nuclear chemists at IHEP also began their R&D on Gd-LS in 2004. Their recent work has focused on preparing solid organo-Gd complexes, that could be cleaned of chemical contaminants by washing with water prior to being dissolved in the solvent LS.
- C. The JINR chemists, who have long experience in the development of plastic scintillators, have been studying the characteristics of different LS solvents, especially Linear Alkyl Benzene. They have also been involved in procuring, purifying, and studying the PPO wavelength shifter.

4.4.1 Selection of Solvents

Several aromatic (organic compounds based on benzene) scintillation liquids were studied to test their applicability as solvents for Gd-LS:

1. Pseudocumene (PC), which is 1,2,4-trimethylbenzene (and mesitylene, the 1,3,5-isomer), has been the most commonly used solvent for Gd-LS in previous neutrino experiments. But it has a low flash point (48° C) and aggressively attacks acrylic plastic.
2. Phenylcyclohexane (PCH) has a lower reactivity than PC, but only half of the light yield.
3. Both di-isopropylnaphthalene (DIN) and 1-phenyl-1-xylyl ethane (PXE) have optical absorption bands in the UV region below 450-nm that cannot be removed by our purification procedures.
4. Linear Alkyl Benzene, (LAB) [10], is an excellent solvent for Gd-LS. LAB is composed of a linear alkyl chain of 10–13 carbon atoms attached to a benzene ring, and has an appreciable light yield. LAB also has a high flash point (130° C), which significantly reduces safety concerns. It is relatively inexpensive, since it is an article of commerce, with worldwide annual production of hundreds of thousands of tons, mainly for the manufacture of biodegradable detergents.
5. Mineral oil (MO) and dodecane (DD) both have very good light transmission in the UV-visible region so that no further purification is required. They produce little or no scintillation light. It has been reported that mixtures of PC and mineral oil will not attack acrylic.

The chemical properties and physical performance of these scintillation solvents, plus mineral oil and dodecane, are summarized in Table 4.12.

LS	Gd Loading in LS	Density (g/cm ³)	abs ₄₃₀	Purification Method	Relative Light Yield	Flash Point
PC	Yes	0.889	0.002	Distillation	1	48°C
PCH	Yes	0.95	0.001	Alumina	0.46	99°C
DIN	Yes	0.96	0.023	Alumina	0.87	$\geq 140^{\circ}\text{C}$
PXE	Yes, but is not stable	0.985	0.022	Alumina	0.87	167°C
LAB	Yes	0.86	0.002	Alumina	0.98	130°C
MO	No	0.85	0.001	Not needed	NA	215°C
DD	No	0.75	0.000	Not needed	NA	71°C

Table 4.12. Properties of Selected Liquid Scintillators, abs₄₃₀ is the absorption of 430 nm light measured in a 10-cm optical cell.

Because of its attractive properties, LAB has been selected as the LS for Daya Bay. It is produced by two different companies in China, Fushun and Nanjing, and in the West, by Petresa in Canada and in Spain. Figure 4.29 shows the optical absorption spectra for samples of Petresa and Fushun LAB. It is still an open question as to whether or not the LAB received from the manufacturer will have to be purified, although we have routinely been using columns of activated alumina to purify our LAB samples to ensure that they all have uniform properties.

4.4.2 Preparation of Gadolinium Complexes

One of the major research challenges is how to dissolve Gd into the liquid scintillator. It is difficult to add inorganic salts of Gd into the organic LS, which is an organic aromatic (benzene-like) compound. The

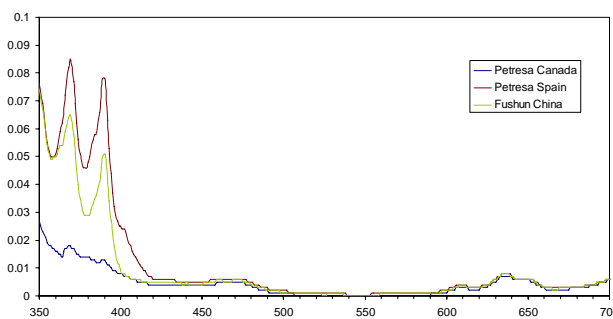


Fig. 4.29. Comparison of the UV-visible spectra of LAB samples as received from the Fushun and Petresa companies

only solution to this problem is to form complexes of Gd with organic ligands that are soluble in the organic LS.

The recent Chooz and Palo Verde antineutrino experiments used different methods to produce their Gd-doped liquid scintillator. In the Chooz experiment, $\text{Gd}(\text{NO}_3)_3$ was directly dissolved in the LS, resulting in an unstable scintillator whose attenuation length decreased at a relatively rapid rate, 0.4% per day. As a result, Chooz had to be shut down prematurely. On the other hand, the Palo Verde experiment used the organic complex, Gd-ethylhexanoate, yielding a scintillator which aged at a much slower rate, quoted as 0.03% per day.

In the Periodic Table, Gd belongs to the lanthanide (Ln) or rare-earth series of elements. Lanthanides can form stable complexes with organic ligands that contain elements such as oxygen, nitrogen, and phosphorus, e.g., carboxylic acids, organophosphorus compounds, and beta-diketones. Over the years, several recipes for Gd-LS based on these organic ligands have been developed by different groups. We briefly summarize some of the BNL and IHEP work below.

The main complexants that we have studied are carboxylic acids, ‘R-COOH’, which can be neutralized with inorganic bases such as NH_4OH to form carboxylate anions that can then complex the Ln^{3+} ion. Some work has also been done with organic phosphorus-oxygen compounds, ‘R-P-O’, such as tributyl phosphate (TBP), or trioctyl phosphine oxide (TOPO), that can form complexes with neutral inorganic species such as LnCl_3 [11]; the extraction of Ln is effective, but the attenuation length is only a few meters and the final Ln-R-P-O complex in LS was not stable for more than a few months. On the other hand, the carboxylic acids form organo-metallic complexes that can be loaded into the LS with $\geq 90\%$ efficiency. The carboxylic acids are preferable to the phosphorus-containing compounds because they are less expensive and easier to dispose of as chemical waste. In principle, the chemical reactions are

- neutralization at $\text{pH} \sim 6.85$ to 7.05, $\text{RCOOH} + \text{NH}_4\text{OH} \rightarrow \text{RCOO}^- + \text{NH}_4^+ + \text{H}_2\text{O}$ in the aqueous phase, followed by
- Ln-complex formation, $\text{Ln}^{3+} + 3\text{RCOO}^- \rightarrow \text{Ln}(\text{RCOO})_3$,

which is soluble in the organic LS but is relatively insoluble in the aqueous phase. These reactions are very sensitive to pH: the neutralization step to form the RCOO^- depends on acidity (the ‘ pK_a ’ of the carboxylic acid); and hydrolysis of the Ln^{3+} can compete with formation of the $\text{Ln}(\text{RCOO})_3$ complex by forming Ln-hydroxo species.

A range of liquid carboxylic acids with alkyl chains containing 2–9 carbon atoms has been studied. It was found that acetic acid (C2) and propionic acid (C3) have very low efficiencies for extraction of Ln into the organic phase. Isobutyl acid (C4) and isovaleric acid (C5) both have strong unpleasant odors and require

R-P-O ligands to achieve high extraction efficiencies for Ln. Carboxylic acids containing 6 to 9 carbons are suitable: the best complexants found to date are the C6 compound, 2-methylvaleric acid, $C_5H_{11}COOH$ or ‘MVA’, the C8 compound, 2-ethylhexanoic acid, $C_7H_{15}COOH$ or ‘EHA’, and the C9 compound, 3,5,5-trimethylhexanoic acid, $C_8H_{17}COOH$ or ‘TMHA’. To date, many hundreds of Ln-LS samples have been synthesized, including scores of Gd-LS. [12]

Several instrumental and chemical analytical techniques have been used as guides for optimization of the synthesis procedures for Gd-LS. Besides the measurements of light yield and optical attenuation length that will be described below, are measurements in the LS of

1. the concentration of Gd^{3+} by spectrophotometry
2. the concentration of the total carboxylic acid, R-COOH, by acid-base titrations
3. the concentration of the uncomplexed R-COOH by IR spectroscopy (of the characteristic carboxylic-acid dimer peak at $\sim 1710\text{ cm}^{-1}$ wavenumbers)
4. the concentrations of the different Gd-carboxylate complexes in the organic liquid by IR spectroscopy
5. the concentration of the H_2O by Karl-Fischer titration
6. the concentrations of the NH_4^+ and Cl^- ions by electrochemistry with specific ion-sensitive electrodes

These measurements indicated that the chemistry of the Gd-LS is more varied and complicated than what is expected from the simple chemical reactions (a) and (b) listed above. The Gd molecular complex in the LS is not simply $Gd(RCOO)_3$, but contains some OH as well, and the form of this complex changes with changing pH. So, even though the long-term studies consistently show that the Gd-LS is chemically stable for periods ≥ 2 years, there is the lingering concern that hydrolysis might occur in the LS over long time periods. Close attention to chemical details, especially pH control, is crucial, as is long-term monitoring of the Gd-LS.

During our R&D at BNL, the Gd carboxylate was formed in the presence of the LS so that it immediately dissolved in the organic liquid (solvent extraction). At IHEP, the solid Gd-carboxylate complex was first synthesized and then dissolved in the LS.

After the Gd-complex is introduced into the LAB, a primary fluorescent additive and a secondary spectrum shifter (both called ‘fluors’) must be added so that the effective wavelength of the emitted light is in the blue region, where the PMTs are most sensitive. The final concentration of the solutes includes 1 g/L Gd ($\sim 0.1\%$ Gd by weight), 3 g/L (0.3% by weight) of the primary wavelength shifter, PPO, and 15 mg/L of the secondary shifter, bis-MSB. The resulting liquid is then filtered through a $0.22\text{-}\mu\text{m}$ pore-size filter and bubbled with nitrogen to remove air (and Rn). Figure 4.30 shows how the light production of the LS varies with the concentration of PPO. We selected the 0.3%-concentration to optimize the light output while reducing the cost of the PPO, which is rather expensive.

4.4.3 Purification of Gd-LS

Most purification steps in principle should be applied before and during the synthesis of the Gd-LS [13] because chemical separation schemes that would be used after the Gd-LS has been synthesized would likely remove some of the Gd as well as other inorganic impurities. However, the removal of non-radioactive chemical impurities could increase the transmission of the light in the LS and enhance the long-term stability of the Gd-LS, since some impurities might induce slow chemical reactions that gradually reduce the transparency of the Gd-LS.

Chemical purification steps that have been developed include the following:

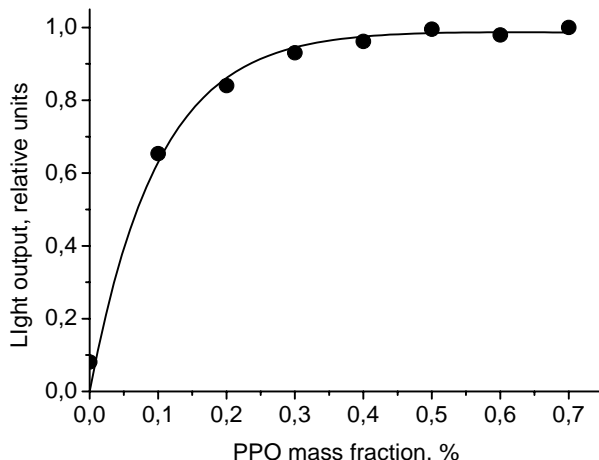


Fig. 4.30. Variation of the light output of LS containing different concentrations of PPO.

1. The purification of chemical ingredients in the aqueous phase, such as ammonium hydroxide and ammonium carboxylate, is done by solvent extraction with toluene mixed with tributyl phosphine oxide (TBPO).
2. LAB, which has low volatility, is purified by absorption on a column of activated alumina, Al_2O_3 .
3. High-volatility liquids, such as the carboxylic acids, are purified by temperature-dependent vacuum distillation at ≤ 0.04 bar. Distillation should remove any radioisotopic impurities, including radon. The distillation temperature is kept as low as possible to avoid chemical degradation of the organic liquid.

The purification of radioactive impurities associated with Gd, mainly the U and Th decay chains and Ra, is an important current R&D area because concentrations of radioactive impurities ≤ 1 ppb (10^{-9} g/g) in the Gd, or ≤ 1 ppt (10^{-12} g/g) in the final 0.1% Gd-LS, are needed to fulfill our criterion of a random singles rate below 50 Hz. We note that some initial assays of the radioactive impurities in samples of the solid $\text{GdCl}_3 \cdot 6\text{H}_2\text{O}$ that is used in the Gd-carboxylate syntheses have already been done with a variety of low-level counting methods, for example, by γ -ray spectroscopy at the New York State Department of Health and at the KamLAND underground laboratory, and by liquid-scintillation counting in the SNO laboratory. However, these initial results were inconsistent; some values were less than the detectable limits, 10 ppb, while others were in the hundreds of ppb.

4.4.4 Characterization of Gd-LS

The long-term stability of the Gd-LS preparations is being monitored in an ongoing Quality Control (QC) program by measuring their light absorbance and light yield. Samples from the same synthesis batch are sealed respectively in 10-cm optical cells for UV absorption measurements, and in scintillation vials for light yield measurements. Monitoring the UV absorption spectrum as a function of time gives a more direct indication of chemical stability than does the light yield.

Fig. 4.31, illustrates representative UV absorption values at 430 nm (measured over time in the UV spectrometer) of several Gd-LS samples that had been prepared by solvent extraction, for different concentrations of Gd from 0.2% to 1.2% by weight in a variety of solvent systems — pure PC, pure LAB, and mixtures of PC + dodecane and of PC + LAB. The figure shows that the samples have been stable since their

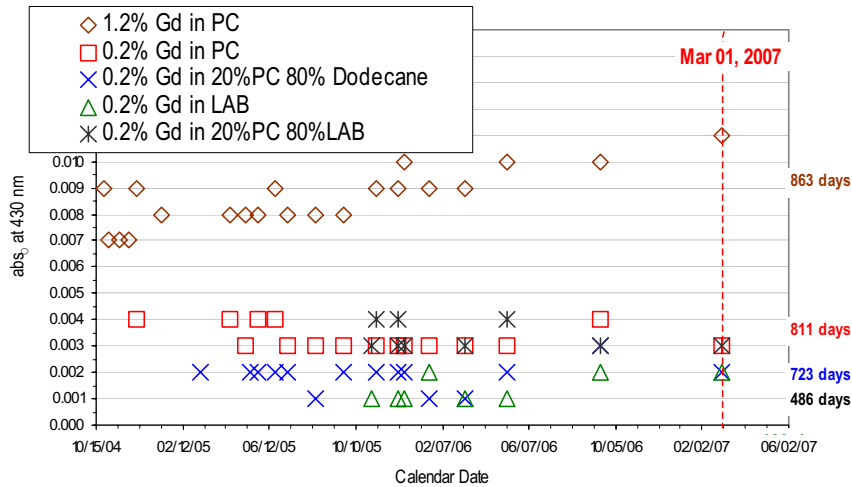


Fig. 4.31. The UV absorption values of Gd-LS prepared by solvent extraction, and measured at 430 nm over the period 2004–2007

synthesis, for periods up to ~ 2.5 years. Analogous values obtained for samples prepared by dissolving solid Gd-carboxylate in LAB are shown below.

Another optical parameter, the attenuation length, L , is extrapolated from the UV absorption data. It is defined as the distance at which the light transmitted through the sample has its intensity reduced to $1/e$ of the initial value: $L = 0.434 d/a$, where a is the absorbance of light (at a reference wavelength, usually 430 nm) measured in an optical cell of length d . Note that for $d = 10$ cm, a value of $a = 0.004$ translates into an attenuation length $L \sim 11$ m. However, it is difficult to extract accurate optical attenuation lengths from these short pathlength measurements because the a values are close to zero. Measurements over much longer pathlengths are needed. BNL has constructed a system with a 1-meter-pathlength, horizontally aligned quartz tube. The light source is a He-Cd, blue laser with $\lambda = 442$ nm. The light beam is split into two beams with 80% of the light passing through the 1-m tube containing the Gd-LS before arriving at a photodiode detector. The remaining 20% of the light passes through an air-filled 10-cm cell and reaches another photodiode detector to measure the fluctuations of the laser intensity, without any interactions in the liquid. Values from this dual-beam laser system with 1-m pathlength agreed to $\leq 10\%$ with the attenuation lengths extrapolated from the measurements with the 10-cm cell in the UV Spectrometer. For 0.2% Gd in a 20% PC + 80% dodecane mixture without fluors, the 1-m measurement gave 95.23% transmission, corresponding to an attenuation length ~ 22 m. This agreed nicely with the value that was extrapolated from the measured $a = 0.002$ in the 10-cm cell.

The long-term stability and other properties of ~ 700 L of Gd-LS have been studied in a prototype detector at IHEP. Data for that Gd-LS sample obtained with a UV-Vis spectrophotometer with a 10-cm optical cell over a period ~ 200 days are shown in Fig. 4.32.

IHEP has also constructed an optical system with a variable vertical pathlength up to ~ 1 m and a single-beam blue LED light source, in order to measure the attenuation length L more accurately. L is measured by varying the liquid level and fitting the measured intensity of transmitted light vs. pathlength with an exponential curve. An example of this type of measurement is shown in Fig. 4.33.

The attenuation length of the unloaded LAB is measured to be 23.1 ± 0.9 m. In phase I of the Daya Bay prototype detector (See Section 15.3.1), 700 L of pseudocumene-based unloaded LS was used. In phase II, 700 L of LAB-based Gd-LS has been synthesized and filled into the detector. Samples of these LS and Gd-

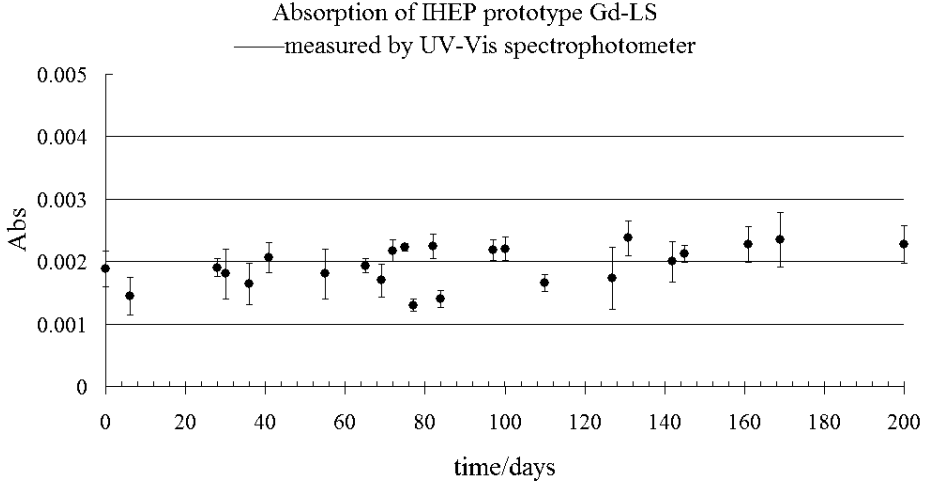


Fig. 4.32. Long-term Stability Test of Gd-LS with 0.2% Gd as a function of time (from phase II of the IHEP prototype: LAB with 5 g/L PPO and 10 mg/L bis-MSB).

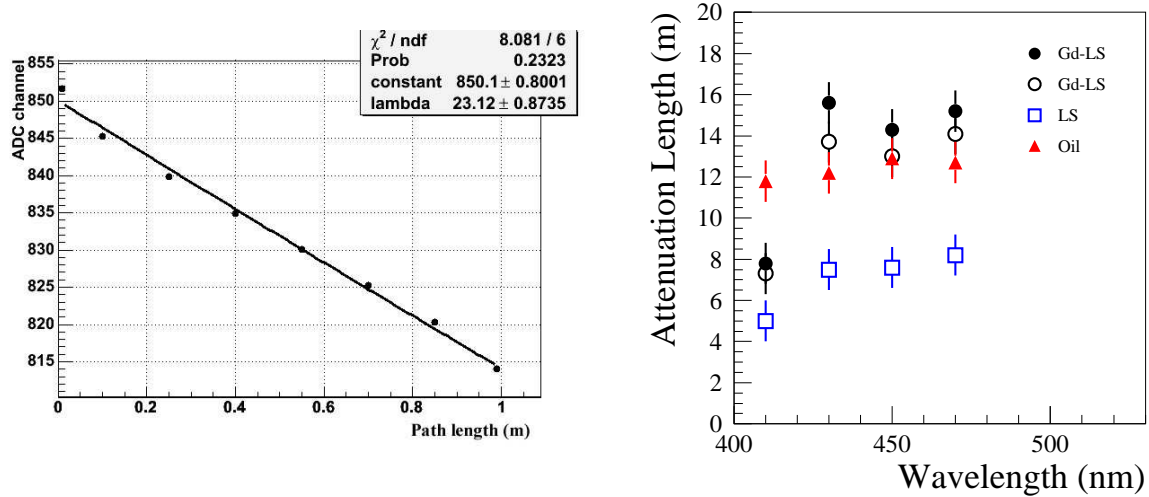


Fig. 4.33. Left: an example of the attenuation length measurement using the 1-m vertical tube system. The transmission values for different pathlengths are fitted with an exponential curve. Right: Closed and open circles are attenuation lengths obtained with samples of the 700-L LAB-based Gd-LS used in the prototype at IHEP. Squares are for PC-based unloaded LS; triangles are for mineral oil.

LS, as well as of the buffer mineral oil, have been removed from the filled detector and measured using the 1-m tube system, as shown in Fig. 4.33. The Gd-LS has been measured twice. The open circles show the first measurement done immediately after the Gd-LS filling. The closed circles show the second measurement two weeks later. The attenuation length of the Gd-LS is ~ 15 m at 430 nm.

The emission spectrum of the Gd-LS was also studied. No remarkable differences were found for the Gd-LS with different solvents (LAB or PC + Oil) or with different complexants (TMHA, EHA, or TOPO).

The emission spectrum of Gd-LS with 5 g/L PPO and 10 mg/L bis-MSB was shown previously in Fig. 4.9. The peak of the emitted light overlaps very well with the most sensitive range of the 8" PMT candidates.

The light output of Gd-LS samples is also measured at BNL, IHEP, and JINR. A scintillation vial containing 10 mL of Gd-LS plus the wavelength-shifting fluors, PPO (3 g/L) and bis-MSB (15 mg/L), is used for measurement of the photon production. The value of the Gd-LS light yield, which is determined from the Compton-scattering spectrum produced by an external ^{137}Cs γ -ray source that irradiates the sample, is quoted in terms of S%, relative to a value of 100% either for pure PC with no Gd loading or for anthracene. Measured S% values are respectively 95% for a mixture of 95% LAB + 5% PC, and 55% for 0.1% Gd in 20% PC + 80% dodecane.

Table 4.13 lists the light yield for several Gd-LS samples, relative to a value of 100% for an anthracene crystal. It is seen that the concentration of Gd loading does not have any major effect on the light yield for concentrations up to 2%.

Gd(g/L)	Scintillator	Complex	Solvent	Light Yield
—	PPO bis-MSB	—	PC:dodecane	0.459
—	PPO bis-MSB	—	LAB	0.542
1.5	PPO bis-MSB	Gd-ethylhexanoate	2:8 PC:LAB	0.538
2.0	PPO bis-MSB	Gd-ethylhexanoate	2:8 PC:LAB	0.528
1.5	PPO bis-MSB	Gd-isobornanoate	LAB	0.492
2.0	PPO bis-MSB	Gd-isobornanoate	LAB	0.478

Table 4.13. Light yield for several Gd-LS samples measured relative to an anthracene crystal.

Fig. 4.34 shows the stability of the light yields of the Gd-LS over a period \sim 120 days for two different γ -ray sources, ^{137}Cs and ^{60}Co .

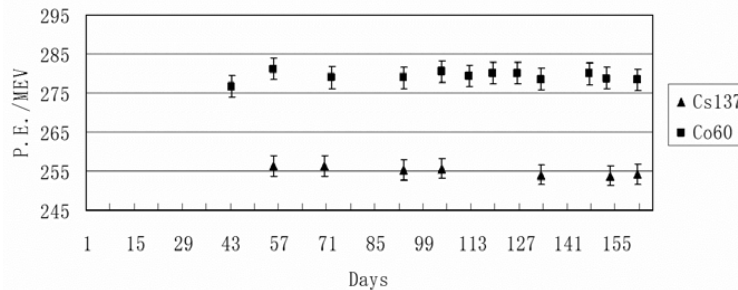


Fig. 4.34. The variation of the light yield vs. time of the Gd-LS taken from the Daya Bay Phase II prototype, measured over a period \sim 120 days for two different γ -ray sources.

It should be noted that beginning in June 2007, measurements have been going on at the University of Hong Kong (HKU) of Daya Bay Gd-LS samples that are being maintained there at room temperature and at a few other temperatures up to a maximum of 40° C (in so-called ‘aging tests’ to accelerate any possible deterioration of the samples). Several \sim 50-L samples of Gd-TMHA in LAB were prepared there by the LS chemists from BNL and IHEP working together. These measurements, which include UV spectra, 1-meter attenuation lengths, and light yields, are being continued to monitor the long-term stability of the Gd-LS.

So far, the synthesized Gd-LS samples have been chemically stable at 40° C for 4 months, with attenuation lengths ~ 8 m. Note that the LAB used in these syntheses had not been purified. The attenuation length is expected to increase after purification of the LAB.

4.4.5 Large Scale Production of Gd-LS

The two different chemical synthesis methods, namely solvent extraction and solid dissolution, that we had pioneered for the synthesis of Gd-LS, have produced very similar Gd-LAB products with LS properties that are equally suitable for the Daya Bay experiment. However, we realized that there could be serious logistical problems associated with the solvent extraction method, in terms of producing ~ 20 T of 1% Gd-LS elsewhere and then shipping it to Daya Bay where it would be diluted to ~ 200 T of 0.1% Gd-LS. It seemed simpler to prepare ~ 1 T of solid Gd-TMHA offsite (at IHEP) and to ship it to Daya Bay for the preparation of the ~ 200 T of 0.1% Gd-LS. However, the Gd solid would have to be dissolved underground in the LS Hall. These activities in the LS Hall would be on the project's critical path so that any unanticipated difficulties encountered in the dissolution process would be potential sources of delay. Nevertheless, we were unanimous in choosing the Gd-solid dissolution process as the project's baseline, and agreed to focus on this option (with the solvent-extraction method preserved as a potential backup).

However, we also realized that there are several important R&D tasks concerning the solid dissolution of water that still must be resolved. Several of these tasks involved determining the permissible concentration range of water that can be accommodated in the liquid Gd-LS:

1. too much water can affect the optical properties of the Gd-LS, by quenching the production of light by the LS and by reducing the optical transmission in the liquid; and
2. insufficient water can affect the solubility and long-term stability of the Gd-carboxylate complex in the Gd-LS.

We have begun studying a variety of methods to remove water from the moist solid Gd-carboxylate, such as mechanical pressing/squeezing and drying under vacuum over a range of temperatures. To date, we have found that the vacuum-drying process is very effective, and superior to mechanical pressing, in producing a dry solid Gd-carboxylate with a constant weight. However, such dry samples have unexpectedly proven to be difficult to dissolve completely in LAB, giving cloudy liquid samples. On the other hand, samples containing some residual water dissolve fairly quickly, over a period of ~ 1 hour and do lead to optically clear liquid samples over a period of ~ 24 hours. However, we still have R&D to do, to determine optimal values of the concentration of water in the Gd-LS and of the standing time required to have the Gd-LS become optically transparent.

We are also doing other R&D concerning:

1. The radiochemical separation procedures to reduce radioactive contaminants in Gd.
2. The commissioning and start of data taking with a more sophisticated setup of a 2-meter-long, dual-beam vertical optical system to measure light attenuation.
3. The effects of filtration on the concentrations of Gd and fluors in the Gd-LS, which may impact our goal of preparing eight identical detector modules for the Daya Bay experiment.

Additional tasks that we are undertaking involve the development and acquisition of large-scale chemical production equipment that would be used for liquid filtration in the LS Hall. Some risks still remain in the large-scale production process that must be addressed:

1. At the production site of the solid:

- (a) As discussed above, we will need to produce a suitably moist solid Gd carboxylate and package it appropriately in a sealed container so that it neither dries out nor absorbs water from the air during its shipment from IHEP to Daya Bay.
- (b) Transportation of the solid to Daya Bay may be a concern. We will need to pay attention to shipment details (e.g., air freight vs. overland shipment) to avoid large temperature fluctuations, especially at $\geq 40^\circ\text{C}$.

Fig. 4.35 shows a schematic of the flow chart for the chemical processes that will be done to prepare the solid Gd carboxylate. We will use a closed synthesis system that will operate in an automated mode and will eliminate exposure of the Gd-LS to air. It is not yet certain if we will need the box type filter press that is shown in the flow chart. This offsite production of the solid Gd-complex is not on the project's critical path.

Flow Diagram of Synthesis of Solid Gd-carboxylate to be done Off-site

Designed by Engineers at Beijing University of Chemical Technology

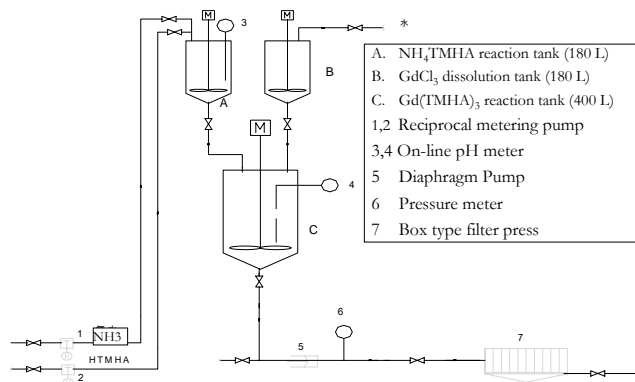


Fig. 4.35. Flow chart for the chemical processes that will be used to prepare the solid Gd carboxylate.

2. During the dissolution of the solid in LAB in the LS Hall:

- (a) Our space requirements for this process in the LS Hall include at a minimum, two separate 1-T tanks for the dissolution in LAB (i) of the solid Gd carboxylate and (ii) of the fluors, and a 4-T tank in which the contents of tanks (i) and (ii) will be mixed. The planned production schedule calls for five weeks of operations in the LS Hall, at five hours per batch and two batches a day. Our recent R&D indicates that the baseline mixing plan cannot achieve this goal of finishing each batch in 5 hours, and it may take upwards of 24 hours for the solution of Gd carboxylate in LAB to become optically clear. Further research on this point is being carried out. If our results show that a standing period of ~ 24 hours will indeed be required for the Gd-LAB solution to clear up, before it is to be added to the 4-T mixing tank, then additional 1-T holding tanks will have to be installed in the LS Hall. Two such tanks will be needed per production batch, one tank for the Gd in LAB and one tank for the fluors in LAB. The current plan is to prepare two batches per day, so that a total of four additional 1-T holding tanks will be needed. There is sufficient space available in the LS Hall to accommodate these extra tanks.
- (b) If the 24-hour standing period described in item (a) above is to be implemented, then the production schedule will be staggered over a two-day cycle, as follows: On day one, the Gd-LAB

solution and the LAB-fluors solution will be prepared for batches 1 and 2 and placed in the four holding tanks. On day two, these solutions, which will have cleared up, will be transferred to and mixed in the 4-T tank, first for batch 1 and then for batch 2; the resulting mixtures will then be transferred into the storage pool for the Gd-LS. Also on day two, the Gd-LAB solution and the LAB-fluors solution will be prepared for the new batches 3 and 4. These solutions will be placed in the four emptied holding tanks, to stand for 24 hours before being transferred to and mixed in the 4-T tank on day 3. This schedule of preparing two batches each day and then waiting 24 hours before doing the mixing step will be continued throughout the full five-week cycle for preparing the Gd-LS. All of the LS Hall activities are on the critical path.

Fig. 4.36 shows a schematic of the flow chart for the dissolution of the solid Gd carboxylate underground in the LS Hall at Daya Bay. This will be a closed automated system to minimize exposure to air. It is possible that the centrifuge shown in the figure will not be needed.

Flow Diagram of 0.1% Gd-LS Dissolution On-site in Hall 5 (Preliminary design)

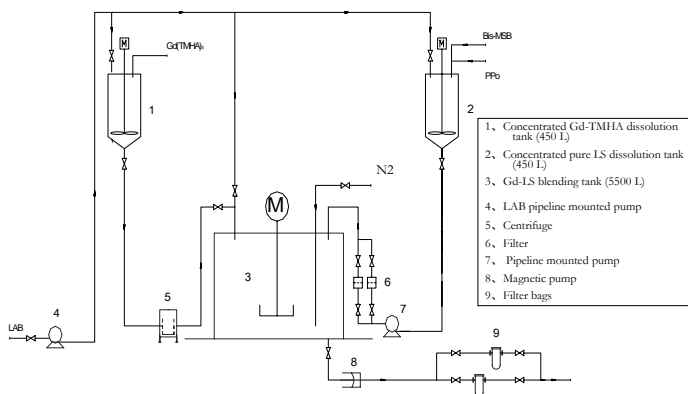


Fig. 4.36. Flow chart for the dissolution processes that will be done to prepare the final Gd-LS in the LS Hall at Daya Bay.

- (c) Fig. 4.36 also shows equipment to be used in filtering the mixed solution. However, note that we have recently begun research to answer the following two questions: Does the dissolved Gd in LAB, at the 0.1% concentration level, need to be filtered before it is transferred into the antineutrino detector modules? What will be the effects of such filtration?

Other R&D issues still require study, e.g., the optimal water content of the solid Gd carboxylate and the ES&H of working in a confined underground space with a dispersible solid.

We have defined some approximate Gd-LS milestones, listed below:

1. Because additional technical assistance will be needed both for the production of the Gd solid and for the dissolution, additional personnel will have to be identified and trained prior to August 1, 2008
2. Production of solid Gd-carboxylate to start at the latest by August 1, 2008.
3. Preparation of the solid Gd-carboxylate to end by November 1, 2008.
4. Solid Gd-carboxylate to arrive at Daya Bay by November 15, 2008 and immediately go into the underground LS Hall, where production will start.

In addition, milestone dates are being developed for the completion of the final design of the process systems and for placement of purchase orders for the system components.

There are other LS-related tasks that are ongoing or will be undertaken in the next several months. Many of these were discussed in the collaboration's internal review that was held at IHEP in mid October 2007:

1. Continue the QC monitoring program of long-term stability of the Gd-LS preparations, at BNL, IHEP, and HKU.
2. Use standardized tests to study the chemical compatibility of the LS with the materials that will be used to construct the detector vessel, e.g., acrylic.
3. Use standardized tests to study the chemical leaching into the LS, the mineral oil, and the ultra-pure water, from materials that are being considered for use in constructing the antineutrino detectors.
4. Explore methods to measure accurately, with high precision, the concentration ratios of C/H and Gd/H, and the concentrations of H and C in the Gd-LS.

4.4.6 Storage of Gd-LS, LS and Mineral Oil at Daya Bay

The current design of the Daya Bay antineutrino detector requires ~ 200 T of 0.1% Gd-loaded LS (consisting of ~ 1 T of solid Gd carboxylate, ~ 75 kg of PPO and a few kg of bis-MSB, all dissolved in 200 T of LAB) for the inner antineutrino target, ~ 200 T of unloaded LS (LAB + ~ 0.7 T of fluors) for the γ -catcher, and ~ 400 T of mineral oil for the buffer region, to be divided equally among the eight 'identical' detector modules. To ensure that the chemical components for all detector modules are as identical as possible, the total amounts of each of the organic liquids needed for each detector region will have to be accumulated on-site and stored separately before filling the detectors. The collaboration has designed a Liquid Scintillator Hall (LS hall) underground, close to the DYB near hall, for liquid scintillator mixing, storage, and filling. The procedures, precision requirements and engineering designs of liquid filling are discussed in Section 4.8. The advantages of underground storage are (1) no transportation is needed of the final products between surface to underground, which neatly solves the problem that storage space for such large volumes of liquids has not been included in the design of the Surface Assembly Building ; (2) easier control of the local environmental conditions, such as the temperature; and (3) the solvents can be transferred to the AD through pipes underground.

The LS hall is designed to be 30 m long and 12 m wide. The maximum height along the center line is 8.5 m and the minimum height on the side is 7 m. The layout of the LS hall is shown in Fig. 3.15. There are three storage pools in the LS hall to store three different kinds of liquids. Since the designs of the storage pools have not yet been finalized, further discussion is needed among the groups involved with LS, Integration, and Monitoring. The sizes of the storage pools are shown in table 4.14. The total liquid volume

	Length (m)	Width (m)	Height (m)	Volume (m^3)	Liquid Volume (m^3)
Gd-LS pool	10	5	5	250	217
LS pool	10	6	5	300	230
Oil pool	10	5	5	250	422

Table 4.14. Sizes of the storage pools. The oil pool is designed to contain only one half of the total mineral oil, which will have to be delivered in two batches.

is the volume for liquids needed for eight ADs, plus liquid for one spare AD and ~ 10 -T wastage. The Oil Pool is designed to contain only one half of the total mineral oil, which will have to be delivered in two

batches. All 400 T of LAB will be procured in one batch to ensure the chemical components for all detector modules are identical. They will be filled into the Gd-LS pool and the Oil Pool first. The LAB in the Gd-LS pool and partially in the Oil Pool will be used for LS mixing and be transferred to the LS pool step by step as the mixing occurs. The Gd-LS mixing will start after the LS mixing is complete. The LAB remaining in the Oil Pool will be pumped out for Gd-LS mixing and will be transferred to the LS pool. When Gd-LS and LS mixing is done, the emptied Oil pool will be cleaned and filled with mineral oil, ready for AD filling. When the oil in the pool is used up after filling four ADs, the other batch of oil will be procured and filled in. Since the mineral oil is used only as shielding in AD, the possible component variation batch by batch has no impact on detector identity.

The basic requirements to the storage pools are

- Compatibility with Gd-LS, LS, and Oil for the long term (see Section 4.8.5 for details);
- Air-tight and covered with nitrogen to prevent oxidation of the liquids;
- Being able to mix the liquid around to ensure homogeneity of the liquid in the pool;
- Monitoring such as air pressure, temperature, and oxygen, etc;
- Easy to clean.

To ensure the quality of the liquids after storing for one year, a reliable and cost efficient method to construct the storage pool is to line concrete pools with acrylic. The concrete pools will be a part of the civil construction. The floor of the pool is designed to have a 0.5% slope for draining the pool and making the cleaning easier. Several companies have been contacted for the acrylic lining. The detailed techniques are slightly different. Large acrylic sheets, e.g. 3 m × 2 m, will be fixed on the side wall and the floor with bolts. The bolts are covered with acrylic then, to avoid contact to the liquid. The sheets are glued together using polymerization. Fig. 4.37 shows the scheme of the lining on the side wall.

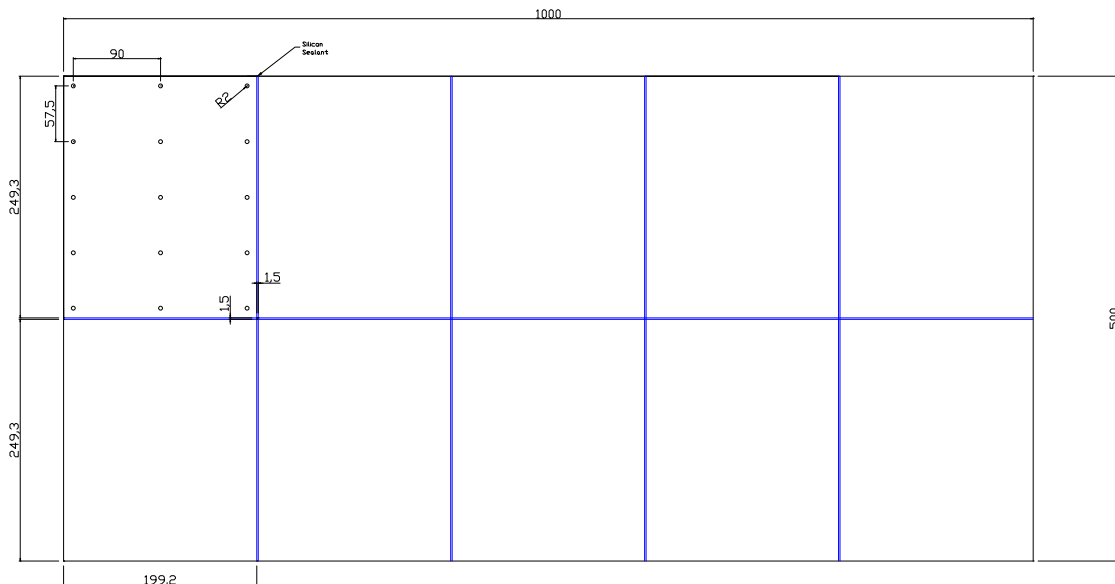


Fig. 4.37. Lining of acrylic on the side wall of the storage pool.

The pools will be sealed with acrylic lids to be air-tight. The design of the lid has not been finalized yet and it may depend on the selected company. The lid will be bonded to the acrylic wall by polymerization

or silicone sealant, or other glues. R&D is being carried on to study the possible contamination from the glue if sealing other than polymerization is used. An example of sealing using silicone sealant is shown in Fig. 4.38.

SCALE 1:10

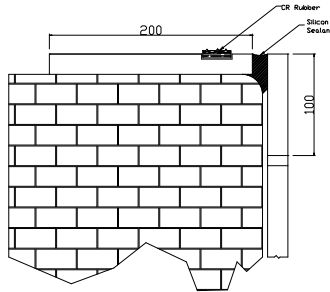


Fig. 4.38. One option to glue the acrylic lid of the storage pool to the wall using silicone sealant.

To make the stored 200-T liquid homogeneous in the pool, piping will be built to recycle the liquid, besides the need to fill in and pump out the liquids. Acrylic or Teflon pipe is required to have good compatibility with the liquids. The pumps will be made of Teflon or be Teflon coated. In case of leaks of liquids from pipes, valves or the storage pool, the floor of the LS hall will have a 0.5% slope. The leakage will flow into a collection well of $5\text{ m} \times 4\text{ m}$ and 5 m in depth, located at the corner of the hall.

4.5 PMT System

4.6 PMT System

The performance of the PMTs in the AD is of critical importance for the Daya Bay experiment since the antineutrino events are reconstructed from the signals provided by the PMT arrays. In the following, we first describe the various requirements for the PMT detector system in order to achieve the physics goals of the Daya Bay experiment. These requirements lead to various specifications for the selection of the PMTs and for the design of the PMT bases. The layout of the PMT system, together with the mechanical support structure and the HV/signal cable routing scheme, will then be presented.

4.6.1 PMT Requirements

The design of the PMT system is based on the various considerations listed below in the following sections.

4.6.1.1 Efficiency for detecting antineutrinos

Antineutrinos are identified from the detection of the prompt positron signal in coincidence with the delayed neutron capture signal. To optimize the sensitivity of the experiment, the PMTs should be capable of detecting the prompt signal at the lowest possible energy of 1 MeV (corresponding to a pair of 511 keV photons emitted from annihilation of positrons produced at rest) with a high efficiency. For a given geometric coverage of the PMT system, the highest efficiency is obtained by optimizing the quantum efficiency of the PMTs. To achieve a high quantum efficiency, the PMT cathodes must have a spectral sensitivity well matched to the spectrum of photons emitted by the liquid scintillator. Table 4.15 lists the requirement of PMT spectral response at various wavelengths. The quantum efficiency is defined as the ratio of the first dynode

current (after subtracting the dark current) over the incident flux of filtered light uniformly illuminating the active cathode area.

For the antineutrino prompt and delayed signals, a large fraction of the fired PMTs would only generate a single photo-electron (s.p.e.) signal. The PMTs should be operated at a reasonable HV to achieve a sufficiently high gain ($\sim 10^7$) in order to observe the s.p.e. signal efficiently. It is also important that the PMTs have good s.p.e. resolution (s.p.r.). As listed in Table 4.15, the peak-to-valley ratio for the s.p.e. charge spectrum should be greater than 2.5 at a gain of 10^7 .

The presence of the earth magnetic field in the direction transverse to the PMT axis would lower the quantum efficiency of the PMT. This consideration leads to the requirement listed in Table 4.15 that the variation of the anode efficiency of the PMT when operated in an external transverse magnetic field of 450 mG should not be worse than 15%.

4.6.1.2 Energy resolution

Good energy resolution for the prompt positron signals is essential for performing the spectral analysis for the neutrino oscillation. The energy resolution depends on the design of the AD, as well as the geometric coverage and the performance of the PMT system. The photo-electron statistics is a main factor for the overall energy resolution. Hence, all considerations related to the optimization of quantum efficiency discussed above also apply here. In addition, the variation of the quantum efficiency over the position where light hits the photocathode is required to be less than 15%. Moreover, as the measured energy is proportional to the total number of photo-electrons, the PMT anode pulse must have good linearity. As shown in Table 4.15, the deviation from linearity is required to be less than 5% over the dynamic range of 0-1 nC. A tapered voltage divider (type B) is required for optimal linearity.

Excessive pre-pulsing and after-pulsing rates, as well as high dark pulse rate, would deteriorate the overall energy resolution. The requirements on the dark pulse rate and on the probability of pre-pulsing and after-pulsing are also listed in Table 4.15.

While the gain of each PMT will be calibrated and monitored regularly, to obtain optimal energy resolution it is essential that the PMT gains remain relatively stable with time and with respect to temperature variation. The requirements on the PMT gain stability are listed in Table 4.15.

4.6.1.3 Timing response

The requirements on the rise and fall times, as well as the transit time spread (TTS), are listed in Table 4.15.

4.6.1.4 Radiopurity

Due to the close proximity of the PMTs to the liquid scintillator, it is of critical importance to minimize the radioactive impurities (^{40}K , ^{232}Th , and ^{238}U) contained in the PMTs. In particular, low radioactivity borosilicate glass is required. The radiopurity specified in Table 4.15 implies a singles rate of ~ 10 Hz.

4.6.1.5 Mechanical strength

The PMTs should have sufficient mechanical strength to withstand the acceleration invariably encountered during transportation, handling, and installation. As the PMTs will be immersed under mineral oil and/or water of several meters depth, the PMT glass envelop must survive an external static pressure of 300 kPa. The number of bubbles in the glass envelop should also be minimized.

4.6.1.6 Uniformity and long-term reliability

In order to ensure similar performance for all AD modules, it is required that the pertinent PMT characteristics (quantum efficiency, s.p.r., timing response, etc.) should have small variations among all PMTs.

Item	Requirement & Justification
Spectral Sensitivity	PMT Quantum Efficiency peak to be greater than: 25% at 420 nm, 8% at 300 nm, 12% at 320 nm, 1% at 600 nm
Gain	$\geq 10^7$ for all PMTs with appropriate tapered resistive base. PMTs must achieve a gain of 3×10^7 at HV ≤ 2 kV
Single Photoelectron Resolution	peak to valley ratio ≥ 2.5 at a gain of 10^7
Magnetic Field Sensitivity	spe response (gain, resolution, timing) should not change by more than 20% in the presence of transverse magnetic field of 450 mG. The anode efficiency should not change by more than 15%
Photocathode Uniformity	maximum quantum efficiency non-uniformity not to exceed 15%
Pulse Linearity	PMT anode pulse linearity must be better than 5% over the dynamic range of 0–1 nC at a gain of 10^7
Dark Pulse Rate	≤ 25 Hz/cm ² at 20° C. fractional increase in dark count rate in going from a gain of 1.0×10^7 to a gain of 3.0×10^7 shall not be more than 30% greater than the increase in dark pulse rate in going from a gain of 0.3×10^7 to a gain of 1.0×10^7
Pre- and After- Pulsing	probability for the PMT anode signal pre-pulsing and afterpulsing not to exceed 1.5%. PMT anode signal not to exhibit after-pulsing with probability of more than 1.5% for photoelectron within 100 ns interval of the defined after-pulse interval (0.1–40 μs)
Gain Stability	less than 5% drift per week and less than 10% drift over a period of one year. Temperature dependence must be less than 1% per °C
Rise and Fall Times	rise time not to exceed 6.5 ns and a fall time not to exceed 10 ns for a single photoelectron pulse
Transit Time Spread (TTS) (FWHM)	not to exceed ~ 3 ns at a gain of 10^7 for a spe
Radioactivity	use borosilicate glass with radioactivity in each PMT not to exceed: ^{40}K : 2.7 Bq, ^{232}Th : 0.5 Bq, ^{238}U : 0.7 Bq
Mechanical Strength	must withstand a sinusoidal vibration of 1.34 mm amplitude at 15 Hz (equivalent to an acceleration of 2 G) for 30 seconds with less than 10% change in gain or timing responses. all PMTs must survive a pressure of 300 kPa

Table 4.15. Requirements on the PMTs.

Failed PMTs would also lead to differences between different ADs, and the failure rate is required to be less than 2% in 5 years of operation.

4.6.2 PMT Acquisition

There are currently three 8" Photomultiplier candidates being considered for the Daya Bay. These are Electron Tube 9354KB, Hamamatsu R5912 and Photonis XP1806. A PMT specifications document was generated based on the requirements of the experiment. The document was reviewed by the collaboration and was finalized in late September 2007. A Request For Proposals (RFP) was initiated in late October 2007. The deadline for the proposals was November 26, 2007. The proposals received from the vendors will be evaluated by a committee appointed by the collaboration based on several criteria including, but not limited to, adherence to the specifications and lowest cost.

We expect to complete the PMT selection by January 2008. Following the CD-2 review the selected vendor will be contracted to provide the photomultipliers based on supplied schedule. The selected vendor must supply the collaboration with a 1 kg sample of the low radioactivity crushed glass used in the fabrication of the PMTs. The sample will be tested and verified by LBNL and if it meets the radioactivity specifications the vendor will be cleared to proceed with the fabrication of the PMTs. If more than one batch of glass is used in the PMT production process a sample of each glass must be provided in advance for testing and verification.

We expect the first 200 PMTs to be delivered within three months of the placement of the order. The PMTs will be shipped directly to the Dongguan University in Guangdong province where the PMT fabrication and testing facilities will be located.

4.6.3 PMT Burn-in

The primary reason for the burn-in and testing process is to ensure compliance of the PMT characteristics with the requirements of the experiment, and to identify the PMT and bases which will fail due to 'infant mortality'. Therefore upon delivery each PMT will have to undergo a rigorous process of inspection, burn-in and testing. In what follows we give details of the processes which will be implemented to achieve the above mentioned goals.

Upon delivery to Dongguan University, all PMTs will be unpacked and labeled with barcodes, and will be physically inspected for any visible damage, excessive bubbles on the glass bulb or nonuniformity of glass. The serial numbers for damaged PMTs will be recorded along with photographs of the PMTs and a description of the damage. The damaged PMTs will be repacked and returned to the manufacturer for replacements.

The PMTs which pass the initial inspection will be photographed and weighed. The mass of the PMTs measured by weighing them along with impurity measurements performed on the fabrication samples of the glass will be used to estimate the amount of radioimpurities present in each PMT. The serial numbers and other manufacturer supplied information for each PMTs will be entered into a QC data base.

The PMT bases shipped from US will be installed on the photomultipliers tubes. The serial number of each base and PMT will be entered into a QC data base as a partially assembled unit. The photomultiplier and base assemblies used in the AD do not have potted shells. These PMT assemblies will be installed into the burn-in setups. Each burn-in box accommodates 8 PMTs. The PMT cables will be attached internally to the panel connectors which will allow them to receive HV from the external power supplies and transmit their pulses to the external electronics. Each PMT station inside the burn-in box will be equipped with a blue LED pulser which is set to pulse at a rate of 10 kHz with an intensity equivalent to 50 photoelectrons. Once the PMTs are installed and the burn-in box cover is closed and locked the external HV will be turned on and set to HV values provided by the manufacturer which establishes a gain of 10^7 . The PMTs will be operated at this gain for a period of 3–5 days. The main purpose of the burn-in process is to identify the early mortality cases in PMT assemblies, and to a lesser extent to stabilize the PMT behavior.

The outputs of the PMTs will be monitored on a daily basis with a digital sampling oscilloscope and associated waveforms will be captured and saved into the QC database for each PMT+base assembly. Any failed assemblies will be removed from the burn-in setup and undergo detailed testing to identify the cause of the failure. The failed PMTs will be disconnected from the associated bases and will be shipped back to the manufacturer. All acquired information about the failure will be recorded in the QC data base for each failed PMT. The failure of an assembly is defined as an excessive change in gain, excessive increase in the dark count rate or high quiescent current on the associated HV channel.

In the case a PMT base is identified as the source of the problem it will be removed from the assembly, its serial number and associated failure mode will be noted in the QC data base and will be replaced with a spare base. The failed unit will be set aside for further diagnostics to identify the failure mode.

The PMT assemblies which have passed the burn-in process will be stored in a dark room until they are further tested.

4.6.4 PMT Testing

The photomultiplier assemblies that pass the burn-in process will be tested and characterized in the PMT test setup. The purpose of this testing program is to insure that certain performance characteristics of each PMT such as relative quantum efficiency, linearity, gain, timing resolution, pre- and after- pulsing and dark noise rate adhere to the requirements of the experiment. Measurements of these parameters require fast and relatively stable optical pulse trains in wavelengths of interest.

Figure 4.39 shows the block diagram of the PMT test setup. It consists of an optical block, the dark

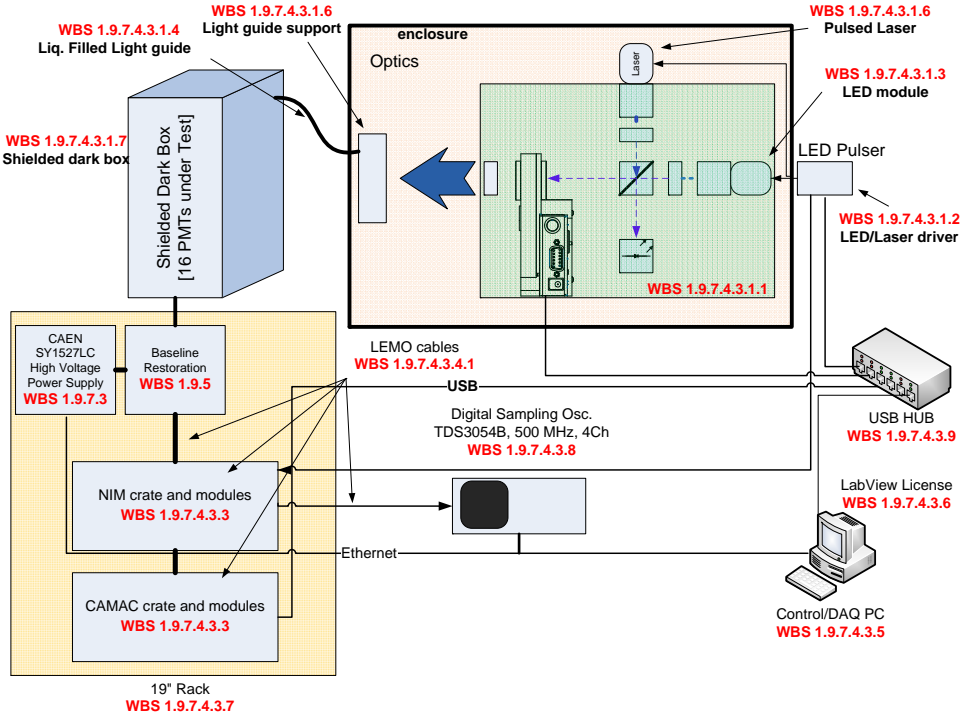


Fig. 4.39. Block diagram of the PMT test system.

box, the HV system, a NIM-CAMAC based DAQ and PC. The optical system consists of two optical pulsed sources. A pulsed blue LED system provides fast optical pulses which are filtered with a 420 ± 10 nm optical bandpass filter. This assembly along with the pulse generator labeled as pulser generates a sequence of

pulses using two banks of 10 LEDs, labeled A and B. Bank A is set to an intensity equivalent to $\frac{1}{5}$ of bank B. Banks A and B are pulsed in the sequence A, B and A+B. The amplitude and frequency of the electrical pulses driving the LEDs are fixed and will not be changed. This allows the outputs of the LEDs to stabilize since the temperature of the p-n junctions generating these pulses will be stable. The LED output beam will be split into two paths. A photodiode, shown at the bottom of the optical system block will monitor the LED output and will be used to compensate for the long term variations due to aging and drift. The second LED beam will be transmitted through a 12 station discrete neutral density filter wheel. The wheel will be controlled by the computer to attenuate the optical radiation by up to a factor of 10^5 . This will be the primary method of varying the optical pulses. A Lambertian diffuser is used to scatter the pulsed optical light and uniformly illuminate 16 liquid filled optical light guides. These six foot long light guides will transmit the light to the PMTs located in the PMT test setup dark box.

This setup will test up to 15 PMT at a time. In addition to the 15 PMTs tested there will be a ‘reference PMT’ in the PMT test setup. The reference PMT is a unit which has been extensively tested and characterized by the collaboration. Its characteristics have been measured and it would be used to compare with the characteristics of the PMTs under test with. In particular the relative anode and photocathode efficiencies of all PMTs will be measured with respect to the reference PMT.

Figure ?? shows the details of the PMT test setup DAQ for one PMT channel. The PMT pulses enter the

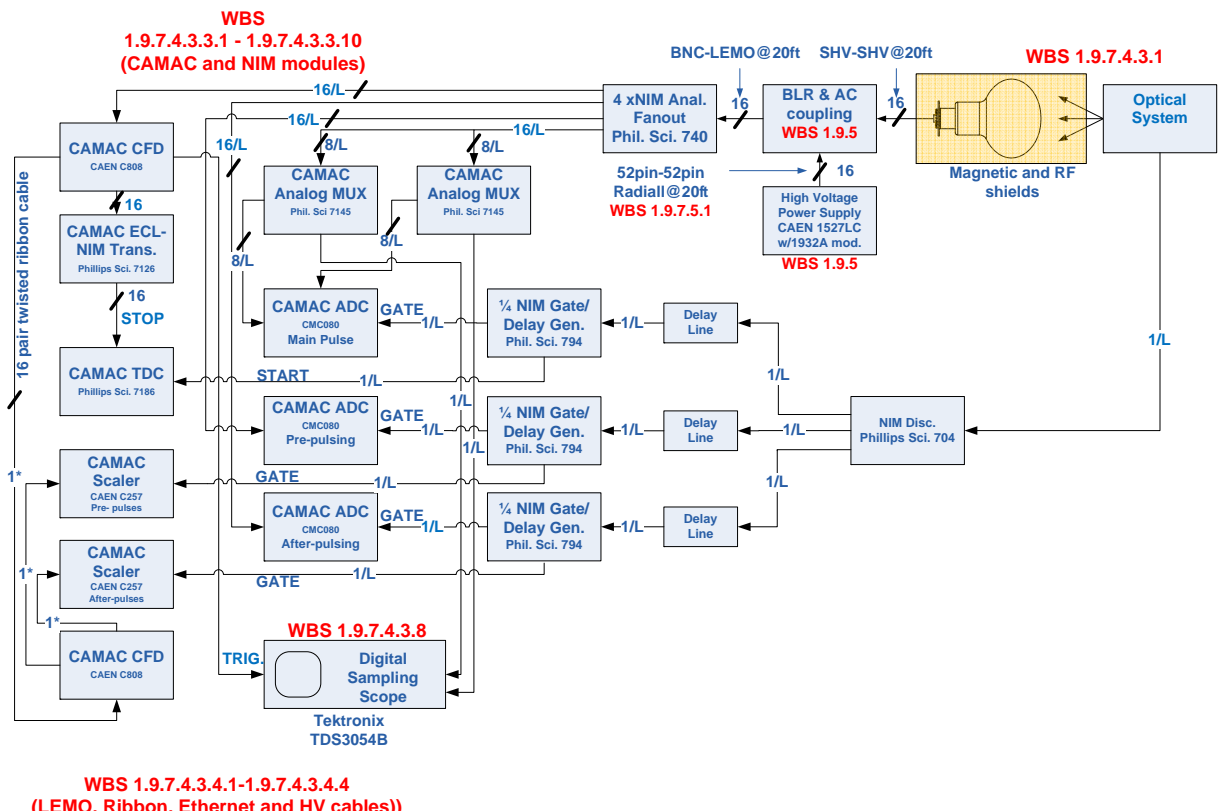


Fig. 4.40. Block diagram of the PMT test DAQ system.

BaseLine Restoration (BLR) unit where the signals are decoupled from the high voltage, and the baseline distortion due to AC coupling is removed. The BLR outputs are fed into NIM analog fanout units and are fed into three separate ADC units as well as a Constant Fraction Discriminator. The ADCs are gated from three gate generators whose output phases are such that they sample the PMT signals during periods defined as pre- after- as well as during the main pulse. In addition the CFD outputs are scaled and also are used to generate STOP pulses to the TDCs. The TDCs are used to measure the PMT output jitter and timing resolution.

A digital sampling oscilloscope is also used to measure rise time, fall time, width and pulse shapes of each PMT at 50 as well as single photoelectron levels.

The dark box used in the PMT test system has 16 testing locations. As mentioned earlier one station will be permanently occupied by the reference PMT. Each station will be optically isolated from the neighboring stations and will be magnetically shielded. The interior surface of the box will be covered with a copper mesh which will be electrically connected to each mu-metal shield on the PMT stations.

The pulsed LED system will allow measurements of the gain vs. HV, relative Quantum Efficiency of each PMT with respect to the reference PMT, linearity of each PMT and pre- and after- pulsing ratios. While the laser pulser system will be used to measure the transit time jitter, the rise time, the fall time and the pulse shape of each PMT. With different LED wavelengths we could also study the relative QE response at shorter wavelengths such as 320 nm.

4.6.5 PMT Base

The AD photomultiplier assemblies will be immersed and operate in the mineral oil for a long period of time. Furthermore to reduce the cable volume in the AD a single coaxial cable will supply the high voltage to the PMTs as well as transmit the PMT signals to the front end electronics. To ensure the integrity of the photocathode and the surrounding PMT bulb we have selected to operate these with positive high voltage, which forces the photocathodes to be set at ground potential. The AC decoupling is performed outside the AD.

The AD response to antineutrinos is typically 1–50 p.e. with an expected maximum around 500 p.e.; however, a cosmic ray muon could deposit a signal as large as 2000 p.e. Therefore it is required to have good linearity for the range 1–500 p.e. and large enough dynamic range to allow the PMT base to rapidly recover from a 2000 p.e. optical pulse. In addition it is important to maintain a high photoelectron collection efficiency over the ensemble of all PMTs operating at a gain of 10^7 . To achieve this goal the PMT base design requires a tapered voltage division ratio augmented by a high and fixed potential difference between the photocathode and the first dynode. Figure 4.41 shows a sample design for the Hamamatsu R5912 8" photomultiplier tube. As shown in this figure, up to six 150 V zener diodes are used to establish a constant potential of up to 900 V between the photocathode and the first dynode stages. Using a three zener diode stage a gain of 10^7 was achieved at 1350 V using a sample R5912. Several other bases have been designed which accommodate the ET 9354KB and recycled MACRO ETL and Hamamatsu R1408 PMTs. Figure 4.42 shows the details of the printed circuit board design based on schematics shown in Fig. 4.41 for the Hamamatsu R5912.

Figure 4.43 shows a photograph of the completely assembled base installed on a R5912. Note that the PMT base along with the mirrored face of the PMT bulb will be coated with black epoxy. This will not only protect the PMT base components from damage and the mineral oil from contamination, it will also minimize the reflection of photons from the back of the base which could give rise to long tails to the signals.

4.6.6 PMT High Voltage System

Figure 4.44 shows various components of the AD PMT system. The High voltage system shown in this figure is based on CAEN SY1527LC mainframe equipped with 1934A modules. Each mainframe could house up to eight 1934A 48-channel high voltage distribution modules. These modules supply positive

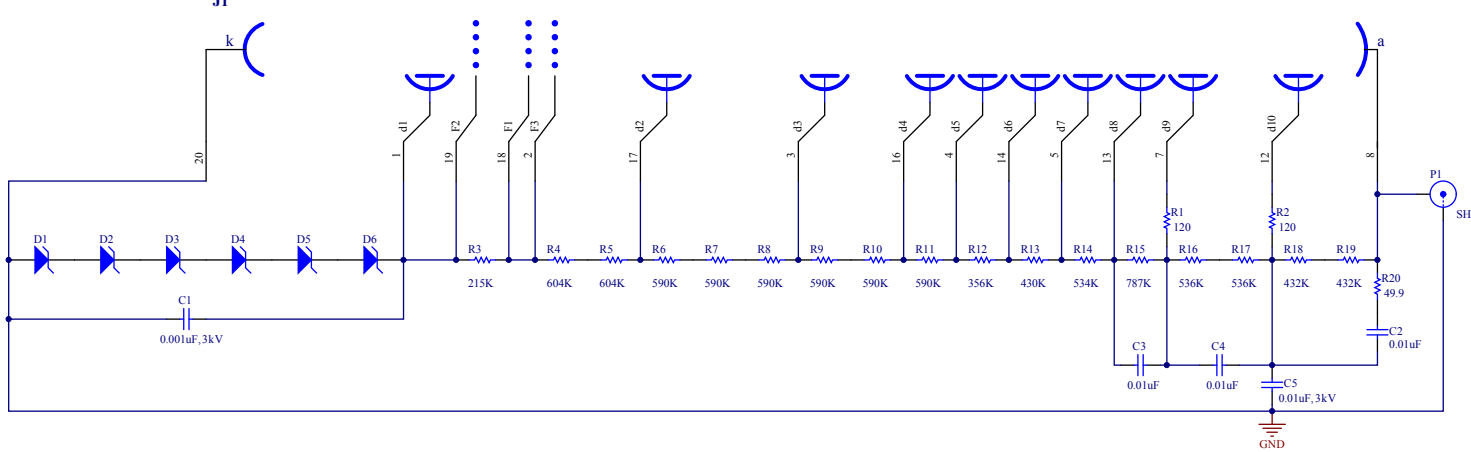


Fig. 4.41. Schematics of the tapered voltage divider used for Hamamatsu R5912 PMT.

high voltage up to 3 kV at a maximum current of 0.5 mA per channel. The outputs are all floating and have a common ground. Each module has a single high voltage generation unit which could be set to any

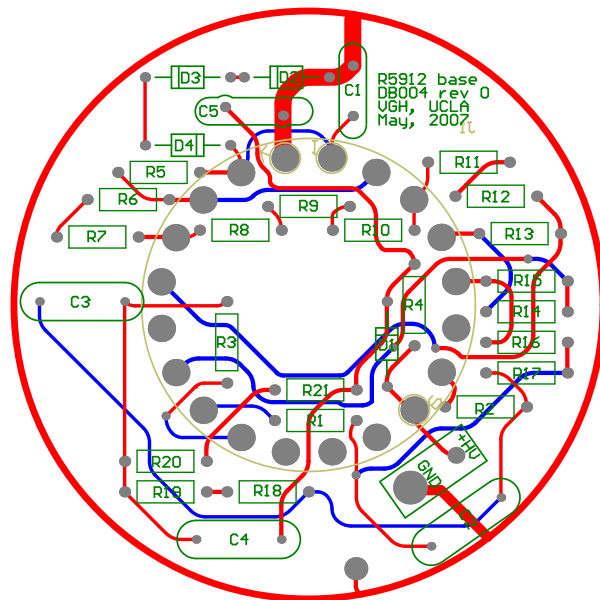
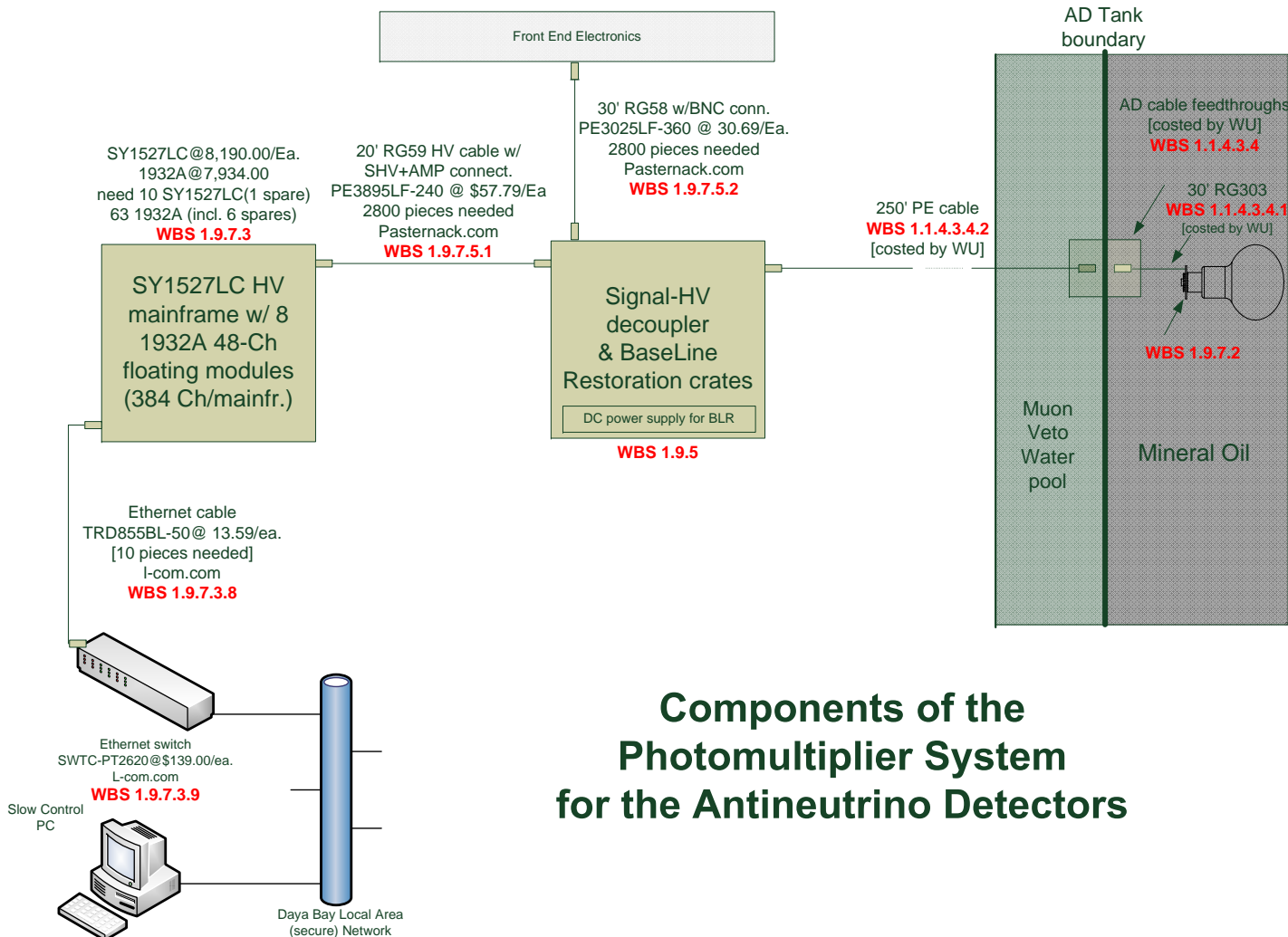


Fig. 4.42. A view of the two layer PC board base for the Hamamatsu R5912 PMT.



Fig. 4.43. Photograph of the PMT base assembled on the Hamamatsu R5912 PMT.

voltage; however, the 48 outputs could be set to a maximum potential difference of 900 V with respect to the generator. These units were selected for their high density, low channel cost and the fact that LabView



Components of the Photomultiplier System for the Antineutrino Detectors

based slow control software already exists for these mainframes and is readily available from IHEP. The slow control system PC will communicate with the high voltage system via Ethernet. Each channel will be

Fig. 4.44. A block diagram view of the AD PMT system showing different components of the system.

individually controlled and its output current and voltage will be monitored and archived in the slow control database. Additionally a hardware limit will be set on the output voltage and currents to limit these quantities in case of error or component failure in the base.

4.6.7 PMT Signal and HV Coupling

Figure 4.45 shows an oscilloscope trace of a sampled PMT pulse which is coupled using a simple AC coupling scheme with a 10 nF capacitor and 50 Ω termination at the scope input. It can be seen that the pulse

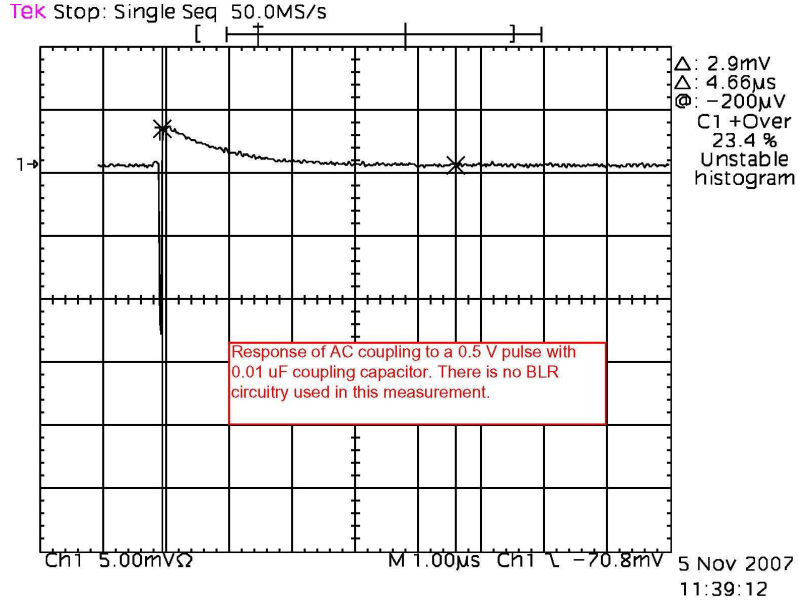


Fig. 4.45. Oscilloscope trace of a large PMT pulse AC coupled via a 10 nF capacitor to the DC coupled 50 Ω terminated Oscilloscope.

is differentiated due to the AC coupling and has a 25% overshoot. More importantly the overshoot distorts the baseline after the main pulse for a period of 4.66 μs. This long period introduces an unacceptable dead time.

While traditionally CR-RC shaping schemes have been used to address this kind of problems, due to the fact that the AC decoupling of signal occurs a long distance away from the PMT at the end of a 50 Ω transmission line which is at high positive potential and which must be terminated in order to prevent reflections, one needs to use alternative approaches. One such technique is the active baseline restoration. The schematic of an active baseline restoration circuit [17] is shown in Figure 4.46. A three channel printed circuit board was designed based on the circuit of Figure 4.46. Figure 4.47 is a photograph of the three channel printed circuit board designed to test functionality, characteristics and cross talk of the circuit. In this photograph only one channel was populated for the initial testing. The neighboring channel is shown to have an RF shield. All channels once assembled will be instrumented with such shield to minimize cross-talk and distortions due to noise. The BLR circuit utilizes a 1.8 GHz bandwidth operational amplifiers (Op-amps) with fast Schottky biased diodes to eliminate the positive overshoot due to the AC coupling. In addition both the input and the output stages of the circuit are terminated in 50 Ω which minimizes the reflection in the transmission lines. It is important to note that the BLR circuit utilizes the Op-Amp in the inverting mode; therefore a second inverting stage is added to the output of the BLR to restore the phase of the pulse. Figure 4.48 shows the small signal response of the BLR circuit to a fast pulse from a pulser. The pink trace represents the input pulse which is delayed and inverted while the black trace is the direct output

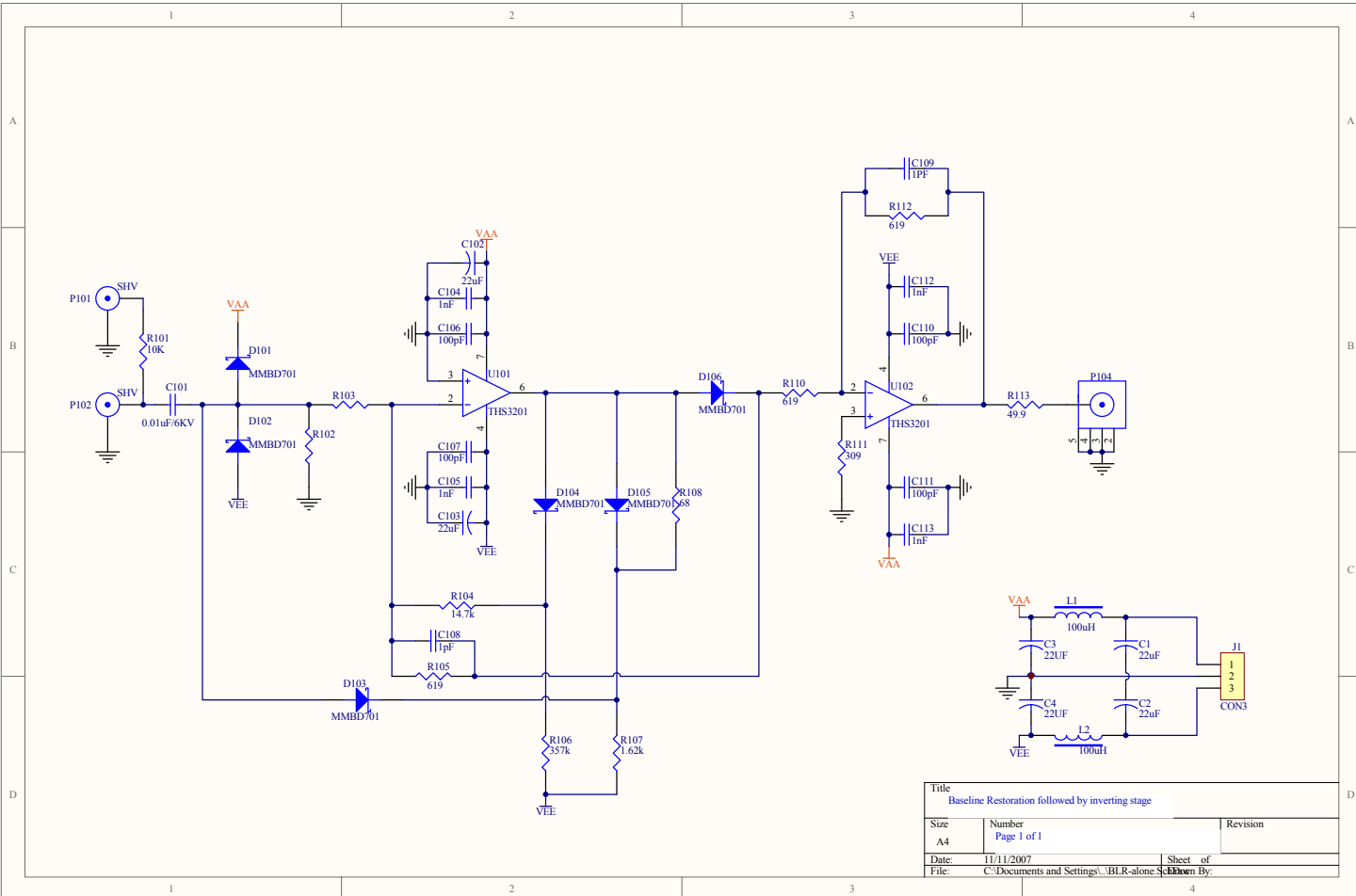


Fig. 4.46. Schematic diagram of the three channel BLR circuit.

of the BLR stage only. The distortions on the pink trace are due to the grounding scheme used for the scope probe.

Figure 4.49 shows the effect of the BLR on the PMT signal baseline on a long time scale. The PMT

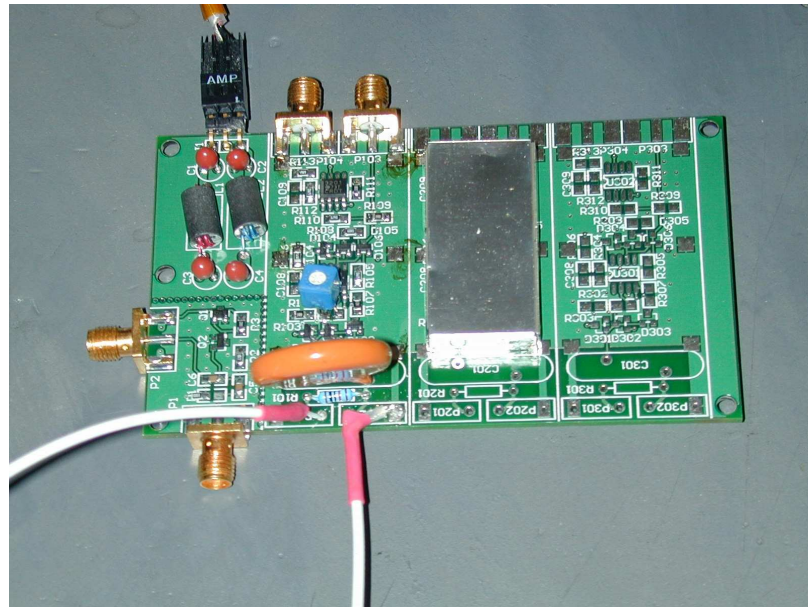


Fig. 4.47. Photograph of the three channel printed circuit board designed for testing the functionality and performance of the BLR circuit.

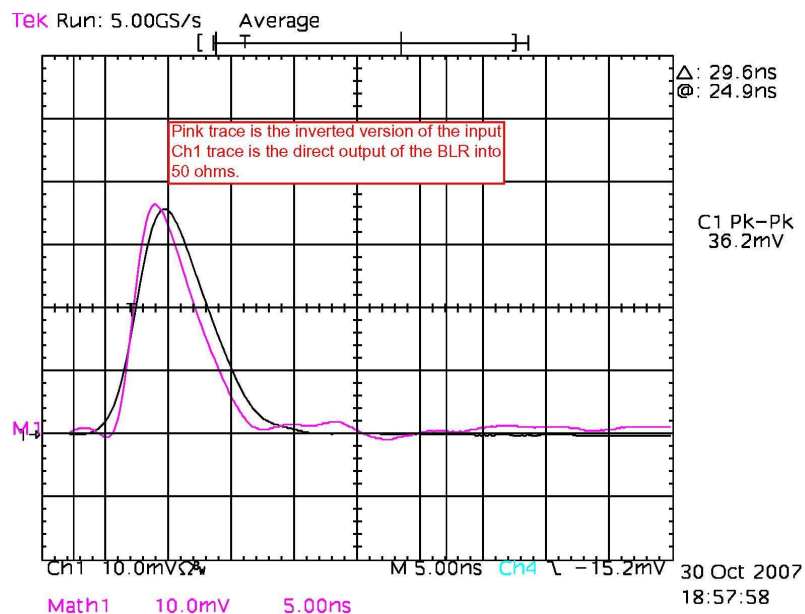


Fig. 4.48. The response of the BLR to small signals.

pulse was generated using a LED. The trigger position is centered in the middle of the scope display and the sweep timebase is set to $1 \mu\text{s}/\text{cm}$. No significant baseline distortion can be detected on the 2 mV vertical scale.

Further tests are planned to test the cross talk and linearity of the BLR circuit. Further optimization would be required to minimize the output offset; however, this is not a critical parameter of the design. The

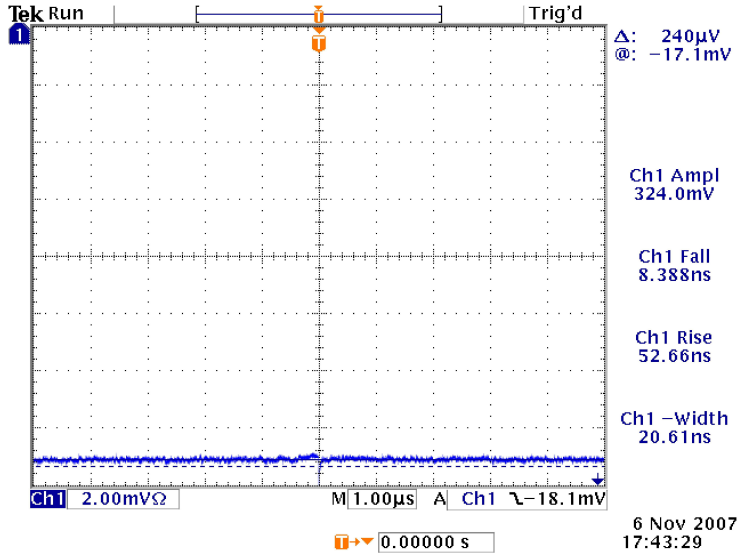


Fig. 4.49. The baseline restoration of the BLR circuit on long time scales.

circuit, when finalized, will be packaged into a high density VME crate.

4.6.8 PMT Support Structure

The PMTs are held in individual mounts and secured in the antineutrino detector using a PMT support structure. In this section we describe the design considerations for the PMT mounts and the support structure. To simplify the design process and make the production of the PMT mounts more economical we plan to use the same (or similar) PMT mounts both in the antineutrino detector and the muon system.

Past experiments such as KamLAND and MiniBooNE have mounted PMTs in individual frames that are directly attached to the wall of the detector tank. This approach is economical and uses the least amount of materials but requires labor-intensive mounting of the PMTs on the walls of the detector tank. This can be complicated especially in a small tank of the size we are considering for the Daya Bay detectors. Also, to simplify the assembly of the antineutrino detectors at Daya Bay we plan to pre-mount all PMTs on a support structure which can then be installed as a module in the detector tank, as shown in Fig. 4.50.

The individual PMTs are mounted to the support structures via the mount structures shown in Fig. 4.51. The PMT cabling will be integrated into the support structure and brought out of the antineutrino detector through penetrations in the wall of the outer steel cylinder of the detector. After passing a quality-assurance procedure, eight sections with 24 pre-mounted PMTs are lowered into the stainless steel vessel through vertical guides attached to the vessel. In addition to simplifying the installation process, a modular support structure allows the easy replacement of any bad PMTs before the detector is sealed. This structure is made of suitable strong, radioactively pure, and non-magnetic material. Figure 4.52 illustrates this concept. A more detailed view is shown in Fig. 4.53.

The PMTs are mounted on the curved frame of the ladder-like structure before it is installed inside the stainless steel tank. There are eight such support structures for each antineutrino detector (see Fig. 4.52). Each structure holds a total of 24 PMTs. Together they form the circular PMT arrangement. The PMTs are mounted radially on the inner rim of the circular support structure. The PMT support structure holds 24 PMTs in 8 rows equally spaced around the circumference of the structure, or a total of 192 PMTs. A detailed model of the PMT arrangement on the support structure and of the PMTs mounts is shown in Fig. 4.53.

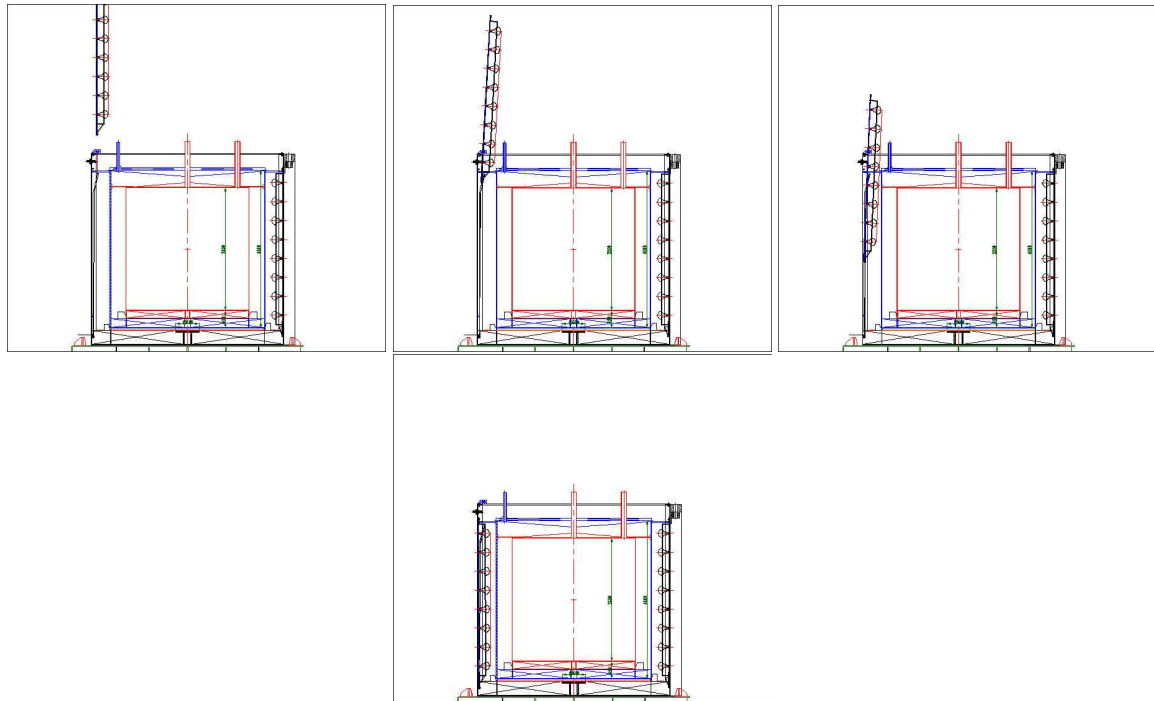


Fig. 4.50. Installation sequence of the PMT support structure. All the PMTs are pre-mounted on the support structure.

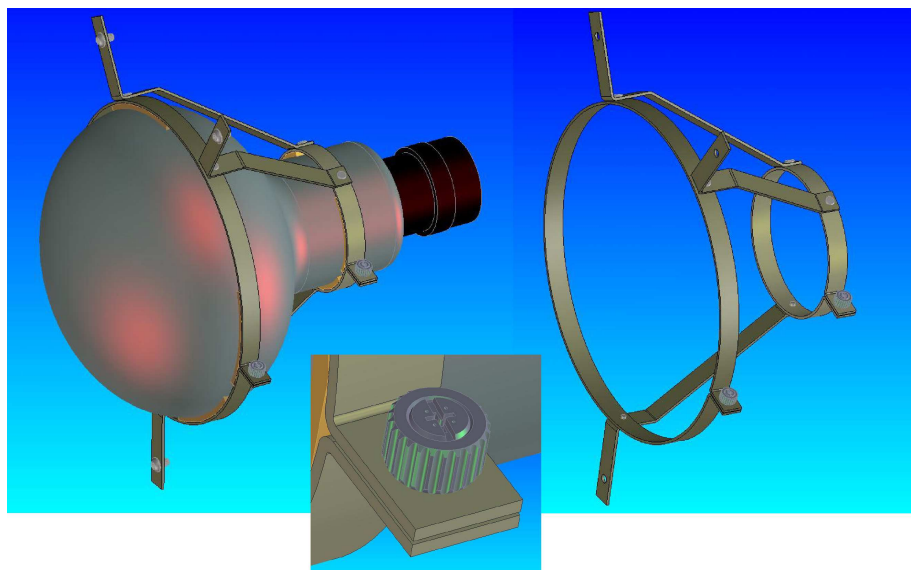


Fig. 4.51. Engineering model of the PMT mounts. The entire mount is fabricated out of strips of stainless steel. The circumference of this holder is adjusted with a screw.

The mounts features include:

- the PMT is held in place with an adjustable collar wrapped around the equator of the glass bulb

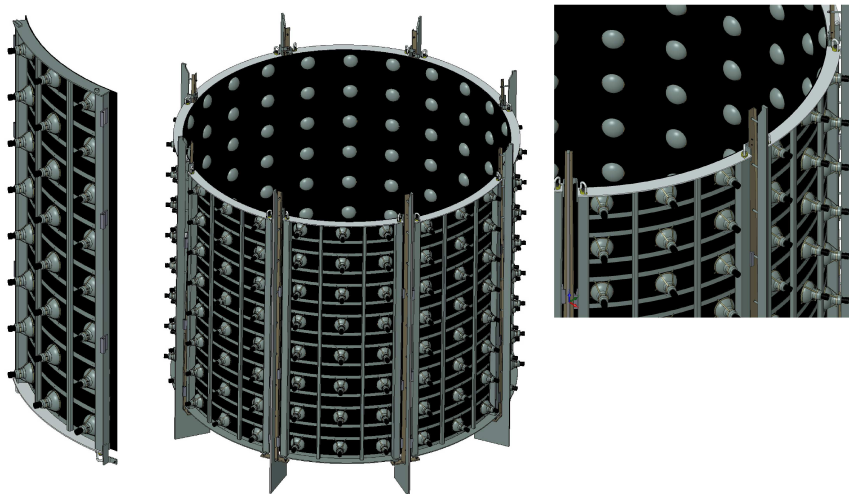


Fig. 4.52. Engineering model of the PMT support structure. The support structure is made of eight angular sections. Each section carries 24 PMTs in equal circular spacing. Together they form a complete ring. The sections can be vertically lowered into the antineutrino detector and secured. The PMTs are held by the mounts shown in the above figure on a ladder.

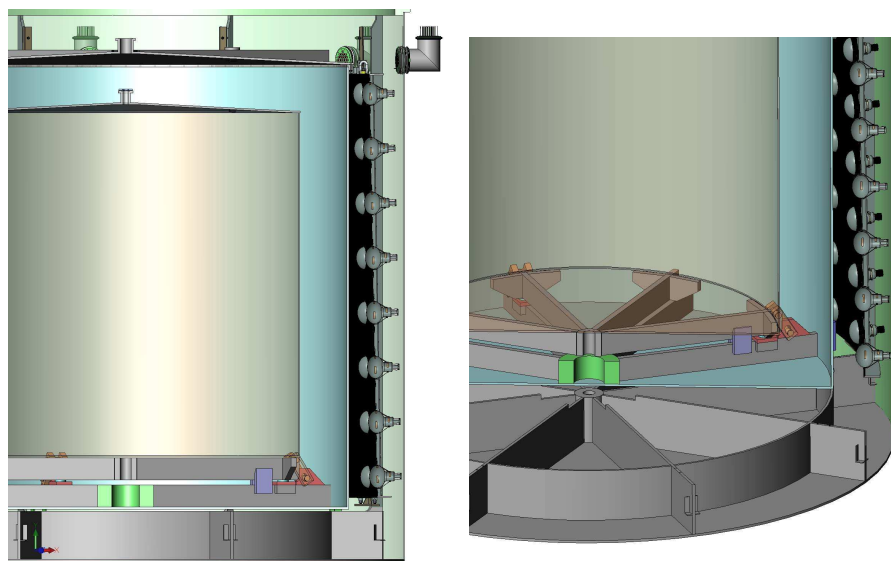


Fig. 4.53. Cross-sectional view and detail of the PMT ladder structure inside the antineutrino detector. The PMTs are arranged radially looking inward towards the center of the detector. A dry box on the outside of the detector wall in form of a right-angle tube is used to make the connection between the cables inside the AD and outside.

- the mount will be attached directly to the structure of the support ladder
- the PMT is facing radially inward, perpendicular to the wall of the detector tank

The current plan is to use a slightly modified version of the AD PMT mount for the muon system PMTs. The mounts will be identical in the interface with the tubes, but the connection to the support structure will be adjusted to accommodate the muon system support frames. The PMT mounts for the muon system must also allow for variations in the PMT geometry as both new PMTs and recycled Macro PMTs will be used.

4.6.9 PMT Cable Penetrations and Cable Routing

Cable penetrations in the wall of the ADs (see Fig. 4.54) and in the cover of the muon pool are needed to

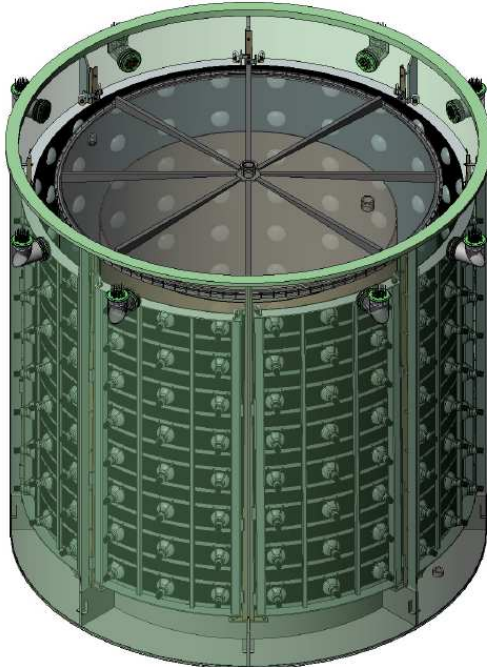


Fig. 4.54. Transparent antineutrino detector model with view of the PMT support ladders and the dryboxes that are used to make the cable connections between the inside of the antineutrino detector and the outside. The dry boxes are arranged symmetrically around the detector to line up with the PMT ladders and to minimize the cable lengths between the PMT ladders and their respective dry box.

connect the PMTs inside the ADs with the front-end electronics and the high-voltage system in the control room. The AD PMT cables have to be routed inside the AD from the PMT base to the AD PMT cable penetrations (see Fig. 4.55) and outside the AD between the ADs and the penetrations in the muon water pool cover. To make the connection between the PMT base and the high-voltage and front-end electronics in the electronics room requires a coaxial cable capable of submersion in ultra-pure water in the muon water pool, which penetrates the AD tank, continues on a path through mineral oil, and connects to the bases attached to the AD PMTs. (The assembly process of the AD tank penetrations is shown in Fig. 4.56.) The PMT cable penetrations and the cable routing are part of the AD PMT mechanics. The electrical PMT cables are discussed as part of the PMT section.

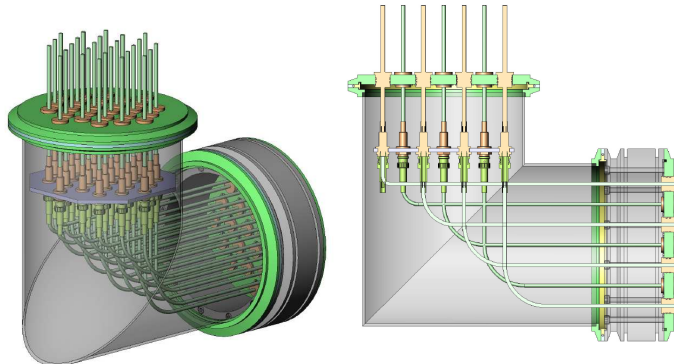


Fig. 4.55. Engineering model of the dry boxes for the PMT cable feedthroughs on the antineutrino detector. They are made of commercial stainless steel elbows with vacuum flanges and a patch panel inside.

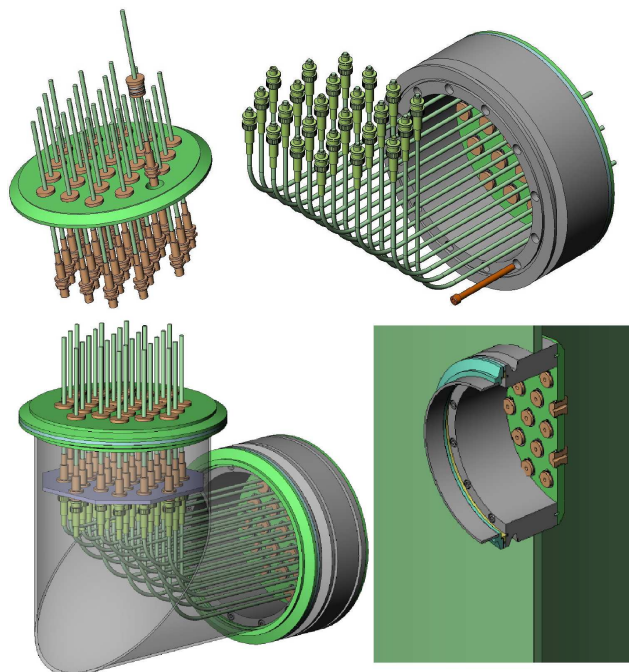


Fig. 4.56. Engineering and assembly model of the dry boxes for the PMT cable feedthroughs. Upper left: Patch panel and flange with cables from outside AD. Upper right: Flange on AD tank wall with cable ends from inside the AD. Lower left: Complete assembly of dry box. Lower right: flange in AD tank wall with seal plugs.

Different PMT cables are chosen to satisfy the different mechanical requirements in the different regions of the cable path. The mechanical requirements for the PMT cables, cable penetrations, and cable routing can be summarized as follows:

- PMT cable penetrations in AD wall
 - must withstand ultrapure water for more than 5 years on the outside

- must withstand mineral oil on the inside for more than 5 years
- must be reliable, serviceable, leak tight for 5 years
- must prevent contamination of the mineral oil by the proper selection of materials and design of the feedthrough penetrations
- must allow us to disconnect cables on the outside of the AD for lifting and transport
- must in principle allow us to replace a PMT cable if it is bad or requires service
- PMT cables and cable trays outside AD in muon water pool
 - must withstand ultrapure water for more than 5 years
 - minimizes the light obstruction in the muon water pool
 - can be disconnected for the lifting and transport of the ADs
 - does not interfere with the functionality of the muon water pool
- PMT cable penetrations in muon pool cover
 - must be leaktight against light for more than 5 years. Penetration can be made in cover gas volume above level of ultrapure water.

4.6.9.1 PMT Cable Penetrations in AD Wall

For the PMT cable penetrations in the AD wall we have chosen a dry-box concept with two elements:

- Each PMT coax cables has an integral seal with the dry-box flange.
- A mechanical dry-box and flanges allow all cable connections to be made in dry air. The PMT cable connectors are not exposed to either mineral oil or ultrapure water.

The connection between the PMT base and the feedthrough in the wall of the AD is made with a cable that is compatible with mineral oil. Ideally, a Teflon coated cable is used such as RG303. Each RG303 cable inside the AD is prepared with an integral seal plug. The seal plug utilizes a bonding technology and makes a leak tight connection to the cable. We found that for Teflon cables a special seal plug is required that provides a full-wire bond. Part of the Teflon cable jacket is removed so that the seal plug can be bonded to the inner layers of the cable (see Fig. 4.60).

For non-Teflon cables the bonding of the seal plug is much easier (see Fig. 4.57). A mechanical seal version is also available as shown in Fig. ???. The seal plug is commercially available from Douglas Electric and other companies. On the other side the seal plug makes an O-ring tight seal with the flange to the dry box. For each PMT ladder there is a dry-box with corresponding flanges. The inner flange to the dry box is attached to the PMT cables in the SAB and travels with the PMT ladder. The seal plugs can be sealed and tested inside the SAB prior to the installation of the PMT ladder in the AD. When the PMT ladders are installed in the AD, the flange with the cable bundle bolts on the flange in the AD wall. The fasteners are inserted from outside the AD so that they don't fall into the AD or damage the PMTs.

Inside the dry-box a connection is made between the cables coming from the inside of the ADs and the cable coming from the outside of the AD. An access flange allows us to make this connection from outside the AD during assembly in the SAB. The access flange is a round, standard O-ring flange. For the connection between the cable inside and outside the AD we plan to use Huber+Suhner SHV 50- Ω connectors. The bulkhead connectors are held in a mounting plate inside the dry box. Each dry box has two gas ports for leak checking the dry box

The PMT cables connecting to the AD from the outside are again prepared with seal plugs from Douglas Electric. These seal plugs fit into the flange that connects to the top of the dry box. For the cables outside the AD RG58 or a similar cable which is compatible with ultrapure water can be used.

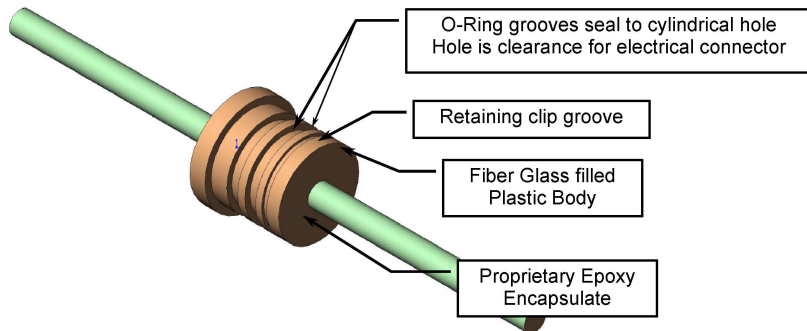


Fig. 4.57. Engineering model of a bonded seal plug for each AD PMT cable. O-rings provide the seal between the seal plug and the flange to the dry box. Both the PMT cables inside and outside the AD are prepared with the seal plugs. This design is the baseline method.

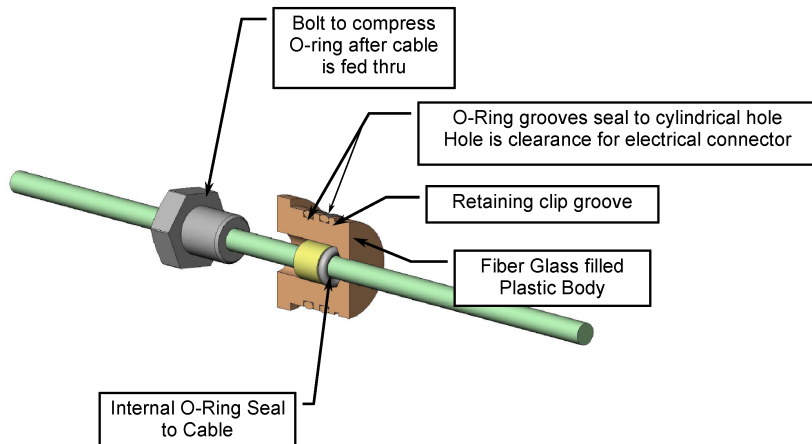


Fig. 4.58. Engineering model of a mechanical seal plug for each AD PMT cable. In this case the seal plug is not bonded to the cable jacket. Instead an O-ring compression seal provides the seal to the cable jacket.

Figure 4.58 shows the model of a Douglas Electric seal plug. It is bonded to the cable and has O-ring grooves. The epoxy encapsulate is a proprietary technique. Figure 4.59 shows the seal plugs inside and outside the AD.

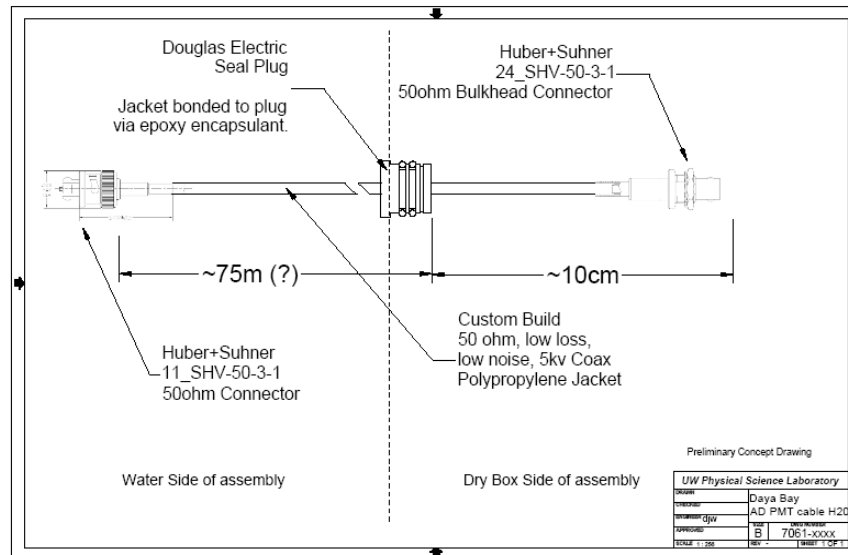
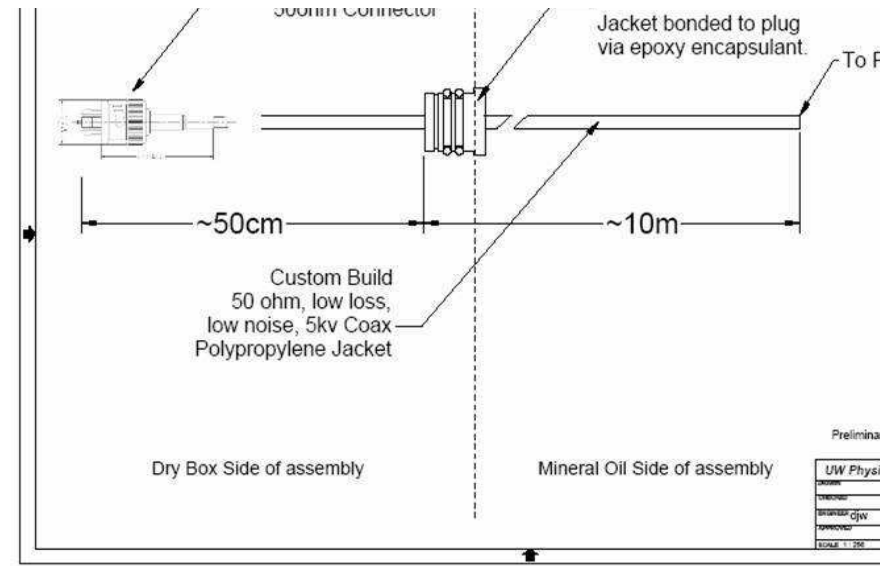


Fig. 4.59. Drawing of the seal plugs on the PMT cables inside and outside the AD. The inside cables go through mineral oil while the outside cables go through ultrapure water.

The dry boxes for the AD PMT cable feedthrough flanges are positioned around the top rim of the AD as shown in Fig. ??.

There is one dry box for each PMT ladder. The width of the AD with the dry boxes as shown here is 5.1 m. The position of the dry boxes can be shifted somewhat if needed. This will require close coordination

with the design of the steel tank and its support and lifting structure. With eight dry boxes we have one dry box per PMT ladder. This simplifies the assembly, testing, and installation procedure inside the SAB.

The seals on the PMT cables and the dry boxes can be leak tested prior and during the assembly of the ADs. For the leak tests halogenated compounds can be used to avoid danger to the PMTs from He. Refrigerant 507 is environmentally safe and can be used in both the US and Europe without a license. The leak check procedure would involve the following steps:

- Install all connectors and seal all flanges
- Pump dry air box to vacuum
- Fill dry box with mixture of R-507 and N₂ to required pressure
- Use leak detector to sniff around each cable plug and flange seam
- After checking is completed pump leak check mixture out of the box back in to storage container
- Backfill dry box with air or N₂ gas.

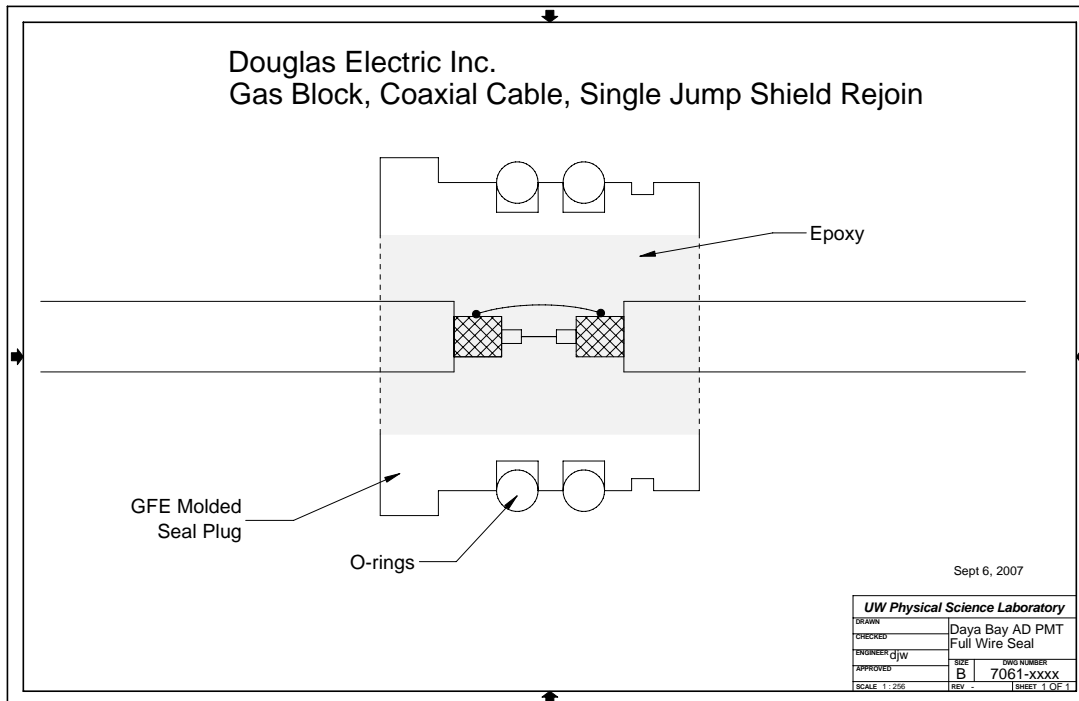


Fig. 4.60. Schematic of the full-wire seal plug for bonding to Teflon cables. For achieving a reliable, leaktight seal plug with Teflon jacketed cables it is necessary to create a full-wire seal. Studies have shown that the electrical characteristics of the cable and the frequency response remain the same with this bonding method.

4.6.9.2 PMT Cables and Cable Trays Outside AD in Muon Pool

From the AD dry boxes the AD PMT cables will be run on cable trays horizontally towards the wall of the muon pool and vertically upward along the wall of the pool. The cable trays will be made out of stainless steel. This is compatible with ultrapure water. The support posts for the cable trays can be made out of stainless or possibly acrylic. This would minimize the light obstruction in the muon water pool. The support for the AD PMT cable trays will also support the dry tube for the AD calibration and sensor cables.

4.6.9.3 PMT Cable Penetrations in Muon Pool Cover

The design of the AD PMT cable penetrations through the muon pool cover will follow the design of the cable penetrations used by the muon system.

4.6.10 PMT R&D Results

We have purchased six R5912 PMTs from Hamamatsu, and six ET9354KB from Electron Tubes for prototyping electrical and mechanical components as well as for evaluating the properties of these devices.

The characterization is carried out with a blue LED, driven by a pulser, housed inside a dark box along with the PMT under study. The DAQ system of the test stand is CAMAC-based. The key properties of the PMTs that are/will be studied are the radioactivity purity, single photo-electron spectrum, absolute gain, linearity, response to the local magnetic field, dark rate, pre- and after-pulsing, and quantum efficiency.

4.6.10.1 Radioactivity background

The amount of natural radioactivity of the glass samples for the R5912 and 9354KB provided by Hamamatsu and Electron Tubes respectively is measured at the low-background counting facility at LBNL. A sample of Photonis XP1806 is crushed and the radioactive purity of the glass is then determined. The results are shown in Table 4.16. The statistical uncertainty of the measurement is about 5 ppb. In the case of Elec-

	^{238}U (ppb)	^{232}Th (ppb)	^{40}K (ppb)
R5912	100	150	15
9354KB	81	73	15
XP1806	229	81	20

Table 4.16. Measured natural radioactivity of glass samples used in R5912, 9354KB, and XP1806 PMTs.

tron Tubes, a sample of the other components used in fabricating a 9354KB tube is also radio-assayed. The contamination is found to be 20 ppb of ^{238}U , < 20 ppb of ^{232}Th , and 3.5 ppb of ^{40}K .

4.6.10.2 Single Photo-electron Spectrum

The observed s.p.e. spectrum of an R5912 operating at roughly a gain of 10^7 is shown in Fig. 4.61. The peak-to-valley ratio is about 2.5. The charge resolution is better than 20%. However, these two parameters dependent on the orientation of the PMT with respect to the local magnetic field as demonstrated below.

4.6.10.3 Effect of Local magnetic Field

The study is done with the PMT axis normal to the local magnetic field. Using the polarized key, a notch, in the socket of the base as the reference, the charge of the waveform is recorded as a function of the angle of rotation about the axial axis of the PMT. The luminosity of the LED is kept constant during the study. As shown in Figs. 4.63 and 4.64, the ET 9354KB tubes show a large variation in the collected charge

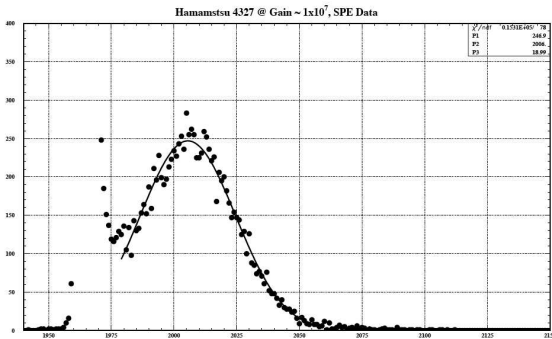


Fig. 4.61. Single photo-electron spectrum of an R5912 PMT running at a gain of 1×10^7 . The x-axis is the ADC channel.

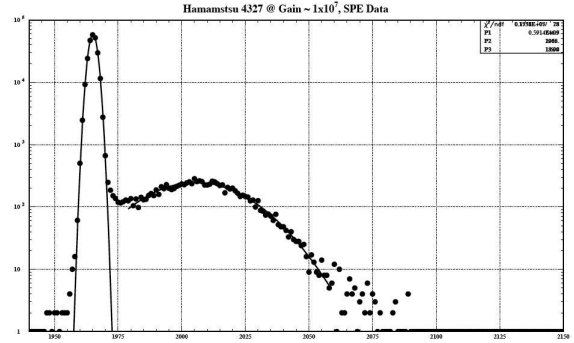


Fig. 4.62. Single photo-electron spectrum of an R5912 PMT running at a gain of 1×10^7 . The y-axis is in log scale.

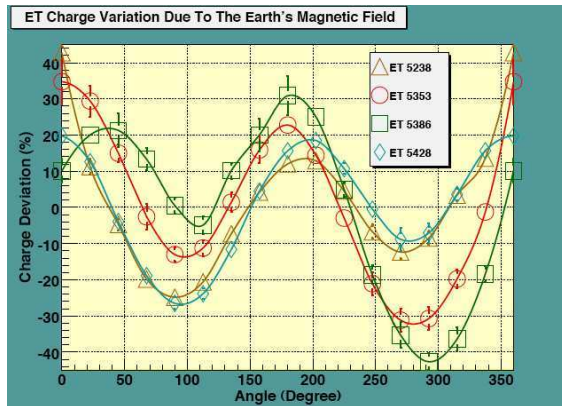


Fig. 4.63. Measured charge of ET 9354KB PMTs as a function of orientation in local magnetic field.

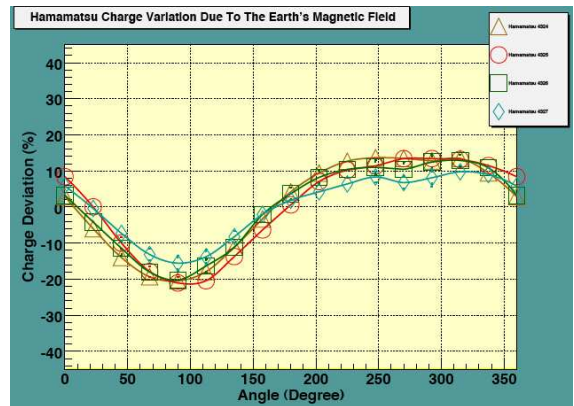


Fig. 4.64. Measured charge of Hamamatsu R5912 PMTs as a function of orientation in local magnetic field.

for a given tube as well as among the four samples. The Hamamatsu R5912 PMTs display a variation of about 30% but do not show any significant change from tube to tube. Close examination of the single photo-electron spectra obtained for different rotation angles for a given PMT indicates that the location of the s.p.e. is insensitive to the local magnetic field. However, the peak-to-valley ratio and the charge resolution do depend on the relative orientation of the field.

Simulation has been carried out by varying the collection efficiency as well as the s.p.e. resolution of the PMT according to the previous measurements of the effect of the Earth's field (e.g. Auger). The results indicate that the impact of the Earth's field on the reconstructed energy resolution of the detector is negligible. It is thus not necessary to use any shield to reduce the impact of the Earth's magnetic field.

4.6.10.4 Absolute Gain and Linearity

The absolute gain of the PMT at a given applied voltage is determined by measuring the total amount of charge of the single photo-electron spectrum after subtracting off the background. Fig. 4.65 is a summary of the absolute gain of four Hamamatsu R5912 PMTs.

The linearity of the PMT as a function of the current at a given gain will be determined in the future.

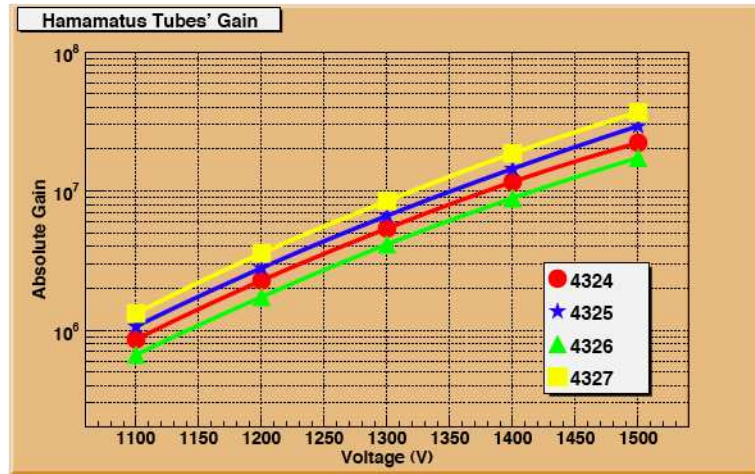


Fig. 4.65. Absolute gain of R5912.

4.6.10.5 Dark Rate

The dark rate of a PMT as a function of time has been studied for two different conditions. For a given PMT, it is first exposed to ambient light for a few minutes before placing it in a dark environment with a high voltage applied. The dark rate is determined at a threshold. When the dark rate has reached an asymptotic value, the high voltage to the PMT is turned off for a few minutes and then turned back on to continue with the measurement.

The measured dark rate of an Electron Tube 9354KB operating at a gain of 10^7 as a function of time is shown in Fig. 4.66. It takes approximately a day for the ET PMT to reach a steady rate of 1.4 kHz. Once this stage is reached, as long as the PMT is not exposed to light again, the dark rate restores to its asymptotic value in less than 15 minutes after power-cycling. In addition, the dark rate is determined as a function of threshold and the result is shown in Fig. 4.67. If the gain is changed to 2×10^7 , the dark rate in the steady state is increased to about 2 kHz at the 0.25 p.e. threshold (about 2 mV).

4.6.10.6 Pre- and After-pulsing

- The temporal distribution of pre-pulsing of the PMT is studied with the main pulse corresponding to about 50 p.e. and a threshold of 1/4 p.e.. Fig. 4.68 is the measured time distribution of pre-pulsing of a Hamamatsu R5912 PMT. The peak at ~ 18 ns is the pre-pulse due to the incident photons striking the first dynode directly. The probability of pre-pulsing between 4 ns and 20 ns before the 50 p.e. main pulse is estimated to be less than 1%. This should be compared to a typical value of 0.5% and a maximum of 2% as stated in the data sheet of R5912.
- The after-pulse is a delayed signal correlated with the main pulse. This phenomenon typically occurs on the microsecond time scale. After-pulsing of the Electron Tubes and Hamamatsu PMTs has been studied for a main pulse of about 50 p.e. The threshold of the TDC is set to about one photo-electron to reduce noise. The time window is chosen between 200 ns and 1 ms after the main pulse. In addition to an unexplained narrow structure between 350 and 500 ns, all PMTs have a broad peak around $2 \mu\text{s}$ and another one in the vicinity of $6\text{--}7 \mu\text{s}$. The time distribution of the first signal recorded after the main pulse for one of the Hamamatsu PMTs operating at a gain of about 2×10^7 is shown in Fig. 4.69. In general, all R5912 PMTs do not have after-pulsing beyond $10 \mu\text{s}$. However, the PMTs of Electron Tubes tend to have different after-pulsing after $10 \mu\text{s}$ and does not end till $20\text{--}30 \mu\text{s}$ for some PMTs.

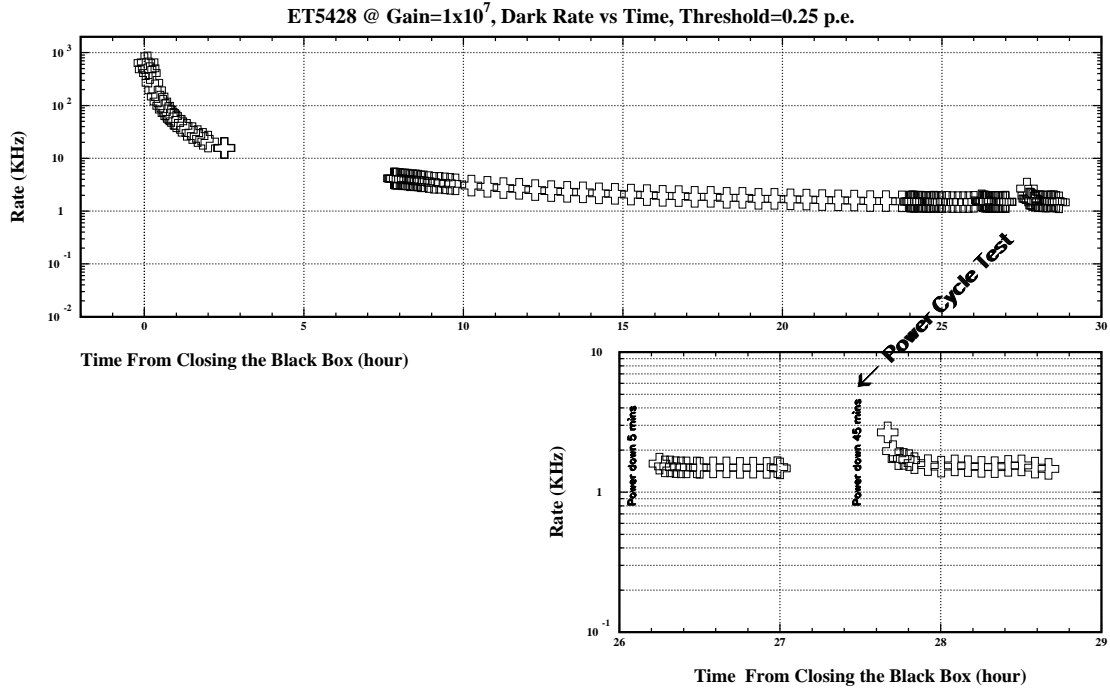


Fig. 4.66. Measured dark rate of an ET 9354KB as a function of time. The PMT is first exposed to light before high-voltage is applied to the tube in the dark. High voltage is power-cycled when the dark rate has reached an asymptotic value.

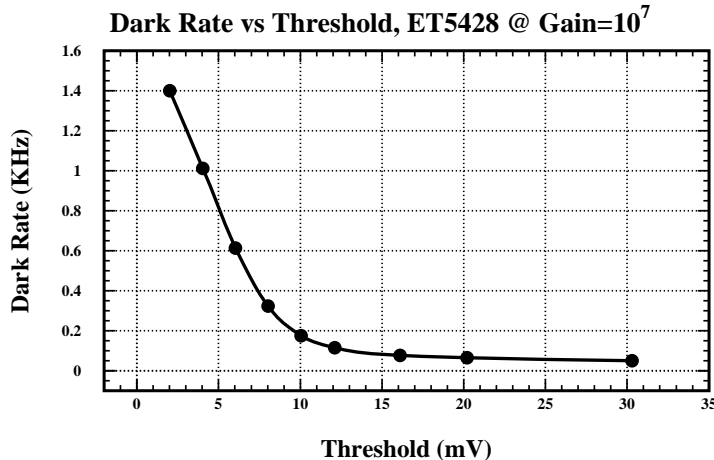


Fig. 4.67. Dark rate of an ET 9354KB as a function of threshold. The threshold corresponding to a 0.25-p.e. (s.p.e.) cut is about 2 mV (10 mV).

4.6.10.7 Quantum Efficiency

Determining the quantum efficiency as a function of the wavelength of the incident light is non-trivial. It will require modifying extensively the current setup. A monochromator will be used as the light source. The

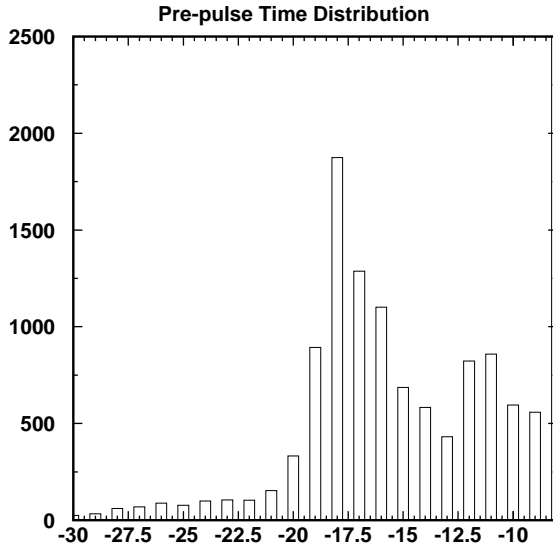


Fig. 4.68. Pre-pulse distribution of a Hamamatsu R5912 as a function of time (ns). The negative value means the signal arrives earlier than the main pulse.

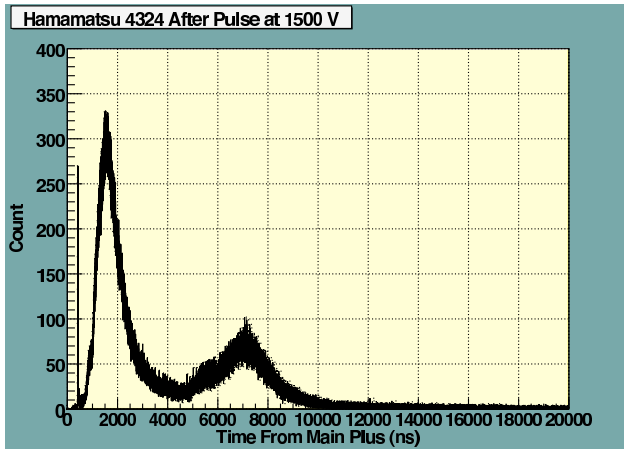


Fig. 4.69. Time distribution of the after-pulse of a Hamamatsu R5912.

incidence light from the monochromator will be split into two. One beam will be sent to a reference PMT and the other beam will be to illuminate the photocathode of the PMT under study. The quantum efficiency of the PMTs will be first determined relative to that of the referent tube. The absolute quantum efficiency of the latter tube will be measured by the manufacturer. Besides the average quantum efficiency, its position and incident-angle dependence will be mapped out for the sample PMTs.

4.7 Monitoring and Instrumentation for the Antineutrino Detectors

This section outlines the proposed instrumentation for the antineutrino detector. The goal of this instrumentation is to:

- ensure the safety of the antineutrino detector and its acrylic vessels during transport, filling, and lifting

- evaluate the geometric identity of the antineutrino detectors
- precisely measure the Gd-loaded liquid scintillator target mass and the LS γ -catcher mass during filling and monitor it during data taking
- monitor the environmental conditions of the antineutrino detectors

The requirements for the detector instrumentation and monitoring program are summarized in Table 4.17.

Item	Requirement	Justification
Measure acrylic vessel dimensions	<2–3 mm	Determine volume prior to fill
Fill level balancing	<1 cm	Avoid load on vessels during filling
Measurement of level in overflow tank	<1 liter	Measure target mass
Cover gas monitoring	Monitor N ₂ supply for O ₂ , H ₂ O, flow rate	Verify that radon is not introduced
Acrylic vessel positions	<0.5 cm	Determine change in γ catcher thickness

Table 4.17. Requirements on instrumentation/monitoring of the antineutrino detector.

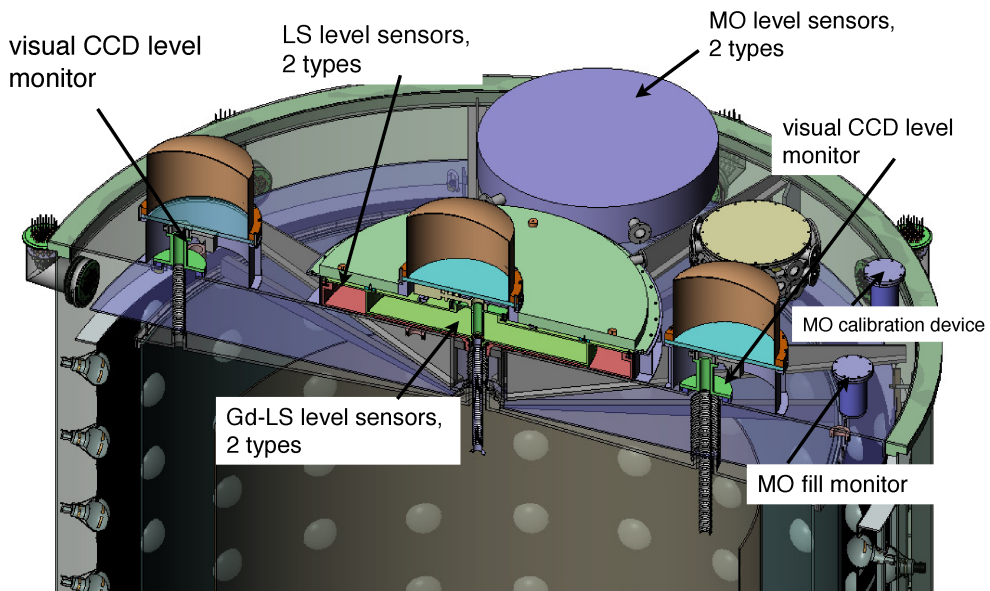


Fig. 4.70. Engineering model of the antineutrino detector lid with indications of the various instrumentation used for liquid level sensing and monitoring during filling and operation of the antineutrino detectors.

4.7.1 Survey of As-Built Detector Geometry

Purpose:

- To provide an as-built geometry of the steel tank, the acrylic vessels, and the position of the PMTs.
- To determine the volume of the as-built acrylic vessels prior to their fill.
- To be used as input to the detector simulations and to establish the geometric identity of the antineutrino detectors.

Instrumentation:

- laser-based optical survey device

We intend to precisely measure the dimensions of each acrylic tank and calculate the as-built volume from the data. Differences between tank volumes will impact the amount of scintillator required to fill each antineutrino detector. As discussed in Section 4.7.5 accurate knowledge of the filled target mass is obtained from the knowledge of the total mass filled into the detector and the liquid level monitoring in the overflow tanks. To fill the detector to a level within the allowable range in the overflow tanks it is necessary to determine the as-built volume of the target vessels. Furthermore, differences in the geometry of the detectors also imply differences in the mass distribution. It must be recognized that sagging of the tank in air will impact the geometry. Loads to the acrylic walls and in particular to the top and bottom faces will be drastically different when the detectors are filled. Modeling calculations to estimate the sensitivity of the antineutrino detector to deflection induced geometry changes are in progress at the University of Wisconsin. The results of this modeling will determine how much effort we must expend to keep track of deflection induced geometry changes.

4.7.2 Visual Monitoring of Inside of Antineutrino Detector

Purpose:

- To provide a visual monitor of the inside of the antineutrino detector and the behavior of the acrylic vessels during filling, transport, and lifting.
- To visually check the liquid levels during filling as they reach the critical acrylic boundaries between the oil and the γ -catcher, and the γ -catcher and the inner Gd-LS target.

Instrumentation:

- Infrared-sensitive CCD camera enclosed in acrylic inside the antineutrino detector (for general purpose inspection).
- CCD cameras enclosed in acrylic enclosure mounted on PMT ladders at the height of the interfaces between oil/ γ -catcher and γ -catcher/target. These cameras can be installed inside the tank (radioactivity permitting)(for monitoring liquid levels). We expect to use 2-3 CCD cameras per tank with infrared lighting.

4.7.3 Monitoring of Acrylic Vessel Positions

Purpose:

- To measure the concentric positioning of the nested vessels, and
- To provide a monitor for possible lateral shifts of the acrylic vessels with respect to the steel tank and to the other acrylic vessels during transport, filling, and lifting.

Instrumentation:

- Laser or ultrasonic thickness gauge inside the mineral oil volume of the antineutrino detector steel tank.
- We may also employ designed calipers or other special tools for a mechanical inspection and measurement.

Ideally, we would like to track both translations and rotations if possible. Several distance gauges will be needed to determine translation and rotational shifts. In addition, monitoring with the in-situ CCD cameras will provide invaluable information on the orientation of the vessels inside the steel tank. Interpretation of the camera images may not be entirely straightforward. For example if the acrylic top surfaces are not perfectly normal to the camera line of site, then the relative position of cross hairs or targets may change after tank filling even if there is no motion of any solids. Lighting may be provided by a ring of infrared LEDs around the camera. An interlock system and/or a lockout procedure on the PMT high voltage systems may be needed to protect PMTs. We are considering the use of infrared cameras to provide an additional layer of safety for the PMTs.

4.7.4 Motion Monitoring

Purpose:

- To provide a record of the motion of the antineutrino detector during its entire lifetime: From the assembly in the surface assembly building to the filling in the filling hall and the installation in the experimental halls. This will help us correlate any potential changes in the antineutrino detector with events during the transport, filling, or lifting.

Instrumentation:

- Accelerometers (on outside of antineutrino detector)
- Tilt sensors (on outside of antineutrino detector)

These devices must either be wireless or connected to a computer/DAQ moving with the detectors. The sensors can provide feedback to operators of the transporter and crane. They can be either removable or permanent and can be covered by a dry box or watertight enclosure if they are permanently attached to the outside of the detector.

4.7.5 Target Mass Monitoring During Filling and Operation

Purpose:

- To measure to an accuracy of <0.1% the mass of the Gd-loaded liquid scintillator target filled into the antineutrino detector and to monitor the mass inside the target volume during transport and data taking.

Instrumentation:

- Load cells on reference tanks (intermediate storage tanks used for filling detectors).
- Mass flow meters between storage and reference tanks and antineutrino detector.
- Instrumentation for measuring the temperature and density of the liquid scintillator, Gd-loaded liquid scintillator, and mineral oil between reference tanks and the antineutrino detector.
- Volume flow meters between reference tanks and antineutrino detector.

- Liquid level sensors for Gd-liquids scintillator and undoped liquid scintillator in antineutrino detector overflow tanks.
- Liquid level sensor in antineutrino detector mineral oil region during filling.

Control of the delivered mass will be achieved with a combination of flow meters and load cells. Two competing methods of mass measurement are under consideration and described in Section 4.8.

Accurate knowledge of the liquid levels is crucial during the filling process. Potentially destructive load forces can be generated if the three tank levels are not precisely controlled. The instrumentation for the detector filling is designed under the assumption that liquid levels must be matched to ± 1 cm during filling. Finite element analyses show that the proposed design of the acrylic vessels can withstand up to 30 cm of difference in the filling levels before the stress and load levels become unacceptably high.

The oil level during fill is the easiest and least expensive to monitor because direct insertion of a probe into the oil is possible. Monitoring of the GD-LS and the LS levels requires the use of non-contact solutions or sensors that are compatible with these liquids. We have performed R&D on three different methods that meet these requirements: Visual monitoring with CCD cameras in the off-center, acrylic calibration ports, pressure sensing with Teflon coated sensors, and in-liquid ultrasonic measurements. radar based measurements. Internal CCD cameras will be useful to calibrate and verify these level sensors.

An accurate measurement of the liquid levels is critical during both data taking as well as transport and lifting. Temperature variations or tank distortions will cause fluid to enter and leave the overflow volumes. A 100 L overflow tank constrained to be less than 300 mm high will rise about 1 mm for every 2 L of added fluid. Thus we require a Teflon covered contact sensor accurate to 1 mm or better with a dynamic range of 300 mm.

The relative density of the three loaded fluids critically influences loading forces on the acrylic tanks and therefore their geometry. We will use Coriolis flow meters to accurately measure the fluid densities. However we must point out that it is not sufficient to simply measure the as-delivered fluid densities. It will be necessary for the collaboration to specify the fluid densities ahead of time and use density measurement as one of several criteria for acceptance or rejection of the fluid deliveries to ensure that the loads on the acrylic vessels are within tolerances.

4.7.6 Gas Supply Monitoring (dry N₂ and ambient)

Purpose:

- Maintain a continuous nitrogen cover gas to the detector and the calibration domes.
- Monitor the pressure, flow, and quality of the dry N₂ purge gas provided to the detectors
- Monitor the pressure, flow, and quality of the dry N₂ purge gas exiting the detectors and detect any leaks into the gas purge system.
- Monitor the gas pressure above/in each overflow tank and calibration dome
- Verify that tank purging is complete prior to filling of the antineutrino detector
- Protect personnel and detect any leaks of flammable liquids from inside the antineutrino detector

Instrumentation:

- Pressure monitors: supply line, above each fluid type, in calibration domes, and in detector exit line.
- Gas flow monitors: supply line, calibration & flow volumes, exit line.

- O₂ sensors trace amounts: N₂ supply and exit lines
- Humidity sensors on exit line: check for water leaks into dry-box or cable tubes.
- O₂ sensors ambient gas: Connected to oxygen deficiency hazard alarm.
- Flammable liquid sensor: Ambient gas. Connected to alarm.
- Humidity sensor: ambient gas.
- Differential pressure sensors between calibration and overflow volumes to protect against pressure surges and between the three detector fluids to protect against tank bulging.
- Gas pressure in cover gas, in calibration boxes, and in overflow tanks.
- Smoke/heat sensor.

A continuous flow of dry N₂ must be provided to every gas space in the antineutrino detector. Numerous strategies can be devised to accomplish this, but to protect the acrylic vessels all solutions must strictly restrict the possibility of differential pressure developing between the three antineutrino detector fluids. A failsafe design that is based on gas conductances and self equalization of pressure is preferred. Separated flow systems require some type of interlock system and are not desirable. A schematic diagram of the N₂ cover gas system is shown in Fig. ?? and ??.

Regulation of the N₂ supply based on pressure and/or flow measurements will be required. Trace O₂ sensors are needed to monitor the quality of supply gas. Leaks into the purge system can be detected by trace O₂ sensors and water sensors in the exit gas. Flammable liquid sensors are desirable for the ambient gas but if LAB type scintillator is used the vapor pressure may be too low for typical sensors to detect. Differential pressure monitors will be required across the isolation gate valve between tank liquids and calibration dome to prevent pressure surge upon opening. If a gate valve is used some form of interlock will be required to protect against untimely closure when the calibration hardware is lowered into scintillator. Both the mineral oil and LAB scintillator are flammable. Smoke and heat sensors above and downwind from the detectors are needed for safety.

4.7.7 Temperature Monitoring

Purpose:

- To monitor the temperature of the antineutrino detector and provide warning if the external temperature of the antineutrino detector exceeds the pre-defined specifications of the detector environment.
- To measure the temperature gradient (top vs bottom) of the buffer oil inside the detector as an input to convection calculations of the detector liquids.
 - temperature at bottom of antineutrino detector (outside antineutrino detector and thermally isolated from the stainless steel tank)
 - temperature at top of antineutrino detector (outside antineutrino detector and thermally isolated from the stainless steel tank)
 - temperature of buffer oil inside antineutrino detector at top and bottom

The temperature sensors must either be compatible with ultra-pure water or they must be demountable.

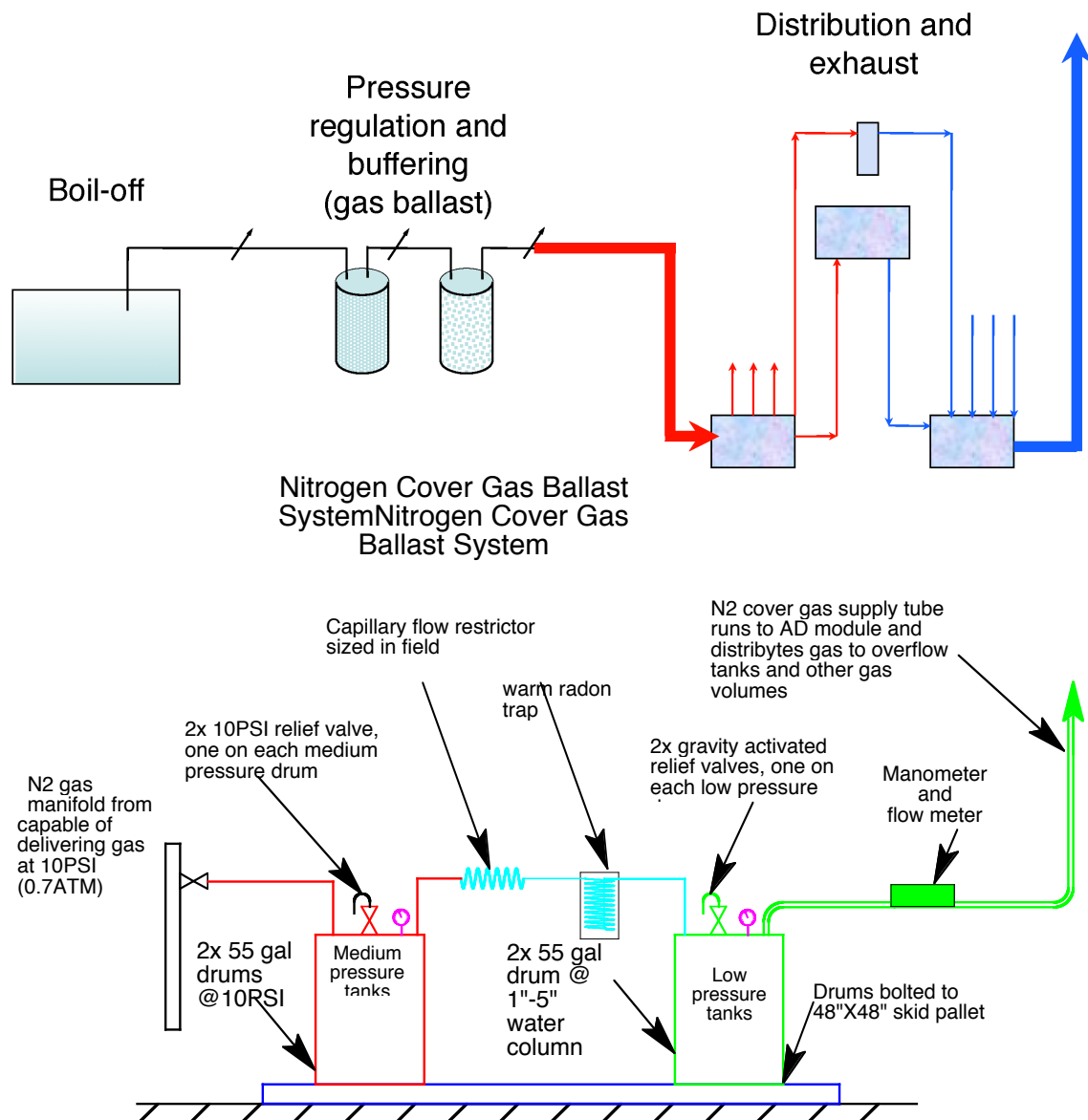


Fig. 4.71. Top: Schematic of the N₂ cover gas supply and ballast system for the antineutrino detectors. Boil-off nitrogen is used as a source of clean, radiopure cover gas for the detector. Bottom: Conceptual layout of the supply lines for the N₂ cover gas system.

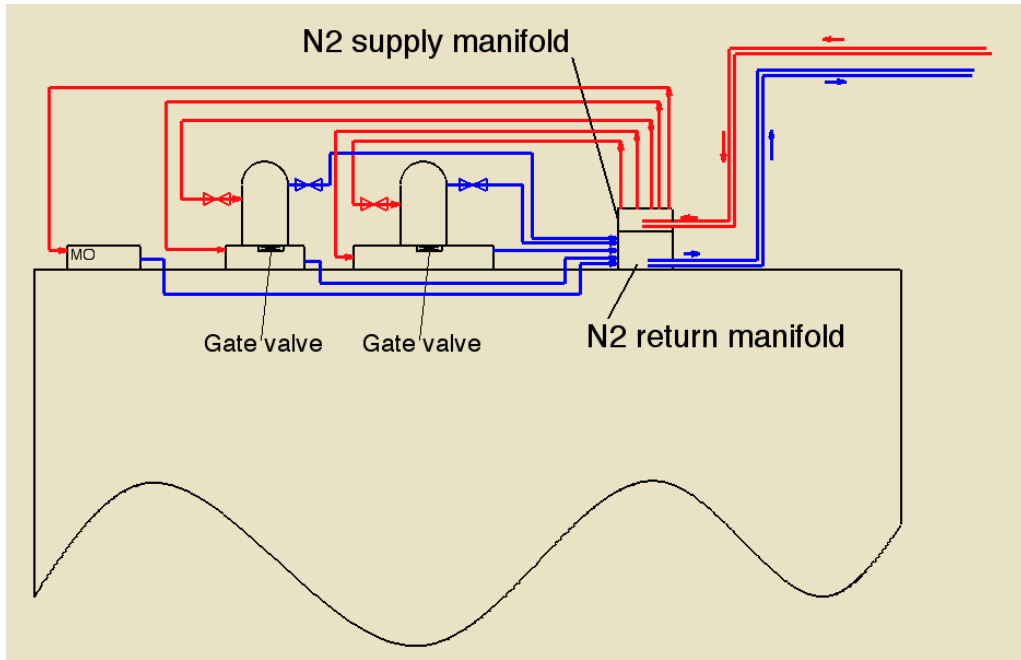


Fig. 4.72. Schematic of the N₂ supply and return lines for the overflow tanks and calibration boxes on top of the AD. The supply and return lines run through common supply and return manifolds so that potential pressure differences between the calibration box and the overflow volumes or across the gate valve can be avoided.

4.7.8 Monitoring of LS Leaks

Purpose:

- To provide early warning to filling and transporting operators in case of a scintillator leak
- To provide warning to the experiment during the operation of the experiment

Instrumentation:

- Resistive wet pads as a liquid indicator under pumps and selected fittings during filling, transport, and storage.
- In-situ detector data distributions as indications for the separation of the gamma catcher and the Gd-LS target during operation and data taking in the water pools

Resistive pads can provide invaluable early warning in case of a water leak. Tests will be required to see if this simple method works with LAB scintillator, or if a more sophisticated liquid sensor technology will be necessary. A wide variety of commercial sensors exist for the detection of liquids.

Once the detector is deployed and installed in the water pool access to the inner regions of the detector is very limited. In this case the in-situ detector distributions can be used to monitor any time-dependent variations and look for indications of mixing of the gamma catcher LS and the target Gd-LS through leaks in the acrylic vessel. A leak in the steel vessel will likely result in degradation of the mineral oil properties and impact the optical parameters of the detector buffer region.

4.7.9 In-Situ Monitoring of the Mineral Oil Attenuation Length

Purpose:

- To monitor in-situ and independent of the calibration sources the attenuation lengths and optical quality of the liquids in the antineutrino detector.

Instrumentation:

- laser-based attenuation length measurement in the mineral oil volume

The objective is to provide a semi-continuous monitor of the optical clarity of the mineral oil in the buffer region. This device uses a port on the top of the antineutrino detector. The monitoring device itself is part of the project's calibration scope and program.

4.8 Filling the Antineutrino Detectors and Measuring the Target Mass to High Precision

The Daya Bay experiment requires the construction of eight multi-ton detector modules. Each module utilizes 20 T of Gd-doped scintillator filled into a centrally located sub-tank. That sub tank forms the center of a system of three concentric nested tanks each filled with a different fluid. The detector modules are to be constructed as matched pairs so that one detector of each pair can be deployed at one of the near sites while the other one will be deployed at the far site. The concept of matched pairs ensures that the Gd-LS target liquid will be identical between pairs of near and far detectors. Hence, a direct comparison of the antineutrino interaction rates can be done.

One of the requirements of the matching is that the amount (weight) of Gd-doped scintillator fluid in a matched pair be equal to within $M_1/M_2 = 1 \pm 0.0005$ or better, where M_1 and M_2 denote the target mass of detectors 1 and 2. The module filling process requires that three concentric tanks be filled with different liquids simultaneously and that during the filling process the column levels of the three tanks match to within a well-specified tolerance of ± 1 cm or so. The tolerable level difference will be determined from the ongoing engineering calculations. Only the central tank has the strict mass balance requirement stated above. It is desirable to match the mass and volume of the γ -catchers similarly but the requirements are less stringent.

Two of the fluids to be filled are flammable and sensitive to air exposure and temperature excursions. During the filling process the detector and the fluids cannot be exposed to mine air. The entire system is to be kept in a nitrogen atmosphere at all times to avoid radon exposure. Ideally, the detectors will only be filled once. Draining the system and starting from scratch in the case of a filling error is not acceptable. We only envision draining the detectors (or pumping them out) if a major repair of the detectors became necessary or at the end of the experiment.

At the required level of accuracy the experimental risk is significant if a single methodology is employed. A number of redundant techniques will be employed to ensure the precise mass measurement of the Gd-LS target:

1. Weighing of the Gd-loaded liquid scintillator
2. Mass flow meters
3. Volume flow meters + temperature + density measurements
4. Geometry surveys of the target volume + density measurement of the Gd-loaded liquid scintillator

Specifically, commercial Coriolis mass flow meters are stated to have the required accuracy but in cases of interrupted flow, power outages or trapped gas, their performance is questionable. Because they integrate a rate over time, they must operate flawlessly during the entire filling process which is expected to take on

the order of one to several days. We therefore require a system that is robust against power interruptions and gas bubbles, both microscopic and macroscopic.

Our goal is to develop a methodology that:

1. allows the precise, simultaneous filling of pairs of detectors
2. provides a way to measure or limit the variation of the target mass between pairs of detectors
3. is redundant and repeatable over a time period of months or years
4. allows recovery from power outages and other unexpected occurrences without impacting the precision of the target mass measurement

The method described here employs the instrumentation listed above and meets the requirements of such a fill system.

4.8.1 The Filling Process

To understand the complexity of the filling process we first consider some hydrostatic issues of the nested fluid design of the antineutrino detectors. The acrylic tanks have thin walls with thicknesses ranging from 10-20mm and therefore will flex considerably in response to unequal hydrostatic pressure between the inside and outside of each tank. Figure 4.73 illustrates the (imaginary) situation where all three tanks are filled so that the overflow levels are equal and the inner tanks are in their neutral (undistorted) positions. This is a stable condition only for all three liquids having the same density. If mineral oil is more dense than scintillator with a specific gravity 1% greater than scintillator, then the outer acrylic vessel would float and must be held to the bottom of the stainless tank against a buoyant force of ~ 400 kg. At the same time the entire outer acrylic vessel would experience a compression which varies with height. The bottom surface sees the largest force, about 450 kg for every 1% specific gravity difference. The top sees about 50 kg. The cylindrical wall will also deform but this effect is undoubtedly smaller than the deflection of the flat bottom surface. The outer acrylic deflection reduces its volume and its overflow level rises. In response to the outer acrylic's higher overflow level, the inner acrylic experiences additional compressive force and its overflow level also rises. The final resting levels for the three overflow volumes in this imaginary exercise depend sensitively on the strength of the acrylic vessels, on the particular specific gravity of the fluids and on the diameter of the overflow columns. A small correction is required to account for the acrylic density which will differ from the liquid densities. In the case that mineral oil is less dense than scintillator the argument is the same but the scintillator overflow level drops.

In practice we expect to fill all three vessels simultaneously. At first only mineral oil is filled (zone A in Fig. 4.73) until its level reaches the bottom of the outer acrylic vessel. At that point filling of the outer acrylic begins (zone B). Liquid delivery rates must be matched to keep the two column heights close to each other. If the two column heights are not equal the force generated on the bottom surface of the outer acrylic vessel is 106 kg for every cm of column mismatch where we assume liquid densities of 0.85 g/cc and a face diameter of 4 m. The same consideration requires that the liquid level of the inner acrylic be close to the outer acrylic level as filling enters zone C. The force on the inner acrylic bottom face is 64 kg for every cm of column mismatch assuming an inner face diameter of 3.1 m. Liquid flow profiles are shown in Fig. 4.74.

As filling proceeds past the top of the inner acrylic (zone D) the situation becomes more complicated. In Fig. 4.73 we assume that the overflow column diameter of the inner acrylic in the region of penetration through the other two vessels (zones D and E) is relatively small, about 5 cm. One might expect that at the lower cm boundary of zone D, flow to the inner acrylic should be dramatically reduced but should not be zero. In fact, if at this point all filling were temporarily stopped and an amount was added to the inner vessel sufficient to raise the overflow column 10 cm there would only be a temporary rise in the column height; the increased hydrostatic pressure would expand the inner vessel and the level would return to almost the same

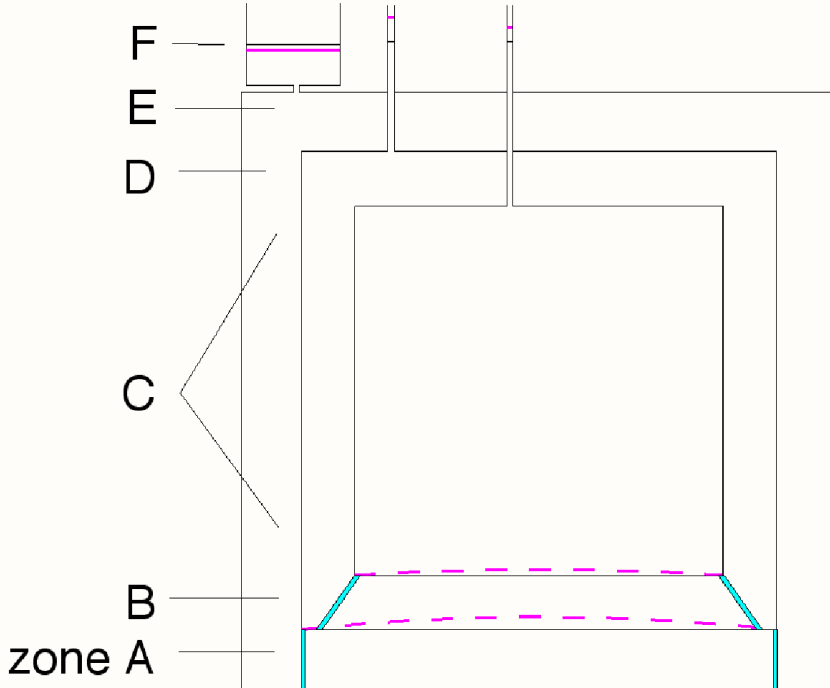


Fig. 4.73. Schematic of the different liquid zones of the antineutrino detector during filling. Zone A: only mineral oil is filled into the detector. Zone B: Mineral oil and LS are filled simultaneously into the detector. Zone C: MO, LS, and Gd-LS are filled simultaneously into the detector. Zone D: This is almost the complete reverse of the previous situation except that calibration pipes penetrate the different regions at the top of the detector. Mostly MO and LS are filled into the detector with some Gd-LS going into the calibration pipes. Zone E: In this zone the detector is filled mostly with MO until it is full with LS and Gd-LS going into the calibration pipes. Zone F: Once the detector is completely full all liquids MO, LS, and Gd-LS will rise into the overflow tanks.

as before the fluid addition. The stiffness of the inner acrylic vessel determines how much additional liquid would be required to raise the inner column height one cm. In effect, this geometry is equivalent to a huge hydraulic cylinder.

We can assume that in zone D no additional liquid is added to the inner tank. As the filling in zone D proceeds, the inner acrylic column level will rise so that the pressure caused by the deflection of the inner tank equals the difference between the inner and outer scintillator columns. If the inner tank is not very stiff then the two scintillator levels will be similar even though no liquid was added to the inner tank. If the acrylic overflow columns have small diameter only small tank deflections are needed to adjust the column height to the equilibrium levels. The smaller the diameter of the column the stiffer the acrylic vessel appears to be. A similar effect on the outer acrylic column will be seen as the filling enters zone E. An intuitive explanation can be found by imagining two water filled balloons. One is connected to a 3 cm diameter glass tube and the other to a very tall capillary tube. The static force required to squeeze out 100 cc of liquid is different for the two cases.

Once the detector is filled, temperature drifts will cause changes in the fluid densities. Away from

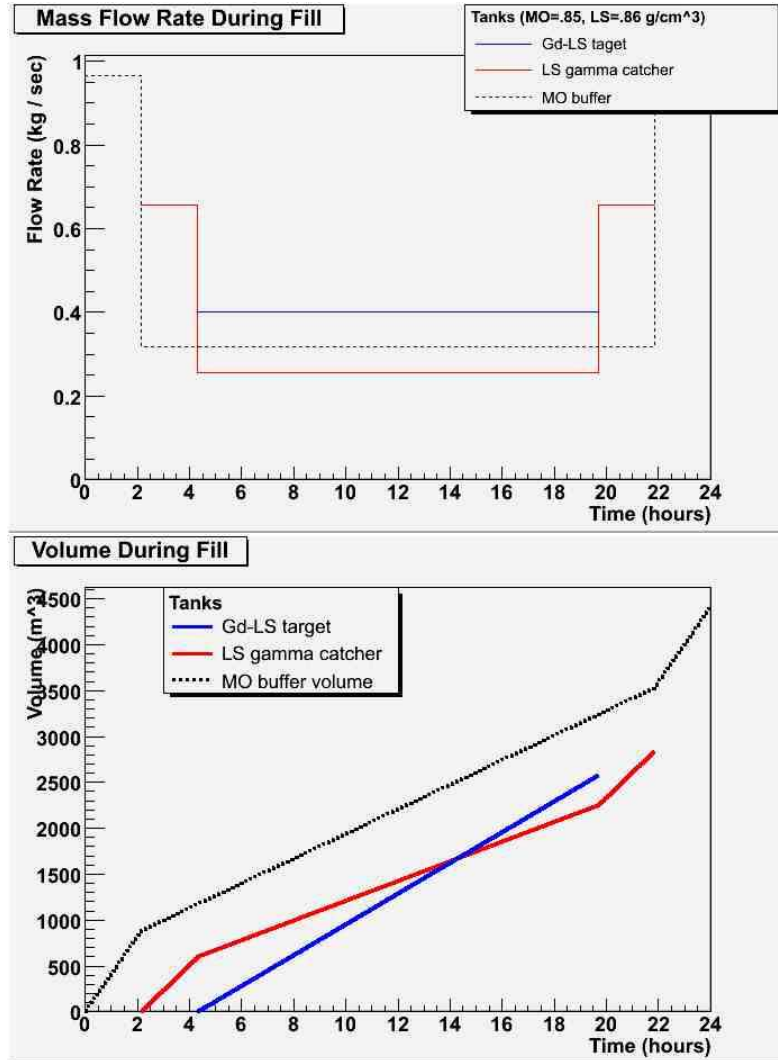


Fig. 4.74. Top: Mass flow rate of the three different detector liquids for a detector fill with a total duration of 24 hrs. The discontinuities indicate the points where the liquids reach acrylic vessel boundaries. Bottom: Cumulative liquids volumes during the detector fill. Again, we assume a total fill duration of 24 hrs. The contribution of liquids in the calibration pipes at the top of the AD is neglected in this graph.

thermal equilibrium the outer layer of mineral oil will respond first because of its contact with outside conditions and the metal vessel it is in. The mineral oil thermal expansion is expected to be larger than scintillator expansion. We estimate 17 L expansion per 1° C temperature rise for scintillator.

As for the filling, we conclude:

- The two acrylic vessels should be thought of as highly elastic structures.
- To fill the three liquid volumes to equal overflow heights with a pre-specified mass we need to know more than the geometry of the three tanks. We also need to know the precise density of the three fluids and we need the stiffness of the acrylic vessels. Assuming the outer steel tank has no load deflection introduces only a small error.

- The stiffness of the acrylic vessels and their ability to deform ($\Delta V/V$ at failure) is a critical design issue. In turn, the requirements on these two parameters depends critically on difference in the three liquid densities.
- It could be possible to fill the acrylic tanks to the point that they fail by expansion even though the column heights are not excessively different. This threat is most likely if the mineral oil is less dense than scintillator. We are investigating possibilities to monitor the curvature of the acrylic bottom surfaces during filling.
- Unstiffened acrylic tank bottoms have a disadvantage that during filling they could be flexed beyond their elastic limit. But they have the great advantage that, because of their ability to flex, the active volume of scintillator is stable against changes in mineral oil density. However, if the ratio of scintillator density to mineral oil density differs from 1 by more than about 2% the forces on the bottom face might be excessive and ribbing or adding a pre-formed dome shape could be required. If mineral oil and/or scintillator of specified density could be manufactured this would greatly simplify the design of the acrylic tanks. We may have to obtain several batches of mineral oil with different densities to mix the oil to the desired density if needed.
- To first order, the change in active scintillator mass as a function of detector temperature is inversely related to scintillator overflow column diameter. On the other hand a large mineral oil overflow column is desirable.
- Liquid level monitoring to an uncertainty of ± 1 cm is required for all three fluids during the filling process. Active regulation of the filling rates based on measured fluid levels should be employed. Level differences of only a few cm could damage the acrylic vessels. Interlocks and visual monitoring of the fluid levels are recommended. We are investigating the possibility of using infrared CCD cameras inside the antineutrino detector that allow us to do this.

4.8.2 Measuring the Target Mass to High Precision of <0.1%

There are only two practical methods we are aware of to directly measure the mass of fluids pumped into the AD modules:

- Coriolis mass flow meters, and
- strain gage based precision load cells

We will utilize both of them for redundancy and systematic cross-checks. Of the two we have chosen a load cell system for our primary measurement because of the achievable accuracy and the immunity of load cells to gas bubbles and interruptions of the delivery stream of liquid. Only the Gd-LS mass filled into the inner acrylic tank needs to be determined to a precision of $M_1/M_2 = 1 \pm 0.0005$ or better requiring the use of a load cell system. The plain LS for the gamma catcher and mineral oil masses can be determined to sufficient accuracy with precision volume flow meters and simultaneous measurements of temperature and density.

Due to space and other considerations we plan to fill only one detector at a time in the LS the LS Hall. However we will wait until two AD modules are fully assembled before filling them. In this way the time interval between fillings will be short, on the order of two weeks. Over this short time interval drifts between the properties of filled scintillator and stored scintillator can be considered negligible and the concept of matched pairs of antineutrino detectors can be maintained.

Therefore, the concept of matched pairs of antineutrino detectors is based on

- filling the antineutrino detectors from a common reservoir of Gd-LS, LS, and MO,
- within a short amount of time (that is ~ 2 weeks).

The relatively thin walls of the acrylic vessels require us to pump all three types of fluids simultaneously and to control the filling rates to maintain equalized pressures on the acrylic walls at all times as described in the beginning of the previous sub-section. Because the three fluids are to be stored in large acrylic lined tanks on the floor of the LS Hall we must first pump 20 T (23,530 L) of Gd-LS into an intermediate Teflon-lined reference tank.

The reference tank will rest on four precision load cells as shown in Figs. 4.75 and 4.76. The vendor



Fig. 4.75. A central element of the target mass measurement system is the precision scale for ~ 25 T of liquid scintillator. An ISO reference tank mounted on precision load cells will be used to measure the target mass to $<0.1\%$. The top panel shows the picture of a standard, commercial ISO tank. The bottom pictures show a commercial C6 load cell (left) and the arrangement of the load cells underneath the ISO tank.

(Sartorius) claims an accuracy for the load cells of 0.008%. The load cells can be calibrated using NIST traceable procedures. It is interesting to note that at the stated accuracy of the loadcells we will need to

ISO Reference Tank Mounting System

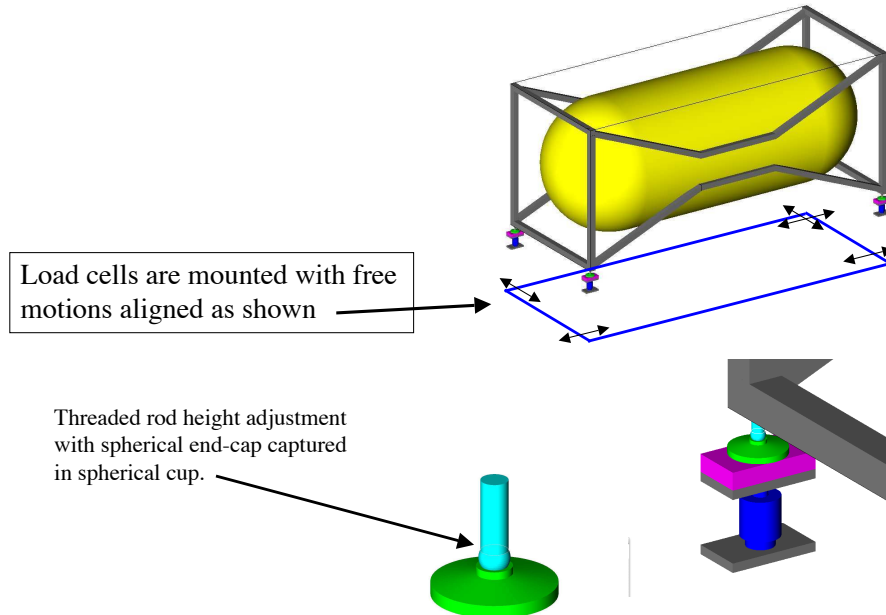


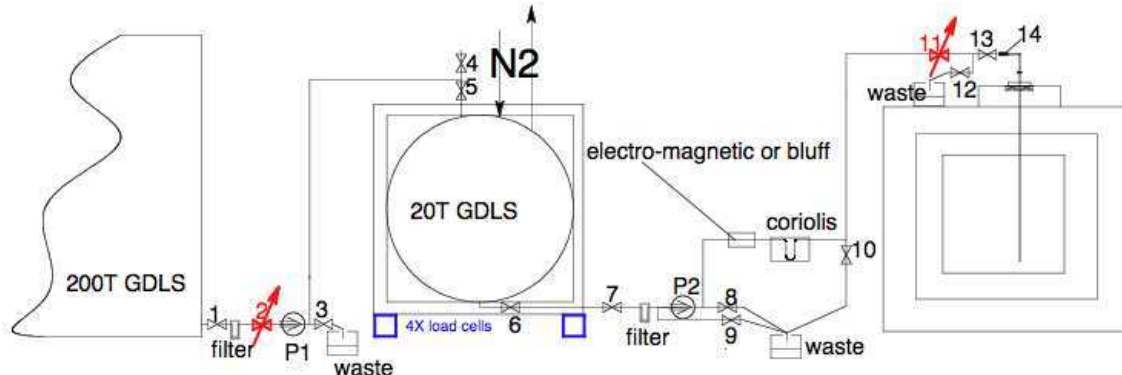
Fig. 4.76. ISO tank mounting details showing orientation of the free motions of the load cell mounts and the application of spherical swivel mounts to absorb load-induced tank frame distortions.

correct for the buoyancy force of the atmosphere on the reference tank. Strict avoidance of any horizontal forces or torques on the load cell system is required if the stated load cell accuracy is to be obtained. Figure 4.76 shows how we intend to eliminate these influences. Three of the load cells are mounted in a support frame that allows motion along one axis only. The fourth cell can move freely in a horizontal plane. By mounting the load cell frames as shown in the figure we allow for thermal and load induced expansion without inducing lateral forces on the load cells. Loading of the ISO tank with fluids will cause the tank frame to bend and this can introduce torques on the load cell mounts. We avoid this problem by resting the four corners of the ISO tank on high capacity spherical swivel mounts. Adjusting the threaded rods on those mounts can equalize the loads on the four corners.

During the detector filling, Gd-LS will be drawn from the reference tank but the plain LS and the mineral oil will come directly from their respective 200 T storage tanks. Plumbing schematics for these two cases have been developed and are shown in Fig. 4.77.

It can be seen that there will be three independent plumbing systems. Each fluid will have a variable speed pump and two flow meters in series. One flow meter is a high precision Coriolis meter with 0.1% precision. The other is a volume flow meter as a backup. The Coriolis meters provide an accurate measurement of fluid density simultaneous with their measurement of mass flow. A system of valves and waste containers allows the plumbing lines to be N₂ purged and primed just prior to the start of filling. Except for the two

GDLS block schematic



LS and MO block schematics

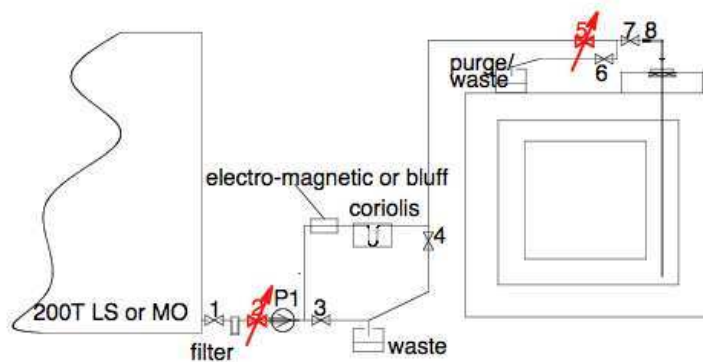


Fig. 4.77. Top panel: Schematic of the filling system for the Gd-LS target liquid. The liquid is pumped through an intermediate ISO storage and weighing tank. Mass and volume flowmeters provide independent measurements of the target mass. Bottom Panel: Schematic of the filling system for the LS and MO filling systems. In this case the mass is determined based on mass and volume flowmeters alone. A total of three, parallel filling systems will be installed in the LS Hall. One for each kind of liquid.

valves shown in red, we will employ only manually actuated valves. The valve status, i.e. open/closed, will be sensed and routed to an interlock system. In the case of operator error or some other emergency condition the two shutoff valves shown in red will automatically close.

The mass of delivered fluid will be determined by the difference between load cell readings. Thus it is not necessary to know in advance the precise mass required to fill the Gd-LS reservoir. This flexibility allows us to terminate or extend fluid delivery to accommodate variations in acrylic tank volume due to construction variation. For example a 3 mm deviation in the inner acrylic tank diameter from its nominal 3100 mm corresponds to a relative volume error of 2×10^{-3} or 45 L.

Zero drift of load cells can be a significant source of weighing error. Generally, the problem is minimized by reducing the time between zeroing the scale and the measurement. In our case filling the reference tank may take as much as two days. The load cells we will use have been purchased and will be subjected to a rigorous testing program. If we find problems with zero drift we can reduce the error by monitoring the zero during the filling process. A system of hydraulic jacks can be employed to briefly lift the reference tank off the load cells. Another potential source of error is long term stability of the sensitivity of the load cells. It could be as long as two years between the filling of the first pair of AD modules and the last pair. To protect against drift of the target pair mass fill over time it will be necessary to periodically calibrate the load cells. Commercial NIST traceable calibration services are available for this purpose.

4.8.3 Control and Operation of the AD Filling and Target Mass Measurement

The AD filling and target mass measurement is a critical one-time process. We expect to fill the ADs only once at the beginning of the experiment and drain them during de-commissioning after the experiment is concluded. In case of emergency repair of the ADs it is possible to pump the liquids back out of the AD into the storage tanks or other intermediate storage containers. However, this operation is reserved for emergencies and not part of the routine plan for liquid handling in the LS Hall. Therefore, the successful and flawless operation of the AD filling and target mass measurement system is critical. To achieve this flawless one-time operation we will rely on a combination of

- computer control and readout
- a trained team of experts
- written check sheets that are followed by trained operators

The instrumentation and pumps of the AD filling system will be controlled by a LabView Realtime PXI-based control system. A UPS system will be used to allow enough time (15–30 minutes) for the AD filling system to be shut off safely in case of an underground emergency. Furthermore, the system is designed in such a way that an unforeseen power failure will not damage any equipment or create a risk of damaging the ADs and their acrylic vessels during filling.

The computer control system will provide the following features:

- Computer readout and display of the mass flow measurement and all instrumentation and pumps associated with the AD filling and target mass measurement system
- Status-read of all valves in the system. Only the emergency shut-off valves will be operated in real-time by computer control and by emergency shut-off buttons. All other valves will be operated by hand following written procedures and check sheets.
- Web-based monitoring and observation of the detector status during filling.
- The control system will link to the experiment's slow control system to provide slow control data on the status of the system and environmental variables.

The filling of the ADs will be performed by a trained team of experts under supervision from the University of Wisconsin. The responsibility for the operation of this system is with the group from the University of Wisconsin and the Physical Sciences Laboratory. The actual filling process will take of the order of 1–3 days. This will be a continuous, 24-hr. process. A trained team of shifts with at least 2 persons per shift will monitor and control the filling process.

The entire AD filling system will be assembled and tested at the Physical Sciences Laboratory prior to its shipment to Daya Bay. Figure 4.78 shows the facilities at PSL that are available for setting up and testing the AD filling system. During this test period written procedures and check sheets will be developed for the



Fig. 4.78. Photograph of the facilities of the Physical Sciences Laboratory (PSL) at the University of Wisconsin. The assembly space at PSL allows us to completely assemble and test the ISO tank load scale and AD filling tank system before shipment to Daya Bay.

operation of the AD filling system underground.

4.8.4 Use of the Liquid Scintillator (LS) Hall for Detector Filling

The filling operation described in the previous section will take place in the LS Hall. An overhead view of the floor space is shown in Fig. 4.79. As can be seen from this layout nearly half of the hall is occupied by the three 200 T storage tanks. Nevertheless the remaining space is sufficient for conducting the filling operations. For the reference tank we will purchase a Teflon-lined 25,000 L ISO tank. ISO tanks conform to the international intermodal container dimensions and, when empty, are readily transported by truck, boat or rail. The 2.6 m × 6 m footprint for our reference tank is shown to scale in Fig. 4.79. To its right is shown one AD module resting on the AGV transporter.

The fluid pumps and flow meters are shown only schematically in the figure. Space is reserved for electronics racks for monitoring and control of the filling process.

Underground air contains radon and over time there can be a buildup of long lifetime radon daughters in the detector. We will make use of a radon free dry nitrogen system supplied as part of the LS Hall infrastructure. The N₂ gas will be used to continuously purge the AD module and the storage tanks. In an effort to reduce the overall level of Radon in the hall, its air supply will be obtained directly from above ground. That air will be conditioned and filtered to class 100,000 and fed into the LS Hall at a slightly elevated pressure compared to the access tunnel. Despite all these precautions we are concerned about the possibility that dirt will enter the detector volume during our manipulations of the filling probe. Both the probe itself and the acrylic vessels will be exposed to ambient air during the preparations for filling. Therefore we intend to construct a clean tent around the detector modules during filling. The present design shown in Fig. 4.79 consists of a tent with flexible cylindrical walls suspended from the ceiling.

The walls form a cylinder about the same diameter as the AD module and extends about one meter below its top surface. Air is filtered to class 10,000 and ducted into the top of the clean zone. A top to bottom laminar flow is established in the clean zone and will enable workers to prepare the AD module for filling. The entire tent assembly will be anchored to the ceiling. A system of ropes will allow the curtain wall to be bundled together in between module fillings and during the motion of the AD in and out of the LS Hall.

4.8.5 Materials Compatibility of Liquid Scintillator with the Target Mass Measurement and AD Filling System

The design of the AD filling and target mass measurement system will follow the general criteria for materials compatibility with mineral oil, liquid scintillator, and Gd-doped liquid scintillator. All elements of the system that have a chance of coming in long-term contact with the LS will be coated in Teflon, made out of Viton or acrylic. Long-term contact is defined as the exposure over several days, weeks, and months. Before and after use of the AD filling system it will be necessary to drain out unnecessary liquids and dry and backfill the entire system with boil-off nitrogen. Nevertheless some elements such as the reference tank may come in long-term contact with the Gd-LS. We expect it will be impossible to completely dry out this tank after each use. To avoid long-term effects one possibility is to line the reference tank with fluoropolymer coating. Reliable 1 mm thick coatings are available. See for example Fisher-Moore at <http://www.fluoropolymer.com> or <http://www.edlon.com>. In the baseline design of the AD filling and target mass measurement system we foresee the use of a Teflon-lined ISO tank. All pumps and piping will be made out of stainless, Viton, or Teflon.

4.8.6 Emptying the Antineutrino Detectors

During the normal operation of the experiment the ADs will only be emptied at the end of the experiment. The emptying of the ADs will also occur in the LS Hall. During the removal of the liquids from the ADs the same care needs to be taken in controlling the liquid levels so that the nested acrylic vessels are not damaged. During emptying of the ADs the liquids can either be pumped back into the liquid storage tanks or in other liquid containers that are positioned in the Hall or in the tunnel outside the LS Hall. Cleanliness control in the LS Hall during the de-commissioning of the experiment may not be as critical. It will depend on how the liquid scintillator from the ADs will be re-used or disposed of.

More challenging is the emptying of an AD in case of a critical repair on the AD before or during the experiment. In principle, the AD filling system can also be used to pump out the ADs. However, the intermediate storage of the liquids from the AD during the repair or maintenance period of the detector is a challenge. Also, the clean handling of the liquids will be critical to ensure that they can continue to be used in the experiment.

If the emptying of an AD becomes necessary we can either pump the liquids back into the LS and

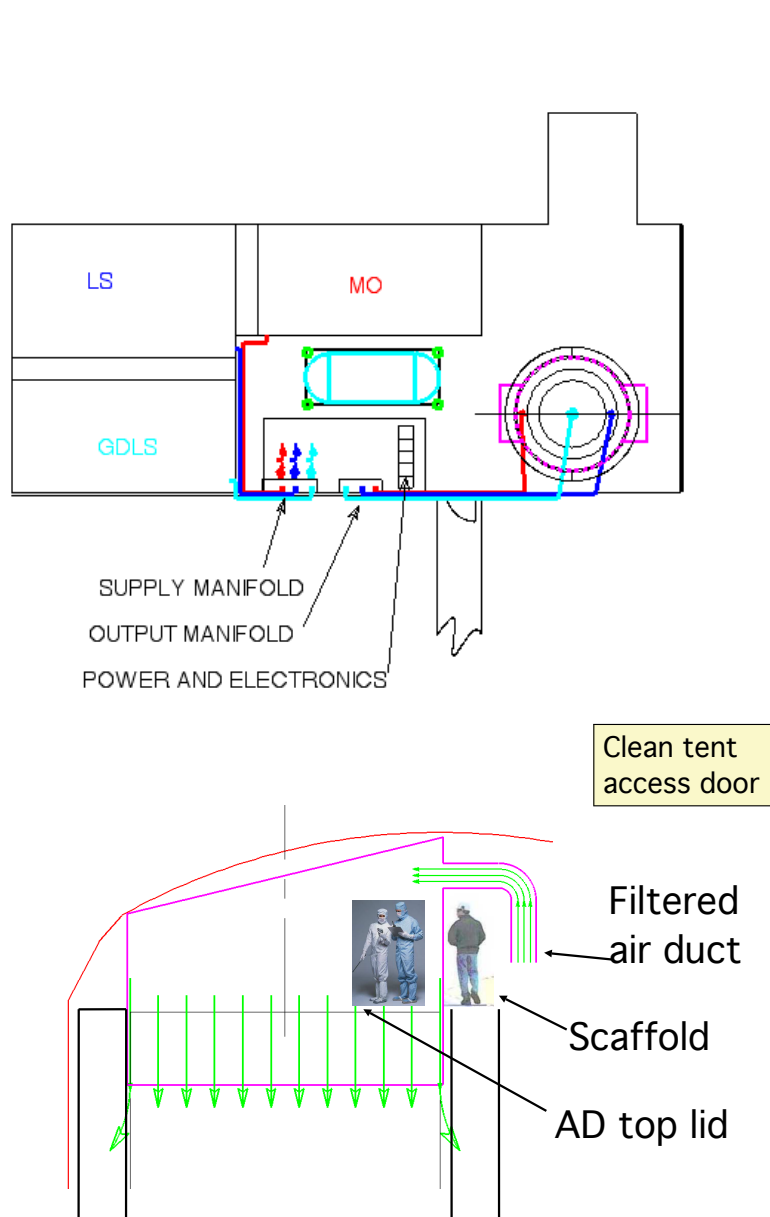


Fig. 4.79. Top panel: Layout of the LS Hall for the filling of the antineutrino detectors. The ADs will be filled one at a time from the MO, LS, and Gd-LS storage tanks. An ISO tank instrumented with load cells is used for the precision mass measurement of the Gd-LS target mass. Bottom panel: To prevent contamination of the inner detector and the Gd-LS during filling the top of the AD will be enclosed in a class-10,000 clean room. Personnel will enter the clean room to insert the AD filling probe and to connect the AD to the filling system.

Gd-LS 200 T storage tanks or find intermediate storage containers. There is a risk that the remaining liquid in the storage tanks could be contaminated if liquid is pumped out of the ADs back into those tanks. These scenarios will need to be considered carefully if these situations arise.

4.9 Risk Assessment

The design of the antineutrino detectors for the Daya Bay experiment is based on liquid scintillator technology and photomultipliers. This technology has been used in similar form in previous reactor antineutrino experiments such as KamLAND, Chooz, and others. A novel feature of the Daya Bay experiment is the concept of a 3-zone design with nested acrylic vessels that contain the γ -catcher and the target mass. The separation of the target in different volumes requires the leaktight separation of the target liquids into different volumes over the lifetime of the experiment. The long-term stability and integrity of the detector is of concern for a precision experiment with a predicted duration of operation of at least 3-5 years. In addition to the mechanical integrity of the detector, the long-term stability of the Gd-loaded liquids scintillator is of particular interest. To achieve the required statistical precision we require the experiment to operate for at least five years. To facilitate the construction of eight identical detector modules and to allow for the possibility of swapping, the detectors will be transported to the experimental halls after they have been assembled and filled. The detector systems and design issues that pose the highest risk are:

- **Acrylic Vessels:** The construction of eight nested acrylic vessels to contain the detector fluids with penetrations for calibration sources and other instrumentation is a non-trivial task. The acrylic vessels must meet stringent geometric and cleanliness specifications and be leak tight during detector filling, transport, and the entire duration of the experiment. *The construction of these vessels poses a schedule, cost, and physics risk to the experiment.*
- **Liquid Scintillator:** The experiment will use Gd-loaded and non-loaded liquid scintillator. Both must have good optical properties for the duration of the experiment. The baseline recipe and default synthesis and mixing procedure for the Gd-loaded scintillator has been chosen. A large-scale production process that allows the production of 200 T of Gd-loaded liquids scintillator is under development. The long-term stability and compatibility with materials in the antineutrino detector is of particular concern. *The production of the liquids scintillators is mostly a schedule and physics risk to the experiment.*
- **Transportation and Lifting:** A novel concept of this experiment is the transport of the fully-assembled and filled detectors over distances of up to 2 km to the experimental halls. It is critical not to damage or alter the detector during this process. While engineering studies have established the feasibility of this approach it is an unproven concept. Much of the ongoing R&D is dedicated towards understanding the detector response during transport and developing instrumentation to monitor the detector during the movement. *We consider the transport and lifting mainly a physics risk.*
- **PMT, Bases and Cables:** The risks involved in the delivery schedule are minimal. The main risk is the delay in availability of funding. The production work will not start without the funding. In addition there is a minor risk due to the fact that 50% of the initial production effort coincides with holidays in the US. This could reduce the initial delivery to about 250. Every effort will be made to start the fabrication as early as possible in FY08 to avoid these delays. Additional risks involve failure of a certain percentage of the PMT/base assemblies due to improper sealing or breakage of PMT bulbs. Based on past experience we expect these to be at a level of less than 0.2%. Note that PMT failures, while rare, will be detected before the bases are glued in permanently. This detection will be done in two distinct stages:
 1. During the initial physical inspection stage after the delivery of the PMTs

2. During the PMT burn-in process. During this period each PMT/base will be tested with LED pulsers for a duration of 2–4 weeks.

Our proposed R&D in 2008 will address these critical issues and focus on mitigating the risks associated with the above described detector elements.

4.10 R&D Plan

4.10.1 PMT System

The photomultiplier tube is one of the critical elements of the detector system. Therefore it is important to understand its performance in the antineutrino detector as well as the muon Cherenkov system to the required systematic precision of the experiment. An extensive R&D program is underway to develop or measure the following. Much progress has been made on these items in 2007:

- Study the characteristics of the PMT that are the most important to Daya Bay i.e. single photoelectron response of the PMTs, peak to valley ratio, absolute gain, dark current/pulse rate vs. high voltage, linearity vs. pulse height, stability, absolute quantum efficiency, variation of quantum efficiency vs. position, effect of magnetic field on s.p.e. and gain.
- Measure the radioactivity of materials used in the PMT (radioassay for the candidate PMTs) and associated hardware.
- Develop and optimize PMT bases: optimize linearity in the required dynamic range of the experiment. Reduce internal ringing due to dynode capacitance and minimize external reflections due to the base.
- Study the effect of prolonged exposure of PMT glass to the highly purified water and mineral oil under pressure.
- Develop a reliable water-proof base to be used in the water Cherenkov detector.
- Develop several automated large-scale PMT test setup (about 50 PMTs at time) for onsite PMT testing and characterization based on pulsed UV LEDs.
- Develop a signal-HV decoupler system.
- Characterize coaxial cables for underwater/oil operations, signal attenuation and low-noise operation.
- Develop and optimize a mu-metal shield for the PMTs.
- Develop support structures for the PMTs to allow easy installation and alignment of the PMTs in the antineutrino detector and muon systems. While we do not foresee prototyping a complete PMT support structure, we plan to build individual PMT mounts and test them with selected PMTs.
- Develop and test a waterproof cable feedthrough or suitable cable patch panel for all PMT cables coming out of the antineutrino detector.
- Develop QA procedures for final onsite testing and characterization of the PMTs.

Many of these tasks are currently underway and some results are documented in the Section 4.6.

4.10.2 Acrylic Vessels

The antineutrino detector uses a pair of nested acrylic vessels to contain the target mass and provide high-efficiency for the detection of antineutrinos. The design, fabrication, and assembly of the nested acrylic vessels is a unique technical challenge. It requires precision and tight tolerances as well the flexibility to accommodate the dynamics of a moving detector. The collaboration plans to prototype the critical elements of the vessels and test them for structural strength, integrity, and leak tightness. This R&D program will be performed jointly between the US, China, and Taiwan. The University of Wisconsin and the Physical Sciences Laboratory plans to design the critical and high-risk elements shown below. In parallel, collaborators from National Taiwan University will work closely with Nakano Ltd. in Taiwan to prototype these parts, seek their engineering input, and test the manufacturing process of these items.

- Fabricate and test a full-size, bolted acrylic flange with O-ring seal for the connection of calibration ports.
- Fabricate and test a full-size acrylic penetration of a calibration pipe through the top of a vessel with a suitable O-ring or U-seal.
- Design, prototype, and test alternative seals such as U-seals, silicone seals, etc.
- Develop and test of a flexible coupling between the acrylic tanks and the steel tank such as a composite coupling using corrugated Teflon tubing.
- Design and construct a full-size prototype overflow tank with ports for liquid monitoring instrumentation.
- Machine and test a prototype flange for a removable lid to the acrylic vessels.
- Test the machining capabilities for a conical top/bottom to the acrylic vessel.
- Test the structural strength and properties of acrylic ribs, feet, or vessel support structure.
- Fabricate a prototype reflector using a sandwiched construction of highly reflective film between two acrylic plates. The adhesive to bond this structure and risk of possible air gaps needs to be studied.
- Perform extensive materials compatibility tests of acrylic with Gd-loaded liquid scintillator and undoped liquid scintillator studying both the optical as well as the structural properties.
- Characterize the optical properties of possible acrylic supplies through a series of systematic and well-characterized transmission measurements.

4.10.3 Instrumentation&Monitoring

Measurement of the target mass and monitoring of the state of the antineutrino detector during assembly, filling, and operation is key to understanding the systematics of the experiment. We plan to test individual units of all key instrumentation of the antineutrino detector prior to their installation in the detector. Key instrumentation tests will include the following:

- Accuracy and long-term stability of load cells and flowmeters for target mass measurements.
- Accuracy, reliability, and materials compatibility of liquid level sensors in overflow tanks.
- Test laser surveying method for determining the as-built geometry of the acrylic vessel.
- Test leak tightness of windows in tank against oil for visual monitoring.
- Characterization of accelerometers and motion monitor for detector transport and lifting.

4.10.4 Assembly&Integration

The antineutrino detector will consist of a pair of nested acrylic vessels inside a steel tank surrounded by a structure of photomultipliers. The nested geometry and multiple zones of the detector pose unique challenges to the assembly and integration of all subsystems. During the R&D phase in 2007 we will develop a procedure for the assembly of the detector paying particular attention to the mitigation of assembly risks and the reduction of labor intensive steps which could pose risks for human errors and schedule. A small-scale, simplified mockup model of the detector may be built to develop and practice the assembly sequence of the Daya Bay antineutrino detector and better understand the assembly sequence.

4.11 Manufacturing Plan

The antineutrino detector is jointly designed and built between the China, Taiwan, Russian, and US groups of the Daya Bay collaboration. Figure 4.80 shows the contributions of the various countries in terms of detector subsystems. In this subsection we outline the manufacturing plan for the detector and its subsys-

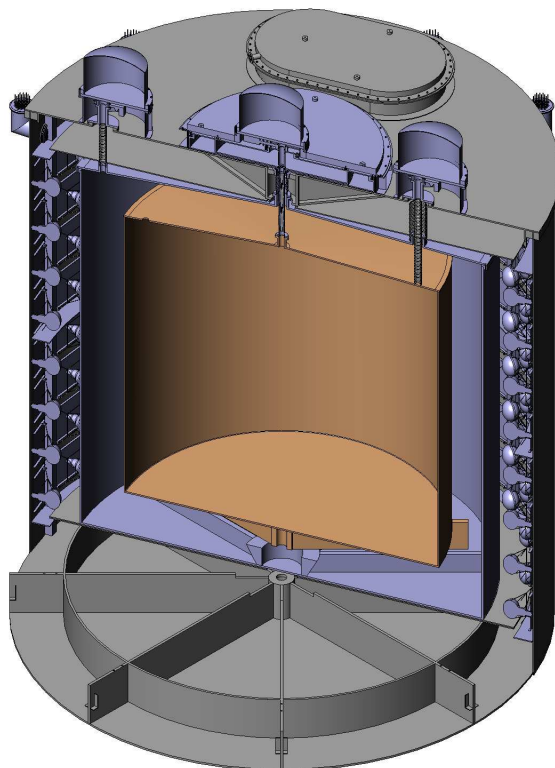


Fig. 4.80. Color-coded model of the antineutrino detector showing the various contributions to the detector from the different countries: China (grey), US (blue), and Taiwan (yellow).

tems:

- **Detector Tank:** The detector tank is a stainless steel construction that provides the outer support for the inner acrylic vessels and liquids. The detector tank will be designed and manufactured in China. The steel tank will be welded and constructed at the manufacturer and shipped to the Daya Bay site as a complete assembly. Some parts of the detector lid and the steel tank are provided by the US.

This includes the flanges for the PMT cable feedthrough connections and some flanges on top of the stainless lid as specified in the Memorandum of Understanding. These parts will be manufactured or procured in the US and delivered to China as specified in the integrated project schedule. Once the tank arrives on-site it will be cleaned and prepared for the detector assembly in the cleanroom of the surface assembly building. Preparations of the tank in the SAB prior to the assembly of the detector include:

- cleaning of the tank's inside
- survey of inner and outer tank dimensions
- lubrication of all threads on the inside with compatible, clean mineral oil

- **PMT Cables, Feedthroughs, and Routing:**

The PMT cable feedthroughs, dry boxes, and hardware for the routing of the AD PMT cables will be fabricated in the US under the supervision of the University of Wisconsin. The interface flanges that represent the mounting points for the PMT cable feedthroughs and dry boxes will be machined in the US and delivered to China for welding into the steel tank. The AD PMT cables will be procured through the University of Wisconsin and then shipped to Douglas Electric for the attachment of the seal plugs. The seal plugs form the core of the cable penetration. The leak plugs will then be leak tested at UW-PSL before the cables are shipped to the base assembly location (external vendor in the US) where they will be soldered to the bases. In the case of the muon system these boards will be first installed into potting shells, the cables will be fed through, and soldered to the PC boards. At this point the cables will have the cable strain relief glued into them by Douglas electric. After the cables have been attached to bases, this assembly will be shipped to the US institution in charge of the base testing, at which point they will be tested with HV and will be conformally coated. They will then be shipped to Dongguan University where after the testing they will be coated with Epoxy (along with the bottom portion of the PMT). In the case of muon potted bases they will be potted with Epoxy. These operations will be performed at Dongguan University. The mechanical hardware for the PMT feedthroughs, the surrounding dry boxes and the AD PMT cable trays in the water pool, are fabricated or procured in the US and shipped directly to Daya Bay for installation.

The PMT cables and seal plugs form an integral unit. The fabrication and assembly sequence for the AD PMT cables is as follows:

- order coax cables and connectors
- ship to Douglas Electric
- Douglas Electric adds seal plug, connectors, and end treatment
- Receive and leak check cable plug assemblies at UW-PSL
- Ship to assembly house for attaching PMT cables to PMT base
- Test base+cable assemblies with HV
- Conformal coating of base
- Ship base+cable assembly to Dongguan University
- Test PMT+base+cable assembly at Dongguan University

- **Acrylic Vessels:** The design of the acrylic vessels is done by the US together with engineering support from China and Taiwan. Two manufacturers for the acrylic vessels have been identified: Reynolds Polymer Technology in Grand Junction, Co, USA and Nakano, Gold Aqua in Taiwan. The default plan

is to build the 3-m vessel at Nakano and the 4-m vessel and related support structures at Reynolds. The acrylic vessels will be shipped individually to Daya Bay and assembled into a nested pair on-site. Preliminary cleaning of the acrylic vessels and hardware will be done by the manufacturer during and after fabrication. The vessels will then be packaged under cleanroom conditions and prepared for transport. Multiple layers of wrapping and packaging will allow us to protect the cleanliness of the acrylic vessels during transport. At Daya Bay the acrylic vessels will be moved into the SAB and unwrapped layer by layer as they are moved inside the cleanroom. The layered packaging will ensure that the vessels can be kept clean during the receiving process and during the preparation for assembly. Specialized acrylic hardware including acrylic bolts, flanges, and overflow tanks may also be fabricated elsewhere. In this case we will attempt to choose the same UV transmitting Lucite.

- **Reflector:** The reflectors increase the light collection and energy resolution. They consist of a reflective foil sandwiched between acrylic plates. China will design and fabricate the reflectors for the antineutrino detector and ship them to Daya Bay.
- **Overflow Tanks:** Overflow tanks outside the antineutrino detector are needed to accommodate the expansion of detector fluids during temperature variations. The MO overflow tanks will be made out of stainless steel. They are integrated into the stainless steel structure of the lid. The overflow tanks for the LS and Gd-LS must be fabricated out of acrylic to meet the materials compatibility requirements with the detector liquids. They will be manufactured at Reynolds Polymer Technology, or some other suitable manufacturer in the US. We plan to use the same acrylic for the overflow tanks as for the main acrylic vessels to minimize the number of different materials that will come in contact with the liquid scintillator. The tanks are to be instrumented with liquid level sensors and temperature sensors to precisely monitor the target mass inside the detector and the overflow volumes. The overflow tanks and related instrumentation are designed by the University of Wisconsin and PSL together with IHEP. Their design is closely related to the design of the acrylic vessels and the steel detector tank. The LS and Gd-LS overflow tanks will be manufactured and assembled in the US, tested for leaktightness, and then cleaned and packaged before shipment to Daya Bay. We plan to perform as much of the assembly and testing work in the US so that on-site activities can be minimized.
- **Liquid Scintillator:**
 - 0.1% Gd-loaded liquid scintillator for inner antineutrino target: The Daya Bay Project selected a baseline plan for its Gd-LS production in July 2007 and will prepare 200 T of 0.1% Gd-LS on-site. Several key R&D studies related to the Gd-LS quality and large scale liquid processing in the LS Hall must be completed as described in Section 4.4. With the current schedule of filling the first pairs of detector modules in early 2009 and the anticipated production time of three months, the production is scheduled to start in August 2008.
 - Unloaded LS for γ -catcher: Two linear-alkyl-benzene (LAB) manufacturers, Fushun in China and Petresa in Canada, have been approached by IHEP and BNL. Both suppliers are capable of providing \sim 400 T of LAB with a short turn-around time (for example, the yearly production of Petresa LAB is \sim 120,000 T) and working closely with Daya Bay scientists. LAB samples drums provided from both companies have been tested at IHEP and BNL. The chemical qualities of LAB from both vendors are rather similar and proven to be satisfactory. Daya Bay will continue the studies and will select the final supplier in October 2008.
 - Mineral oil for buffer region: mineral oil will be purchased from China and delivered to the Daya Bay site without any further chemical processing. The batch-to-batch variation of the chemical properties and quality for mineral oil is well known. IHEP and BNL will impose quality-

assurance criteria for the acceptance of mineral oil from the vendor. We expect to accumulate 400 T of mineral oil in six months, starting in January 2009.

- **PMT Support Structure: Mounts and Ladders** The PMT support structure will be designed by the US and fabricated either in the US or China. This is yet to be decided taking into account cost and logistics considerations as well as the PMT support requirements. The fabrication and delivery of the PMT supports is US scope. The University of Wisconsin, UCLA, and Berkeley are currently working together on a design that meets the PMTs specifications and installation requirements for the antineutrino detector. This work is done in close collaboration with the IHEP group in China to define the interface points with the stainless steel tanks. Lawrence Berkeley National Laboratory leads the design of the PMT support structures and will oversee the fabrication and shipment to Daya Bay China. The PMT mounts and ladders will be fabricated and pre-assembled before shipment to Daya Bay. The final assembly of the PMTs into the mounts and their installation on the ladders will take place in the SAB at Daya Bay.
- **PMTs and bases:** The PMTs will be procured by UC Berkeley/LBNL and tested by Berkeley, UCLA, and other institutions. Some of the testing work will be done in China in collaboration with university groups. The bases for the PMTs will be designed and manufactured at UCLA. The potting of the PMT bases will be performed in China.

The mechanical parts of the water-proof, potted PMT base housings will be designed and fabricated at UCLA. The design will be developed as part of the ongoing Daya Bay R&D and start in April 2007. We expect to complete the design and prototyping of these bases by the end of July 2007. Based on similar designs, the UCLA machine shop has estimated that the production of each mechanical housing will take ~ 2.5 hours. Assuming availability of funding by Oct 1 2007, we expect to produce 100–200 housings per month after an initial setup period of 1 month. This will result in delivery of 100–200 units per month starting early January 2008.

The PMT base printed circuit fabrication and the assembly will be done by external vendors. Based on past experience we expect that by January 2008 we will have 500 PMT bases tested and available for shipment to China. The remaining bases could be delivered at a rate of 200–400 units per month following the initial delivery.

The PMT base printed circuit boards and the housings will be assembled in China mainly by the Chinese members of the Daya Bay collaboration. The assembly process involves attachment of the PMT bases to the PMTs and injecting the housings with potting compound. This will result in a sealed PMT assembly. The procedures and quality assurance steps to pot and seal the PMT-base assemblies will be developed during the initial design and prototyping of the bases. Therefore, an initial 100% underwater testing program of the first 20–50 assemblies followed by a random sample testing of 5% of the assemblies should suffice to insure the integrity of the seals.

- **Monitoring Instrumentation:** The monitoring instrumentation for the antineutrino detector is mostly commercially available. R&D and testing of this instrumentation is currently being performed at the University of Wisconsin and the Physical Sciences Laboratory as well as IHEP and other Chinese universities. UW and IHEP will oversee the design of the instrumentation package and coordinate its procurement and integration into the detector design. The instrumentation for the AD will be procured and provided by China and the US as outlined in the Memorandum of Understanding. After appropriate tests at the responsible institutions the instrumentation will be shipped to Daya Bay where it can be integrated into the antineutrino detector
- **AD Filling and Target Mass Measurement System** This system will be designed, assembled, and tested at UW-PSL and then shipped to Daya Bay.

The assembly, filling, and installation of the antineutrino detectors is described elsewhere.

4.12 Quality Assurance During Fabrication and Assembly

The detectors will be built in a worldwide collaboration. Fabrication of subsystems will take place in the US, China, and Taiwan. A few materials will also be procured from Russia. To ensure the quality and performance of the assembled antineutrino detector a few guiding principles will be followed. We distinguish between the fabrication and assembly phase. During the fabrication phase the manufacturers carry the responsibility to meet the specifications of the collaboration. The Daya Bay subsystem managers will oversee the manufacturing process and enforce quality assurance. In the assembly phase, however, the Daya Bay collaboration carries the overall responsibility of defining the assembly process and finding a team of scientists, engineers, and technicians with the right set of skills to perform the assembly. For the US subsystems the assembly will be performed by a team of expert engineers and scientists with support of the Daya Bay integration team and local technician support from China. The ultimate responsibility for the successful detector assembly will be with the L2 managers.

Fabrication of Subsystems

- During the design and R&D phase the Co-L2 managers of the detector will visit potential vendors, establish working relationships, and personal contacts. Local collaborators preferably at the L3 level will be the point of contact and responsible person for overseeing the fabrication of a part or subsystem in a respective country. In some cases design and fabrication will be done in different countries. In this situation it is important for the groups responsible to understand the manufacturing capabilities in advance and vice versa. The R&D phase will be used to develop a manufacturing plan and establish working relations between the design groups and manufacturing facilities.
- The fabrication of all parts and subsystems of the detector will follow detailed written specifications and milestones in English. If specifications in languages other English are required a translated document will be prepared with the same level of technical detail. Translation services may be used for translating the technical documents.
- Procedures and quantitative measures for the quality assurance of all parts and subsystems will be developed by the L2 and L3 managers.
- For each part or subsystem a set of milestones will be developed during the R&D phase and written into the manufacturing plan.
- During the fabrication the L2 detector managers together with local L3 contacts will regularly visit the fabrication sites to review quality assurance and fabrication progress. Regular phone conferences will aid in updating the task groups on progress and discussing manufacturing and quality problems as they arise.
- A document summarizing the as-built characteristics and results from all quality assurance tests will be prepared for all subsystems and made available to the collaboration.

Assembly of the Antineutrino Detector

- The assembly of the antineutrino detectors will follow strict written procedures that are developed by the detector group and approved by the L2 managers and the collaboration prior to the assembly on-site.
- Electronic and paper check sheets will be used to organize the assembly effort.

- A Daya Bay collaborator with scientific and technical experience (preferably the L2 managers or designated representative) will be present on-site during the entire assembly process for the antineutrino detector to discuss and approve any change in the assembly procedure. It is unavoidable that certain decisions regarding the assembly have to be taken in real-time and cannot first be discussed via phone or video conference. In addition, we require that L3 managers (or designated representative) will be on-site and available for discussion when their respective subsystem is integrated into the antineutrino detector.
- Regular phone and video conferences will be used to monitor the assembly progress and inform the collaboration.

4.13 ES&H

A discussion of the hazard analysis and safety considerations for the antineutrino detector systems is given in Chapter 13 and the separate document Daya Bay Project Hazards Analysis Document (HAD).

REFERENCES

1. E.H. Bellamy *et al.*, Nucl. Inst. Meth. A339, 468 (1994).
2. M. Apollonio *et al.* (Chooz Collaboration), Phys. Lett. B420, 397 (1998); Phys. Lett. B466, 415 (1999); Eur. Phys. J. C27, 331 (2003).
3. <http://www.3m.com/product/information/Vikuiti-Enhanced-Specular-Reflector.html>
4. <http://anomet.com/cgi-bin/online/storepro.php>
5. <http://www.detectors.saint-gobain.com/>
6. <http://www.texloc.com/corrugated.html>
7. Boehm *et al.* (Palo Verde Collaboration), Phys. Rev. Lett. 84, 3764 (2000) [arXiv:hep ex/9912050]; Phys. Rev. D62, 072002 (2000) [arXiv:hep-ex/0003022]; Phys. Rev. D64, 112001 (2001) [arXiv:hep-ex/0107009]; A. Piepke *et al.*, Nucl. Instr. and Meth. A432, 392 (1999).
8. H. Back *et al.* (LENS-Sol Collaboration), Proceedings of the 5th International Workshop on Neutrino Oscillations and Their Origin (NOON 2004), World Scientific Publishing Co., Eds. Y. Suzuki, M. Nakahata, S. Moriyama, Y. Koshio (University of Tokyo, Japan), June 2005.
9. M. Yeh, A. Garnov, and R. L. Hahn, Nucl. Instr. and Meth. A578, 329 (2007).
10. C. Kraus, *et al.* (SNO+ Collaboration), Prog. Part. Nucl. Phys. 57 (2006) 150–152.
11. M. Yeh, R. L. Hahn, A. Garnov, and Z. Chang, AIP Conf. Proc. 785 (2005) 209.
12. M. Yeh, A. Garnov and R. L. Hahn, Gadolinium-Loaded Liquid Scintillator for High-Precision Measurements of Antineutrino Oscillations and the Mixing Angle, θ_{13} , submitted to Nucl. Instr. and Meth. A (2006)
13. R. L. Hahn, Prog. Part. Nucl. Phys., 57 (2006) 134–143.
14. K. Eguchi *et al.* (KamLAND Collaboration), Phys. Rev. Lett., 90 (2003) 021802 [arXiv:hep-ex/0212021]; 94 (2005) 081801 [arXiv:hep-ex/0406035].
15. <http://www.hamamatsu.com/>.
16. <http://www.electrontubes.com/>.
17. C. Arnaboldi, and G. Pessina, Nucl. Instr. Meth. A512, 129 (2003).
18. J. Boger *et al.* (SNO Collaboration), Nucl. Instr. and Meth. A449, 172 (2000).
19. <http://www.emcohighvoltage.com/>.
20. Gold Aqua, <http://www.goldaqua.com>
21. Nakano Ltd. <http://www.nakano.com.tw>
22. Reynolds Polymer Technology, Inc. <http://www.reynoldspolymer.com>
23. www.fluent.com

5 Calibration and Monitoring Systems

The measurement of $\sin^2 2\theta_{13}$ to a precision of 0.01 in the Daya Bay experiment will require extreme care in the characterization of the detector properties as well as frequent monitoring of the detector performance and condition. The physics measurement requires that the neutrino flux be measured with *relative* precision that is substantially better than 1%. This is accomplished by taking ratios of observed event rates in the detectors at near and far sites to identify the oscillation effects. This will require that differences between detector modules be studied and understood at the level of $\sim 0.1\%$ and the changes in a particular detector module (over time or after relocation at another site) be studied and understood at $\sim 0.1\%$. Achieving these goals will be accomplished through a comprehensive program of detector calibration and monitoring, as described previously in Section 2.2.2.

5.1 Radioactive Sources

The response of the detectors at the far and near sites may have small differences, which can lead to distortions in the measured anti-neutrino energy spectra. Therefore, it is necessary to characterize the detector properties carefully before data taking and monitor the stability of the detectors during the whole experiment. Calibration sources must be deployed regularly throughout the active volume of the detectors to simulate and monitor the detector response to positrons, neutron capture gammas and gammas from the environment.

Sources that will be used in the calibrations are listed in Table 5.1. These sources cover the energy range

Sources	Calibrations
Neutron sources: Am-Be, ^{252}Cf , Pu(C)	Neutron response, relative and absolute efficiency, capture time
Positron sources: ^{22}Na , ^{68}Ge	Positron response, energy scale trigger threshold, and PMT QE (relative)
Gamma sources: H neutron capture ^{22}Na ^{60}Co Am-Be $^{238}\text{Pu}-^{13}\text{C}$ Gd neutron capture	Energy linearity, stability, resolution spatial and temporal variations, quenching effect 2.223 MeV annih + 1.275 MeV 1.173 + 1.333 MeV 4.43 MeV 6.13 MeV ~8 MeV

Table 5.1. Radioactive sources to be used for calibrations. All of these sources can be used in the manual calibration system with few constraints on the source activity. For the automated calibration system, we choose to use ^{68}Ge and low rate ^{252}Cf neutron sources.

0.5–10 MeV and thus can be used for a thorough energy calibration.

The Am-Be source can be used to calibrate the neutron capture detection efficiency by detecting the 4.43 MeV gamma in coincidence with the neutron. The $^{238}\text{Pu}-^{13}\text{C}$ source will similarly provide a 6.13 MeV gamma in coincidence with the neutron. The absolute neutron detection efficiency can be determined with a ^{252}Cf source, because the neutron multiplicity is known with an accuracy of about 0.3%. The delayed neutron capture signal provides the energy scale calibration at ~ 8 MeV (n-Gd) and 2.2 MeV (n-H). In addition, neutron sources allow us to determine the appropriate thresholds for neutron detection and to measure the neutron capture time for the detectors.

The positron detection threshold can be calibrated by a ^{68}Ge source. ^{68}Ge decays via electron capture into ^{68}Ga , which then immediately decays and emits positrons. The ionization energy of the positron will be absorbed by a layer of polyethylene, and the two 511 keV annihilation gammas which can be used to calibrate the threshold for positron detection.

All sources will be encapsulated in small containers to prevent any possible contamination to the ultra-pure liquid scintillator. They can be regularly deployed at known locations in the target and γ -catcher. The detailed geometry of the sources will be described in Section 5.5 (see Fig. 5.8).

5.2 LED Calibration System

LEDs have proven to be reliable and stable light sources that can generate fast pulses down to ns widths at similar wavelengths (430 nm) to the light propagating in liquid scintillator from ionizing radiation. They are therefore ideal light sources for checking the optical properties of the liquid scintillator, the performance of the PMTs and the timing characteristics of the data acquisition systems. The features of the LED calibration system are described briefly below.

1. T_0 : The diffuser ball on the central axis of the detector module will be lowered to the level of each ring of PMTs and then light pulses of a full width of about 5 ns are emitted to set the t-zero of events for that ring of PMTs.
2. Optical attenuation length: The calibration PMTs at the top/bottom of the detector will measure the light intensity emitted from the descending central diffuser ball to monitor the light attenuation length of the Gd-LS. Similarly the diffuser ball and calibration PMT in the γ -catcher will monitor the light attenuation length of the LS in the γ -catcher (see Fig. 2.3).
3. PMT gains: The gains of the PMTs are monitored by lowering the central diffuser ball to the appropriate ring of PMTs and then pulsing the LEDs to give single photoelectron signals in the PMTs.
4. The LED pulser can be triggered after an muon passing through the detector to test the electronics response following energetic muon events.

The LED driver will be triggered by an external TTL trigger pulse. During an automated calibration cycle (see description in Section 5.5), the same pulse will also trigger the anti-neutrino detector DAQ. The LEDs will be sealed inside spherical diffuser balls, which will emit blue light isotropically. The deployment scheme for the diffuser balls is illustrated in Fig. 5.1. A diffuser ball can be automatically lowered to any height through three ports at different radial position at the top of the detector. There will also be three diffuser balls located at fixed vertical positions in the oil buffer, as shown in Fig. 5.1. Six 2" low background PMTs (e.g. Electron Tubes 9813B) are located at the top and bottom of the detector tank. As elaborated in Section 2.2.2.5, these PMTs will be used together with the LED system to measure the optical properties of the detector. These 2" PMTs will be using the same electronics as the main 8" PMTs. They will be constantly read out by the DAQ during normal and calibration running.

The LED automated deployment system is illustrated in Fig. 5.2. The driver board will be mounted on the rotating wheel that deploys the LED. The external trigger pulse (TTL, about 100 ns in width) will come in through a coaxial cable, transmitted through an electric slip ring onto the wheel and driver board. A thin and flexible coaxial cable will be attached to the board on one end, while the other end is attached to the LED (sealed in the diffuser ball). The coaxial cable winds on the deployment wheel and through the pulley, which serves as the deployment cable as well.

We have selected a commercial laser diode driver board from Directed Energy, part No PC0-7110-40-4, with a 430 nm LED by Industrial Fiber Optics (IF-E92A). A vendor for very thin (0.4 mm OD) coaxial cable with a Teflon jacket has also been identified (Cooner Wire). The timing characteristics of the LED has

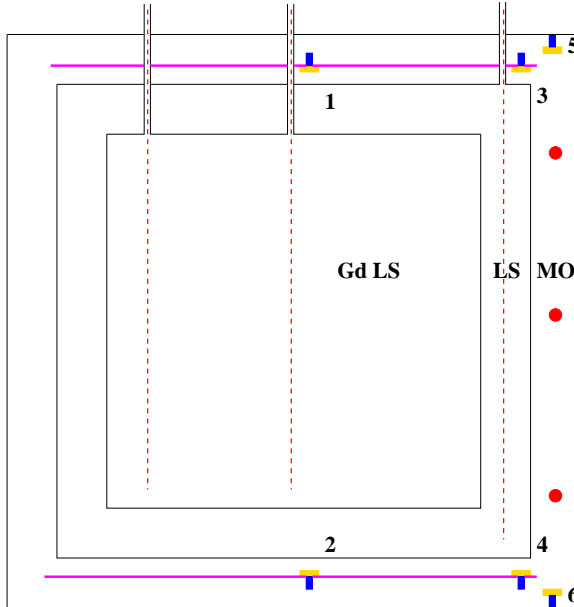


Fig. 5.1. Same figure as Fig. 2.3. A diagram illustrating the deployment scheme for the LED diffuser balls. Three vertical dashed lines indicate the range of the automated deployment axes. The red balls represent the fixed diffuser balls in the oil buffer. The 2" calibration PMTs are shown as blue blocks with yellow faces. The magenta thick lines on the top and bottom represent the reflectors.

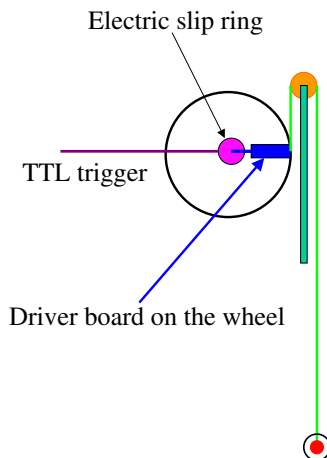


Fig. 5.2. Conceptual diagram of the LED deployment system.

been studied. Fig. 5.3 shows a scope capture of the LED light flash (~ 10000 photons per pulse) detected by a 2" phototube *. The TDC spectrum (started by the trigger pulse when the same light pulse was filtered down to single photoelectron level) is given in Fig. 5.4. One observes rise and fall times of 1.6 ns and 2.7 ns respectively, which is sufficiently fast for the purpose of T_0 calibration. The impact of the slip ring on the

*To minimize the timing width, a small inductor (~ 100 nH) was mounted in parallel with the LED and coaxial cable assembly.

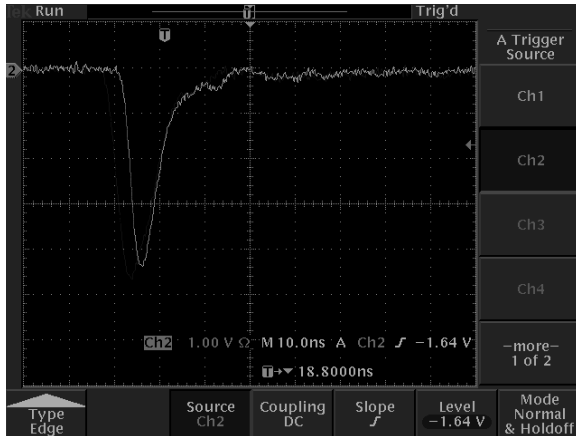


Fig. 5.3. Scope capture of the LED light pulse detected by a phototube.

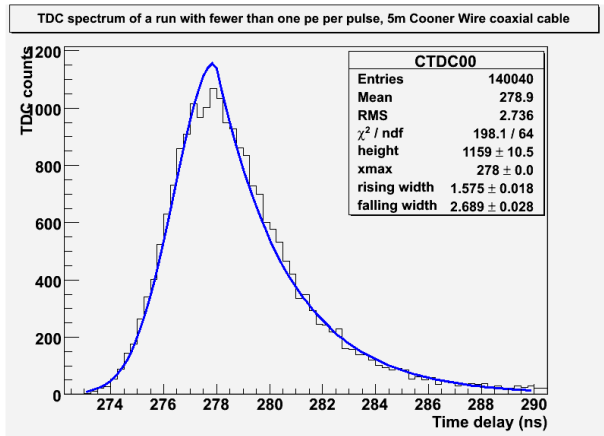


Fig. 5.4. TDC spectrum of the LED light pulse. For details see text.

timing characteristic of LED light pulses has also been studied. No difference is observed in the LED light timing when the TTL trigger signal is transmitted directly onto the board or through the slip ring.

The diffuser ball is an acrylic spherical shell filled with nanoparticle-loaded epoxy. The LED is sealed inside the acrylic ball, and the junction is sealed by glue and reinforced by a concentric Viton and acrylic tube. A Teflon heat shrinkage tube provides final protection of the junction. The coaxial cable/LED/diffuser ball assembly will be fully compatible with the liquid scintillator. A small weight (stainless steel with an acrylic shell) will be attached to the diffuser ball to hold the cable straight during the deployment while minimizing the light obstruction.

5.3 In-situ Detector Monitoring

Each detector module will be equipped with a suite of devices to monitor in-situ some of the critical detector properties during all phases of the experiment. The in-situ monitoring includes load and liquid sensors for the detector mass, attenuation length measurements of the Gd-LS target and the LS γ -catcher, a laser-based monitoring system for the position of the acrylic vessel, accelerometers, temperature sensors, and pressure sensors for the cover gas system.

The purpose of these tools is to monitor the experiment during three critical phases:

1. detector filling
2. data taking
3. detector transport and swapping

During filling of the modules, the changing loads and buoyancy forces on the acrylic vessels and the detector support structure are carefully monitored with load and level sensors to ensure that this dynamic process does not exceed any of the specifications for the acrylic vessels.

Most of the time during the experiment the detectors will be stationary and taking data. Experience from past experiments has shown that the optical properties of detectors will change over time due to changes in the attenuation lengths of the liquid scintillator or changes in the optical properties of the acrylic vessel. It is important to track these characteristics to be able to explain any possible changes in the overall detector response as determined in the regular, automated calibration. In-situ monitoring of the LS attenuation length and regular extractions of LS samples from the detector modules will help monitor some of the basic detector properties.

The transport of the filled detectors to their location and the swapping of detectors over a distance of up to ~ 1.5 km is a complex and risky task that will require close monitoring of the structural integrity of the detector modules during the move. The proposed swapping scheme of the detectors is a novel method without proof-of-principle yet. While conceptually very powerful, extreme care has to be taken in the calibration and characterization of the detectors before and after the move to be able to correct for all changes in the detector response or efficiencies. The accelerometers, pressure sensors, and the monitoring of the acrylic vessel positions will provide critical real-time information during this procedure to ensure that the detectors — and in particular the acrylic vessels and PMTs — are not put at risk. Recording any changes in the detector modules will also help us understand possible differences in the detector response before and after the move. The acrylic vessel position monitoring system will use a laser beam and reflective target on the acrylic vessel surfaces. By measuring the angular deflection of the laser beam over the length of the detector, transverse displacements of the acrylic vessel can be monitored quite precisely.

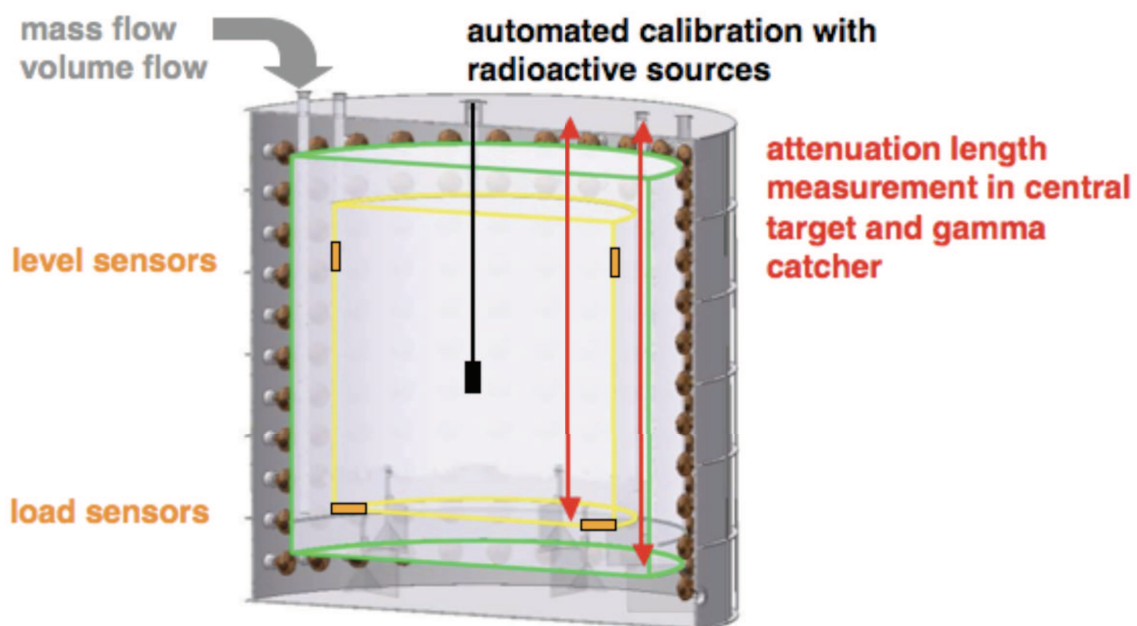


Fig. 5.5. Diagram illustrating the variety of monitoring tools to be integrated into the design of the antineutrino detector modules.

5.4 Detector monitoring with data

Cosmic muons passing through the detector modules will produce useful short-lived radioactive isotopes and spallation neutrons. These events will follow the muon signal (detected in the muon system as well as the detector) and will be uniformly distributed throughout the detector volume. Therefore, these provide very useful information on the full detector volume which is complementary to the information obtained by deploying point sources (see Sections 5.5 and 5.6). For example, such events are used by KamLAND to study the energy and position reconstruction as well as to determine the fiducial volume. As with KamLAND, the Daya Bay experiment will use primarily spallation neutron capture and ^{12}B decay ($\tau = 29.1$ ms and $Q = 13.4$ MeV). The rates of these events for Daya Bay are given in Table 2.5.

Regular monitoring of the full-volume response for these events, compared with the regular automated source deployments, will provide precise information on the stability (particularly of optical properties of the detector, but also general spatial uniformity of response) of the detector modules. With the addition of

Monte Carlo simulations, this comparison can be used to accurately assess the relative efficiency of different detector modules as well as the stability of the efficiency of each module.

The spallation neutron events are particularly valuable as they provide an abundance of neutron capture events following cosmic muon events. In addition to accurately monitoring the stability of the 8 MeV capture signal, these events will facilitate monitoring of the relative neutron capture time. As discussed in Section 2.2.3.4, this parameter is directly related to the fraction of Gd captures which is a component of the neutron detection efficiency. Monitoring the stability of this quantity provides an important constraint on the variation of the neutron detection efficiency. For the near sites, we will obtain sufficient statistics in about three days to constrain the Gd capture fraction to 0.1%. For the far detectors, we will need about one month to reach this precision.

5.5 Automated Deployment System

Automated deployment systems will be used to monitor all detector modules on a routine (weekly or bi-weekly) basis. Each detector module will be instrumented with three identical automated deployment systems. Each system will be located above a single port on the top of the detector module, and will be capable of deploying three different sources into the detector volume (see Fig. 5.6). This will be facilitated by

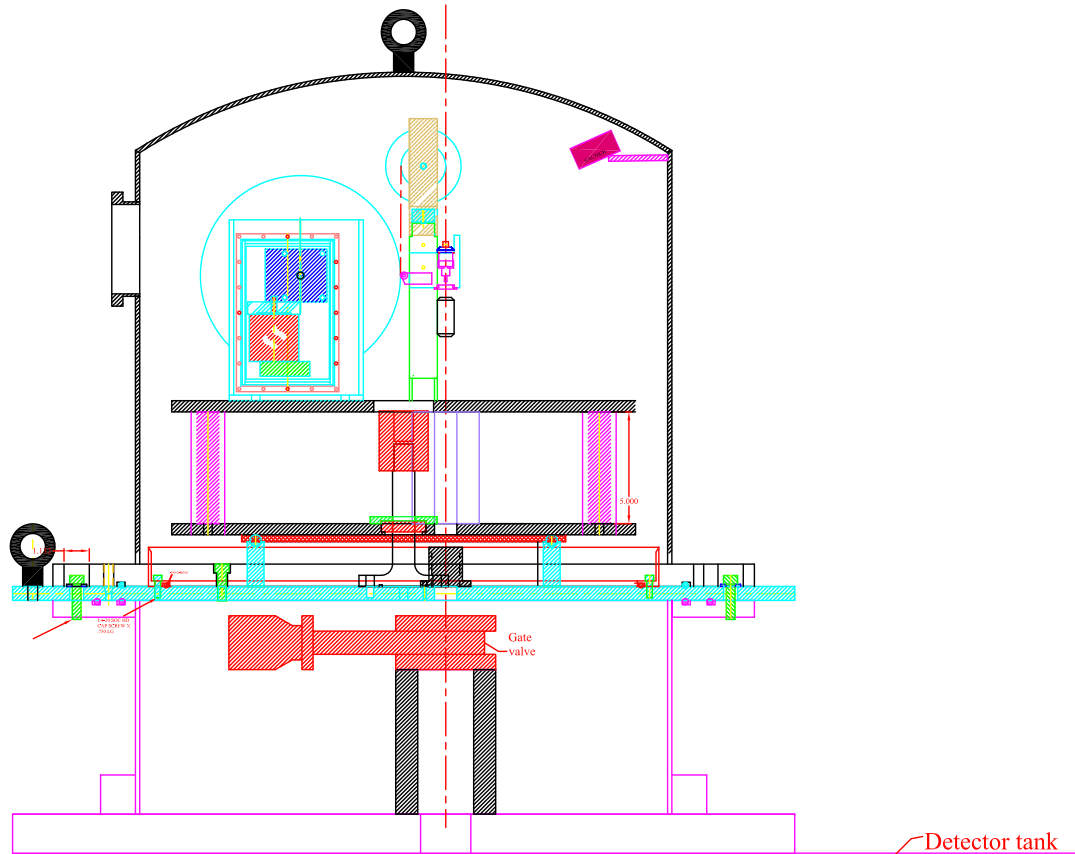


Fig. 5.6. Design drawing of the automated source deployment system. The central motor and gear box to rotate turntable is omitted for visual clarity. The bottom plate of the calibration box (with the eye bolt) is 35 inches in diameter.

three independent stepping-motor driven source deployment units all mounted on a common turntable. The

turntable and deployment units will all be enclosed in a sealed stainless steel vessel (calibration box) to maintain the isolated detector module environment from the outside (ultra-pure water). Double o-ring seals will be employed between the calibration box and its support spool, so that the volume between the two o-rings can be pumped out for leak-checking and to ensure seal quality. All internal components must be certified to be compatible with liquid scintillator. The deployment systems will be operated under computer-automated control in coordination with the data acquisition system (to facilitate separation of source monitoring data from physics data). Each source can be withdrawn into a shielded enclosure on the turntable for storage. The deployed source position will be known to <1 cm.

Below is a list of safety features incorporated into the design of the system:

- The deployment motor drives the wheel with a worm gear box. Since one can not back-drive a worm gear, this system is power fail-safe even during a deployment. In addition, the gear box reduces motor torque by a factor of >30 ;
- A Teflon roller (pink in Fig. 5.6) between the wheel and the pulley post keeps the cable in the groove;
- Two weights (one above and the other below the source, not shown in Fig. 5.6) keep the tension in the deployment cable when the source accidentally hit the bottom. This mitigates the risk of cable slipping out of the groove when losing tension.
- A load cell is sensing the tension in the deployment cable constant. It serves as a downward motion “kill” switch when detecting a sudden decrease in the cable tension;
- An upward motion limit switch is served both as a “kill” switch to prevent the source from being retracted too far, and a “zeroing” switch of the stepper motor [†];
- Optical motion encoder is implemented on each stepper motor to ensure position precision and reproducibility.

At present, we anticipate including two radioactive sources on the first two deployment motor units:

- A ^{68}Ge gamma source. The ^{68}Ge provides two coincident 0.511 MeV γ rays to simulate the threshold positron signal.
- A ^{252}Cf source to provide neutrons that simulate the neutron capture signal on Gd to calibrate the 6 MeV neutron energy threshold. The neutron capture on hydrogen also provides an energy scale calibration at 2.2 MeV.

The detector responses to these sources have been carefully studied. As an example, shown in Fig. 5.7 is the delayed energy spectrum of a ^{252}Cf source in the IHEP prototype detector (see Section 15.3.1). Excellent agreement is observed between the measured and simulated spectra.

The third motor unit will be used to deploy a LED diffuser ball into the detector, as described in Section 5.2.

The radioactive source designs are shown in Fig. 5.8. The sources will be contained inside welded stainless steel cylindrical containers (1 mm thick). These cylindrical containers are encased in acrylic capsules to avoid detrimental effects of the SS on the Gd-LS. The sources are suspended by Teflon coated stainless steel cables. The ^{68}Ge is at the center of a CH_2 cylinder which is used to stop the positrons emitted from the ^{68}Ge source. The positrons annihilate in the CH_2 , yielding two 511 keV gamma rays. The source strength will be about 100 Hz. The ^{252}Cf source is sealed inside a 3.6 cm long and 1 mm thick stainless steel cylindrical

[†]The “zero” of the stepper motor should only need to be calibrated by the limit switch once at the beginning of the commissioning, and during the run if some error occurs (e.g. power outage).

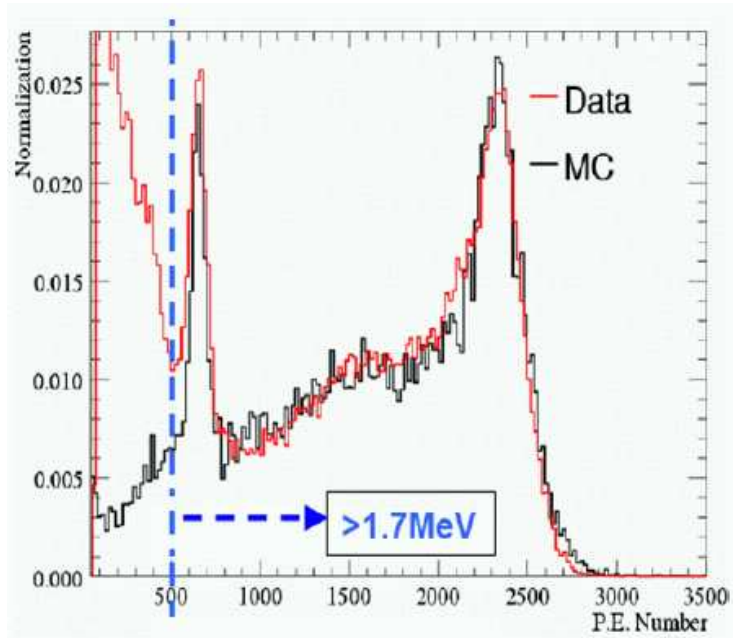


Fig. 5.7. The measured and simulated delayed energy spectra of a ^{252}Cf in the prototype detector.

containers with 1 cm OD. There is CH_2 in between the source and the steel to reduce the high energy gamma background from neutrons captured on steel (see below).

When not in use, sources are “parked” inside shielding cylinders in the calibration boxes above the detector tank. The leaked-in events will be background. For a ~ 100 Hz ^{68}Ge source, due to the fact that the two 511 keV gammas are emitted back-to-back and the shielding from the mineral oil and gamma catcher, the residual background rate above the trigger threshold will be completely negligible. The situation for the neutron source is subtler. Neutrons can capture on steel (e.g. Fe, Mn, Cr, Ni, etc) and emit high energy gamma rays (>6 MeV). When they penetrate into the detector, these events produce “neutron-like” background, and are difficult to shield. To avoid a significant level of correlated background when in accidental coincidence with natural radioactivity background, the rate of the neutron source has to be limited to ~ 1 Hz (0.2 nCi ^{252}Cf). In addition, the neutron source will be retracted into a 7 cm thick and 8.75 cm high borated polyethylene (BPE) cylinder (shown as the purple blocks in Fig. 5.6) when at the “parking” position. In addition, a BPE disk with 4.4 cm thickness and 6 cm radius (not shown in Fig. 5.6) will also be needed at the “parking” position underneath the BPE cylinder.

The sources described above can be deployed in sequence by each of the systems on each detector module. During automated calibration/monitoring periods, only one source at a time would be deployed in each detector module. The three automated systems for each detector module are located as follows:

- Central axis
- A radial location in the central Gd-LS volume near (20 cm inside) the inner cylindrical acrylic vessel wall
- A radial location in the γ -catcher region.

In Table 5.2, the program of a typical automated calibration cycle is outlined. The entire cycle takes about 4 hours (including overhead).

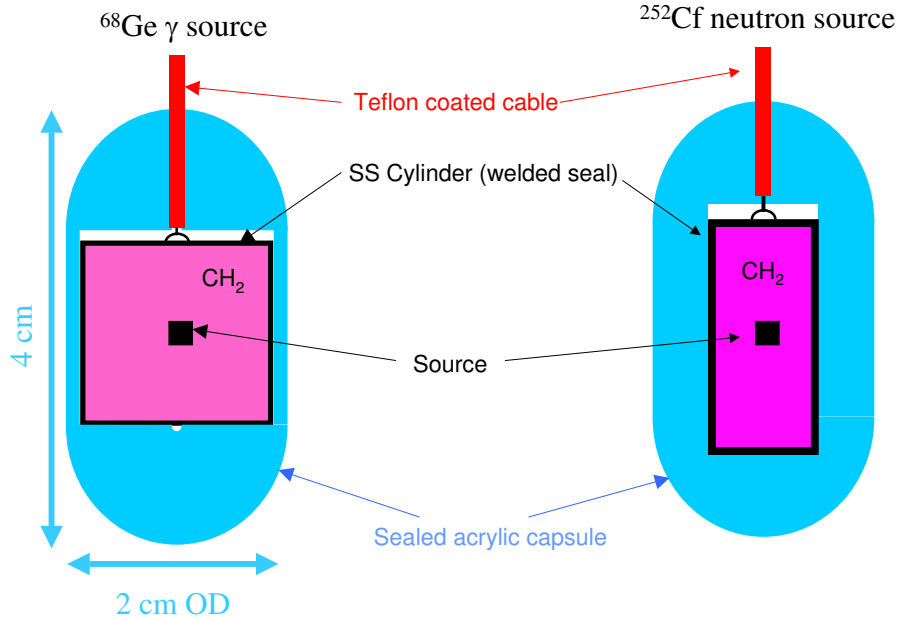


Fig. 5.8. Schematic diagrams showing designs of radioactive sources for the automated deployment system. On the left is the combination gamma source and on the right is the Pu(C) source.

Simulation studies indicate that we can use these regular automated source deployments to track and compensate for changes in:

- average gain of the detector (photoelectron yield per MeV)
- number of PMTs operational
- scintillation light attenuation length

as well as other optical properties of the detector system. Examples of these are detailed in Section 2.2.2.5.

Cables come out from the calibration boxes through sealed feedthroughs. The cables from all three calibration boxes are brought together into an interface box, and are guided up through the water pool in stainless steel conduit, as illustrated in Fig. 5.9. The cables that carry the trigger signals for the LEDs will be coaxial, and all other electrical cables will be multi-conductor twisted pair AWG22 cables. We will also need to run three compressed air lines (per detector module) to control the gate valves. For each detector module, in total there will be six 50-conductor twisted pair AWG22 cables, six RG175 coaxial cables, and three compressed air hoses, which are quite manageable under the scheme laid out in Fig. 5.9.

The control/monitor software of the automated calibration system has been developed in LABVIEW 8.0. A screen-shot of the control screen for a single calibration box (three deployment units on the same turntable) is shown in Fig. 5.10. Each deployment and turntable motor has its own status display. The stepper positions and the tension in the deployment cable are constantly monitored. The automated deployment sequence will be pre-programmed, and normally no human intervention is needed. If there is an error during the procedure, the entire system will be interrupted for diagnosis and intervention by an expert.

Two axes in target			Axis in gamma catcher		
Source	Position in z (cm)	Duration (min.)	Source	Position in z (cm)	Duration (min.)
^{68}Ge	150	5	^{68}Ge	180	5
^{68}Ge	75	2	^{68}Ge	90	2
^{68}Ge	0	2	^{68}Ge	0	2
^{68}Ge	-75	2	^{68}Ge	-90	2
^{68}Ge	-150	5	^{68}Ge	-180	5
^{252}Cf	150	5	^{252}Cf	180	5
^{252}Cf	75	3	^{252}Cf	90	3
^{252}Cf	0	3	^{252}Cf	0	3
^{252}Cf	-75	3	^{252}Cf	-90	3
^{252}Cf	-150	5	^{252}Cf	-180	5
LED	150	5	LED	180	5
LED	75	2	LED	90	2
LED	0	2	LED	0	2
LED	-75	2	LED	-90	2
LED	-150	5	LED	-180	5

Table 5.2. Summary of a typical automated calibration cycle. The left table lists the sources and positions for the two calibration axes in the target region, and the right table is for the axis in the gamma catcher. Note the difference in the z accessibility between the two tables, reflecting the larger height occupied by the gamma catcher. The origin of z is defined at the “equator” of the detector. The time to deploy the source to a given position is taken into account in the “Duration” column.

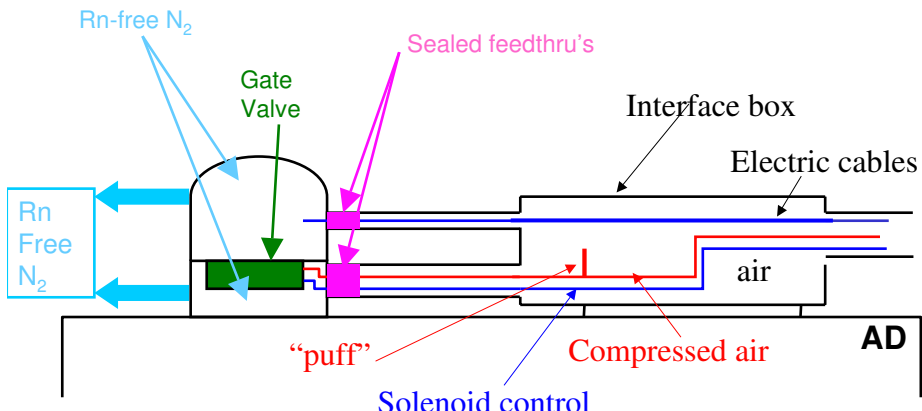


Fig. 5.9. A schematic diagram of the cabling scheme for the automated calibration system, and the concept of an interface box.

The periodic automated calibration will be performed simultaneously on all the detector modules. We envision that the sequence to interrupt normal data taking, perform the calibration, and resume data taking will be under main DAQ control. The calibration control software will write the system status into a slow control database, which is monitored by the main DAQ system constantly.

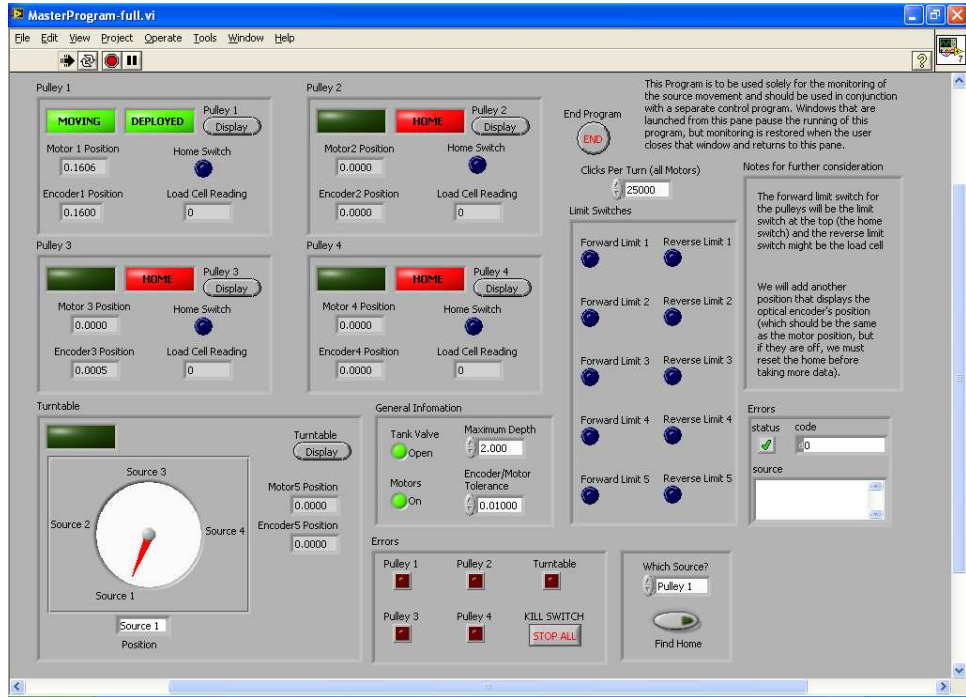


Fig. 5.10. Screen shot of the LABVIEW control/monitoring program for the automated calibrate system (one turntable and three deployment unit).

5.6 Manual deployment system

A mechanical system will be designed to deploy sources throughout the active volume of the detectors. The source inside the detector can be well controlled and the position can be repeated at a level less than 1 cm. The whole deployment system must be treated carefully to prevent any contamination to the liquid scintillator. The system must be easy to setup and operate, tolerate frequent use and must have a reliable method to put sources into the detectors and to take the sources out as well. The space for operation should not be too large. Figure 5.11 shows a schematic view of the manual source deployment system. When performing the manual calibration, one meter of water is required above the detector to suppress the ambient background. As illustrated in the picture, an operation platform will be installed temporarily during the manual calibration cycle. To limit the total length, the vertical pipe has a telescope mechanism that will be activated when lowering the source into the detector tank. After reaching the desired depth, the lowest segment (arm) can rotate in the horizontal direction about a “hinge joint” operated by a miniature rope and pulley mechanism. The details of this joint are depicted in Fig. 5.12. One can control the depth as well as the orientation of the arm quite easily. Also shown in Fig. 5.12 is an additional mechanism that is capable of deploying the source along the horizontal arm. A simpler (and perhaps more robust) alternative would be to have the source at a few fixed positions along the arm.

We envision that the manual calibration would be performed during the commissioning period. About 100 positions in the target region will be sampled by the composite ^{68}Ge and neutron sources.

5.7 Manufacturing Plan

The automated deployment systems will be fabricated in the Kellogg Laboratory at the California Institute of Technology (Caltech). Substantial components such as gate valves, stepping motors, slip rings, and stainless bell jar lids are commercially available. Many custom components such as the pulley wheels,

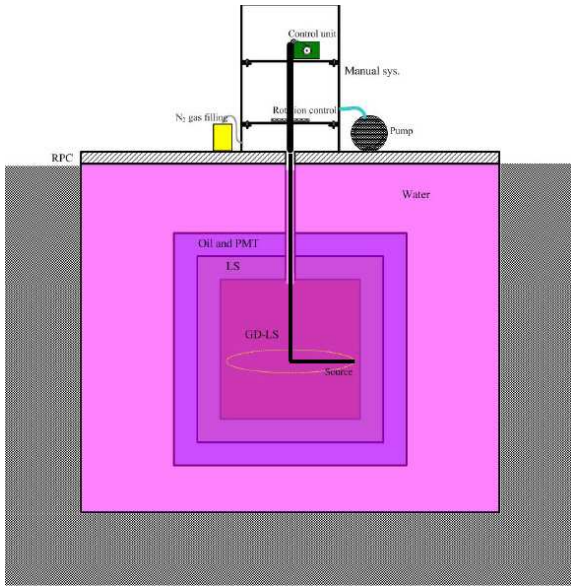


Fig. 5.11. Schematic diagram of the manual source deployment system.

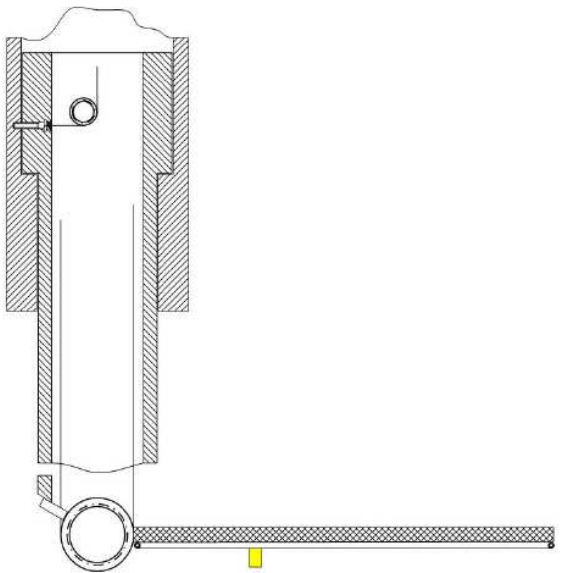


Fig. 5.12. Details of the rotating joint.

turntable, and miscellaneous parts will be machined in shops at Caltech. The LED pulser units and fiber optics will be supplied by Hong Kong University and installed at Caltech. Each deployment system will be fully assembled and tested at Caltech prior to shipment to China. After arrival at the Daya Bay site, the units will be tested, installed and commissioned on the detector modules.

Radioactive sources will be procured, prepared, and tested at the China Institute for Atomic Energy (CIAE).

The manual deployment system will be fabricated at CIAE. CIAE is responsible for testing, installation and operation of the system.

5.8 Quality Assurance

The assembled automated systems will be fully tested at Caltech prior to shipment to China. Positioning accuracy of 1 cm, reliability, and fail-safety of interlocks will all be established during this testing program. In addition, each unit will be checked for leaks before shipment. The assembled system in the underground hall, including cable conduits, will be checked for leaks before filling the water pool.

The manual system will be tested at CIAE prior to shipment to the Daya Bay site. Positioning accuracy of 2 mm, reliability, and fail-safety of interlocks will all be established during this testing program.

Radioactive sources will be tested to certify that they are leak-tight. This will include soaking in acid or other solvent and counting the soak liquid. Absolute activity of each source will be measured and documented.

5.9 ES&H

The calibration systems do not involve flammable materials or gases, high voltage, or other hazards. The radioactive sources are of very low activity, typically 100 Bq or less, and will be operated in a shielded environment so that they do not represent a hazard to humans. Personnel involved in the installation and testing of the sources will need to be properly trained and monitored. The dose rates will be extremely low, of order $\mu\text{rem}/\text{hr}$.

The calibration box will be constantly flushed by dry nitrogen. This will minimize the amount of liquid

scintillator or its vapor to avoid possible contamination. The amount of liquid scintillator “clinging” on the surface of the deployment cable will be quantitatively measured in a prototype unit.

5.10 Risk Assessment

The primary risk associated with the calibration systems is the interface with the detector module. Interlocks must insure that the pressure in the calibration system is equalized with the detector before opening the gate valve and deploying a source. The sources and materials must be tested to be compatible with the liquid scintillator to avoid contamination of the detector. The design and testing protocol of the containment vessel and associated conduits for cabling will insure that water from the veto pool will not leak into the system.

The primary schedule risk in the calibration system is the delayed delivery of the manual calibration system. Two key purposes of the manual calibration system are a) to directly measure the neutron detection efficiency and to precisely measure the 6 MeV energy scale using a high rate Pu-C source at the detector center (see Secs. 2.2.3.4 and 5.1), and b) to measure the energy response of the detector throughout the target region from 1 to 8 MeV. If the manual calibration system is not ready by the detector commissioning period, we will pursue an alternative plan as follows:

- During the detector commissioning, use automated calibration system to deploy a high rate Pu-C source (\sim 40 Hz tagged neutrons) to the detector center. This will allow the measurement of neutron detection efficiency and a precise calibration of 6 MeV neutron threshold at the detector center.
- Use the spallation neutrons with the position reconstruction to measure the detector response (at 2.2 MeV and \sim 8 MeV) as a function of position. Monte Carlo simulation has shown that to calibrate the 8 MeV peak to a 0.5% precision in a given pixel of 200 kg (100 per detector) takes 1(10) days in each near(far) detector. Note that this measurement is *in situ* during normal data taking, and will be complemented and benchmarked by the radioactive source measurements along the vertical axes using automated calibration system. See details at the end of Sec. 2.2.2.5.

6 Muon System

The main backgrounds to the Daya Bay Experiment are induced by cosmic-ray muons. These backgrounds are minimized by locating the detectors underground with maximum possible overburden. Background due to muon spallation products at the depths of the experimental halls as well as ambient γ background due to the radioactivity of the rock surrounding the experimental halls is minimized by shielding the antineutrino detectors with 2.5 meters of water. Gammas in the range of 1–2 MeV are attenuated by a factor ~ 10 in 50 cm of water [1]. Thus the 2.5 meters of water provides a reduction in the rock γ flux of roughly five orders of magnitude. This “water shield” also attenuates the flux of neutrons produced outside the water pool.

Events associated with fast neutrons produced in the water itself remain a major potential background. A system of tracking detectors will be deployed to tag muons that traverse the water shield. Events with a muon that passes through the water less than 200 μs before the prompt signal, which have a small but finite probability of creating a fake signal event, can be removed from the data sample without incurring excessive deadtime. By measuring the energy spectrum of tagged background events and having precise knowledge of the tagging efficiency of the tracking system, the background from untagged events (due to tagging inefficiency) can be estimated and subtracted statistically with small uncertainty. Our goal is to keep the uncertainty of this background below 0.1%.

The muon system will also have some ability to identify showering muons. Such muons have an enhanced likelihood to produce other cosmogenic backgrounds, of which ^9Li is the most important. This capacity supplements the ability of the AD to identify such muons. Although, as discussed in Section 2.3.3, we plan to measure and subtract this background, it may also be possible to suppress it without unacceptable deadtime by identifying likely parent muons and rejecting subsequent apparent signal candidates. While such tagging may help to suppress the ^9Li background, the working assumption is that no extra requirements are imposed on the muon system in order to reduce this background.

The current baseline configuration for meeting these challenges is shown schematically in Fig. 6.1. The antineutrino detectors are separated by 1 m from each other and immersed in a large pool of highly-purified water. The pools are all octagonal in cross-section. The Far Hall pool has the cross-section of a 16 m square with corners cut off at 45° such that the shortest distance from the walls to an AD is 2.5 m. The near hall pools have the cross-section of 16 m \times 10 m rectangles with corners cut off according to the same principle as for the Far Hall. The minimum distance between the detectors and any point on the walls of the pools is 2.5 m. The water shield is divided into inner and outer sections of the pool and instrumented with phototubes to detect Cherenkov photons from muons impinging on the water. The outer side and bottom sections of the pool are 1 m thick, read out by phototubes spaced periodically. The outer sections are separated from the inner pool by Tyvek film 1070D reflectors stretched over a stainless steel frame. The frame holds PMTs for both the inner and outer sections of the pool. The muon tracker is completed by four layers of Resistive Plate Chambers (RPCs) above the pool. The top layers extend 1 m beyond the edge of the pool in all directions, both to minimize the gaps in coverage and to allow studies of background caused by muon interactions in the rocks surrounding the pool.

Expected rates of cosmic ray muons in the components of the muon system can be found in Table 7.3.

6.1 Muon System Specifications

Note that it is not envisioned that this system will act as an online veto. This will allow ample opportunity for careful offline studies to optimize the performance of the system.

Requirements of the muon system are summarized in more detail in the following subsections.

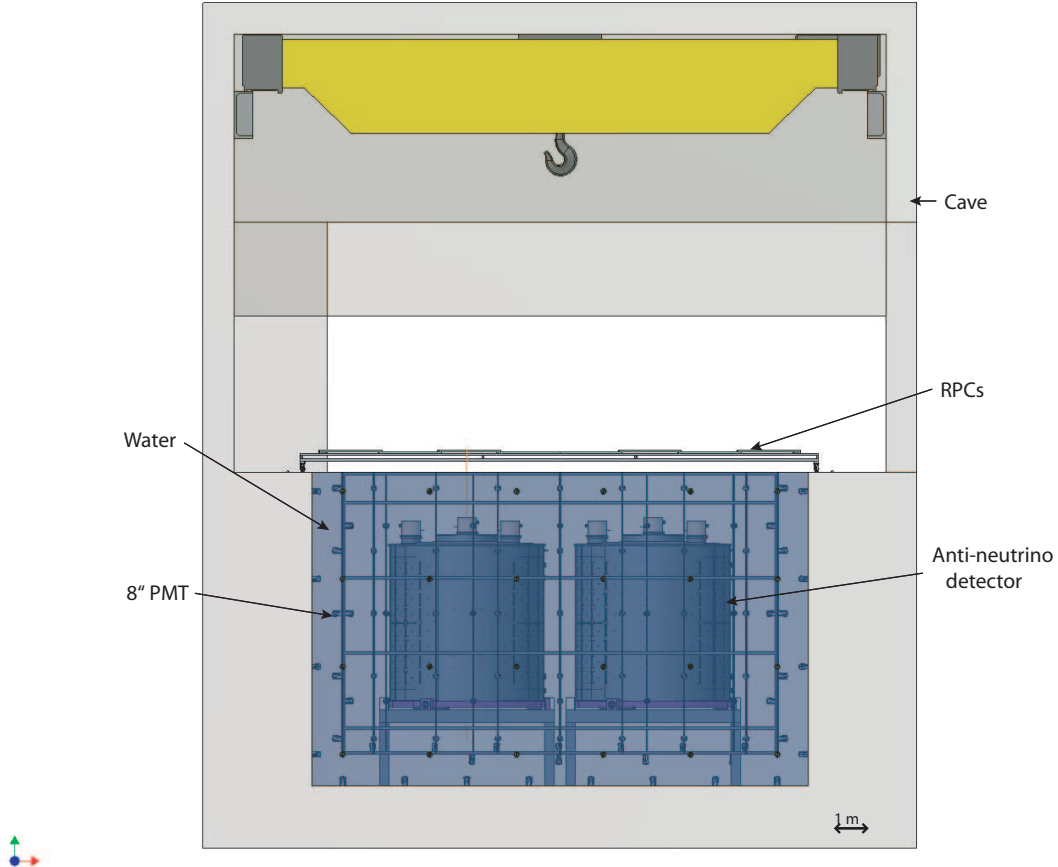


Fig. 6.1. Elevation view of an experimental hall, showing the baseline design for the muon system. This includes a layer of RPCs above a water pool with at least 2.5 m of shielding for the antineutrino detectors, two layers of 8" photomultipliers in the water, with compartmentalization of the outer 1 m of water for position resolution and redundancy.

6.1.1 Muon Detection Efficiency

The overall efficiency of the muon system has to exceed 99.5%, with an uncertainty $<0.25\%$. This is driven by the need to reject the fast neutron background from muon interactions in the water and to measure its residual level. As can be seen in Table 2.10, without suppression, our simulations predict this background would otherwise be ~ 50 times that of the fast neutron background from muon interactions in the surrounding rock, *i.e.* at a level roughly 2% of that of the signal. According to our simulation, a factor of 200 reduction in this rate brings the fast neutron background from the water safely below that from the rock, and the total residual fast neutron background down to the 0.1% level. The requirement on the uncertainty in the efficiency brings the systematic due to the uncertainty on the fast neutron background from the water to a level at which it is small compared with other systematics.

6.1.2 Muon System Redundancy

It is difficult to achieve the requisite efficiency with only one tagging system. Moreover it is necessary to have a method of determining the residual level of background after the imposition of the muon rejection cuts. Therefore it is desirable to have two complementary tagging systems to cross-check the efficiency of

each system and allow detailed comparison with simulation.

As discussed below, the current baseline design is to instrument the water shield as a Cherenkov tracker by deploying 8" PMTs in the water with $\sim 0.6\%$ coverage. Such systems are expected to have $>95\%$ efficiency. A second tracking system, in our baseline a combination of RPCs [2] [3] above and outer water sections at the sides and bottom of the water pool, can give an independent efficiency of $>90\%$. The two systems compliment each other, with the probability of a background-producing muon being missed by both systems below 0.5%.

6.1.3 Spatial Resolution

The fast neutron background due to muons interacting in the water shield falls rapidly with the distance of the muon track from the AD. The spatial resolution of the muon tracker should be sufficient to measure this falloff. Measurements from previous experiments show that the characteristic falloff distance is about 1 meter [4]. A spatial resolution of 50–100 cm in the distance between the muon trajectory and the ADs is necessary in order to study this radial dependence. The technologies we are proposing are capable of achieving sufficient resolution in each coordinate.

6.1.4 Timing Resolution

There are several constraints on the timing resolution. The least restrictive is on the time registration of the muon signal with respect to that of the candidate event. To avoid compromising the veto rejection to a significant extent, this resolution need only be in the range of fractions of a microsecond. More stringent requirements are imposed by other, technology-dependent, considerations. The water shield PMTs need ~ 2 ns resolution to allow spatial reconstruction of the muon trajectory.

6.1.5 Water Shield Thickness

As mentioned above the shield must attenuate γ rays and neutrons from the rock walls of the cavern by large factors to reduce the accidental background in the antineutrino detectors. A minimum thickness of 2 m of water is required; 2.5 m gives an extra margin of safety.

6.1.6 Summary of Requirements

The requirements discussed above are summarized in Table 6.1

Item	Requirement	Justification
Thickness of water shield	≥ 2 m	Attenuate fast neutrons and γ rays from nearby rock
Total inefficiency for detecting muons	$\leq 0.5\%$	Reduce fast-neutron background to a level below ${}^9\text{Li}$
Uncertainty of efficiency	$\leq 0.25\%$	Maintain fast neutron uncertainty well below that of ${}^9\text{Li}$
Random veto deadtime	$\leq 15\%$	Avoid undue impact on statistical precision
Uncertainty in random veto deadtime	$\leq 0.05\%$	Keep well below other systematic uncertainties
Position resolution	0.5–1 m near AD	Study radial dependence of cosmogenic background
Timing resolution	± 2 ns (Cherenkov) ± 25 ns (RPCs)	Allow spatial reconstruction of muon trajectory Limit random veto deadtime from false coincidences to $\mathcal{O}(1\%)$

Table 6.1. Requirements for Muon system.

6.2 Water Shield

The antineutrino detectors will be surrounded by a shield of water with a thickness of at least 2.5 meters in all directions. Several important purposes are served by the water. First, fast-neutron background originating from the cosmic muons interacting with the surrounding rocks will be significantly reduced by the water. Simulation shows that the fast-neutron background rate is reduced by a factor 1.5–2 for every 50-cm of water. Second, the water will insulate the antineutrino detectors from the air, reducing background from the radon in the air as well as γ rays from surrounding rocks and dust in the air. With the low-energy γ ray flux reduced by a factor ~ 10 per 50-cm of water, the water can very effectively reduce the accidental background rate associated with the γ rays. Third, the water shield can be instrumented with PMTs for observing the passage of cosmic muons via the detection of the Cherenkov light.

The active inner and outer water shield sections, together with the RPCs, form an efficient muon tagging system with an expected overall efficiency greater than 99.5%. The ability to tag muons with high efficiency is crucial for vetoing the bulk of the fast-neutron background. Finally, the large mass of water can readily provide a constant operating temperature for the antineutrino detectors at the near and far sites, eliminating one potential source of systematic uncertainty.

6.2.1 Water Shield Design

The schematic of the water shield is illustrated in Fig. 6.1 for the water pool configuration. The cylindrical antineutrino detector modules are placed inside an eight-sided cavity filled with purified water, *i.e.* a water pool configuration. As mentioned above, the maximum dimensions of the water pool are 16 m \times 16 m \times 10 m (high) for the far site, and 16 m \times 10 m \times 10 m (high) for the near sites. The four detector modules in the far site will be immersed in the water pool forming a 2 by 2 array. As shown in Fig. 6.6, the adjacent detector modules are separated by 1 meter and each module is shielded by at least 2.5 meters of water in all directions. For the near sites, the two antineutrino detector modules are separated by 1 meter. Again, any neutrons or γ rays from the rock must penetrate at least 2.5 m of water in order to reach the antineutrino detector modules. The weight of water is 2170 ton and 1400 ton, respectively, for the far site and for each of the two near sites.

The water shield is divided into inner and outer sections separated by Tyvek partitions. The outer sections are 1 m thick covering the sides and bottom of the pools.

Tyvek panels are supported on the same frames that support the water shield PMTs. A section of these frames are shown in Fig. 6.2. The side frames are constructed of a series of stainless steel unistrut modules. The modules span a face of the pool horizontally and are of two different heights. The lowest modules are 1 m high above which are stacked three 3 m high modules to make up the entire 10 m height of the water. The modules are fixed to anchors in the concrete floor and the sides of the pool. The anchors are fixed to the concrete as shown in Fig. 6.3 A similar structure covers the floor of the pool, but it cannot be prepared in advance because of the presence of the support legs of the AD table (visible in Fig. 6.2). Instead it is constructed in place. Details of the connection between the side and bottom frames and the anchoring of each is shown in Fig. 6.4.

The sides of the ADs within the pools are also covered with Tyvek. The current plan is to accomplish this with essentially no impact on the AD structure as described in this document.

This will be accomplished by construction of separate stainless steel circular frames placed upon the ADs after they are fully assembled, as shown in Fig. 6.5. Threaded studs of diameter 0.5 cm and length 4 cm are tack-welded to each frame as shown. These studs will be separated by 15 cm, so that there will be approximately 100 per AD. Each AD will contain 4 Tyvek sheets. The size of each sheet will be approximately 4 m by 5 m.

The Tyvek sheets will be supported by the frame as shown in the Fig. 6.5. The sheets will be cut so that they will not interfere with structures on the AD outer wall. Each Tyvek sheet will be hung from the

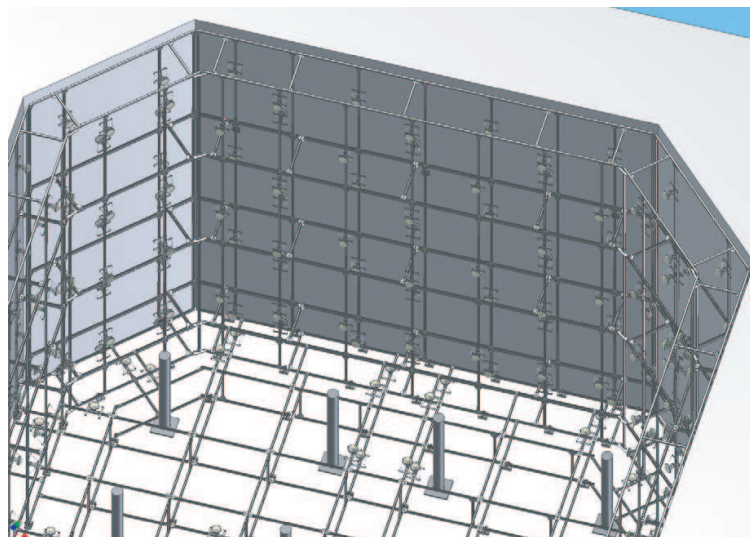


Fig. 6.2. Section of pool with PMT support frames (shown without Tyvek panels).

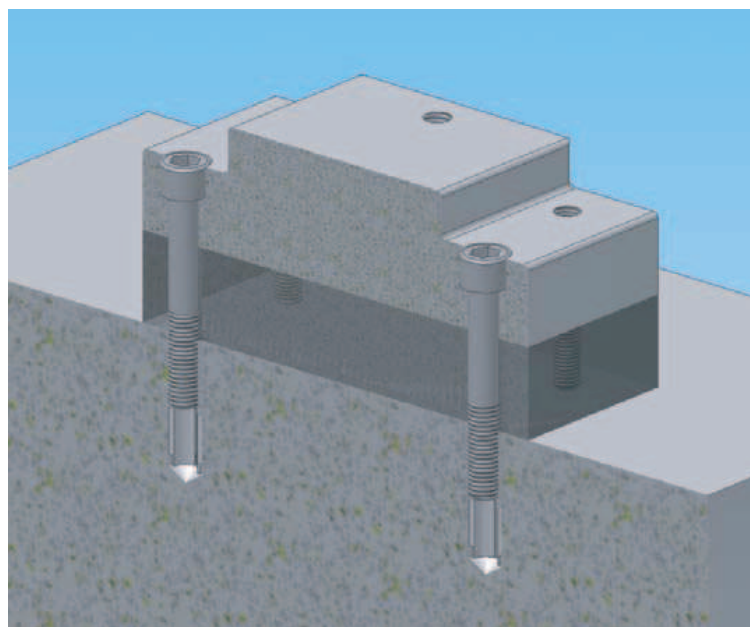


Fig. 6.3. Support pad/anchor bolted to the concrete. Half of one anchor is shown so that the method of fastening can be seen. Each anchor is bolted on, then leveled by a separate set of screws and finally grout is inserted between the anchor and the concrete.

frame by means of steel grommets arrayed at their tops to fit over the studs. They will be held in position by threaded nuts. To insure horizontal and vertical stability, the bottom of each Tyvek sheet will be fastened to its two adjacent sheets by specially design metal fasteners that will also serve as weights. Once the Tyvek sheets are installed, and all components, including water, are in place in the muon shield, there will be no further movement of the Tyvek sheets.

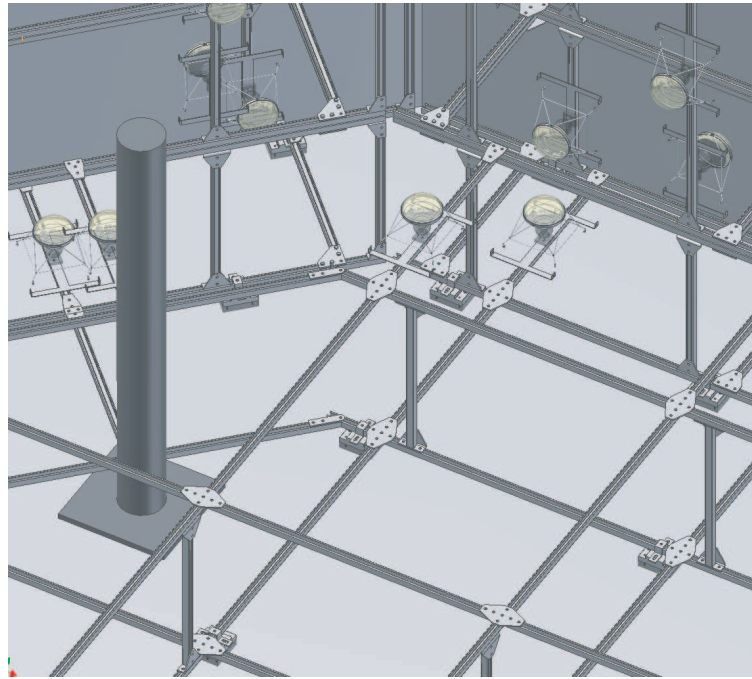


Fig. 6.4. Intersection of the side and bottom PMT support frames at one corner of the pool. Support leg of the AD table is also visible.

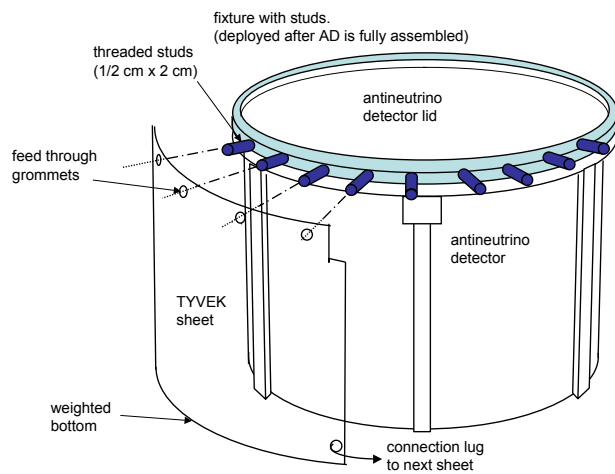


Fig. 6.5. Scheme for covering antineutrino detectors with a reflective covering

6.2.2 Water Shield PMT layout

In the baseline design the inner water shield will be instrumented with arrays of hemispheric 8" PMT as shown in Fig. 6.6. Inward-facing PMT arrays will be mounted on frames placed at the sides and on the

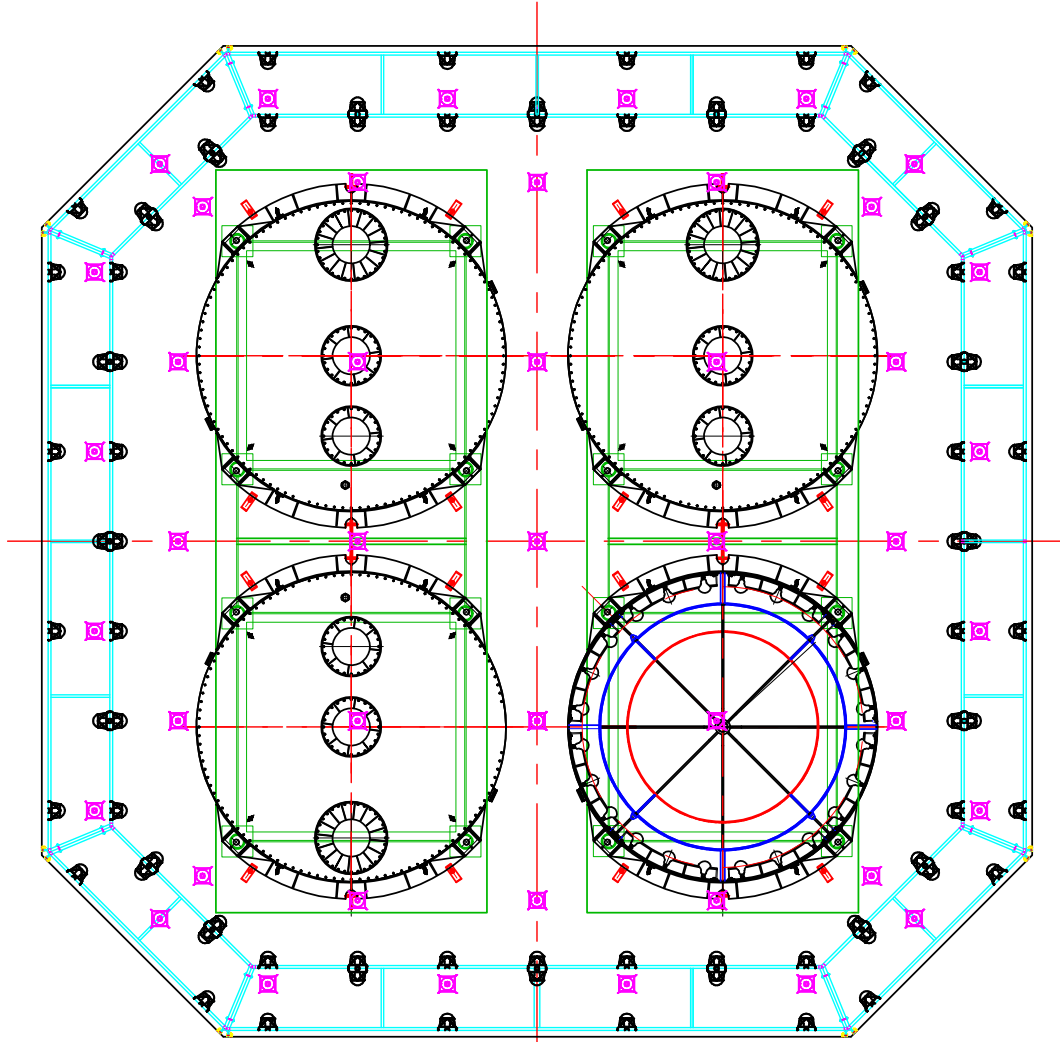


Fig. 6.6. Plan view of Far Hall configuration.

bottom of the pool, abutting the inner surfaces of the outer sections (which will be covered with Tyvek). The PMTs will be approximately evenly distributed forming a rectangular grid with a density of 1 PMT per $\sim 8 \text{ m}^2$. This corresponds to a 0.5% areal coverage. The total number of PMTs for the far site and the two near sites is 392, as detailed in Table 6.2. The outer shield has inward-facing PMTs on the sides and bottom of the pool and outward-facing PMTs on the side partitions, all at densities of one per $6\text{-}7 \text{ m}^2$. The numbers are summarized in the same table. Bases for these PMTs will be custom designed and manufactured potted and encapsulated. The final design will be completed after we choose a PMT. Figure 6.7 shows the current conceptual design for the base enclosure.

The HV system will be very similar to that described in Section 4.6.6 for the antineutrino detector PMTs. Our baseline PMT support scheme is shown in Fig. 6.8. The PMTs must be supported against their own weight in air but also against a much larger buoyant force when they are under water. In this scheme they are supported at the widest part of the bulb by a stainless steel ring with a Teflon liner. The ring is welded to stainless steel wires at four points and these in turn are themselves welded to a wire square. Four legs extend from the corners of the square and are fixed onto an I-shaped stainless steel frame. This frame is bolted onto the PMT support structure. There is also a cable support (not shown) to relieve stress on the base.

Site	inner bottom	inner sides	inner total	outer in-facing	outer out-facing	outer total	grand total
DB Near	20	96	116	109	64	173	289
LA Near	20	96	116	109	64	173	289
Far	32	128	160	128	96	224	384
All three	72	320	392	346	224	570	962

Table 6.2. Number of PMTs for the water shield.

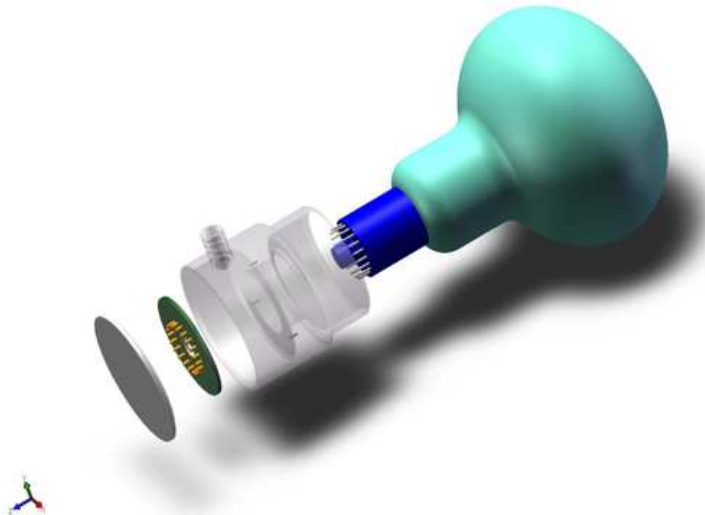


Fig. 6.7. Design of a phototube base enclosure suitable for use in ultra-pure water.

Efficiency, position resolution, timing resolution, etc. are being further optimized by Monte-Carlo simulations now in progress. The baseline and a number of other possible arrangements of PMTs have been studied so far.

6.2.3 Water Shield Front-End Electronics

Extrapolation of the curves in Figs. 6.13 and 6.22 indicates that although the number of photoelectrons per PMT has a long tail, only about 0.01% of the struck PMTs see more than 100 photoelectrons. Thus the performance of the antineutrino detector electronics, as listed in Table 7.1, should certainly be adequate for the water shield readout. However the reduced dynamic range requirement may indicate that less expensive options should be considered for the pulse height measurement. In addition to the pulse height information, timing information will also be provided by the readout electronics. The 0.5 ns/bin TDCs, do not limit the timing resolution of 2 ns expected for a single PMT channel. The energy sum of the PMTs as well as the multiplicity of the struck PMTs will be used for defining the muon trigger (see Section 7.2.3).

6.2.4 Calibration of the Water Shield PMTs

The timing and gain stability of the water Cherenkov PMTs will be calibrated and monitored by a system of distributed light sources. The light sources will consist of LEDs embedded in diffuser balls, like the system described for the antineutrino detectors in Section 5.2. The light sources will be permanently mounted at several locations throughout the water volume. The exact locations of sources has not yet been optimized, nevertheless, one key requirement is that regions illuminated by neighboring light sources must

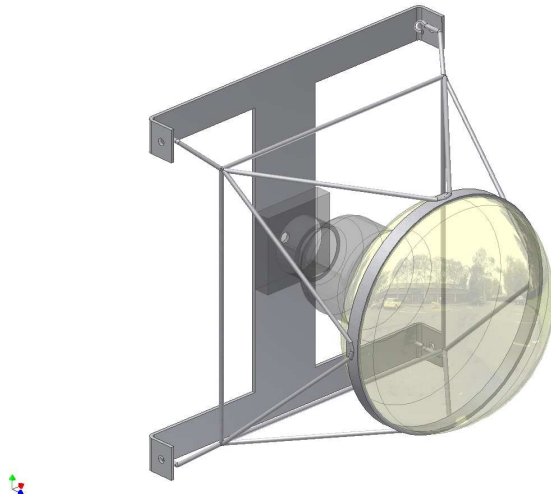


Fig. 6.8. PMT support scheme for water pool.

Table 6.3. Water conditioning systems used in previous experiments.

Experiment	Vol (m ³)	Flow (gpm)	Vol/Flow (days)	Att Len (m)	Resistivity & Radon (MΩ-cm) (Bq/m ³)
IMB	8000	80	18		
SuperK	50,000	130	71	100	> 18 < 0.002
SNO	1700	40	7.8		≈ 0.001
KamLAND	3200	35	16.8		0.5 10 ⁴
BaBar/DIRC	6	4	0.28	≥ 50	18 → 10
Milagro	≈ 4000	190	3.9	20	
DYB Far Pool	2560	17	28		
DYB Near Pools	1600	11	27		

overlap so that the timing offset for the different regions can be determined. Relative timing offsets for the inner and outer veto regions, and between the veto and antineutrino detectors, will be measured with cosmic rays.

No radioactive sources will be required.

6.2.5 Water Conditioning

The pool water needs to be conditioned to meet specifications

necessary for acceptable performance. Most important of these specifications is water clarity, which dictates the stages of purification and recirculation speed. Other specifications include radioactivity and temperature stability. Our water system design is based on purification systems for previous experiments, tailored to meet our particular circumstances.

Water systems used in other experiments, and the specifications they achieved, are summarized in Table 6.3. Note that the only two experiments which carefully measured their attenuation lengths (SuperK and BaBar/DIRC) made use of deionization stages in their water conditioning and achieved extremely clear water. Milagro did not make use of deionization, and observes a significantly lower optical attenuation length,

albeit not determined with a particularly careful measurement.

Our clarity specification is a requirement that the attenuation length for Cherenkov light be on the order of the pool dimensions or larger. For micron sized particles, this translates to a particle density of $10^{10}/\text{m}^3$ or less. We expect to use a filter stage followed by reverse osmosis to meet many of our specifications. Such a system has been used to reduce suspended particles down to $1 \mu\text{m}$ and other dissolved solids in water to a level of 4 ppm [5], far lower than necessary for water clarity.

Ion removal is important for clarity because dissolved ions have much larger scattering cross sections for visible and ultraviolet light than do water molecules. Indeed, ultrapure water in contact with stainless steel is known to degrade in clarity rapidly [6,7], particularly in systems with relatively large surface-to-volume ratios [8]. Still, ions at very low concentrations (on the order of parts per million) are enough to reduce water resistivity well below the theoretical maximum of $18 \text{ M}\Omega\text{-cm}$. It is best to rely on empirical evidence to determine how “pure” we need to make the water in order to meet our clarity specification.

Bacterial growth in the water must also be minimized, at least for the sake of clarity. To first approximation, this is accomplished using an ultraviolet sterilization stage [9,10]. Gas removal, aimed at radon, will also be used to remove dissolved oxygen.

Most radioactive backgrounds will be carried on suspended particles and removed to a satisfactory level by the filters. However, radon dissolved in the water is a potentially serious background for the antineutrino detectors. The ^{214}Bi isotope in the ^{222}Rn decay chain emits an energetic ($> 1\text{ MeV}$) photon in roughly 80% of its active region with a significant probability. We would like to keep the rate in the AD from radon at 1 Hz or below, in which case it is essentially negligible compared to other singles background sources. A simple estimate suggests that an AD rate of 1 Hz is equivalent to a radon concentration of $0.5 \text{ Bq}/\text{m}^3$. A simulation shows that this number is rather conservative, and that about $3(6) \text{ Bq}/\text{m}^3$ corresponds to 1 Hz, for a photon threshold of $0.5(1.0) \text{ MeV}$.

Note that ^{222}Rn has a half life of about four days. Also, ^{214}Bi and the intermediate daughters have much shorter half-lives, so that the four-day half life controls the concentration of the dangerous radionuclides. Our water conditioning system contains gas removal stages using standard de-aerators. Such systems have been used to reduce the radon level in SNO and Super-K to levels near $10^{-3}\text{Bq}/\text{m}^3$ (see Table 6.3), although this is primarily due to letting radon decay away (and keeping it from getting in) since the turnover rate is generally much longer than the decay half life. In the case of Super-K, the starting point was raw mine water, with an activity close to $10^3 \text{ Bq}/\text{m}^3$, or a suppression of 10^6 . Not only does the Daya Bay water conditioning system start with domestic water (which, although not known precisely, would naturally have a much lower radon level thanks if just in part to the 4 day half life) but measurements from bore holes at the Daya Bay site show that the radon emanation rate into the water system gives a much lower steady state activity, even ignoring the water conditioning system and the potential effect of liners.

The water pool will effectively serve as a temperature stabilization medium for the antineutrino detectors. Keeping the temperature constant to $\pm 1^\circ \text{C}$ is required by the AD design and equalizing the temperatures between the near and far halls to the same level is necessary to achieve ‘identical’ detector pairs. The current design is shown in Fig. 6.9. Domestic, potable water is delivered through gravity-fed piping to the ‘Fill/Makeup’ (F/MU) system for initial processing. (The tunnel entrance is at a reference height of +10 m, while the F/MU system/water storage pool is at -18.3 m, and the DYB, LA, and Far hall pools are at -20 m, -16 m, and -15 m respectively.) Initial purification includes a biocide feeder, water softener, filters, and a reverse osmosis (RO) unit. The RO system produces a significant amount of waste water, which is fed into the drainage stream which leads to the DYB hall. An electric 75 kW heating unit is proposed, which may be necessary to optimize the RO performance, depending on the temperature of the input water. The next stages of the F/MU system consist of a Continuous Deionizer (CDI), LiquiCel de-aerator, ultra-violet sterilization (UV) stage, filter, and controls. We choose a CDI over mixed resin bed deionization because of significant maintenance costs expected with this first stage of deionization. Pumps will need to be added for direct transfer to the experimental halls.

A water storage ‘hold up’ pool has been provided by the civil construction. This pool will be used to hold water that is transferred out of the experimental halls when access is needed to the apparatus. The second stage of the F/MU system (i.e. from the CDI onward) can be used as in a 35 gpm polishing loop if water is stored in the hold up pool for a long period of time. Vertical turbine pumps at the bottom of the pool will be used for this circulation, and also for transfer to the experimental halls if necessary.

We note that a 35 gpm ($190 \text{ m}^3/\text{day}$) transfer rate will fill the far hall pool in about two weeks.

Once delivered to the experimental hall, the water is continuously maintained through a polishing loop including mixed resin bed deionizers (MBDI), particle filters, and LiquiCel de-aerators, driven by vertical turbine pumps in the bottom of the pool. The MBDis are arranged in pairs so that any one can be switched out and replaced for recharging the resin bed when necessary. Local electric heater units are supplied for each polishing loop. The circulation rate is 45 gpm for the DYP and LA pools, and 70 gpm for the Far Hall pool. All of the water circulates through the heater, and $\sim 1/3$ is diverted through the purification loop.

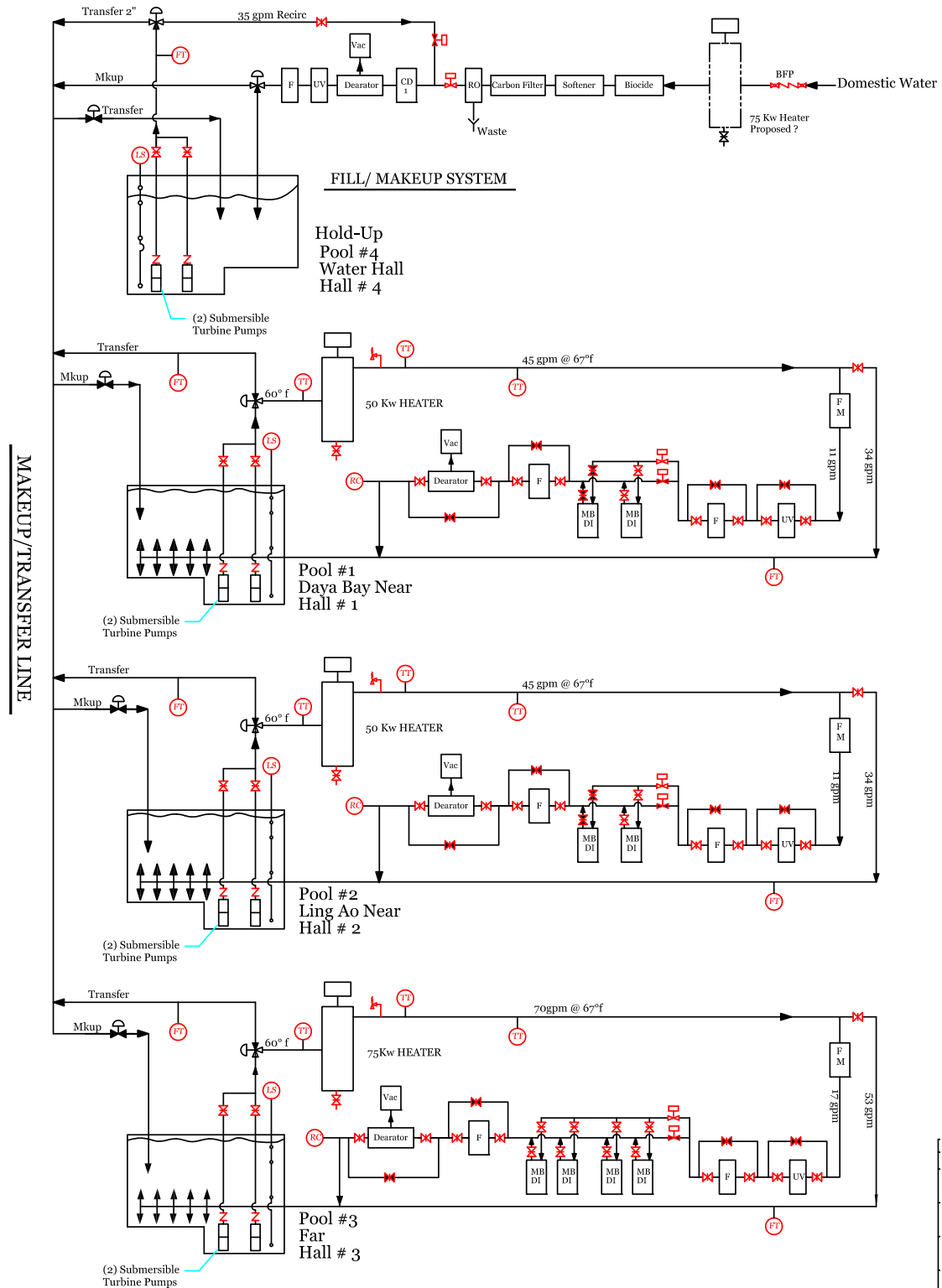


Fig. 6.9. Schematic diagram of the water conditioning system designed for the three experimental halls and central storage pool.

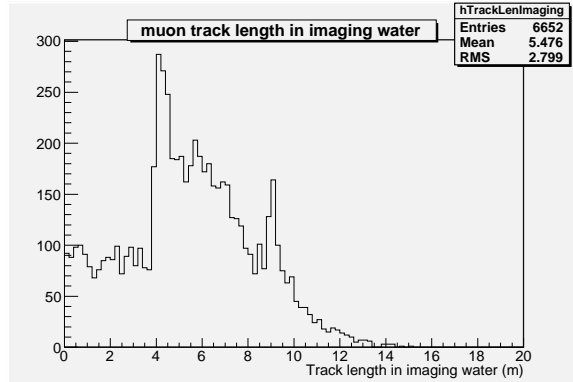


Fig. 6.10. Track length of muons in the inner water shield for the Far Hall. The edge at around 4 m is due to muons that penetrate the water and the ADs approximately vertically while the edge around 9 m is due to those that miss the ADs.

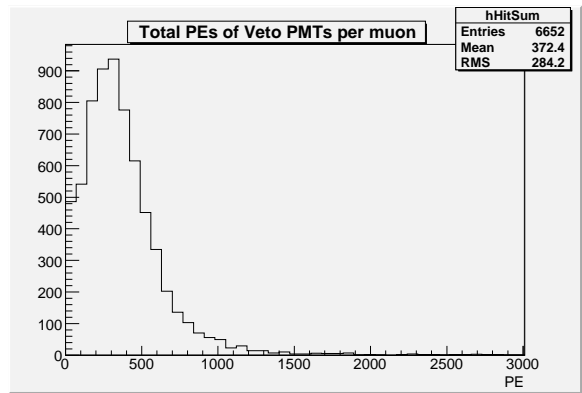


Fig. 6.11. Total number of photoelectrons observed in baseline configuration in the inner shield of the Far Hall.

6.2.6 Inner Water Shield

6.2.6.1 Inner Water Shield Simulation Studies

Figure 6.10 shows the simulated distribution of track length of cosmic ray muons in the inner water shield of the Far Hall. The mean distance traveled through the water is about 5.5 m. With our $\sim 0.5\%$ geometric coverage and assuming a typical bialkali photo-cathode, our simulation predicts that the average number of photoelectrons collected is ~ 372 for the baseline configuration. The distribution can be seen in Fig. 6.11. Our simulation indicates that 2/3 of these photoelectrons are due to reflected photons. A photon collection time of 200 ns and Tyvek reflectivity of ~ 0.8 are assumed. The PMT threshold is assumed to be $\sim 1/4$ of a photoelectron. We conservatively assume an attenuation length of 30 m. These photoelectrons are spread over an average of ~ 72 PMTs as seen in Fig. 6.12, and the resulting distribution of photoelectrons in a single PMT is shown in Fig. 6.13. As expected the average for events with non-zero PMT counts is about 5 photoelectrons, although there is a long exponential tail.

Muons are identified in the Monte Carlo by demanding a minimum number of PMTs to fire. Results on efficiency of the inner water shield as a function of the number of PMTs demanded are shown in Fig. 6.14. In each case a threshold number of PMTs is determined by the requirement that the deadtime due to random coincidences be $< 1\%$. Conservatively an effective singles rate (dark current plus radioactivity) of 50 kHz/PMT was assumed for this calculation. For the baseline configuration described above, this level was reached at a threshold of 11 PMTs, yielding an efficiency of 97.1% as can be seen from the lower curve in Fig. 6.14*.

Studies of the ability of the inner shield to determine the muon trajectory are in the early stages but are very promising. Fig. 6.15 shows a result of a least squares fit to the muon trajectory using the PMT time and pulse height information. The difference between the actual and reconstructed distance of closest approach of the muon trajectory to the center of the water pool is determined with a central RMS of ~ 50 cm.

*Note that since virtually all muons entering the inner water shield must have penetrated the RPCs or the outer water shield, the overall efficiency is higher than this.

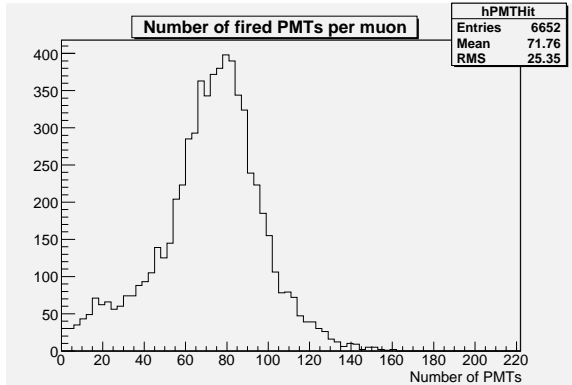


Fig. 6.12. Number of inner shield phototubes hit in baseline configuration of the Far Hall.

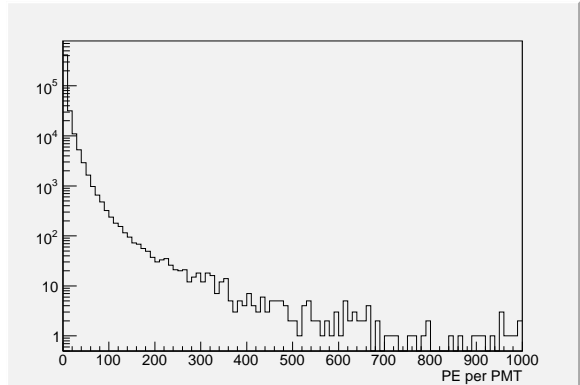


Fig. 6.13. Photoelectrons observed per inner shield PMT in baseline configuration of the Far Hall.

6.2.7 Outer Water Shield

Combined with the RPCs to be discussed below, the outer water shield forms a nearly hermetic muon tagging layer that can determine the path of muons through the region of the antineutrino detectors. In addition, it can measure the efficiency of the inner water shield for muons.

As mentioned above, the water pool is divided into inner and outer sections by reflecting dividers supported on stainless steel frames as shown in Fig. 6.16. The outer sections are 1 m thick. The dividers are multilayer films supported by stainless steel frames. Outer layers of Dupont Tyvek film 1070D sandwich an inner layer of thin white plastic. These films separate the inner and outer water pools optically. Similar films line the sides and bottom of the pool. Figure 6.17 shows these films on a section of PMT support module and Fig. 6.18 shows how the panels are attached to the frames. The frames are also used to support the inner water shield PMTs and some of the outer water section PMTs (the rest are supported on the pool side and bottom walls). The PMTs, bases, electronics and PMT support scheme for this region will be the same as those for the inner pool. However the outer shield will have its own front-end electronics and trigger.

6.2.7.1 Performance of the Outer Water Shield

The distribution of track lengths in the outer shield is shown in Fig. 6.19. Here the average path length is about half that of the inner shield. However, as shown in Fig. 6.20, the number of photoelectrons collected is about 80% of that of the inner shield, because the overall density of PMTs is higher in the outer shield.

Figure 6.21 shows the number of phototubes excited by the passage of a muon through the outer shield. This is about 72% of the case of the inner shield. Figure 6.22 shows the distribution of the number of photoelectrons per phototube for the outer shield. Once again as in the case of the inner shield there is a long tail. The upper curve in Fig. 6.14 shows the efficiency of the outer shield as a function of the number of PMTs required in the trigger. Using the same random rate criterion as for the inner shield, the threshold number of PMTs is 13 and the outer shield efficiency for tracks that hit the water is 97.7%. Note that the events missed by both systems are predominantly corner-clippers that have a very short path length in the water. This can be seen in Fig. 6.23. This implies that the muons missed by the water shield are those which are furthest from the ADs and therefore the least likely to cause fast neutron background. The overall water pool efficiency taking an OR of the inner and outer pool is 98.3%.

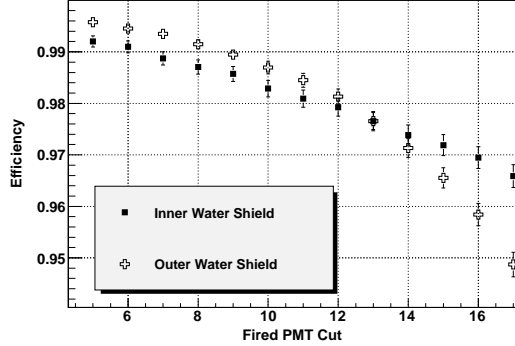


Fig. 6.14. Muon efficiency of the inner and outer water shields as a function of the number of hit PMTs demanded. For the inner shield the threshold level needed to reduce the random rate to 50 Hz is 11 PMTs, for the outer it is 13 PMTs. Approximately 12,000 muons are simulated for each curve.

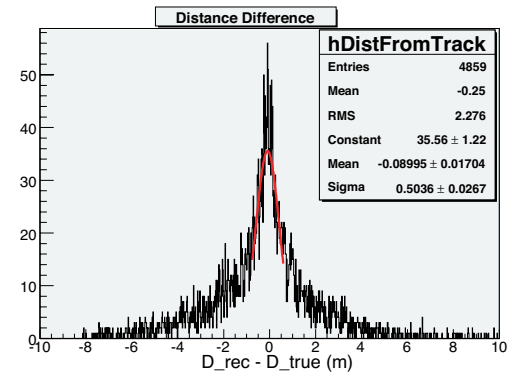


Fig. 6.15. Distribution of reconstructed minus actual muon distance of closest approach to the center of the Far Hall pool.

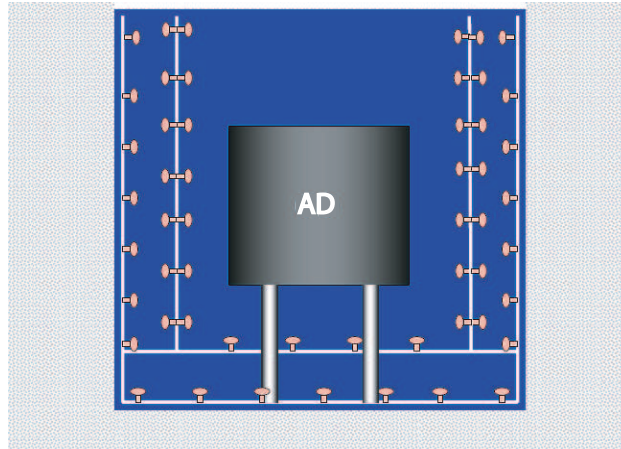


Fig. 6.16. Inner and outer sections of a near hall water pool.

6.3 Resistive Plate Chambers (RPC)

The RPC is an attractive candidate tracking detector for instrumenting large areas. RPCs are economical, and are simple to fabricate. The manufacturing techniques for both Bakelite (developed by IHEP for the BES-III detector [2]) and glass RPCs (developed for Belle [3]) are well established.

An RPC is composed of two resistive plates with gas flowing between them. High voltage is applied on the plates to produce a strong electric field in the gas. When a charged particle passes through the gas, an avalanche or a streamer is produced. The electrical signal is registered by pickup strips placed outside the plates and sent to the data acquisition system. In our case, the RPCs will operate in the streamer mode.

We plan to use RPCs developed at IHEP for the BES-III muon spectrometer for the Daya Bay Experiment. These RPCs were constructed using a new type of phenolic laminate developed at IHEP. The

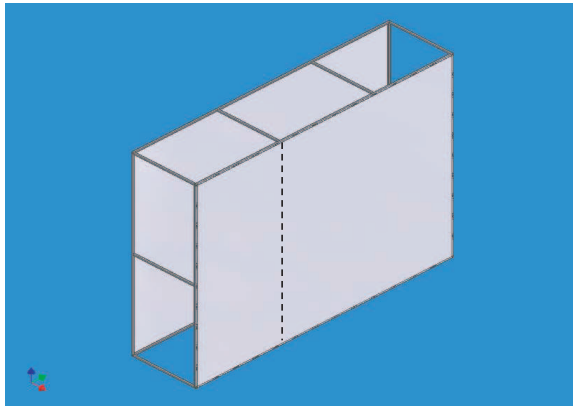


Fig. 6.17. Tyvek pool liner and inner-outer pool separator on PMT support frame.

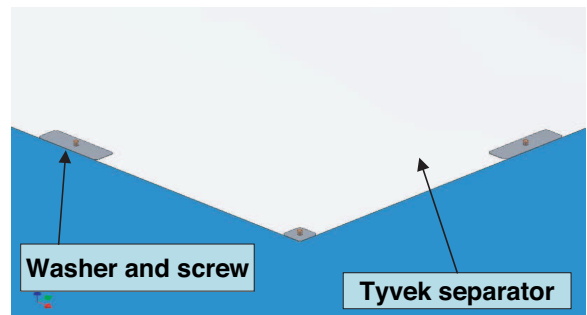


Fig. 6.18. Anchoring scheme for separator panels.

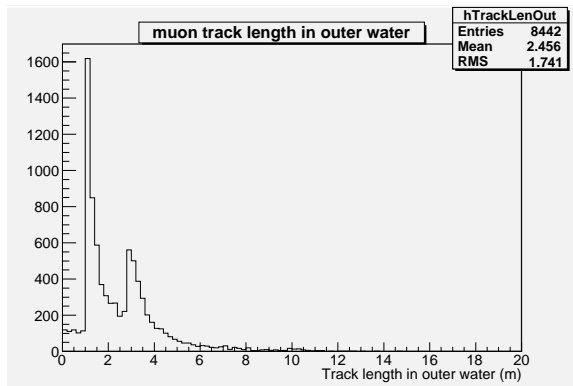


Fig. 6.19. Track length of muons in the outer water shield for the Far Hall. The structure starting just below 3 m is due to muons that enter the side and exit the bottom section of the outer shield.

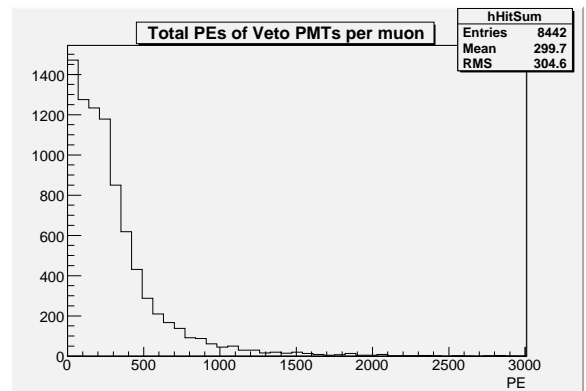


Fig. 6.20. Total number of photoelectrons observed in the outer shield PMT in baseline configuration of the Far Hall.

surface quality of these plates is markedly improved compared to the Bakelite plates previously used to construct RPCs. The resistivity of the laminates can be controlled to any value within a range of 10^9 – 10^{13} Ω·cm. These RPCs can operate without linseed oil coating. Applying linseed oil to the Bakelite plates is a time-consuming step in the production.

About 1000 IHEP-style bare chambers (~ 1500 m 2) have been produced for BES-III. Tests show that the performance of this type of RPC is comparable to that of RPCs made with linseed oil treated Bakelite or with glass.

The efficiency and noise rate of the BES-III RPCs have been measured. In Fig. 6.24, the efficiencies versus high voltage are shown for threshold settings between 50 and 250 mV. The efficiency plotted does not include the dead area along the edge of the detector, but does include the dead region caused by the insulation gasket. This kind of dead area covers only about 1.25% of the total detection area. The efficiency of the RPC reaches a plateau at about 7.6 kV, and rises slightly to 98% at 8.0 kV for a threshold of 150 mV. There is no discernible difference in efficiency above 8.0 kV for thresholds below 200 mV.

It is a standard practice at IHEP to subject a new RPC to 10 kV high voltage in Argon for three or more

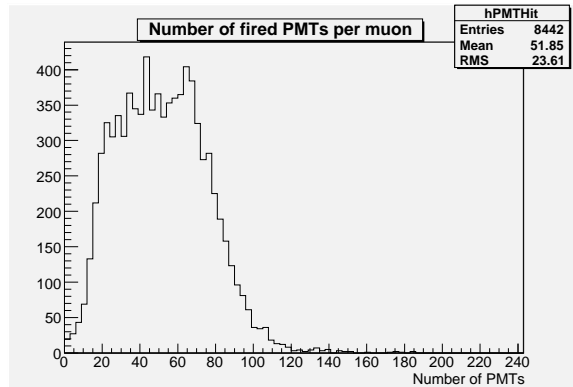


Fig. 6.21. Number of outer shield phototubes hit in baseline configuration of the Far Hall.

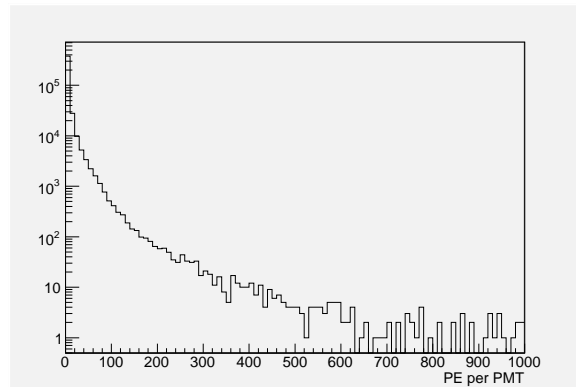


Fig. 6.22. Photoelectrons observed per PMT in baseline configuration of the outer shield of the Far Hall.

days, a process known as “training”, to burn off dust and corona points in the chamber. The singles rate of an RPC trained for three days is typically $<0.1 \text{ Hz/cm}^2$. The singles rate will drop significantly below this if the training lasts for more than one month. Figure 6.25 shows the singles rates at various thresholds of an RPC that had been trained for more than a month.

Although the typical singles rate after training is $<0.1 \text{ Hz/cm}^2$ at thresholds above 150 mV, the noise rate increases significantly when the high voltage is raised above 8 kV.

In cosmic-ray tests of ~ 600 BES-III RPCs, the average efficiency was 97%, and only 2 chambers had an efficiency less than 92%. Figure 6.26a shows the efficiency distribution; the efficiency was obtained without excessive chamber noise. Figure 6.26b shows the singles rates of the RPCs. The most probable noise rate was $\sim 0.08 \text{ Hz/cm}^2$. Only 1.5% of these tested chambers had a noise rate higher than 0.3 Hz/cm^2 .

6.3.1 RPC Design

6.3.1.1 Overall considerations

For the Daya Bay experiment, the main function of the RPC detector is to provide a highly efficient hermetic muon tracker on top of the water shield with an efficient trigger for muons. The spatial resolution requirement is quite modest, of order 0.5 m, which can be satisfied by strip readout of rather coarse segmentation. Multiple RPC layers (with alternating x and y readout) will improve the trigger efficiency. The number of layers is determined by the trigger efficiency requirement. Table 6.4 gives the efficiencies under different trigger requirements, assuming an efficiency of 95% per layer (x or y). For four layers, the efficiency for a trigger requiring hits in 3 out of 4 layers is 98.6%. If one of the layers is not working, the trigger requirement can be changed to requiring hits in 2 out of 3 layers, with an efficiency of 99.28%. While this is actually a higher efficiency than a 3-out-of-4 trigger, it comes at the expense of a higher accidental trigger rate. This is acceptable for a small percentage of modules with a “dead” layer. With regard to muon tracking, the loss of coordinate information from a single dead layer is not detrimental. The current plan calls for four layers.

To cover the near and far halls of respective pool areas $18 \text{ m} \times 12 \text{ m}$ and $18 \text{ m} \times 18 \text{ m}$, a modular design is simple and workable. Considerations of practical constraints on mechanical strength, RPC materials, packaging and transportation of the RPCs, lead to a choice of module size of about $2 \text{ m} \times 2 \text{ m}$.

The RPCs will be constructed in layers, with alternating layers giving x and y coordinates, i.e., the readout strips in alternating layers are oriented perpendicularly to one another.

Avoiding dead-space is the primary concern in the design of the RPC modules. This affects the overall

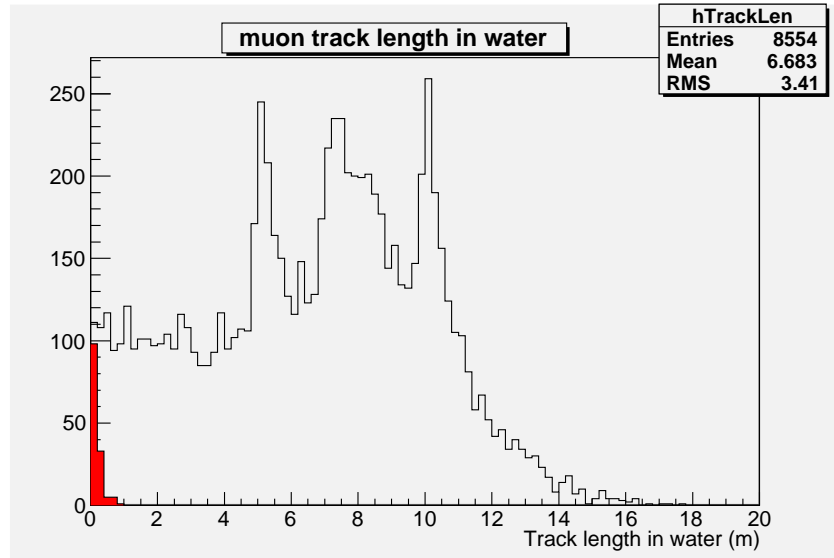


Fig. 6.23. Total track length of muons in the water shield for the Far Hall. Red histogram is events that were missed by both the inner and outer shields.

Layer	≥ 1 criterion	≥ 2 criterion	≥ 3 criterion	≥ 4 criterion
1	95%			
2	99.75%	90.25%		
3	99.987%	99.275%	85.74%	
4	99.999%	99.952%	98.598%	81.45%

Table 6.4. Trigger efficiency as a function of layers and coincidence level

design, the support structure, and the installation of the modules. The dead-space between $2 \text{ m} \times 2 \text{ m}$ modules can be avoided by overlapping them in 9×6 and 9×9 modules in the near and far halls, respectively. Figure 6.27 shows the slanting mode where each module is tilted by a small angle from horizontal, allowing overlap of the modules. All the “odd” rows overlap in the same way, whereas the “even” rows are placed on top of the adjacent “odd” rows. The slanting mode also ensures that each module has at least one side accessible, an advantage in designing gas and high voltage connections.

6.3.1.2 Module Design

In addition to 4 layers of RPC chambers and readout strips, ground planes, separation planes, support and shielding layers are also needed. The thickness of each RPC layer is 6 mm. This includes two PET insulating films, each 0.15 mm thick, one above and one below the chamber. To achieve good conductivity and grounding, the readout strips and ground planes are copper-clad G10 sheets. A polypropylene (PP) honeycomb panel (1 cm or 2 cm thick) is used to separate the adjacent layers. The support shielding layers at the top and bottom of the module have to provide mechanical strength and rigidity, as well as meet grounding requirements. Fiberglass honeycomb panels have good mechanical strength and rigidity, and are the ideal material for this. Fiberglass honeycomb panels with skin thickness of 1.0 mm will be used. A conductive fabric layer between the fiberglass and PP panels will form the ground in the outer shell of the module. The compact and thin Insulated Media RPC module design (denoted by IM_R_IV), shown in Fig. 6.28, with the RPC sandwiched between the strip and ground planes, will be the baseline design because this arrangement

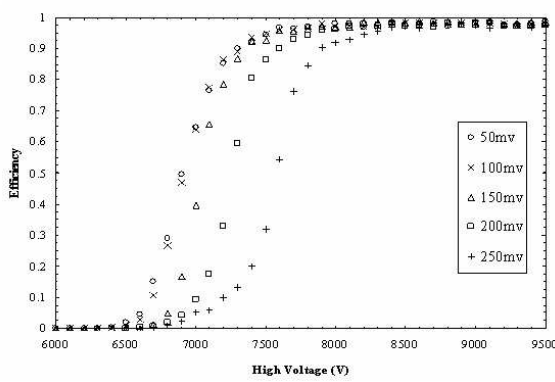


Fig. 6.24. Efficiency of the BES-III RPC versus high voltage for different thresholds.

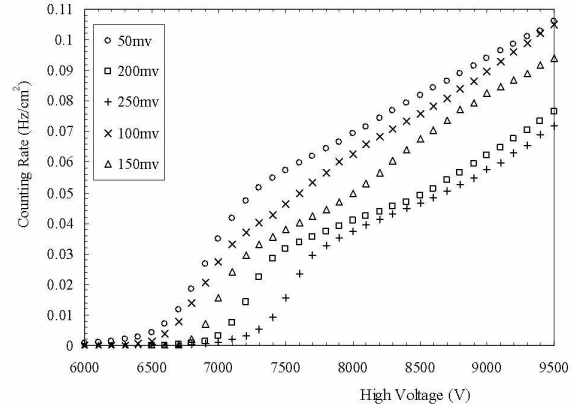


Fig. 6.25. Noise rate of the BES-III RPC versus high voltage for different thresholds.

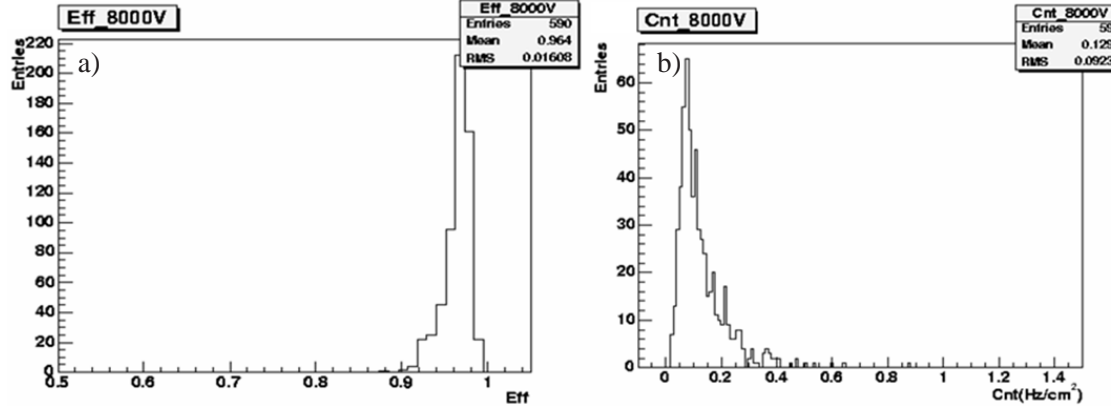


Fig. 6.26. Distributions of a tested RPC a) Efficiencies. b) Singles rates.

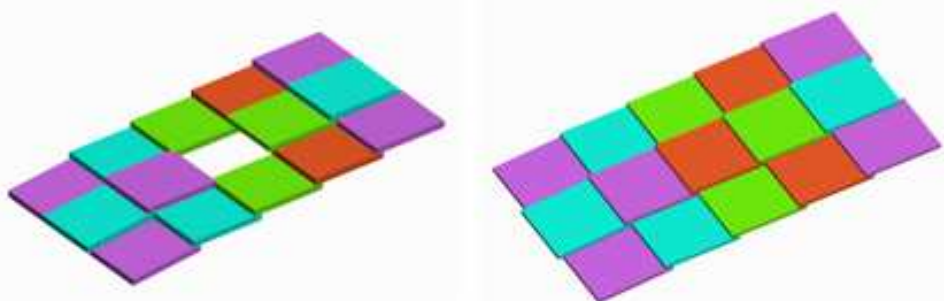


Fig. 6.27. Two 3-D models of the slanting mode. **Left:** the columns are aligned (the white space is a module removed to reveal the overlap). **Right:** there is an additional offset in the even (middle) row, with all the even modules offset slightly to the left.

gives a larger signal than the other arrangements that were considered.

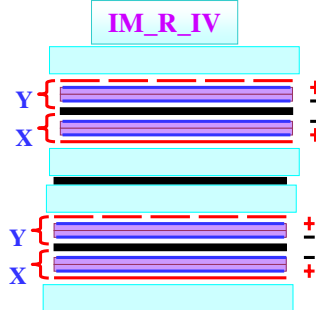


Fig. 6.28. The layer structure of the "IM_R IV" module design

In order to cover the entire $18 \text{ m} \times 12 \text{ m}$ and $18 \text{ m} \times 18 \text{ m}$ sensitive areas, modules slightly larger than $2 \text{ m} \times 2 \text{ m}$ dimensions are needed to provide sufficient overlap. The overlap space between adjacent modules is determined by two factors. First, there has to be some free space around the perimeter of the module for gas, HV, and readout electronics distribution lines. From the experience of the muon detector at BESIII, the width of this free space has to be $> 3 \text{ cm}$. Second, to ensure that there is no dead-space for muons with incident angles up to about 75° (normal incidence is 0°), the thickness of the module has to be

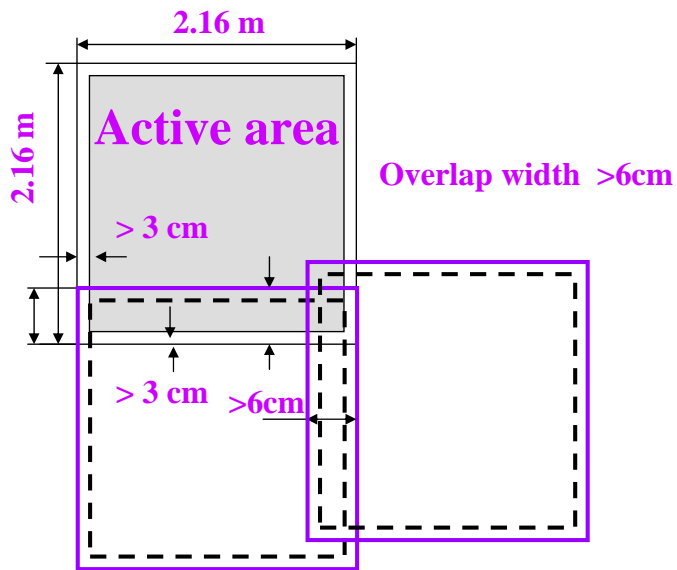


Fig. 6.29. Module dimensions and overlap width. See also Fig. 6.27.

Since the Bakelite sheets are made by industry in $2.4 \text{ m} \times 1.2 \text{ m}$ sizes, the largest width one can obtain, after removing some unusable edges, is 1.1 m . Therefore, each RPC layer has to be constructed from two side-by-side single-layer RPCs of dimensions $2.1 \text{ m} \times 1.1 \text{ m}$ and $2.1 \text{ m} \times 1.0 \text{ m}$. There is a 10 mm edge

frame in the RPC, leaving some dead area between these side-by-side RPC layers. Since there are 4 layers of RPCs, the dead-space between RPCs can be minimized by an appropriate stacking of the RPCs, as shown in Fig. 6.30. Figure 6.31 shows the simulation results for the four stacking schemes considered. The current

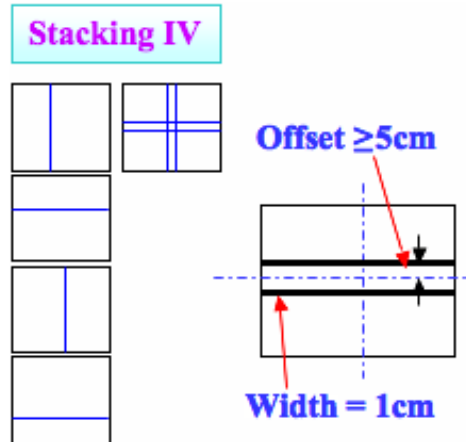


Fig. 6.30. Stacking scheme of the RPC layers within a module. The layers are shown, expanded vertically, with a projection of all four layers shown at the right.

baseline design, “Scheme IV”, which rotates the dead-space between two RPCs successively by 90 degrees, has the smallest overall dead-space of the schemes considered.

6.3.1.3 Module mechanical structure

The overall mechanical structure of the RPC module is shown in Figs. 6.32 and 6.33. The outermost part is constructed with 30 mm × 2 mm aluminum channels and 40 mm x 5 mm reinforced steel plates. Combined with the top and bottom honeycomb panels, they provide the main fixing and support functions. The four vertical steel ribs provide a lifting ring of 10 mm diameter for the lifting of the module. The lifting ring, connected through a U-channel steel piece and another connecting piece, is riveted to the steel ribs. Inside the U-channel connector there is an inverted U-shape PVC connector, which can be used to fix the RPC and the honeycomb panels, transferring the force to the steel ribs. In the horizontal direction, there are four 50 mm x 3 mm aluminum ribs. The aluminum rib is pressed underneath the steel rib, with no rivets at the intersections. The aluminum channel protects the cables and gas lines inside, and serves to connect the top and bottom honeycomb panels together (screw holes are spaced 200 mm apart for this purpose). This increases to some extent the overall mechanical strength of the module, as well as allowing the module to be disassembled easily for repair and maintenance.

6.3.1.4 Signal Readout

The spatial resolution requirement for the RPC readout is quite modest, of order 0.5 m. This can be satisfied, in principle, by strips of 1 m pitch. Through extensive measurements of signals with wide strips, we propose to use strips of 25 cm pitch of zigzag design, as shown in Fig. 6.34. The effective width of the strip is 6 cm. The effective length of 8 m does not cause degradation of the signal. There are 8 readout channels per layer. Since there are 32 channels in one Front End Card (FEC), each module can be served by one FEC.

The signal amplitude is equivalent to that of 6.5 cm strips, and is comparable to that of the commonly used 2-5 cm strips. The y readout strips come out of the top of the module. The x readouts come out of both

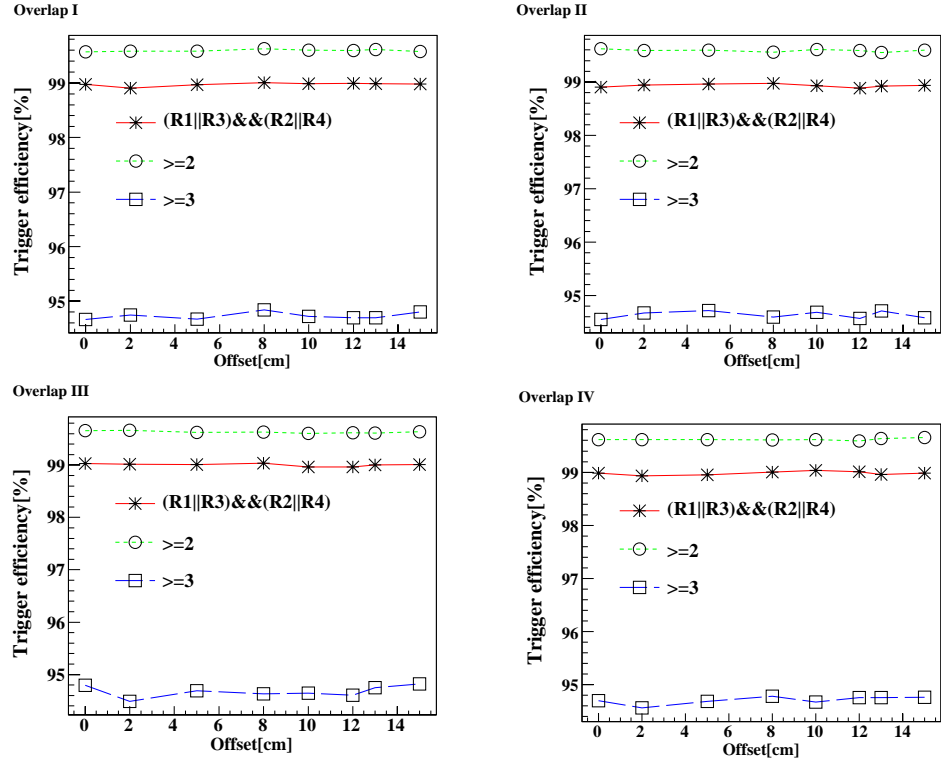


Fig. 6.31. Comparison of the trigger efficiency for the four stacking schemes.

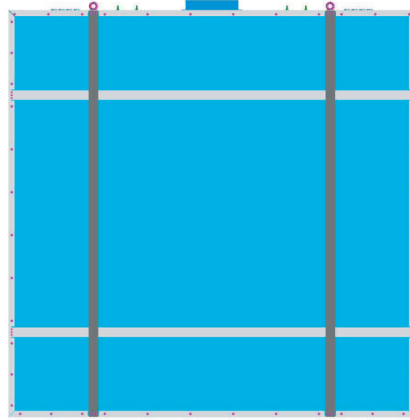


Fig. 6.32. RPC module mechanical and services structure. The gas and HV connections are at the top. The lifting rings (red) are connected to the steel vertical supports (gold/brown, two of the four are shown). Two of the four aluminum horizontal supports are shown in light gray.

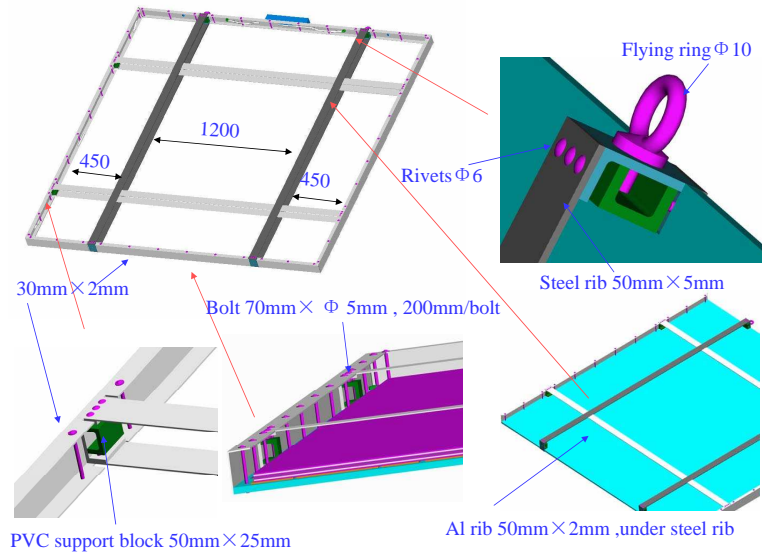


Fig. 6.33. RPC module support structure.

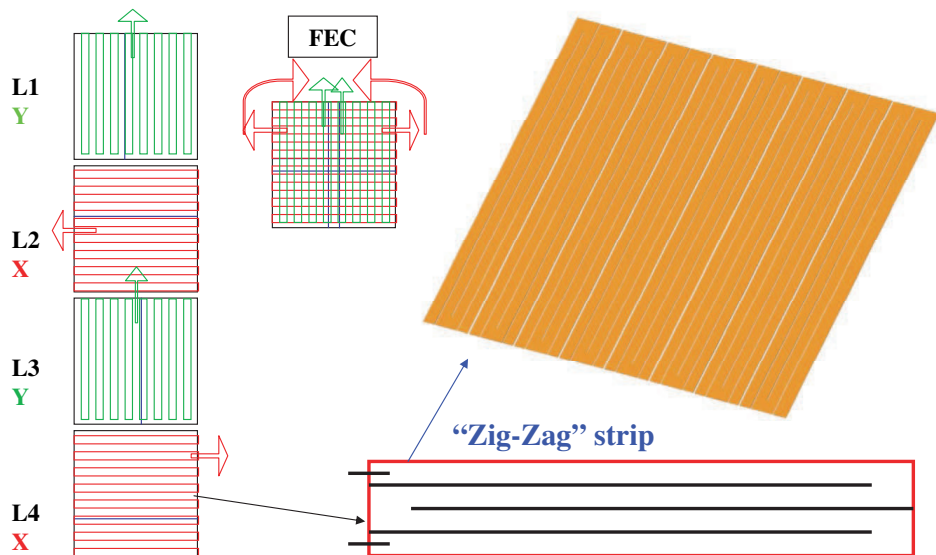


Fig. 6.34. Module size and overlap width.

sides, and are routed to the top of the module. There is an electronics socket on the side of the module. The signal wires from the four strip layers are connected to the four connectors in the FEC as shown in Fig. 6.35. Fig. 6.35 is an illustration of the electronics box assembly structure.



Fig. 6.35. The assembly structure of the electronic box.

6.3.1.5 Gas Distribution

To avoid the adverse effects of large flow resistance of series gas flow, cross-contamination of parallel flow, and aging effects due to fluoride ions, each module will be supplied by two independent gas channels. Each gas channel is connected to 4 RPCs in series, with a volume of 17.64 liters, supplied independently from outside. The gas connectors will be located according to the diagonal flow (cater-corner) principle. To ensure that the gas inlets and outlets are always on the top (accessible) side of the module, the first and third layers are daisy-chained together, and the second and fourth layers are daisy-chained together, as shown in Fig. 6.36.

6.3.1.6 High Voltage Connector Arrangement

The high voltage copper electrode is attached to the graphite surface of the RPC by conductive epoxy. One end of the copper plate protrudes slightly beyond the edge of the RPC, for convenient soldering of the copper plate to the high voltage cable. Since the copper plate is very thin and easy to break, we normally tape the copper plate to the gas connector, allowing the gas connector to protect and support the copper plate. Therefore, the arrangement of the high voltage is the same as that of the gas. For the IM_R_IV baseline design, the high voltage of the top-most layer is positive, in the sequence "top:+- -++- -:bottom". Hence the positive and negative high voltage distributions, as shown in Fig. 6.37, basically separate the positive and negative high voltage cables. In the left and right sides of the top of the module, there are 4 high voltage outlets, the left outlet corresponds to two negative high voltage channels, right outlet for positive high voltage channels. From outside to inside, we have the corresponding high voltages of 1 to 4 layers of RPCs. From left to right, the high voltage is 1-, 2-, 3-, 4- and 4+, 3+, 2+, 1+. This arrangement is good for the independent load increase and control of the high voltage for each layer. A grommet is inserted in every outlet, to ensure good insulation between the high voltage and the aluminum frame, and avoid abrasion of the high voltage cable.

6.3.2 RPC Gas System

The RPC gas system will be similar to that used in the BELLE [11] and BABAR [12] experiments, in which a gas mixing system distributes gas to the individual RPCs through simple "flow resistors", with the output flow from each chamber separately monitored by a low-cost electronics bubbler [13]. A high-level diagram of the system for one of the Near Halls is given in Fig. 6.38.

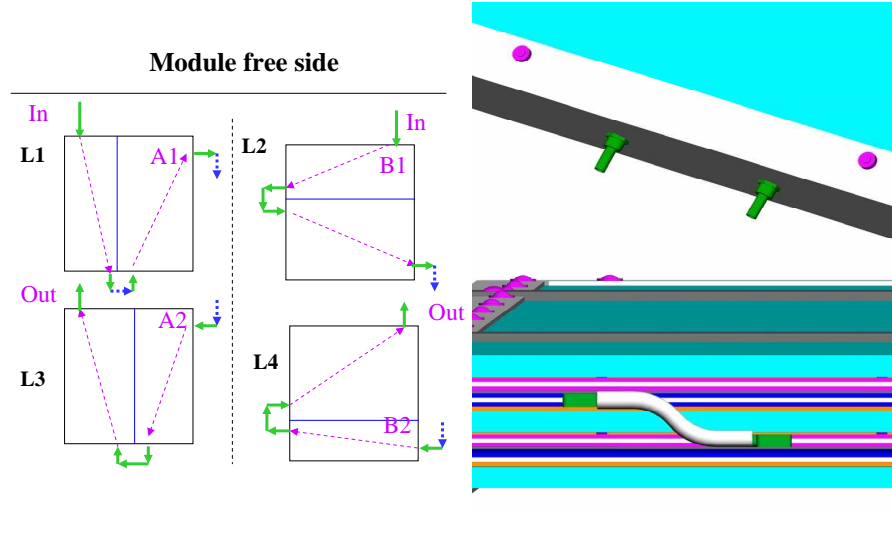


Fig. 6.36. Arrangement of two-in two-out gas flow.

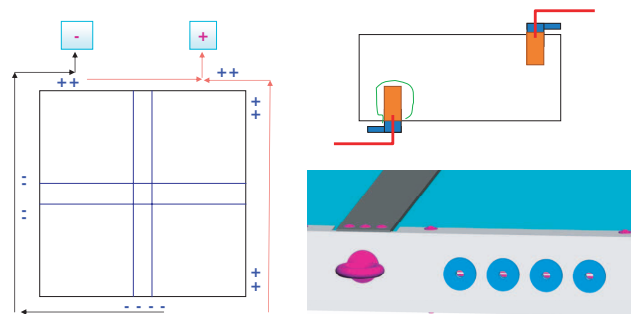


Fig. 6.37. Two-in two-out high voltage arrangement.

Mixing of the chamber gases is performed with mass flowmeters, as sketched in Fig. 6.39. It may be advantageous to use “drop-in” modular mixing components recently developed for the semiconductor processing industry, such as the Integrated Gas System of Fujikin [15].

A four component gas mixture, Ar/R134A/Isobutane/SF₆ (75.4/20/4/0.6 % fractions by volume), will be used. The small admixture of SF₆ permits the RPCs to be operated with good efficiency at significantly lower voltage [16].

The electronic bubbler system [13] monitors the chamber gas flow by counting gas bubbles in a small oil bubbler as they pass a photogate, as indicated in Fig. 6.40. There will be one bubbler for every four RPCs, Detailed histories of the input and output gas flow will be available via the online slow-control system.

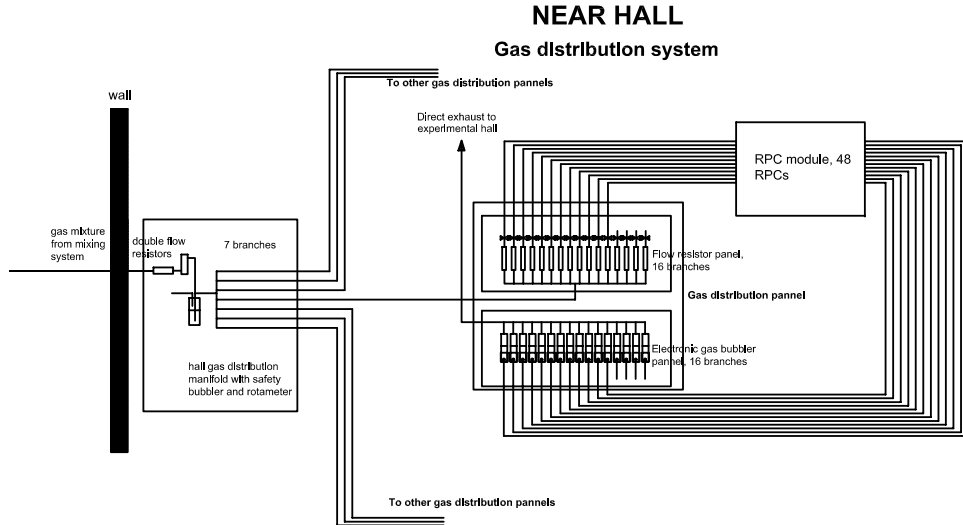


Fig. 6.38. Overall process diagram of the RPC gas system in one of the Near Halls.
From [19].

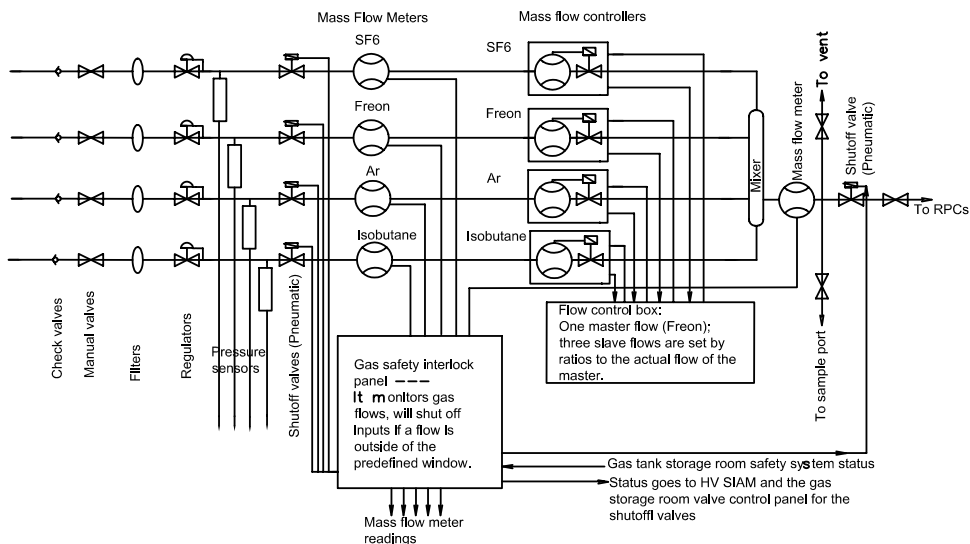


Fig. 6.39. Process diagram for the gas mixing subsystem. From [19].

The gas will be input from multiple, switchable sources to minimize interruptions of the gas flow during chamber operation. However, the gas flow rate will be only ≈ 1 chamber volume per day ($6 \text{ m}^3/\text{day} = 5 \text{ kg/day}$), so that short interruptions of the flow will be of little consequence. The used gas will be exhausted into the return ducts of the detector hall air-handling system.

While a mixture of isobutane and air is flammable for isobutane concentrations between 1.8 and 8.4% by volume, the region of flammability is reduced by the presence of an additional inert component of the gas. In the RPC gas mixture the inert component is Ar/R134A/SF₆ with volume percentages 78.4/20.8/0.6. The range of flammability of this particular inert gas mixture together with isobutane and air has not been studied in detail, but it should be similar to that when using Ar/C₂F₆ (70/30), as was calculated in the Fire Hazard Analysis for the BaBar experiment [20]. As shown graphically in Fig. 6.41, there is no region of flammability for a gas mixture in which the ratio of isobutane to the inert component of the RPC gas is 4%

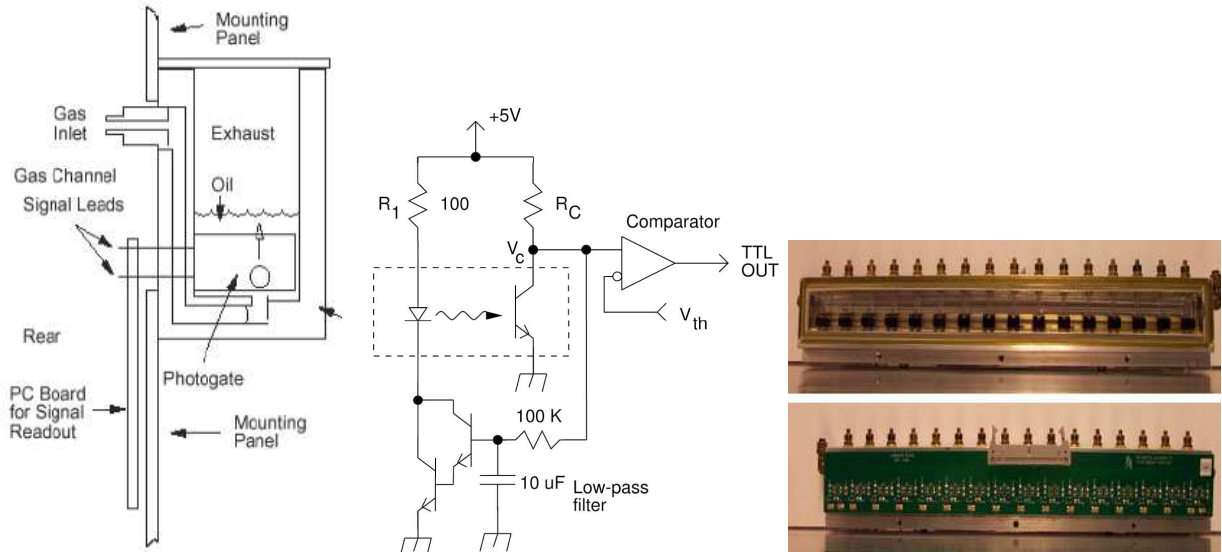


Fig. 6.40. Concept, circuit diagram and photographs of the electron bubbler system. From [13].

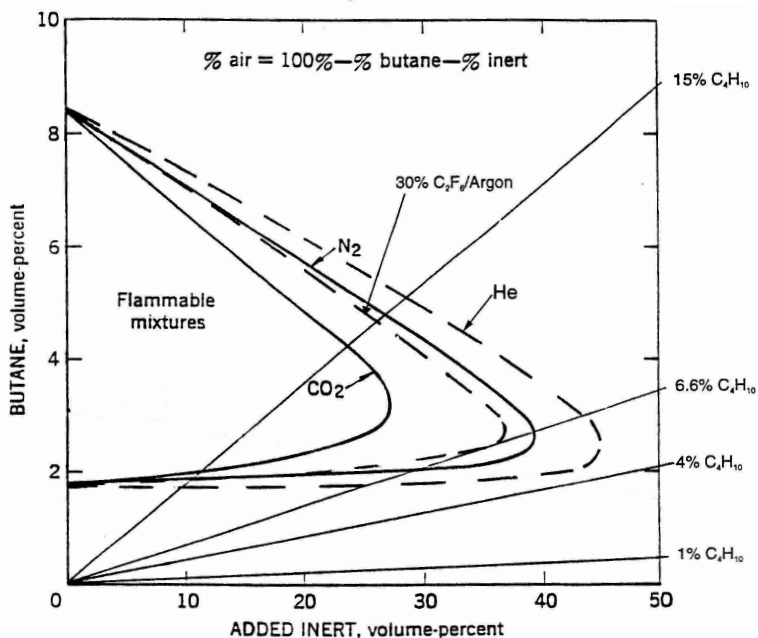


Fig. 6.41. Flammability regions for isobutane gas mixtures. There is no region of flammability for a gas mixture in which the ratio of isobutane to the inert component of the RPC gas is 4% or less. From [20].

or less. Hence, the RPC gas mixture is nonflammable when exhausted into the air-handling system, even in the event of prior air leaks into the RPCs.

An extensive safety system with status monitors and interlocks will be implemented via the slow-control system. For a recent example of a muon-chamber-gas safety system, see [14].

Each detector hall will have its own gas distribution system. The layout of the system in one of the Near

Halls is sketched in Fig. 6.42.

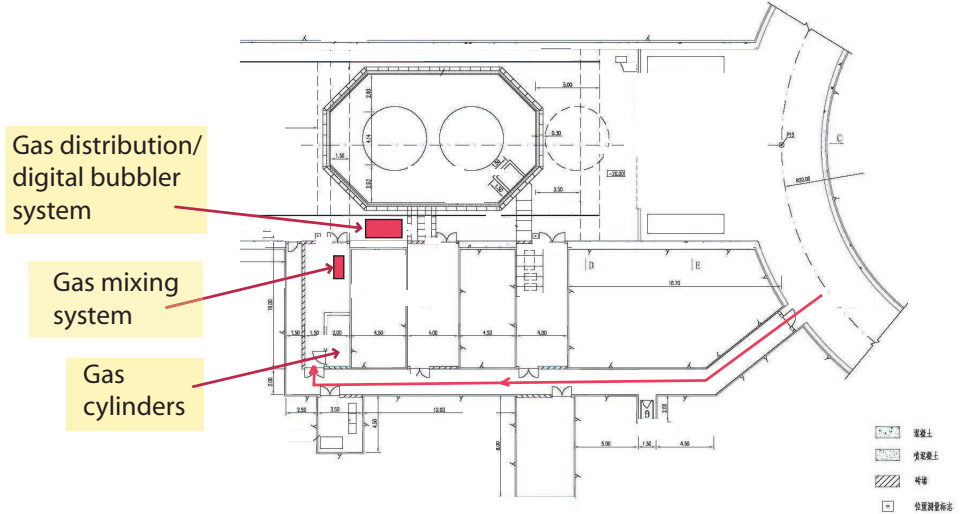


Fig. 6.42. Layout of the RPC gas system in the Daya Bay Near Hall.

6.3.3 RPC High Voltage System

The RPC high voltage system is composed primarily of commercial parts from CAEN [21]. All gas gaps will be operated with an ~ 8 kV gap. This will be achieved by using ~ 5.5 kV positive supply in conjunction with a ~ 2.5 kV negative supply. The positive supply will be the A1526P model, which provides up to 15 kV at 1 mA in each of six channels. Two cards will be used at each site. At the near sites each positive spigot will supply HV to 18 2 m by 2 m RPC planes with an expected current draw of less than $500 \mu\text{A}$, while at the far site each channel will supply 28 gaps with a current draw of less than $700 \mu\text{A}$. The negative supply will be the A1932AN, which has 48 channels at up to 3 kV and 0.5 mA. Again two cards will be used at each site and up to 4 RPC planes will be powered by each channel with a per channel current of less than $100 \mu\text{A}$. At each site the high voltage will be powered and controlled by a CAEN multichannel power supply mainframe (model SY1527LC) which will house both the positive and negative supply cards.

6.3.4 RPC Performance

Taking into account inefficiencies due to dead-spaces, we expect the overall efficiency of a single layer to be $\varepsilon \sim 96\%$. If we adopt the definition of a track as hits in at least three out of the four layers within an area of $\sim 50 \text{ cm} \times \sim 50 \text{ cm}$, the tracking efficiency is calculated to be at least 99.1%. Assuming a conservative bare chamber noise rate, r , of 1.6 kHz/m^2 (twice the BES-III chamber measurements), a signal overlap width τ , of 25 ns (40 MHz clock rate), and a coincidence area, A , of 0.25 m^2 , the accidental rate would be about $6 \times 10^{-5} \text{ Hz/m}^2$. For the far hall, this gives a total accidental rate of 0.02 Hz and a negligible contribution to the deadtime in the case that a muon signal is defined by a track in the RPCs alone (*c.f.* the cosmic ray muon rate of 16 Hz in the Far Hall). A test of a 3 layer configuration with prototypes of the Daya Bay chambers, using a track definition of two out of three planes hit, found a coincidence efficiency of $99.5 \pm 0.25\%$, which is consistent with that calculated. The efficiency curves are shown in Fig. 6.43.

Initial simulation results based on measurements of radioactivity in the Aberdeen Tunnel predict singles rates from radioactivity of $\sim 650 \text{ Hz/m}^2$

Note that when the RPCs are added to the simulation of the veto system efficiency, they raise the overall efficiency of the three components of the system in OR to 99.2%. When the probability of each muon to

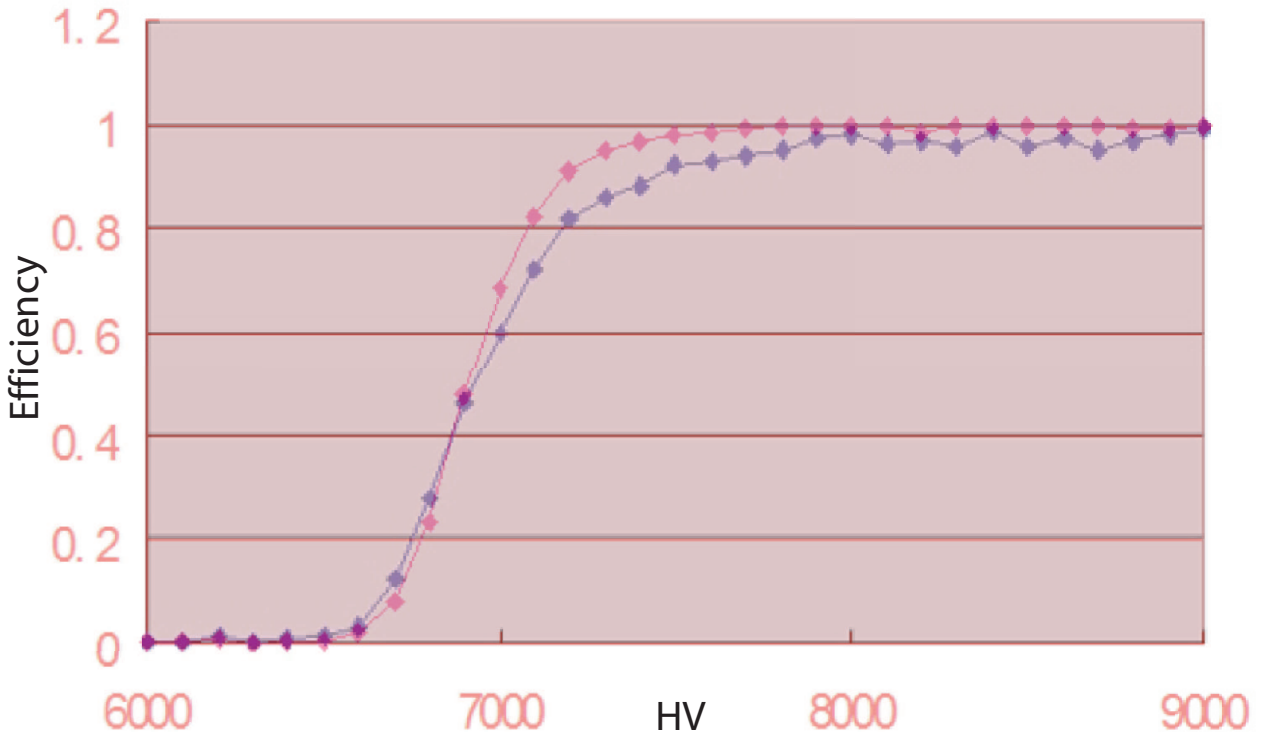


Fig. 6.43. Efficiency as a function of gap voltage for the individual modules of the Daya Bay prototype RPCs (blue) and for the system when two out of three hit modules are required (red).

create a fast neutron background event as a function of distance of the muon trajectory to the nearest AD is taken into account, since the muons that are missed are those furthest from the ADs, the effective efficiency will meet the 99.5% requirement.

6.3.5 RPC Support Structure

6.3.5.1 Physics Requirements

The RPC tracker has to be supported over the water pool by a mechanical structure. The top of the mechanical support structure has to be less than 750 mm from the water surface. The four sides of the tracker have to extend 1 m beyond the edge of the pool, tracking muons entering the rock surrounding the water pool for background study. The far hall water pool is 16 m in maximum length and 16 m in maximum width, and the near hall water pools are 16 m in maximum length and 10 m in maximum width. Two sets of RPC support structures are called for, one with length 18 m, width 18 m for the far hall, and a second set with length 18 m, width 12 m, for the near halls, as shown in Fig 6.44.

6.3.5.2 Mechanical Structure Requirements

The RPC support structure has to provide support and anchor for the RPC modules. The RPC modules have dimensions: length 2 m, width 2 m, height 7 mm, and weight less than 40 kg/m^2 . Each RPC module has to be positioned and surveyed. Taking into account the weight of the positioning fixtures, the RPCs are assumed to have a weight of 50 kg/m^2 . The main support structure will be constructed with steel H-beam with transverse and diagonal braces. Details of the Far Hall structure are shown in Fig. 6.45.

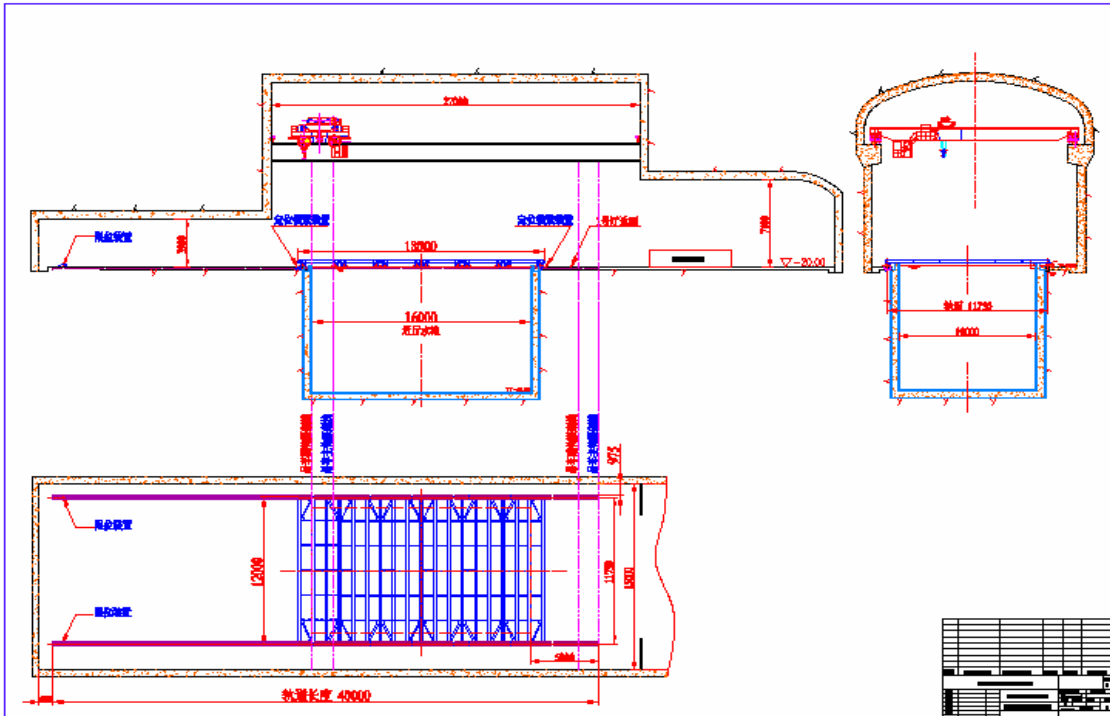


Fig. 6.44. Diagram showing RPC main mechanical support.

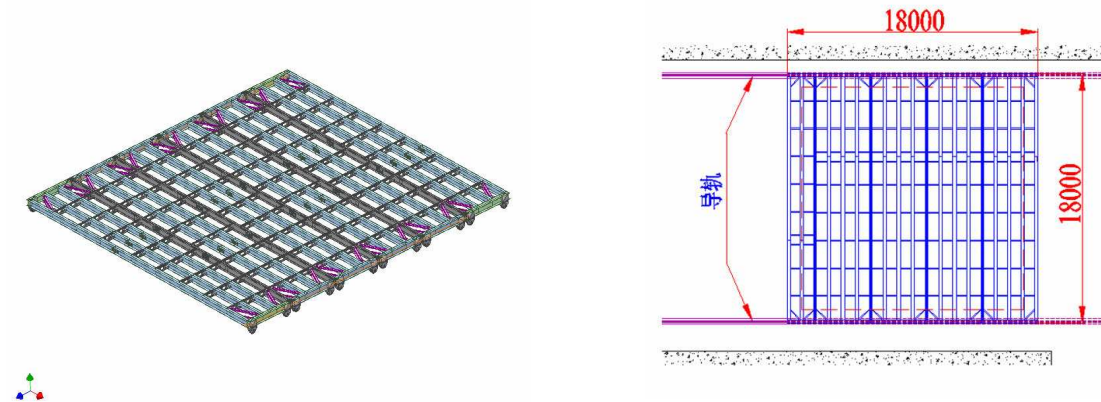


Fig. 6.45. RPC support structure for the far hall ($18 \text{ m} \times 18 \text{ m}$).

6.3.5.3 Moving Mechanism Requirements

Since the neutrino detector in the water pool has to be hoisted and removed, in order to be replaced by another neutrino detector to meet the swapping requirement, we have to be able to move the RPC support structure away to allow access to the neutrino detectors. Therefore, we place rails on both sides of the water pool and wheels underneath the RPC support structure, equipped with two driving wheels and two follower wheels as shown in Fig. 6.46.

The main mechanical structure when fully loaded with RPCs has to be able to move along a straight

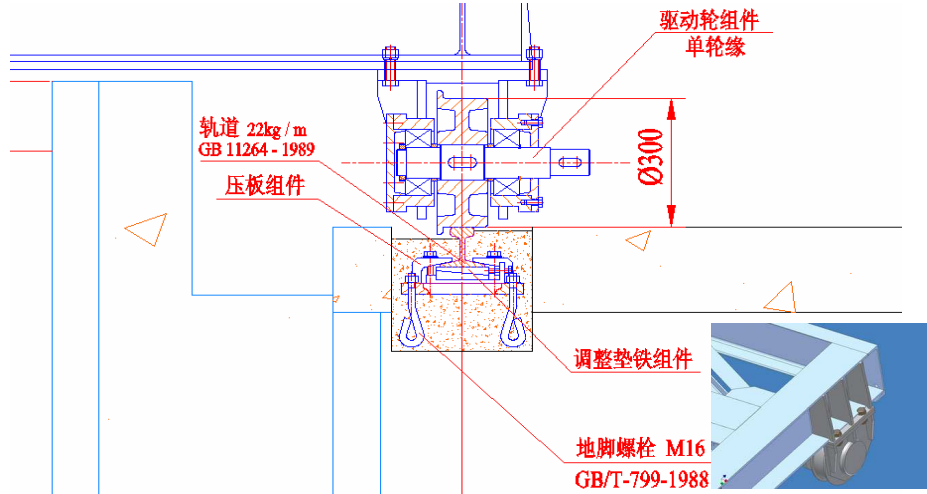


Fig. 6.46. Wheels and track.

track, of 18 m length; the moving structure is required to be stable, safe and reliable, with little vibration. The guiding track has to be constructed precisely such that there is no jamming of the wheels in the track. The travel along the track direction will be limited by start and stop. Locking devices will be constructed at the operating position and its parking position to expose the water. The movement will be driven by a motor, the drive train from a motor, decelerator, to the driving wheels. The two sets of driving equipment are controlled by a frequency converter, starting at the same time, and synchronized in their operation. The moving speed is 0.03 m/s, taking about 10 minutes to reach the final position. The electrical control includes overload protection, over-current protection functions.

6.3.5.4 Design details

The material will be Carbon steel, Q235A GB/T 700-1988. To facilitate the fabrication, assembly and transportation on the road and in the tunnel, the RPC mechanical structure is subdivided into smaller pre-assembled subunits. The subunits will be welded from the components in the factory, and assembled in the factory by bolting the subunits together. After the units passed the adjustment, tests and measurements, they will be connected as a unit. The wheels will be put on the units, and tested on rails. After the units passed the test, they will be disassembled and transported to the job site to be re-assembled. Details are shown in Figs. 6.47 and 6.48.

During the construction and assembly, the local deformation and overall deformation of the subunits and units are controlled.

The surface of the support structure will be sand blasted, and painted with a primer and a final coat. This will prevent the contamination of the steel to the pure water; it also prevents rusting of the steel due to the moisture in the environment.

6.3.5.5 Strength Analysis of the Mechanical Structure

(1) RPC support structure I The main beam uses hot rolled H-beam HM350X250. The total amounts of material needed for the structures are 36 tons and 40 tons for the far and near halls, respectively. The maximum deflection of the main beam in the far hall without the RPC load is given by

$$Y_{max} = -\frac{5qL^4}{384EI} \quad (30)$$

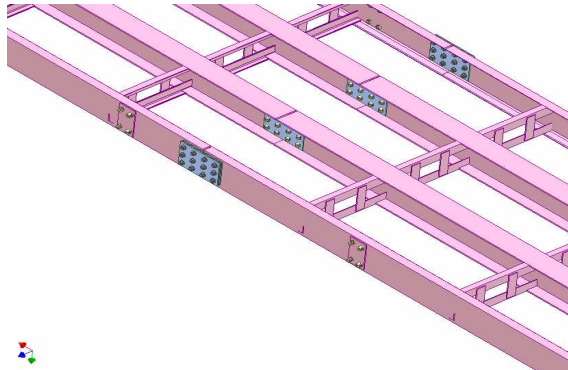


Fig. 6.47. Subunits assembled into a unit.

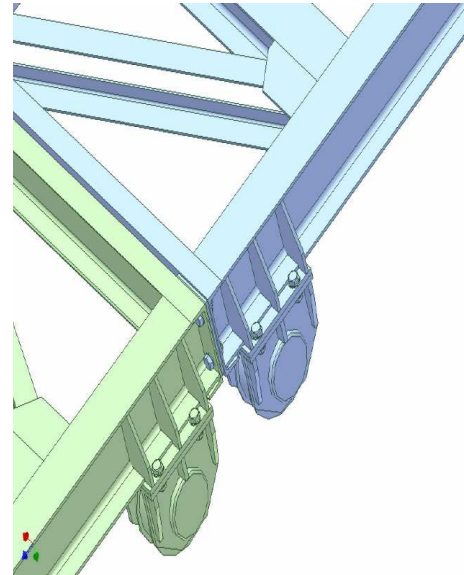


Fig. 6.48. Units assembled together.

where Y is the maximum deflection in mm, q is a uniform load of 0.797 N/mm, due to a total load of 36 tons for the 18 m beam, L is the span of the main beam, 18000 mm, E is the Young's modulus, 206 GPa, and I is the cross sectional moment of inertia, $I = 2.17 \times 10^8 \text{ mm}^2$.

The maximum deflection due to its own weight is about 24 mm. If we add the weight of the RPC detector, the fixture, and installation fixture all on the single main beam, estimated to be 0.5 N/mm, the maximum deflection is about 40 mm.

(2) RPC support structure II: Using the same material for the H-beam, the maximum deflection of the main beam in the near halls, which is 12 m long, is calculated from Equation ?? to be about 6.6 mm.

If we include the weight of the RPC detector, the fixture, installation fixture all on the single main beam, the maximum deflection is 12 mm.

6.3.5.6 RPC Support Structure Finite Element Analysis

We set up a quarter model, shown in Fig. 6.49, for a finite element analysis. The structure, under a load consisting of its own weight and the weight due to the RPC detector, is supported at both ends by a simple support force. Results can be seen in Figs. 6.50 and 6.51.

$$\begin{aligned} \sigma_{max} &= 70.2 \text{ MPa} \\ [\sigma] &= \frac{\sigma_s}{n} = \frac{235}{1.3} = 181 \text{ MPa} \\ \sigma_{max} &< [\sigma] \end{aligned} \quad (31)$$

The safety factor is 2.6.

6.4 Manufacturing Plan.

6.4.1 Commercial Components

6.4.1.1 Commercial Components for the Water Shield

The main commercial components are the ~600 8-inch phototubes. We are considering the three manufacturers, Hamamatsu (R1512), Electron Tubes (9354KB), and Photonis (XP1806). In addition there are

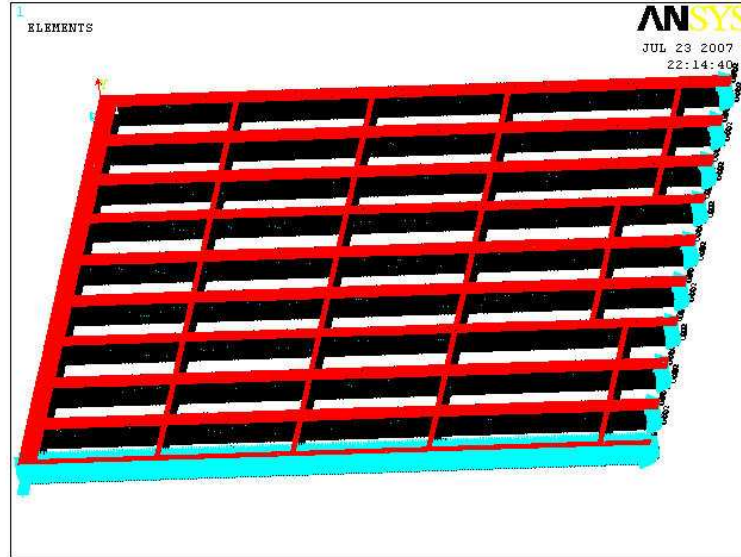


Fig. 6.49. Model for calculations.

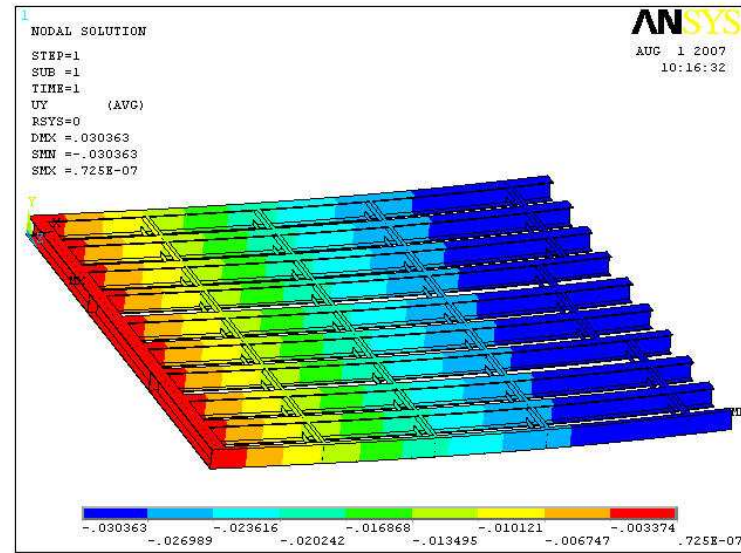


Fig. 6.50. Maximum deflection 30.36 mm.

approximately 500 legacy PMTs from the MACRO experiment, most of which can be used in the muon system. Bases may also be bought from the manufacturers although we are leaning toward fabricating them ourselves. We will test all the MACRO PMTs to determine the best ones to use. A decision on the type of new PMT to be purchased will be made by January of 2008. Since the PMT requirements of the AD system are more stringent than those of the veto, in order to minimize the overhead of having multiple PMT types and to get the benefit of possible volume discounts we will use the same PMTs as that system, unless there is a significant financial penalty for doing so. If we purchase the PMTs (R5912) and bases from Hamamatsu, they can deliver approximately 200/month to Daya Bay starting three months after the order

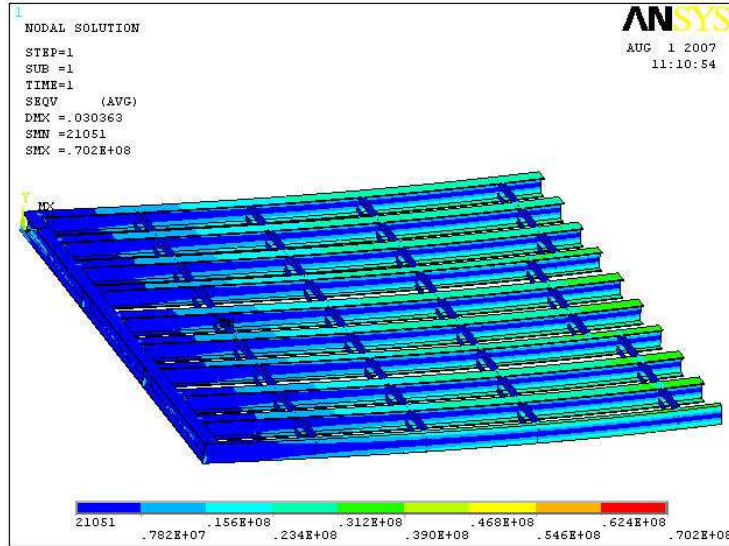


Fig. 6.51. Maximum stress 70.2 MPa.

Component	Number	Source
PMTs/bases	1000	Hamamatsu/ET/Photonis/in-house
PMT electronics	1000	IHEP
RPCs	800	IHEP
RPC FEEs	6400	USTC
PMT support structure		IHEP
RPC roof support		IHEP

Table 6.5. Components of muon system

is placed. Assuming CD-3A approval is secured in March of 2008 and the order is placed immediately, PMTs will begin to be delivered in June of 2008. The complete order for the muon system and the ADs could be completed by January of 2010. Sufficient PMTs for both the ADs and the muon system of the Daya Bay Near Hall could be delivered by October 2008. In our baseline, the HV supplies will be commercial (probably from CAEN or Wiener), although R&D on a home-built system is underway.

6.4.1.2 Commercial Components for RPCs

The production of the Daya Bay RPC chambers will take place in Beijing, China. A local company, called Beijing Gaonengkedi Science and Technology Co. Ltd. (GNKD), will be contracted to produce all the bare RPCs. This company has the experience of producing 1500 similar bare RPCs for the BESIII muon detector.

GNKD will obtain its Bakelite sheets from an outside supplier. Right now, a few Bakelite production companies, including the one which produced the Bakelite plates for the BESIII RPC detectors, are under consideration. Once the Bakelite producer is selected, the production of all the Bakelite plates will take only about 20 days, tentatively scheduled starting at the end of December, 2007.

All the RPC bare chambers will be assembled in GNKD. The assembly procedure includes gluing the spacers between the Bakelite sheets and applying a graphite layer on top of each Bakelite sheet. All the

production fixtures, including a large clean room, are in place. The staff at GNKD will test the chambers for gas tightness and HV integrity. The bare chambers which meet the acceptance criteria will be transferred to IHEP for further testing and assembly into modules. The RPC bare chamber production rate will be about 10 m^2 per day (include the weekends). The Daya Bay muon tracker requires about 3500 m^2 of RPCs; the bare RPC production can be accomplished in about 1.5 years. ($3500 \text{ m}^2 / 10 \text{ m}^2/\text{day} = 350 \text{ days}$.)

The bare chambers will be trained for 1-3 days. The trained RPCs will be tested for performance including dark current, singles rate, and efficiency.

6.4.2 Components to be Fabricated In-house

6.4.2.1 Components to be Fabricated In-house for Water Shield and Outer Water Sections

6.4.2.1.1 PMT base fabrication

The main components to be fabricated for the water shield are the PMT bases if we fabricate them ourselves. This fabrication will include 40–60 meters of Polyethylene-jacketed high voltage 50Ω coaxial cables for transmitting HV and signals. These cables will be soldered to the bases and potted with epoxy at one end and will have an SHV connector at the far end. Fig. 6.52 shows a prototype base with the end removed. The mechanical parts of the water proof potted PMT base housings will be designed and fabricated



Fig. 6.52. Prototype water-proof base for muon system PMTs.

in UCLA. The design will commence in April 2007. We expect to complete the design and prototyping of these bases by the end of January 2007. Based on similar designs, the UCLA machine shop has estimated that the production of each mechanical housing will take 2.5 hours. Assuming availability of funding by

March 2008, we expect to produce 100–200 housings per month after an initial setup period of 1 month. This will result in delivery of 100–200 units per month starting in April 2008.

The PMT base printed circuit fabrication and the assembly will be done by external vendors. Based on past experience we expect that by July 2008 we will have 500 PMT bases tested and available for shipment to China. The remaining bases could be delivered at a rate of 200–400 units per month following the initial delivery if required.

The PMT base printed circuit boards and the housings will be pre assembled in US and will be shipped to Dongguan University for final testing and potting mainly by the Chinese members of the Daya Bay collaboration. The assembly process involves attachment of the PMT bases to the PMTs and injecting the housings with potting compound. This will result in a sealed PMT assembly. The procedures and quality assurance steps to pot and seal the PMT-base assemblies will be developed during the final design and prototyping of the bases. Therefore, an initial 100% underwater testing program of the first 20–50 assemblies followed by a random sample testing of 5% of the assemblies should suffice to insure the integrity of the seals. Expert US personnel will be present to oversee quality control at the beginning of the assembly and testing process

The risks involved in the delivery schedule are minimal. The main risk is the delay in availability of funding. The production work will not start without the funding approval.

Additional risks involve failure of a certain percentage of the PMT/base assemblies due to improper sealing or breakage of PMT bulbs. Based on past experience we expect these to be at a level of less than 0.2%. Please note that the PMT failures, while rare, will be detected before the bases are glued in permanently. This detection will be done in two distinct stages:

1. During the initial physical inspection stage after the delivery of the PMTs
2. During the PMT burn-in process. During this period each PMT/base will be tested with LED pulsers for a duration of three days.

The main ES&H challenge of the base fabrication is the potting compound which needs to be handled under a hood. The bases need to be tested at high voltage, but the power supplies are current limited the electrocution hazard is not high. In addition the connections made are only SHV and there is no exposure to open HV during the testing stage.

Since a single coaxial cable will carry both (+) HV and signal, there must be splitters to separate the two. The Baseline Restoration (BLR) units will incorporate the AC decoupling and baseline restoration of the signals due to AC coupling. These units will be designed at LBNL. A preliminary design and prototype of the BLR has been discussed in the PMT section. This design will be finalized and produced by LBNL.

6.4.2.1.2 PMT supports

Stainless steel unistrut and other components will be shipped directly to the SAB and a design engineer will be present for receiving and inspecting it. US personnel (L3 manager, an engineer and one postdoc) will be present to supervise the assembly of the modules and their installation in the Daya Bay Hall. For subsequent halls the L3 manager will supervise.

6.4.2.2 Components to be Fabricated In-house for RPCs

6.4.2.2.1 RPC module fabrication

The RPC module assembly and testing will be done at IHEP.

The assembly will take place in work stations, about 2 m × 2 m, slightly smaller than the size of the module.

Before the assembly of the module, all the parts will be checked and inspected. The holes in the top and bottom honeycomb panels, as well as the support positions of the 60 mm × 30 mm U-channels will be pre-drilled.

When the preparation work is finished, the two vertical steel reinforced ribs will be placed on the work station, followed by the two horizontal aluminum reinforced ribs.

The layers will then be assembled, from the bottom to the top. Before the last honeycomb panel is placed on top, the matching resistors, the high voltage and gas connections will be attached and tested.

After we place the top honeycomb panel on top, the aluminum reinforced rib will be placed on top and riveted to the reinforced steel rib. A plastic PVC fixture will be inserted in the support position. The gas connections, high voltage and the electronics will be attached. The assembly is completed by attaching the lifting rings.

The performance of the fully assembled modules will be tested with full readout electronics in a cosmic ray hodoscope.

The present manufacturing schedule does not pose any risk to the overall schedule of the Daya Bay Experiment. The main time bottleneck is the bare chamber production. The other steps generally proceed faster than the chamber production, although the testing of chambers and modules may take some time to set up at the beginning.

The main ES&H challenges of the RPC manufacture will be the adhesive used in the chambers which must be handled under a hood, the isobutane component of the gas used for testing the chambers, and the HV needed in the QA tests. Single RPC panels when assembled weigh about 25kg so can be handled without cranes. Gases will be premixed in non-flammable proportions. The factory floor is level and the building is well-ventilated, minimizing ODH hazards. Routine testing will involve only one chamber at a time, reducing the electrical hazard. Open HV connections will be avoided and surge trips will be built into the circuits.

There are technical, cost and schedule risks associated with the RPC fabrication. We assume most of the technical risks (unacceptable efficiency, stability, noise rate) will be eliminated by R&D now in progress. The main cost and schedule risks are related to possible underestimates of the labor required to assemble and test the chambers. These are unlikely because of the recent and very relevant experience of GNKD in RPC fabrication.

6.4.2.2.2 RPC support manufacture

The RPC support structure will be designed at IHEP and fabricated by an outside vendor.

6.4.3 Quality Assurance During Fabrication and Assembly

6.4.3.1 Quality Assurance During Fabrication and Assembly of the RPCs

6.4.3.1.1 Quality Assurance of Raw Materials

A. Production and QC of Bakelite sheets In the production of Bakelite sheets, the first step is the vigorous inspection of raw materials, including the phenolic resin and paper substrate. Before the production of the Bakelite laminates, there will be a pre-production run of about 10 sheets to ensure all properties meet the specifications. When the Bakelite sheets are transported to GNKD, the resistivity of each sheet will be measured carefully. Prior to the resistivity measurements, the Bakelite sheets will be kept at a constant temperature of 20° C for at least 24 hours. The resistivity of each sheet will be measured at nine points. The resistivity has to be in the range 2×10^{11} to 2×10^{12} cm. The percentage variance of the nine measurements has to be less than 30%. The smoothness of the surface of the Bakelite sheets will be measured by a laser smoothness instrument, requiring the smoothness to be within 80% of that of a glass reference sample.

B. Inspection of epoxy Each batch of epoxy will be inspected very carefully. In addition to the routine visual and transparency inspections, strength test of glue joints will be conducted. The strength of the glue

joint between the spacer and Bakelite sheet has to exceed 5 kg. The whole batch of epoxy will be discarded if the strength test is not satisfied.

C. Inspection of edge frames and spacers The edge frames and spacers will be visually inspected individually for cracks and impurity contaminations in the material.

D. Inspection of gas inlets and outlets The gas inlets and outlets will be inspected for contaminations, impurity in the material, and visual defects. There should be no blockage in the gas channel.

E. Graphite test Using trial spray runs, the graphite will be tested for resistivity, granularity and adhesive strength.

6.4.3.1.2 Quality Control of the Production Process of the the RPCs

A. Professional quality controllers

We will appoint full-time quality controllers whose sole responsibility is to monitor the production process and ensure that all personnel follow production procedures.

B. Signature system

Operators in each job step are required to sign off on the work, and are responsible for the work. Future problems in quality can be traced to the operator(s) who performed a specific job step.

C. QC data base

A data base will be established for QC. The data and measurement results of each Bakelite sheet and RPC will be recorded in the data base. The data for the properties of the raw materials and components of an RPC can be located in the data base. In this way, any future problems in quality can be traced promptly to the source so as to guarantee the quality of every RPC.

D. Graphite coating and surface resistance test

The graphite coating of the Bakelite sheets will be done in a special dedicated production line. The graphite coating will be dried in the drying channel. The surface resistance of the graphite coating will be measured 4 hours after it is dried. Nine measurements at nine different points will be taken. The surface resistance has to be in the range 0.2 to 1 M Ω . The percentage variance of the nine measurements has to be less than 30%.

E. Cleaning of components

The spacers will first be cleaned by water. They will then be cleaned in an alcohol ultra-sound bath for 10 minutes. The edge frames and Bakelite sheets will be rinsed by water before they are transported into the clean room. They will be cleaned by alcohol and dried by a silk cloth shortly before use.

F. RPC gluing and strength control

The spacers will be glued to the Bakelite plates by vacuum pressure at 50 mb (50 cm of water) for more than 20 hours. Glued RPCs will be removed from the clean room to undergo a gluing strength test. In the gluing-strength test, the RPC will be under a gauge pressure of 50 mb, connected to a U-tube water manometer. A Plexiglas rod will be rolled on top of the RPC. If there is no change in the water level in the U-tube, the RPC passes the gluing-strength test. Any discernible change in the water level in the U-tube during this test indicates that there is breakage in the spacer glue joint.

G. Gas tightness test

The gas tightness of the RPCs will be tested by the change in under-pressure using a U-tube water manometer. A negative pressure of 20 cm of water will be applied to the chamber. The pressure will be recorded at half-hour intervals. An RPC with a pressure reading difference of more than 5 mm of water will be checked for leaks. Leaks, if found, will be repaired. An RPC that fails the gas tightness test 3 times will be rejected.

H. HV training

RPCs that passed the glue-strength and gas-tightness tests will be filled with pure Argon and trained at 8000 V for 24 hours. Trained RPCs will be transported to IHEP for further tests.

I. RPC dark current, singles rate and efficiency measurements.

Three RPCs with strip readout will be used to form a muon telescope. The strip signals from the three RPCs, after discrimination, form a three-fold coincidence signal. The signal is fanned out to several channels. One channel goes to a scaler with counts denoted by N1. The RPC to be tested is placed between the three RPCs. The strip signals from the RPC under test are discriminated, and are used to form two logic signals; the one in coincidence with N1 is sent to the scaler N2. The raw signals are sent to the scaler N3. The high voltage for the RPCs will be provided by the CAEN SY127 system. The positive HV plug-in unit provides +3/4000 V up to 3/4 mA current. The negative HV plug-in unit provides -6000 V up to 1 mA. The current of the negative plug-in unit is read out by a C139 unit with a resolution of 1 μ A,

The efficiency and singles rate of the RPC under test are given by N2/N1 and N3/(strip area \times time), respectively.

For a gas mixture of Ar: R134a: Isobutane = 50:42:8, the dark current at 8 kV has to be $\leq 10\mu$ A/m². This gas mixture (standard mix) will be used for all tests unless indicated otherwise.

Singles rate : the singles rate has to exhibit a visible plateau, and the rate at 7.5 kV has to be $\leq 8000\text{Hz}/\text{m}^2$. Detection efficiency: Using the muon telescope, for HV 5.5 to 9 kV and standard gas mixture, there has to be a plateau in efficiency with a knee at 7.0 kV. The efficiency in the plateau has to be $>90\%$.

6.4.3.1.3 RPC Module Assembly and Testing

A. RPC module assembly : Special full-time technical personnel will be responsible for the assembly of the RPC modules. They will supervise every facet of the assembly to ensure good quality of the products.

B. Performance testing: By using four RPC modules (or scintillators), two on top and two on bottom, as a muon telescope, the muon trajectories can be determined. The local detection efficiency of an RPC module can be measured. For each RPC, at least 1 million events will be collected for the standard mix and normal operating HV (8000 V).

6.4.3.2 RPC Installation

Specialized personnel from IHEP will be present to oversee the RPC module tests in the SAB, the installation of the RPC support system and the installation and testing of the RPC modules. In addition US personnel (L4 managers) will be present to oversee the connection of the RPC HV and gas systems and the installed module tests.

6.4.3.3 Quality Assurance During Fabrication and Assembly of the RPC support structure

Specialized personnel from IHEP will visit the support vendor when the each section of each experimental hall's support structure has been manufactured. The section will be mounted on rails like those to be used in the halls and moved along to make sure it has been correctly manufactured and aligned.

REFERENCES

1. Hubbell, J.H. and Seltzer, S.M. (2004), “Tables of X-Ray Mass Attenuation Coefficients and Mass Energy-Absorption Coefficients” (version 1.4). [Online] Available: <http://physics.nist.gov/xaamdi> [2006, August 2]. National Institute of Standards and Technology, Gaithersburg, MD.
2. J. W. Zhang *et al.*, Nucl. Instr. Meth. A **540**, 102 (2005).
3. A. Abashian *et al.*, Nucl. Instr. Meth. A **449**, 112 (2000).
4. M. Aglietta *et al.* [LVD Collaboration], “Measurement of the neutron flux produced by cosmic-ray muons with LVD at Gran Sasso,” arXiv:hep-ex/9905047.
5. R. Becker-Szendy *et al.*, “IMB-3: A Large water Cherenkov detector for nucleon decay and neutrino interactions,” Nucl. Instr. Meth. A **324**, 363 (1993).

6. Frank M. Sogandares and Edward S. Fry. Absorption spectrum (340-640 nm) of pure water. I. Photo-thermal measurements. *Applied Optics*, 36:8699–8709, 1997.
7. Robin M. Pope and Edward S. Fry. Absorption spectrum (380-700 nm) of pure water. II. Integrating cavity measurements. *Applied Optics*, 36:8710–8723, 1997.
8. Edward S. Fry. Private communication, 2007.
9. Y. Fukuda *et al.*, “The Super-Kamiokande detector,” *Nucl. Instr. Meth. A* **501**, 418 (2003).
10. J. Boger *et al.* [SNO Collaboration], “The Sudbury Neutrino Observatory,” *Nucl. Instr. Meth. A* **449**, 172 (2000) [arXiv:nucl-ex/9910016].
11. A. Abashian *et al.*, *The $K_{L/\mu}$ detector subsystem for the BELLE experiment at the KEK B-factory*, *Nucl. Instr. Meth. A* **449**, 112 (2000).
12. S. Foulkes *et al.*, *Gas system upgrade for the BaBar IFR detector at SLAC*, *Nucl. Instr. Meth. A* **538**, 801 (2005).
13. M. Ahart *et al.*, *Flow Control and Measurement for RPC Gases*, Belle Note 135 (Aug. 26, 1996), <http://wwwphy.princeton.edu/~marlow/rpc/gas/flow.ps>
14. R. Messner, *The LST Gas Mixing System* (Oct. 4, 2004),
http://puhep1.princeton.edu/~mcdonald/dayabay/BaBar_gas_system/messner_LST_gas_system.pdf
15. *Fujikin Integrated Gas System Brochure*, <http://www.technofittings.com/pdf/igs/igsbroc.pdf>
16. A. Bergnoli *et al.*, Tests of OPERA RPC Detectors, *IEEE Trans. Nucl. Sci.* **52**, 2963 (2005).
17. G. Benelli *et al.*, *The BABAR LST Detector High Voltage System: Design and Implementation*, *IEEE Nucl. Sci. Symp. Conf. Rec.* **2**, 1145 (2005),
<http://www.slac.stanford.edu/cgi-wrap/getdoc/slac-pub-12069.pdf>
18. Extensive documentation of the BABAR LST high voltage system is available online at
<http://www.physics.ohio-state.edu/~klaus/LST/HV/osu/OSUHV.htm>
19. C. Lu and K. McDonald, *Daya Bay RPC Gas System: Design Report & Budget Estimate* (July 28, 2007), <http://puhep1.princeton.edu/~mcdonald/dayabay/Lu/GasSystemReport.pdf>
20. Appendix A of *Fire Hazards Analysis for BaBar Detector Project*, Hughes Associates, Inc., Baltimore, MD 21227 (Dec. 19, 1996),
<http://www.slac.stanford.edu/BFROOT/www/Organization/Spokesperson/safety/documents/FHA/FHA.pdf>
21. CAEN Short Form Catalog 2007.

7 Electronics, Trigger, and Data Acquisition Systems

The readout electronics and the trigger event selection, with estimated rates, are presented along with the timing synchronization between all of the electronic elements. The processing of the trigger data from the front-end modules through data storage is discussed, along with the detector control system. Each detector module (AD, inner muon, outer muon, RPC) is designed to have a readout system independent of the other modules, except for a common clock signal. We are building into the system the capability to readout any module based on information from any adjoining module.

7.1 PMT Front-End Electronics

The Front-End Electronics (FEE) readout system is designed to process PMT output signals. Even though the requirements for the muon system are not as stringent as those for the AD, we plan to use the same FEE electronics for both systems. The essential functions are as follows:

- Provide fast information to the trigger system
- Determine the charge of each PMT signal to measure the energy deposit in the liquid scintillator or water. This will enable us to identify muon events, select neutrino events, reject backgrounds, and deduce the antineutrino energy spectrum.
- Provide precision timing information (PMT-to-PMT) that can be used in event reconstruction, to study and reject potential backgrounds, and increase the precision of the measured trigger signals.

7.1.1 Requirements for the PMT Front-End Electronics

When a reactor antineutrino interacts within the target volume, its energy is almost completely transferred to the positron and ultimately converted into ultraviolet and visible light, some of which will ultimately be transformed into photoelectrons (p.e.) at the photocathodes of the PMTs. Monte Carlo simulations predict (for a given PMT) that the number of p.e. produced per antineutrino event will range from 0 to 50, depending on the location of the interaction within the detector. The passage of cosmic muons through the detector may produce as many as 2000 p.e. in individual PMTs. It seems prudent to provide sufficient headroom to accommodate more photo-electrons than the current simulation predicts; as such, we choose a full dynamic range from 0 to 4000 photoelectrons. This range is more than sufficient to accommodate the needs of the Cherenkov water shield. In order to maintain precision below 400 p.e., two pairs of amplifiers and ADCs will be used, resulting in a fine range from 0–400 p.e., and a coarse range from 0–4000 p.e.

The intrinsic energy resolution for a single p.e. is typically about 40% with some variation from PMT to PMT, while the threshold for a PMT signal is constrained by the dark noise, typically at the level of about 1/3–1/4 of a p.e. The electronic noise and charge resolution of the readout electronics should not further contribute to these limitations. Therefore, we require the RMS noise due to the electronics to be less than 10% of a p.e., and the charge resolution of the electronics to be better than 20% of a p.e.

In addition to measuring the pulse size and shape, we can determine (with precision) the arrival time of the signal from the PMT relative to a common stop signal, for example, the trigger signal. The time jitter of a PMT signal for a single p.e. is about 1–2 ns, caused by the PMT transit time spread, the PMT rise time, and the time walk effect of the discriminator. The design goal for the time resolution of the readout electronics should therefore be better than 1.0 ns. The dynamic range of the time measurement depends on the trigger latency and the maximum time difference between the earliest and the latest arrival time of light to PMTs. Guided by simulations, this range is chosen to be from 0 to 500 ns. By comparing the arrival time at various PMTs, we can roughly reconstruct the position of the event within the detector. Although such a method is more suitable for large detectors similar to KamLAND, it provides a second position measurement that

complements the charge-gravity method that is often used with smaller detectors, and thus offers a cross-check of systematic uncertainties and an additional handle for studying backgrounds. The precision to which we measure the trajectory of the muon also depends on the PMT timing precision.

The requirements for the electronics used to read out the PMTs are summarized in Table 7.1.

Item	Requirement	Justification
Linear Range	0–200 p.e.	Accurately measure inverse beta decay events
Full Range	0–1000 p.e.	Large enough to reasonably measure cosmic muons
Resolution	<0.1 p.e. @ 1 p.e.	Sufficiently fine to resolve 1 p.e. distribution
Noise	<10% @ 1 p.e.	Electronics should not contribute to overall noise
Time range	0–500 ns	Allows for trigger latency and photon propagation
Timing resolution	<1 ns	Event reconstruction
Sampling rate	≥40 MHz	Accurately determine PMT pulse shape
Channels/module	≥12	Can fit each AD into one VME crate
VME standard	VME64xp-340 mm	DAQ architecture requirement

Table 7.1. Requirements for the electronics used to read out the PMTs.

7.1.2 PMT Front-End Electronics (FEE) Boards

The PMT readout electronics for each detector module is housed in a single 9U VME crate with up to 16 FEE boards, one trigger board, and one fan-out board. In such an arrangement, moveable boards can be easily realized, and correlations among modules can be minimized. In order to make the readout electronic system simple and easy to maintain, the same front-end electronics (FEE) boards will be used for both the Antineutrino Detectors and Water Shield PMTs.

Each FEE board accepts 16 PMT signals and performs the time and charge measurements. The number of channels over threshold and the total charge observed by the FEE board is fed to the trigger system for a fast trigger decision. After collecting information from all readout boards, a trigger signal may be generated and distributed to each FEE board and used as a common stop for the TDCs. It also initiates readout of the ADC and TDC data.

The input PMT signal is immediately amplified and used to drive three distinct circuits, a discriminator (threshold decision and TDC start pulse), a charge summing circuit (for the energy sum trigger), and a pulse shaping circuit whose output is sampled to accurately measure the charge of the pulse. A simplified circuit diagram of the electronic readout system, showing its main functions, is given in Fig. 7.1.

A stable threshold is set using a 14-bit DAC (AD7247) [?] controlled from the VME processor. This level of precision is required in order to achieve the required TDC time resolution. The rising edge of the discriminator output signal is used to start the TDC. The TDC is realized by using internal resources of a high-performance Field Programmable Gate Array (FPGA) with key components of two ultra high speed Gray-code counters. The first counter changes at the rising edge of an internal 320 MHz clock, while the second one changes at the falling edge. Each time bin is 1.563 ns. The RMS of the time resolution is less than 0.5 ns. The FPGA also uses the discriminator output to increment the NHIT counter, a sum of all channels that went over threshold that clock cycle.

To measure the charge of the PMT signal, an ultra low-noise FET input amplifier (AD8066) is selected for the charge integrator. A CR-(RC)⁴ shaping circuit is used to obtain a smooth signal peak after shaping. An RC time constant of 25 ns is chosen, corresponding to an output signal width (1% amplitude to 1% amplitude) of about 325 ns. The RC is implemented using discrete surface mount components. The shaped signal is sent into two amplifiers with different gains, a gain of ×10 for the fine range and a gain of ×1

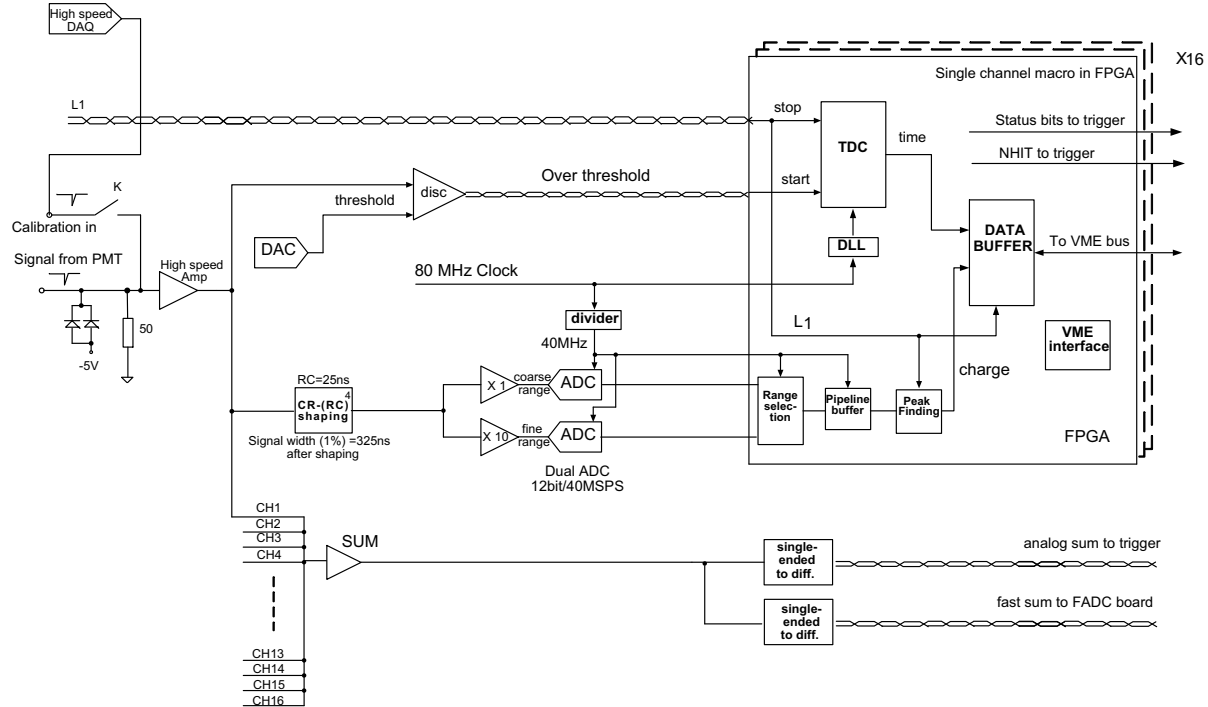


Fig. 7.1. Block diagram of front-end electronics module for PMT readout.

for the coarse range. These two analog signals are digitized using two 12-bit Flash ADCs (AD9222) with a 40 MHz sampling rate (one for the course range and one for the fine range). The digitized samples go directly into the FPGA, in which all data processing (*e.g.* range selection, peak finding, data pipelining, pedestal subtraction, nonlinearity corrections, and data buffering) will be implemented. Since data manipulation takes place within the FPGA, we maintain flexibility in choosing how best to record the size and shape of the pulse.

The FEE boards readout using a standard VME A24:D32 interface. Up to 256 32-bit data words are saved locally and readout through the VME backplane by the MVME5500 DAQ processor. The time-ordered ADC data will be saved inside the FPGA for up to a few hundred microseconds. This data can be accessed and retrieved on command should we wish to examine the untriggered activity within a given detector module prior to, for example, a signal from a different detector module (something we call a look-back trigger). Look-back triggers will be used to study backgrounds (primarily muon induced backgrounds).

The last of the three branches is for the energy sum trigger. Signals from all 16 channels are sent into an analog sum circuit. The result is converted into two differential signals, one for the trigger board and the other for a 200-MHz Flash ADC board.

The NHIT information is generated every clock cycle (80 MHz clock). The NHIT can be from 0 to 16, which is encoded in a five bit binary word that is sent as LVPECL on twisted-pair cable to the trigger board through the front panels. This information is used to form a multiplicity trigger, described below.

Self testing and calibration is accomplished (in part) using a programmable pulse generated by a fast on-board DAC chip and sent as a calibrated input simultaneously to all channels on the board.

7.1.3 RPC Front-End Electronics

Building on their experience designing RPC electronics for BESIII, the University of Science and Technology of China (USTC) is developing a custom RPC readout system for the Daya Bay Experiment. As shown in Fig. 7.2, one Front-End Card (FEC) is used to readout each RPC module (eight channels in each of four layers). The FEC transfers data and trigger information, and receives clock, external trigger, and control

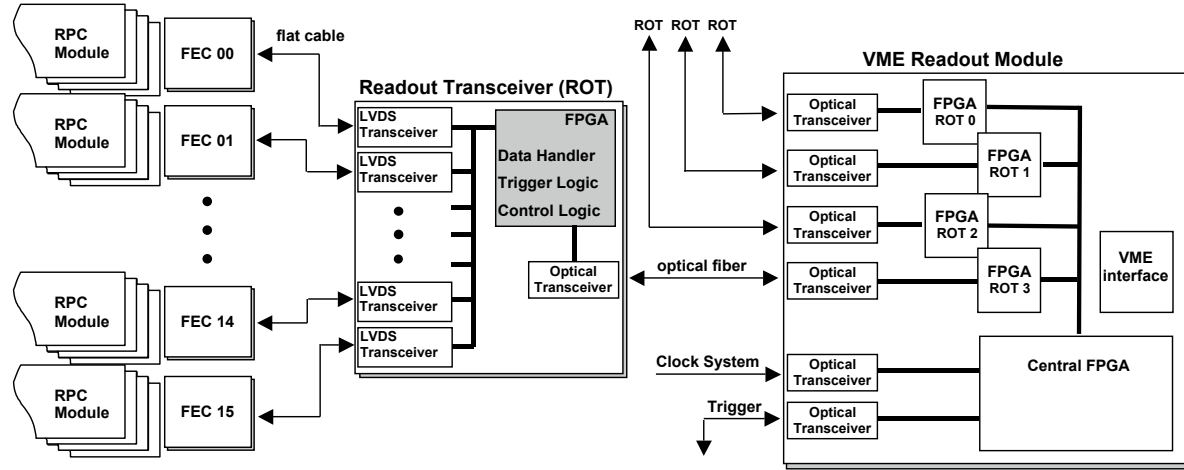


Fig. 7.2. Configuration of the RPC electronics & readout system.

logic from a ReadOut Transceiver board (ROT). Each ROT can receive data from up to 16 FECs, or 512 RPC channels, using differential LVDS signals. The data is sparsified and stored in a data buffer awaiting DAQ processing. The ROT, in turn, communicates with a VME Readout Module (ROM). Each ROM can manage up to 4 ROTs. As such, we only require one ROM for each near hall and 2 ROMs for the far hall.

The main tasks of the Front End Card (FEC) are to discriminate the raw signals from the RPCs and to decide when this information should be recorded (i.e trigger). It also converts the signals into a digital format and passes the data to the ROT module. The logical design of the card is shown in Fig. 7.3.

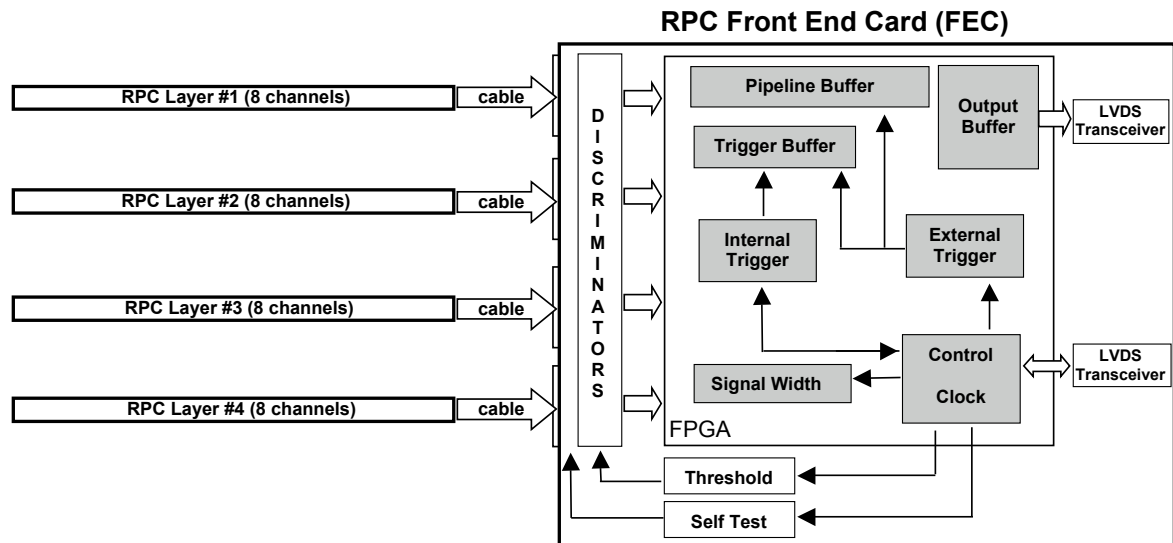


Fig. 7.3. Block diagram for the FEC.

The discriminator circuit transforms the analog signals from the strips into a digital bit map. The threshold is controlled using a 10-bit DAC (AD5313) in conjunction with an LM324 amplifier. The range of the threshold is 0 and 130 mV. The threshold setting circuit is shown in Fig. 7.4. The DAC is also used with a

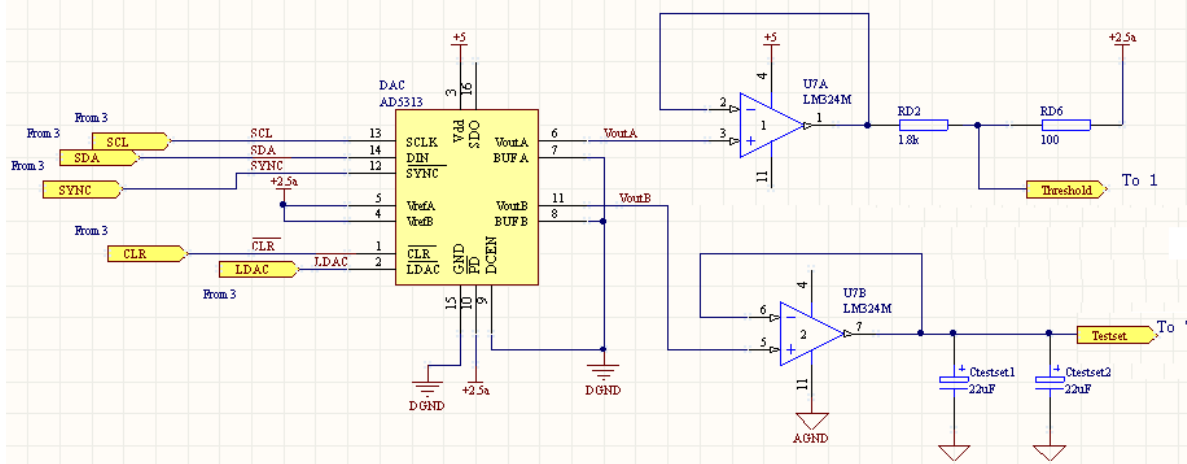


Fig. 7.4. Diagram of the FEC threshold forming circuit.

second LM324 to set the level for the self-test mode. Discrimination is accomplished using an ADCMP604 comparator with a 4 ns rise/fall time and a propagation delay of only 1.5 ns. The comparator circuit is shown in Fig. 7.5. The FEC has a separate comparator circuit for each input channel. The self-test feature

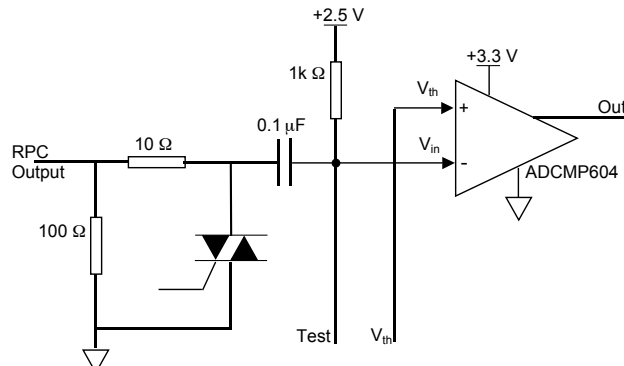


Fig. 7.5. Diagram of the FEC discriminator circuit.

is modeled after that used for BESIII and uses an ADG781 quad analog switch (eight ICs per FEC). The output pulse voltage is controlled with the DAC (see above) with control signals from the FPGA. This feature allows us to test individual electronic channels with a variety of pulse sizes. The digital pulses from the comparators are inputs to the FPGA (an Altera EP3C25Q240C8) and stored in a buffer to wait for a trigger signal. All subsequent signal processing and trigger logic is accomplished within the FPGA.

The width of the input data pulses (coincident window) are set by the FPGA. An internal trigger is generated when at least one hit in at least two layers overlap in time. The coincident window is adjustable, but will likely be set to 100 ns. The trigger selected data is time stamped, serialized, and stored in the output buffer. LVDS transceivers transmit the data to the ROT. The FEC may also receive an external trigger signal from the ROT. This also causes the data to be time-stamped, serialized, and readout. Data without a trigger are cleared. Configuration commands and configuration files will be sent to the FEC via the ROT, enabling the FEC to be updated without having to physically fetch the boards.

7.2 The Trigger System

The trigger system of the Daya Bay experiment makes trigger decisions for the antineutrino and muon detectors to select neutrino-like events, muon-related events, periodic trigger events and calibration trigger events. The primary physics trigger for the antineutrino detectors and for the muon water pools will be a multiplicity of PMTs over threshold within a defined coincident window. The trigger will have high efficiency for events which deposit more than 0.7 MeV in an AD, enabling a complete energy spectrum analysis that increases our sensitivity to θ_{13} . The trigger is sensitive to events with neutron capture on both Gd and H. We will also implement an energy sum trigger. The RPC detectors will primarily be triggered using a coincidence of 2 out of 4 layers within a single module. The following sections will describe the requirements and technical baseline for the trigger system. A block diagram for the overall trigger system is shown in Fig. 7.6.

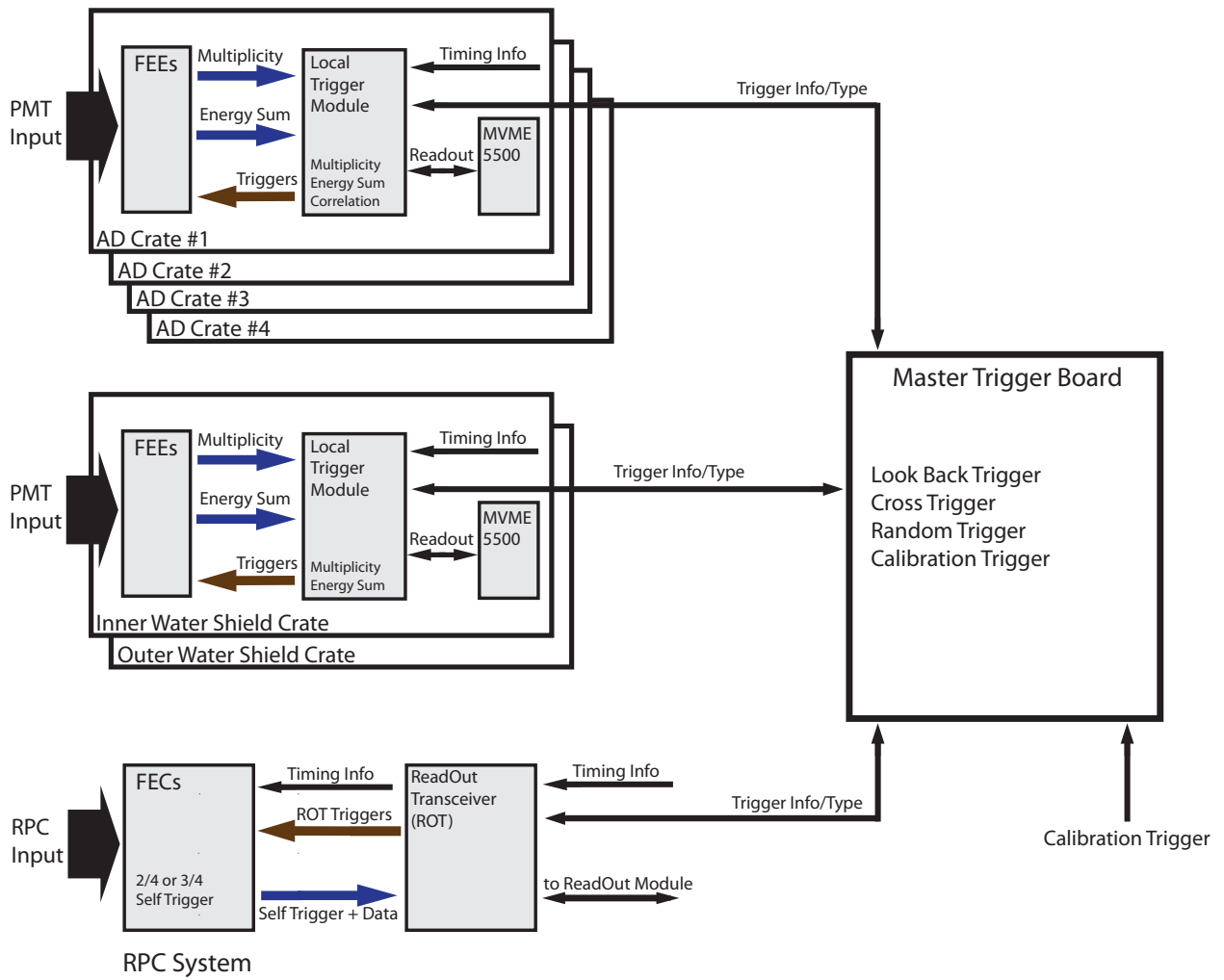


Fig. 7.6. A block diagram of the Daya Bay trigger system.

7.2.1 Trigger System Requirements

The signature of a neutrino interaction in the Daya Bay antineutrino detectors is a prompt positron annihilation (with a minimum energy of 1.02 MeV) followed by neutron capture on Gd. About 90% of the

neutrons are captured on Gadolinium, giving rise to an 8 MeV γ cascade. The lifetime of a thermal neutron in the Gd-doped liquid scintillator is about 28 μ s. The major backgrounds in the antineutrino detectors are fast neutrons produced by cosmic muon interactions in the rock or water, cosmic muon induced production of $^8\text{He}/^9\text{Li}$, and accidental coincidences between (for example) natural radioactivity and neutrons or beta emitters produced by cosmic muons. All three major backgrounds are related to cosmic muons, necessitating a high efficiency muon trigger. Furthermore, since an antineutrino event is a coincidence of the prompt positron annihilation followed by a delayed neutron capture, the time interval between these signals is a crucial parameter for the physics analysis. The precision of this interval is linked to the trigger signal which is synchronized to the 80 MHz system clock. The following are the main trigger requirements imposed by the physics goals of the Daya Bay experiment:

The requirements for the trigger system are summarized in Table 7.2.

Item	Requirement	Justification
Efficiency	>99%	High efficiency to maintain small systematic uncertainty
Time of Trigger	13 ns	Measurement of delay in neutron capture time
Energy Threshold	~ 0.7 MeV	High acceptance for prompt signal
Flexibility	dynamic algorithms	Functionality under a variety of conditions
Reproducibility	< a few ns	Consistency between AD modules
Redundancy	>1 algorithm	Ability to measure trigger efficiency

Table 7.2. Requirements for the trigger system.

Trigger efficiency: A precise spectrum analysis requires an energy-independent trigger efficiency for the entire signal energy region (from 0.7 MeV through 12 MeV). A parallel trigger algorithm (e.g. energy sum trigger) will be used to measure the trigger efficiency. A random periodic trigger (with no requirement on the energy threshold) will also be employed. In the early stages of the experiment, the trigger efficiency is required to be as high as possible for both signal and background, provided that the event rate is acceptable and does not introduce dead time. After an accurate characterization of the backgrounds, the trigger system can be tuned (if necessary) to increase background rejection while retaining high efficiency for antineutrino interactions.

Trigger time stamp: Since neutrino events are constructed offline from the time correlation between the separately recorded prompt positron annihilation signal and the neutron capture signal, each readout crate must be able to create consistent and accurate time-stamps. The trigger board must provide a local system clock and a global time-stamp to the DAQ and FEE readout boards in the crate. The trigger board in each crate will receive timing signals from a global GPS based master clock system as described in Section 7.3. Events recorded by the antineutrino detectors and muon systems can thus be accurately associated in time offline using time-stamps. It should be possible to use the PMT TDC data to further increase the precision of the trigger time measurement.

Energy dependence: The trigger is required to independently trigger on both the prompt positron annihilation signal ($E \geq 1.02$ MeV) and the delayed neutron capture on Gd (photon cascade of ~ 8 MeV) with very high efficiency. In order to avoid potential bias, we intend to use a multiplicity trigger as our primary trigger (as opposed to an energy sum trigger). The multiplicity trigger must have high efficiency for events with an energy of 0.7 MeV and above. This low threshold requirement fulfils two trigger goals, allowing the DAQ to record all prompt positron signals produced from neutrino interactions, and for background, it allows the DAQ to register enough uncorrelated background events due to either PMT dark noise or low energy natural radioactivity to enable a detailed analysis of backgrounds offline.

Flexibility: The system must be able to easily implement various trigger algorithms using the same basic trigger board design for different purposes such as

- Using different thresholds to adapt to the possible aging effect of liquid scintillator, or for triggering on calibration source events which have lower energy signatures.
- Using different hit multiplicities to increase the rejection power due to the uncorrelated low energy background and for special calibration triggers.
- Implementing pattern recognition for triggering on muon signals in the various muon systems.
- Using an OR of the trigger decision of different trigger algorithms to provide a cross-check and cross-calibration of the algorithms as well as a redundancy to achieve a high trigger efficiency.
- Implementation of a correlated positron-neutron trigger.

Independence: Separate trigger system modules should be used for each of the antineutrino detectors and components of the muon system. This is to reduce the possibility of introducing correlations between triggers from different detector systems caused by a common hardware failure.

7.2.2 The Antineutrino Detector Trigger System

Neutrino interactions inside a detector module deposit an energy signature that is converted to optical photons which are then detected by a number of the PMTs mounted on the inside of the detector module. Two different types of triggers can be devised to observe this interaction:

- A multiplicity trigger (with or without pattern recognition).
- An energy sum trigger.

In addition to physics triggers, the antineutrino detector trigger system needs to implement several other types of triggers for calibration and monitoring:

- Calibration triggers of which there are several types:
 1. Triggers generated by the LED pulsing system that routinely monitors PMT gains and timing.
 2. Special energy and multiplicity triggers used to test detector response using radioactive sources
- A periodic trigger to monitor detector stability and random backgrounds.
- An energy sum and/or multiplicity trigger prescaled with looser threshold and multiplicity requirements. This trigger may be initiated by a delayed trigger from the muon system to study muon induced backgrounds.
- A readout of a detector module initiated by information from a different detector module.

A VME module with on-board Field Programmable Gate Arrays (FPGAs) is used to implement the antineutrino detector trigger scheme outlined in Fig. 7.7 based on experiences gained at the Palo Verde [1] and KamLAND experiments.

The multiplicity trigger is implemented with FPGAs which can perform complicated pattern recognition in a very short time. FPGAs are flexible and can be easily reprogrammed should trigger conditions change. If necessary, different algorithms can be downloaded remotely during special calibration runs which make use of customized radio-active sources or LED based flashers. As described in Section 7.1, each FEE board

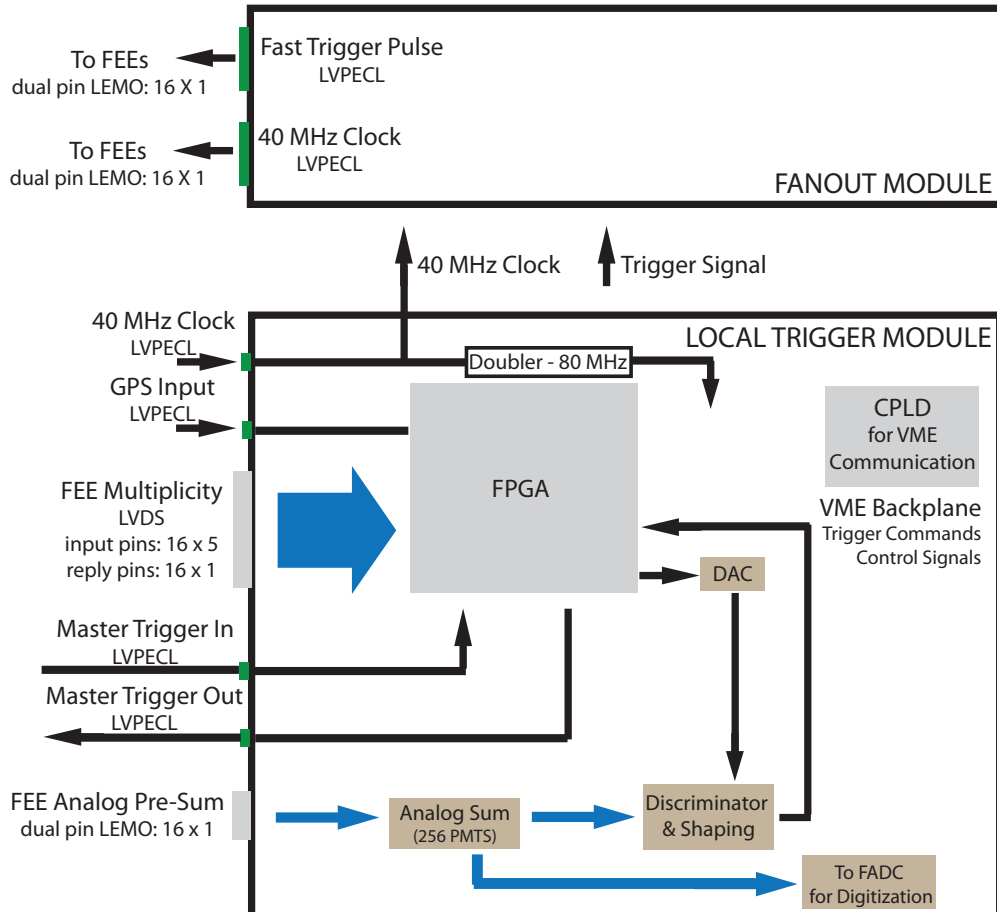


Fig. 7.7. Simplified trigger board.

delivers to the trigger board a count of the total number of PMTs crossing threshold that clock cycle. The dark current rate for the low activity PMTs is typically around 5 kHz at 15° C. For a detector with N total PMTs, a dark current rate of f Hz, and an integration time of τ ns, the trigger rate R given a multiplicity threshold m is

$$R = \frac{1}{\tau} \sum_{i=m}^N i C_N^i (f\tau)^i (1-f\tau)^{N-i}, \quad f\tau \ll 1 \quad (32)$$

where C_N^i are the binomial coefficients.

To be conservative, we will assume a PMT dark current rate 10 times larger than expected (50 kHz) when estimating the multiplicity trigger rate due to dark current. A coincidence window of 100 ns will also be used. The rate thus calculated using Eq. 32 as a function of the number of coincident PMTs is shown in Fig. 7.8. We expect that multiplicities of 10 or more PMTs within a 100 ns coincidence window should occur due to dark currents with a rate less than about 1 Hz.

The energy sum trigger is the sum of the signals received from the PMTs through the FEE boards and integrated with a 50 ns shaping time, and then discriminated. The threshold of the discriminator is generated with a programmable DAC which can be set via the VME backplane bus. The energy sum is digitized using a 200 MHz flash ADC (FADC) on the trigger module. We plan to have an energy trigger threshold of 0.7 MeV or less. At such low energy thresholds, the trigger will be dominated by two types of background:

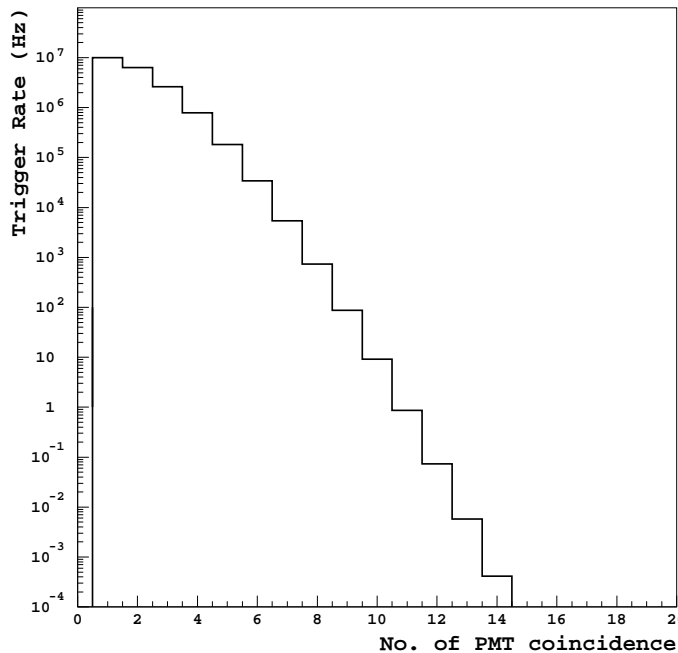


Fig. 7.8. Calculated trigger rates caused by PMT dark current as a function of the multiplicity threshold. For this study, we assumed that the maximum number of PMTs was 200. The PMT dark current rate used was 50k with a 100 ns coincidence window.

one is natural radioactivity originating in the surrounding environment (shown to be less than 50 Hz in Section 2.3.4), and the other is from cosmic muons (negligible at the far site). At this threshold, the energy sum trigger rate from the PMT dark current with a 100 ns coincidence window is negligible.

Tagging antineutrino interactions in the detector requires measuring the time-correlation between different trigger events. The time-correlation will be performed offline, therefore each triggered event needs to be individually time-stamped. It may become necessary to have a correlated event trigger in case the background rate is too high. A periodic trigger to monitor the PMT dark-current, background activity, and detector stability will be included.

7.2.3 The Muon Trigger System

The muon system will utilize two separate DAQ VME crates, one for each of the muon water shield detector systems. The inner water shield Cherenkov detector surrounds the ADs while the outer water shield Cherenkov detector covers the sides and bottom around the edges of the water pool. The 4-layer RPC system that tracks muons coming through the top of the detector system will be readout by ROMs situated within one of the existing water shield VME crates.

The presence of a muon which goes through any of the water Cherenkov detector regions can be tagged with energy sum and multiplicity triggers using a similar scheme and hardware modules as used for the antineutrino detector. In addition, a more complicated pattern recognition scheme using localized energy and multiplicity information (e.g. localized to one segment of the outer water shield) may be used. The trigger rate in the water Cherenkov detector from cosmic muons is estimated to be <16 Hz in the far hall and <300 Hz in the near halls (see Table 7.3). The PMTs used in the water Cherenkov detectors are assumed

Detector	Description	Trigger Rates (Hz)			Occ	Ch No.	data rate (kB/s)
		DB	LA	Far			
$\bar{\nu}$ module	cosmic- μ	36×2	22×2	1.2×4	100%	192	1408
	Rad.	50×2	50×2	50×4			
Inner water shield	Rad & noise	50	50	50	10%	123/169	31
	cosmic- μ	250	160	15			526
Outer water shield	Rad & noise	50	50	50	10%	168/212	41
	cosmic- μ	250	160	15			309
RPC	Rad.	2000	2000	3000	10%	32/module	217
	cosmic- μ	186	117	11			11
site totals	(kB/s)	1042	788	714			2544

Table 7.3. Summary of data rate estimations. kB/s = 1000 bytes per second.

to have a singles rate of 50 kHz per PMT from noise and radioactivity. The trigger rates from PMT singles in the water Cherenkov systems can be controlled by adjusting the multiplicity trigger requirements. The requirement for the water Cherenkov detector systems is <1% trigger deadtime due to radioactivity and PMT noise. The multiplicity thresholds required for the various proposed PMT configurations in the inner water shield system are discussed in detail in Section 6.

In addition to the segmented water shield Cherenkov detector triggers, muons could also be tagged by a system of multiple-layer RPCs placed above the water pool. As discussed above, each RPC module consists of eight strips in each of four layers. These channels are all readout by a single FEC card. The FEC employs an internal trigger which initiates a readout of the RPC module, and all adjacent modules, should 2 out of the 4 layers have coincident hits. A muon signal (three out of four RPC layers) can then be reconstructed offline using information from the adjacent modules.

The RPC response to radioactivity was measured using several BES-III modules placed in the Aberdeen tunnel (see Section 6.3.4), which is expected to have similar ambient radioactivity levels as that in the Daya Bay site. A simulation of the three out of four layer coincidence rate in the RPC system due to radioactivity based on the Aberdeen tunnel measurements was carried out. The trigger rate from radioactivity is thus estimated to be ≤ 1 Hz/m². This corresponds to a radioactivity trigger rate of about <300 Hz in the far hall.

The global muon trigger decision is an OR of the three muon detector trigger systems: RPC tracker, inner water Cherenkov and outer water Cherenkov systems. The muon trigger decision may be used to launch a higher level delay trigger looking for activity inside the antineutrino detector at lower thresholds and/or multiplicities for background studies.

7.3 The Timing System

The design of the trigger and DAQ system is such that each antineutrino detector and muon detector sub-system has independent triggering. In this design it is necessary to synchronize the data from the various trigger streams offline. This is particularly important for tagging and understanding the backgrounds from cosmic muons that are reconstructed offline from data originating from independent sub-systems (the inner and outer water shields, the RPCs, and ADs). Reconstructed cosmic muon candidates can be time correlated with activity in the antineutrino detector to study muon induced backgrounds. To this end, the Daya Bay timing system is required to provide a global time reference to the entire experiment, including the trigger, DAQ, and front-end boards for each sub-system at each site. By providing accurate time-stamps to all components various systematic problems can easily be diagnosed. For instance, common trigger bias, firmware failure, and dead time can all be tracked by looking for time-stamp disagreements in the data output from

each component. Furthermore, by having multiple sites synchronized to the same time reference, it will be possible to identify physical phenomena such as supernova bursts or large cosmic-ray air showers.

The timing system can be conceptually divided into three main parts: the GPS Driver Module, the Central Clock Generator, and the local Clock Fanout. The likely configuration is illustrated in Fig. 7.9.

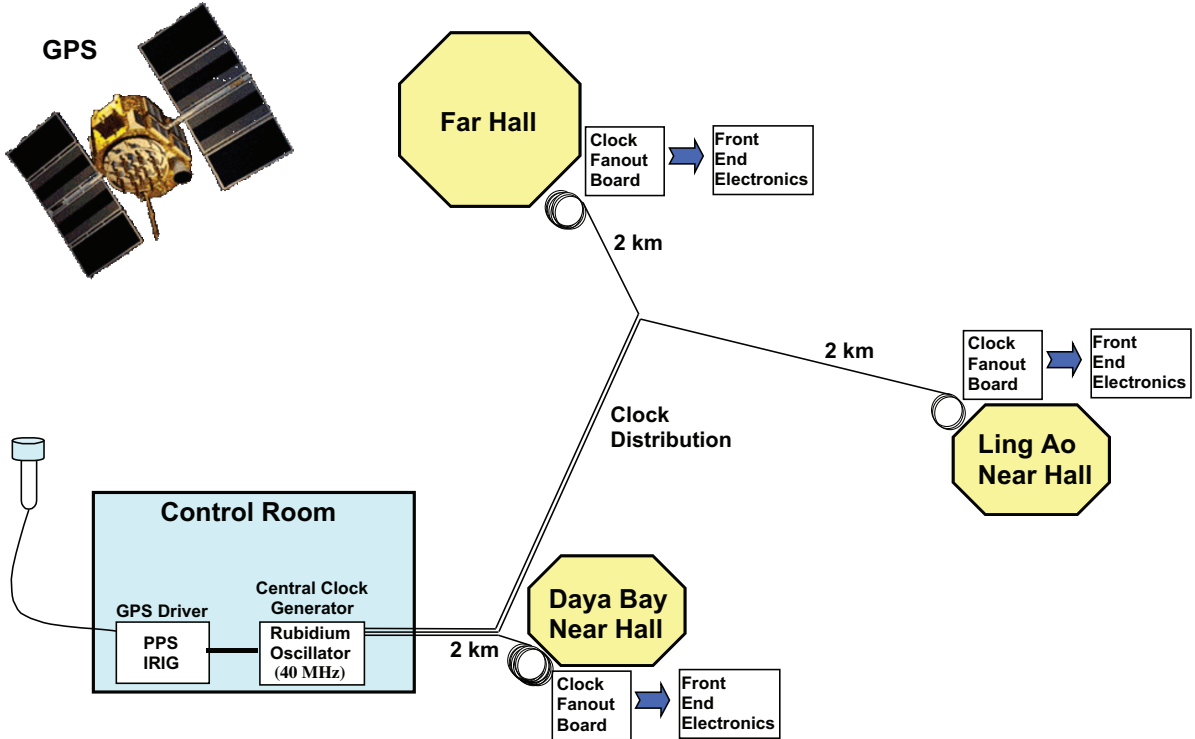


Fig. 7.9. Schematic layout of the global clock.

7.3.1 GPS Driver Module

The global timing reference can easily be produced using a GPS (Global Positioning System) receiver to provide a UCT (Universal Coordinated Time) reference. Commercially-available units are typically accurate to better than 200 ns relative to UCT [2,3]. For redundancy, two GPS receivers will be employed, placed either in the surface assembly building or control room. The GPS Driver receives the GPS signals and provides a one pulse per second (PPS) signal and encoded absolute time information to the Central Clock Generator across optical fibers.

7.3.2 Central Clock Generator

The Central Clock Generator (CCG) uses a precision Rubidium oscillator as the source for our system clock. The Rubidium oscillator synchronizes to the GPS using the PPS signal as an input. The 10 MHz output frequency is quadrupled using a PLL to 40 MHz. The 40 MHz system clock, the PPS signal, and the IRIG information are distributed separately to each detector hall. The GPS information is also used to synchronize a local computer. This computer can then be used as a Tier-1 network time protocol (NTP) peer for all experimental computers. The CCG will be equipped with a backup 10 MHz oscillator to be used when the Rubidium clock is not available.

7.3.3 Local Clock Fanout

At each site a Clock Fanout Board (CFB) receives the signals from the CCG and distributes them to the Local Trigger Boards and ROTs. Each CFB is also equipped with a separate oscillator circuit capable of delivering a 40 MHz clock and PPS signal. This method allows each site to operate independently of the central clock during commissioning or in the case of hardware failure. The 40 MHz clock is passed through the Local Trigger Module and ROT to the FEEs and FECs. In the FEE case, the LTM uses a fanout board, which also distributes fast trigger signals. The system clock is doubled locally to provide 80 MHz clock, where needed.

7.4 The Data Acquisition System

The main task of the data acquisition (DAQ) system is to record antineutrino candidate events observed in the antineutrino detectors. In order to understand the backgrounds, other types of events are also recorded, such as cosmic muon events, low energy radiative backgrounds... etc. Therefore, the DAQ must record data from the antineutrino and muon detectors with precise timing information. Offline analysis will be used to select antineutrino events and to study the muon related backgrounds in the antineutrino detectors. This section presents the DAQ main design requirements, the system architecture and the DAQ software.

7.4.1 Requirements

- Architecture and control requirements:** The architecture requires multiple independent DAQ systems at each detector site. Each antineutrino detector module will have a separate VME readout crate that contains the trigger and DAQ modules. In addition, the inner and outer water shield detectors will have their own VME readout crates. The readout Modules for the RPC detectors will reside in one of the water shield crates. The trigger and DAQ for the antineutrino and muon detector modules are kept separate to minimize correlations between them.

The run control should be configurable and flexible, allowing it to work seamlessly for data taking controlled from the surface or in a detector hall. Run control should allow both global operation of all detector systems in all three detector halls, and operation of parts of detector halls whenever debugging or commissioning is required. The system should allow each sub-system in any detector hall to start its own run control in order that debugging and commissioning can be conducted in parallel.

- Event rates** The trigger event rates at the Daya Bay, Ling Ao and Far site from various sources are summarized in Table 7.3. The rate of cosmic muons coming through the top of a detector are calculated using Table 2.9. For these calculations, we have assumed that the trigger rate due to radioactivity and noise equal the largest estimated value. We also assumed that the only other significant contribution is due to cosmic muons, as the rate of anti-neutrino interactions is negligible.

To turn this into a volumetric rate, we use a MC simulation to calculate the ratio of muon rates entering from the top to all muons entering the detector's volume. The total rates from cosmic muons in the inner and outer water shield muon detector systems are shown in Table 7.3. At the far site, the trigger rates in the ADs are dominated by natural radioactivity (<50 Hz/detector) and at the near sites both cosmic and natural radioactivity contribute.

The trigger rate in the water shield detectors caused by the singles rate from PMT noise and γ rays will be adjusted to be ≤ 50 Hz (<1% deadtime requirement) by varying the multiplicity and energy trigger requirements.

The RPC noise rates are scaled from the BES chamber measurements in Section 6.3.4. The RPC noise rate when requiring a localized coincidence in three out of four layers is considered negligible. The singles rates shown in Table 7.3 are the natural radioactivity rates in the RPC systems at the various sites.

While the trigger rate in the antineutrino detectors at each site is of order a few 100 Hz, an OR of the three muon trigger systems could produce a maximum trigger rate of 1 kHz. The Daya Bay trigger and DAQ system will be designed to handle a maximum trigger rate of 1 kHz. In addition, to trigger on the correlated neutrino and fast neutron signals in the antineutrino detector, the DAQ needs to be able to acquire events that occur ≥ 300 ns apart.

3. **Bandwidth** Table 7.3 summarizes the trigger rates, channel counts, and data throughputs required at each site and for each detector system. In order to estimate the required data bandwidth, we need to first define the data structure and size. The data structure should consist of a data description record followed by a raw data record. The format of the data descriptor is roughly defined as follows:

event size header: 32 bits

Detector hall and subsystem identification: 8 bits

Trigger record: 16 bits

timestamp: 48 bits

status and error information: 24 bits

The size of the event description record is of fixed length, 128 bits or 16 bytes.

The raw data record of PMT events is defined as:

Address: 8 bits (for data sparsification)

Timing: TDC: 32 bits

Charge: 6 ADC samples @ 12 bits/sample: 72 bits

The address includes module number of FEE and channel number within the module. The number of TDC values per data record is variable since a multi-hit TDC will be implemented within the FEE. The RPC raw data record assumes 1-bit per channel (a hit map of one RPC detector module) along with the module identification number.

For our estimates, we assume zero suppression will occur. A hit-map of the triggered module and its adjacent modules are readout for the RPC detector. The expected data throughput from each site is estimated by combining the number of readout channels with the trigger rates and occupancies as shown in Table 7.3, and includes a 128 bit event description header word for each subsystem per trigger. The variable data of TDC and ADC per channel is not considered in estimate of data throughput for simplicity, but we will leave enough safety margin for total data throughput.

Table 7.3 shows data throughput for each subsystem in each detector hall for the baseline trigger scheme. We estimate that the expected data throughput rate is <1.5 MB/second/site. The total data throughput rate for all 3 sites is estimated to be about 3000 kB/s. These estimates would increase should we decide to implement full waveform digitization or additional triggers.

In addition to consideration of data bandwidth from the baseline trigger scheme, there are other type of trigger events as described in 7.2, e.g., look back trigger, that consumes more data throughput. In contrast with baseline trigger, look back trigger will read out all hit information of PMT and RPC module in time windows of look-back. The data throughput contribution of muon water shield and RPC for look back trigger may be as high as 4 MB/s and 1.6 MB/s, respectively, for a look-back time window of 200 microseconds. However, the system design has sufficient flexibility so that we can adjust the trigger scheme to keep the throughput rate manageable should the trigger rate be higher than expected.

4. **Dead-time:** The DAQ is required to have a negligible readout dead-time ($<0.5\%$). This requires fast online memory buffers that can hold multiple detector readout snapshots while the highest level DAQ CPUs perform online processing and transfer to permanent storage. It may also require some low level pipelines at the level of the PMT FADCs.

7.4.2 The DAQ System Architecture

The data acquisition (DAQ) system is used to:

1. Read data from the front-end electronics.
2. Concatenate data fragments from the FEE boards into a complete event, crate by crate.
3. Record event data on archival storage.
4. Run control and monitoring.

The DAQ architecture design is a multi-level system using advanced commercial computer and network technology as shown in Fig. 7.10: VME front-end readout, event builder and event storage.

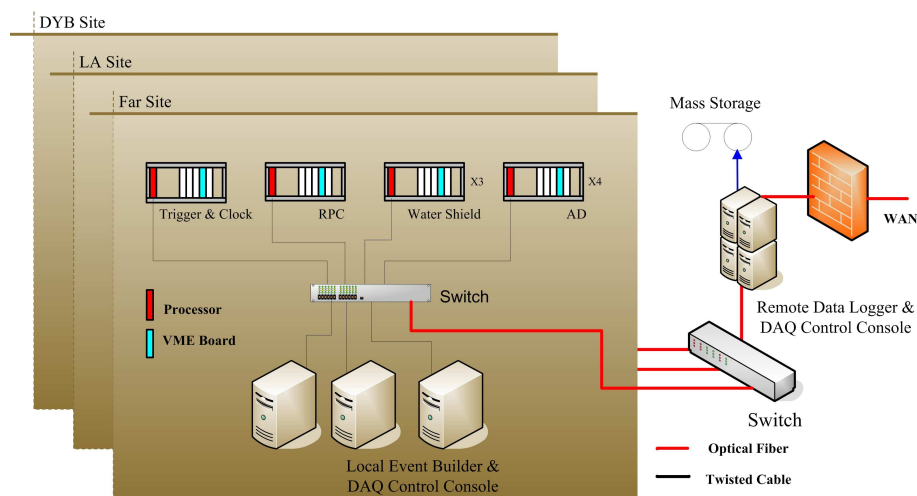


Fig. 7.10. Block diagram of data acquisition system.

DAQ software of Daya Bay will be developed based on the framework of BESIII DAQ software and ATLAS TDAQ software. Functionally, the DAQ software can be divided into two parts: data flow software and online software.

The data flow software is responsible for receiving the detector data and transporting the data to mass storage. Since the DAQ system is required to be dead time free, each DAQ level should have a data buffer capability to handle a fluctuation in data rate. In addition, both the VME bus and network switches should have enough margin of data bandwidth to deal with the data throughput of the experiment.

The online software is responsible for all aspects of experimental and DAQ operations and control during data-taking, and during testing and calibration runs.

The DAQ system can be separated into two parts, front-end and back-end.

7.4.2.1 VME front-ends readout

The lowest level is the VME based front-end readout system. It is the interactive interface of DAQ system with front-end electronics systems, trigger and detector. Its main tasks are configuring FEE modules, reading out data of FEE modules, assembling event data inside one VME crate and transmitting data through ethernet.

Each VME crate is responsible for one detector or muon system. Each module of the antineutrino detector will have its own independent VME crate.

Therefore, The lowest level VME readout system of the far detector hall will consist of the trigger boards for each system, the front-end readout boards from three muon systems, and the four antineutrino detector readout boards. All readout boards are expected to be 9U VME boards. The Far and Near detector halls, will have the same DAQ architecture but with different number of VME readout crates to accommodate the different number of readout channels in the Far/Near halls.

The front-end readout system is a real-time system based VME bus. Each VME crate holds a VME system controller, some front-end readout (FEE) modules and at least one trigger module which supplies the clock signals via the VME backplane to the FEE modules. The VME controller, an embedded single-board computer, is used to collect, preprocess, and transfer data. It is based on a PowerPC CPU MPC 7455 with a 1GHz clock and Universe II chip for VME bus interface. TimeSys, the operating system run on the controller, is a commercial embedded real-time Linux with version 2.6.9 kernel. The controller can read data from an FEE board via D8/D16/D32/MBLT 64 transfer mode, allowing a transfer rate up to 80 MB/s per crate, which is sufficient to meet the bandwidth requirements. All readout crates of the entire DAQ system at a single site are connected via a fast asynchronous Ethernet switch to a single local event builder computer.

7.4.2.2 Event Builder

At each site an Event Builder computer collects the data from the different VME crates for the different detectors and concatenates the FEE readout to form single antineutrino or muon events. Each type of sub-event, muon events, or antineutrino events, have a different data stream and will be recorded as separate data files in permanent storage. This scheme complies with the DAQ system design principle of keeping each detector system completely independent for both hardware and software. The Event Builder computers for each site may also be deployed to a surface building for ease in the maintenance of hardware.

According to the different trigger sources all sub-systems (detector, FEE, Trigger and DAQ) can be partitioned into several independent parts. Each part is a collection of equipment and resources, called a partition. There are independent run-control, data acquisition and data storage in every partition which is configurable. If every detector module is a partition, there are 17 partitions in the Daya bay experiment.

7.4.2.3 Data Storage and Logging

Data from the Event Builder computer at each site are sent via fast optical fiber link through a dedicated switch at a single surface location where it is then transferred to local hard disk arrays. The hard disk arrays act as a buffer to the remote data archival storage or as a large data cache for possible further online processing. Each day will produce about 0.3 TB of data that needs to be archived. Although implementation of data logging has not yet been finalized, there are two obvious options:

1. Set up a high bandwidth network link between Daya Bay and the Chinese University of Hong Kong, China, and distribute the data to Beijing and the US from there. This is the preferable scheme.
2. Record the data locally on disk (or tape) and deliver to Hong Kong by car, where they would be copied and distributed via the network.

Whichever option is realized, the local disk array should have the capability to store a few weeks worth of data in the case of temporary failures of the network link.

7.4.2.4 Online Software

The Online Software encompasses the software to configure, control, and monitor the DAQ system but excludes the management, processing, and transportation of physics data. It is a customizable framework which provides essentially the 'glue' that holds the various sub-systems together. It does not contain any elements that are detector specific as it is used by all the various configurations of the DAQ and detector instrumentation. It cooperates with the other sub-systems and interfaces to the DataFlow, the detector control system and the Offline Software. It also provides the interface between the human user and the DAQ system.

An important task of the Online Software is to provide services to marshal the DAQ through its start-up and shutdown procedures so that they are performed in an orderly manner. It is responsible for the synchronization of the states of a run in the entire DAQ system and for process supervision. Configuration database services are provided for holding the large number of parameters which describe the system topology, hardware components, software components, and running modes. During data taking, access is provided to monitoring information like statistics data, sampled data fragments to be analyzed by monitoring tasks, histograms produced in the DAQ system, and also to the errors and diagnostic messages sent by different applications. User interfaces display the status and performance of the DAQ system and allow the user to configure and control the operation. These interfaces provide comprehensive views of the various sub-systems for different types of users and operations.

The Online Software architecture is based on a component model and consists of three high level components, called packages. Each of the packages is associated with a group of functions of the Online Software. For each package, a set of services which it has to provide is defined. The services are clearly separated one from another and have well defined boundaries. For each service a low-level component, called a sub-package, is identified.

Each package is responsible for a clearly defined functional aspect of the whole system.

- **Control** contains sub-packages for the control of the DAQ system and detectors. Control sub-packages exist to support DAQ system initialization and shutdown, to provide control command distribution, synchronization, error handling, and system verification.
- **Databases** contains sub-packages for configuration of the DAQ system and detectors. Configuration sub-packages exist to support system configuration description and access to it, record operational information during a run and access to this information.
- **Information Sharing** contains classes to support information sharing in the DAQ system. Information Sharing classes exist to report error messages, to publish states and statistics, to distribute histograms built by the sub-systems of the DAQ system and detectors, and to distribute events sampled from different parts of the experiment's data flow chain.

The interaction between the Online Software packages is shown in Fig. 7.11. The Control makes use of the Information Sharing and of the Databases packages. The Databases package is used to describe the system to be controlled. The Information Sharing package provides the infrastructure to obtain and publish information on the status of the controlled system, to report and receive error messages, and to publish results for interaction with the operator.

7.5 Detector Control and Monitoring

The detector control system (DCS) controls the various devices of the experiment (e.g., high voltage systems, calibration system, etc.), and monitors the environmental parameters and detector conditions (e.g., power supply voltages, temperature/humidity, gas mixtures, radiation, etc.). Some safety systems, such as rack protection and fast interlocks are also included in the DCS.

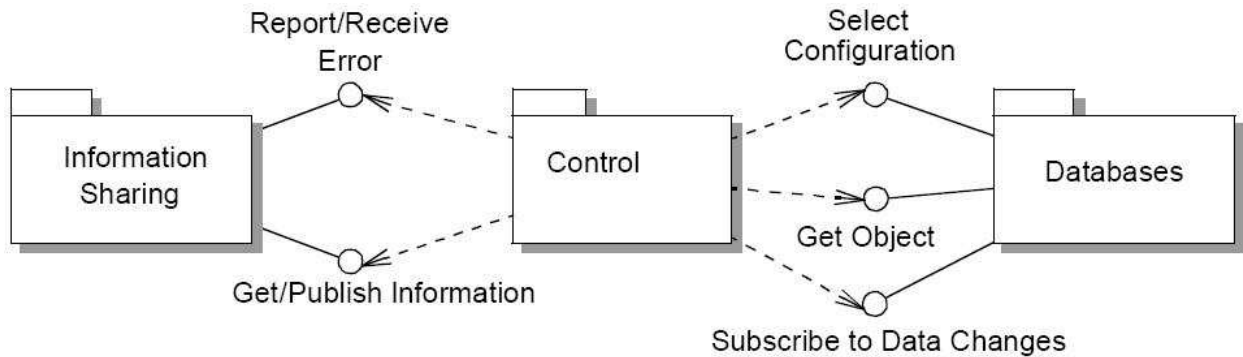


Fig. 7.11. Internal interaction between the Online Software packages.

The DCS will be based on a commercial software package implementing the supervisory, control, and data acquisition (SCADA) standard in order to minimize development costs, and to maximize its maintainability. LabVIEW with Data logging and Supervisory control module is a cost effective choice for the DCS. The BESIII system will act as a model from which the Daya Bay system is developed.

The endpoint sensors and read modules should be intelligent, have digitalized output, and conform to industrial communication standard. We will select the minimum number of necessary fieldbus technologies to be used for communication among the SCADA system and the readout modules.

7.6 Manufacturing Plan, Quality Assurance, ES&H (Environment, Safety and Health) and Risk Assessment

7.6.1 Manufacturing Plan

The PMT readout electronics (*e.g.* FEE boards), are being designed by IHEP and will be manufactured in China. Front end electronics for the RPCs will be manufactured and tested at the University for Science and Technology in China. Final stage testing of all components together with the RPCs will take place on site at Daya Bay. The trigger and clock systems are being designed by Tsinghua University in Beijing in concert with the electronics group at IHEP. These systems will use a mixture of commercial electronics (including GPS receivers) and custom made boards either purchased or manufactured in China. The DAQ software is being designed and developed at IHEP, with some support from the US. The VME crates, power supplies, processors, cables and other miscellaneous components are available from commercial vendors, as are electronic racks and cooling systems. The crates and rack hardware will be acquired in Asia. Computer systems are readily available from numerous sources. The monitoring and control system will use a mixture of commercial hardware and software, and some custom software. University resources (students and post-docs) will be used to develop both hardware and software components of the electronic systems. Testing and integration of the system will be done by physicists, primarily in Asia, but also within the US.

7.6.2 Quality Assurance

The electronic designs will be thoroughly reviewed by experienced electronic engineers not directly involved with the design effort prior to prototyping and production of electronics boards. Prototypes will be tested both in China and in the US. Custom electronics boards will use commercial off-the-shelf components and products that are available in China. Furthermore, ADCs and FPGAs will be selected from pin-compatible family lines allowing for unanticipated upgrades. Full production will occur only after a complete system integration test involving all parts. Software will be exercised by several groups during development to identify problems and bugs, both in China and within the US. Responsibility for maintenance

and repairs (as needed) will remain with the original design team during installation and commissioning. Finally, a programmable calibration pulse can be generated by a fast DAC chip on-board the PMT FEE which is sent to the input of every channel on that board. We will use this feature as a reliable self test and calibration for the full readout system.

7.6.3 Environment, Safety, and Health

The principle hazard is exposure to electrical power (220 VAC and various high-current, low-voltage DC power lines). Local standards and regulations will be followed for installation of AC power into the electronics racks. Appropriate commercial class-2 cable, outlets, and plugs will be used throughout. High current DC power supplies will be mounted inside the racks. Voltage distribution will use appropriate high current cables, with all connectors properly covered to prevent accidental human contact or short-circuits. Custom PCBs will be fused to prevent/reduce fire hazards. Cooling fans will have appropriate covers to limit contact with spinning fan blades. Sensors mounted within the rack will automatically shut-off power in emergency situations. Hazard and hazard mitigation plans will be reviewed internally by engineers not directly involved with the original design. Written procedures will be drafted to advise people working with Daya Bay electronics on proper safety procedures.

7.6.4 Risk Assessment

There is a risk that experimental conditions will be different than those experienced during integration testing. A sample of possible risks include:

1. excess noise
2. unanticipated cross talk
3. failure of the GPS clock system
4. trigger rates larger than anticipated
5. detector response outside original design expectations
6. environmental conditions outside expectations

Mitigation:

To mitigate these risks, designs are being kept as simple and flexible as possible with built-in redundancies (*e.g.* using a precision oscillator as a backup clock), where possible. We will require that about 50 percent of the FPGA resources on each module remain available to accommodate upgrades and modifications for both the readout and trigger systems. Isolation transformers will minimize the impact of external sources of electronic noise. The rack environmental design will be flexible enough to allow for improvements and upgrades should any aspect prove inadequate.

REFERENCES

1. G. Gratta *et al.*, Nucl. Instr. and Meth. **A400**, 54 (1997).
2. Trimble Navigation Ltd. <http://www.trimble.com/acutime2000.html>.
3. TrueTime Ltd, <http://www.truetime.net/software-winsync.html>

8 Offline

This section describes the Daya Bay Offline Software and Computing Project. The project covers all developments of offline software for the Daya Bay experiment, the definition of the computing environment, the provision of hardware and manpower resources, and the operation of the offline computing systems. Offline software and computing is connected to, but distinct from, online software and computing which is conducted in real-time in conjunction with raw data acquisition.

In particular, the Daya Bay Offline Software and Computing Project is responsible for the provision of the software framework, development and computing environment, experiment databases, data management system, and external software as well as provision of the hardware and networking required for offline processing and analysis of Daya Bay data.

The development of detector-specific algorithmic code for simulation, calibration, alignment, trigger and reconstruction is under the responsibility of each detector subsystem, but the Software and Computing Project plans and coordinates these activities across detector boundaries and supplies and supports the non-detector-specific software and tools that the detector subsystems use.

Daya Bay Offline Software and Computing, as in any experiment, serves evolving roles during the course of the project. These different roles can be assigned to chronologically ordered stages, but two or more different stages are often concurrent. The consequence of this is that offline software and computing resources are already in one stage of production running and must be smoothly evolved to meet the requirements of each new stage, in place, while running, and without interrupting ongoing work for concurrent stages.

The distinct stages of Offline software and computing can be categorized as:

1. **Experiment Design:** Alternative detector designs are simulated and tested in software. These designs evolve with time as physics, mechanical, fabrication, and cost influences are explored and refined. For each new design or configuration, the impacts on physics signal, efficiency, and uncertainty are simulated and studied.
2. **Physics Preparation:** Physics analysis software is developed, tested, and refined, including simulation of realistic detector signals, background, and geometry. During this phase, data processing and analysis software is prepared to the point that physics analysis can be done on day one of data taking.
3. **Detector Commissioning:** This phase involves commissioning and testing of detectors as they are prepared for data taking. Detector calibration and detector diagnostics software coupled with DAQ raw data I/O and some slow controls data I/O are needed for determining detector and electronics health.
4. **Data Taking & Analysis:** Production running requires full DAQ raw data I/O, full slow controls data I/O, end-to-end reconstruction and data processing software and physics analysis software. Our goal is for offline software and computing to be prepared for day one data processing and physics analysis.

8.1 Offline Requirements

Current requirements for offline focus on the simulation of detector designs and physics signatures, and on software development for physics preparation. They are summarized in Table 8.1. Detector commissioning will require much, but not all, of the same software as production data taking, some network connectivity into the Daya Bay site, but not much CPU and storage resources. As data taking begins, all software, hardware, and networking components must be in place on day one to ensure calibration and characterization of detectors and rapid first results from data. Once data taking reaches steady-state, the offline requirements will shift towards data management, data processing and ease of access to the data and software for all Daya Bay collaborators.

Item	Requirement	Justification
End-to-end data transfer rates	0.5 TB/day	Entire data volume plus 50% recovery capacity
Mass storage volume	800 TB	Sufficient for 5 years of raw and processed data
Cluster specs	225 kSpecInt2000	Four full production passes per year
First production software release	11/2008	Ready for commissioning at Daya Bay near site
Second production software release	2/2010	Ready for full operations

Table 8.1. Requirements for Offline.

8.1.1 Networking, Computing and Software Distribution

Computing hardware, archival storage, and networking requirements for Daya Bay are not extraordinary for modern physics experiments. However, the international and distributed aspect of the collaboration impels special attention to networking and data archiving, as well as strong coordination of US and Chinese resources and ease of access to experiment resources for all collaborators.

Offline software must be easy for Daya Bay collaborators to download, install, and use at Daya Bay institutions. Software and infrastructure must require a low level of long-term maintenance effort. Offline software must run on all validated and supported platforms and must allow integration of Daya Bay collaborator-written code specific to the experiment with commonly used tools and packages such as Geant4 [13] and ROOT [28].

Daya Bay requirements on Networking, Computing, and Software Distribution include:

1. **Commissioning Network Bandwidth:** As the civil construction ends and on-site detector construction, commissioning, and testing begin, there will be a constant onsite presence of scientists, engineers, and technicians who will need Internet access for email, web browsing, and video conferencing with outside collaborators. Some relatively small amount of data transfer will also use network bandwidth. As well, those researchers not on site during this time will need access to onsite/online monitoring and communication with onsite personnel.

2. **Steady-state Network Bandwidth:** End-to-end network bandwidth from the DAQ disk buffer at the Daya Bay reactor site to the Castor [4] data archive at IHEP must be able to deliver an aggregate of ~ 100 TB/year of recorded raw data. Sufficient additional bandwidth is required for remote access by Daya Bay scientists to the on-site computers as well as normal incidental use by researchers at the reactor site (e.g. email, web access, video conferencing).

End-to-end network bandwidth from the Castor data archive at IHEP to the HPSS [17] data archive at LBNL must be able to deliver the same raw data rates. Trans-Pacific network bandwidth must also allow US-sited collaborators the same access to off-site monitoring and control as China-sited collaborators. In addition, bandwidth between IHEP and LBNL is required for exchange of processed data, simulated data, database synchronization, etc. Trans-Pacific bandwidth required beyond raw data transfer is estimated at $\sim 100\%$ of the raw data rate.

3. **Recovery Network Bandwidth:** End-to-end network bandwidth from the DAQ disk buffer at the Daya Bay reactor site to the data archive in Beijing must be sufficient to recover from periodic network

outages or interruptions. Surplus bandwidth for such recovery should be approximately 50% of the steady-state data rate, sufficient to drain the DAQ disk buffer without interfering with nominal data transfer. This model drains the DAQ disk buffer over a time-period twice the length of the network outage.

4. **Network Connectivity:** The maximum time to recovery and mean time between failures of the end-to-end network connectivity from the DAQ disk buffer at the Daya Bay reactor site to the data archive in Beijing must not overflow the DAQ disk buffer. The DAQ disk buffer will be \sim 20 TB, which is sufficient for \sim 1 month of recorded raw data. In theory, this implies that the maximum time to recovery of the network must be less than 1 month, and that the aggregate down-time of the end-to-end network connectivity must not exceed 33%. In practice, the maximum time to recovery should be less than 1 week, and the aggregate availability should be greater than 96% (i.e. 2 weeks aggregate outage per year).
5. **Computing Power:** Dedicated, validated computing resources must be sufficient to allow 2 full production passes through a year's worth of raw data per year using less than 50% of the total compute power. Thus we allot resources sufficient for 4 full production passes for a full year of data with the remaining 50% dedicated to user-level analysis and simulation.
6. **Software Releases and Distribution:** Daya Bay software releases must be installed on each of the three official clusters (BNL, IHEP, LBNL). Software releases must be available for download and installation on other institutional resources running supported operating systems and software loads (i.e. suite of loaded external software versions).

8.1.2 Simulation

Daya Bay simulation, like most modern physics experiments, is done using GEANT4. Daya Bay requires specific physics processes be properly implemented in the physics engine, the ability to easily compare alternate detector designs, configurations, and options, and that the output of the simulations permit the development of offline algorithms well before detector turn-on. Existing physical processes in GEANT4 essential to Daya Bay are validated against external data when available or other simulation packages such as MCNPX [22], FLUKA [11] and GEANT3. Additional processes or phenomena specific to Daya Bay such as the photon spectrum after neutron capture on Gadolinium, cosmic muon flux, and specific radioactive decays are provided by custom-built additions.

The Daya Bay simulation is modified as design decisions are reached and test-stand data are available to gradually improve the degree of realism of the program. Early use of simulation is focused on detector design. As the experiment evolves, the simulation will be improved to eventually generate data with the raw data format for detailed studies of triggering algorithms, calibration techniques, data transfer and processing, and data analysis methods. Experimental data obtained during detector commissioning will be used to refine and expand the simulation which will, in turn, be used to validate and examine the signal acceptance and background estimation techniques. In addition, the simulation will be expanded to accommodate alternative studies such as supernovae detection or large cosmic-ray air showers.

8.1.3 Data Processing and Analysis

The offline software must support data reduction, reconstruction and analysis. The algorithms that make up this processing, and the data objects they produce, are varied and complex. Many authors will contribute algorithms which must work together in a manageable manner. The software must manage the necessary complexity and present a cohesive and easy to use system to the physicist programmers and users.

In tension, there is a limited number of software developers available to work on the core software that manages this complexity. We require a solution that best uses Daya Bay software developer time. For this

we leverage existing expertise from the HEP community, and in particular draw from high quality software that has been produced for LHC experiments and adopted by many others.

Specifically, we require the software to be written in the context of the Gaudi framework[12]. This framework is to be used for processing raw data, real or simulated, marshalling reconstruction and analysis algorithms, and driving analysis software. While all production processing will be done using Gaudi based algorithms, support must exist for using the popular analysis tool ROOT[28] for doing ad-hoc analysis.

Detector description and event data visualization is required. This must integrate into Gaudi. It currently includes an OpenInventor based display for detector geometries and may be extended to display event information.

The data produced by the Daya Bay experiment is a set of independently triggering sub-detectors, unlike accelerator experiments where the readout is synchronized with accelerator spills or collisions. This means that, unlike accelerator data, the grouping of data into physics 'events' is not known a priori but rather must be inferred from the data itself. Hence the offline software must support a data model where sufficient data is available at any particular time so that algorithms can reconstruct complete physics events. For instance, as in similar experiments like KamLAND [19], Daya Bay production analysis of anti-neutrino events will be predicated upon sliding time windows on data within an AD and between ADs and the veto system. The offline framework must provide a natural interface to this kind of data analysis and allow users to configure the time-window size and other appropriate parameters without recompiling.

Daya Bay requirements on Data Processing and Analysis include:

1. **Gaudi Integration:** Gaudi is the framework in which all Daya Bay specific offline software will be written. This includes services such as detector description information, simulation, persistency as well as official data processing and user analysis codes.
2. **ROOT Support:** ROOT is a very popular analysis package. While the majority of the offline software does not require ROOT, users are expected to want to use it for doing high-level ad-hoc analysis. The offline software must support this. In addition the data persistency will use ROOT I/O.
3. **Data Model:** The data model used by the offline framework must support the real data from the DAQ and results of the simulations. It must be possible to navigate a sufficient range of time-stamped data so that complete physics events can be constructed.
4. **Data Processing Model:** The offline analysis framework must permit the time-window data processing model expected by Daya Bay raw data processing. Other data processing models required by subsequent analysis must be supported.
5. **Data Access:** The complete picture of the detector's state is composed of sets of data whose rates of change differ significantly, for example the calibration data can be expected to change on the order of days or weeks, while physics data change in the order of milliseconds or less. Data processing needs access to all of these various streams of data and thus the offline framework needs to provide efficient access to storage of these quantities.

8.1.4 Data Movement and Networking

Daya Bay data will initially be distributed to a few collaboration-funded computer clusters to be calibrated, processed, and archived. The processed data are then made available to all collaborators for analysis at these official clusters or at local, institutional machines (e.g. local desktops and/or university clusters). The Offline subsystem must provide tools for the automatic and manual movement and management of data coming out of the DAQ system. Offline must also provide the tools for management of data provided by the utility company (e.g. reactor power levels, etc).

8.1.5 Online Interface

The online system will be responsible for merging the data streams from all detector subsystems (e.g. ADs, Muon system, and RPCs) into a single, time-ordered stream for subsequent offline analysis. Past this point of the experiment’s data processing, the management of data files, tools for data transfer and accounting, and software for I/O and processing are the responsibility of the Offline group. Before this point in the data flow, responsibility resides with the Online group.

Daya Bay requirements on the Online/Offline interface include:

1. **Slow Control and Reactor Data:** Detector slow control data are those data which monitor detector and trigger state and/or configuration, environmental conditions such as temperature and humidity, etc. These data change slowly over time and will be recorded in a relational database by the DAQ along side the main data stream. Reactor data will be provided by the utility company with some significant latency (probably hours, days, or even weeks after data are taken). These slow control and reactor data are needed to analyze and normalize our detector data stream in order to achieve baseline sensitivity. The offline processing and analysis software must provide access to all salient slow control and reactor data and allow Daya Bay analysis software to correlate in time the detector data stream with the proper database data.

8.2 Data Management, Networking and Computing

Daya Bay is an international collaboration with commensurately international hardware resources and globally distributed scientists requiring access to Daya Bay data, compute resources, and software. All managed data transfers are made via national and international networks. We expect to make use of Grid resources and tools for data transfer and job submission where appropriate. However, the modest data volumes and compute requirements of Daya Bay simulation, processing, and analysis as well as the limited manpower available suggest that more than a small investment in customizing Daya Bay software and/or hardware resources to a specific Grid is not cost-efficient. Therefore, we do not expect to fully Grid-enable our system, rather we will use a subset of easily adopted tools.

8.2.1 Data Movement

During steady-state data taking mode, data taken by the detectors are transferred by network from the reactor site in China to at least two permanent data archives (one in China, one in the US).

The first stage of data processing (i.e. calibration, reconstruction, and event filtering) will occur at one or both clusters, using validated production Daya Bay software running in the Daya Bay offline analysis framework. We may want to replicate processing at both clusters as a QA measure (i.e. process twice and compare results to ensure reproducibility). Results from each stage of data processing and subsequent data analysis steps are centrally archived and available to all collaborators for local and/or remote processing. Full data archiving, data processing, and data analysis will be done at the LBNL and IHEP clusters. Data processing and analysis will also be done at the BNL cluster and data analysis will be done at other institutional computing resources.

Daya Bay data are recorded by the DAQ system at the Daya Bay reactor site and stored on a local disk buffer large enough to hold ~ 1 month’s worth of recorded raw data (see Data Rate Estimate in Section 7.4.1). Data are transferred by network concurrently to two major Daya Bay data archives on NERSC’s [26] HPSS system at LBNL in Berkeley, CA, and on IHEP’s Castor system in Beijing, China. Integrity of the network data transfers are checked by comparing checksums of the data at either end. Failure of the integrity check triggers a retransmit of the data file.

Once data are transferred and validated, the original master copy at the Daya Bay reactor site on the DAQ disk buffer is marked as redundant and deleted using a high-watermark/low-watermark algorithm. This

scheme can accommodate temporary outages of the network and/or data migration tools without impact on the science output of the experiment.

Most of the data migration effort will be either automated or use tools which minimize the manual effort involved and reduce the likelihood of human error. Examples of this are: Bookkeeping for the disk buffer at the Daya Bay site will be done by a database loaded programmatically, rather than manually, from a spyder-like service which will keep watch on well-defined file system directories on the disk buffer. All data migration and high-watermark/low-watermark processes will work from this bookkeeping database.

8.2.2 Networking

Daya Bay depends upon several externally funded national and international networks and upon two network links funded specifically for use by Daya Bay. Specifically, the networks upon which Daya Bay depends include:

1. **CSTNet:** Built on the Chinese Academy of Science Network (CASNET) and the National Computation Facilities of China (NCFC), CSTNet [8] (The China Science and Technology Network) is the first public non-commercial network for research and education in China. CSTNet provides a 1 Gbps backbone and 1 Gbps connection to IHEP which will be used for all Chinese network traffic to and from IHEP.
2. **GLORIAD:** GLORIAD [15] (Global Ring Network for Advanced Application Development) is a high-speed computer network used to connect scientific organizations in Russia, China, United States, the Netherlands, Korea and Canada.

GLORIAD provides 4 parallel OC12 (622 Mbps) links between StarLight in Chicago and Hong Kong. Of these 4 OC12 links, one is publicly available and is being used today by Daya Bay and other experiments in the US and China. Though Daya Bay does not directly contribute to the funding of GLORIAD, we have been working with US and Chinese GLORIAD representatives to ensure sufficient Trans-Pacific bandwidth for Daya Bay raw and processed data flows.

3. **TransPAC2:** TransPAC2 [32] is an NSF-funded high-speed international circuit connecting research and education networks in the Asia-Pacific region to those in the US. TransPAC2 is part of the NSF's International Research Network Connections (IRNC) program.

The TransPAC2 network is currently engineered as a single OC-192 circuit between Los Angeles and the APAN network in Tokyo.

Daya Bay would use TransPAC2 as a geographically diverse backup circuit in case of service interruption of the GLORIAD Trans-Pacific link.

4. **ESNet:** ESNet [10] (The Energy Sciences Network) is a high-speed US national network serving Department of Energy (DOE) scientists and collaborators worldwide. Managed and operated by the ESNet staff at Lawrence Berkeley National Laboratory, ESNet provides direct connections to all major DOE sites with high performance speeds, as well as fast interconnections to more than 100 other networks. Funded principally by DOE's Office of Science, ESNet services allow scientists to make effective use of unique DOE research facilities and computing resources, independent of time and geographic location.

Current ESNet national bandwidth is 10 Gbps with 10 Gbps connectivity to both LBNL and BNL.

5. **DayaNet-OC3:** We have dubbed the connection from the Daya Bay site to the outside world **DayaNet**. DayaNet has two distinct implementations. The high bandwidth DayaNet will be an OC3 (155 Mbps) provisioned from on site to the Chinese CSTNet with bandwidth sufficient to provide for maximum,

predicted raw data flows, recovery from any network outages, and offsite monitoring and control of the experiment.

6. **DayaNet-DSL:** DayaNet-DSL is a lower bandwidth (~ 1 Mbps) DSL connection which will be placed into production at the earliest possible date to provide scientists, engineers, and technicians on site to communicate with outside collaborators through email, web, and video-conferencing. DayaNet-DSL will also provide some limited data transfer and experiment monitoring and control for early tests before DayaNet-OC3 is available.

DayaNet-DSL will be kept in production throughout the lifetime of the experiment as a failsafe network in the case of network interruptions on DayaNet-OC3, and to allow video-conferencing and incidental use without introducing contention on DayaNet-OC3.

7. **Institutional:** BNL, IHEP, and LBNL are each connected to their respective national networks at full speed. Both BNL and LBNL are connected at 10 Gbps to the 10 Gbps ESNet backbone and IHEP is connected at 1 Gbps to the 1 Gbps CSTNet backbone.

Because we are depending upon externally funded networks for our data transfer, it is important for Daya Bay be in close communication with those network providers so that we can ensure our bandwidth and connectivity requirements will be met. Beginning in April 2007, US and Chinese Daya Bay network engineers have been talking with GLORIAD, ESNet, and CSTNet network engineers to establish expectations and channels of communication for the eventual end-to-end network testing and trouble shooting required to move data between the Daya Bay site and each of the Daya Bay computer and storage resources in the baseline data flow model for the experiment.

DayaNet-DSL will be provisioned in the 2nd quarter of calendar year 2008 so that collaborators working on assembling, commissioning, and testing detectors on the Daya Bay site and in the SAB will have communication with collaborators outside Daya Bay. This network will also be used for initial tests of off-site monitoring and experiment control. Experience has shown that DSL bandwidth rates of even as low as 600 Kbps are sufficient to do video-conferencing, and more than enough for VOIP (Voice Over IP) and other normal Internet activities anticipated for the experiment.

DayaNet-OC3 will be provisioned in Fiscal Year 2008 at 155 Mbps which will be dedicated to Daya Bay data transfers and site access. This will be more than sufficient for the Daya Bay steady-state data taking rate (up to ~ 260 GB/day), leaving headroom for recovering from data migration and/or network interruptions and providing access to the site for remote monitoring of the experiment for researchers offsite.

The expected data rate estimated for Daya Bay is ~ 260 GB per day (see Data Rate Estimate in Section 7.4.1). However, to calculate the network bandwidth to provision from the Daya Bay site to the outside world we start with the Maximum theoretical DAQ rate of 500 GB/day. A maximum DAQ rate of 500 GB/day is ~ 50 Mbps. Assuming that we would want to increase data transfer rates by 50% during periods of recovery (e.g. it would take 36 hours to recover from a 24 hour outage) sets the recovery data transfer bandwidth to ~ 75 Mbps. Estimating the online control, video conferencing, email, web-browsing and incidental network usage is impossible, but we know that video conferencing with even 0.5 Mbps is acceptable, so predicting 10 Mbps is more than sufficient. All networks try to run at $\sim 30\%-40\%$ capacity for smooth package traffic without collisions. Network engineers at LBNL think that we can get at most 80% capacity if we tune TCP buffers, use state-of-the-art data transfer protocols, etc. Steady-state usage of 60 Mbps nominal bandwidth usage on a 155 Mbps OC3 is 39% occupancy. 85 Mbps recovery bandwidth usage on a 155 Mbps OC3 is 55% occupancy.

From China to the United States, Daya Bay will rely on two R&E (Research & Education) networks. GLORIAD, which connects to ESNet in Chicago is currently 2.5 Gbps across the Pacific and already in use by Daya Bay. TransPAC2, which connects to Internet2 in Los Angeles, is part of the NSF's IRNC

(International Research Network Connections) program. This international diversity of connection ensures that no single Trans-Pacific network outage will interrupt data flow to the US.

Once in the US, the DOE-funded Energy Science Network (ESNet) provides a high-reliability 10 Gbps IP backbone to all DOE Office of Science facilities including the NERSC PDSF cluster at LBNL and to BNL where the Coop Cluster is located.

Networking within China and connection to IHEP in Beijing relies on the Chinese national network (CSTNet) which provides a 1 Gbps backbone and 1 Gbps connectivity to IHEP.

The final network topography for Daya Bay is not yet fully settled. The connection from the Daya Bay reactor site could land in Hong Kong (CUHK) or connect directly to CSTNet in Shenzhen, or even to the alternate Chinese national R&E network, CERNET at Zhoushan University. This will depend upon final service negotiations and costs.

8.2.3 Data Archiving

All Daya Bay data (raw data, calibrations, reactor data, processed data, and collaboration analysis objects) will be archived in at least two locations. At LBNL's National Energy Research Scientific Computing (NERSC) [26] Facility we will store our raw data on the HPSS (High Performance Storage System) mass store. This system has a current total capacity of 8.8 PB and is allocated via the normal NERSC allocation process. At IHEP, the Castor system in use for LHC experiments will be replicated or extended to provide archival storage for Daya Bay.

Data from these two archives will be available to all collaborators via the use of standard data transfer tools such as FTP, scp, and/or GridFTP. A bookkeeping database will allow users to query all centrally managed data files.

8.2.4 Databases

A relational database will be used to hold time-varying data needed to analyze detector data. It will hold such information as reactor power, calibration parameters, detector environmental or other “slow control” values. It will also hold surveyed offsets from ideal detector geometry as well as information on changing detector configuration. There will be a single, authoritative database. It will allow for read-only replication at other collaborating sites in order to optimize access times.

The main role this database provides is efficient time based random access to its data. Every entry of a particular type of data has an associated range of time when it is considered valid. Given a specific point in time, the software interface to the database will select the correct entry. When entries have overlapping validity ranges the entry with the most recent creation date is selected. This versioning mechanism allows improved quantities to be entered without the need to delete values and provides a way to reproduce past results.

Accessing this database in a simple manner is done through a the DatabaseInterface (DBI) package adopted from MINOS. Daya Bay has collaborators that also collaborate with MINOS and have a good understanding of using this DBI package.

8.2.5 Computing Resources, Operations, and Data Processing

The offline computing resources needed for simulation and for data management, processing, and analysis will be met at three officially supported computing clusters at BNL, IHEP, and LBNL and at two tape archives at IHEP and LBNL. The manpower required to administer and operate the resources will be supplied by the host institutions. Daya Bay operational manpower will be required to manage data files and batch jobs on the systems, as well as installing and validating the official Daya Bay software load.

Daya Bay simulations, data analysis, and software development are currently making use of the BNL's Coop Cluster, LBNL's PDSF, and IHEP's computer cluster as well as smaller, institutional clusters. We are

also centrally storing and serving simulated data from LBNL’s HPSS as well as from several web-accessible data servers at BNL and IHEP.

Because of our limited available effort, we must limit the number of officially supported platforms to those run on the clusters. Official support means that the core group will assure that releases compile and run on these platforms. When platform-specific problems develop on unofficial platforms resolution support will be provided on a best effort basis. Majority of such support is expected to come from a “champion” of the unofficial platform. We explicitly do not support any platforms that are not Unix-like.

The officially supported platforms are Scientific Linux[29] (SL), a slight variant of Red Hat Enterprise Linux maintained by FNAL, and Debian GNU/Linux[30]. IHEP and LBNL clusters currently run SL4 and the BNL cluster runs Debian 4.0.

Portability is emphasized when developing new software or including additional dependencies on external, third party packages. The number of these external dependencies are minimized but this is balanced against the philosophy to adopt rather than develop, described more below.

8.2.5.1 BNL Cluster

The BNL Cooperative Cluster (coop) [7] is a relatively small cluster currently with >50 CPU AMD Opteron 2GHz cores and ~8 TB disk. It serves the MINOS, Daya Bay and other experiments with priority given dependent on the size of the hardware contribution and experiment provides. US Daya Bay will eventually add ~40 CPU and 10 TB disk.

BNL hosts a large computing facility for the RHIC and ATLAS experiments as well as a number of smaller ones. If required, Daya Bay can obtain CPU, disk, tape and human resources through the facility.

8.2.5.2 IHEP Cluster and Tape Archive

IHEP has several medium and large Linux clusters for experiments including CMS [6], ATLAS [2], BESIII [3], Argo [1], and HXMT [18] (Hard X-ray Modulation Telescope). The BESIII experiment includes a Castor tape archive system of 4.8 PB capacity.

CAS will deploy another cluster of ~100–200 CPUs with ~20 TB of disk and another Castor system with ~200–500 TB tape capacity dedicated to Daya Bay. This system will be managed in parallel with the other clusters, initially running Scientific Linux 4.

8.2.5.3 LBNL Cluster and Tape Archive

At LBNL, the Parallel Distributed System Facility (PDSF) [27] is used by approximately 20 different nuclear physics and high energy physics experiments. These experiments are able to pool their resources allowing a much larger and professionally managed central resource than they could realize individually. PDSF supplies currently approximately 600 processors, 150 TB of shared disk space, and 150 TB of local disk space. All CPUs are running Linux operating system and allow the user to specify at run time the software load (via the modules facility [25]) and operating system (via the chos utility [5]), which allows simultaneous usage by the widest variety of applications.

US Daya Bay will add another ~100 processors and ~20 TB of shared disk to the PDSF system. This will guarantee a minimum fair share of the overall resources. Additional CPU resources are available depending on usage by other stake-holder experiments.

PDSF is part of the NERSC facility and well coupled to the HPSS mass storage system [17]. The NERSC HPSS system consists of 8 large STK tape robot silos with an aggregate capacity of 8.8 PB and a large (100 TB) disk cache. The maximum throughput for the system is 3.2 GB/sec. Users can access the system through a variety of clients such as hsi, htar, ftp, pftp, and grid clients.

The NERSC facility is operated for the Department Of Energy (DOE) as an open resource for DOE’s Office of Science researchers. Allocations of NERSC computer time and archival storage are awarded by

DOE to research groups whose work reflects the mission of DOE's Office of Science. The allocations are administered by NERSC and managed by DOE. The research groups are awarded project accounts, known as repositories, from which they draw resources throughout the allocation year.

Requests to use NERSC resources are submitted annually via a web form known as the ERCAP (Energy Research Computing Allocations Process) Request Form. ERCAP is accessed through the NERSC Information Management (NIM) web interface and is available year-round.

Daya Bay currently has mass storage allocation of 25 TB on NERSC's HPSS system and will apply annually for additional storage up to a maximum of \sim 600 TB to archive all raw, simulated, and processed data sets.

PDSF and HPSS are administered by computing professionals and adhere to defined metrics for availability, uptime, and performance. The only Daya Bay operations manpower necessary is that required to submit and manage jobs and data files.

8.3 Offline Core Software and Infrastructure

Daya Bay has adopted an object-oriented approach to software and is written primarily in the C++ programming language. We have chosen a philosophy of adopting existing quality software where it fits our needs and focus our efforts on providing any missing, Daya Bay specific software.

We recognize a major division in software development. On one side, which we term Physics software, consists of data reduction, reconstruction and analysis algorithms specific to the experiment. It also includes information such as detector description, reactor output and other experiment specific parameters. On the other side is the Core software which supports the Physics software. It provides processing frameworks, data access services, a database for time varying information such as calibrations. The development of Physics software itself is not covered by this project, rather the supporting Core software is.

It is recognized that the Core software has further divisions based on task. These include the following:

1. **Processing and Analysis:** This division is the bulk of the effort. It includes the support for data reduction and event reconstruction algorithms and the application of calibrations, efficiency studies and final physics results.
2. **Simulation:** This is a specific subset of processing and analysis. It includes the generation of initial particle kinematics and the detectors' response to them, as finally the effects of the electronics and trigger conditions. It results in data which looks identical to that from the real DAQ in addition to the simulated "truth" information.
3. **Infrastructure and Process:** This includes managing software development and collaboration through tools such as bug tracking and documentation systems, code repositories, installation method and electronic mailing lists.

These elements are described in more detail in the following sections.

8.3.1 Processing and Analysis Software

The primary component of the core software for offline processing and analysis is the offline framework. The framework provides a common software environment in which user codes run and cooperate. It is the software which controls what code gets called for which data and when.

Applying the above philosophy we have adopted the Gaudi Data Processing Application Framework as the basis of our offline framework. In addition we have selected a number of Gaudi-based packages for adoption from the LHCb offline software project (from which Gaudi was initially developed). These packages are largely independent from LHCb specific tasks and logically could be ported to Gaudi, proper.

These packages provides the basic units of processing such as a common in-memory transient data store (TDS), algorithm management, configuration management. It also provides detector description and event data model implementation and their visualization.

Some reasons for selecting Gaudi as our software basis include:

1. **Reduced Developer Burden:** Gaudi is an existing and well supported framework which has been developed and tested in large collaborations with much more manpower than Daya Bay can bring to bear on development of our own framework. Several much smaller experiments in HEP have adopted Gaudi for the same reason.
2. **Collaboration Expertise:** Gaudi is used by Chinese collaborators in BES III and has been used by US collaborators and potential collaborators from ATLAS. Hence, we are able to draw upon both US and Chinese technical expertise.
3. **Reduced User Burden:** Gaudi minimizes user coding. Users generally only have to write Algorithms that interact with the common in-memory data store for data access and automatic data I/O.
4. **Integration with other software:** Gaudi supports integration with other important major software packages such as Geant4, ROOT and Python.
5. **Provides needed services:** Gaudi provides many needed services including particle properties, histograms and ntuples, pseudo-random number generation, logging.

Our evaluation of Gaudi focused on several aspects of usability and applicability to Daya Bay including:

1. **Source code:** Daya Bay will maintain our own version of Gaudi and LHCb Gaudi-based packages as well as the LCGCMT project used in building them in our software repository. This lets us decouple our development with that of Gaudi itself. We can immediately apply bug fixes or Daya Bay specific modifications. Where applicable we feed changes to the upstream developers.
2. **Installation:** While LHC experiments largely rely on distributing binaries we feel it is important to be able to compile all software from source. This allows supporting the varied computing platforms Daya Bay necessarily has, as well as finding and fixing problems that do not affect LHC experiments. Building this large amount of software is a daunting task. It is done through a suite of scripts that handle downloading and building external, third party software (Geant4, ROOT, boost++, CLHEP, etc), Gaudi and related and finally Daya Bay software itself. This has been shown to work on platforms not supported by LHC binaries including Debian GNU/Linux and Mac OS X. We may, at some point, distribute the binary results of these builds so that some sites can avoid the effort in performing their own builds.
3. **Event Processing Model:** The processing models for accelerator-based experiments are typically based upon separate, uncorrelated triggers which are processed one-by-one. Daya Bay data processing will involve analyzing data records from multiple detectors and triggers within the execution of an algorithm. We have determined such a model is supported by Gaudi.
4. **Support and Upgrades:** Daya Bay is a small experiment relative to ATLAS and LHCb (the main developers of core Gaudi). We need assurances that we can expect some level of support from these authors when we find bugs and request or contribute feature additions. We have already engaged the Gaudi community and helped foster greater communication by creating the "Gaudi-Talk" mailing list hosted at BNL.

5. Geometry: We have adopted LHCb detector description based on DetDesc and related packages. It provides us in-memory objects, XML based persistency and OpenInventor based visualization. It is important to have the same source of detector description used during analysis as was used during simulation. This is accomplished through the Gaudi Interface to Geant4 (GiGa). Minimal Daya Bay specific software is needed, and instead attention is focused on describing the detectors in simple XML files.

8.3.2 Simulation Software

In the past, simulating the Daya Bay experiment has been focused on simulating initial kinematics and the detectors' response. The initial particle kinematics for various event types were simulated with a suite of programs written in Fortran. Their output is saved to text files or directly piped into the detector simulation. These will be converted into Gaudi algorithms. Initially they will continue to be executable sub-processes. If this proves to be unmanageable they will be refactored into Fortran subroutines and wrapped in C++.

The current detector simulation is a Geant4-based monolithic program called G4dyb. While successful for initial R&D studies it has become relatively difficult to extend further. We plan to gradually refactor it to be more modular. This will start with replacing the current, hard-coded detector description described with the one described above. From there we intend to investigate the possibility of converting the rest to a pure GiGa implementation.

8.3.3 Infrastructure and Process

To support software development and collaboration we again follow the philosophy of adopting quality software before considering to develop our own. Our tools are largely Internet based and distributed among the major laboratory collaborators. The following software is in service:

SVN We manage our source code and define our releases using a Subversion (SVN) repository served by IHEP. The repository is mirrored in a read-only fashion at some other institutions.

Code browsing This is done with Trac served from National Taiwan University, WebSVN from IHEP and Doxygen from BNL.

CMT Our software build and runtime management system, like that of Gaudi, is based on Configuration Management Tool (CMT). As described above, software builds are largely automated though a custom written build script suite.

Mantis Issue (bug) tracking is handled by the Mantis Bug Tracker and is served from LBNL.

MediaWiki Collaborative, web-based documentation is performed through MediaWiki wiki software served from BNL.

DocDB Formal documents, meeting presentations and minutes, and external talk material are managed by DocDB, a product of FNAL and served from IHEP.

MajorDomo Electronic mailing lists are served by MajorDomo from LBNL.

8.4 Risk Assessment

Offline computing does not pose environmental, health or safety risks.

8.4.1 Schedule

Offline software by its nature is heavily front-loaded in the schedule. In order for scientists to commission, debug, and characterize detectors as they are installed into the Daya Bay site, the software for reading and processing detector data must be in place before detector installation. This requires that researchers develop, test, and debug detector-specific code, define data structures and data I/O formats, and are familiar with processing and analyzing simulated detector data using the offline framework and data analysis tools. This implies that the offline framework and analysis tools themselves (the environment in which researchers develop, test, and debug their own code) have already been developed, tested, debugged, and deployed to the collaboration.

Schedule Pipeline: The front-loading of offline software carries risk to the overall schedule for detector specific software and consequently to the ability of the experiment to be prepared at turn-on to commission the experimental hardware in a timely fashion.

Mitigation:

- We are leveraging work done by other experiments with far more resources than Daya Bay, such as adopting the Gaudi framework with targeted ATLAS extensions. We are drawing upon Gaudi expertise of LBNL collaborators currently working on ATLAS and on Chinese expertise of collaborators from BES III.
- We are leveraging MINOS experience and software in adopting the Data Base Interface (DBI) used for time-varying data.
- We have prototyped event data model structures with an option to build a framework specific to Daya Bay data analysis or incorporate those data model structures to the Gaudi-based framework.

8.4.2 Cybersecurity

Cybersecurity risks posed to the Offline Software and Computing Project relate to the experiment's information and information systems. Much of the computing and data is housed at US or Chinese national labs.

Those in the US are subject to the Federal Information Systems Management Act (FISMA). Compliance with FISMA entails, among other things, enumeration of risks in terms of their effect on the confidentiality, integrity and availability of the information and information systems. Risks must be mitigated through security controls and any residual risk must be accepted by the lab's DOE representative. Currently one lab (BNL) has completed the Certification and Accreditation process under FISMA. LBNL is still in the process but has gotten good evaluations from past security audits.

The IHEP cluster also is managed with explicit attention to cybersecurity best practices for WAN-accessible Linux clusters and is part of the IHEP security enclave. IHEP cybersecurity practices are subject to the classified criteria for security protection of computer information system (GB 17859-1999). In order to understand the current status of the information security programs and controls to make informed judgments and investments that appropriately mitigate risks to an acceptable level, IHEP has completed the Security Self-Assessments Compliance which GB 17859-1999 entails. IHEP uses defense in depth to elevate cybersecurity above that required by GB 17859-1999.

Besides the general risks covered by the above there are specific risks posed to this project.

Data transfer: Raw data from the detectors must be transferred from the DAQ disk array to offsite locations at IHEP and LBNL for initial processing and subsequent distribution. There is a risk of data loss or corruption during this transfer.

Mitigation:

- File checksums are computed before transferred. The cached file is removed only after it is confirmed that the copied files have matching checksums. A corrupt or lost file is retransmitted.
- Copies of data at more than one site (at least IHEP and LBNL) provide redundancy against loss or corruption after the initial transfer.

Prevention of Malicious code insertion: The offline software is developed by many people in parallel and used on information systems at many institutions. In principle, malicious code can be included that could alter results or provide avenues to attack collaboration computing systems.

Mitigation:

- Committing code requires username and password authentication unique to each contributor.
- The contents of each commit is monitored by the offline group through email notifications.
- If malicious code is found it can easily be excised from the repository.
- Elevated privileges are not required to run the software so a local vulnerability must exist for any attack to spread beyond the account running the code.
- Individual institutions have general mitigations against malicious software affecting their computing systems.

REFERENCES

1. <http://argo.na.infn.it/>
2. <http://atlas.web.cern.ch/Atlas/index.html>
3. <http://bes.ihep.ac.cn/>
4. <http://castor.web.cern.ch/castor/>
5. <http://www.nersc.gov/nusers/resources/PDSF/chos/index.php>
6. <http://cms.cern.ch/>
7. <http://www.phy.bnl.gov/coop/doc/coop.html>
8. <http://www.cstnet.net.cn/>
9. <http://docdb.fnal.gov/doc/>
10. <http://www.es.net/>
11. <http://www.fluka.org/>
12. <http://cern.ch/gaudi/>
13. <http://cern.ch/geant4/>
14. <http://www-glast.slac.stanford.edu/>
15. <http://www.gloriad.org/>
16. <http://harp.web.cern.ch/harp/>
17. <http://www.nersc.gov/nusers/resources/HPSS/>
18. <http://www.hxmt.cn/english/>
19. <http://kamland.lbl.gov/>
20. <http://lhcb.web.cern.ch/lhcb/>
21. <http://www.mantisbt.org/>
22. <http://mcnpx.lanl.gov/>
23. <http://www.mediawiki.org/wiki/MediaWiki>
24. <http://minerva.fnal.gov/>
25. <http://www.nersc.gov/nusers/resources/software/os/modules.php>
26. <http://www.nersc.gov/>
27. <http://www.nersc.gov/nusers/resources/PDSF/>
28. <http://root.cern.ch/>

29. <https://www.scientificlinux.org/>
30. <http://www.debian.org/>
31. <http://subversion.tigris.org/>
32. <http://www.transpac.org/>

9 Installation and Testing Plan

Careful logistical coordination will be essential for the delivery, staging, assembly, installation, and testing of all detector components and subsystems. This chapter discusses some of the basic considerations in the installation process and outlines a plan for the staging, assembly, installation, and testing of experimental subsystem components at the Daya Bay facilities.

The installation of subsystems, system testing of experimental equipment and deployment of detectors begins as beneficial occupancy of the facilities is obtained. Well-coordinated activities underground and on the surface are essential for the timely start of the experiment. While the civil construction of the underground tunnels and halls is underway, the assembly and testing of the first detectors will be started above-ground in the Surface Assembly Building (SAB) so that they can be deployed as early as possible.

The Collaboration has a wide range of experience in the installation and operation of large detector systems including underground installations at SNO, KamLAND, GALLEX (at the Gran Sasso Laboratory), IceCube (at the South Pole) and STAR. Members of the Daya Bay Collaboration have also been involved in the engineering and installation activities at MINOS and other large accelerator based experiments. Chris Laughton, an underground engineer from FNAL with extensive experience, is directly involved in the evaluation of the tunnel design and specifications for the civil construction at Daya Bay.

The logistics of assembly, installation and test of detector systems include:

- Testing of components and subsystem assemblies in the SAB.
- Preparation of components and subsystem assemblies in the SAB for transport underground.
- System assembly and/or installation in underground experimental halls.

The effort of WBS 1.7 supports the overall planning, staging, control and execution of the final assembly, installation, test and commissioning of the experimental hardware on site at Daya Bay. It includes labor, consumable materials and universal equipment (not including any custom installation and test hardware required for individual detector elements) required to perform these functions. It includes all technical, trades, supervisory and engineering labor required to install the detector elements, but not the physicist and engineering effort supporting the installation and test activities of an individual subsystem.

The effort of WBS 1.1, 1.2, 1.3 and 1.4 will provide system experts and cognizant engineering oversight along with relevant procedures and installation documentation for assembly and installation of the subsystem elements while in the SAB, in the experimental halls and subsequent in-situ system testing.

The management and supervision of all resources at the Daya Bay facilities will fall under the purview of the L2 Installation Managers. They are responsible for insuring the availability of qualified resources, tools and equipment, engineering documentation and procedures, appropriate supervision and safety oversight for the timely execution of installation and test tasks as defined in the project resource loaded schedule. The subsystem management structure will consist of two co-L2 managers responsible to the project office for cost, schedule, tracking and reporting. At the Daya Bay site the Local Installation Manager (LIM) and his deputy, the Facilities/Technical Supervisor, serve as the local managers and work control coordinators for the L2/L3 managers and the technical and trade staff working at the facilities. They report to the Installation Managers. On a weekly basis the Installation Managers will conduct a scheduling meeting (in person or by video conference) with the LIM to review progress to date, schedule tasks by work order for the coming week and discuss safety issues and requirements to accomplish this effort. Attendance at these meetings is required by all managers, supervisors, visiting L2/L3 managers or experts that plan to work or supervise the work of others under their control at the facilities that week. All work tasks to be performed at the site requires a task work order to be completed by all L2/3 managers prior to this scheduling meeting for review and approval by the LIM or Facilities/Technical Supervisor and the local safety coordinator (LSC). These

two managers will provide work control coordination for the facilities by review and approval of each work order for:

- scope of effort
- list of personnel
- special equipment required
- training/qualifications
- personnel protective equipment
- special permits (LOTO, working hot, critical lift, working at heights, etc.)
- safety concerns

The special permits will be reviewed by the Chief Engineers and special committees convened by the ESSH Policy committee. Each work order will be reviewed and approved at these weekly installation scheduling meetings by the LIM and LSC.

9.1 AD Deployment Plan

The planned deployment sequence for the ADs into the underground halls is shown in Fig. 9.1. The

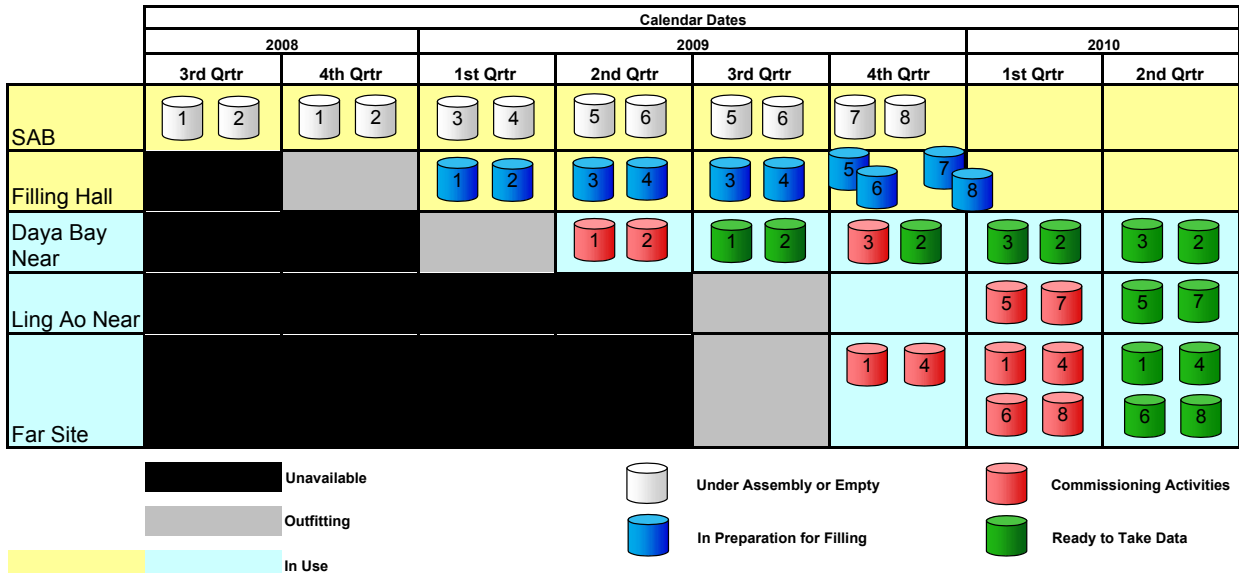


Fig. 9.1. Diagram of the planned deployment of the AD modules into the experiment.

entire process from completed assembly in the SAB, through filling in the LS hall and deployment into the experimental halls is shown by quarter. In this plan the first AD module will be moved from its initial deployment in the Daya Bay hall to its final deployment in the far hall and will provide an opportunity to test the swapping of detectors. All other detectors will be deployed to their final locations.

9.2 Receiving and Storage of Detector Components

The logistics of receiving, storing, staging, assembling, and testing components for the Daya Bay experiment requires the construction of suitable surface facilities including the SAB. As detector subsystem elements arrive at the Daya Bay site, they will be delivered to the SAB. Special arrangements will be made for the handling of the detector liquids: the unloaded LS, Gd-LS, and mineral oil. The major elements of the experiment (antineutrino detector outer vessel, acrylic vessels, calibration systems, muon detectors and PMTs) will arrive on a well coordinated timeline to avoid space problems and to allow the assembly of two detector modules at a time in the SAB. The SAB will contain storage space for two steel outer vessels plus two sets of nested acrylic vessels as well as several large muon detector panels and a large quantity of PMTs.

The logistics underground also requires special consideration: the storage and mixing tanks and the associated hardware for Gd-LS, LS and mineral oil will need to be in place as soon as the LS hall is available as this is on the critical path.

9.2.1 Surface Assembly Building

A surface assembly building (as described in Section 3.3.7) is required to assemble and test components of the muon system, the calibration system, PMTs and two antineutrino detectors at once. This building will be large enough to accommodate the assembly of two detector tanks and their associated acrylic vessels and store components for the next pair of AD's while testing PMTs and assembling and testing RPC components. Integration workshops have reviewed many possible layout options for optimal usage and a schematic layout of the on-site assembly facilities is shown in Fig. 9.2. The SAB layout will meet the following requirements:

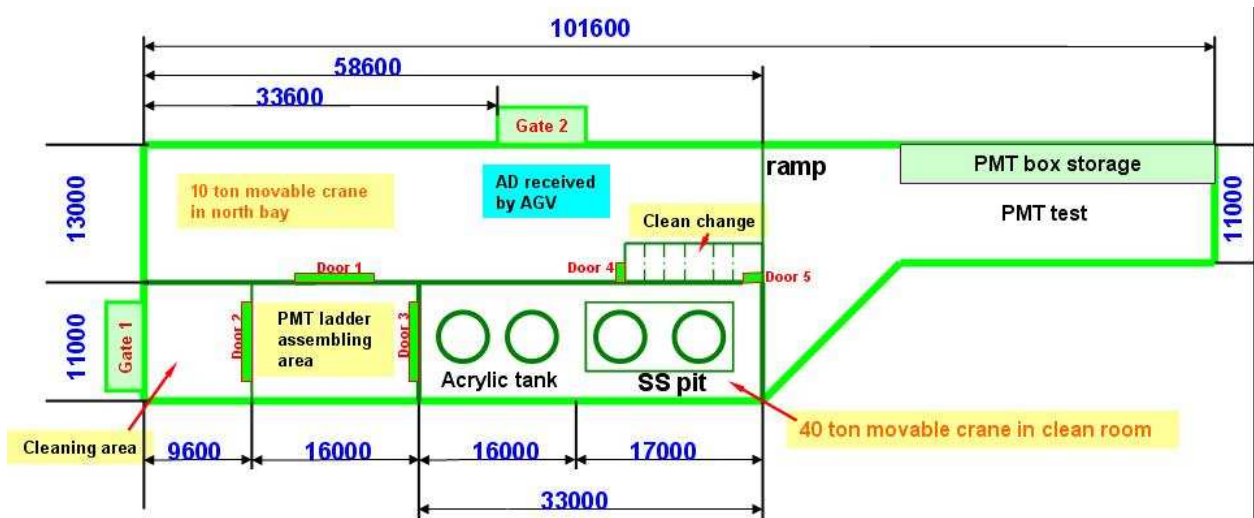


Fig. 9.2. Schematic layout of the proposed surface assembly building showing locations for storage and assembly of detector subsystems.

1. The North Bay will be approximately 13-m wide and 58-m long and have a 10-T capacity overhead bridge crane.
2. Directly east will be an additional assembly and storage area without crane coverage.
3. The South Bay will be 11-m wide and 58-m long and have a 40-T overhead bridge crane for AD assembly inside the AD assembly clean room area that will be capable of lifting the assembled (but dry) AD's onto the transporter.

4. The Southwest area of this bay inside gate-1 is used for AD vessel cleaning while on the AGV.
5. The adjoining area to the east is for AD PMT ladder assembly.
6. Continuing east is the AD clean room assembly area with a large pit in the floor at the far end for AD assembly.

When AD vessels are delivered to the Nuclear Power Plant (NPP) site by truck they will be off-loaded by boom crane onto the AGV transporter. The AGV will transport all vessels into the north bay through gate-2. Stainless steel vessels will be directly placed on temporary support stands by the AGV while acrylic vessels can be off-loaded using the bridge crane. During AD assembly in the SAB AD vessels will be transported by AGV from the north bay out gate-2 and into gate-1 for cleaning. They will then continue on the AGV into the clean room area and off-loaded with the bridge crane for assembly. Once the detector modules are assembled and tested as required, they will be moved underground with the AGV for filling and subsequent installation in the experimental halls.

In parallel with the assembly of the antineutrino detectors, space will be provided for the storage, inspection and testing of the PMTs in the north east bay area. Several inspection and testing stations as well as a station for survey and alignment will be prepared. An area for pre-assembly and testing of RPC panels is provided as well. The availability of the two bridge cranes will allow all of the assembly work to proceed in parallel without compromising the cleanliness of the AD assembly area.

To accomplish these multiple testing, assembly, and QA tasks, appropriate test stations will be assembled. We plan to provide appropriate gases and high and low voltage power as well as a low-noise test environment with suitable electrical shielding and grounding. Mechanical noise is expected to play a minor role in these tests.

The SAB will be designed to ensure several levels of cleanliness control. Detector components arriving on site will be stored under sealed conditions in the SAB. During the assembly of the detector modules, stringent cleanliness requirements apply. Both the level of particulates and the environmental air will have to be monitored. The AD assembly area will be maintained as a class 1000–10000 cleanroom to provide the appropriate environment for the detector assembly.

9.3 AD Assembly, Testing and Transport

All of the assembly work on the antineutrino detector modules except for the mixing of the LS, filling the liquids into the AD and the installation of the calibration boxes and cable dry-boxes will be performed above ground in the SAB, as described in Section 9.2.1 below. This will provide a facility for the assembly and testing of two antineutrino detector modules at a time. Some elements, such as the liquid mixing tanks, will arrive ready for installation. However, elements such as the antineutrino detector vessels will require assembly and system testing under cleanroom conditions prior to transportation underground and filling.

The logistics of assembly and installation of the antineutrino detector include:

1. All detector modules will be fully assembled and tested with inert gas under cleanroom conditions in the SAB.
2. Unfilled detector modules will be moved down the portal access tunnel to the underground facilities. During initial transport from the surface to the underground LS hall, the antineutrino detectors are unfilled and weigh 30 T, or approximately 25% of their final weight.
3. All detector liquids will be transported underground to the LS hall in special ISO liquid tanks to ensure clean and safe handling of all liquids.
4. AD liquids will be mixed and stored in large tanks in the LS hall.

5. The detector modules will be filled sequentially in the underground LS hall using highly accurate mass flow systems and a single reference tank instrumented with precision load cells to ensure “identical” target mass and composition for each AD.
6. Once an AD module has been filled, the detector will be moved to one of the experimental halls.
7. Once a module is filled with liquid it will be moved in the horizontal tunnels (<0.5% grade) between the experimental halls (EH) and lifted by crane into the pool.
8. The AD filling system will be designed to allow for the draining of all detector modules at the end of the experiment.

9.3.1 Assembly of the Antineutrino Detectors

The major components of the antineutrino detectors will be fabricated at different places worldwide and shipped to the Daya Bay site for assembly and testing. The tasks involved in the assembly of the detector modules include:

1. Cleaning and inspection of stainless steel tank
2. Cleaning and inspection of the acrylic vessels
3. Lifting the acrylic vessels into the detector tank
4. Installation of the PMTs and cabling inside the detector tank
5. Installation of monitoring equipment in the tank
6. Precision survey of PMT ladders, tank and acrylic vessel geometry
7. Installation of stainless steel tank lid.
8. Connecting all fill lines, calibration, and instrumentation ports
9. Final cleaning of the entire system
10. Pressure/leak testing of acrylic vessels and detector tank after assembly
11. Test installation of automated calibration systems (to be removed before transport underground)

The entire assembly of the detector modules will be performed in class 1000–10000 cleanroom conditions. This complex assembly and integration task will require close coordination of several working groups (detector design, engineering, calibration, monitoring) and the on-site presence of key scientific and technical personnel. The detector assembly is shown in Fig. 9.3.

9.3.2 Precision Survey of the Antineutrino Detectors

During assembly and before transporting the antineutrino detector modules underground, the geometry of the detector module internal components will be surveyed to high precision using modern laser surveying techniques. The precision commonly achieved in modern equipment over the scale of the antineutrino detector (~ 5 m) is of the order of $<100 \mu\text{m}$ in both the radial and the longitudinal direction. This will serve as a baseline reference for the as-built detector geometry. In-situ monitoring equipment inside the detector modules will then be used to track any changes during the transport or filling of the modules. Relating internal system geometries to external fiducial points in the experimental halls will ultimately allow a precise relative understanding of detector geometry to the experimental hall and the outside world. This task will be the responsibility of the AD subsystem group.

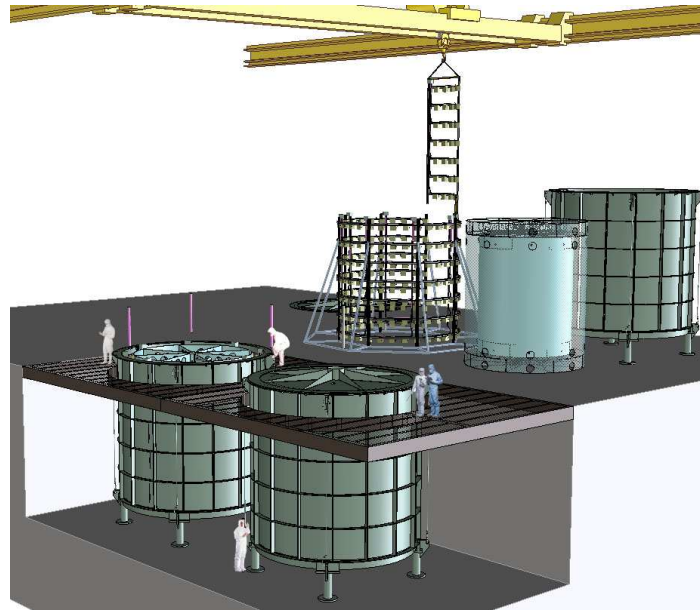


Fig. 9.3. Illustration of the envisioned detector assembly process in the SAB outside the underground tunnel at Daya Bay.

9.3.3 Antineutrino Detector Subsystem Testing

Following the assembly of detector modules and subsystems, testing becomes a critical task to ensure a smooth turn-on and commissioning of the detectors underground. The collaboration's quality assurance (QA) and quality control (QC) program will be invaluable in preparing subsystems, getting them ready, and finally installing them underground with a high success rate.

All incoming equipment will be inspected for obvious damage. For system elements that are completely assembled and tested to meet specifications at far away sites (the US and Beijing, for example) we require a limited retest to ensure that no internal damage occurred during shipment, such as for the PMTs and calibration modules. Appropriate test stations will be assembled and utilized in the SAB. Appropriate infrastructure including low- and high-voltage, laboratory gases, and other supplies will be provided for the on-site system tests.

Once the antineutrino detectors have been assembled in the SAB, we plan to perform a suite of tests of their mechanical integrity and functionality including:

1. pressure and leak tests of the detector tank and acrylic vessels with an inert gas
2. running the PMTs and all cabling with a gas fill inside the detector zones
3. testing the functionality of all ports, calibration, and monitoring equipment

The pre-assembly and test of the calibration system will include:

- Mount calibration boxes on AD overflow tank and lid.
- Test the functionality and operation of the calibration system in the dry AD by moving the sources up and down.
- Test the automated calibration sequence in SAB with the dry AD by operating all three boxes simultaneously; go through the sequence for different sources and positions.

- Perform visual checks of source motion of calibration system using cameras inside the AD.
- Test for gas leak tightness of calibration system.
- Test gas flow and overpressure control of nitrogen cover gas system with calibration box and gate valve.
- Install the calibration PMTs in the AD.

Once a detector module passes this series of tests, it is wrapped to maintain cleanliness and is ready for transport underground.

9.3.4 Antineutrino Detector Transport to LS Hall

Detector modules will be transported to the LS hall and then on to experimental halls from the SAB using an automatic-guided-vehicle (AGV) transporter. There are several issues associated with this task that make it somewhat more difficult than simply using conventional transportation equipment:

1. Due to cost and construction constraints, the tunnel itself is not very large as compared to an AD on the transporter.
2. Entrance to the underground laboratory is through an access tunnel with an incline of 9.6%.
3. Transport systems have to be compliant with ventilation and underground safety requirements.
4. The transport vehicle must be self leveling of the full AD (115 T capacity) on a 0.5% grade.
5. Transport vehicle should be narrow enough to allow it to drive under an AD on a temporary stand and lift it and drive off.

Because of this, the transport vehicle should meet the following requirements:

1. have a low bed height (≤ 0.5 m)
2. be powered by an electric drive or a very clean burning fuel.
3. be capable of accurate tracking along a predetermined guided route.
4. have stabilizer outriggers to prevent tipping of the load.

This AGV transporter will be capable of picking up a fully assembled AD (unfilled) from the SAB off of a temporary support stand. Then it will transport the AD into the underground tunnel down a 9.6% grade and to the LS hall. The detector modules will be dropped off on a temporary support stand and then be filled in the underground LS filling hall; then transported in the horizontal tunnels ($< 0.5\%$ grade) between experimental halls after they have been filled. During the transport to the experimental halls, the antineutrino detectors are filled and have a total mass of ~ 110 T. We have identified a suitable transportation system that meets these requirements. Figure 9.4 shows an illustration of the transporter we are considering for use at Daya Bay.

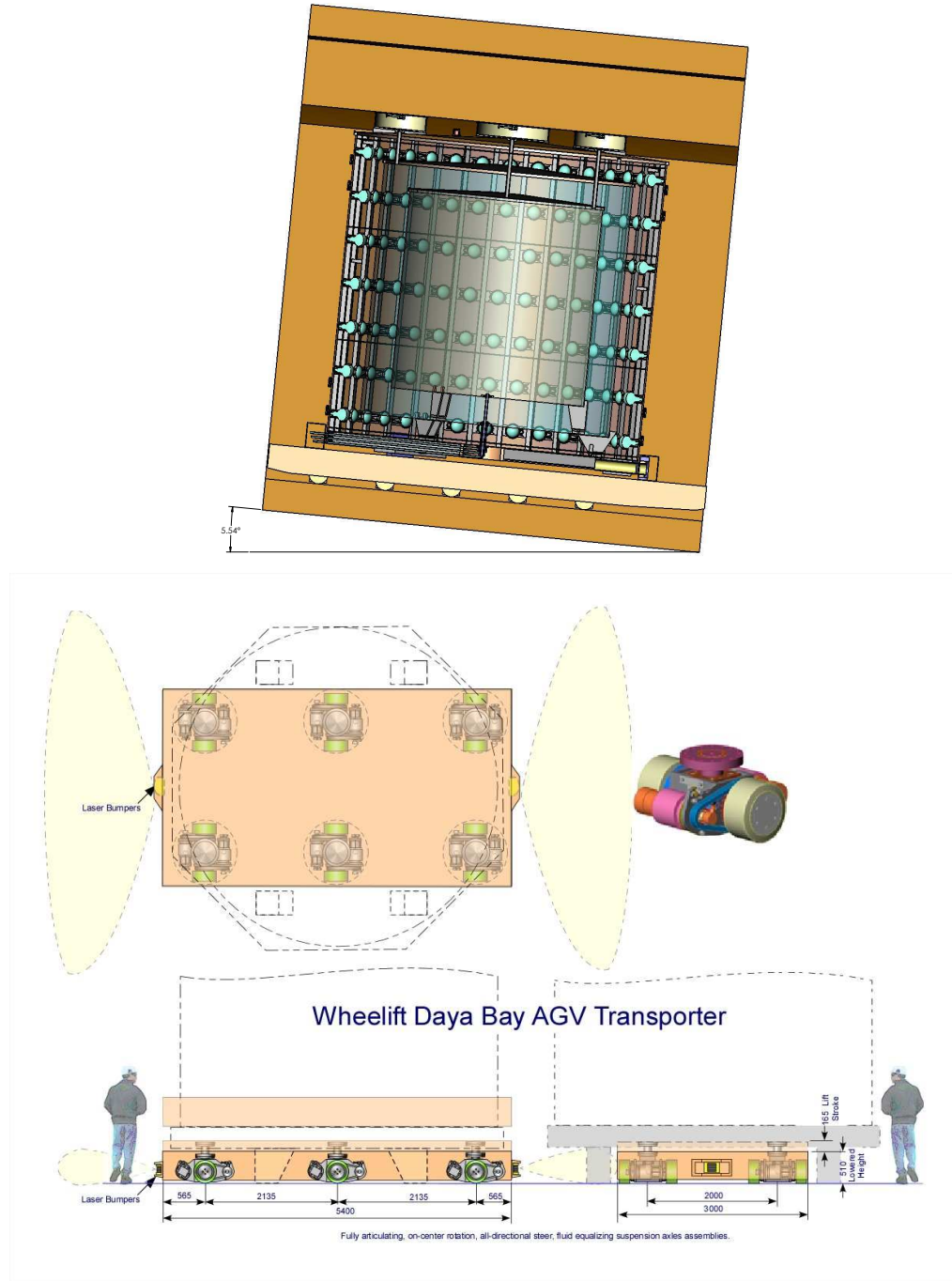


Fig. 9.4. *Top:* Antineutrino detector on transporter during transport down the access tunnel. *Bottom:* Illustration of the Wheelift transporter being considered for the transport of the antineutrino detectors [1].

9.3.5 Filling the Antineutrino Detector Modules

The underground LS hall (see Fig. 9.5) is designed to allow for the delivery, mixing and storage of detector liquids and then the precise filling of the antineutrino detectors to the required precision of $\leq 0.1\%$

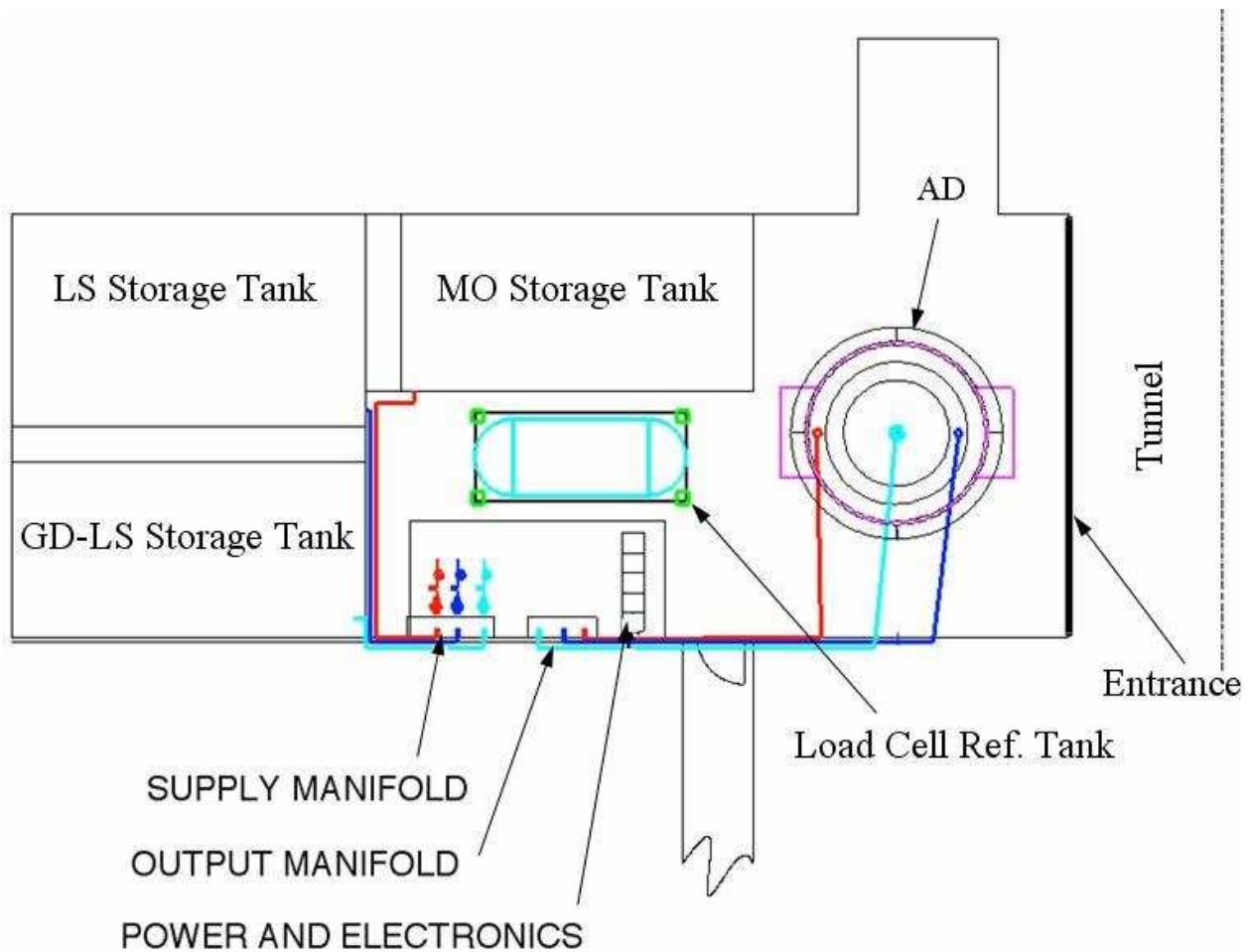


Fig. 9.5. Schematic plan view of the LS hall during filling of one AD with load-cell reference tank and pumping systems.

in target mass. The delivery, mixing and storage of AD liquids in the LS hall takes place well before the first AD arrives with beneficial occupancy of the hall; this process is detailed in the AD section of this document. For AD filling the LS hall is designed to accommodate a single detector module during the filling process. The detectors will be filled sequentially in pairs. The three components: Gd-LS, LS and mineral oil will be filled simultaneously in order to maintain equal liquid levels in each vessel and minimize stresses on the acrylic vessels. The goal is to ensure the same target mass and composition in pairs of detectors. Having one uniform batch of each type of liquid will further ensure the identical nature of the different detectors. The first pair of detectors can then be deployed at the Daya Bay site for a check of the relative detection efficiency before one is moved to the far site (as shown in Fig. 9.1).

The filling process of the antineutrino detectors and required instrumentation are described in detail in Section 4.8. The filling station will be equipped with a variety of instrumentation on the storage tanks and the fill lines for a precise and redundant measurement of the target mass and composition. In addition, all fill lines will be equipped with the necessary filtration and liquid handling systems. After filling, the detector modules will be picked up from the temporary stand and deployed in the appropriate experimental halls using the transporter system.

9.3.5.1 Antineutrino Detector Transport from the LS Hall to the Experimental Halls

Once the detector has been filled in the LS hall it is ready for transport to the experimental halls. In preparation for the transport to the experimental halls the following steps will be taken:

1. Measure temperature in the tunnel and experimental hall rock compared to the LS hall and LS. Apply insulation to the outside of the AD if necessary.
2. Wrap the detector in clean plastic foil to prevent dust and environmental contamination.
3. Move the transporter into LS hall and under the antineutrino detector on its temporary stand.
4. Raise the antineutrino detector from the floor using the transporter. Monitor the inside of the AD with all available detector instrumentation during this initial lift and the subsequent transport.
5. Program the transporter for semi-automatic guiding from the LS hall to the experimental hall.
6. Move the AD out of the LS hall and along the tunnel to experimental hall.
7. Move the detector into experimental hall (paying attention to minimizing the environmental contamination of the experimental hall from the tunnel).
8. Lower the detector onto a temporary stand on the floor of the experimental hall.
9. Move the transporter out of experimental hall.
10. Remove the dust cover from the detector.

An antineutrino detector transport team consisting of the following personnel with appropriate communication devices will be needed during this operation:

- operator for transporter
- scientific project leads for the antineutrino detector
- personnel for observing the move of the detector through the tunnel
- personnel for monitoring the detector instrumentation including cameras of acrylic vessels, accelerometers, etc.

Once an AD has been delivered to an experimental hall it will be deposited on a temporary stand by the AGV transporter. The AD will then be installed in the water pool when required based on the resource-loaded-schedule (RLS) of tasks for the overall experiment installation plan. This installation process is detailed in later sections for installation of detectors in experimental halls.

9.4 Detector Installation in the Experimental Halls

The Daya Bay experiment consists of several detector systems that require technical resources for assembly and/or installation, and test at the experimental halls:

1. Muon veto pool.
2. Muon RPC system .
3. Antineutrino detectors.
4. AD Calibration.

5. LS Mixing Systems.

6. PMT assemblies.

7. Electronics.

The logistics of assembly and installation of these detector systems include:

- Testing of components and subsystem assemblies in the SAB
- Preparation of components and subsystem assemblies in the SAB for transport underground
- System assembly in underground halls

As standard practice all incoming equipment will be inspected for obvious damage. For system elements that are completely assembled and tested to meet specifications at remote sites (the US and Beijing, for example) we require a limited retest to ensure that no internal damage occurred during shipment. Testing for broken channels or shorts in RPC chambers, PMTs, and calibration systems will all be required. To accomplish these tasks, appropriate test stations will be assembled and utilized in the SAB. The test stations will be manned by technicians, grad students, post-docs and scientists and will utilize a small set of simple electrical tests performed to written test specifications. Appropriate infrastructure including low- and high-voltage, laboratory gases, and other supplies will be provided for on-site system tests.

The installation sequence of these detector systems into an experimental hall are outlined below following a likely time ordered sequence as defined in the resource-loaded-schedule and starts with beneficial occupancy of the experimental hall. Beneficial occupancy of the experimental halls (see Fig. 9.6) includes:

- Completion of all excavation and concrete work.
- Completion of all AC power feeds with grounding systems for both clean and dirty power distribution.
- Operational acceptance of HVAC system.
- Acceptance of standard and emergency lighting.
- Acceptance of fire/smoke detection/alarm systems.
- Load test and acceptance of the overhead bridge crane.
- Completion of supply and return muon water pipes from surface source to Hall-4 water storage through tunnels to experimental halls.
- Completion of miscellaneous punch-list civil items.
- BO of the Daya Bay, LS and water halls also includes a temporary safety barrier separating experimental activities from ongoing construction work.

In general most experimental hall installation activities will start with the following;

1. Beneficial occupancy acceptance of the experimental hall.
2. Survey the concrete water pool and install external reference target monuments in experimental hall; these will be used to establish water pool detectors in each EH with above ground reactor core locations.
3. Deliver the AD and Muon water pool concrete anchor plates to EH.

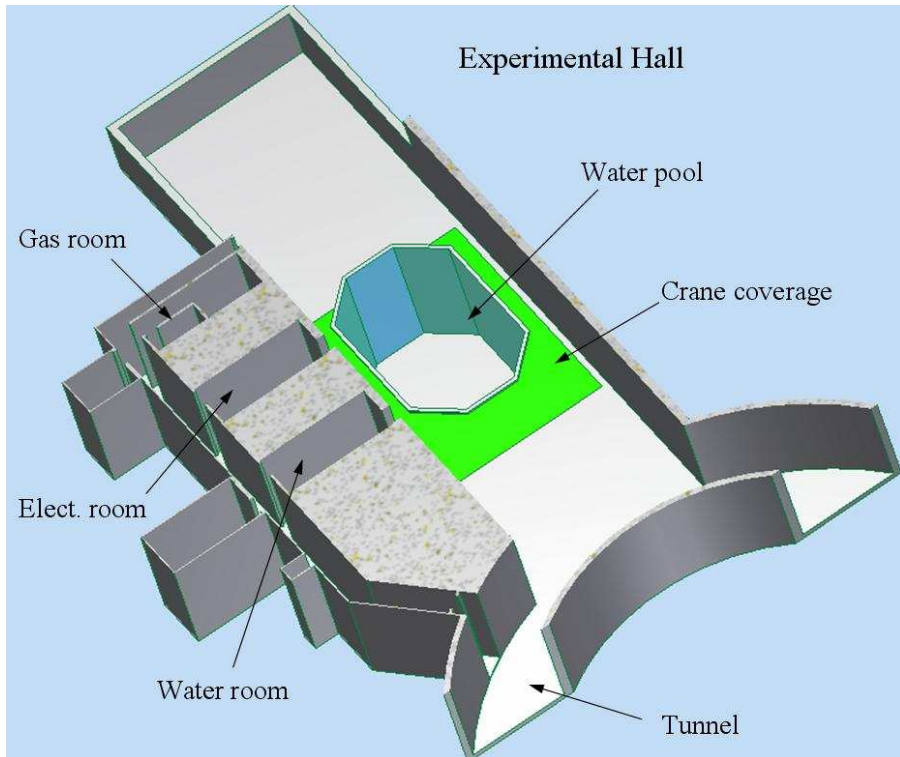


Fig. 9.6. Daya Bay near hall at Beneficial Occupancy shows tunnel entrance to hall, overhead crane coverage (green floor area), water pool and equipment rooms.

4. Locate/survey, core-drill, install and grout all muon veto support structure and water system pipe anchors in walls of concrete water pool using scissor man-lift for access. Mask off clear areas of anchor plate surface.
5. Locate/survey, core-drill, install and grout all muon veto support structure and AD support stand floor anchors in concrete floor of water pool. Mask off clear areas of anchor plate surface.
6. Thoroughly clean and wash interior of concrete water pool in preparation for concrete sealant application; this may require specific surface treatment based on coating material.
7. Apply spray-on concrete liner to the interior surface of water pool. Note: we are investigating two possible commercially available concrete sealant products that can be applied to the concrete water pool surfaces and anchor plates; water contamination and cost will be deciding factors on selection of liner materials.

At this point many of the subsystems can begin installation of their systems in parallel when appropriate in the experimental halls. Many of these systems have been previously delivered to the SAB and undergoing assembly and testing in preparation for delivery and installation at an EH. It will require careful scheduling of deliverables and staging of equipment into each EH. The times required for each of these steps will be specified in the Resource Loaded Schedule. There are a few interface constraints that will require certain items from one subsystem to be installed prior to another and there are life safety constraints that limit rigging and construction of equipment above workers; these will be noted in further sections of subsystem installation.

9.4.1 Installation of the Muon Veto System

The installation of the muon veto subsystem begins after civil construction beneficial occupancy; when the concrete water pools have had subsystem support anchors installed and the concrete liner has been applied as outlined in the previous section. This subsystem encompasses and requires the installation of, water pumping and filtration systems, RPC modules and support systems, RPC gas system, water PMT system, pools cover and nitrogen purge gas. The following will detail the installation of these systems (as shown in Fig. 9.7):

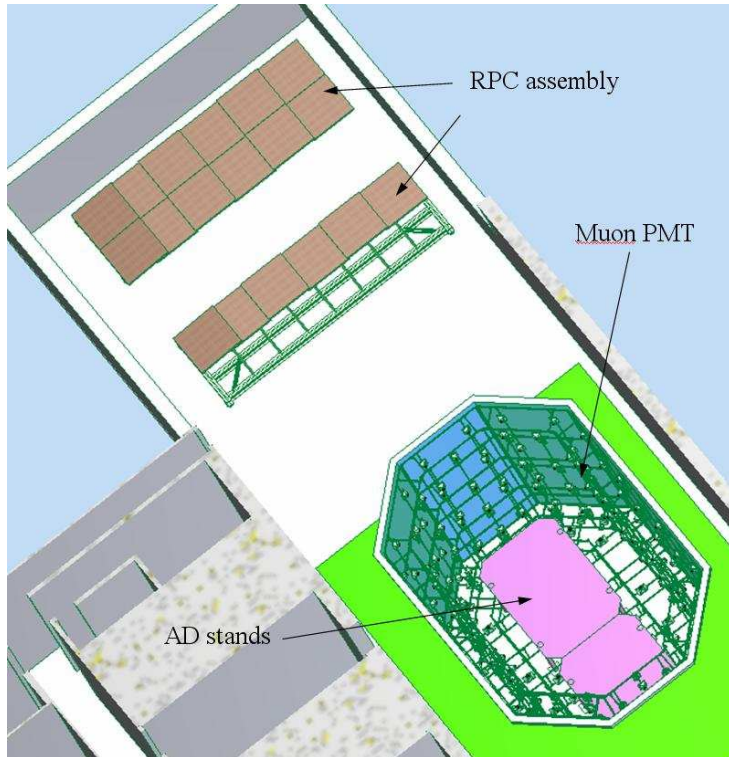


Fig. 9.7. Installation of RPC and muon PMT detectors shown proceeding in parallel in the Daya Bay near hall.

A. The water pumping and filtration systems require the following tasks:

1. Deliver the water system filtration skids to the SAB for transport underground to the three experimental halls and the fill/makeup hall-4.
2. Transport with AGV from SAB the fill/makeup water systems skid to hall-4. Set and anchor skid on concrete pad.
3. Install fill and drain piping lines into hall-4 storage pool.
4. Connect the electric power feeds and compressed air to the water systems skid.
5. Connect the surface feed-water and EH supply lines to the water system skid in the fill/makeup hall-4.
6. Run and test hall-4 fill/makeup water system.
7. Transport with AGV from SAB to the EH the appropriate water systems skid.

8. With overhead crane rig skid into water equipment room, set and anchor skid on concrete pad.
Note: this can be performed in parallel with other muon systems installation; care should be taken not to rig equipment over personnel working below.
 9. Install fill and drain piping lines into EH water pool.
 10. Connect the electric power feeds and compressed air to the water systems skid.
 11. Connect the hall-4 water supply and return lines to the water system skid in the water equipment room.
 12. Run and test the EH water pumping and filtration water system when required and scheduled for by the project RLS. Note: this could be performed after completion of muon PMT water pool system and prior to installation of ADs in the pool or possibly wait until after ADs have been installed. Figure 6.9 shows a conceptual-design schematic of the overall water filtration system.
- B. The PMT burn-in, test, and assembly in holders will occur in parallel with item “A” and will be a continuous process either at a collaborative university or in the SAB until all are ready for installation.
1. Setup the PMT burn-in and testing area.
 2. Start phased delivery of the 8” PMTs.
 3. Burn-in of the 8” PMTs. This will achieve stable PMT performance, and eliminate any flawed PMTs with a short lifetime, reducing the expense and effort of replacing some number of PMTs that would otherwise be likely to fail shortly after installation.
 4. Testing of the 8” PMTs. This ensures that only PMTs with a stable performance, and within specified requirements of efficiency, gain and current draw will be installed, further reducing the expense and effort of replacing installed PMTs, or, worse, the compromise to the experimental goals that would result from sub-par performance PMTs being installed.
- C. Install the muon PMT support structure after completion of item “A”.
1. Deliver the support frame materials, the Tyvek materials and PMT assemblies from the SAB to the EH.
 2. Assemble the individual PMT support substructure modules in the EH starting with the wall modules; install PMTs and Tyvek panels on each module.
 3. Using overhead crane rig and stack each wall module into the pool using scissor man-lift for access. Route individual module cables in end trays to the module stacked above.
 4. Complete wall module installation leaving out one corner section for access until after floor modules are installed.
 5. Transport the AD support stands from the SAB to the EH and with the overhead crane install the support stands in the pool and secure them to the floor anchors. Note: these stands need to be installed after completion of the wall modules in the previous step and before installation of PMT floor modules.
 6. After AD support stand installation complete installation of PMT floor modules and route cables to the vertical trays in wall modules.
 7. Complete installation of final wall module and cable routing to top surface modules.
 8. Install cable patch panels at surface modules.
 9. Route PMT cables from water pool patch panels in trench to the electronic equipment room.

10. Fill the pool with water, install cover and begin system testing of the water muon detector. Note: this test can be performed prior to AD installation into the pool if there is adequate time in the project schedule.

D. RPC support structure installation in parallel with item “C”.

1. Deliver the disassembled structural framing and rails to the experimental halls.
2. Install the rails, level, anchor and grout on either side of pool.
3. Assemble on the floor of the EH the individual 4 m wide RPC support frames with wheels.
4. With overhead crane set them on the rails at far end of water pool. Make sure there are no personnel working under the load during the lift.
5. Roll the structure off of pool under RPC storage area.
6. Connect the drive units and test-roll each 4 m wide structural support. Structure is ready for RPC module installation at this point.

E. Install RPC on structural supports after completion of item “D”.

1. Deliver RPC panels to the SAB for storage and testing.
2. After testing is complete transport appropriate number to EH for installation on a structural support.
3. Using a portable gantry crane over individual 4-m wide supports at the far end of the EH, install the individual RPC panels.
4. Complete installation on all individual structures with RPC modules and join all structures, complete all cabling and gas connections for a complete RPC system test.

9.4.2 Installation of the Antineutrino Detectors

After the antineutrino detectors have been filled they will be slowly transported through the tunnels to the appropriate experimental hall where they will be deployed onto their stands in the water pool. The detectors will be staged onto temporary stands on the floor of the hall by the transporter. After installation of the lifting fixtures the detectors will be lifted onto their stands in the water pool by crane. The installation of all detector systems in the experimental halls is a complex procedure that requires good coordination by the installation team and between the various subsystems. Detailed check lists and procedures will have been developed and rehearsed for these tasks. The lifting and installation procedure will be practiced with a lightweight mockup frame that resembles the antineutrino detector and has the same dimensions. The installation process is illustrated in Fig. 9.8.

The installation of the antineutrino detector will include the following steps. Estimates for the time it will take to perform each step are given.

1. Set the antineutrino detector on temporary floor stands on the near side area of the experimental hall using the transporter. Remove the transporter from the experimental hall.
2. Remove external dust cover from the AD and thoroughly clean the detector of all contamination.
3. Use the scissor man-lift for access around antineutrino detector to attach the lifting fixture to the stainless steel tank. Using the overhead crane, attach the lifting fixture to the stainless steel tank of the antineutrino detector paying particular attention to safe work practices 5 m above the floor (note that the attachment process may be automated). (*1 day*)

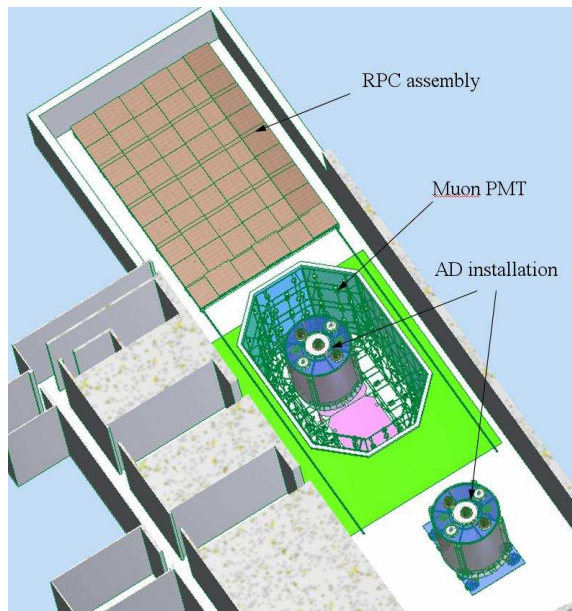


Fig. 9.8. One AD shown installed in water pool on support stand while a second AD is transported into the Daya Bay near hall for installation using the overhead crane.

4. Prepare the water pool for the installation of the antineutrino detector after support stands and muon PMT support structure installation is complete. (*4 days*)
 - Drain water pool when the muon system testing is complete.
 - Clear unnecessary personnel and equipment from the water pool and verify that there is no obstruction in the lifting path of the antineutrino detector. (We may want to practice the steps in the lifting procedure using only the lifting fixture.)
 - Position several spotters in and around the water pool to observe and guide the lifting of the antineutrino detector. Provide communication with 2-way radios.
5. Lift the antineutrino detector into the water pool: (*2–3 days*)
 - Using the overhead crane lift the antineutrino detector vertically off the temporary floor stand, and move it slowly over the water pool using appropriate tag lines for control of load.
 - Lower the antineutrino detector onto the support stand in the empty water pool with mechanical stops for guiding the antineutrino detector into place.
 - Disconnect lifting fixture from antineutrino detector and raise it out of the way.
 - Install AD work platform, roll personnel access bridge into place over pool and connect access stairs from bridge to AD work platform to access the top of the antineutrino detector.
 - Manually secure the antineutrino detector to the stand in the water pool using the work platform to access the bottom of the antineutrino detector and the top of the support stands.
6. Using the AD work platform make all the necessary connections at the top of the antineutrino detector. During this work all personnel will use appropriate fall protection and personnel protective equipment. (*2 days*)

- Lower the automated calibration boxes (200 kg each) onto the antineutrino detector.
 - Install automated calibration boxes with sources, N_2 gas supply lines, and calibration control cables. Perform a leak and functionality check on each calibration box. The leak check contains two steps: a) overpressure the calibration box with Argon and use Argon sniffer for leak detection, and b) flush the interior of the calibration box with dry nitrogen, pump out the volume between the double o-ring seal, and see if the vacuum holds.
 - Install the AD cable tray from edge of water pool to the AD top flange.
 - Install the PMT HV, signal and instrument cables in tray from edge of pool to the AD.
 - Make dry box cable connections and instrumentation cable connections on the antineutrino detector.
 - Perform leak check of dry box areas by using pressurizing the dry box and watching for a slow pressure drop with time.
7. With the work platform in place perform a system check of the antineutrino detector: (*3 days*)
- Deploy all calibration sources into the different regions of the antineutrino detector using all three automated calibration boxes.
 - PMT HV test.
 - Test the readout of all other instrumentation of the antineutrino detector.
8. Once the antineutrino detector has been determined to be functional, the access stairs and bridge along with the AD work platform can be disconnected and removed. (*1 day*)

We estimate that it will take approximately three weeks to install each pair of detectors in the experimental hall. This estimate assumes that the work is not manpower limited. Standard tools and equipment needed for the installation of the antineutrino detectors will be provided for by the civil construction (facility cranes) or installation (transporter and general rigging equipment). Any specialized equipment will be the responsibility of the AD subsystem. Some of the installation related requirements include the following:

- temporary floor stands for AD's in the SAB, LS hall and experimental hall where detector can sit until it is ready for next task,
- 125 T bridge crane for lifting of full antineutrino detectors into water pool.
- 5 T crane for lifting equipment such as calibration boxes and work platforms into water pool.
- scissor man-lift in experimental hall to attach lifting structure (if necessary).
- access bridge, stairs and work platform in water pool to access AD, install calibration boxes, and make connections for cables and gas lines.
- mechanical system that guides the antineutrino detector into the correct position on the support platform in the water pool.
- fall protection systems for personnel working at heights of 4–8 m above floor of experimental hall or water pool.
- rescue cage and other provisions to lift injured worker out of empty water pool.



Fig. 9.9. ADs shown installed in the water pool at Daya Bay near hall. Personnel can gain access to an AD using an access bridge, stairs and work platform atop the AD, as shown.

One of the important elements of this installation are personnel access systems that provides safe access to the detector for securing it to the support stands and at the top of the detector for making all required cable and pipe connections and for performing the necessary system checks. One possible solution for personnel access to the AD in the water pool being considered (see Fig. 9.9) Here a work platform can be lowered by crane atop the AD. Then an access bridge can be rolled across the pool and stairs from the bridge to the AD work platform are installed. This platform will be supported by the AD itself and additional access ladders can be secured over the sides of the platform for access to the AD stands. The other possible solution is a floating platform on the water in the half-filled pool of the muon veto. Such floating work platforms have been used in other experiments such as Super-Kamiokande and SNO. The water level can be adjusted to allow access to the detector at any height inside the water pool. The water and platform would help protect the PMTs but access to several levels of the detector at the same time is difficult. The operational issues related to these options still need to be evaluated in detail.

Only trained and authorized personnel will be used for the entire lifting operation of the antineutrino detector or access to detectors in the water pool. The safety considerations, hazards and warnings of the installation of the antineutrino detectors will be documented in a critical lift procedure to be used by all personnel involved. During the installation and final testing of the antineutrino detectors in the experimental hall, we require the presence of a number of subsystem experts. The personnel needed during this complex installation process include:

- qualified operators for the transporter and cranes
- critical lift person-in-charge and safety officer
- engineering and scientific project leads for the antineutrino detector
- calibration subsystem experts for installation and final testing

- instrumentation subsystem experts for installation and final testing
- PMT and HV subsystem experts for final testing
- general technician support

9.4.3 Precision Alignment and Survey

Precise knowledge of the ‘global’ location of each hall with respect to the reactor cores is important for the accurate determination of the distances between the reactor cores and each neutrino detector. Permanent survey monuments in each experiment hall will serve as reference marks for the positioning of the detectors. These survey monuments will be placed and known to a precision of better than tens of centimeters, with respect to the outside world, even though the halls are hundreds of meters inside underground tunnels. This precision is commonly achieved in the construction of tunnels and in mining.

Within the experimental halls, the position of the detectors can be determined quite accurately. The antineutrino detectors will be placed and anchored in precisely known locations on their stands at the bottom of each water pool. The knowledge of the location of each antineutrino detector with respect to the fiducial monuments in the halls will be at the sub-mm level. The location of the muon system elements also can be surveyed and understood at the same sub-mm level. This is both with respect to the antineutrino detectors and to the experimental hall.

With this information, the distance between the detector modules and the reactor cores will be known to the required precision of better than 30 cm. A summary of the required positioning accuracy is provided in Table 9.1.

Item	Requirement	Justification
Detector location relative to reactors	$\mathcal{O}(10 \text{ cm})$	Control systematic uncertainty in baseline

Table 9.1. Positioning accuracy of the principal elements of the Daya Bay experiment.

The Muon Systems will require survey of PMT locations within each water pool as well as a survey of the location of each RPC. The positioning requirements for these components are not as severe as for the AD’s.

REFERENCES

1. Wheelift Systems Group, ultraheavy capacity transporters, <http://www.wheelfit.com/>

10 Integration

The scope of effort for this subsystem is to assist experimental subsystems and their managers in developing, defining, and controlling the mechanical systems, electrical systems, experimental assembly, safety systems, and civil construction interface between each subsystem. To this end the Integration Group will act as liaisons between each subsystem to coordinate and document efforts in resolving all physical interface issues. Engineering and design effort is being devoted to ensure that subsystem hardware can fit together, be assembled and serviced, and have minimal negative impact on other subsystem performance. This group will communicate integration issues and their resolution based on change control policy to L2 managers, project management and the collaboration in general on interface issues. The integration group must approve and process all Engineering Change Request and Engineering Change Notice (ECR/ECN) dealing with subsystem interface, experimental assembly and physical envelope related issues. To accomplish this effort the subsystem has been subdivided into five WBS L3 subcategories: WBS 1.8.1: Mechanical Systems Integration, WBS 1.8.2: Electrical Systems Integration, WBS 1.8.3: Experimental Assembly, WBS 1.8.4: Safety Systems Integration and WBS 1.8.5: Subsystem Management.

10.1 Mechanical Systems Integration

The primary goal is subsystem mechanical hardware interface coordination, by assisting in defining and developing subsystem component hardware geometry. It is important to develop 3-D envelope drawing documentation of the maximum dimensional subsystem mechanical hardware, and its operational location within the experimental complex. Subsystems nominal dimensional detail and assembly drawings will likely differ as their designs evolve and mature due to manufacturing and alignment tolerances. These integration drawings will differ as they represent simple geometric volumes that bounds a subsystem dimensional hardware limits and stay clear zone. It will also define and document mechanical hardware interfaces between subsystems where mechanical support connections are required.

An early project effort will be the civil construction of the Daya Bay experimental complex, with its access tunnels, experimental halls, surface assembly building and utility requirements. The integration group will assist in defining these areas and the development of experimental requirements as they pertain to the civil construction. We will interact formally with the civil contractor in defining and documenting civil and experimental interfaces. We will maintain as-built documentation and 3-D envelope drawings of the civil complex when the facilities are complete, and will update the drawings whenever modifications are made.

The integration group will assist in specifying and documenting the experimental mechanical utility requirements for detector installation and operation. Below ground tunnel and experimental hall ambient temperature, humidity and air exchange requirements will help determine the appropriate HVAC system to be installed. Overhead crane requirements in the experimental halls and surface assembly building will be specified. Antineutrino Detectors (AD), each weighing 110 tons full, will have to be transported from Liquid Scintillator (LS) filling station to each experimental hall. The AD transporter to be used for this operation will have to be specified and an appropriate vendor found that can deliver this specialty equipment. The Muon system water pools require highly filtered water with excellent clarity. The water filtration and pumping system for each experimental hall pool will be specified along with determination of capable vendors. Discussions are underway with CGNPG over the use of ultra-pure water from the reactor. Experimental gas systems will need to be defined and documented within each experimental hall and surface support building along with compressed gas bottle and dewar storage racks. Mechanical utilities (piping and ducting) routing for experimental needs through the complex will be defined and documented by the integration group along with interface mounts to the facility and interconnection points to subsystems.

10.2 Electrical Systems Integration

Electrical power requirements will be divided into two parts; facility electrical power and experimental electrical power. Facility electrical power is defined as the supply and distribution network extending from the main feeder lines down to and including distribution panels and wall receptacles as provided in the civil construction of the complex. This network will supply both conventional (rotary equipment) and isolated clean power for experimental use. The integration group will assist in determining conventional power requirements for water systems, gas systems, LS filling station, and experimental HVAC systems as required.

Detector electronics systems used to collect data are adversely affected by the electrical noise generated by conventional electrical equipment. Therefore an isolated clean power distribution network is required to supply power for all subsystem electronics. In conjunction with this network a grounding plan for all AC power systems must be developed and implemented to eliminate clean power ground loops and minimize electrical noise on the system. The experiment is responsible for this network and grounding plan, and the integration group will assist in determining and documenting this network capacity and distribution.

To minimize operational downtime and loss of data caused by electrical utility power dips and short term disruptions (<30 minutes), uninterruptible power supplies (UPS) will be used on the isolated clean power network. Integration will assist each subsystem in determining and documenting the need and capacity throughout this network.

Emergency power requirements will be needed for the facility electrical power network to maintain life safety system during long term disruption of utility power. At this time it is not clear if the isolated clean power network has the same emergency power needs, possibly during LS filling, but the integration group will work with each subsystem to make this determination.

Electrical utilities (tray and conduit) routing for experimental needs through the complex will be defined and documented by the integration group along with interface requirements to both facility and specific subsystems.

10.3 Experimental Assembly

Each subsystem is responsible for the delivery to the Daya Bay surface assembly building of fully or partially assembled component hardware for installation. It is the installation subsystem that provides the resources needed to complete subsystem assembly and final operational installation in the complex. The integration group will assist individual subsystems in defining and documenting a hand-off interface with the installation group. This interface will specify the deliverable hardware configuration, quantity, timeline, and initial staging of the hardware when delivered. It should include any requirements for use of surface assembly building floor space for additional hardware assembly or component testing.

The integration group will assist in the development of an overall experiment installation plan. This plan will be documented in solid model drawings showing the assembly flow of subsystem hardware through the complex in a timeline sequence starting at beneficial occupancy of the surface assembly building. The time interval will be directly coupled to installation milestone dates through to project completion.

10.4 Safety Systems Integration

Environmental, Safety, Security and Health issues for the project will fall within those policies established by the host country, China, and must meet minimum standards, as negotiated, for all collaborative members working at the experimental complex. These policies will include life safety concerns for radiological controls, chemical inventory controls (MSDS), emergency egress and access controls, fire protection and suppression systems, laser operation, cryogens, oxygen deficiency hazards, fall protection, personnel protective equipment, electrical and mechanical hazards, and liquid spill confinement and cleanup controls. The integration group will assist in evaluating, defining and documenting these life safety hazards as they

pertain to this project and will work with each subsystem on engineered solutions and/or procedures required to mitigate these hazards.

Equipment protection systems will also be incorporated into the experimental operational safety envelope. A system will be developed using a programmable logic controller (PLC) as the heart of a safety interlocks system to alarm subsystem fault conditions and automatically bring experimental hardware to a preprogrammed safe state. These fault interlock conditions will automatically valve off liquid and gas sources and/or turn off electrical power to designated hardware based on cooling water leak detection and/or detection of flammable gases and liquids. It will also alarm and interlock AC power for smoke detection near electronics, and alarm and ventilate for ODH and flammable gas conditions. The integration group will assist in developing and documenting these equipment protection and life safety interlock systems, and provide guidance in the implementation of hardware and logic for system operation.

10.5 Subsystem Management

The integration group will provide the necessary management, engineering, design, and administrative effort needed to assist all subsystems in fulfilling our project interface objectives, as outlined herein. To this end there will be two L2 subsystem co-managers from both the China and United States collaborative groups whose primary responsibilities will be to ensure subsystem goals and objectives are successfully accomplished. They will report directly to project management their subsystem tracking of schedule and cost progress. They will work with project management and L2 subsystem managers as members of the Technical Board in reporting, resolving, and documenting all subsystem interface issues through the engineering change control process. They will hire and manage the engineering, design and administrative resources needed to develop and maintain this subsystem effort.

The integration group will develop general standards and controls that include engineering document standards to be used project wide for CAD file exchange, engineering drawings and design notes, specifications and procedures, engineering change request and engineering change notice (ECR/ECN) process, and a document numbering system. Engineering design standards will be developed outlining analytical methods and factors of safety, along with industry standards and codes to be applied in the design, fabrication or procurement of both mechanical and electrical experimental components. The integration group will assist in defining an experimental component reference name and coordinate system standard to identify, by unique name, designation subsystem components and their operational location in the complex. The integration group will develop and maintain a project wide cable/fiber/connector database with unique name designation along with from-via-to location information. Integration will also maintain all documentation related to alternative value engineering design studies used in the development of the baseline project experimental hardware.

11 Value Engineering

The Integration Office (discussed in Section 16.1) oversees the value engineering program of Daya Bay. This group provides high level systems and value management oversight over all technical aspects of the Project. The project has established a mechanism of design reviews (as described in Section 14.1.4) that are a key component of the value engineering process — assuring that alternatives are considered and an optimized cost-benefit solution is obtained. These reviews and their reports and action items are recorded in the experiment’s DocDB document storage system. A number of value management studies have been undertaken as outlined in the rest of this chapter. Value management was integrated into the project’s scope split between the U.S. and China, in which purchases on the world market are generally part of U.S. scope, whereas purchases in China and most of the installation labor are part of China’s scope.

11.1 Antineutrino Detector

The AD is the major cost driver for the experimental detector.

11.1.1 Comparison of 3-zone vs. 2-zone Detectors

The possibility of adopting a detector module design with a 2-zone structure, by removing the γ -catcher from the current 3-zone design, has been carefully studied. A 2-zone detector module with the same outer dimension as the 3-zone structure has a target mass of 40 T (keeping the same oil buffer and γ -catcher thicknesses). The efficiency of the neutron energy cut at 6 MeV will be $\sim 70\%$, compared to $\sim 90\%$ with the γ -catcher and the 2-zone 40 T detector module will have only $\sim 60\%$ more detected events than the 3-zone 20 T detector module. The reduction of efficiency in the neutron energy cut will introduce a larger uncertainty due to the energy scale uncertainty. This uncertainty is not removable by the near/far relative measurement, in the different detector modules due to differences in the energy scales.

The energy scale is possibly site-dependent due to variation of calibration conditions in the different sites. According to the experience gained from KamLAND, a 1% energy scale stability at 8 MeV and 2% at 1 MeV can be readily achieved. The uncertainties in neutron detection efficiency for a 1% relative energy scale uncertainty have been studied by Monte Carlo for the 2-zone 40 T detector module and the 3-zone 20 T detector module. The uncertainty in the relative neutron detection efficiency for the 2-zone detector module is 0.4% at 6 MeV as compared with 0.22% for the 3-zone detector module. Similar uncertainties at 4 MeV have also been studied, see Table 11.1. This uncertainty will be the dominant residual detector uncertainty

Configuration	6 MeV	4 MeV
2-zone	0.40%	0.26%
3-zone	0.22%	0.07%

Table 11.1. Uncertainty of the neutron energy threshold efficiency caused by uncertainty in the energy scale for 2-zone and 3-zone detector modules. The energy scale uncertainty is taken to be 1% and 1.2% at 6 MeV and 4 MeV, respectively.

(see Table 2.8), while other uncertainties are cancelled by detector module swapping this one is not (e.g., a doubling of this uncertainty will significantly degrade the $\sin^2 2\theta_{13}$ sensitivity that can be achieved).

As shown in Table 11.1, lowering the energy cut to 4 MeV can reduce the neutron energy threshold efficiency uncertainty. However, the intrinsic radioactivity from the Gd-doped liquid scintillator and the acrylic vessel will cause a significant increase of the accidental background rate. For external sources (such as radioactivity from the PMTs and the rock) only γ rays, with an upper limit of ~ 3.5 MeV, can enter the detector module. For internal sources, however, γ rays, but also β and α particles contribute — these can produce significant rates of signals above 3.5 MeV (e.g. ^{208}Tl has an endpoint of 5 MeV) as observed by

KamLAND. Chooz has also observed a significant number of events of delayed energy of 4–6 MeV (see Fig. 11.1). In addition, gadolinium has contamination from ^{232}Th which increases the rate of ^{208}Tl decay

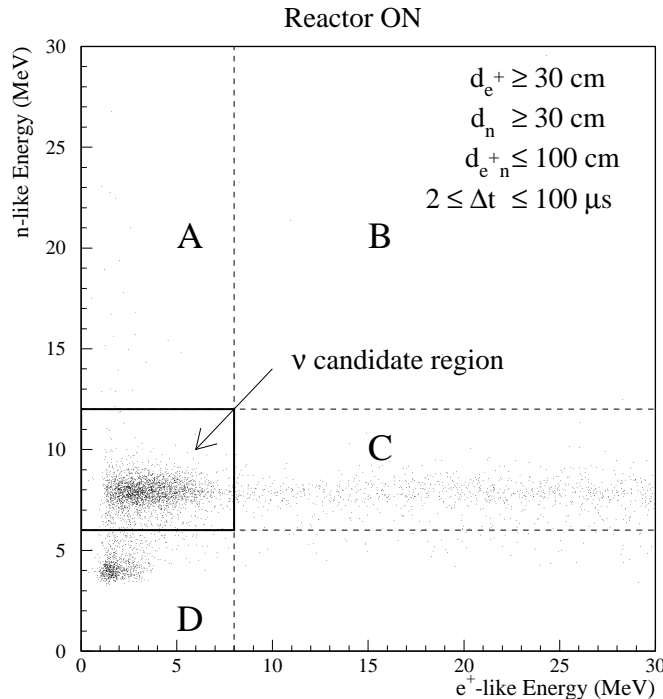


Fig. 11.1. The energy distribution observed by Chooz, horizontal axis is the prompt signal energy; the vertical axis is the delayed signal energy. In the region labelled D there are many background events with delayed signal falling into the 3–5 MeV energy range.

in the scintillator. All of these factors make a reduction of the neutron threshold from 6 MeV to 4 MeV undesirable. The accidental background rate would be a couple of orders of magnitude larger with the lower threshold at 4 MeV.

11.1.2 PMT Magnetic Shields

The effect of the Earth's magnetic field (whose typical strength is 0.3–0.5 Gauss) on the performance of a PMT is twofold:

- The trajectories of photoelectrons are affected such that the collection efficiency at the first dynode is a function of the orientation of the PMT relative to the magnetic field.
- The trajectories of secondary electrons in the dynode chain are affected such as to increase fluctuations in the PMT gain. This causes a lower “peak to valley” ratio for single photoelectrons, and increases the average transit time for the signal.

For example, an unshielded 8" Hamamatsu R5912 PMT showed about $\pm 10\%$ gain variation as a function of orientation relative to the Earth's magnetic field as shown in Fig. 4.64. Note that the gain of a well-designed PMT such as the Hamamatsu R5912 is largely unaffected by magnetic fields smaller than $\sim 1/3$ of the Earth's field.

Since the effects of the Earth's field are not large, many experiments such as LSND [7], MiniBooNE [8] and the Pierre Auger Project [9] operate large-aperture PMTs without using any magnetic shield.* Other experiments, including Super-Kamiokande [10], SNO [11], KamLAND [12] and BOREXINO [13], surround the entire detector with field-compensating coils to cancel some components of the Earth's field.

We have considered using a μ -metal mesh cage, pioneered by the DUMAND Collaboration [14], suitable for shielding large-aperture PMTs. As shown in Figure 11.2, the shield is a hemispherical mesh, made of ~ 1 -mm diameter wires with permeability of $\mu \sim 10^5$. This kind of mesh shield can achieve a transparency of $\sim 92\%$ in the NESTOR project [15], and $\sim 96\%$ for ANTARES [4–6].

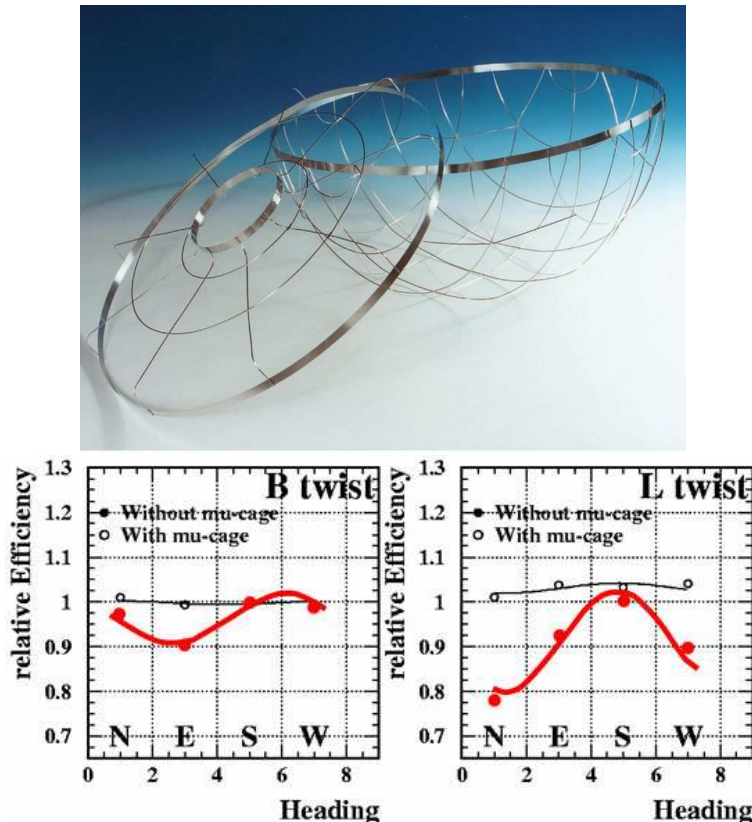


Fig. 11.2. *Top:* Hemispherical magnetic shield. Image from [4]. *Bottom:* Variation of the PMT efficiency with and without μ -metal cage.

The ANTARES shield reduces the magnetic field strength at the PMT by a factor of ~ 3 (and ~ 8 for the NESTOR shield), with the resulting improvement in the single-photoelectron peak-to-valley ratio and transit time as shown in the figures at the top of the page. The variation of PMT gain with orientation is almost completely eliminated [4]. The suppression of the magnetic field by the wire-mesh shield however is not fully effective at radii within about one mesh spacing of the mesh itself [16].

11.1.3 PMT Size

We have analyzed the option of using 8" vs. 10" PMTs using a comparison of the characteristics of the 8" and the 10" Hamamatsu PMTs. At an additional cost of \$840k we will achieve a $\sim 25\%$ improvement in the energy resolution if we keep the same number of the PMTs in each AD (192/AD). However, this will

*The standard technique of shielding a PMT with a μ -metal cylinder greatly reduces the angular acceptance of the PMT.

also double the singles rate due to increased radioimpurity of the PMT glass bulb, and also due to the dark noise of PMT photocathodes.

The reduction of 1" in the gamma catcher due to increase in the length of the 10" PMT will decrease the efficiency of the gamma catcher. The increase in the PMT length also reduces the space between the PMT bulbs and the AV during the insertion of the ladders into the SS tanks. This introduces additional risk factor during the installation process.

Another critical parameter is the higher susceptibility of the larger PMTs to the magnetic fields. Since the baseline design of the AD PMT system does not include a magnetic shield option for the PMTs this becomes an important factor in favor of selecting the 8" PMTs which are known to have acceptable magnetic field behavior.

If we chose to keep the total active area fixed by using the 10" PMTs then it is possible to reduce the overall cost of the PMT system by a large amount ($\sim \$100\text{--}300k$). However this option reduces the PMT redundancy in AD. Furthermore the cost savings may be offset by the additional design effort that would be required to develop new designs, perform simulations and further measurements. This could result in substantial delays in the schedule.

In both options a new set of simulations would be needed to further study the impact of the 10" PMT on the AD response. In addition we would need to implement a new R&D program to evaluate the 10" PMTs. New AD ladder design would be needed which could impact the overall design of the SS tank.

11.1.4 LS Process

In reaching consensus on the choice of the baseline chemical procedures to produce the needed liquid scintillator with Gd loading, we were aware that we had developed two viable alternative chemical synthesis methods, (1) solvent extraction of the Gd-carboxylate directly from aqueous medium into the organic scintillating solvent, LAB, and (2) preparation of the solid Gd-carboxylate followed by its dissolution into LAB. Both of these methods gave equally suitable final products of the Gd-LS.

However, the logistics of the two processes were different. (a) For the solvent extraction procedures, $\sim 20\text{ T}$ of 1% Gd-LS would have to be prepared at Daya Bay in the Surface Assembly Building or prepared offsite and then shipped in ISO containers to Daya Bay. At the Daya Bay site, this 1% Gd-LS would be diluted tenfold with LAB in a mixing tank to produce the final product, $\sim 200\text{ T}$ of 0.1% Gd-LS. (b) For the solid preparation, $<1\text{ T}$ of dried solid Gd-carboxylate would have to be synthesized in batches offsite and then packaged for shipment to Daya Bay. At the Daya Bay site, this solid would be dissolved and mixed in LAB in a mixing tank to produce the final product, $\sim 200\text{ T}$ of 0.1% Gd-LS.

We realized that either of these options associated with the solvent extraction process was more complicated than working with the solid Gd-carboxylate. Furthermore, since the solid would be prepared offsite (the site chosen for this work is at IHEP in Beijing), its preparation would not be on the project's critical path. Only the final dissolution and mixing steps, which would be done at Daya Bay in the underground LS Hall, would be on the critical path. The estimated time to complete these final tasks, if all goes well, should be ~ 5 weeks. Based upon these considerations, we chose as the project's baseline the preparation of the solid and its subsequent dissolution to produce the final Gd-LS.

The savings from this choice that should accrue to the project are mainly in terms of the reduced risk of slippage in the schedule. To a lesser extent, there might also be some monetary savings due to the fact that the scale of the equipment needed to prepare the solid at IHEP is smaller than what would be needed to synthesize and transport the $\sim 20\text{ T}$ of LS containing 1% of Gd. We also note that the equipment needed for these chemical steps can either be fabricated by us or is readily available for purchase from industry, e.g., apparatus for dissolution, dilution and mixing, vacuum drying, distillation, centrifugation.

11.1.4.1 Handling and storage of AD organic liquids underground

In addition to the one mixing tank that will be needed underground in the LS Hall, there will be three storage vessels; this number of vessels has been kept to a minimum for storage of the Gd-LS, for the unloaded LS, and for the mineral oil. The scheduled sequence of how these tanks will be used with the different liquids has been worked out carefully, to minimize the number of vessels, one per kind of organic liquid, and the number of steps that will be needed in handling each of the liquids. The main savings that will be realized are in time and in the cost of any additional vessels.

Around 200 ton Gd-LS, 200 ton unloaded LS, and 400 ton mineral oil need be handled. To reduce systematic uncertainties by near/far relative measurements with identical detectors, the liquids should be prepared either by one batch for all 8 ADs, or at least by one batch for each pair ADs. Otherwise, industrial organic liquids from different batches will have different density and H/C ratio, and different batches of Gd-LS may have different H/Gd ratio. However, preparation in pairwise will lower the sensitivity of side-by-side calibration of ADs at the same site. Preparation in 4 batches at different stages of the construction may also introduce additional schedule risk and logistic problems. Thus we will prepare all liquids in one batch with some affordable cost increase for larger storage.

11.1.5 LS Storage

Building LS storage underground will increase the cost of civil construction for extra excavation. It is preferred comparing to storage above ground due to 1) ground building for the storage and its temperature maintenance for the stability of Gd-LS in a year cost similar to the extra excavation. 2) storage above ground need extra liquid handling to fill ADs underground. 3) extra safety review will be required by the power plant and Nuclear Safety Agency if not underground.

Storage using Teflon lined ISO tanks probably works for pairwise liquid preparation, which requires storage for 40 T Gd-LS and 40 T unloaded LS. Mineral oil can be stored in normal ISO tanks. The cost is estimated to be ~\$300k. However, it doesn't work for one batch liquid preparation due to the four times cost and much larger space required for the ISO tanks.

Building three 200-ton storage with acrylic has been considered. The quote we got is ~\$500k. Making storage of steel and lined with Teflon or acrylic cost similar. Both need on-site fabrication.

Our baseline storage option is to make the storage with concrete and lined with ~10 mm thick acrylic sheet. The cost is \$150-200k. The on-site fabrication need two months. Acrylic lining in such a large concrete pool has certain technical risk. Careful R&D is required. At the same, epoxy painting on the concrete surface is planned to mitigate the risk.

An alternative option using balloon made of fluor-plastic film in the concrete pool is also being actively studied. Several candidates, such as PVF, PVDF, and fiber glass covered with Teflon film, are identified. Bags will be made to test the welding technique and compatibility with Gd-LS. If feasible, it will further reduce the cost and time.

11.1.6 AV Supports

The 3 m vessel rests on supports inside the 4 m vessel. These supports must be designed to meet five requirements.

1. They must support the load of the 3 m vessel. This load is greatest when the vessels are empty but acrylic is denser than LS so there some long-term load when they are full.
2. The supports should have enough vertical compliance that the load stays distributed over an area (instead of line or point) as the bottoms of the vessels flex in or out slightly due to internal pressure variations.

3. The supports should position the 3 m vessel laterally as well as hold it in the correct rotation about its vertical axis. The positioning should be tight enough that the vessel cannot creep out of place with thermal cycling or vibration.
4. The supports must allow slight dimensional changes due to lifting or thermal expansion without stressing the acrylic vessels.
5. There should be some sort of hold down to keep the vessel from floating out of place if the vessels are filled unevenly by accident.

Requirements 4 and 5 can come into conflict with each other unless the supports are “kinematic” — that is they constrain enough degrees of freedom of the vessel to prevent rigid body motion. The 3 m vessel is accurately located but not overconstrained.

These requirements can be easily satisfied with an elaborate mounting system. However, in this case that is undesirable because of cost but, more importantly, because of a prohibition of many of the usual materials in the LS and because of a desire to keep unnecessary equipment in the LS to a minimum.

Effort has been put into devising a system that is as simple as possible yet which will achieve all of these goals.

11.1.7 Cable Feedthroughs

Each of the 192 PMTs in each AD need to be electrically connected to the BaseLine Restoration (BLR) circuit that supplies the High Voltage (HV) and separates the analog signal. This cable must be sealed where it penetrates the tank wall separating the water from the Mineral Oil (MO). There must be at least one break in the electrical path to allow for the AD to be moved from one hall to another. The design adopted has an additional electrical break very near the Stainless Steel Tank (SST) wall. This allows a relatively short pigtails (10m) with SHV connector to be attached to each PMT. This makes the transportation, mounting and testing of the PMTs easier. The design introduces a plug that is epoxied to each cable. This plug makes a reliable double O-ring seal to a flange. The hole for the plug is large enough to allow the electrical connector to pass. This means individual phototubes and cables can be replaced. The seals to both the cable and the flange can be tested individually and as a group. If there is a problem an individual seal can be replaced. The electrical connection is not submerged in the water, but rather protected by an air space created in a dry box outside the tank. This design provides a double seal (water air, and air MO) between the water and the MO. If there is a leak, the air space could be pumped or purged to allow detector operations to continue. This space also facilitates leak checking. The plugs, connectors, and dry box hardware have significant monetary cost, but they make assembly, testing, and repair easier while introducing redundancy and failure recovery to this important seal. The technical “cost” is the introduction of a break in the cable that will produce signal drop and reflection. This effect is minimized by using high quality impedance matched connectors. Measurements of the connection show it will have an insignificant impact on the signal. In addition to cost savings during assembly and testing there is a potential direct cost savings by allowing the MO portion of the cable to be of a different material than the water portion of the cable. The present baseline Teflon RG303 that meets MO compatibility tests is substantially more expensive than more conventional RG58 cables that will work for the water portion of the cable. While we are still working to identify a less costly MO cable, the dry box electrical connection insures the majority of the cable can be relatively inexpensive.

11.1.8 Optimization of the AD Stainless Steel Vessel

The SSV design went through many design iterations and several detailed finite element structural analyses over the past 18 months. The design was reviewed broadly and had formal Preliminary and Final Design Reviews; many people provided input to the design.

While the focus of the later review and input had to do with the structural support of the Acrylic Vessels and PMT Ladders as well as the many ports and interfaces around the Lid area, early efforts focused on the optimization of structural architecture, the lifting approach and stability as well as minimizing the material volume to keep cost down.

Prior to finalizing the design, the following studies were performed:

1. Lift point: while bottom support is optimal from point of view of minimizing the material needed in the cylinder, stability of the lift dictated lift points high on the cylinder walls.
2. Ribbed and ringed cylinder vs thicker cylinder wall: a slightly thicker wall meant a cleaner inside surface for mounting the PMT Ladders, less welding, less clean up and simpler/cheaper manufacture.
3. External ribbing vs internal: internal top and bottom ribs meant lower overall AD height because we could take advantage of the mineral oil buffer filling the gaps between the sparsely arranged ribs.

11.2 Muon System

The muon system is the second leading cost driver for the detector.

11.2.1 PMT Optimization

The optimization in density of PMTs has been checked in a number of studies (e.g. DocDB-1518), assuming a simple multiplicity trigger. The philosophy of the studies was to probe changes in our assumptions to determine how close to the “edge” our baseline densities were. Overall muon efficiencies less than 99% were considered unacceptable (separate studies showed that 99% in overall muon efficiency correlates to 99.5% efficiency for potential background events). It was found when the maximum water attenuation length assumption was reduced from 30 m to 20 m, the efficiency fell below 99%. Similarly, there were conditions under which a failure of $\sim 10\%$ of the PMTs led to an efficiency less than 99%.

11.2.2 Water Hall

The three pools for the experimental halls constitute roughly 5000 cubic meters of filtered, de-ionized, and de-aerated water. The pools may well need to be filled and drained several times throughout the lifetime of the experiment, and managing this water volume is nontrivial. For cost and environmental reasons, we have build a fourth pool into the civil design, which will serve as an intermediate storage facility for the water, with the capacity for continuous conditioning if necessary.

Use as an intermediate storage facility is justified on the basis of cost. We estimate that each pool will eventually be emptied and filled four to five times, for calibrations and repairs. Including the water, electricity, and cost of consumables, it is roughly an equal expense to dig the fourth pool, rather than dispose of the water. Furthermore, there is the added advantage of not disposing large amounts of water to the terrain outside the tunnel, adjacent to the site of the power plant. In addition, the water quality is higher, especially since it need not be transported over large distances, when it comes to refill the pool, if we are using water already conditioned and stored in the fourth pool.

Including the capacity for continuous conditioning is a simple by product of this decision. If necessary, the Fill/Makeup system can be used as a polishing loop for pool four. In this way, a consistently high quality water supply is available for all three experimental halls, with roughly equal contamination from being transported about the same distance from the source to the hall.

11.2.3 Pool Shape

The initial shapes of the water pool were square for the Far hall and rectangular for the near halls. Eight-sided shapes with the corners clipped in a manner than maintained our 2.5 m water buffer were found to be adequate for background rejection ($< 10\%$ increase in all backgrounds), and to have a number of

advantages. About 500 T of water is saved, and 500 m³ less of rock needs to be removed. The density of PMTs can be increased without increasing their number. Less material is needed for the PMT supports, and water circulation is improved.

11.2.4 RPC Strip Size

For the Daya Bay experiment, the main function of the RPC detector is to provide a highly efficient hermetic muon tracker on top of the water shield with an efficient trigger for muons. The spatial resolution requirement for the RPCs is quite modest, about 0.5 m, to be commensurate with the expected spatial resolution of the water Cherenkov detector.

The accidental rate due to noise and ambient gammas in the RPC modules is reduced to an acceptable level for four layers of RPCs. The readout electronics channel count is minimized by reading out only one coordinate per RPC layer. Four layers of readout strips provide two *x* and two *y* coordinate measurements, sufficient to locate the entry point of a muon entering the water shield.

Even though the spatial resolution can be satisfied by strips of 1 m pitch, the signal falls below the threshold of the front-end electronics, tentatively set at 30 mV, if the strips are wider than 25 cm. In our RPC R&D work, it was noticed that the signal was not degraded by the length of the strips up to 8 m while the signal pulse height scales roughly as the inverse of the strip width.

We optimized the strip readout by using the so-called zigzag strip design. Each 2 m × 2 m strip readout plane is segmented into eight 25 cm wide strips. Each 2 m × 25 cm strip is configured as an 8 m × 6.3 cm strip. The noise rate per strip depends on the total area of the strip, and is therefore the same for the zigzag design. The extra propagation delay of the signal in the zigzag strip, about 40 ns, is small compared to the coincidence window of 100 ns assumed in trigger logic in the front end card.

11.3 Electronics

The 40 MHz sampling rate used by the FEE was selected as the most cost effective solution. The pulse shaping has a time constant of 25 ns, and results in a width at the base (1% to 1% width) of a bit more than 300 ns. Consequently, a 25 ns sampling period (40 MHz sampling frequency) is sufficient to accurately measure the waveform. Considering the fact that higher speed ADCs are significantly more expensive, the 40 MHz IC was selected.

11.4 Offline

Daya Bay physicists do continuous simulation and analysis throughout the experiment which produce the fundamental quantitative products in support of our scientific conclusions. This involves development of software which do the physics calculations, and of software which perform infrastructure actions such as dynamic library loading, service instantiation, data I/O, memory management, database management, component execution, etc. The physics calculation software developments are specific to the Daya Bay detector, data, and physics goals. However, much of the infrastructure software can be quite generic. Rather than spend potentially many man-years over the life of the experiment on developing our own software framework infrastructure, we decided to adopt the already existing Gaudi software framework which is used by the ATLAS, LHCb, GLAST, BES-III, and MINERvA experiments. This reduced the amount of Daya Bay effort required to deliver the framework, results in a robust and feature-rich framework which has been heavily tested by other experiments, provides us with an active community of experts and users who provide support, and allows us to take advantage of internal Daya Bay experts from ATLAS and BES-III. The manpower required to design, develop, debug, document, and deploy a similar system could be prohibitive for Daya Bay.

One fundamental component of scientific inquiry is reproducibility of scientific results. This is as true when the results are from computer simulation or data analysis as it is from physical measurements. The reproducibility of computational science results depends upon sound code management and documentation

tools and adopting best practices in the use of those tools. In an experiment the size of Daya Bay, this must be done in a way which does not impose an onerous burden on the scientists. To that end, we have adopted several open-source and HEP-community tools including Subversion (SVN) for code management, Configuration Management Tool (CMT) for controlling software builds, MediaWiki and DocDB for documentation, DBI database interface from MINOS, and Mantis for bug and feature request tracking. Each of these tools allow us to “roll back” to earlier versions of code, configuration, documentation, etc when it is necessary to understand and interpret a new result. Each of these tools were installable out-of-the-box with little effort or learning curve for the experiment. This allows us to gain the capability necessary to support and confirm our scientific results with very little Daya Bay invested effort.

Hardware resources for Daya Bay are not exceptional compared to large, modern experiments at LHC, RHIC, the Tevatron, or PEP-II. However, they can still require significant system administration and maintenance to ensure their availability, cybersecurity, and performance. Annual recurring costs for man-power for administration, for cooling, and for electricity for stand-alone computer clusters and especially for large tape storage systems can dwarf the original hardware purchase price. In Daya Bay, we are able to take advantage of the large established infrastructures at the two national labs (BNL, LBNL). At NERSC in Berkeley Lab, we will be adding our computer resources for CPU and disk to the large PDSF Linux cluster for Nuclear Physics and High Energy Physics. This means that sharing of resources can increase the effective CPU we can use, and that all system administration tasks are well managed and covered by NERSC manpower. For the tape storage of our raw, simulated, and processed data, we are using the NERSC HPSS (High Performance Storage System) — an 8-robot tape library with a 22 Petabyte capacity supported by DOE’s Office of Advanced Scientific Computing Research (ASCR) for use by DOE researchers. This allows us to store the 150 Terabytes per year of data we project without any Daya Bay financial burden. All tape storage is covered by DOE allocations from the Office of High Energy Physics. At Brookhaven Lab, we are adding to the BNL Coop cluster in place and working for the MINOS experiment. Though this requires some Daya Bay collaborator effort, it leverages the expertise and effort required for the MINOS experiment and thus is only incremental effort from Daya Bay’s perspective. We are in conversation with the RHIC and ATLAS Computing Facility (RACF) at BNL to investigate whether we can leverage their expertise and efforts to provide Daya Bay additional computing resources without diverting additional Daya Bay effort.

11.5 Civil/Installation

The civil and installation tasks represent a major portion of the cost of the experiment. Several tradeoffs between civil construction costs and detector design were considered. A couple of these are described in this section.

11.5.1 SAB Design

The early designs for the Daya Bay Surface Assembly Building (SAB) called for a 25-m × 50-m structure that could be used for both storage and staging of delivered experimental components and the assembly and pre-testing of systems prior to delivery underground (see Fig. 11.3). It was soon realized that a much larger building would be required to integrate all of the AD vessels storage and assembly along with muon RPC assembly and PMT assembly and test. Integration/installation workshops were conducted amongst subsystem stakeholders with many options being considered. The area to the south east was then incorporated into the SAB design (see Fig. 9.2). This larger floor area allowed for the integration planning for storage and staging of AD stainless steel outer vessels, acrylic inner vessel, a washing area, a large clean room AD assembly area all under overhead crane coverage. Now that we have converged on a workable SAB design solution the construction of the building has begun with the demolition of an existing warehouse that was located directly on the site (Fig. 11.4).

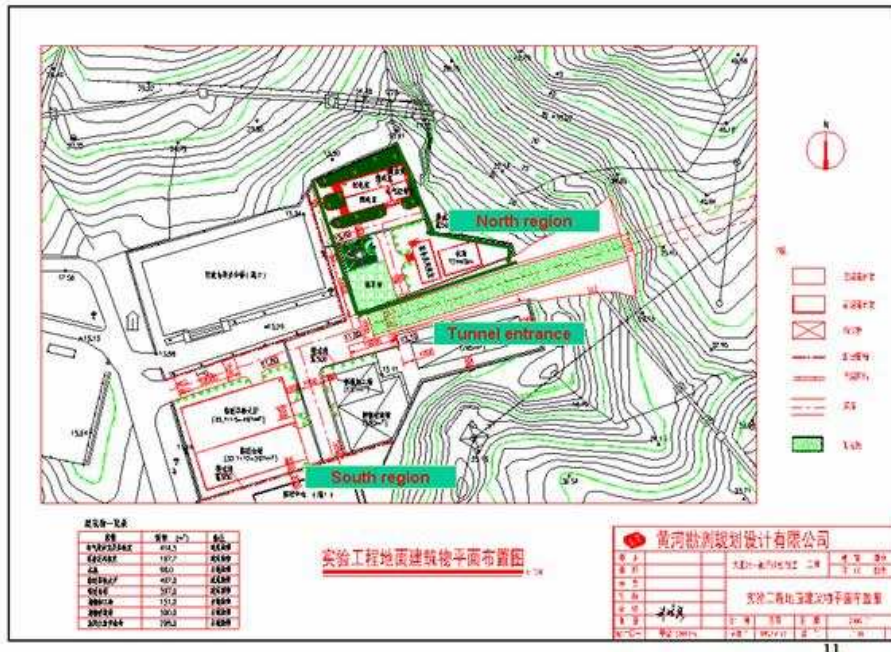


Fig. 11.3. Early civil layout of the above ground facilities showing the SAB in the south region, the site utilities in the north region and the tunnel portal entrance.

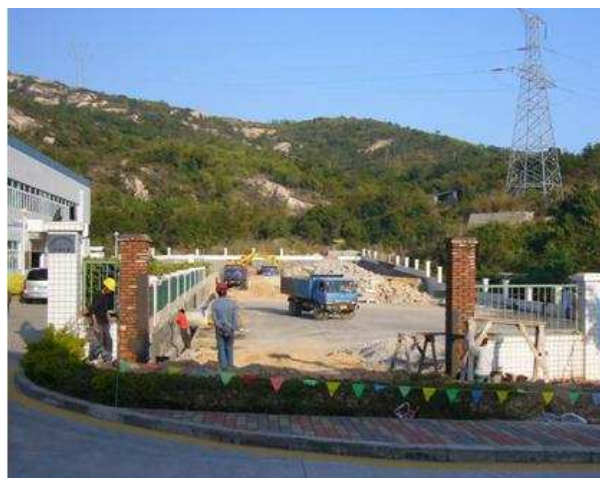


Fig. 11.4. Photo looking east at demolition of warehouse at the site of the SAB. Road to the left will be the tunnel portal entrance.

11.5.2 Transporter

The antineutrino detector design calls for eight units that are approximately 5-m diameter cylinders 5.3-m high and weighing 110 T each. To transport these detectors underground through tunnels to the experimental halls requires a low profile large capacity vehicle maneuverable in close quarters. The original concepts called for standard construction vehicles and low-boy tractor trailer vehicles as shown in Fig. 11.5. These vehicles along with the size of the AD directly affected the cross-section of the tunnel which at that



Fig. 11.5. At left is a flatbed high capacity vehicle with a load bed close to 2-m above the ground. At right is a typical low-boy tractor trailer combination that can't be reversed out of tunnel and with a load bed height of 1-m.

point was approximately 7-m wide by 8.5-m high (see Fig. 11.6). By reducing the tunnel cross-section the

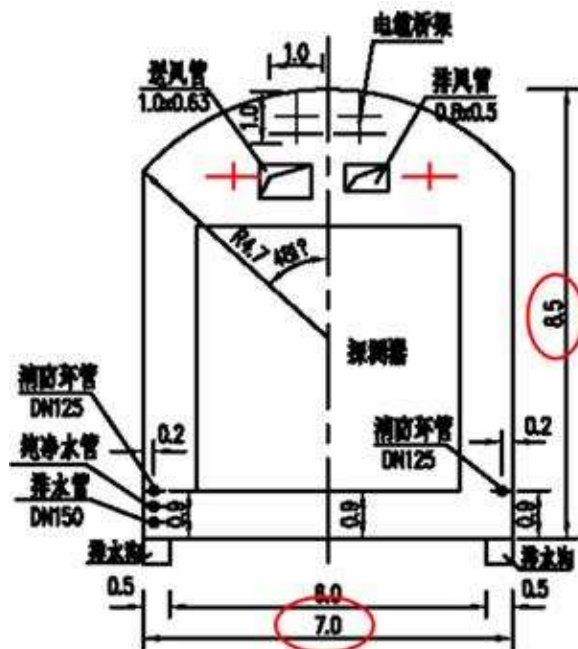


Fig. 11.6. Typical tunnel cross-section based on most common heavy capacity vehicles available.

civil cost for excavation could be greatly reduced. A search for a high capacity low profile specialty vehicle uncovered a suitable vehicle at the Doerfer Company, a maker of automatic-guided- vehicles. Discussions with the company and their engineers produced a vehicle design with a maximum load capacity of 128 metric-ton and a load bed height of 0.55-m (see Fig. 11.7). The use of this vehicle greatly reduced the cross-section of the tunnel to 6.2-m wide by 7.1-m in height (see Fig. 3.16), along with the civil cost of excavation.

REFERENCES

1. P. Ranin *et al.*, *Study of the Influence of the Earth's Magnetic Field on PMTs for Pierre-Auger Surface Detectors* UCLA-Cosmic/2001-02 (May 3, 2001)
2. A.K. Tripathi *et al.*, *Effect of Earth's Magnetic Field on Production Photonis PMTs* UCLA-



Fig. 11.7. Photo of typical automatic-guided-vehicle produced by Wheelift, a division of Doerfer Company.

Cosmic/2001-04 (Dec. 1, 2001)

3. A.K. Tripathi *et al.*, *A systematic study of large PMTs for the Pierre Auger Observatory*, Nucl. Instr. and Meth. **A497**, 331 (2003), Nucl. Instr. and Meth. **A504**, 1 (2003)
4. P. Vernin and J.-P. Schuller, *The Eyes of ANTARES* (Mar. 8, 2002)
5. P. Amram *et al.*, *The ANTARES Optical Module*, Nucl. Instr. and Meth. **A484**, 369 (2002)
6. J.A. Aguilar *et al.*, *Study of large hemispherical photomultiplier tubes for the ANTARES neutrino telescope*, Nucl. Instr. and Meth. **A555**, 132 (2005)
7. C. Athanassopoulos *et al.*, *The liquid scintillator neutrino detector and LAMPF neutrino source*, Nucl. Instr. and Meth. **A449**, 172 (2000)
8. I. Stancu *et al.*, *The MiniBooNE Technical Design Report* (May 14, 2001), http://puhep1.princeton.edu/~mcdonald/dayabay/MiniBooNE/detector_tdr.pdf
9. J. Abrahman *et al.*, *Properties and performance of the prototype instrument for the Pierre Auger Observatory*, Nucl. Instr. and Meth. **A523**, 50 (2004)
10. S. Fukuda *et al.*, *The Super-Kamiokande detector*, Nucl. Instr. and Meth. **A501**, 418 (2003)
11. J. Boger *et al.*, *The Sudbury Neutrino Observatory*, Nucl. Instr. and Meth. **A449**, 172 (2000)
12. A. Suzuki (for the KamLAND Collaboration), *Present Status of KamLAND*, Nucl. Phys. B (Proc. Suppl.) **77**, 171 (1999)
13. A. Brigatti *et al.*, *The photomultiplier tube testing facility for the Borexino experiment at LNGS*, Nucl. Instr. and Meth. **A537**, 521 (2005)
14. S. Matsuno *et al.*, *Single photon light detector for deep ocean applications*, Nucl. Instr. and Meth. **A276**, 359 (1989).
15. E.G. Anassontzis *et al.*, *The optical module for the NESTOR neutrino telescope*, Nucl. Instr. and Meth. **A479**, 439 (2002)
16. M. Taiuti, *Wild Ideas on Photon Detection* (Oct. 8, 2003), <http://www.vlvnt.nl/talks/P5/P5.5-Taiuti.pdf>

12 Operations of the Daya Bay Experiment

The routine monitoring of the experiment and daily maintenance work will be performed by the scientific members of the collaboration with support from technical personnel. The control room (see Fig. 3.17) is located near the access portal for monitoring and data taking. Daily walk-around checks in the underground facility, in addition to regular remote monitoring, will ensure the safe operation of all underground systems. The training of shift personnel will meet the safety requirements of underground work for the Daya Bay collaboration at the Daya Bay power plant. The shift leader will be trained in emergency response as the Local Emergency Coordinator (see Section 13).

The operations of the detector will consist of monitoring the detector performance and data quality, routine calibration, and online data analysis. The calibration procedure will include automated calibration runs to be performed by shift members operating the detector. Special manual calibration runs are to be performed by expert personnel.

All shift duties related to data taking and monitoring will be shared between the members of the Daya Bay Collaboration. On-site shifts as well as remote, off-site shifts will be part of running the Daya Bay experiment. Groups responsible for specific subsystems will make arrangements for performance monitoring and the maintenance of their detector subsystems.

The scientific and technical team of the Daya Bay experiment will have support from the China Guangdong Nuclear Power Group (CGNPG) which operates the Daya Bay reactor complex, and which is a collaborator on the experiment.

Operation of the Daya Bay Experiment requires a variety of tasks including:

1. Data taking with the detectors deployed in the experimental halls.
2. Automated calibration of each AD. (see Table 5.2 in Section 5.5).
3. Full-volume calibration of the AD as needed.
4. Monitoring of the underground lab conditions.
5. Monitoring of the state of the AD.
 - (a) Monitoring of AD temperatures and liquid levels.
 - (b) Monitoring the AD liquids (i.e. Gd-LS, LS and mineral oil) and chemical assays on the liquid scintillator samples. (It would be valuable to make chemical assays on a regular basis of the Gd-loaded liquid scintillator and the unloaded liquid scintillator in the antineutrino detector. Such assays would complement in-situ measurements with lasers or calibration sources to check optical transparency and light yield. These assays would have to be done offline in a remote laboratory. Sampling ports on the inner vessel containing the Gd-loaded liquid scintillator and the intermediate vessel containing the liquid scintillator would be required. However, it is very difficult to access the target liquids in the detector when they are installed in the water pool and we are currently studying the feasibility of such sampling ports in the design of the antineutrino detector.)
6. Monitoring and maintenance of the muon system.
7. Maintenance and repair of the calibration systems.
8. Monitoring, maintenance, and repair of electronics and data acquisition system.

Operation of the Daya Bay experiment may include data taking with the detector modules in different configurations. The default configuration as well as other optional configurations are outlined in the following section.

12.1 Configurations of Detector Modules

This section describes the different possible detector configurations of the Daya Bay experiment and their possible use during different phases of the experiment. The deployment options and run scenarios are currently being evaluated from the point of view of logistics, cost and physics reach:

- 1. Initial Detector Deployment:** The eight detector modules are built, assembled, and filled in pairs to ensure that their characteristics and target mass and composition are as identical as possible. Once the first detector pair has been filled underground the detectors will be deployed together at the Daya Bay near site for a commissioning run, detailed study of their properties and check of their relative efficiencies.

A commissioning run of both detectors at the near hall is a unique opportunity to test the operation of each detector module before one of them is deployed at the far site. The intrinsic detector background, the cosmogenic background at the near site, and the relative detection efficiency of the detector modules can be checked during this commissioning phase. A drawing of this detector configuration is shown in Fig. 12.1. Including the time for detector installation and start-up, the total time for such a



Fig. 12.1. Commissioning run of the first pair of detectors at the Daya Bay near site. With sufficient runtime of several months, systematic checks of the detectors and a relative comparison of the detector response is possible.

commissioning run is likely to be ~ 6 months.

- 2. A Mid Site:** If additional funding could be obtained a mid-site would be constructed near the central tunnel junctions at a distance of 1156 m from the Daya Bay cores and 873 m from the Ling-Ao cores. A mid-site would allow for a variety of possible systematic cross checks and a different oscillation signature as a function of energy.
- 3. Default Configuration of Full Experiment:** To achieve the best sensitivity in the Daya Bay experiment two 20-ton detector modules are deployed at both the Daya Bay and Ling-Ao near sites along with four 20-ton detector modules at the far site. The total active target mass at the far site is 80 T. It is possible to operate in this configuration either with or without the swapping of pairs of detectors. A drawing of this detector configuration is shown in Fig. 1.12.

4. **Optional Swapping in the Daya Bay Run Plan:** Swapping of detector modules is an option but not a necessity in the Daya Bay experiment. The target sensitivity of $\sin^2 2\theta_{13} < 0.01$ at 90% C.L. can be achieved without swapping detectors. The design of the Daya Bay experiment provides the option of swapping detectors for systematic checks and to ultimately increase the sensitivity of the experiment to about $\sin^2 2\theta_{13} < 0.006$ (see Table 2.15).

The collaboration plans to consider swapping of detectors after the initial taking data for 2–3 years.

12.2 Early Occupancy of the Experimental Halls

The civil construction of the underground laboratory including the experimental halls and tunnels will take about 24 months. The time scale is set by the excavation of the tunnels between the experimental halls. The Daya Bay near site will be completed about a year before the Ling Ao and far site are finished. This early completion of the experimental hall at the Daya Bay near site provides the opportunity to commission the detector modules at this near site.

The use of the experimental hall during the ongoing excavation and construction of the tunnel to the far site has been built into the civil construction plan and schedule. Beneficial Occupancy of the Daya Bay hall will include a fire proof separating the Daya Bay tunnel segment from the other tunnel segments and allowing experimental access to the Daya Bay, LS and Water halls. Other experimental facilities such as KamLAND in the Kamioka mine have demonstrated that data taking with a sensitive neutrino experiment is possible while a new underground hall is excavated some few hundred feet away (the KamLAND liquid scintillator purification hall was built in 2006). A similar situation can be found at SNOLab in the Creighton mine in Canada which is being constructed during the active phase of the Sudbury Neutrino Observatory.

The possibility of commissioning the detector modules at the near site is of great value for gaining experience in operating and calibrating the experiment, as well as in determining backgrounds and detector systematics. The experiment plans to start commissioning the detector in early 2010.

12.3 Servicing and Maintenance of the Antineutrino Detector

Once the antineutrino detectors are installed and the pools filled with water the detectors cannot be easily accessed. Service or repair of the calibration boxes, instrumentation attached to the antineutrino detector, cables or gas lines requires that the water pool is at least partially drained and a work platform is installed. The basic steps required to access the lid of the antineutrino detector, perform the service, and ready it again for data taking are:

- Stop data taking and shut down HV.
- Slide RPCs off the pool. (*0.5 day*)
- Partially drain the water pool to uncover the top of the AD. (*2 days*)
- Install scaffolding or work platform in the water pool to access the top of the antineutrino detector. (*1 day*)
- Remove dry covers from cables and cable penetrations. (*0.5 day*)
- Perform service or repair on calibration boxes, patch panels, gas lines, or instrumentation. (*1–2 days*)
- Perform leak check on dry box systems as described in the installation procedure. (*0.5 day*)
- Dismantle work platform and lift out of water pool. (*1 day*)
- Refill the water pool. (*2 days*)

- Move the RPCs back into place and close up water pool. (*0.5 day*)
- Turn on HV and take calibration data. (*0.1 day*)
- Start data taking.

We estimate that the operational turn-around time for servicing the antineutrino detector from the time we stop data taking to the time we can resume data taking will be of the order of 10–14 days. This is based on the assumption that the water pool can be drained to a suitable level and filled in about two days respectively. The details of the purification system for the water pool are described in Section 6.2.5.

12.4 Detector Swapping

The purpose of swapping detectors has been described in Sections 1 and 2. An overview of the steps involved in the swapping procedure is given below. Detector swapping will utilize the standard transportation methods developed for the underground movement of the detectors. As such, detector swapping uses all of the same techniques and procedures developed for the initial deployment of the detector. It is important to characterize any change in detector performance when swapping, so the detector must be carefully calibrated both before and after the swap.

12.4.1 Logistics of Detector Swapping

We anticipate that the transport of each detector module in the tunnel can be performed in less than a day. With a transportation speed of ~ 5 m/minute a distance of 1500 m can be covered in less than 7 hrs.

Detector swapping includes the following sequence of steps:

1. Perform final detector calibration to establish detector response immediately prior to the move.
2. Shut down HV and DAQ.
3. Slide RPC off water pool.
4. Fully drain water pool (Replace with fresh, filtered water when refilling.)
5. Install scaffolding to allow safe access to the top of antineutrino detector.
6. Disconnect PMT HV and signal cables, LS overflow plumbing, etc. as required to prepare for move.
7. Remove calibration system & piping as required from top of antineutrino detector.
8. Attach the lifting device to the antineutrino detector.
9. Using a 125 T crane, lift the antineutrino detector vertically out of pool and translate it horizontally onto a transporter.
10. Transport the antineutrino detector to the new location.
11. Reverse the operation at the previously prepared new location.
12. Calibrate the detector in the new location to establish the detector response immediately after the move.

12.5 Maintenance and Operations Costs

At this time, just prior to the CD-2 review, it is approximately three years before the Daya Bay Collaboration begins full operation of the experiment. It is not possible to provide a formal pre-operations and operations scope and cost plan with any kind of accuracy at this time. In the interest of providing an initial estimate we are preparing this initial concept for Pre-operations and Operations. This forms the basis of part of the international MOU. We will improve our understanding of what this plan entails and the US cost of these items in the coming months.

There are many assumptions in this conceptual pre-operations and operations plan. The most significant one is that the DOE and NSF base program will support the physicists, postdocs and grad students associated with Daya Bay to perform detector testing, commissioning and on-going data analysis. And, that their associated travel and living expenses will be covered as well. This means that the only labor and travel/per-diem costs included here are associated with technical and engineering resources.

12.5.1 Pre-operations Costs

Pre-operations are expected to begin after assembly and initial check out of the first two ADs. More specifically, we would like this to occur after initial check out of the two ADs and Muon System and their associated electronics and online system in the Daya Bay Near Hall. It is estimated that this will occur approximately nine months prior to CD-4b approval for operations of the entire three-hall, eight-AD experiment. Initial Pre-Operations could occur as early as late 2009 or early 2010.

At this point in time, we will begin taking physics data but with only a portion of the entire experiment. This will represent an end-to-end slice of the full technical detector. The offline system (hardware and software) will be in initial start-up mode and will be capable of detecting anti-neutrino events, i.e. sorting, time-ordering and processing the data making it ready for preliminary data analysis. The Daya Bay Project, because of its identical detector systems, in three experimental halls, lends itself nicely to this plan.

Initiating pre-operations could require the project to complete a CD-4a (initiate early operations) review. Pre-operations will require funding for the items shown below. It is envisioned that the US will be responsible for maintenance and operations of at least the US scope deliverables or for a large (up to 50%) portion of the entire experiment.

1. The US share of common costs (such as power, gasses, DI filter beds, etc)
2. Spares (breakage and failure of items like PMTs and CPUs)
3. Maintenance technician labor, travel and living expenses (for replacing consumables and repairing failed systems)
4. Pre-operations Planning and Management labor and travel/expenses
5. Pre-operations Safety personnel labor and travel/expenses
6. Computing and software
7. Office space, supplies and accommodations for US collaborators
8. Miscellaneous and unforeseen expenses

These preoperations costs listed above will be associated with the Daya Bay Research Program.

The expected monthly cost of these items is \$200k. This cost is roughly budgeted in the following manner:

1. \$85k/month. for consumables

2. \$10k/month for spares
3. \$40k/month for technical/engineering labor, travel and per-diem
4. \$25k/month for planning and management labor, travel and per-diem
5. \$15k/month for safety labor, travel and per-diem
6. \$10k/month for computing and software
7. \$5k/month for space and supplies
8. \$10k/month for miscellaneous expenses

It is expected that pre-operations would last until the experiment begins full regular operations or approximately nine months (\$1,800k).

12.5.2 Operations Costs

Operations will begin after we have successfully completed DOE CD-4b review and approval — begin full experiment operations. At this time, we would have completed the construction, assembly, installation and initial check-out of all technical systems — the full, eight-AD, three-Hall, experiment — and the Daya Bay Research Program will begin. This could occur as early as July 2010. Steady-state operations will evolve over time. Initially, we will be able to leave the detectors alone except during maintenance and repair situations. But, after 2–3 years of operation, we may want to ‘swap’ ADs between halls to further reduce systematic uncertainties. In years where ‘swapping’ will occur, a somewhat larger Technical and Engineering labor force may be necessary. The cost estimate below is for a normal (non-swapping) maintenance and operations year. Steady-state operations (non-swapping year) will require funding for the following items:

1. Shared costs
2. Spares
3. Maintenance tech and engineering labor, travel and per-diem
4. Operations Office labor
5. Safety Office labor
6. Computing and Software
7. Office space, supplies and accommodations for US collaborators
8. Miscellaneous and unforeseen expenses

The expected annual cost for these items totals \$3M ± \$0.5M per year. This is budgeted approximately in the following manner:

1. \$1000–1400k/yr. for shared costs (including consumables)
2. \$150–250k/yr. for spares
3. \$500–750k/yr. for maintenance tech and engineering labor, travel and per-diem
4. \$250–350k/yr. for operations office labor

5. \$200–250k/yr. for safety office labor
6. \$100–200k/yr. for computing and maintenance
7. \$50–100k/yr. for space and supplies
8. \$200k/yr. in miscellaneous and unforeseen expenses

At this point no considerations towards an upgrade program have been developed.

12.6 Decommissioning of Experiment

A reverse of the procedures described in Section 12.3 will be used during the decommissioning phase of the experiment. During decommissioning special attention will be paid to the appropriate disposal of all liquids and materials involved to assure that no potential ecological or safety problems arise.

13 Environment, Safety and Health

Protecting the environment and personnel safety is of the highest priority for the Daya Bay Project. This requires an adherence to safety regulations of both the host country and those of the U.S. The Project is integrating safety into all phases of project development and will work to assure a positive worker attitude towards safety. The safety organization and responsibilities are described in the Integrated Safety Management (ISM) plan.

The project will use the BNL SBMS (Standards Based Management System) to incorporate safety standards into the design, installation, work practices and operation of the Daya Bay experiment. The BNL SBMS incorporates integrated safety management (ISM) into the overall management system. In addition the system is available on the web for easy access. All standards must meet or exceed the local Chinese standards and those of the power plant. If Chinese requirements are less stringent than the BNL SBMS requirements then the collaboration has a mechanism to adopt a compromise standard. All environmental releases at the Daya Bay Experiment will follow the Chinese requirements.

The collaboration has developed a safety organization to address Environment, Safety, Security and Health (ESSH) issues. The roles and responsibilities of the collaboration and the project personnel are discussed in the Daya Bay Integrated Safety Management plan. The Daya Bay safety organization is shown in Fig. 13.1. The U.S. and Chinese Safety Officers are responsible to assure the Project managers that the

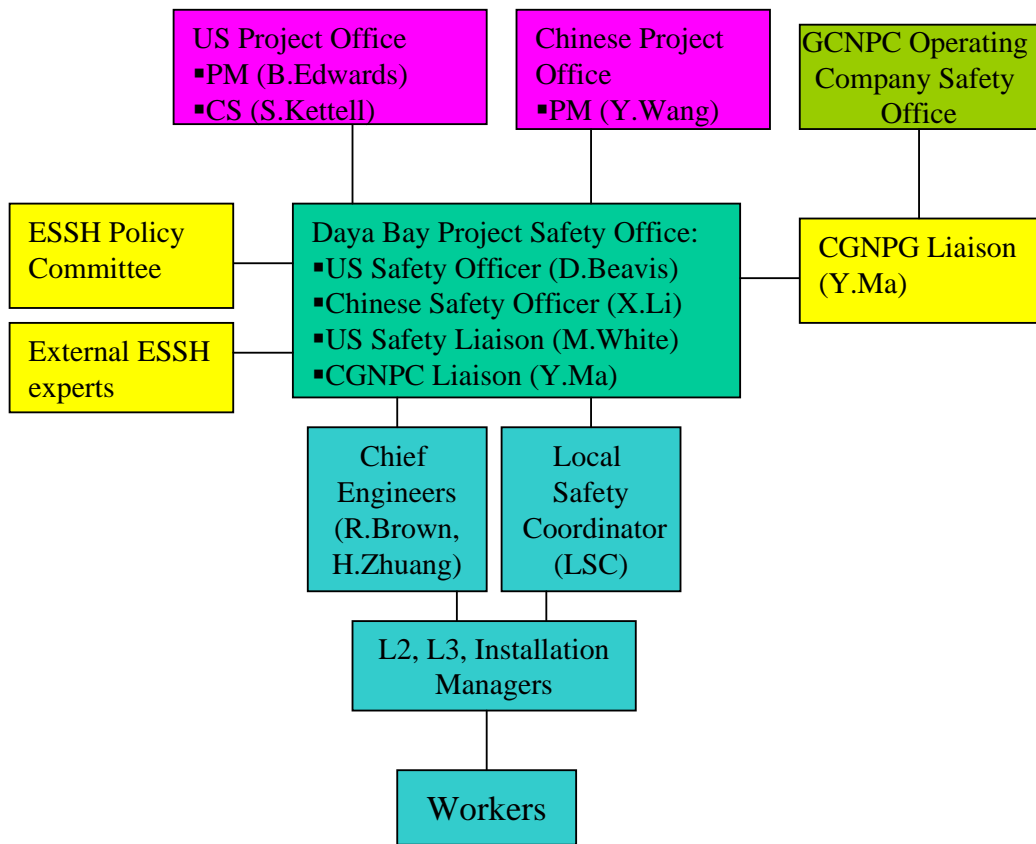


Fig. 13.1. Daya Bay Project Safety organization chart.

design, installation, work practices and operations of the experiment are following the safety guidelines. The U.S. Daya Bay Safety Officer reports directly to the US Project Manager and also serves as the L3 Manager for Safety in the Integration Office and draws upon the safety organizations at BNL and LBNL.

The project has a Safety Liaison, which is supported by WBS 1.10.1 to assist in collecting the necessary safety resources for reviewing the project and assisting with mitigation efforts. The Chinese Safety officer reports to the Chinese Project manager. A liaison safety officer has been assigned to work with CGNPG to ensure that all requirements for working on the power plant property are satisfied and incorporated into the Daya Bay working rules. The Safety Officers run the Daya Bay Project Safety Office, which will evolve into the Operations Safety Office as the project ends.

The Project's liaison to the power plant has begun discussions to determine the scope of support that the power plant will be able to provide to the Project through their existing safety organization during the construction and operations phases.

The project has three distinct phases. In the first phase, the civil construction (which is entirely funded by China) will be the only activity at the experimental site and all personnel working at the site will work safely under guidelines imposed by Chinese authorities, including the power plant, and overseen by the Chinese Daya Bay Project Safety Officer. The Chinese Safety Officer will notify The Project Managers and US Safety Officers if any major injuries or equipment damage occur during the civil construction. Special provisions will be put into effect for visits by Project personnel during this phase. Simultaneous with civil construction the design and prototype testing of experimental components will occur at numerous institutions. The safety officers will ensure that the detector designs meet the standards for the Daya Bay experimental site. The work at each institution will follow all appropriate local regulations.

During the second, detector construction phase, all safety guidelines established by Chinese and U.S. authorities will be applied to all personnel working at the Daya Bay site under the direction of the local safety coordinator (LSC) and the local installation manager (LIM). The safety officers are available to assist with any safety issues at the site or at remote institutions. Finally, during the operations phase the Operations Office will support the continued presence of the Safety Officers. The safety organization is expected to evolve from the present project organization.

The Project has overseen the development of a hazard analysis document that includes the identification and analysis of safety hazards associated with the construction and operation of the Daya Bay Project. This document has been developed in conjunction with the appropriate L2 Managers and is summarized below (Section 13.1). The Project has consulted with a number of underground construction and safety experts as well as with conventional safety experts at BNL and LBNL. An Underground Safety Review Committee chaired by Howard Hatayama (EHS Division Director at LBNL) has been convened and has been offering advice to the Project on safety issues. A more detailed discussion of underground safety issues can be found in Section 13.3.

The Project will work with the power plant and IHEP to develop a training program and a Job Training Assessment (JTA) program. All personnel entering the facilities will have site training. Short-term access without training will only be allowed if the individuals are escorted by a qualified escort. The training will include how personnel should report and respond to emergencies, including egress to the safe refuges. All personnel going into the underground facility are expected to sign-out and carry tokens, which are linked to the specific area where they will be working. In the event of an emergency the tokens will provide information about the number of personnel in the facility and their expected locations. The Training Program will likely be tied to the issuance of Identification Badges by the power plant to allow site access. All work will be planned, with appropriate considerations for 'Worker Planned Work' and specialized training as needed.

The experiment will have a designated local emergency coordinator (LEC). A qualified LEC will be required to be on site and in immediate contact if an emergency should arise. The LEC will be trained in the appropriate response procedures and be fluent in the native language. The primary responsibility of the LEC is to provide information to emergency response personnel.

We understand that the power plant will provide emergency response, including fire, police and emergency medical response. These resources are connected to the local government, but administratively report

to the power plant. The Project will discuss issues regarding mine rescue training of the emergency response teams. We anticipate that the power plant will provide sufficient on-site security for the Project's needs.

13.1 Identification and Mitigation of Safety and Environmental Hazards

The Project's hazards analysis and mitigation strategy are described in the Hazards Analysis Document (HAD). A short discussion will be given here.

The primary concern for the Daya Bay Experimental areas is smoke and fire. Steps are taken to eliminate or mitigate the risk of generating smoke and creating fire. The facility systems provide for detection, suppression, communications, fire rated doors, alarms, refuge rooms, and a smoke clearing mode for ventilation in the experimental halls.

Additionally all equipment will be reviewed for the risk of fire. All electronics will be reviewed for proper fusing and design. The electronics racks in the electronics room will have smoke detectors with interlocks to the rack power. The room will have additional detection and suppression provided by the facilities safety systems (FSS).

Controls will be established to limit the use of materials that are flammable or highly combustible. All flammable and highly combustible liquids will be inventoried, limited in quantity and transported under well defined procedures.

Storage and use of large quantities of low combustible materials will conform to the requirements of NFPA520. This includes mineral oil, liquid scintillator, Gd-doped Liquid scintillator and Bakelite.

The storage and use of flammable gas for the RPCs will conform to the requirements of NFPA520. At present the power plant has not consented to the storage of flammable gas above ground as a security measure for the reactors. The working and spare isobutane gas cylinders will be placed in a special room in a corner of the gas mixing room in each experimental hall. This storage area will have detectors, interlocks and alarms as mitigation. Once the gas has been mixed the distribution and mitigation will be similar to any accelerator experiment.

There are several potential issues besides fire related to electrical distribution. Breakers and high power crates will be examined for flash arc hazards. All HV cables and connectors will be properly rated for the planned voltages. The experiment will ground all experimental equipment.

A Material Safety Data Sheet (MSDS) for each chemical used by the experiment has been posted on the web. Handling and usage procedures for these chemicals will follow MSDS recommendations.

Radiation is not a concern for the Project. The sealed sources are very weak and the experiment will follow good practices for inventorying, storing, and handling.

Mechanical hazards will be addressed in the design and work procedures. The chief engineers review the mechanical design and the procedures for mitigating mechanical hazards. The appropriate worker Personal Protective Equipment (PPE) will be identified during procedure reviews. The required training for the installation and assembly tasks will be established.

13.2 Environmental Stewardship

The Project is committed to protecting the environment. All Project work that is performed in the U.S. will be performed in accordance with all applicable local, State and Federal laws and regulations. Project work performed at the Daya Bay site will conform to all applicable Chinese regulations. The primary environmental concerns are with releases of RPC gases, possible spills of liquid scintillator and mineral oil and the use of cleaning solutions. The largest normal release will be seepage water and waste water from the reverse osmosis water system, neither of these is expected to require mitigation. The LS hall, where LS and Gd-LS are mixed and LS, Gd-LS and mineral oil are filled into the ADs, will have a secondary containment vessel to trap any spills. When the experiment is finished these fluids will be disposed of following Chinese regulations. The amount of RPC gas is small and we anticipate that it will be below Chinese regulatory

concern. The amount of cleaning solution is also small. We do not anticipate any radiological issues, but all sealed sources will be inventoried and tracked and radon will be monitored.

13.3 Underground Safety

The Project is learning from the experiences of others in underground experimental physics work. Our underground safety committee has benefited from the experience of people working at Yucca Mountain, the Nevada Test Site and has consulted with others involved with safety issues in the NuMI tunnel, the Soudan mine and SNO.

Current priorities include:

- Compare the facility designs to US design requirements. We want to understand the safety standards implemented in the design and to what extent those design standards may be different than equivalent standards in the U.S. We will evaluate the design to assure ourselves that safety concerns are being properly addressed. This is particularly necessary where the facility systems are being used to mitigate hazards.
- Working with the power plant to understand the capabilities of the local emergency response and what will be needed to ensure appropriate mine rescue and firefighting training and equipment.
- Establishing the appropriate safety design and operational mitigation of safety risks associated with the use of flammable gases and liquids underground.

14 Quality Assurance

In this chapter, we discuss the quality management system we will employ and the various kinds of tests planned for each subsystem as well as for the integrated Daya Bay detector. Section 14.1 provides an overview of the quality management approach, as well as the design codes and standards utilized, the drawing exchange and archiving system and our use of design, manufacturing and safety reviews throughout the life of the Project.

14.1 Quality Assurance and Testing

The Daya Bay quality assurance program is designed to assure that the detector performs according to our specifications. Each institution's Quality Assurance program will be implemented for procurements from that institution; however, an overall quality assurance for the Daya Bay Project will also be applied. The standard for the Daya Bay quality assurance program will be comparable to that of the LBNL or BNL institutional standard (e.g., BNL-QA-101 and LBNL/PUB-3111-Rev.8).

14.1.1 Quality Management Plan

The purpose of the Quality Management (QM) Plan is to implement quality management methodology throughout the various project management systems and associated processes in order to:

- Plan and perform project operations in a reliable and effective manner to minimize the impact on the environment, safety, and health of the staff and the public;
- Standardize processes and support continuous improvement in all aspects of project operations; and
- Enable the delivery of products and services that meet the Project's requirements and expectations.

This policy is applicable to all Daya Bay Project activities and items involving construction, operations, maintenance, and research, including the procurement of equipment for these activities. A graded approach to quality is used to place the most emphasis on and allocate proper resources to those items and/or processes that may have the greatest effect upon personnel, environment, safety, health, cost, data, equipment, performance, and schedule. The graded approach is a process for determining that the level of analysis, management controls, documentation, and necessary actions are commensurate with an item's or activity's potential to:

- Create an environmental, safety, or health hazard;
- Incur a monetary loss due to damage, or to repair/rework/scrap costs;
- Reduce the availability of equipment;
- Adversely affect the program objective or degrade data quality;
- Unfavorably impact the public's perception of the Daya Bay or DOE mission.

This provides a methodology for establishing a level of analysis, documentation, and actions commensurate with the programmatic and/or ES&H impact. The scope of the quality-related activities is a function of its risks and programmatic issues. Quality classification designations, A1 (Critical); A2 (Major); A3 (Minor); and A4 (Negligible), may be used to aid in selecting applicable quality-related activities, as appropriate. The graded approach does not allow internal or external requirements to be ignored or waived, but allows the degree of controls, verification, and documentation to be varied in meeting requirements based on ES&H risks and programmatic issues. This policy can be found in the BNL Standards Based Management System (SBMS) in the subject area: "Graded Approach for Quality Management".

14.1.2 Design Codes and Standards

Engineering design standards and guidelines that will be applied in the design of experimental hardware have been defined collaboration wide policy and documented in the Daya Bay DocDB document control system. Conflicts between this policy and local institutional policies require that the more stringent or conservative approach be taken. The policy defines design loads to be applied to structural analysis of experimental hardware, fixtures and tooling including applicable seismic codes. The policy suggests sources for data on materials selection, certification and their properties as defined in American Association and Society standards. The policy defines analytical methods to be used based on load application and failure criteria of the materials being selected. The policy defines Factor of Safety and gives specific guidelines for the application of factor of safety used in the design of project experimental hardware. Lastly it defines a method and format for documenting all engineering analysis performed in the design of project experimental hardware.

14.1.3 Drawing Exchange and Archiving

Engineering drawing control systems have been developed for use project wide and are documented in the Daya Bay EngDB drawing control system. The scope of this system details the engineering drawing standards for dimensioning and tolerancing, along with a system of units. It defines a common language for all notes and specifications, a system for revision, drawing format sizes to be used along with a global project title box. A method for handling, transferring and archiving electronic drawing files has been defined collaboration wide. A drawing number scheme along with WBS L2 drawing number assignments is detailed and the policy for released drawings is defined.

14.1.4 Design Reviews

To promote value engineering in the design process and insure that all experimental hardware meets or exceeds minimum engineering design standards and safety policies, a series of design reviews are held for all experimental hardware designs prior to drawings release for procurement or fabrication. Each subsystem undergoes a preliminary and final design review. The project office assigns chairs for these reviews and forms a committee of appropriate experts for this peer review process. The preliminary review will be early in the design process when conceptual designs have been firmed up based on scientific requirements, engineering analysis, conceptual design drawings, cost and schedule. The outcome of this review and the action items generated should promote and enhance the design process towards a finished hardware design. The final design review is conducted when subsystem hardware detailed design drawings and engineering analysis are complete and the L2 manager is ready to release drawings for procurement or fabrication. The charge for the final design review will insure that previous action items and issues have been satisfactorily resolved, meets the functional experimental requirements, is within the integration interface envelope, meets engineering design and drawing standards and policies, the hardware can be assembled, installed, tested and operated in a safe manor and it is within the project cost and schedule definition.

14.1.5 Test Plans

Each subsystem will provide a staged testing plan for all elements. This includes a QA test plan for the manufacturer, testing upon receipt of materials, testing prior to and after shipping to China and testing prior to and after installation, as appropriate. These plans will continue to be developed by each subsystem as design decisions are made. Preliminary versions or outlines of test concepts are described in some detail in each of the technical chapters of this document.

15 R&D Plan

There are several key aspects of the Daya Bay Risk Program. First, there was the early identification of potential risks in each of the detector elements as well as the system as a whole. Second, there was an early R&D program that focused on understanding, reducing or eliminating the identified risks. Third, there is the formal tracking of the remaining risks and mitigation strategies throughout the life of construction phase of the experiment. And lastly, there is an accounting for technical, cost and schedule risk in developing the contingency analysis for the experiment.

15.1 Risk Assessment and Tracking

Subsystem Managers have performed a risk assessment of their technical systems as described in the Daya Bay Risk Management Plan. These risks are listed in the Risk Registry. The Risk Registry includes the probability and consequences of each of these risks and aids in the establishment of priorities. The Risk Registry also contains a brief summary of the mitigation strategy. The highest priority risks are tracked most closely. Updates to the risk list and status will occur quarterly or as risk status changes.

15.2 Risk Mitigation

Several key project risks were addressed in the project R&D. A number of prototypes have been designed and the built.

15.3 R&D Program

R&D efforts have focused on development of suitable technologies to help the collaboration make wise technology and cost decisions in designing the Daya Bay experiment. These efforts were also very useful in understanding and reducing risk. The major R&D efforts are summarized below.

1. Detailed physics simulation of various detector geometries to optimize performance for science requirements while minimizing cost and risk
2. Engineering studies and analysis of various detector geometries and elements
3. AD: including the development of 3-D models of the AD (acrylic vessels, steel tank, drain and fill ports, overflow tanks), assembly and installation planning, prototypes (fill mechanism, overflow tanks, calibration ports, feedthroughs and seals), test instrumentation for the target mass measurement system, test survey equipment, conceptual design of filling station, planning for characterization of ADs, test instrumentation for safety systems (overpressure protection, cover gas, flammable gas/liquid detection)
4. PMTs: including PMT mount design, characterization and testing plan, supplier validation, optimization of PMT base and magnetic shielding design, production test stand, validation of cables and feedthroughs for use under water (and in oil/water interface)
5. Gd loaded LS: including recipe and process development and testing, materials compatibility testing, Gd-LS for prototype AD in Hong Kong, procedures for scaling up LS production to multi-ton quantities, radio-assay procedures and measurement capabilities.
6. Acrylic vessels: prototyping of acrylic vessel elements and full scale models, development of a viable vendor for the acrylic vessels
7. Water Cherenkov system: including materials compatibility testing in high purity water, water purity specification development (including attenuation length measurement), water purification system prototype tests and water systems design, optimization of PMT count and location with simulation and

engineering studies, optical reflectivity studies of various materials, evaluation and characterization of MACRO PMTs, potted PMT base design and validation in water, PMT mount design (10 lb. buoyancy force vs. 1 lb. weight), water pool PMT structural support conceptual design, water pool cover systems design

8. RPC system: including structural support conceptual design, operation in high humidity environment, design and optimization of strip size, gas system and HV system
9. Calibration system: including simulation of sources and spallation products, design development for automated source deployment system, design, construction and testing of prototype automated system, source design and testing, source shielding design, final automated system design, simulation studies for detailed calibration plan
10. Electronics: including design review of key electronics designed in China (FEE, Clock, Trigger), construction of a test stand to certify and verify prototype electronics
11. Software and Computing: including development of software framework, evaluation of pre-existing software framework packages, core software infrastructure and data management development, design and evaluation of network transfer and data archiving, software tutorials for collaboration users
12. Installation: including the development of as-built 3-D models of facilities and subsystems to assist installation planning and staging and to provide early identification of possible areas of interference, the creation and implementation of project controls and policies for engineering documentation and drawing standards, change control policies, analysis and design standards, QA and safety policies.
13. Integration: including the development of installation and test plan for the overall detector installation, with a timeline for delivery, storage, staging, assembly, transport, installation and testing, develop overall installation and test plan, based on plans from each subsystem, with resource loaded schedule and milestones
14. Project Development: including the development of overall project cost, schedule, risk, hazard analysis and the preparation for CD-1 and CD-2/CD-3a reviews

Some elements of the R&D plan will be described in detail in the rest of this Section, including the AD prototype detector at IHEP.

15.3.1 Antineutrino Detector Prototype

Valuable data on the performance of the antineutrino detector has been obtained from a scaled down prototype at the Institute of High Energy Physics, Beijing, China. The goal of this R&D work was multifold: 1) to verify the detector design principles such as reflectors at the top and the bottom, uniformity of the response in a cylinder, energy and position resolution of the detector, etc.; 2) to study the structure of the antineutrino detector; 3) to investigate the long term stability of the liquid scintillator; 4) to practice detector calibration; 5) to provide necessary information for the Monte Carlo simulation.

15.3.1.1 Prototype Detector Design

As shown in Fig. 15.1, the prototype consists of two cylinders: the inner cylinder is a transparent acrylic vessel 0.9 m in diameter and 1 m in height with 1 cm wall thickness. The outer cylinder is 2 m in diameter and 2 m in height made of stainless steel. The prototype experiment is done in two phases, phase-I using undoped liquid scintillator, and phase-II using 0.1% Gd-doped liquid scintillator.

In phase-I from Mar. 2006 to Jan. 2007, the acrylic vessel was filled with 0.54 T of normal liquid scintillator. The liquid scintillator consists of 30% mesitylene, 70% mineral oil with 5 g/l PPO and 10 mg/l

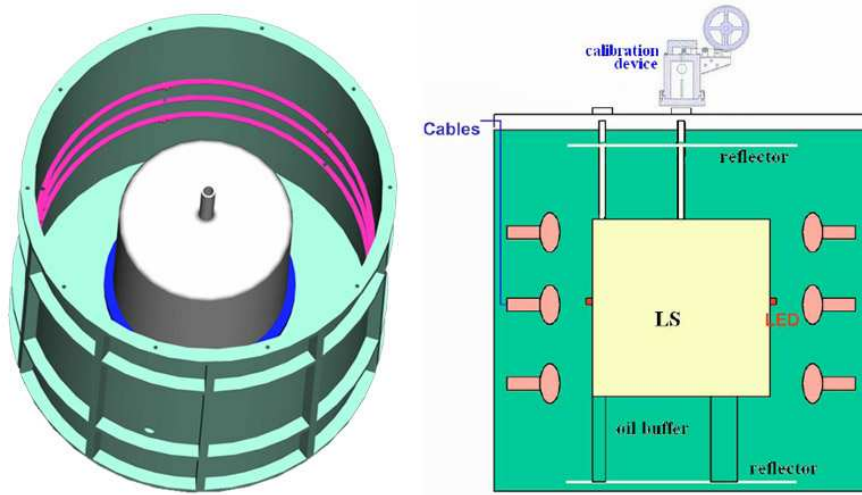


Fig. 15.1. Sketch of the antineutrino detector prototype (Left) Top view, (Right) Side view.

bis-MSB. The space between the inner and outer vessel was filled with 4.8 T of mineral oil. A total of 45 8" EMI9350 and D642 PMTs, arranged in three rings and mounted in a circular supporting structure, are immersed in the mineral oil. The attenuation length of the LS is measured to be 10 m and that of the mineral oil is 13 m. An optical reflector of Al film is placed at the top and bottom of the cylinder to increase the effective coverage area from 10% to 14%. The scintillator light yield is about 10000 photons/MeV, and the expected detector energy response is about 200 p.e./MeV.

The prototype is placed inside a cosmic ray shield with dimensions of $3\text{ m} \times 3\text{ m} \times 3\text{ m}$. It fully covers five sides (except the bottom). The top is covered by 20 plastic scintillator counters (from the BES Time-of-Flight system), each 15 cm wide \times 3 m long. The four side walls are covered by 36 1.2 m \times 1.2 m square scintillation counters from the L3C experiment. Figure 15.2 shows a photograph of the prototype test setup, before and after the muon counters were mounted.

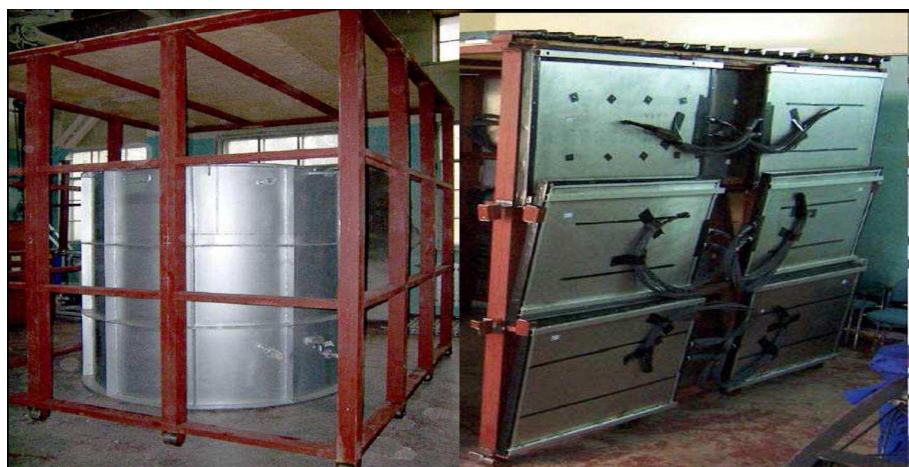


Fig. 15.2. The antineutrino detector: before (left) and after (right) the muon detectors were mounted.

The readout electronics were designed as prototypes for the antineutrino detector, according to the requirements discussed in Section 7.1. The trigger system, DAQ system and online software are all assembled as prototypes for the experiment (see Chapter 7).

In phase-II starting from Mar. 2007, the normally liquid scintillator was replaced with 0.1% Gd-LS. The Gd-LS was prepared with the solid dissolution method described in Chapter 4. The solid complex is dissolved in pure LAB, as well as 3 g/L PPO and 15 mg/L bis-MSB. The light yield of the Gd-LS was measured to be similar to the phase-I LS and the attenuation length is ~ 12 m, longer than phase-I LS because of the less UV absorption of LAB. To try more options, the top reflective panel was replaced with the ESR. At the same time, 4 bad PMTs have been replaced.

15.3.1.2 Prototype Detector Test Results

Several radioactive sources including ^{133}Ba (0.356 MeV), ^{137}Cs (0.662 MeV), ^{60}Co (1.17+1.33 MeV) and ^{22}Na (1.022+1.275 MeV) are placed at different locations through a central calibration tube inside the liquid scintillator to study the energy response of the prototype. The gain of all PMTs are calibrated by using LED light sources, and the trigger threshold is set at 30 p.e., corresponding to about 110 keV.

Figure 15.3 shows the energy spectrum after summing up all PMT response for the ^{137}Cs and ^{60}Co sources located at the center of the detector. A total of about 160 p.e. for ^{137}Cs is observed, corresponding to an energy response of 240 p.e./MeV, higher than naive expectations. The energy resolution can be obtained from a fit to the spectra, resulting in a value of about 10%. A detailed Monte Carlo simulation is performed to compare the experimental results with expectations, as shown in Fig. 15.3. Very good agreement is achieved, showing that the detector behavior is well understood.

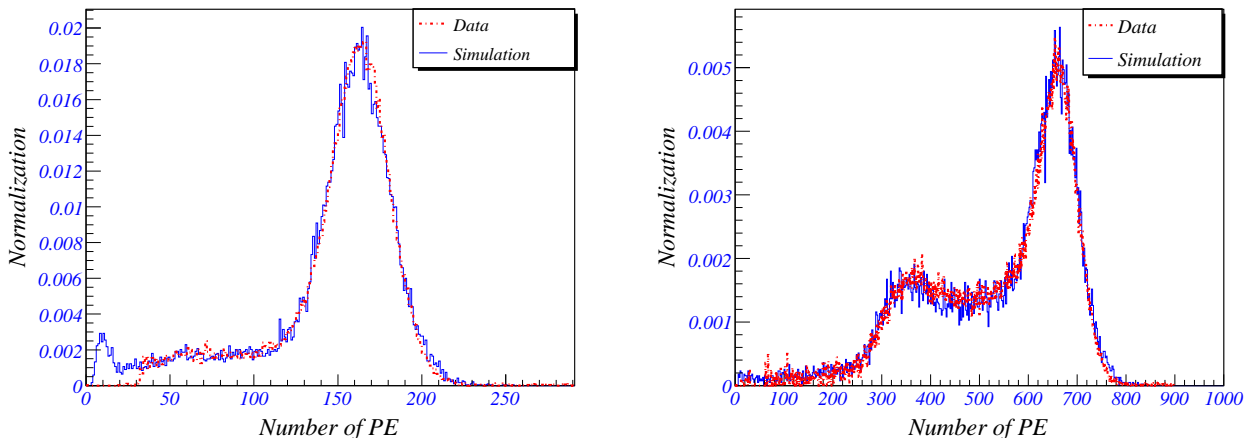


Fig. 15.3. Energy response of the prototype to ^{137}Cs (left) and ^{60}Co (right) sources at the center of the detector with a comparison to Monte Carlo simulation.

All of the sources were inserted into the center of the detector; the energy response is shown in Fig. 15.4 (left). Good linearity is observed, although at low energies non-linear effects are observed which are likely due to light quenching and Cherenkov light emission. The energy resolution at different energies is also shown in Fig. 15.4 (right), following a simple expression of $\sim 9\%/\sqrt{E}$, in good agreement with Monte Carlo simulation as shown in Fig. 15.3.

The energy response as a function of vertical depth along the z-axis is shown in Fig. 15.5. Very good uniformity (better than 10%) over the entire volume of the liquid scintillator shows that the transparency of the liquid is good, and the light reflector at the top and the bottom of the cylinder works well as expected. The fact that the data and Monte Carlo expectation are in good agreement, as shown in Fig. 15.5, demonstrates

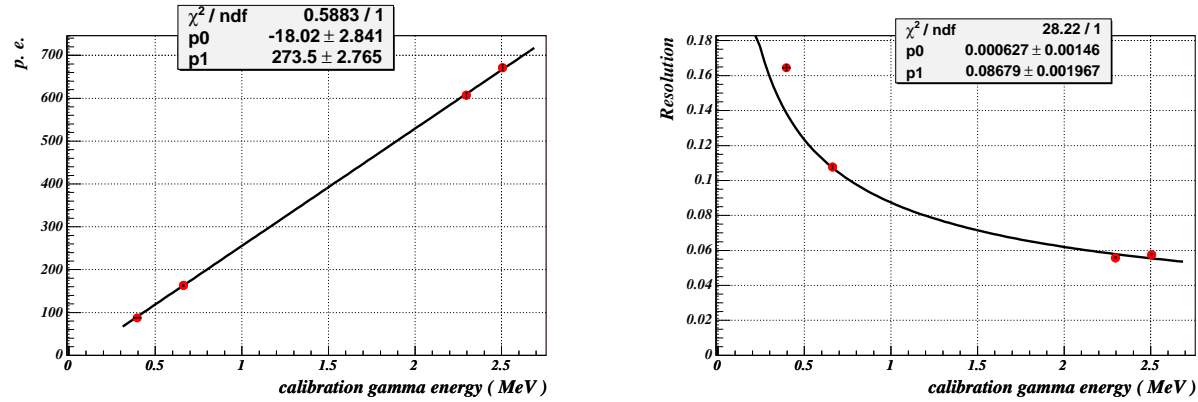


Fig. 15.4. Linearity of energy response of the prototype to various sources at the center of the detector (left), and the energy resolution (right).

that the prototype, including its light yield, light transport, liquid scintillator, PMT response, and the readout electronics is largely understood.

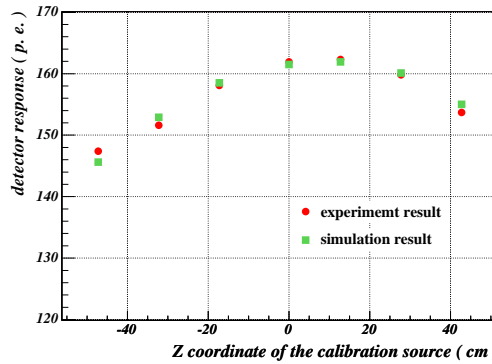


Fig. 15.5. Energy response of the prototype to a ^{137}Cs source as a function of z position, and a Monte Carlo simulation.

In phase-II, similar studies have been carried out but special efforts are put on the neutron sources ^{252}Cf and Pu-C. Using ^{137}Cs and ^{60}Co sources, a higher p.e. yield, ~ 300 p.e./MeV was observed, comparing to 240 p.e./MeV in phase-I. The increase was understood to be a combination of three contributions: replacement of four bad PMTs, longer attenuation length of Gd-LS, and higher reflectivity of ESR, $\sim 99\%$ comparing to $\sim 86\%$ of Aluminum film. For the neutron sources, the data was analyzed by assuming prompt-delayed signal coincidence. Due to high backgrounds on the surface laboratory and high radioactivity of the sources, the events can not be cleanly selected without interlacing. To reduce the interlacing, a cut was applied to require that there is no event in 1 ms precedent to a pair of prompt-delayed events. The data and Monte Carlo comparison of ^{252}Cf is shown in Fig. 15.6, where the left plot shows the prompt signal and the right one shows the delayed signal. In the delayed signal, which is supposed to be a neutron, the first peak corresponds to an energy of 2.2 MeV and the second one corresponds to 7.8 MeV.

A similar study is done for Pu-C sources (see Fig. 15.7). The delayed signal is similar to that of the ^{252}Cf source. There are two peaks in the prompt signal. The first corresponds to 4.4 MeV. It is understood as the

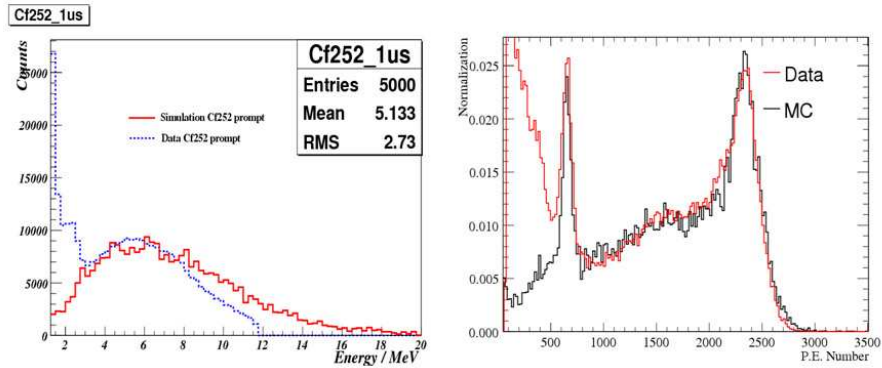


Fig. 15.6. Data and MC comparison of ^{252}Cf . Left: the prompt signal. Right: the delayed signal.

gamma emitted from the excited carbon nuclei by neutrons. The second peak corresponds to the 6.13 MeV gamma of the Pu-C source.

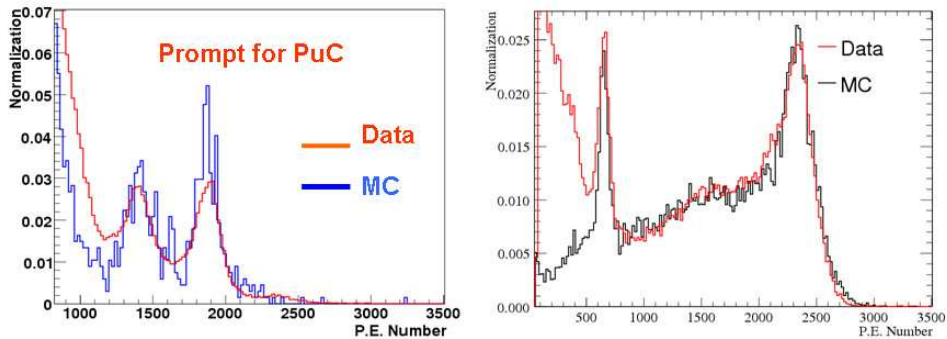


Fig. 15.7. Data and MC comparison of Pu-C source. Left: the prompt signal. Right: the delayed signal.

16 Organization and Management

The Daya Bay Project is international in scope, funding and organization. In this chapter, we present an overview of the international Project organization as well as some of the management approaches. We also present a summary of the planning and scheduling process as well as our proposed tools. While there will be oversight by many international agencies and many reviews of the Project, here we only summarize the planned function of the U.S. standing and ad-hoc committees and the technical review process. For example, the function of the Project Advisory Panel (PAP) as well as the expert ad-hoc technical reviews, are described.

A detailed project management plan has been described in the Project Execution Plan (or PEP) document. In addition to the management organization and standing committees described here, this document further describes the management organization details, management processes, periodic technical reviews and change control.

16.1 Daya Bay Project Organization

The U.S. Project's reporting and decision making from the perspective of DOE is summarized in Fig. 16.1

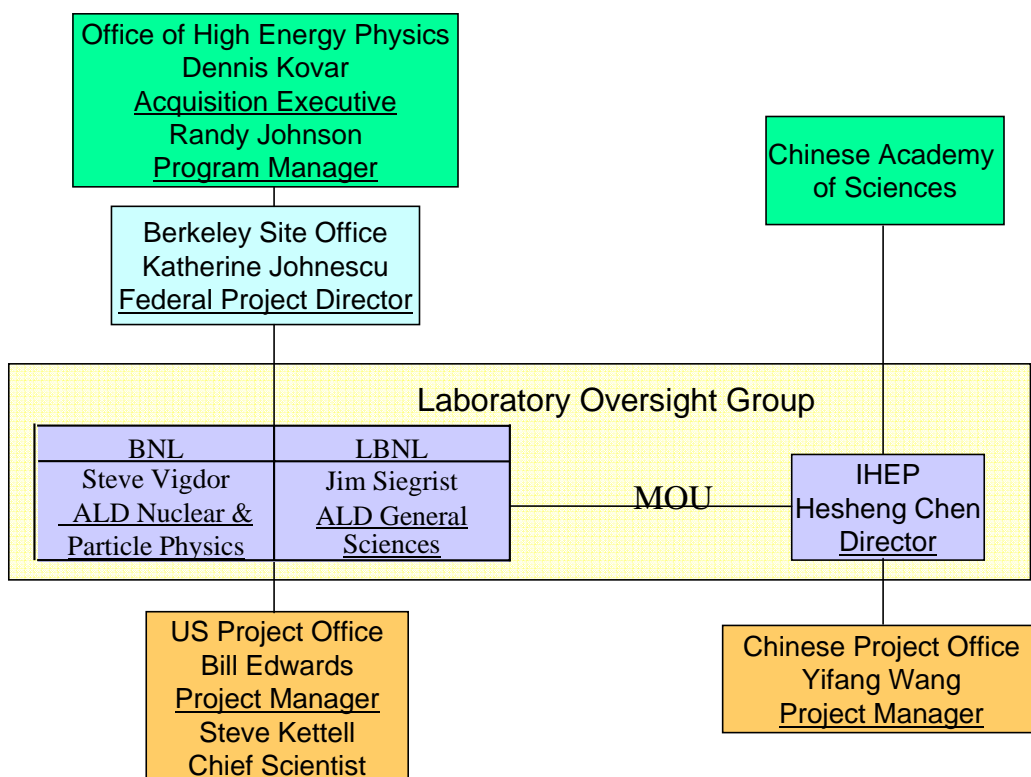


Fig. 16.1. U.S. Daya Bay Project reporting and responsibility organization chart, with an emphasis on the relationship to DOE.

The Daya Bay Laboratory Oversight Group (LOG) and International Finance Committee (IFC) will aid the international oversight of the Project. The IFC meets in conjunction with the regularly scheduled U.S.-China meetings. A Charter was approved at the November 20, 2007 meeting.

The LOG has among its members Steve Vigdor (Associate Laboratory Director for Nuclear and Particle Physics, Brookhaven National Laboratory), Hesheng Chen (Director, Institute of High Energy Physics) and

Jim Siegrist (Associate Lab Director for General Sciences, Lawrence Berkeley National Laboratory). This oversight group will meet regularly with the leadership from the Daya Bay Collaboration and the Project leadership to assess progress and plans. They will report their views regularly to the U.S. DOE, Chinese Academy of Sciences (CAS), Chinese Ministry of Science and Technology (MoST), the National Natural Science Foundation of China, Guangdong Provincial Government, Shenzhen Municipal Government, China Guangdong Nuclear Power Group and the rest of the international funding agencies.

The IFC will have representatives from the international funding agencies and will meet annually to receive an overview of Project financial status and future funding requirements. Both of these groups will provide reports of project status to the multiple funding agencies.

Figure 16.2 highlights the internal organization of the Project and its oversight boards and panels. The

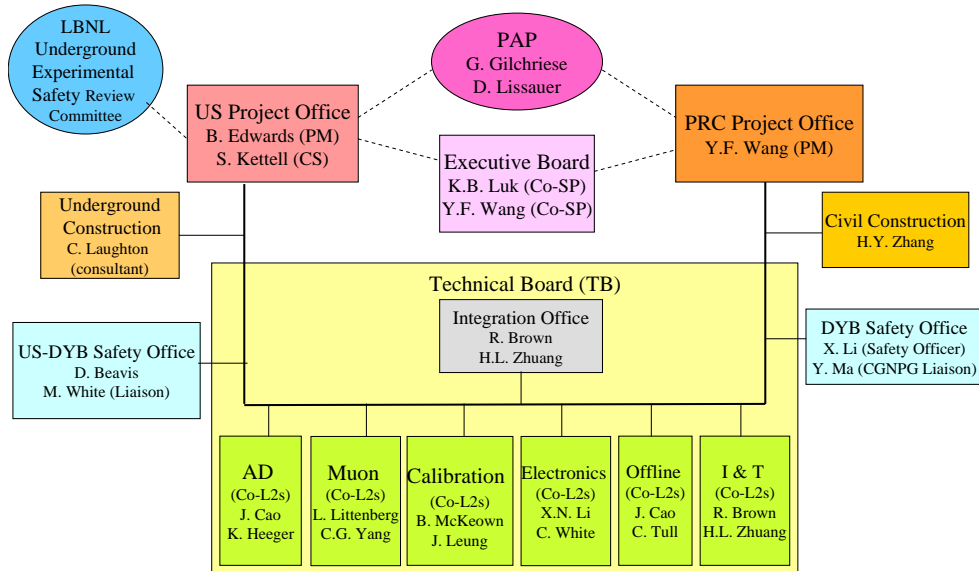


Fig. 16.2. Daya Bay Project organization chart.

Spokespersons are part of the Collaboration's Executive Board (Spokespersons are Yifang Wang and Kam-Biu Luk, the rest of the Executive Board is Bob McKeown [U.S.], Karsten Heeger [U.S.], Changgen Yang [China], Jun Cao [China], Ming-Chung Chu [Hong Kong], Yee Bob Hsiung [Taiwan], Alexander Olshevsky [Russia]) which will help guide the Project organization in its goal of delivering the experimental apparatus and software that will meet the scientific goals/requirements of the Daya Bay Collaboration. The Project Officers are *ex-officio* members of the Executive Board.

The Project Advisory Panel (PAP) is a panel with expertise in large projects gathered from the relevant international community. This panel will provide valuable guidance and advice to the Project over the course of the construction lifecycle. The PAP is charged by and reports to the LOG.

16.1.1 U.S. and China Project Management Offices

Because there are two countries providing the major funding for Daya Bay (China and the U.S.), and because each country's funding agencies have their own project management and control requirements, there are two Project Offices, one in the U.S. and one in China. This way, each country has an organization overseeing and reporting on their portion of the construction effort to their funding agencies. The complication of splitting the project office in this way is obvious. The key to making this work is agreement between the two Project Offices on the project scope and goals as well as frequent communication of issues and plans. The Daya Bay Memorandum of Understanding (MOU) between the lead laboratories in the U.S. and China

(BNL, LBNL and IHEP) defines a mutually agreeable set of scope deliverables for all countries and the terms of cooperation on the experiment.

The U.S. Project Office personnel includes: Project Manager Bill Edwards, Chief Scientist Steve Ketell, Chief Engineer Ralph Brown, Safety Officer Dana Beavis and Project Controls Officer Mike Barry. The Chinese Project Office personnel includes: Project Manager Yifang Wang, Deputy Project Managers Changgen Yang and Jun Cao, Chief Engineer Honglin Zhuang and Safety Officer Xiaonan Li. This organization has been in place and functioning well together for more than a year now.

The Integration Group, shown in Fig. 16.2, is headed by the two Chief Engineers, Ralph Brown and Honglin Zhuang, and is responsible to make sure that the design efforts are well coordinated and that plans for the detector installation are clearly defined.

A Technical Board, composed of the Project Offices and L2 managers (see Section 16.1.2) is responsible for technical decisions regarding the detector design and construction.

The Daya Bay Collaboration holds several collaboration meetings per year at which status, issues and plans are discussed and agreed upon face-to-face. Additionally, the Collaboration's Technical Board meets by phone conference bi-weekly. This frequent high-level communication provides the connection which binds the project together and enables joint decision making, problem solving and planning.

16.1.2 Project Subsystem Organization

The current roster of U.S. and Chinese Co-Subsystem Managers (at Level 2 of the WBS) are listed below in Table 16.1. This table also represents the makeup of our Technical Board. The WBS 1.9 PMT

WBS	Description	U.S. Manager	Chinese Manager
1.1	Antineutrino Detector	K. Heeger	J. Cao
1.2	Muon System	L. Littenberg	C. Yang
1.3	Calibration System	R. McKeown	J. Leung
1.4	Trig/DAQ	C. White	X. Li
1.5	Offline	C. Tull	M. Wang
1.6	Conventional Construction	—*	H.Y. Zhang
1.7	Installation & Test	R. Brown	H. Zhuang
1.8	System Integration	R. Brown	H. Zhuang

Table 16.1. The Daya Bay Subsystem Managers. * Chris Laughton of FNAL has been providing valuable consultation services to the Daya Bay Collaboration on civil construction issues.

system is listed at level 2 in the resource loaded schedule, but is managed at level 3 under both AD and Muon systems.

16.2 Technical Reviews

In addition to the various agency review processes, the Project has held many internal reviews at appropriate points in the development of the Project and its subsystems. Early in the subsystem development process preliminary design reviews are held. Later in the process and prior to initiating large procurement activities final design reviews are held. Each of these reviews will have uniquely assembled committees, utilizing relevant expertise, both internal and external to the Collaboration as necessary, to ensure the subsystem designs are optimal.

16.3 Change Control

The Change Control process is documented in the PEP.

17 Schedule, Scope and Cost

In this chapter, an overview of the project schedule and the international division of scope and cost is provided. The U.S. scope is outlined. Details of the scope for the international partners can be found in the Daya Bay MOU. Detailed breakdowns of the US cost and schedule can be found in the RLS. This is a joint project with an international collaboration, and the cost accounting approaches differ substantially from country to country. Project cost accounting in the Peoples Republic of China is quite different from the approach taken in the U.S. For example, in China essentially all labor costs (Physicist, Engineer and technician) do not appear in the estimate. The primary cost items in China are materials and equipment. The price of labor for items such as tunnel mining is very much less than the price in the U.S. As a result, it is very difficult to review the cost of a Chinese scope element by applying typical U.S. costing standards.

17.1 Project Schedule

Briefly, the first significant construction event of the Daya Bay experiment schedule begins with the initiation of civil construction on the tunnels in the fall of 2007. The Project's goal is to complete the civil construction of the tunnels, experimental halls and utility infrastructure before the fall of 2009.

There is an additional goal to complete the Daya Bay Near Hall (and LS and Water Halls) as early as possible — approximately 12 months earlier than the final (far) hall. The schedule for the detector elements is therefore driven by the completion of the first two antineutrino detectors and one third of the muon system hardware by the spring of 2009 in order to deploy these in this first experimental hall by the summer of 2009. This Daya Bay Near Hall will be used as an early opportunity to install, test and begin partial experiment operations — a chance to debug and gain insight into detector operations. This would occur in the winter and spring of 2010.

The remainder of the detectors will be installed and commissioned in the Ling Ao Near and Far Halls by the end of calendar 2010 so that the full complement of near and far detectors can begin data taking. Some major milestones are listed in Table 17.1.

17.2 Project Scope

The project's entire technical scope has been described in the previous chapters. The total Daya Bay project includes the civil construction of the experimental facility at the Daya Bay nuclear reactor complex as well as the construction of the detector elements (antineutrino detectors, muon system, calibration system, DAQ/Trigger/Online and offline). Crucial to all of these activities are the project integration elements: Installation and Test, System Integration and Project Management.

17.2.1 U.S. Project Scope

The U.S. Project scope is detailed in Appendix A of the Daya Bay MOU to be signed between BNL, LBNL and IHEP. A summary of the major elements of U.S. scope deliverables follows:

1. Antineutrino Detector:
 - (a) Design and 50% of the fabrication costs of the Acrylic Vessels,
 - (b) materials (Gd complex, Bis-MSB, etc), processing equipment and critical expertise for the production of the LS and Gd-LS
 - (c) PMTs with bases, cables and high voltage power supplies
 - (d) PMT support system (PMT frames, mounts and ladder structures)
 - (e) portions of the system for measuring physical properties and monitoring systems
 - (f) the filling system for precisely filling the ADs with the three liquids
 - (g) overflow tanks and N₂ cover gas system for maintaining an inert gas environment inside the ADs

Milestone	Description	Date	Level	RLS line#
	Chinese Funding Secured	3/07	L2	
1	US CD-1 Review	4/07	L1	1457
2	Start Civil Construction	10/07	L2	
3	US CD-2/3a Review	1/08	L1	1458
4	FDR of long lead complete	1/08	L2	
5	CD-3a Approval	3/08	L1	1459
6	US CD-3b Review	6/08	L1	1460
7	SAB BO	7/08	L2	798
11	Daya Bay hall BO	11/08	L2	802
12	LS Mixing begins	1/09	L2	942
15	1 st AD pair assembly complete	5/09	L2	957
18	Overall System test in DB hall	8/09	L2	1113
20	LA hall BO	9/09	L2	807
21	far hall BO	9/09	L2	811
22	DB hall ready for physics	10/09	L2	1114
25	US CD-4a Request	2/10	L1	
28	Overall System test in LA hall	4/10	L2	1116
30	LA hall ready for physics	6/10	L2	1117
32	Overall System test in far hall	9/10	L2	1119
33	far hall ready for physics	11/10	L2	1120
34	US CD-4b Request	4/11	L1	

Table 17.1. Selected Daya Bay milestones.

- (h) portions of necessary tools and equipment for the assembly and installation of ADs
 - (i) some of the necessary safety equipment elements for the AD system
2. Significant portions of the Muon System:
- (a) Water Cherenkov PMTs, bases, cables and high-voltage power supplies
 - (b) PMT support structure
 - (c) Water Pool liner and cover
 - (d) water purification system
 - (e) high-voltage and gas mixing/control system for Resistive Plate Chambers (RPC)
 - (f) portions of necessary tools and equipment for the assembly and installation of PMTs
 - (g) components of the safety elements for the Muon System
3. Calibration system:
- (a) automated deployment system for radioactive and LED sources
 - (b) monitoring system.
4. Integration & Installation:
- (a) Transporter (AGV) system for moving the ADs
 - (b) Some installation and test equipment for activities in the SAB and experimental halls (e.g., rigging equipment, meters and oscilloscopes, hand tools)
 - (c) Financial support for some of the installation manpower on site at Daya Bay contracted by IHEP.
5. Joint Project Management control and oversight
- Additionally, many detector elements will be cooperatively developed:
1. front-end and trigger electronics design for both the antineutrino and muon systems
 2. Portions of online and onsite data production facility
 3. many of the infrastructure items (e.g., online and offline software)
 4. system design integration
 5. installation and test planning

17.2.2 U.S. Project Cost

The U.S. Cost associated with the above scope is detailed in the RLS and Cost Books. The TEC cost for the U.S. scope, in at-year U.S. dollars, is \$31.2M. The TPC cost is \$34M. The total includes contingency at the level of ~35% of the total U.S. base cost. Contingency is currently estimated at L3 or below of the WBS. It is based on the level of design maturity and the level of risk associated with the element, the level of cost basis and the level of risk associated with the element and is described in detail in the risk and contingency documentation.

The costs are fully captured in the RLS and Cost Book. The basis of estimate is captured in a web based file system.

A Acknowledgements

This work was supported in part by the Chinese Academy of Sciences, the Ministry of Science and Technology of China (contract no. 2006CB808100), the National Natural Science Foundation of China (Project numbers 10225524, 10475086, 10535050 and 10575056), the Guangdong provincial government, the Shenzhen Municipal government, the China Guangdong Nuclear Power Group, the Ministry of Education of China under the Program for New Century Excellent Talents in University, the Research Grants Council of the Hong Kong Special Administrative Region of China (Project number 400805, 703307 and 704007), the focused investment scheme of CUHK and University Development Fund of The University of Hong Kong, the MOE program for Research of Excellence at National Taiwan University and NSC fund support, the United States Department of Energy (Contracts DE-AC02-98CH10886, DE-AS02-98CH1-886, DE-FG02-92ER40709, DE-FG02-07ER41518 and DE-FG02-91ER40671 and Grant DE-FG02-88ER40397), the U.S. National Science Foundation (Grants PHY-0653013, PHY-0650979, PHY-0555674 and NSF03-54951), the University of Houston (GEAR Grant number 38991), the University of Wisconsin, the Virginia Polytechnic Institute and State University, the Thomas F. and Kate Miller Jeffress Memorial Trust, the Ministry of Education, Youth and Sports of the Czech Republic (Project numbers MSM0021620859 and LC527), and the Joint Institute of Nuclear Research in Dubna, Russia.

B Acronyms

AC	alternating current
Access	database program from Microsoft Corporation
AD	Daya Bay antineutrino detector
ADC	analog to digital converter
APS	American Physical Society
BES	Beijing Spectrometer at the Beijing Electron Positron Collider
BINE	Beijing Institute of Nuclear Energy
BNL	Brookhaven National Laboratory
BO	Beneficial Occupancy
BPE	borated polyethylene
Bugey 3	Reactor antineutrino experiment in France
CAS	Chinese Academy of Sciences
CDR	conceptual design report
CC	charged-current neutrino interactions
CCD	charge coupled device
CCG	central clock generator
CD-1	Critical Decision #1 — Site Selection (CDR)
CD-2	Critical Decision #2 — Cost/Schedule/Scope well defined (TDR)
CD-3a	Critical Decision #3a — Long lead procurements
CD-3b	Critical Decision #3b — Start of Construction
CD-4a	Critical Decision #4a — Initiate early operations
CD-4b	Critical Decision #4b — begin full experiment operations
CERN	European Organization for Nuclear Research
CFB	Clock Fanout Board
CGNPG	China Guangdong Nuclear Power Group (Daya Bay owner)
C.L.	confidence level
CMT	Configuration Management software package
<i>CP</i>	charge, parity symmetry
<i>CPT</i>	charge, parity, time reversal symmetry
CSE	Computing Science Engineering
CVS	code versioning system
DAC	digital to analog converter
DAQ	data acquisition
DB	Daya Bay
DC	direct current
DCS	detector control system
DOE	U.S. Department of Energy
ES	elastic neutrino scattering
ES&H	environment, safety & health
FADC	flash ADC
FEA	Finite Element Analysis
FEC	front-end card
FEE	front-end electronics
FET	field effect transistor
FPGA	field programmable gate array
FSS	Facility Safety Systems
FY	fiscal year
FWHM	full width at half maximum
GALLEX	Gallium Experiment
Gd-LS	Gd loaded liquid scintillator
GEANT	detector description and simulation tool

GNO	Gallium Neutrino Observatory
GPS	Global Positioning System
GW _{th}	reactor's thermal power in GigaWatts
H/C	ratio of hydrogen to carbon
H/Gd	ratio of hydrogen to gadolinium
HV	high voltage
IBD	inverse beta decay
IFC	International Finance Committee
IGG	Institute of Geology and Geophysics
IHEP	Institute for High Energy Physics
ILL	Institut Laue-Langevin
ISO	International Standards Organization
IRNC	International Research Network Connections
JINR	Joint Institutes for Nuclear Research
JTAG	electronic standard for testing & downloading FPGAs
KamLAND	Kamioka Liquid Scintillator Antineutrino Detector
K2K	KEK to Kamiokande neutrino oscillation experiment
KARMEN	Karlsruhe Rutherford Medium Energy Neutrino experiment
KEK	High Energy Accelerator Research Organization in Japan
Kr2Det	Two Detector Reactor Neutrino Oscillation experiment at Krasnoyarsk
L/E	distance divided by energy
L3C	L3 cosmic ray experiment
LA	Ling Ao
LAB	Linear Alkyl Benzene
LabVIEW	Laboratory Virtual Instrument Engineering Workbench
LBNL	Lawrence Berkeley National Laboratory
LEC	Local Emergency Coordinator
LED	light emitting diode
LENS	Low Energy Solar Neutrino Spectrometer
LIGO	Laser Interferometric Gravity Observatory
LMA	Large Mixing Angle solution
Ln	lanthanides
LOG	Laboratory Oversight Group
LS	liquid scintillator
LSND	Liquid Scintillator Neutrino Detector
LTM	Local Trigger Module
LVDS	low voltage differential
MBLT	Multiplexed Block Transfer
m.w.e.	meters of water equivalent
MC	Monte Carlo
MIE	Major Item of Equipment
MINOS	Main Injector Neutrino Oscillation experiment
ML	Maximum Likelihood
MoST	Ministry of Science and Technology of China
MOU	Memorandum of Understanding (Daya Bay MOU to be signed by BNL, LBNL and IHEP)
MSB	1,4-bis[2-methylstyryl]benzene
NC	neutral current neutrino interactions
NHIT	counter for number of hits
NIST	Natioanl Institute of Standards and Technology
NSFC	Natural Science Foundation of China
NPP	nuclear power plant
NTP	Network Time Protocol

NuSAG	Neutrino Science Assessment Group
NWW	North-West by West
ODH	oxygen deficiency hazard
OPC	Other Project Costs (Project costs not in TEC)
OPERA	Oscillation Project with Emulsion-tRacking Apparatus
p.e.	photo-electrons
P-HAD	Preliminary Hazards Assessment Document
P-PEP	Preliminary Project Execution Plan
PAP	Project Advisory Panel
PC	pseudocumene
PC	personal computer
PLL	Phase-Locked Loop
PMMA	Polymethyl methacrylate (Acrylic)
PMT	photomultiplier tube
PPO	2,5-Diphenyloxazol (Wavelength shifter)
PPS	Pulse Per Second
PRD	Pearl River Delta (elevation above sea level)
PSL	Physical Sciences Laboratory at the University of Wisconsin
PVC	Poly Vinyl Chloride
PWR	pressurized water reactors
QA	quality assurance
QC	quality control
QE	quantum efficiency
QM	quality management
RACF	RHIC and ATLAS Computing Facility
REE	rare earth elements
R&D	research and development
RLS	Resource Loaded Schedule
RMB	Chinese Yuan
RPC	resistive plate chamber
RPT	Reynolds Polymer Technology
RPVC	rigid polyvinyl chloride
RQD	Rock Quality Designation
RS	Richter scale
SAB	Surface Assembly Building
SAGE	Soviet American Gallium solar neutrino Experiment
SBMS	Standards Based Management System
SCADA	supervisory, control, and data acquisition
s.p.e.	single photo-electron
SNO	Sudbury Neutrino Observatory
SNO+	proposed solar and geo-neutrino experiment using liquid scintillator in the existing SNO detector
SS	stainless steel
SAB	surface assembly building
TDC	time to digital converter
TEC	Total Estimate to Complete (total cost of project funded by MIE)
TPC	Total Project Cost (total cost of project including OPC)
TSY	Fourth Survey and Design Institute of China Railways
UCT	Universal Coordinated Time
UV	ultraviolet light
VME	Versa Module Europa
WBS	work-breakdown structure
YREC	Yellow River Engineering Consulting Co. Ltd.

C Requirements

This appendix is a summary of the scientific requirements of the Daya Bay experiment and the subsequent requirements for the Daya Bay detector elements. A full description of the system functions and requirements can be found in the text of the TDR.

Scientific Requirements

Item	Requirement	Justification
Sensitivity in $\sin^2 2\theta_{13}$ (90% C.L.)	≤ 0.01	Goal of the experiment as recommended by NuSAG
Standard error of $\sin^2 2\theta_{13}$	0.006	The value corresponding to 90% C.L. is 1.67 times the standard error for one-parameter
Baseline of the far detector	$1.5 \text{ km} \leq L \leq 2 \text{ km}$	Location of the first oscillation maximum due to Δm_{31}^2
Number of events at the far site	$\geq 170,000$	The minimum number of events to reach the designed sensitivity
Background/signal	$\ll 0.09$	This ratio should be much better than that obtained by Chooz since reactor off data is not expected

Table C.1. Summary of scientific requirements.

Requirements on Uncertainties

Requirement	Near Site	Far Site	Justification
Statistical uncertainty	0.07% per site	$\leq 0.24\%$	Far site should be less than the systematic uncertainty and allow a total uncertainty of less than 0.006. Near sites will have very good statistics.
Detector systematic uncertainty		$\leq 0.38\%/\text{module}$	Must allow a total uncertainty of less than 0.006, should not be much larger than the statistical or background uncertainties
Reactor power systematic		$\leq 0.2\%$	Should be small compared to other uncertainties, is satisfied with two near sites and any reasonable assumption on the uncorrelated power uncertainty on a single core
Background uncertainty	0.3% per site	0.2%	Dominated by ${}^9\text{Li}$; sets a limit on the size of a detector, and is improved by putting detectors deeper. (Motivates siting the halls 20 m below sea level.)

Table C.2. Requirements on uncertainties necessary to achieve the sensitivity goal of $\sin^2 2\theta_{13} < 0.01$ at 90% C.L.

Antineutrino Detector

- **Scientific Requirements**

Item	Requirement	Justification
Target mass at far site	$\geq 80 \text{ T}$	Achieve sensitivity goal in three years over allowed Δm_{31}^2 range
Precision on target mass	$\leq 0.3\%$	Meet detector systematic uncertainty baseline per module
Energy resolution	$\leq 15\%/\sqrt{E}$	Assure accurate calibration to achieve required uncertainty in energy-threshold cuts (dominated by energy threshold cut)
Detector efficiency error	$< 0.2\%$	Should be small compared to target mass uncertainty
Positron energy threshold	$\leq 1 \text{ MeV}$	Fully efficient for positrons of all energies
Radioactivity singles rate	$\leq 50 \text{ Hz}$	Limit accidental background to less than other backgrounds and keep data rate manageable

Table C.3. Physical requirements of the antineutrino detector.

- **Requirements on Steel Tank**

Item	Requirement	Justification
Height	$\leq 5 \text{ m}$	Clear ducts at the ceiling of the tunnels
Diameter	$\leq 5.1 \text{ m}$	Clear cable trays and the walls of tunnels
Height of external ports	$\leq 0.3 \text{ m}$	Clear ducts at the ceiling of the tunnels
Wall thickness	$\leq 2 \text{ cm}$	Minimal material to reduce radioactivity while maintaining strength
Leak tightness	$> 5 \text{ years}$	Data taking requires at least 3 years
Tilt	9.6% when empty	Transport empty AD down sloped access tunnel
Ports	≥ 3	Insert calibration devices, fill and drain liquid
Vessel wall deflection	$< 2 \text{ mm}$	Lift full tank without perturbing acrylic vessels

Table C.4. Requirements on the steel tank of the antineutrino detector.

- Requirements on Photomultiplier Tubes

Item	Requirement & Justification
Spectral Sensitivity	PMT Quantum Efficiency peak to be greater than: 25% at 420 nm, 8% at 300 nm, 12% at 320 nm, 1% at 600 nm
Gain	$\geq 10^7$ for all PMTs with appropriate tapered resistive base. PMTs must achieve a gain of 3×10^7 at HV ≤ 2 kV
Single Photoelectron Resolution	peak to valley ratio ≥ 2.5 at a gain of 10^7
Magnetic Field Sensitivity	spe response (gain, resolution, timing) should not change by more than 20% in the presence of transverse magnetic field of 450 mG. The anode efficiency should not change by more than 15%
Photocathode Uniformity	maximum quantum efficiency non-uniformity not to exceed 15%
Pulse Linearity	PMT anode pulse linearity must be better than 5% over the dynamic range of 0–1 nC at a gain of 10^7
Dark Pulse Rate	≤ 25 Hz/cm ² at 20° C. fractional increase in dark count rate in going from a gain of 1.0×10^7 to a gain of 3.0×10^7 shall not be more than 30% greater than the increase in dark pulse rate in going from a gain of 0.3×10^7 to a gain of 1.0×10^7
Pre- and After- Pulsing	probability for the PMT anode signal pre-pulsing and afterpulsing not to exceed 1.5%. PMT anode signal not to exhibit after-pulsing with probability of more than 1.5% for photoelectron within 100 ns interval of the defined after-pulse interval (0.1–40 μs)
Gain Stability	less than 5% drift per week and less than 10% drift over a period of one year. Temperature dependence must be less than 1% per °C
Rise and Fall Times	rise time not to exceed 6.5 ns and a fall time not to exceed 10 ns for a single photoelectron pulse
Transit Time Spread (TTS) (FWHM)	not to exceed ~ 3 ns at a gain of 10^7 for a spe
Radioactivity	use borosilicate glass with radioactivity in each PMT not to exceed: ^{40}K : 2.7 Bq, ^{232}Th : 0.5 Bq, ^{238}U : 0.7 Bq
Mechanical Strength	must withstand a sinusoidal vibration of 1.34 mm amplitude at 15 Hz (equivalent to an acceleration of 2 G) for 30 seconds with less than 10% change in gain or timing responses. all PMTs must survive a pressure of 300 kPa

Table C.5. Requirements on the PMTs.

- Requirements on Acrylic Vessels

Item	Requirement	Justification
LS vessel volume	$\leq 1\%$	Matched pair filling
Gd-LS vessel volume	Matched to 0.3%	Matched pair filling
Dimension stability	$< 1 \text{ mm}$	Suppress time-dependent systematic problems
Optical properties	Transmittance $> 90\%$ at 400 nm	Maximize detection efficiency
Leakage	No leak at any interface for > 5 years	Simulations ongoing
Surface crazing	Minimal crazing after assembly and transport	Maintain good/stable optical properties

Table C.6. Requirements on the acrylic vessels for the antineutrino detector.

- Requirements on Liquid Scintillator

Item	Requirement	Justification
Chemical stability of Gd-LS	> 5 years	Unchanged during data taking
Attenuation length of oil, LS and Gd-LS	$\geq 10 \text{ m}$	Ensure good light collection and maintain energy resolution
Light yield of liquid scintillators	> 100 detected p.e./MeV	Meet energy-resolution requirement
Radioactive contamination	$< 10^{-12} \text{ g/g}$	Reduce accidental background
Distribution of Gd in LS	Gd uniformly dissolved in LS	Maintain detection efficiency
Batch-to-batch identical properties of organic liquids	Every batch of each liquid (LS, Gd-LS, oil) to be the same as the other batches	Pair-wise filling to control target mass and ensure identical detector properties

Table C.7. Requirements on the liquid scintillator of the antineutrino detector.

- Requirements on Fill/drain Mechanism

Item	Requirement	Justification
Access to all three zones	Fill all volumes simultaneously	Minimize differential stress on the acrylic vessels
Fill Rate	1–2 days	Avoid extended filling time and bubbles from turbulent flow
Bubbles in scintillator	Minimize bubbles during filling	Avoid optical degradation at acrylic boundaries
Drain Rate	1–2 days	Rapid recovery from errors or emergency
Drained liquids	Discard drained liquids	Simplify technical challenges of fill/drain mechanism; Detector can be opened to air during emptying; drained liquids are likely contaminated
Residual liquids	<tens of liters after drain	Avoid standing LS in vessel during repair
Fluid pumping hardware	Non-contaminating vacuum tight; Reversible flow; Interlock to level sensors and emergency stop	Accurate fluid delivery, Radon protection, Preserve fluid properties, Suction flow during draining; drain without dismantling hardware or overstressing acrylic
Fluid measurements	Gd-LS to <0.3% LS & MO to <0.5% $\delta_\rho < 0.1\%$, $\delta_T < 0.5^\circ \text{C}$	satisfy detector systematic error Protect acrylic vessels Determine overflow tank fill levels.
Cover gas	Continuous N ₂ boil-off supply before, during and after filling	Minimize radon contamination

Table C.8. Technical requirements for the fill/drain mechanism of the antineutrino detector.

- Requirements on Overflow Tanks

Item	Requirement	Justification
Height	<300 mm	Tall enough to buffer anticipated fluid expansion/contraction from 5° C change in temperature
Geometry	Simple	Allow measurement of volume
Non-capturing overflow	Passive emptying back into main volume	Avoid loss of target mass and associated systematic uncertainty
Materials compatibility	scintillator compatibility for >5 years	Maintain structural integrity and avoid contamination of LS

Table C.9. Requirements on the overflow tanks of the antineutrino detector.

- Requirements on Instrumentation and Monitoring

Item	Requirement	Justification
Measure acrylic vessel dimensions	<2–3 mm	Determine volume prior to fill
Fill level balancing	<1 cm	Avoid load on vessels during filling
Measurement of level in overflow tank	<1 liter	Measure target mass
Cover gas monitoring	Monitor N ₂ supply for O ₂ , H ₂ O, flow rate	Verify that radon is not introduced
Acrylic vessel positions	<0.5 cm	Determine change in γ catcher thickness

Table C.10. Requirements on instrumentation/monitoring of the antineutrino detector.

Muon System

Item	Requirement	Justification
Thickness of water shield	≥ 2 m	Attenuate fast neutrons and γ rays from nearby rock
Total inefficiency for detecting muons	$\leq 0.5\%$	Reduce fast-neutron background to a level below ${}^9\text{Li}$
Uncertainty of efficiency	$\leq 0.25\%$	Maintain fast neutron uncertainty well below that of ${}^9\text{Li}$
Random veto deadtime	$\leq 15\%$	Avoid undue impact on statistical precision
Uncertainty in random veto deadtime	$\leq 0.05\%$	Keep well below other systematic uncertainties
Position resolution	0.5–1 m near AD	Study radial dependence of cosmogenic background
Timing resolution	± 2 ns (Cherenkov) ± 25 ns (RPCs)	Allow spatial reconstruction of muon trajectory Limit random veto deadtime from false coincidences to $\mathcal{O}(1\%)$

Table C.11. Requirements for Muon system.

Positioning Requirements

Item	Requirement	Justification
Detector location relative to reactors	$\mathcal{O}(10)$ cm	Control systematic uncertainty in baseline

Table C.12. Positioning accuracy of the principal elements of the Daya Bay experiment.

Calibration

Requirement	Description	Proposed Solution(s)
Optical Integrity	Spatial uniformity of response, light attenuation	LED, γ sources
PMT gains	Match gains of all PMTs	LED - single p.e. matching
PMT timing	~ 1 ns timing calibration for each PMT	Pulsed LED
Energy scale	Set scale of energy deposition	Gamma sources
H/Gd ratio	Measure relative Gd fraction	Neutron sources

Table C.13. Requirements for the full manual calibration procedure.

Requirement	Description	Proposed Solution(s)
Mechanical/thermal	Verify these properties are stable	Load sensors, thermometers, etc.
Optical stability	Track variations in light yield	γ sources, spallation products
Uniformity, light attenuation	Monitor spatial distribution of light	γ sources, spallation products
Detection efficiency	Monitor ϵ for neutrons and positrons	γ sources, neutron sources
PMT gains	Monitor 1 p.e. peaks	LED source

Table C.14. Requirements for automated calibration procedure.

Readout Electronics and DAQ

Item	Requirement	Justification
Linear Range	0–200 p.e.	Accurately measure inverse beta decay events
Full Range	0–1000 p.e.	Large enough to reasonably measure cosmic muons
Resolution	<0.1 p.e. @ 1 p.e.	Sufficiently fine to resolve 1 p.e. distribution
Noise	<10% @ 1 p.e.	Electronics should not contribute to overall noise
Time range	0–500 ns	Allows for trigger latency and photon propagation
Timing resolution	<1 ns	Event reconstruction
Sampling rate	≥40 MHz	Accurately determine PMT pulse shape
Channels/module	≥12	Can fit each AD into one VME crate
VME standard	VME64xp-340 mm	DAQ architecture requirement

Table C.15. Requirements for the electronics used to read out the PMTs.

Trigger

Item	Requirement	Justification
Efficiency	>99%	High efficiency to maintain small systematic uncertainty
Time of Trigger	13 ns	Measurement of delay in neutron capture time
Energy Threshold	~0.7 MeV	High acceptance for prompt signal
Flexibility	dynamic algorithms	Functionality under a variety of conditions
Reproducibility	< a few ns	Consistency between AD modules
Redundancy	>1 algorithm	Ability to measure trigger efficiency

Table C.16. Requirements for the trigger system.

Offline

Item	Requirement	Justification
End-to-end data transfer rates	0.5 TB/day	Entire data volume plus 50% recovery capacity
Mass storage volume	800 TB	Sufficient for 5 years of raw and processed data
Cluster specs	225 kSpecInt2000	Four full production passes per year
First production software release	11/2008	Ready for comissioning at Daya Bay near site
Second production software release	2/2010	Ready for full operations

Table C.17. Requirements for Offline.

Installation

Item	Requirement	Justification
Resource loaded Installation and Test plan	4/08	Beneficial occupancy of SAB
Transporter available for use	9/08	Beneficial occupancy of Filling Hall
Documentation of assembly, test and installation procedures	5/08	Prior to AD assembly in SAB

Table C.18. Requirements for Installation.

Integration

Item	Requirement	Justification
Interface drawings/descriptions documented	4/08	Beneficial occupancy of SAB
Safety interlocks installed	10/08	ADs to Filling Hall
Documentation of safety policy/procedures	4/08	Beneficial occupancy of SAB

Table C.19. Requirements for Integration.

D AD simulation parameters and studies

The Daya Bay antineutrino detector (AD) consists of three concentric cylinders that define three different volumes, the Gadolinium doped liquid scintillator (Gd-LS) target whose mass needs to be precisely measured, the liquid scintillator (LS) volume which functions as γ -catcher (GCAT) and the mineral oil (MO) volume which is the buffer zone. The inner two volumes are defined by two cylindrical acrylic vessels (AV) which are transparent to photons with wavelengths above 300 nm (50% at 300 nm). Any structures introduced into the inner two volumes are made of acrylic to minimize the loss of light. Table 4.4 shows the dimensions of the inner and outer AVs of the current baseline design.

The goal of the Daya Bay experiment is to achieve a sensitivity of better than 0.01 to $\sin^2 2\theta_{13}$. Thus systematic uncertainties need to be understood and controlled extremely well. The experiment adopts a near-far detector arrangement to cancel many correlated systematic uncertainties related to neutrino flux, neutrino interaction and detectors. This strategy requires detectors at the near and far sites as identical as possible. In order to understand our detectors, detailed simulation is needed. From the topological perspective, the modeling and the simulation of the AD using GEANT4 can be grouped into three categories:

- Main structures. This includes the AVs and the LS and Gd-LS volumes defined by them.
- Contained structures. This category includes the structures inside the outer AV that support and constrain the inner AV. They can also increase mechanical strength of the AVs.
- Penetration structures. This category includes the filling and calibration pipes connecting the Gd-LS and LS to the corresponding overflow tanks and calibration boxes.

We describe the AD-related simulation work on these three categories in the following. Note that not all simulation results reported here use the latest baseline design of the AD as the design evolved based on simulation results.

First we briefly review the parameters used in the simulation and define metrics used to evaluate AD performance.

D.1 Simulation parameters

The following properties used in the simulation of the AD were determined from measurements using the prototype as described in Section 15.3.1:

1. Scintillation yield per MeV of deposited energy,
2. number of detected photoelectrons per MeV of deposited energy, and
3. non-linear effects such as quenching of scintillation light, emission of Cherenkov light and absorption and re-emission.

From detailed comparisons of the prototype to simulation, we expect a scintillation light yield of ~ 9000 photons per MeV and ~ 105 photoelectrons per MeV.

Additional standalone measurements were made to determine the following properties

1. optical properties of the reflector,
2. LS and Gd-LS emission spectra,
3. LS, Gd-LS, mineral oil and acrylic absorption spectra,
4. refractive indices of acrylic, Gd-LS, LS and mineral oil,

5. transport of optical photons, and

6. PMT response

as described briefly below.

The emission spectra of LS and Gd-LS were measured with a Fluorolog-Tau-3 fluorescence spectrometer in the 200–800 nm range and found to be nearly identical in that wavelength range. The absorption spectra of LS, Gd-LS and mineral oil were measured with a TU1901 UV-vis spectrophotometer with a 10 cm long cell in the wavelength range of 190–900 nm. To minimize systematic effects, the inferred attenuation length in the 10 cm cell is normalized to the measured attenuation in a 100 cm tube at 440 nm. The measured attenuation length at 440 nm as implemented in the simulation was ~ 13 m, ~ 7 m and ~ 12 m for Gd-LS, LS and mineral oil, respectively. The absorption spectrum of acrylic was measured at the National Institute of Metrology of China in the wavelength range 350–850 nm. The refractive index of acrylic, LS and mineral oil was measured at 589 nm with an Abel refractometer and at 486 nm and 546 nm with a V-prism refractometer. The refractive index was assumed to obey the functional form $(n^2 - 1)/(n^2 + 1) = a/(\omega_0^2 - \omega^2)$ where a and ω_0 are parameters and ω is the frequency [1]. Both the specular and total reflectivity of the Al reflector and the ESR reflector used in the prototype 15.3.1 were measured in the 200–800 nm range and the results implemented in the simulation. The wavelength spectrum of the PMT quantum efficiency is taken from the manufacturer's specification sheet. The prototype measurements are used to set the overall light yield of the scintillator thus effectively fixing the product of the quantum efficiency, collection efficiency and light yield used in the simulation to that of the prototype.

D.2 Simulation geometry

Figure D.1 shows the visual output of the geometry of the antineutrino detector in GEANT4 simulation code of Daya Bay, G4dyb, that has been used to optimize detector design as well as verify detector performance.

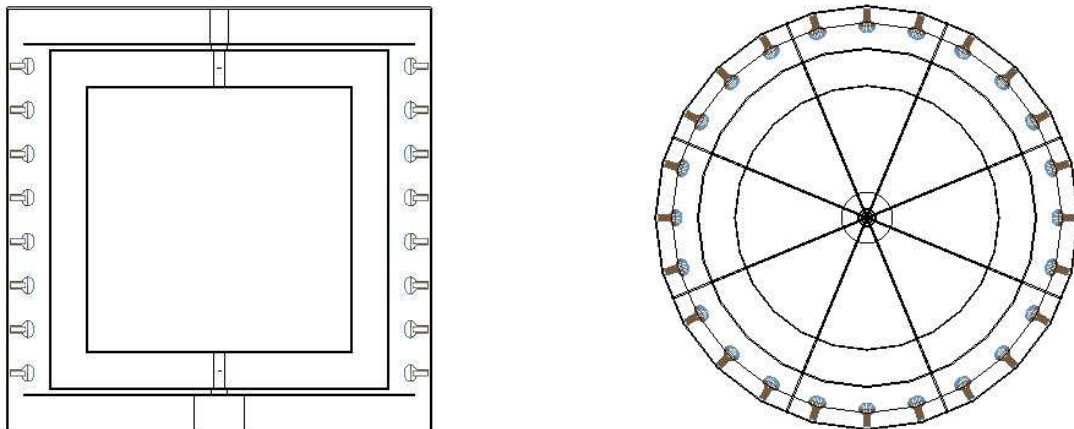


Fig. D.1. Antineutrino detector geometry in G4dyb, the GEANT4 simulation code of Daya Bay. Left: side view. The three regions from the center to the wall are the target, γ -catcher, and buffer mineral oil, respectively. Reflective panels are in buffer oil at the top and bottom. Right: top view. Eight radial reinforcing ribs can be seen. The reinforcing ribs of the stainless steel tank and two acrylic vessels overlap in this view.

Without the penetration structures, the detector is rotationally and up-down symmetric. The center of the detector is set as the origin of the coordinate and z axis points upward.

D.3 Evaluation metrics

From the sensitivity studies (Section 2), the dominant detector-related systematic uncertainty is due to the detection efficiency. We thus define metric to evaluate different AD-design options based on the positron and neutron detection efficiencies.

$$\sigma_{\epsilon}^{\text{sys}} = \frac{|\epsilon((1+s)E_{\text{cut}}) - \epsilon((1-s)E_{\text{cut}})|}{2\epsilon}, \quad (33)$$

where $\epsilon((1 \pm s)E_{\text{cut}})$ is the efficiency evaluated at $\pm s$ of the nominal energy cut E_{cut} where $s = 1(2)\%$ is the estimated energy scale uncertainty at $E_{\text{cut}} = 1(6)$ MeV for positron(neutron) detection. Note that the metric for positron efficiency is based only on the low energy cut used to define the positron and not the 8 MeV cut that defines the upper limit for the positron energy. The 1 and 6 MeV energy scale for different AD designs are calibrated using mono-energetic photons uniformly distributed in the Gd-LS. The energies we refer here are the reconstructed energies of positron annihilations and neutron captures thus energy resolution is automatically considered.

D.4 Main structures

The main structures of the AD obviously have the largest effects on the detector performance. As part of the design optimization, we have compared the performance of two-zone and three-zone AD designs (Section 11.1.1) as well as the performance as a function of the thickness of the GCAT (Section 4.1.4). The AVs will suffer certain geometrical changes due to stress after being filled. The effects of different distortions need to be studied in order to fully understand the detector performance. Currently, we have studied following issues via MC simulation to help with the design and to provide guidance on engineering tolerances:

- Three-zone versus two-zone (Section 11.1.1)
- The thickness of the γ -catcher (Sec 4.1.4)
- The thickness of the mineral oil buffer (Sec 4.1.5)
- The thickness of the AV wall
- Small variations of the outer AV size

D.4.1 The thickness of the AV wall

Any acrylic within the volume contained by the outer AV in the antineutrino detector is effectively inactive or “dead” volume and we would like to minimize its usage. However, the AVs require certain thickness to guarantee the mechanical strength.

The effects of different thickness of the inner AVs are simulated. For each simulation, the outer radius of the inner AV is kept the same so the increase of the AV thickness is equivalent to a reduction in the amount of target mass. A total number of 500k events with optical simulation are produced for each AV wall thickness of 10 mm, 15 mm and 20 mm. One million events for each thickness value are produced without optical simulation as comparison.

Generating millions of events with full optical simulation is onerous, so we also generate events without the optical simulation and with the energy resolution of $13\%/\sqrt{E}$, consistent with the fully simulated resolution as described in Section 4.2, put in by hand. Figure D.2 shows the results of the smearing and that

the 6 MeV energy cut is sufficiently far from the n-Gd capture peaks that the precise value of the energy resolution is not critical to the evaluation of the efficiency and its systematic uncertainty. Since there is no optical simulation, the time window cut is based on the time of the energy deposit in the LS instead of the hit time of the photoelectrons. These simplifications speed up the simulation process and thus provide us prompt feedback on the detector design. We will use the same simplification methods in other investigations.

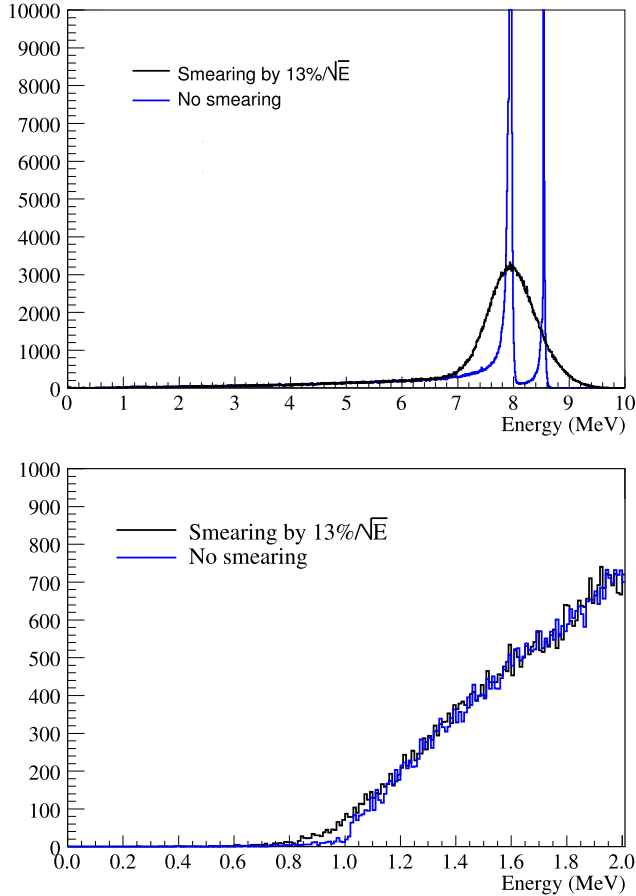


Fig. D.2. Energy smearing to simulate the detector response based on the estimated energy resolution. Skipping the optical simulation at the stage of forming detector designs provides prompt feedbacks. The upper figure is for the delayed neutron capture signal on Gd only and not on hydrogen, and the lower figure is for the prompt signal due to the positron for the same event.

The impact of the AV wall thickness on the efficiencies is summarized in Table D.1 and Table D.2 for the positron and neutron respectively. Here, ϵ is the energy cut efficiency, $\sigma_{\epsilon}^{\text{sys}}$ is the systematic uncertainty of the efficiency (Eq. 33) and $\sigma_{\epsilon}^{\text{stat}}$ is the statistical uncertainty of the MC simulation sample.

Given the high efficiency and relatively small systematic uncertainty of the positron energy cut, it is obvious that the neutron energy cut efficiency and uncertainty is the dominant one between the two. Thus, we concentrate on the neutron detection in the following. The results in Table D.2 indicate that the thinner the AV wall, the higher the energy cut efficiency and the lower the systematic uncertainty. Our baseline design is chosen to be 10 mm for the inner AV.

Table D.1. Effects of the inner AV wall thickness on the positron energy cut efficiency.

Thickness	With optical simulation			Without optical simulation		
	ϵ	$\sigma_{\epsilon}^{\text{sys}}$	$\sigma_{\epsilon}^{\text{stat}}$	ϵ	$\sigma_{\epsilon}^{\text{sys}}$	$\sigma_{\epsilon}^{\text{stat}}$
10 mm	99.80%	0.070%	$\sim 0.020\%$	99.40%	0.075%	$\sim 0.015\%$
15 mm	99.75%	0.075%	$\sim 0.020\%$	99.04%	0.09%	$\sim 0.015\%$
20 mm	99.41%	0.10%	$\sim 0.020\%$	98.73%	0.10%	$\sim 0.015\%$

Table D.2. Effects of the inner AV wall thickness on the neutron energy cut efficiency.

Thickness	With optical simulation			Without optical simulation		
	ϵ	$\sigma_{\epsilon}^{\text{sys}}$	$\sigma_{\epsilon}^{\text{stat}}$	ϵ	$\sigma_{\epsilon}^{\text{sys}}$	$\sigma_{\epsilon}^{\text{stat}}$
10 mm	91.2%	0.23%	$\sim 0.06\%$	90.7%	0.24%	$\sim 0.06\%$
15 mm	91.0%	0.24%	$\sim 0.06\%$	89.8%	0.27%	$\sim 0.06\%$
20 mm	89.7%	0.27%	$\sim 0.06\%$	89.1%	0.30%	$\sim 0.06\%$

D.4.2 Small variations of the outer AV size

Practically speaking, AVs meant to be identical will not be completely identical because of the engineering tolerances. We would like to see how this geometrical difference affects the “identicalness” of the ADs. To examine such effects, different simulations are performed.

The first is to change the dimensions of the outer AV slightly around the baseline design and to see how much this affects the neutron energy cut efficiencies. The simulation is done by keeping the stainless steel tank and the inner AV dimensions fixed while varying the outer AV dimensions. Table D.3 shows the simulation results.

Table D.3. Effects of the outer AV dimension changes.

Outer AV diameter/height (mm)	ϵ	$\sigma_{\epsilon}^{\text{sys}}$	$\sigma_{\epsilon}^{\text{stat}}$
3990	90.7%	0.25%	0.12%
3995	90.5%	0.26%	0.12%
4000	90.7%	0.28%	0.12%
4005	90.6%	0.25%	0.12%
4010	90.9%	0.24%	0.12%

Within the range 3990–4010 mm for the outer AV radius/half height, we do not see any significant change in energy cut efficiencies and the corresponding uncertainties. We can thus conclude that dimensional variations in this range do not have significant effects on detector “identicalness”.

D.4.3 Additional simulation of main structure variations

More simulation work will be done to evaluate the effects on the systematic uncertainties and the “identicalness” of detectors caused by possible mechanical changes. In the future, we will study the following effects:

- Position shifts of the AVs
- Tilting of the AVs
- AV shape changes
- Air bubbles on the AV walls

D.5 Contained structures

To make the main structure mechanically sound, ribs are probably needed to reinforce the AVs. Supporting structures at the bottom of the outer AV are also needed to support the inner AV. Those ribs and supporting structures will displace the LS and may downgrade the performance of our detectors.

Currently, we have performed two specific simulations and one general study:

- The effects of ribs in the outer AV
- The effects of the inner AV kinematic mounts
- General features of effects due to acrylic in the outer AV

D.5.1 The effects of ribs in the outer AV

To support and to constrain the inner, Gd-LS, vessel inside the outer AV, some mechanical structures are needed. One option is to use ribs as shown in Fig. D.3. The design at the time of performing the simulation was up-down symmetric.

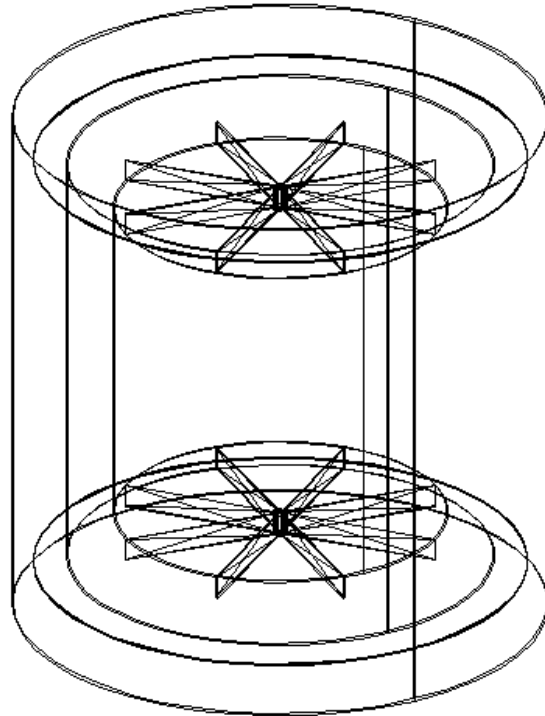


Fig. D.3. The rib structure to support and to constrain the inner AV inside LS.

There are eight ribs symmetrically distributed and connected to a 20 cm cylinder at the center. The rib height of 42.5 cm is determined by the inner and outer AV dimensions. The baseline design is to use 15 mm thick acrylic for these ribs. We study the effects of different thickness.

Table D.4 shows the corresponding dead volumes in the outer AV for different choices of rib thickness and their impact on the positron and neutron energy cut efficiencies and the corresponding uncertainties.

Our conclusion based on this simulation study is that the presence of acrylic ribs in this thickness range has a very small impact on the neutron and positron detection efficiency.

Table D.4. Effects of the rib thickness to energy cut efficiencies and their uncertainties

Rib thickness (mm)	Dead volume (%)	Neutron		Positron	
		ϵ	$\sigma_{\epsilon}^{\text{sys}}$	ϵ	$\sigma_{\epsilon}^{\text{sys}}$
10	0.58	89.72%	0.29%	99.01%	0.09%
20	1.2	89.60%	0.29%	99.02%	0.09%
30	1.7	89.40%	0.29%	98.96%	0.10%
40	2.3	89.34%	0.29%	98.95%	0.10%
50	2.9	89.16%	0.29%	98.92%	0.10%

D.5.2 The effects of the inner AV kinematic mounts

One way to support the inner AV in the LS container is to use kinematic mounts which are made of acrylic. Kinematic mounts can minimize the coupling of the mechanical distortion between the LS and the inner AVs. In the simulation, we approximate the kinematic mounts with solid acrylic cylinders of radius 20 cm and height 15 cm. Figure D.4 shows the simplified geometrical model of kinematic mounts. The effects of the kinematic mounts are summarized in Table D.5.

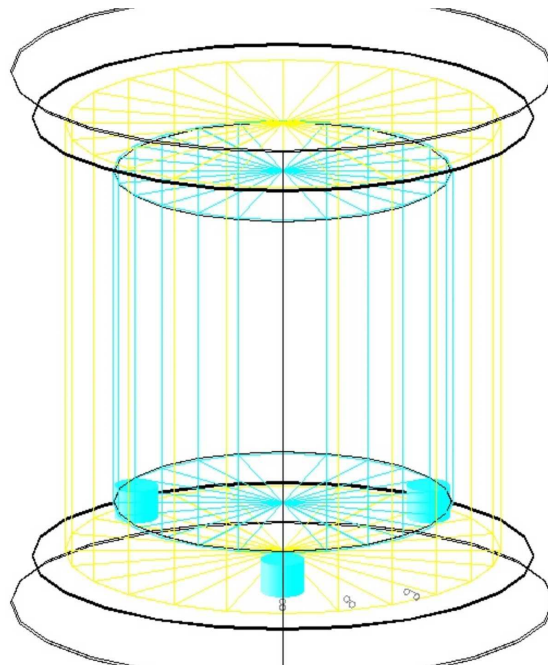


Fig. D.4. The simplified geometrical model of acrylic kinematic mounts in GEANT4. The three small cyan cylinders are the simplified kinetic mounts.

The total volume of kinematic mounts account for 0.297% of the LS volume. From Table D.5, we can see that such kinematic mounts have no impact on the efficiencies.

D.5.3 General features of effects due to acrylic in the outer AV

We would like to know how the evaluation metrics change with respect to the location and the volume of an acrylic cylinder inside the outer AV to provide some general guidance to the design of any contained structure. We use one single acrylic cylinder placed at the bottom of the outer AV to study such effects as shown Fig. D.5.

Table D.5. Effects on the energy cut efficiencies of the inner AV kinematic mounts

Configuration	Neutron			Positron		
	ϵ	$\sigma_{\epsilon}^{\text{sys}}$	$\sigma_{\epsilon}^{\text{stat}}$	ϵ	$\sigma_{\epsilon}^{\text{sys}}$	$\sigma_{\epsilon}^{\text{stat}}$
Baseline	91.57%	0.22%	0.05%	99.77%	0.058%	0.01%
With Kinematic Mounts	91.53%	0.23%	0.05%	99.75%	0.061%	0.01%

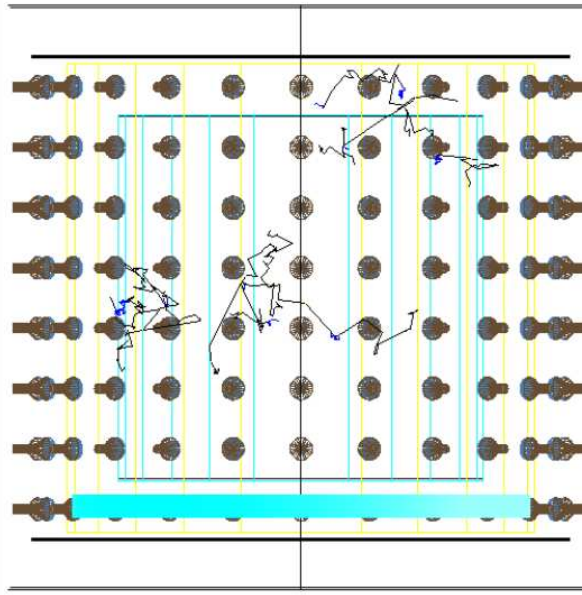


Fig. D.5. A cylinder-shaped acrylic dead volume at the bottom of the outer AV. The plot is the side view of the detector in GEANT4 and the cyan colored strip represents the acrylic cylinder.

First, we study the dependence on the z -position with an acrylic cylinder with a fixed volume of 5% of the LS volume. In order to have enough space for the acrylic cylinder to move in the z direction, we make it flat: Its radius is 1.95m and its height is 0.105m. Table D.6 shows the simulation results. In order to speed up the simulation, we turn off the optical simulation and use the energy resolution to smear the energy deposit as in Section D.5.1.

Table D.7 shows the energy cut efficiency dependence on the radial location of the acrylic cylinder. In this case, the dead volume percentage is fixed at 5% and the z position of the cylinder is at the center of the LS between the inner and the outer AVs, at position $z = -1.77m$. In order to have as much space as possible to move the cylinder away from the center, we make it thin and tall: Its height is 0.4m and its radius is 1m. We only simulate the neutron captures.

Comparing the two cases, we see that the energy cut efficiency has stronger dependence on the z -direction. Now, let us examine how the efficiency changes with respect to the acrylic volume. We will use the LS volume as the normalization volume.

The neutron energy cut efficiency drops as the acrylic volume in the LS increases as shown in Fig. D.6. At the same time, the systematic uncertainty increases as shown in Fig. D.7. The red dots in Fig. D.6 and Fig. D.7 are the results of the rib thickness study but the corresponding dead volume is shifted by 0.6%. This is because the baseline value of the inner AV thickness for the barrel walls was 15mm instead of 10mm used

Table D.6. Z-dependence of the effects on the energy cut efficiencies due to acrylic in the outer AV

z-position(m)	Neutron			Positron		
	ϵ	$\sigma_{\epsilon}^{\text{sys}}$	$\sigma_{\epsilon}^{\text{stat}}$	ϵ	$\sigma_{\epsilon}^{\text{sys}}$	$\sigma_{\epsilon}^{\text{stat}}$
-1.62	88.7%	0.287%	0.01%	96.1%	0.061%	0.006%
-1.72	89.6%	0.272%	0.01%	96.2%	0.060%	0.006%
-1.83	90.0%	0.263%	0.01%	98.3%	0.053%	0.004%
-1.94	90.4%	0.255%	0.01%	98.9%	0.052%	0.003%

Table D.7. Radial dependence of the neutron energy cut efficiencies of acrylic cylinders in LS

R-position(m)	ϵ	$\sigma_{\epsilon}^{\text{sys}}$	$\sigma_{\epsilon}^{\text{stat}}$
0.	89.2%	0.271%	0.01%
0.25	89.2%	0.268%	0.01%
0.5	89.2%	0.270%	0.01%
0.75	89.4%	0.267%	0.01%
0.95	89.5%	0.265%	0.01%

in the rib thickness study. The extra 5mm acrylic covered on the inner AV occupies 0.6% of the LS.

D.5.4 Discussion

Contained volumes are unavoidable in order to make the detector's mechanical structure sound. In order to minimize the loss of photons due to these volumes, we use the acrylic as supporting and reinforcing structures. The amount of acrylic needed inside the LS volume based on the current designs does not change the detector performance significantly.

A general case is studied by placing different acrylic cylinders at different locations inside the LS volume. The results of the specific case and the general case are consistent. This study can provide us general guidance to the mechanical design.

Through our study, we are certain that the contained structures made of acrylic will not hurt the performance of our detectors from the perspective of energy. However, since the contained structures might not be up-down or rotationally symmetric, they may cause asymmetric responses of the detector, which, for example, might affect the vertex reconstruction. Although the Daya Bay experiment is designed to be independent of vertex reconstruction, there may be indirect effects of the energy reconstruction since the energy scale has location dependence. We will study the asymmetric effects due to the presence of contained volumes in the future.

D.6 Penetration structures

Penetration structures consist of the calibration and overflow pipes. The baseline design of the calibration and overflow piping are shown in Fig. 4.24. Although we would like to have all the tubes made in acrylic to reduce the loss of optical photons originating from antineutrino interactions in the Gd-LS, it is important to have the corrugated Teflon tubes (black parts of the overflow/calibration tubes in Fig. 4.24) to provide the flexibility that is needed to accommodate small relative transverse displacements of the AVs. The dimensions of these pipes based on the current design are shown in Table D.9. The total lengths of those tubes are completely determined by the main structures of the detector and the positions of the calibration boxes as we can see from Fig. 4.24.

The penetration structures are not up-down symmetric thus they will cause asymmetric responses. The

Table D.8. Volume dependence of the neutron energy cut efficiencies of the acrylic presence (represented by a cylinder) in LS

Dead Volume (%)	ϵ	$\sigma_{\epsilon}^{\text{sys}}$	$\sigma_{\epsilon}^{\text{stat}}$
None	90.5%	0.26%	0.01%
5	89.2%	0.27%	0.01%
10	87.9%	0.29%	0.02%
15	87.2%	0.29%	0.01%
18.9	86.9%	0.29%	0.01%

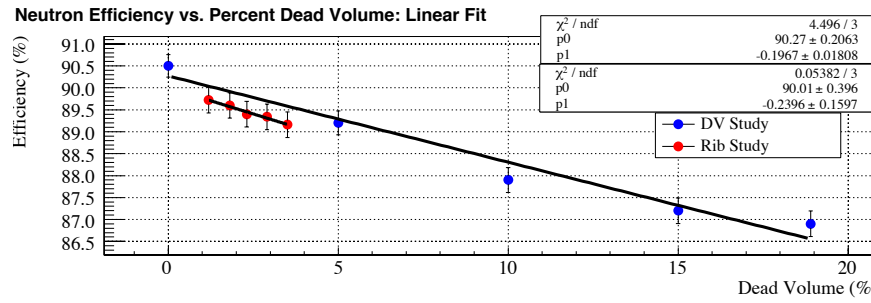


Fig. D.6. The dependence of neutron energy cut efficiency on the percentage of acrylic volume in the LS. The blue points “DV Study” correspond to Table D.8. The red points “Rib Study” correspond to Table D.4.

amount of LS displaced by these pipes is relatively small thus the asymmetric effects are small. However, penetrations introduce localized Gd-LS into the LS volume and localized Gd-LS and LS into MO volume. Based on the current baseline design, the total Gd-LS amount outside of the inner AV due to the central overflow tube and the off-center calibration tube is around $\sim 0.02\%$ of the Gd-LS inside. Though there will be neutron captures inside these overflow and calibration tubes, compared to the goal of the systematic uncertainty on the target mass of 0.1%, the amount of Gd-LS inside the penetration tubes could be ignored. However, we need to give a quantitative evaluation on such effects.

Currently, we have implemented the geometry of the penetration volumes into our GEANT4 Monte Carlo. As we argued above, we are planning to study their effects from the following perspectives:

- Asymmetrical effects. Events at different locations may have different efficiencies and efficiency uncertainties. This simulation work can be done together with the asymmetry studies on the contained structures.
- “Contamination” effects. The Gd-LS confined locally inside the LS and MO volumes can capture neutrons. Such events probably have different visible energy compared with the captures inside the inner AV due to their location. We need to understand the features of such events so we can minimize their effects.

D.7 Summary and future plans

In summary, we have performed some simulations related to acrylic vessels to provide guidance to detector design and the major structures of the detector have been decided. To further optimize the details of the AV design and to evaluate their impacts to the systematic uncertainties, more simulation work is needed. We have listed proposed simulation work in the corresponding sections above.

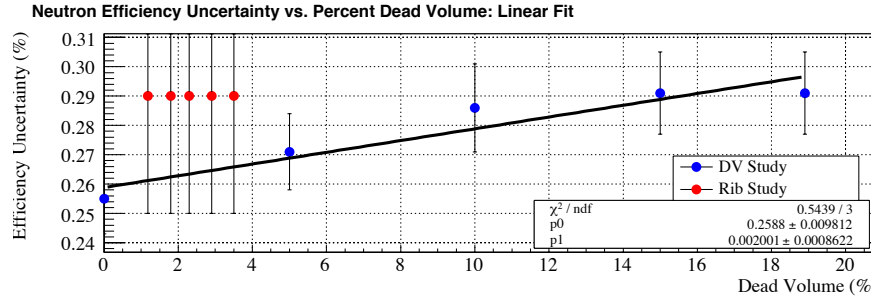


Fig. D.7. The dependence of the systematic uncertainty of neutron efficiency on the percentage of acrylic volume in LS

Table D.9. Dimensions of the penetration tubes. The total lengths of penetration pipes are determined by the main structures: Gd-LS overflow/calibration tubes are 928mm long and LS overflow/calibration tubes are 488mm long. Only Teflon tube lengths are given here. The off-center LS tube I is the one which is concentric with the off-center Gd-LS calibration tube in order to provide a passage for it. The off-center LS tube II is the single calibration tube for the LS volume.

Penetration	Inner Radius	Length(acrylic+Teflon)	Thickness(acrylic/Teflon)
Central Gd-LS	25mm	50mm+478mm	5mm/1mm
Central LS	50mm	50mm+438mm	5mm/1mm
Off-center Gd-LS	25mm	0mm+928mm	/1mm
Off-center LS(I)	50mm	0mm+488mm	/1mm
Off-center LS(II)	25mm	50mm+438mm	5mm/1mm

Different parts of the AV have correlated effects on the detector performance. The current standard reference is a simple 3-zone detector without any contained and penetration structures. As the AV design evolves, we will repeat some of the simulations with the baseline designs including the contained and the penetration structures. As the detector designs are being finalized, we will shift our simulation work more toward the evaluation of detector performance.

REFERENCES

1. http://www.physics.uc.edu/~johnson/Boone/oil_page/refraction/refraction.html